PROCEEDINGS of the 3rd APPLIED SCIENCES RESEARCH INTERNATIONAL CONFERENCE 2024 (ASRIC)

Navigating Global Challenges with Applied Sciences Solutions for a Sustainable Future

ORGANIZED BY:
FACULTY OF APPLIED SCIENCES
UNIVERSITI TEKNOLOGI MARA
PERAK BRANCH , TAPAH CAMPUS
MALAYSIA

CO-ORGANIZED BY:

UNIVERSITAS GADJAH MADA
FACULTY OF MATHEMATICS AND NATURAL SCIENCES

SHARDA UNIVERSITY
Beyond Boundaries

3rd Applied Sciences Research International Conference 2024

(ASRIC 2024)

Faculty of Applied Sciences,

Universiti Teknologi MARA,

Perak Branch, Tapah Campus,

35400 Tapah Road, Perak, Malaysia.

Conference date: 18th September 2024

Publication date: 10th October 2024

Proceedings of Extended Abstracts

EDITORS

Dr. Noor Fadhilah Muhamad Sahapini

Dr. Husna Zulkipli

Dr. Saiyidah Nafisah Hashim

Ms. Putri Shareen Rosman

Ms. Wan Nurul Hidayah Wan Anuar

e-I.S.B.N : 978-629-97630-3-1

Published by Faculty of Applied Sciences, Universiti Teknologi MARA,

Perak Branch, Tapah Campus

Faculty of Applied Sciences,

Universiti Teknologi MARA,

Perak Branch, Tapah Campus,

35400 Tapah Road, Perak, Malaysia.

PREFACE

Welcome to the 3rd Applied Sciences Research International Conference (ASRIC) 2024!

It is with great pleasure that we present this year's conference, a premier gathering of scholars, researchers, and professionals dedicated to the advancement of applied sciences. This conference aims to showcase the latest research, promote networking, foster collaborations, and explore innovative solutions to global challenges. ASRIC 2024 was accomplished virtually on 18th September 2024.

The theme of this year's conference, "Navigating Global challenges with applied sciences solutions for a sustainable future, reflects our commitment to address pressing issues regarding the role of applied sciences in steering humanity towards sustainable future. Our distinguished keynote speakers and presenters bring a wealth of knowledge and expertise, offering invaluable insights into emerging trends and transformative breakthroughs.

We would like to express our heartfelt gratitude to Faculty of Applied Sciences, Universiti Teknologi MARA, Perak Branch, Tapah Campus for the incredible support and assistance provided throughout the conference. The dedication and effort have been the instrumental in the event's success. We also want to extend our sincere gratitude to all the participants and researchers for their invaluable contributions to the conference. Not to forget the thorough evaluations and constructive feedback given by the reviewers. We truly appreciate all the hard work you put in.

As the editor, it is our privilege to present this collection of proceedings. We are honoured to have the opportunity to compile the diverse and insightful contributions from our esteemed speakers and authors. May the ideas shared lead to a new discovery and open more opportunities in research especially in applied sciences navigating the global challenges for sustainable future.

Warm regards,

Dr. Noor Fadhilah Muhamad Sahapini
Dr. Husna Zulkipli
Dr. Saiyidah Nafisah Hashim
Ms. Putri Shareen Rosman
Ms. Wan Nurul Hidayah Wan Anuar

ASRIC 2024 Proceedings Editors

TABLE OF CONTENT

TRACK A

APPLIED BIOLOGY

EXPLORING THE GENETIC DIVERSITY AND POPULATION STRUCTURE IN A SUBSET OF *PTEROPTYX TENER* (COLEOPTERA: LAMPYRIDAE) POPULATIONS ALONG THE SELANGOR RIVER USING MICROSATELLITE MARKERS

Nur Hamizah Ali Akaram[1], Subha Bhassu[2], Shawn Cheng[3]

[1]*Institute of Biological Sciences, Faculty of Science, University Malaya, 50603 Kuala Lumpur, Wilayah Persekutuan Kuala Lumpur.*

s2199590@siswa.um.edu.my

[2]*Institute of Biological Sciences, Faculty of Science, University Malaya, 50603 Kuala Lumpur, Wilayah Persekutuan Kuala Lumpur.*

subhabhassu@um.edu.my

[3]*Forest Research Institute Malaysia, 52109 Kepong, Selangor Darul Ehsan, Malaysia*

shawn@frim.gov.my

ABSTRACT

The synchronous firefly species *Pteroptyx tener* is a popular species in Kuala Selangor due to its unique flashing and lekking behaviour. However, the population of *P. tener* has fluctuated over the years. To better understand the status of this species and address its issues, the genetic diversity and population structure of *P. tener* were analysed in this study. Utilising 11 microsatellite loci, the results revealed low levels of genetic diversity (H_o = 0.240, H_e = 0.417, and SI = 0.714) and high levels of inbreeding (mean F_{IS} = 0.440). The pairwise genetic differentiation (F_{ST}) and gene flow (*Nm*) indices ranged from 0.052 to 0.126 and 1.735 to 4.516, respectively, indicating moderate levels of genetic differentiation despite frequent gene flow among them. The UPGMA dendrogram showed two subclusters within the four populations. The need for an effective conservation management plan for the firefly population is indicated by its small population size and high inbreeding effects.
Keywords: Genetic diversity, *Pteroptyx tener*, inbreeding, conservation

INTRODUCTION

In Peninsular Malaysia, *Pteroptyx* fireflies stand out among other genera found owing to the synchronous flashings produced and the two most prevalent species found are *Pteroptyx tener* and *Pteroptyx bearni* (Coleoptera: Lampyridae) (Nada & Kirton, 2004; Jusoh et al., 2018). Due to its prevalence and dominance in Kuala Selangor, *P. tener* is the focal species of this research. *P. tener* predominantly leks on *Sonneratia caseolaris*, commonly found in estuaries throughout the country. Male fireflies synchronise their flashes with one another while mating, competing with other males, flying, and engaging in different stages of courtship with females. (Case, 1980; Nallakumar, 2003). In Malaysia, *P. tener* is a popular entomotourism activity due to its vivid bioluminescent display and lekking behaviour (Lemelin et al. 2019). Kuala Selangor is home to two important firefly entomotourism sites: Kampung Kuantan, and Kampung Bukit Belimbing According to an unpublished report, their populations have been fluctuating for the past 16 years (Khoo et al., 2023). Concerns have been raised regarding the impact of habitat loss and land conversion on their population numbers (Jaikla et al., 2020). However, the concern was the impact of these fluctuations on their genetic variation. In small populations, random shifts in allele frequency could lead to reduced genetic diversity and increased homozygosity, ultimately impairing the organism's ability to adapt through evolution (Woodruff, 2001). Increased homozygosity and inbreeding lead to inbreeding depression, which decreases fitness and compromises their long-term viability. Thus, preventing inbreeding is an objective in conservation genetics (Gomez-Raya et al., 2015). To the best of our knowledge, little is known about their population genetics. Owing to the possibility of providing insights into the evolutionary background of threatened animals and designing effective management measures, genetics has become essential in conservation biology (Hedrick & Hurt, 2012). However, many Malaysian scientists have only taken the lead in keeping track on their ecology (Prasertkul, 2018). There is limited data available on populations of *P. tener* specifically along the Selangor River. Therefore, there is a need for population genetics research as it provides the fundamental framework for comprehending changes affecting *P. tener* populations and preserving their genetic landscape. We developed a preliminary set of genomic microsatellite markers was developed using the de novo

partial genome assembly of the *P. tener* genome to assess the genetic diversity and population structure of a subset of *P. tener* populations living along the Selangor River in its natural habitat. Microsatellite markers are commonly employed in population studies because they exhibit appropriate levels of genetic polymorphism and codominant inheritance (Collard et al., 2005). This research provides genetic diversity information for *P. tener*, which can support the development of effective conservation and management strategies to revive their populations in the future.

MATERIALS AND METHODS

A total of 71 adult *Pteroptyx tener* samples were collected from four sectors along the river at night. They were then preserved at −20°C. A partially sequenced *P. tener* genome using de novo assembly was used to identify microsatellite regions in the genome. FullSSR was employed to mine for microsatellite-containing loci. Then, Polymerase Chain Reaction (PCR) reactions were prepared with Q5 High Fidelity 2× Master Mix (New England Biolabs, USA); the respective forward and reverse primers; and UltraPure DNase/RNase-Free Distilled Water (Invitrogen, USA) in a final reaction volume of 10 µL. Initial, PCR was performed at the annealing temperature of 48°C and the PCR products were screened. Touchdown PCR was then employed to amplify markers. PCR products were electrophoresed on a 1.5% GelRed-stained agarose gel. Highly specific primer pairs were selected for 5' end linker (M13, M4 and RV) labelling with different fluorophores (FAM™, HEX™, NED™) for the genotyping. The PCR thermal cycling conditions included an initial denaturation step at 98°C for 3 min; 35 cycles of denaturation for 10 s at 98°C; annealing at a temperature of 48°C to 57°C for 30 s (varies according to the T_a of each primer); extension at 72°C for 30 s; and final extension at 72°C for 2 min. The PCR products were injected into the ABI3500xl Genetic Analyzer (Applied Biosystem, USA) with GeneScan 400HD ROX (Applied Biosystem, USA) as the internal standard size. Analysis such as allele scoring, identifying genotyping error and null alleles were performed using GeneMarker Genotyping Software v2.6 (SoftGenetics, USA), MicroChecker software (Oosterhout et al., 2004) and FreeNA (Chapuis & Estoup, 2007). Hardy-Weinberg equilibrium (HWE) deviations was detected by GENEPOP v4.8 (Raymond and Rousset, 1995) and corrected using False Discovery Rate analysis. Genetic diversity and genetic differentiation indices were obtained using Microsatellite Toolkit, Popgene v1.32 (Yeh et al., 1999), FSTAT v2.9.4 (Goudet, 2003). Pairwise population genetic differentiation coefficient and gene flow were all determined by GenAlEx v6.5 (Peakall & Smouse, 2012). A UPGMA dendrogram was constructed using PowerMarker (Liu & Muse, 2005), and visualised using MEGAX v10.1.8 (Kumar et al., 2018).

RESULTS AND DISCUSSION

Out of the 20 microsatellite loci, only 11 of them showed amplification and are informative. Descriptive statistics based on four populations of *P. tener* are presented in Table 1. The number of alleles per locus (*Na*) ranged from 2.727 (Pop4) to 3.727 (Pop3) with an average of 3.136 alleles per locus; 1.629 (Pop1) to 2.043 (Pop3) with an average of 1.828 for the total population (*Ne*); 0.596 to 0.860 (*SI*); 0.155 (Pop1) to 0.312 (Pop3) with an average of 0.240 for the total population (*Ho*); 0.337 (Pop1) to 0.490 (Pop3) with an average of 0.417 for the total population (*He*); the allelic richness showed minimal variations in the values amongst the four populations (*Rs*), ranging from 2.624 (Pop1) to 3.360 (Pop 3). Low SI, lower H_o to H_e ratio, and positive F_{IS} showed low diversity of the species and excess homozygotes in their natural habitat. A higher degree of homozygosity and lower genetic variation were revealed among all of them. It is widely acknowledged that endangered invertebrates typically exhibit lower levels of genetic diversity (Beaurepaire et al., 2024). It may have arisen due to the reduced population size, resulting in inbreeding, bottleneck, selection, or the founder effect (Goodisman and Hahn, 2005).

Table 1. Genetic diversity parameters for four populations of *Pteroptyx tener* along the Selangor River.

Population	Na	Ne	Ho	He	SI	F_{IS}	Rs
Pop1	3.00	1.629	0.155	0.337	0.596	0.547	2.624
Pop2	3.091	1.821	0.235	0.424	0.722	0.454	2.881
Pop3	3.727	2.043	0.312	0.490	0.860	0.370	3.360
Pop4	2.727	1.820	0.259	0.416	0.678	0.388	2.696
Mean	3.136	1.828	0.240	0.417	0.714	0.440	2.890

Generally, it is shown that there is moderate genetic differentiation and high gene flow in *P. tener* individuals among all populations (Table 2). Moderate levels of differentiation may be maintained even if individuals frequently move between populations due to ongoing gene flow (Lenormand, 2002). Despite the high level of gene flow, individuals possibly only interact with neighboring conspecifics and exchange genetic material with close relatives, which leads to a high level of inbreeding. As a result, the two subclusters formed do not show significant differences (Figure 1).

Table 2. Pairwise population genetic differentiation coefficient (F_{ST}) and gene flow (N_m)

No	Populations		F_{ST}	N_m
1	Pop1	Pop2	0.126	1.735
2	Pop1	Pop3	0.102	2.205
3	Pop2	Pop3	0.093	2.442
4	Pop1	Pop4	0.094	2.396
5	Pop2	Pop4	0.081	2.838
6	Pop3	Pop4	0.052	4.516

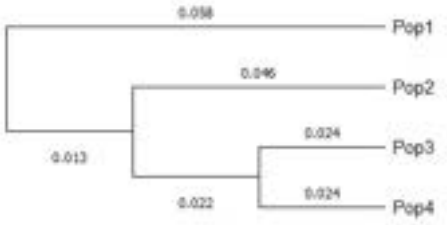

Figure 1. A UPGMA tree of four *P. tener* populations was constructed based on Nei's unbiased genetic distance (Nei, 1973).

CONCLUSION AND RECOMMENDATIONS

To summarize, this study provided insights into the current population structure and diversity of P. tener in a specific region of the Selangor River. The newly developed microsatellite markers revealed relatively low genetic diversity across the four P. tener populations examined. Evidence suggests that a moderate level of genetic differentiation exists, likely due to substantial gene flow among these populations, possibly involving genetic exchange among their closely related conspecifics. This phenomenon may explain the observed low genetic diversity. Analysis of population clustering identified two distinct subpopulations within the four studied groups. The findings of this research will serve as a foundation to offer significant support for the formulation of an effective conservation strategy for these fireflies in the future.

REFERENCES

Beaurepaire, A. L., Webster, M. T., & Neumann, P. (2024). Population genetics for insect conservation and control. *Conservation Science and Practice*, *6*(3), e13095. https://doi.org/10.1111/csp2.13095

Case, J. F. (1980). Courting Behavior in a Synchronously Flashing, Aggregative Firefly, Pteroptyx tener. Biological Bulletin, 159(3), 613–625. https://doi.org/10.2307/1540827

Chapuis, M.-P., & Estoup, A. (2007). Microsatellite Null Alleles and Estimation of Population Differentiation. Molecular Biology and Evolution, 24(3), 621–631. https://doi.org/10.1093/molbev/msl191

Collard, B., Jahufer, Z., Brouwer, J. B., & Pang, E. (2005). An introduction to markers, quantitative trait loci (QTL) mapping and marker-assisted selection for crop improvement: The basic concepts. Euphytica, 142, 169–196. https://doi.org/10.1007/s10681-005-1681-5

Gomez-Raya, L., Rodríguez, C., Barragán, C., & Silió, L. (2015). Genomic inbreeding coefficients based on the distribution of the length of runs of homozygosity in a closed line of Iberian pigs. Genetics Selection Evolution, 47(1), 81. https://doi.org/10.1186/s12711-015-0153-1

Goodisman, M. A. D., & Hahn, D. A. (2005). Breeding System, Colony Structure, and Genetic Differentiation in the Camponotus Festinatus Species Complex of Carpenter Ants. Evolution, 59(10), 2185–2199. https://doi.org/10.1111/j.0014-3820.2005.tb00927.x

Goudet J. (2003). FSTAT, a program to estimate and test population genetics parameters (version 2.9.4). http://www.unil.ch/izea/softwares/fstat.html

Goudet, J. (1999). PCAGEN version 1.2: a program to perform a principal component analysis (PCA) on genetic data. Unil https://www2.unil.ch/popgen/softwares/pcagen.htm

Hedrick, P. W., & Hurt, C. R. (2012). Conservation genetics and evolution in an endangered species: research in Sonoran topminnows. Evolutionary Applications, 5(8), 806–819. https://doi.org/10.1111/j.1752-4571.2012.00259.x

Jaikla, S., Lewis, S. M., Thancharoen, A., & Pinkaew, N. (2020). Distribution, abundance, and habitat characteristics of the congregating firefly, Pteroptyx Olivier (Coleoptera: Lampyridae) in Thailand. Journal of Asia-Pacific Biodiversity, 13(3), 358–366. https://doi.org/10.1016/j.japb.2020.06.002

Jusoh, W. F. A., Ballantyne, L., Lambkin, C. L., Hashim, N. R., & Wahlberg, N. (2018). The firefly genus Pteroptyx Olivier revisited (Coleoptera: Lampyridae: Luciolinae). Zootaxa, 4456(1), 1–71. https://doi.org/10.11646/zootaxa.4456.1.1

Khoo, V. (2023). A study of the habitat requirements of Cyclotropis carinata snails, which are a source of food for firefly larvae, and a study of firefly population monitoring in Kuala Selangor. Unpublished Final report. Lembaga Urus Air Selangor.

Lemelin, R. H., Boileau, E. Y., & Russell, C. (2019). Entomotourism: The allure of the arthropod. Society and Animals, 27(7), 733-750.

Lenormand, T. (2002). Gene flow and the limits to natural selection. Trends in Ecology & Evolution, 17(4), 183–189. https://doi.org/10.1016/S0169-5347(02)02497-7

Lewis, S. M., Wong, C. H., Owens, A. C. S., Fallon, C., Jepsen, S., Thancharoen, A., Wu, C., De Cock, R., Novák, M., López-Palafox, T., Khoo, V., & Reed, J. M. (2020). A global perspective on firefly extinction threats. BioScience, 70(2), 157–167. https://doi.org/10.1093/biosci/biz157

Li, Y.-L., & Liu, J.-X. (2018). StructureSelector: A web-based software to select and visualize the optimal number of clusters using multiple methods. Molecular Ecology Resources, 18(1), 176–177. https://doi.org/10.1111/1755-0998.12719

Nada, B. & Kirton, L.G. 2004. The Secret Life of Fireflies. IRBM Updates. Retrieved from http://www.luas.gov.my/irbm/updates.

Nallakumar, K. (2003). The synchronously flashing aggregative fireflies of peninsular Malaysia. Biodiversity. https://www.tandfonline.com/doi/abs/10.1080/14888386.2003.9712684

Peakall, R., & Smouse, P. (2012). GenAlEx V5: Genetic Analysis in Excel. Populations Genetic Software for Teaching and Research. Bioinformatics (Oxford, England), 28, 2537–2539. https://doi.org/10.1093/bioinformatics/bts460

Prasertkul, T. (2018). Characteristics of Pteroptyx Firefly Congregations in a Human Dominated Habitat. Journal of Insect Behavior, 31(4), 436–457. https://doi.org/10.1007/s10905-018-9687-8

Pritchard, J. K., Stephens, M., & Donnelly, P. (2000). Inference of population structure using multilocus genotype data. Genetics, 155(2), 945–959. https://doi.org/10.1093/genetics/155.2.945

Raymond, M., & Rousset, F. (1995). GENEPOP (Version 1.2): Population Genetics Software for Exact Tests and Ecumenicism. *Journal of Heredity*, *86*(3), 248–249. https://doi.org/10.1093/oxfordjournals.jhered.a111573

Van Oosterhout, C., Hutchinson, W. F., Wills, D. P. M., & Shipley, P. (2004). micro-checker: software for identifying and correcting genotyping errors in microsatellite data. Molecular Ecology Notes, 4(3), 535–538. https://doi.org/10.1111/j.1471-8286.2004.00684.x

Woodruff, D. S. (2001). Populations, Species, and Conservation Genetics. In S. A. Levin (Ed.), Encyclopedia of Biodiversity (pp. 811–829). Elsevier. https://doi.org/10.1016/B0-12-226865-2/00355-2

Yeh, F. C., Yang, R., and Boyle, T. (1999). POPGENE: Microsoft Windows-based Freeware for Population Genetic Analysis. Release 1.31. Edmonton: University of Alberta

SURVEILLANCE STUDY OF BACTERIAL CONTAMINATION ON VEGETABLES AND 'ULAM' SOLD IN JELI MARKET, KELANTAN

Nur Alia Zakaria [1], Khomaizon Abdul Kadir Pahirulzaman [1*]

[1] *Faculty of AgroBased Industry, Universiti Malaysia Kelantan, Jeli Campus, 17600 Jeli, Kelantan, MALAYSIA*

khomaizon@umk.edu.my

ABSTRACT

Jeli wet market is a famous wet market among local where people can find fresh vegetables and poultry for daily consumption. Vegetables and 'ulam' are important to supply high vitamins for human's health. 'Ulam' is Malaysian salad that is eaten raw or slightly processed. However, the consumption of contaminated fresh produce may result to foodborne illness. The impact of this disease associated with foodborne outbreaks that happened with symptoms such as diarrhoea. The common bacteria that able to cause this problem are Escherichia coli, Staphylococcus aureus and Salmonella typhi. All of these bacteria can be found typically in food included in raw vegetables and 'ulam' which obtained either from the farm, transport or in the wet market. In this study, the presence of bacteria in vegetables and 'ulam' sold in Jeli wet market were evaluated and identified. Results show that some fresh produce, such as cassava, Chinese okra, 'pucuk ubi kayu,' and 'pucuk kaduk,' are not safe to consume. The rest of the produce is considered safe, with bacterial levels below 10^6 CFU/mL, as recommended by the World Health Organization (WHO). The presence of bacteria in the fresh produce was confirmed using selective media, Gram staining, catalase tests, and TSI agar tests.

***Keywords*:** Bacterial Contamination, Foodborne Illness, Fresh Produce, Foodborne Outbreak

INTRODUCTION

Vegetables and 'ulam' refer to any type of plant where various parts, from rhizomes to roots, can be eaten raw as salad or cooked in dishes. 'Ulam,' also known as traditional vegetables, has been important in the multicultural Malaysian community for its health benefits and beauty purposes, such as anti-aging, for a long time. Previous studies have recorded more than 100 plant species from various families consumed as 'ulam' [1]. In Kelantan, sellers in the fresh market usually grow their own produce. Small-scale farmers typically use traditional planting methods on farms located near their homes, making it easier for them to care for the plants, such as watering the crops daily. They also decide on the types of fertilizers and pesticides to use during planting. Additionally, these sellers use traditional packaging methods, often using newspaper and rubber bands to pack leafy vegetables. Since the quality of vegetables cannot be improved after harvest, proper packaging is necessary to protect them from damage, contain them, and ensure they last longer.

The well-known wet market in Jeli, Kelantan, is Pasar Besar Jeli. Sellers at this market typically offer produce from village farmers, making it a central place for residents of Jeli to buy vegetables and traditional foods of the Kelantan community. As the district's population has grown, so has the demand for vegetable supplies. Rural farmers rarely have the means to expand their market reach, so they usually sell their produce at the wet market. Due to poor storage facilities, they are compelled to sell their vegetables even during peak times when prices are low [2].

METHODOLOGY

Sample Collection and Preparation

Five types of vegetables (cassava, carrot, Chinese okra, tomato, and cabbage) and five varieties of 'ulam' ('pucuk jenereh', 'ulam raja', 'pucuk ubi kayu', 'pucuk kaduk', and 'pucuk pegaga') were purchased from Jeli Wet Market in Jeli, Kelantan. These samples were freshly bought from the market within 1-2 days before the experiment and stored in separate zip lock bags. All samples were promptly used for bacterial isolation or stored at 4 °C to maintain their quality and prevent contamination from external sources.

Bacterial Isolation

25 g of each of vegetables and 'ulam' samples were placed in a sterile stomacher bags separately and added with 225 mL phosphate buffer solution. The samples were homogenized using BagMixer for 2 minutes. Samples were then serially diluted to 10^{-5} before spread onto nutrient agar media. Plates were incubated at 37 °C

for 24 hours. Colonies grown on culture plates were recorded as colony forming unit per millilitre (CFU/mL). Results were reported following the BAM Chapter 3: Aerobic Plate Count (APC) by Food and Drug Association (FDA) guidelines [3].

Bacterial Identification using Selective Media

The bacterial isolates were identified using selective media: MacConkey agar, XLD agar, and Baird Parker agar to detect *E. coli*, *Salmonella spp*., and *S. aureus*, respectively. Morphologically distinct colonies from isolation plates were streaked onto these selective media. The plates were then incubated at 37 °C for 24 hours. Identification was based on the appearance of colonies on the culture plates: Pink colonies on MacConkey agar indicated the presence of *E. coli*, yellow colonies on XLD agar indicated the presence of *Salmonella spp*., and pale yellow colonies on Baird Parker agar indicated the presence of *S. aureus*. Controls *E. coli* ATCC8739, *S. aureus* ATCC6538 and *S. typhi* ATCC14028 were used for comparison with the isolates.

Bacterial Identification by Gram Staining

The isolated bacteria were further identified by Gram staining. The wire loop was heated to sterilize and used to transfer a small drop of sterile distilled water onto a clean glass slide. After cooling and sterilizing again, the wire loop was employed to transfer a small number of bacterial cells onto the water drop, which were then spread to create a thin smear. The smear was heat-fixed with crystal violet reagent for 1 minute, followed by a quick wash with distilled water for 2 seconds. Iodine was applied and left on the slide for 1 minute before another brief wash with distilled water. Acetone, the decolorizing agent, was flooded onto the slide for 15 seconds and washed off with distilled water. Subsequently, the slide was flooded with safranin for 30 seconds and washed again with distilled water. Results were observed using a brightfield microscope under 100X magnification, revealing that gram-negative bacteria stained pink, while gram-positive bacteria stained purple.

Bacterial Identification using Biochemical Test

The isolated bacteria underwent further biochemical testing using the catalase test and Triple Sugar Iron (TSI) agar. For the catalase test, a small amount of bacterial cells was taken from a well-isolated colony using a sterilized wire loop and placed on a clean glass slide. Several drops of 30% hydrogen peroxide (H_2O_2) were added to the bacterial cells, and the production of bubbles was observed against a dark background, confirming the presence of catalase enzyme. In the TSI test, TSI agar from Merck, Germany was utilized. A well-isolated colony from the isolation plates was inoculated onto the TSI agar slant using a sterilized wire loop. The inoculation involved stabbing into the center of the medium to the bottom of the tube, followed by streaking on the surface of the agar slant. The results were analyzed based on specific observations: A completely yellow color in both the butt and slant indicated that the organism produced significant acid from lactose fermentation. If the butt was yellow and the slant remained red, it meant the organism did not ferment lactose but did ferment some glucose. No yellow color in either the butt or slant indicated that the organism did not ferment lactose or glucose. Additionally, a black color change in the slant indicated that the organism produced hydrogen sulfide (H_2S). Controls *E. coli* ATCC8739, *S. aureus* ATCC6538 and *S. typhi* ATCC14028 were used for comparison with the isolates.

RESULTS

Aerobic Plate Count

The number of colonies that grew on nutrient agar varied between the vegetable and 'ulam' samples. Some samples produced more than 250 colonies, which are reported as too numerous to count (TNTC). Among the vegetable samples, the highest colony count was found in cassava with 6.9×10^6 CFU/mL, followed by Chinese okra with 1×10^6 CFU/mL, carrot with 6.3×10^5 CFU/mL, and cabbage with 2.37×10^5 CFU/mL. The lowest was tomato with 0 CFU/mL. For the 'ulam' samples, the highest CFU/mL value was in ‘pucuk ubi kayu’ with 1.47×10^6 CFU/mL, followed by ‘pucuk kaduk’ with 1.02×10^6 CFU/mL, ‘ulam raja’ with 7×10^5 CFU/mL, ‘pucuk jenereh’ with 1.51×10^5 CFU/mL, and ‘pegaga’ with 1.15×10^5 CFU/mL.

Identification of Bacterial Isolates

The selective media was used to distinguish different types of bacteria isolated from vegetables and 'ulam' samples. Cassava samples formed many colonies on Baird Parker medium indicating presence of *S. aureus*, whereas no colonies were formed from tomato samples. For Chinese okra, numerous colonies were observed on MacConkey and XLD mediums showing presence of *E. coli* and *Salmonella spp*, while none were seen in tomato samples. On Baird Parker medium, 'pucuk ubi kayu' had the most colonies, and 'pegaga' had the least. Colonies formed abundantly on MacConkey medium for all samples except 'pegaga'. On XLD medium, many colonies were seen in all 'ulam' samples except 'pegaga'. Gram staining was used for further confirmation. Isolates from MacConkey and XLD agar plates produce a pink stain, indicating they are gram-negative. In contrast, isolates from the Baird Parker plate produce a purple stain, similar to the control plate, indicating they are gram-positive (Figure 1a).

Biochemical Test of Bacterial Isolates

In the catalase test, all isolated strains produced bubbles, indicating that the isolates produce catalase enzymes (Figure 1b). However, different results were observed when the isolates were grown on TSI agar. Four agar samples turned yellow, one turned black at the butt while remaining red on the slant, one turned yellow on the slant only, and one remained unchanged (Figure 1c).

DISCUSSION

The CFU/mL values for cassava and Chinese okra exceeded the FDA's acceptable limit of 10^6 CFU/mL, indicating high contamination. Cassava, often planted with animal manure and sold uncleaned, had soil on it, which harbors bacteria. In contrast, carrots, also tuber plants, were clean, showing no soil, suggesting they were washed before sale. Soil bacteria thrive in alkaline conditions, like those created by manure. Chinese okra's rough skin traps bacteria, while tomatoes showed no bacterial colonies, indicating they were safe and well-processed. Tomatoes' protective epidermal layer and antagonistic microorganisms help prevent bacterial contamination [4]. The high CFU/mL values in cassava and Chinese okra highlight contamination from sellers or handlers. Vegetables with over 10^6 CFU/mL are unsafe to eat, and appearance isn't a reliable indicator of bacterial presence. Thorough washing with decontaminants like vinegar is essential. The CFU/mL levels in 'pucuk ubi kayu' and 'pucuk kaduk' were above the safe limit, making them risky for raw consumption [5]. Other 'ulam' samples were safe. Leafy greens like 'ulam' are prone to bacterial infections. They grow in varied soil types with minimal care and are often exposed to bacteria in wet markets, increasing the risk of cross-contamination [6]. 'Pucuk ubi kayu' had the highest CFU/mL, possibly due to pests attracted to cassava roots. 'Pucuk kaduk' grows in bacteria-rich soil, often fertilized with poultry manure, increasing contamination. 'Pegaga' appeared clean, suggesting it was washed, unlike 'pucuk kaduk.' 'Pucuk jenereh,' a roadside shade tree in Malaysia, benefits from pruning, reducing bacteria exposure from pests and soil.

Three types of selective agar; Baird Parker, MacConkey, and XLD were used to detect *S. aureus*, *E. coli*, and *Salmonella spp*. in samples. These media can also grow other bacteria, so Gram staining was used to confirm bacterial types. *S. aureus* on Baird Parker medium indicates poor hygiene, often from nasal carriers among farmers and handlers. This pathogen in ready-to-eat vegetables and 'ulam' may come from contaminated surfaces and equipment [7]. *E. coli* on MacConkey medium that stains yellow points to fecal contamination, likely from manure or contaminated irrigation water. *E. coli* can persist in manure-fertilized soil for over 100 days [8]. High levels of *E. coli* in samples may result from poor hygiene or contaminated utensils and can adhere to plant parts even after washing [6]. XLD agar detected *Salmonella spp*., which may come from polluted irrigation water [9,10]. Salmonella spp. can enter plant parts through contaminated soil or irrigation water and from wild animals in wet markets, especially during the rainy season [11]. This bacterium is a significant public health concern linked to serious outbreaks.

Catalase tests identify the presence of the catalase enzyme in bacteria, which breaks down hydrogen peroxide (H_2O_2) into oxygen and water, forming bubbles. This test reveals that all colonies from the isolated media are catalase-positive, meaning they can use oxygen as a terminal electron acceptor for respiration. Low bubble production signifies less catalase activity, which helps bacteria defend against the effects of hydrogen peroxide, a byproduct of aerobic carbohydrate metabolism [12]. Additionally, Triple Sugar Iron (TSI) agar tests were conducted on representative of strains grown on the selective media. Isolate 1 from MacConkey media, isolate 3 from Baird Parker media, control *E. coli*, and control *S. aureus* turned the TSI slant yellow, indicating acidic reactions and the fermentation of dextrose, glucose, and lactose [13]. Isolate 2 from XLD media turned the TSI agar into a red slant with a blackening medium, indicating glucose fermentation and hydrogen sulfide (H_2S)

production [14], similar to *S. typhi* in the control tube. The uninoculated TSI agar remained red, indicating no sugar fermentation or gas production, as no cracks were observed in the agar.

Bacterial pathogens can contaminate fresh produce at any stage of the production and supply chain. This contamination can happen through direct contact with fecal matter during agricultural practices, such as using wastewater for irrigation or applying biosolids and animal manure as fertilizers. There is also a risk of contamination during transportation and handling processes [15,16,17]. Therefore, it is important for consumers to wash fresh produce with running water and use a decontaminant to kill bacteria before consumption to avoid foodborne illness.

CONCLUSION

This study revealed that some fresh produce sold in Jeli market, such as cassava, Chinese okra, 'pucuk ubi kayu,' and 'pucuk kaduk,' had bacterial levels exceeding safe limits, making them unsafe for consumption. In contrast, other produce was found to be safe, with bacterial levels below the WHO recommended threshold of 10^6 CFU/mL. Consuming contaminated produce can lead to foodborne illnesses. Common bacteria responsible for these issues include *E. coli*, *S. aureus*, and *S. typhi*, were also isolated from the vegetable and 'ulam' samples. These bacteria can be introduced to fresh produce at multiple stages, from farming to market handling. The findings highlight the critical need for maintaining good hygiene practices and proper handling to prevent contamination and ensure food safety. Regular microbial testing and rigorous adherence to food safety protocols are essential for minimizing the risk of foodborne illnesses.

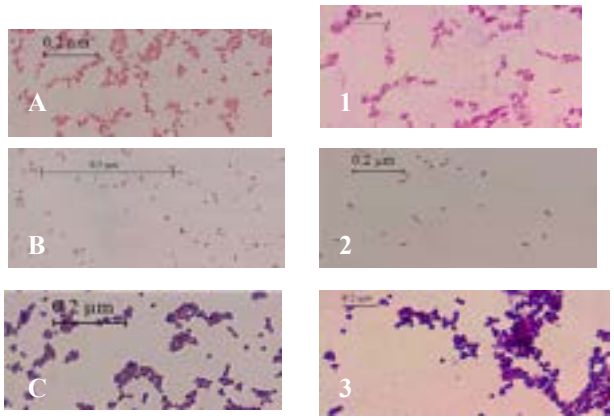

a. Gram staining

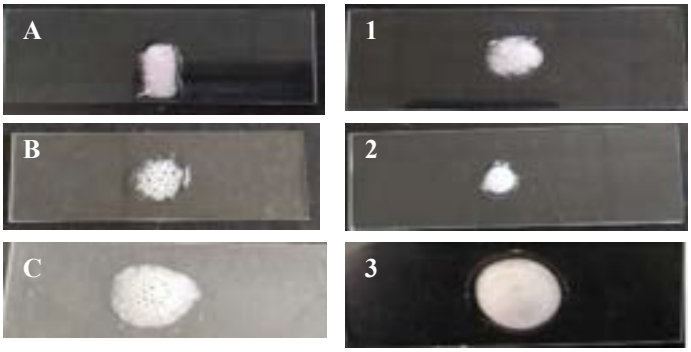

b. Catalase test

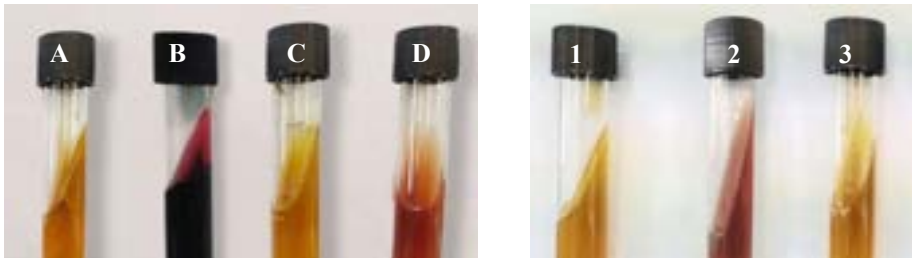

Figure 1. The representative of bacterial isolates (Isolate 1, Isolate 2 and Isolate 3) that were isolated from vegetables and 'ulam' samples. These isolates were compared to controls, which include E.coli (A), S. aureus (B), S. typhi (C) and un-inoculated agar (D).

ACKNOWLEDGEMENT

The authors would like to thank Faculty of AgroBased Industry, Universiti Malaysia Kelantan for the laboratory facilities.

REFERENCES

[1] Awang, N. A., Mat, N., & Mahmud, K. (2020). Traditional knowledge and botanical description of edible bitter plants from Besut, Terengganu, Malaysia. Journal of Agrobiotechnology, 11(1), 32-47

[2] Shariff, A. H. M., Shapiai, N. A., Zakaria, M., Akanda, J. M. H., Noor, N. Q. I. M., Yusop, M. H. M., & Razali, U. H. M. (2019, September). Proximate compositions of *Ipomea aquatic* Forsk.(leaf, petiole and stem) from Lubok Bungor, Jeli, Kelantan. In AIP Conference Proceedings (Vol. 2155, No. 1, p. 020060). AIP Publishing LLC.

[3] Food and Drug Association website. https://www.fda.gov/food/laboratory-methods-food/bacteriological-analytical-manual-bam. Retrieved in 2023.

[4] Bello, O. B., Olawuyi, O. J., Azeez, A. H., Adebisi, O. S., Owoade T. A., 2016. Microorganisms causing postharvest tomato (*Solanum lycopersicum* L.) fruit decay in Nigeria. Scientia Agriculturae, 13(2): 93 – 96.

[5] Kong, X., Jin, D., Jin, S., Wang, Z., Yin, H., Xu, M., & Deng, Y. (2018). Responses of bacterial community to dibutyl phthalate pollution in a soil-vegetable ecosystem. Journal of hazardous materials, 353, 142-150.

[6] Luna-Guevara, J. J., Arenas-Hernandez, M. M., Martínez de la Peña, C., Silva, J. L., & Luna-Guevara, M. L. (2019). The role of pathogenic *E. coli* in fresh vegetables: Behavior, contamination factors, and preventive measures. International Journal of Microbiology, 2019.

[7] Wu, S., Huang, J., Wu, Q., Zhang, F., Zhang, J., Lei, T., ... & Xue, L. (2018). Prevalence and characterization of *Staphylococcus aureus* isolated from retail vegetables in China. Frontiers in microbiology, 9, 1263.

[8] Muhammad, J., Khan, S., Su, J. Q., Hesham, A. E. L., Ditta, A., Nawab, J., & Ali, A. (2020). Antibiotics in poultry manure and their associated health issues: A systematic review. Journal of Soils and Sediments, 20(1), 486-497.

[9] Afolabi, O., and Oloyede, A. (2010). Irrigation water as possible source of borne pathogens in raw vegetables. Journal of Natural Sciences, Engineering and Technology, 9(2), 117–122.

[10] Alegbeleye, O. O., & Sant'Ana, A. S. (2020). Manure-borne pathogens as an important source of water contamination: An update on the dynamics of pathogen survival/transport as well as practical risk mitigation strategies. International Journal of Hygiene and Environmental Health, 227, 113524.

[11] Nguyen, T. K., Bui, H. T., Truong, T. A., Lam, D. N., Ikeuchi, S., Ly, L. K. T., ... & Hayashidani, H. (2021). Retail fresh vegetables as a potential source of Salmonella infection in the Mekong Delta, Vietnam. International Journal of Food Microbiology, 341, 109049.

[12] Kaushal, J., Mehandia, S., Singh, G., Raina, A., & Arya, S. K. (2018). Catalase enzyme: Application in bioremediation and food industry. Biocatalysis and Agricultural Biotechnology, 16, 192-199.

[13] Ahmad, M., Mamun, A. A., Morshed, S., Islam, M. S., Hoque, M. M., Sarwar, N., ... & Ahmed, T. (2018). Microbial safety of drinking jar water and antimicrobial resistant pattern against Escherichia coli in jar water at Chittagong, Bangladesh. International Food Research Journal, 25(2).

[14] Boatemaa, M. A., Ragunathan, R., & Naskar, J. (2019). Nanogold for in vitro inhibition of Salmonella strains. Journal of Nanomaterials, 2019, 1-11.

[15] Chee-Sanford, J. C., Mackie, R. I., Koike, S., Krapac, I. G., Lin, Y. F., Yannarell, A. C., Maxwell, S., & Aminov, R. I. (2009). Fate and transport of antibiotic residues and antibiotic resistance genes following land application of manure waste. Journal of Environmental Quality, 38(3), 1086–1108.

[16] Rahman, M., Alam, M.-U., Luies, S. K., Kamal, A., Ferdous, S., Lin, A., Sharior, F., Khan, R., Rahman, Z., Parvez, S. M., et al. (2022). Contamination of fresh produce with antibiotic-resistant bacteria and associated risks to human health: A Scoping Review. International Journal of Environmental Research and Public Health, 19, 360.

[17] He, Y., Yuan, Q., Mathieu, J., Stadler, L., Senehi, N., Sun, R., Alvarez, P. J. J. (2020). Antibiotic resistance genes from livestock waste: Occurrence, dissemination, and treatment. NPJ Clean Water.

MICROBIAL LEVELS ON COLD-FLAVORED DRINKS SOLD IN KUALA PILAH, NEGERI SEMBILAN

Najihah Moktar[1], Noorlis Ahmad[1]*

[1]*School of Biology, Faculty of Applied Science, UiTM Negeri Sembilan Branch, Kuala Pilah Campus, 72000 Kuala Pilah, Negeri Sembilan*

**anorlis@uitm.edu.my*

ABSTRACT

Food Handling rules are crucial steps to prevent the spread of various foodborne diseases. Even their slightest negligence can impact millions of people's health because they contact with food directly or indirectly before serving their customers. Improper food handling, poor hygienic practices, and scarcity of safe food management knowledge among street hawkers will lead to contamination in the ready-to-drink (RTD) cold-flavored drinks sold in their community area. The objectives of this study are to detect and quantify the presence of common pathogenic foodborne bacteria by using the MPN method in cold-flavored drinks (iced corn milk juice, iced asam boi lemonade, iced cendol, and iced mango juice) sold in Kuala Pilah, Negeri Sembilan. Four samples of cold-flavored drinks were selected to detect, quantify, and identify the common pathogenic foodborne bacteria isolated from cold-flavored drinks sold in Kuala Pilah, Negeri Sembilan by using the biochemical test. The result showed that all samples were contaminated with bacterial load in which 50% of the total samples which are iced corn milk juice and iced mango juice have the highest density of bacterial contamination (>1100 MPN/g). Iced cendol and iced asam boi lemonade have shown a density of bacterial contamination of 240 MPN/g and 43 MPN/g respectively. A total of 70% of bacteria isolated from cold-flavored drinks were identified as *Shigella* spp. Only 30% of the total isolates identified as *Enterobacter* spp. This study showed that the microbial levels of cold-flavored drinks sold in Kuala Pilah, Negeri Sembilan were average and needed to be improved to provide the best food safety and food quality to the local consumers. All the food handlers need to know about food handling and hygiene, as wide contamination in ready-to-eat (RTE) foods and ready-to-drink (RTD) beverages should be treated since it is potentially pathogenic at any level.

Keywords: Microbial levels, bacterial contamination, common pathogenic foodborne bacteria, Ready to Drink (RTD), cold-flavored drinks

INTRODUCTION

Disease caused by foodborne pathogens such as gastrointestinal tract infection is a common thing to happen nowadays. As reported by World Health Organization (WHO) in 2019 that 0.4% of U.S. deaths which about 9955 attributed in diarrheal diseases (Stephenson et al., 2024). The contamination in ready to eat (RTE) food or ready to drink (RTD) beverage can come from various sources such as bacteria, viruses, parasites or chemicals. Therefore, the availability of foodborne pathogen bacteria can be detected in the foods and drinks consumed by the people every day. Especially in the foods and drinks bought from local hawker stalls. The growth of ready to drink (RTD) hawker stalls around Kuala Pilah, Negeri Sembilan has become a major concern as it can be one of the reasons for the spread of foodborne pathogens to the consumers. Hence, the objectives of this study are to detect and quantify the presence of common pathogenic foodborne bacteria by using Most Probable Number (MPN) method and to identify the common pathogenic foodborne bacteria presence by using biochemical test in cold-flavored drinks sold at hawker stalls in Kuala Pilah, Negeri Sembilan. The scarcity knowledge of safe food handling among the local hawkers could be one of the factors of the contaminations in foods and drinks sold at the local hawker stalls in the studied area. Therefore, it leads to the spread of diseases caused by these foodborne pathogens such as diarrhoea, shigellosis and food poisoning. Several scientifical techniques have been performed in this study in order to verify the microbial levels of the drinks such as sampling, pH and temperature measurements, serial dilution, Most Probable Number (MPN) test, streaking on MacConkey agar, transferring of bacterial colonies and lastly identification of the bacterial isolates. In this study, the result showed that all samples were contaminated with bacterial load in which 50% of the total samples which have shown the highest density of bacterial contamination (>1100 MPN/g). Meanwhile the other two samples have density of bacterial contamination of 240 MPN/g and 43 MPN/g respectively. A total of 70% of bacteria isolated from cold-flavored drinks were identified as *Shigella* spp. Only 30% of the total isolates identified as *Enterobacter* spp.

MATERIALS AND METHODS

The materials required in this study were nutrient broth, nutrient agar, MacConkey agar, Gram stain reagent set, Metyl red indicator, sterilized MR-VP both, Tryptophan broth, Kovac's reagent, 5% Alpha-Naphthol, 40% Potassium Hydroxide, *E. coli* positive control, Simmon Citrate slant agar and distilled water. In this study, the sampling activities were conducted at local hawker stalls around Kuala Pilah, Negeri Sembilan where there were four cold-flavored drinks samples including iced milk corn juice *(air jagung susu ais),* iced asam boi lemonade juice *(air lemon asam boi ais),* iced cendol *(air cendol ice)* and iced mango juice *(air mangga susu ais)* that have been bought from four different stalls. A random sampling method has been performed as all the drinks were chosen randomly without any specific types. All the drinks samples were placed separately in a different sealed, sterile, labeled sample tube and immediately brought to the laboratory for analysis. The pH and temperature of each drink samples were measured by using pH paper and thermometer respectively for each sample. Serial dilution was performed where a 9 ml of Nutrient broth were added to each of the test tubes and 1ml of the cold-flavored drink samples were transferred into each of the 9ml of Nutrient broth. These steps were repeated until it reaches the dilution factor of 10^{-9}. After the serial dilution steps, 1 mL of the first test tube with a dilution factor of 10^{-1} were pipetted into three different 1.5 ml microcentrifuge tubes. All the solution in the microcentrifuge tubes were placed in the incubator for 24 hours at 37 °C. The estimation of total bacterial formed was determined by using MPN chart after 24 hours of incubation (Khan et al., 2015). Five tubes that showed positive result from MPN test were streaked on MacConkey agar. Formation of turbidity in the tubes indicates positive result on MPN test. Then, the inoculating loop that have been inoculated with the turbid solution were streaked on MacConkey agar and the all the plates were incubated in the incubator at 37°C for 24 hours (Arshad et al., 2006). The colonies formed on the MacConkey agar after incubation period were observed and transferred on the Nutrient slant agar. The nutrient slant agar was inoculated by drawing the needle upward in a zigzag motion along the agar surface and then were incubated at 37°C for 24 hours (Cappuccino & Welsh, 2018). The bacterial colonies growth from the Nutrient slant agar were tested with biochemical test and further identified with Gram staining. An IMViC (Indole test, Methyl Red test, Voges Proskauer test, Simmon Citrate test) have been conducted to identify the bacterial genus and Gram staining were performed to observe the bacterial morphology.

RESULTS AND DISCUSSION

Most Probable Number (MPN) 3 Tubes Test

The results in Table 1 below shows the Most Probable Number (MPN) of bacteria in four samples of cold-flavored drinks of Air Jagung (AJ_{01}), Lemon Asam Boi (LAB_{02}), Cendol (C_{03}) and Mangga Susu (MS_{04}) that have been randomly bought from local street vendors in Kuala Pilah, Negeri Sembilan for three weeks. These samples were analyzed for enumeration for total bacterial contamination and for the presence and absence of common foodborne pathogenic bacteria such as *E. coli, Salmonella* spp.*, Shigella* spp.*,* and *S. aureus.* For the first sample, Air Jagung (AJ_{01}), the density of bacterial presence in the sample is >1100 MPN/g as refer to the table of most probable number. As shown in Table 1, AJ_{01} showed positive result for all concentration dilution from 10^{-1}, 10^{-2}, 10^{-3} since all microcentrifuge tubes showed turbidity for all tubes when compared to the negative control as shown in Figure 1 below. The most probable number of density of bacterial presence in the LAB_{02} is 43 MPN/g. Meanwhile in sample C_{03}, concentration dilution of 10^{-1} and 10^{-2} showed positive results for all tubes and negative results for all tubes for concentration dilution of 10^{-3}. The most probable number of density of bacterial presence in C_{03} sample is 240 MPN/g. Lastly, for sample MS_{04}, all concentration dilution from 10^{-1} to 10^{-3} showed positive results in all tubes. Thus, the most probable number of density of bacterial presence in the last sample is >1100 MPN/g. Based on these results, it showed that each of cold-flavored drinks collected from local hawker stalls in Kuala Pilah, Negeri Sembilan has been contaminated with bacterial pathogens, most probably by coliform bacteria as the formation of turbidity in MPN test indicates positive result for the test. Positive result in MPN test portrayed the presence of bacteria in a sample.

The analysis of four iced-cold drinks samples showed that the density of bacterial contamination ranging from 43 MPN/g to >1100 MPN/g. However, majority of the samples had MPN value distribution of >1100 MPN/g which showed that half of four cold-flavored drinks samples collected have exceed the limit of >1100 MPN/g values. In the previous research done by Afreen et al. (2019) proven that the street vended drinks samples collected in Rawalpindi City, Pakistan also showed MPN value distribution exceed the limit of >1100 MPN/g. In this research, samples AJ_{01} and MS_{04} showed the highest destiny of bacterial contamination compared to other samples. The lowest bacterial density is shown by the sample LAB_{02} which is only 43 MPN/g. LAB_{02} is a lemonade juice sample with pH range in between pH 4-7. Low acidity in fruit juices between pH 4.8-6.2 are suitable for the growth of pathogenic bacteria (Nawawee et al., 2019).

Table 1. Most Probable Number (MPN) 3 Tubes Test for four samples of cold-flavored drinks in Kuala Pilah, Negeri Sembilan

[a]Samples	10^{-1}	10^{-2}	10^{-3}	[b]MPN/g
AJ_{01}	+++	+++	+++	>1100
LAB_{02}	+++	+--	---	43
C_{03}	+++	+++	---	240
MS_{04}	+++	+++	+++	>1100

[a]Note: Air Jagung (AJ_{01}), Lemon Asam Boi (LAB_{02}), Cendol (C_{03}), Mangga Susu (MS_{04})
[b]Source: Bacteriologic Analytic Manual, 8th ed. Maryland: Food and Drug Administration, 2010.

Biochemical test and Gram staining for bacterial isolates

Five tubes from each sample that showed positive result were streaked on MacConkey agar to observe the grow of Gram-negative bacteria species that presence in the cold-flavored drinks samples collected at the hawker stalls in Kuala Pilah, Negeri Sembilan. Ten slightly pink and translucent bacterial colonies on the MacConkey agar have been isolated and identified in the biochemical test and Gram staining. Based on the result shown in Table 2 below, seven out of ten bacterial isolates have been identified as *Shigella* spp., meanwhile the other three isolates have been identified as *Enterobacter* spp. These presumptive identifications were identified according to Cooper (2019). All the bacteria isolated from cold-flavored drinks were identified as Gram-negative bacteria as it appeared red to pink under a Gram stain as shown in Figure 1 below.

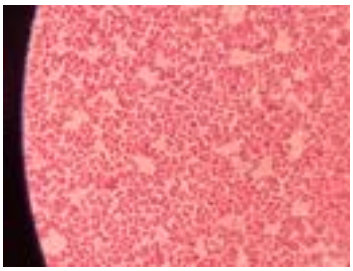

Figure 1. Gram staining result under 100x magnification

Based on Table 2, all bacteria isolated from AJ_{01} and LAB_{02} were presumptively identified as *Shigella* spp., followed by two bacteria isolated from C_{03}. Since the biochemical test (IMViC) has shown negative (-) result for Indole test, positive (+) result for Methyl-Red test, Voges-Proskauer test and Simmon Citrate test. Meanwhile, in MS04 and one isolate from sample C_{03} were identified as *Enterobacter* spp. as the result for IMViC test showed negative (-) result for both Indole test and Methyl-Red test and positive (+) result for both Voges Proskauer test and Simmon Citrate test. Coliform bacteria such as *Salmonella* spp. and *E. coli* were not found in the samples collected from the local hawker stalls in Kuala Pilah, Negeri Sembilan. Similarly, Dominguez-Gonzalez et al. (2022) also reported no prevalence of *Salmonella* in their samples. However, in the same research, Dominguez-Gonzalez et al. (2022) mentioned that there was presence of *Shigella* spp. in the fresh-squeezed orange juices samples purchased from street vendors in Morelia, Mexico which specifically refer to the species of *Shigella sonnei*. It shows the same result as obtained in this research where *Shigella* spp. were found in the iced-cold drink samples bought from local hawker stall in Kuala Pilah, Negeri Sembilan. The contamination of *Shigella* spp. in the drinks may be caused by the use of contaminated utensils or bare hands during drink handling and preparation which has led to cross contamination to the drinks sold. Based on the study done by Dominguez-Gonzalez et al. (2022) where the squeezed orange juice samples were found to have the presence of *Shigella* and *E. coli*, where it followed by the lack of hygiene practice showed by the street vendor such as had a dirty stalls, wore unwashed cloth, use unwashed or dirty orange, had poor water management and finally used unclean water to wash utensils and raw materials.

Based on the result, there was the presence of *Enterobacter* spp. detected in the cold-flavored drinks sold at hawker stalls in Kuala Pilah, Negeri Sembilan. It is similar as reported by Feglo.P & Sakyi.K (2012) that there was the presence of *Enterobacter cloacae* in the samples of ice-kenkey and cocoa drinks collected from street vendors in Kumasi, Ghana. It was observed that the handlers were wearing dirty cloths, practicing improper cleaning of dishes and performing unhygienic handling during the food preparation (Feglo.P & Sakyi.K, 2012).

Table 2. Biochemical Test (IMViC Test) and Gram staining

[a]Samples	Indole Test	Methyl Red Test	Voges Proskauer Test	Simmon Citrate Test	Gram staining	[b]Presumptive Results
Positive Control	+	+	-	-	-	*E. coli*
$AJ_{(1)}$(A)	-	+	+	+	-	*Shigella* spp.
$AJ_{(1)}$(B)	-	+	+	+	-	*Shigella* spp.
$LAB_{(2)}$(A)	-	+	+	+	-	*Shigella* spp.
$LAB_{(2)}$(B)	-	+	+	+	-	*Shigella* spp.
$LAB_{(2)}$(C)	-	+	+	+	-	*Shigella* spp.
$C_{(3)}$(A)	-	+	+	+	-	*Shigella* spp.
$C_{(3)}$(B)	-	-	+	+	-	*Enterobacter* spp.
$C_{(3)}$(C)	-	+	+	+	-	*Shigella* spp.
$MS_{(4)}$(A)	-	-	+	+	-	*Enterobacter* spp.
$MS_{(4)}$(C)	-	-	+	+	-	*Enterobacter* spp.

Note. [a]Air Jagung ($AJ_{(1)}$), Lemon Asam Boi ($LAB_{(2)}$), Cendol ($C_{(3)}$), Mangga Susu ($MS_{(4)}$)
[b]Source: Cooper, C. (2019). *Biochemical Tests to Identify Selected Gram-Negative Bacteria*. Youngstown State University (YSU).

CONCLUSION

As a conclusion, cold-flavored drinks sold in Kuala Pilah, Negeri Sembilan were grossly contaminated with foodborne pathogens as the bacterial contamination density in MPN test has shown the range of 43 MPN/g to >1100 MPN/g in the samples collected from local hawker stalls. After detection by using biochemical test, it can be concluded that the cold-flavored drinks were contaminated with Shigella spp. and Enterobacter spp. The root of contamination was found due to scarcity in the food handlers' knowledge in safe food storing, preparing, handling and serving among the local street hawkers. The level of bacterial contamination in the sample has exceeded the standard set by the Malaysian specifications for ready-to-drink (RTD) beverages (carbonated and non-carbonated) (MS601:1994) and WHO Guidelines for Drinking Water Quality. Additionally, the location of the stalls also plays the main role where it has likely influenced the bacterial contamination in the cold-flavored drink sold. This study suggests that food safety education needs to be exposed to the local hawkers and to the consumer itself in order to make sure the consumer and the food handlers are aware of potential foodborne disease that is caused by these pathogenic foodborne bacteria due to lack of responsible among the food handler as the biosafety and the cleanliness of the utensils, raw material and their hands were ignored during food or drink preparation. Not only bacteria, but also other foodborne pathogens such as viruses, chemicals and parasites also might be presence in the cold-flavored consumed daily by the local consumer, if the biosafety were ignored. Public awareness in choosing the cleanest hawker stalls to get ready to drink (RTD) beverages is essential as it helps to reduce the spread of foodborne diseases. This study might help to maximize food safety practices among street hawkers and to increase local awareness regarding street food safety.

REFERENCES

Afreen, A., Ahmed, Z., Ahmad, H., & Khalid, N. (2019). Estimates and burden of foodborne pathogens in RTE beverages in relation to vending practices. *Food Quality and Safety*, *3*(2), 107–115. https://doi.org/10.1093/fqsafe/fyz007

Arshad, R., Farooq, S., Sayyed, A., & Ali, S. (2006). MANIPULATION OF DIFFERENT MEDIA AND METHODS FOR COST-EFFECTIVE CHARACTERIZATION OF ESCHERICHIA COLI STRAINS COLLECTED FROM DIFFERENT HABITATS. In *Pak. J. Bot* (Vol. 38, Issue 3).

Bacteriologic Analytic Manual, 8th ed. Maryland: Food and Drug Administration, 2010. https://www.fda.gov/food/laboratory-methods-food/bam-appendix-2-most-probable-number-serial-dilutions#tables

Cappuccino James G, W. C. (2018). *Microbiology A Laboratory Manual* (11th ed.). Pearson Education Limited.

Stephenson, M. M., Coleman, M. E., & Azzolina, N. A. (2024). Trends in Burdens of Disease by Transmission Source (USA, 2005–2020) and Hazard Identification for Foods: Focus on Milkborne Disease. *Journal of Epidemiology and Global Health*. https://doi.org/10.1007/s44197-024-00216-6

Cooper, C. (2019). *Biochemical Tests to Identify Selected Gram-Negative Bacteria.* Youngstown State University (YSU). https://crcooper01.people.ysu.edu/microlab/gram-negative-bacilli-chart-2021.pdf

Dominguez-Gonzalez, K. G., Aguilar-Chairez, S., Cerna-Cortes, J., Soria-Herrera, R. J., & Cerna-Cortes, J. F. (2022). Microbiological quality and presence of foodborne pathogens in fresh-squeezed orange juice samples purchased from street vendors and hygienic practices in Morelia, Mexico. *Food Science and Technology (Brazil)*, *42*. https://doi.org/10.1590/fst.10222

Feglo.P & Sakyi.K. (2012). Bacterial contamination of street vending food in Kumasi, Ghana. *Journal of Medical and Biomedical Sciences* , *1*(1), 1–8.

Khan, M. M., Islam, M. T., Chowdhury, M. M. H., & Alim, S. R. (2015). Assessment of microbiological quality of some drinks sold in the streets of Dhaka university campus in Bangladesh. *International Journal of Food Contamination*, *2*(1). https://doi.org/10.1186/s40550-015-0010-6

Nawawee, N. S. M., Bakar, N. F. A., & Zulfakar, S. S. (2019). Microbiological safety of street-vended beverages in Chow Kit, Kuala Lumpur. *International Journal of Environmental Research and Public Health*, *16*(22). https://doi.org/10.3390/ijerph16224463

OPTIMISATION OF FTA CARD PREPARATION FOR DIRECT AMPLIFICATION OF THE SSR-MEGCIR3607 MARKER IN OIL PALM

Nurul Ain Shahira Mohd Asri [1], Mohd Razik Bin Midin[2], Wan Nurhayati Wan Hanafi [1,3]

[1]*Faculty of Applied Sciences, Universiti Teknologi MARA (UiTM), 40450 Shah Alam, Selangor, MALAYSIA*

ainshahira5798@gmail.com

[2] *Kulliyyah of Sciences,IIUM Kuantan Campus, 25200 Kuantan, Pahang Darul Makmur, MALAYSIA*

mohdrazik@iium.edu.my

[3]*Human Genetics and Biochemistry Research Group (Hugeb), Universiti Teknologi MARA*

40450 Shah Alam, Selangor, MALAYSIA

wannurhayati@uitm.edu.my

ABSTRACT

The molecular composition of oil palm (Elaeis guineensis) leaves, characterized by high levels of polysaccharides and secondary metabolites, presents significant challenges for effective DNA extraction and analysis. Although traditional PCR methods have been successful with young leaves, collecting them is labor-intensive and often impractical. Mature leaves, which are more accessible, have been underutilized due to the inhibitory effects of their biochemical content on DNA extraction. This study introduces an innovative solution using Flinders Technology Associates (FTA) cards—a paper-based technology designed to preserve nucleic acids in a stable form and overcome these extraction challenges. FTA cards consist of chemically treated filter paper that lyses cells upon contact, stabilizing the DNA for further analysis. Our objective was to develop a reliable, rapid, and practical alternative to conventional DNA extraction methods. We accomplished this by creating a modified PCR protocol tailored for oil palm DNA analysis using FTA cards. Our findings demonstrate that FTA cards effectively preserve sufficient DNA from mature oil palm leaves for successful PCR amplification, surpassing traditional DNA extraction techniques. This research addresses the challenges of DNA extraction and offers practical applications for oil palm studies. Future research could explore the scalability and cost-effectiveness of FTA card technology, potentially revolutionizing plant genetics research.

Keywords: DNA, Elaeis guineensis, high level polysaccharide, secondary metabolites, Flinders Technology Associates (FTA), PCR amplification

INTRODUCTION

Oil palm (*Elaeis guineensis*) have been cultivated and domesticated in Malaysia since its first introduction in the 1870s and began as an ornamental plant in Malaysia. It has the fastest-growing global demand as a raw material for food, personal care products, livestock feed, bioenergy, and other products (Ferdous Alam *et al.,* 2015). Since then it became a part of the industrialised Malaysia's agricultural economy and has grown into a massive industry because of its crude palm oil (Rahman, 2020).

Molecular marker methods and techniques for DNA have greatly expanded and become the most valuable tools currently accessible and are a complementary study from the traditional approach for plant identification (Nadeem *et al.,* 2018). Molecular approach is essential and become a pre-requisite in this regard, which critical to improve the productivity and quality of oil palm that capable to analyse its genetic material efficiently and accurately. Commonly, traditional PCR analysis methods widely applied by previous researcher (Wong *et al.,* 2015; Sarimana *et al.,* 2021) but often have inherent limitations that hinder research progress. Traditional method are complicated and time-consuming procedures that require specialised equipment and extensive sample handling (Suzana *et al.,* 2015; Ying and Zaman, 2006; Kalyana Babu *et al.,* 2017). In addition, transportation, and storage of genetic samples, which are essential for research collaboration and genetic diversity studies, pose a major logistical challenge. These constraints not only extend research time, but also limit access to genetic analysis in regions with limited resources and infrastructure (Aubakirova *et al.,* 2014).

In response to these challenges, this research endeavors to initiate a paradigm shift in the way we approach PCR analysis of oil palms. Central to this effort is the integration of Flinders Technology Associates (FTA) card technology, a compact and versatile device specifically designed for the collection, preservation, and transport of

nucleic acid samples (Mbogori *et al.*, 2006). This innovative approach aims to eliminate the shortcomings of conventional methods while providing reliability, quick and convenience in genetic analysis.

The main objective of this research is to explore and demonstrate the potential of FTA card technology as a transformative solution for PCR analysis of oil palm. By optimizing the PCR protocol tailored to oil palm DNA using FTA cards, we aim to provide a reliable, rapid, and convenient method that streamlines genetic research processes. It is expected that this method will find wide application not only in oil palm breeding programs, but also in various areas of agricultural research. By optimizing the process of FTA card preparation, it leads to more efficient, reliable, and drive progress in the oil palm industry and contribute to sustainable agricultural practices worldwide.

MATERIALS AND METHODS

Materials and reagents

The reagents and chemicals for that were used in this study are phenol, 99% ethanol, distilled water, boric acid, molecular biology grade water, Tris-base, and EDTA (Ethylenediaminetetraacetic acid), 5x Hot FIREPol blend master mix, QIAGEN QIAcard FTA wash buffer, 1x TE buffer (Tris-EDTA buffer), 10x TBE buffer, gel red nucleic acid staining 10000x water, Quickload 100bp DNA ladder, Solis Biodyne 100bp DNA ladder ready to load, SSR primer (mEgCIR3607), 6x DNA loading dye.

Plant materials and sampling collection

The genetic materials utilised in this study were oil palm leaves sourced from an independent smallholder plantation located in Teluk Panglima Garang, Selangor, Malaysia. A total of 50 samples were collected from two distinct blocks within these plantations, with 25 samples drawn from each block, subsequently designated as P1S1 until P1S25 for plantation 1 and P2S1 until P2S25 for plantation 2.

The collected samples considering having characteristics such healthy and productive condition. The easily reachable mature frond: frond 32-40 were chosen, harvested, cut, placed, and labelled in the zip lock bag individually. The samples were placed in the box and brought back to the laboratory immediately. The samples must be prepared immediately within a 24-hour collection period.

Sample preparation using direct PCR-based

Each leaf tissue was carefully cleaned to eliminate any dust or dirt that could interfere with the DNA extraction process. Precisely 0.4g of the leaf tissue was weighed using an analytical balance. A few drops of water were added to moisten the tissue, which was then crushed using a mortar and pestle. The crushed leaf material was transferred onto the FTA card (specifically onto the circled area) using a pair of tweezers. To prevent the leaf material from adhering to the FTA card cover, small pieces of parafilm were placed over the crushed leaves. A pestle was then used to press and roll over the FTA card to ensure the extraction of the green leaf extract. Upon completion, the FTA card containing the sample was labelled, placed in a zip-lock bag, and stored at room temperature. These steps were repeated for an additional 24 samples and applied across another one block of oil palm plantation.

FTA preparation for direct PCR-based

Based on optimised the washing step, the modified procedure begins with placing clean, sterile PCR tubes on a rack and labelling them according to the PCR gradient temperature. For example, samples from plantation 1 are labelled P1S1_I1, P1S2_I2, P1S3_I3, ..., P1S25_I25, and samples from plantation 2 are labelled P2S1_I1, P2S2_I2, P2S3_I3, ..., P2S25_I25. The Harris MicroPunch was sterilized by punching clean paper. Two discs from the FTA card were punched using the Harris MicroPunch and inserted into labelled PCR tubes. Each sample was washed with 200 µL of QIAcard FTA wash buffer, vortexed, and centrifuged at 6100 rpm and 2°C for one minute. The wash buffer was discarded, and this step was repeated, with the total of two washes with QIAcard FTA wash buffer. Afterwards, 200 µL of TE buffer was added to the PCR tubes, vortexed, and centrifuged at 6100 rpm and 2°C for one minute. The TE buffer was discarded, and this step was also repeated, that makes the total of two washes with TE buffer. The FTA elute was then incubated at 95°C for 5 minutes and air-dried for an hour at room temperature or for 20 minutes in a drying cabinet.

Primer optimisation via FTA card

PCR was performed in a 25 µL reaction volume containing 4 µL of FTA elute, 1 µL of reverse primer (5'- GAGGGGGTTGGGACATTAC-3'), 1 µL of forward primer (5'- TAGCTCACAACCCAGAACTAT-3'), 4 µL of 5x Hot FIREPol Blend master mix, and 15 µL of sterile distilled water. The gradient temperature was set between 5°C below the melting point (Tm). The PCR cycling conditions started with an initial denaturation at 94°C for 4 minutes, followed by 35 cycles of denaturation at 94°C for 30 seconds, annealing at an optimized temperature gradient for 30 seconds and elongation at 72°C for 1 minute. This was followed by a final extension at 72°C for 10 minutes, with the PCR held at ∞ for 10 to 12°C. The amplification was carried out using a thermal cycler. The PCR products were then separated using 1.8% agarose gel electrophoresis with 1x TBE buffer.

RESULTS AND DISCUSSION

According to the manufacturer's protocol (QIAGEN, 2023), FTA discs can be directly used as a DNA source after undergoing the recommended washing steps. However, to ensure that the DNA within the FTA discs is fully unbound during the washing process, several modifications and optimizations in the preparation steps are necessary, particularly when working with high-polysaccharide plants such as oil palm (Wan Hanafi and Abu Bakar, 2019; Adugna et al., 2011; Siegel et al., 2017). Considering these modifications, a preparation method of FTA elute was developed as a as FTA preparation steps of DNA source for PCR amplification. To optimize the FTA card preparation process for direct SSR amplification in oil palm, both FTA discs and FTA elute were tested as DNA sources without altering any PCR components. As illustrated in Figure 1, the use of FTA discs resulted in no PCR product and the presence of primer dimers, whereas the use of FTA elutes produced clear PCR products without non-specific bands. The FTA elute method was further validated using 50 samples from two independent smallholder oil palm plantations. The primer validation process consistently yielded successful PCR amplification with expected product sizes of 190-238 bp and no primer dimers across all 50 samples.

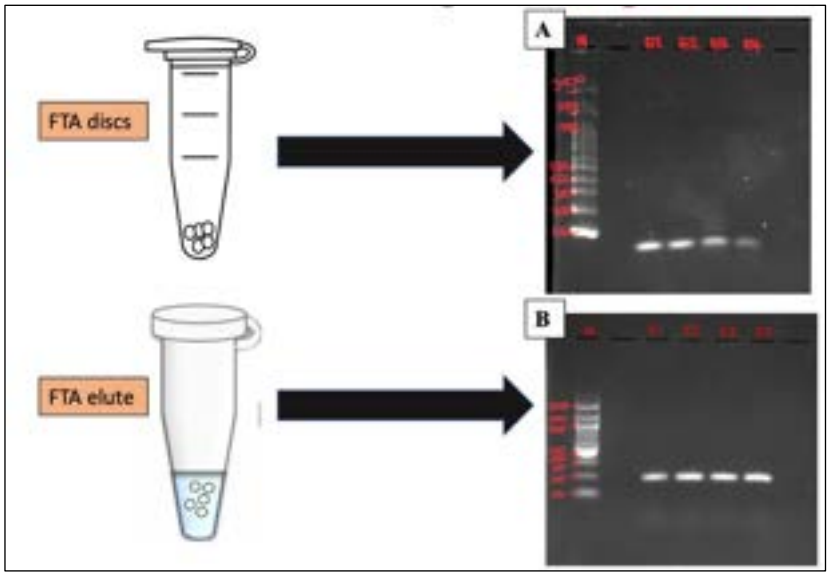

Figure 1. Comparison of outcome for oil palm PCR amplification using DNA source from different FTA card preparation steps

CONCLUSION

The mEgCIR3607 marker-based direct amplification of the SSR in oil palm through the optimisation of FTA card production has proven to be a dependable and reliable for genotyping technique. The results imply that in modified FTA card preparation procedures greatly improve DNA yield and purity, especially in species of plants with high polysaccharide content like oil palm. Although the results are promising, there were few consideration where the FTA discs were unable to generate PCR amplification of oil palm. This implies that additional modification might be required to guarantee the universal applicability of FTA discs, especially in situations where DNA is tightly bonded or the plant material contains with high amount of secondary metabolites. This optimised

procedure highlights the applicability of PCR amplification by enabling consistent and accurate amplification across a variety of samples especially for large scale of plant sampling.

REFERENCES

Adugna, A., Sweeney, P. M., & Snow, A. A. (2011). Optimization of a high throughput, cost effective, and all-stage DNA extraction protocol for sorghum (*Sorghum bicolor*). *Journal of Agricultural Science and Technology*, 5(1), 243 – 250.

Aubakirova, K., Omasheva, M., Ryabushkina, N., Tazhibaev, T., Kampitova, G. & Galiakparov, N. (2014). Evaluation of five protocols for DNA extraction from leaves of *Malus sieversii, Vitis vinifera* and *Armenica vulgaris*. *Genetics and Molecular Research*, 13(1), 1278-1287.

Ferdous Alam, A. S. A., Er, A. C., and Begum, H. (2015). Malaysian oil palm industry: Prospect and problem. Journal of Food Agriculture and Environment, 1313(22), 143-148.

Kalyana Babu, B., Mathur, R. K., Naveen Kumar, P., Ramajayam, D., Ravichandran, G., Venu, M. V. B. and SparjanBabu, S. (2017). Development, identification & validation of CAPS marker for SHELL trait which governs dura, pisifera & tenera fruit forms in oil palm (Elais guineensis Jacq.). PLoS ONE, 12(2), 1-16.

Mbogori, M. N., Kimani, M., Kuria, A., Lagat, M. & Danson, J. W. (2006). Optimization of FTA technology for large scale plant DNA isolation for use in marker assisted selection. *African Journal of Biotechnology*. 5(9), 693-696.

Nadeem, M. A., Nawaz, M. A., Shahid, M.Q., Doğan, Y., Comertpay, G., Yildiz, M., Hatipoğlu, R., Ahmad, F., Alsaleh, A., Labhane, N., Özkan, H., Chung, G., & Baloch, F. S. (2018). DNA molecular markers in plant breeding: status and recent advancements in genomic selection and genome editing. *Biotechnology and Biotechnological Equipment*, 32 (2), 261–285.

QIAGEN. (2023). QIAcard FTA Formats. The QIAGEN website. Retrieved on 31 May 2023 from https://www.qiagen.com/us/products/discovery-and-translational-research/sample-collection-stabilization/qiacard-fta/qiacard-fta-formats

Rahman, S. (2020). Malaysian Independent Oil Palm Smallholders and their Struggle toSurvive 2020. ISEAS-Yusof Ishak Institute, 2020 (144), 1-16.

Sarimana, U., Herrero, J., Erika, P., Indarto, N., Wendra, F., Santika, B., Ritter, B., Sembiring, Z., and Asmono, D. (2020). Analysis of genetic diversity and discrimination of Oil Palm DxP populations based on the origins of pisifera elite parents. Breeding Science Preview, 71(2), 1-10.

Siegel, C. S., Stevenson, F. O., & Zimmer, E. A. (2017). Evaluation and Comparison of FTA Card and CTAB DNA Extraction Methods for Non-Agricultural Taxa. *Applications in Plant Sciences*, 5(2), 1-7.

Suzana, M., Rahimah, A. R., Maizura, I. and Singh, R. (2015). A simple and rapid protocol for isolation of genomic DNA from oil palm tissue. Journal of Oil Palm Research, 27(3), 282-287.

Wan Hanafi, W. N., & Abu Bakar, N. S. (2019). Application of Whatman FTA Card Method in Oil Palm DNA Extraction and PCR Analysis. *Scientific Research Journal*, 16 (2), 17-26.

Wong, W. C., Jit, T. C., Kien, W. C., Mayes, S., Singh, R., & Chin, S. A. (2015). Development of an Effective SSR-Based Fingerprinting System for Commercial Planting Materials and Breeding Applications in Oil Palm. *Journal of Oil Palm Research*, 27 (2), 113-127.

Ying, S. T., & Zaman, F. Q. (2006). DNA Extraction from Mature Oil Palm Leaves. *Journal of Oil Palm Research*, 18(1), 1-6.

POLYHYDROXYALKANOATE GRANULE FORMATION AND THE EFFECTS OF CARBON SOURCES ON THERMOPHILIC GLOEOCAPSA SP.

Abellyna Abraham[1], Nur Izzati Mohd Noh[2*], Fazilah Abd Manan[3], Anthony Nyangson Steven[4]

[1,2*,3]*Department of Bioscience, Faculty of Science, Universiti Teknologi Malaysia*

[4]*Department of Chemistry, Faculty of Science, Universiti Teknologi Malaysia*

abraham.a@graduate.utm.my [1]/ izzati@utm.my [2]*

ABSTRACT

Polyhydroxyalkanoates (PHAs) are intracellular biopolymers that produced naturally by microbes for energy storage. Apart from that, PHAs also assists the microbial cells to survive under biotic stress condition and aid their survival. Unlike heterotrophic bacteria, cyanobacteria are able to accumulate PHA under photoautotrophic growth conditions with the aid of carbon dioxide and sunlight. In this study, a unicellular thermophilic cyanobacteria, *Gloeocapsa* sp. have been employed to asssess its morphology, the presence of PHA granules, and the effect of different carbon source on its growth yield to increase the PHA accumulation. Three *Gleoecapsa* sp. samples were used in this study, which are samples 2DL, Ci, and C. The samples were cultivated to observe its morphology. It was observed that *Gloeocapsa* sp. cells are unicellular cells that has spherical coccus morphology and are tightly packed together within spherical colonies. Moreover, the *Gleocapsa* sp. samples have been cultivated for 21 days to observe the dry cell weight (DCW mg/mL) biomass from four different carbon source media (basic BG11, carbon-rich BG11, flue gas water supplied BG11, and pineapple skin extract supplied BG11). The results obtained demonstrates that *Gloeocapsa* sp. samples recorded the highest growth in basic BG11 media, meanwhile the lowest growth were recorded in flue gas supplied BG11 media. In addition to that, Sample C recorded the highest DCW in all cultivation except for flue gas supplied BG11, meanwhile only Sample 2DL recorded the highest DCW in flue gas supplied BG11 media. This study provides insights on the co-relation between the biomass and carbon source requirements by thermophilic cyanobacteria as well as their ability in forming PHA granules.

***Keywords*:** Thermophilic cyanobacteria (*Gloeocapsa* sp.), Polyhydroxyalkanoate (PHA), Nile Blue A (NBA), Sudan Black B (SBB), Carbon sources

INTRODUCTION

The first study identifying polyhydroxyalkanoates (PHA) in *Gloeocapsa* was conducted by Hai et al. (2001) who investigated the presence of type-III PHA synthases in various cyanobacteria, including *Gloeocapsa* sp. strain PCC 74281. Besides that, western blotting was utilized to verify the PHA granules of cyanobacterial strain including *Gloeocapsa* sp. Even though, both Western blotting and PHA granule staining are both valuable techniques, they serve different purposes and have distinct advantages. Nevertheless, in this study, SBB and NBA staining are chosen for PHA granule detection because PHA granule staining is specifically designed to detect PHA granules within the cells which makes it highly specific for PHA-producing cyanobacterial cells. Moreover, unlike Western blotting, PHA granule staining method allows direct visualization of PHA granules under a microscope and provides immediate insights into the morphology and intracellular localization of PHA granules (Koller & Rodríguez-Contreras, 2015).

Despite that cyanobacteria can accumulate PHAs naturally, their PHA production based on volumetric productivity and cell biomass is critically lesser than that in heterotrophic bacteria. According to Singh & Mallick (2017), the main reason that lower PHA accumulation in cyanobacteria is due to cyanobacterial growth rate, which is typically slower than heterotrophic bacteria. Therefore, cyanobacterial strain improvement by genetic modification, new harvesting techniques, and alternate carbon sources are suggested to enhance the PHA production (Singh & Mallick, 2017). Till date, there are many studies have been conducted for different bacterial strains with various carbon sources such as sugars, waste oils, and lignocellulosic waste biomass to increase the dry cell weight of cells. There is limitation on information regarding the effects of carbon sources on cyanobacterial growth and their PHA accumulation. Thus, the aim of this research is to examine the presence of intracellular PHA granules, and to assess the effect of carbon sources on the growth biomass of thermophilic *Gloeocapsa* sp.

MATERIALS AND METHODS

Thermophilic *Gloeocapsa* sp. cultivation and PHA granules detection

Three thermophilic *Gloeocapsa* sp. strains isolated from different location of Malaysia hot springs were used for this study (Sample 2DL from Kg. Lada, Negeri Sembilan; Sample C and Ci from Ulu Kuang, Perak). All strains were cultivated photoautotrophically in BG11 medium (pH 7.4) at 47 °C with constant light illumination. After a week of cultivation, the morphology and PHA detection of thermophilic *Gloeocapsa* sp. samples were assessed. The morphological features of the thermophilic *Gloeocapsa* sp. samples were observed using light. Primary detection of PHA intracellular granules of *Gloeocapsa* sp. samples was performed using SBB dye as described by Balakrishna Pillai et al. (2018) and observed using light microscopy. For further PHA intracellular granules detection, NBA staining was employed as explained by (Legat et al., 2010) and examined under fluorescence microscope at excitation wavelength for DAPI.

Preparation of different carbon sources

For biomass analysis, three different modified BG11 media (carbon-rich BG11 and flue gas water with BG11, and pineapple skin extract with BG11) were prepared meanwhile basic BG11 media was used as a control. For basic BG11 and carbon rich BG11, the carbon source was derived from sodium carbonate, Na_2CO_3 meanwhile the nitrogen source was from sodium nitrate, $NaNO_3$ Additionally, the concentration of Na_2CO_3 and $NaNO_3$ in carbon-rich BG11 media were increased. The flue gas water was obtained from carbon combustion meanwhile the lignocellulosic waste used was prepared from 1g/mL of pineapple skin extract (PSE). All modified BG11 media were adjusted to pH 7.4.

Thermophilic *Gloeocapsa* sp. cultivation and PHA granules detection

For cultivation, 10% inoculum of the *Gloeocapsa* sp. were prepared in sterilized 1x basic BG11 medium, carbon rich BG11 media, FGW with BG11 media, and PSE with BG11 media. All cultures were cultivated at 47°C under continuous illumination with white fluorescent for 21 days. After cultivation, the cell pellet was collected and dried at 70°C. The dry cell weight (DCW) biomass was calculated using formula [(DCW after dehydration (g)−DCW before dehydration(g)×1000mg)/150mL]

RESULTS AND DISCUSSION

Morphology and PHA granule detection of thermophilic *Gloeocapsa* sp.

Gleocapsa sp. strains 2DL, Ci and C were characterized by a spherical coccus morphology, consisting of individual cells tightly packed together within spherical colonies (Figure 1 **A-C**). The cells are typically small, rounded, and proximity to each other within the colony. The spherical shape enhances their ability to efficiently acquire nutrients and adapt to varying environmental conditions. Notably, sample 2DL and Ci were diploid cells with sample Ci appeared to has thicker mucilaginous sheath compared to sample 2DL (Figure 1**A** and 1**B**). It is known that *Gloeocapsa* sp. cells can exist as unicellular with quadruplet cells wrapped within a mucilaginous sheath, which was the distinct shape of sample C (Figure 1**C**). The presence of quadruplets in certain instances may serve as reproductive strategy, enabling the cells to disperse and colonize new areas (Kumar et al., 2010). These cells were surrounded by a protective mucilaginous sheath. It is also known that mucilaginous sheath serves multiple functions such as shielding the cells from drying out, providing defense against harmful UV radiation and offers structural support to the colony (Souza et al., 2020).

According to Mohammed & Ray (2022), SBB is a non-specific dye for PHA-producing producers. Thus, in this study, Nile Blue A was used to further confirm the presence and accumulation of PHA granules. Sudan Black B-stained culture smear showed cells filled up with dark blue-black stained granules (Figure 1 **D-F**) and the cells stained with Nile Blue A when exposed to UV light at 405 nm, exhibited bright blue cytoplasmic granules (Figure 1 **G-I**). After staining the *Gloeocapsa* cells with SBB and observed under light microscope, the PHA granules were clearly visible in black colour (Figure 1 **D-F**). Nile Blue, being lipophilic can sometimes detect granules of lipids that differ in nature and composition from PHA (Chaudhry et al., 2011). The fluorescence intensity increased with the increase of PHA content from PHA producing cells. PHAs are accumulated intracellularly under the condition of nutrient stress and act as a source of carbon and energy (Ratnaningrum et al.,

2019). The screening result from three *Gloeocapsa* sp. samples (2DL, Ci, C) showed qualitatively by emitting bright blue as they were able to accumulate PHA granules when it was observed under UV light irradiation at 405 nm (DAPI) using fluorescence microscope. As indicated in Figure 1 **G-I**, the *Gloeocapsa* cell contains intracellular PHA granules when stained with 1% of NBA solution. The granules were clearly observed as blue-fluorescence.

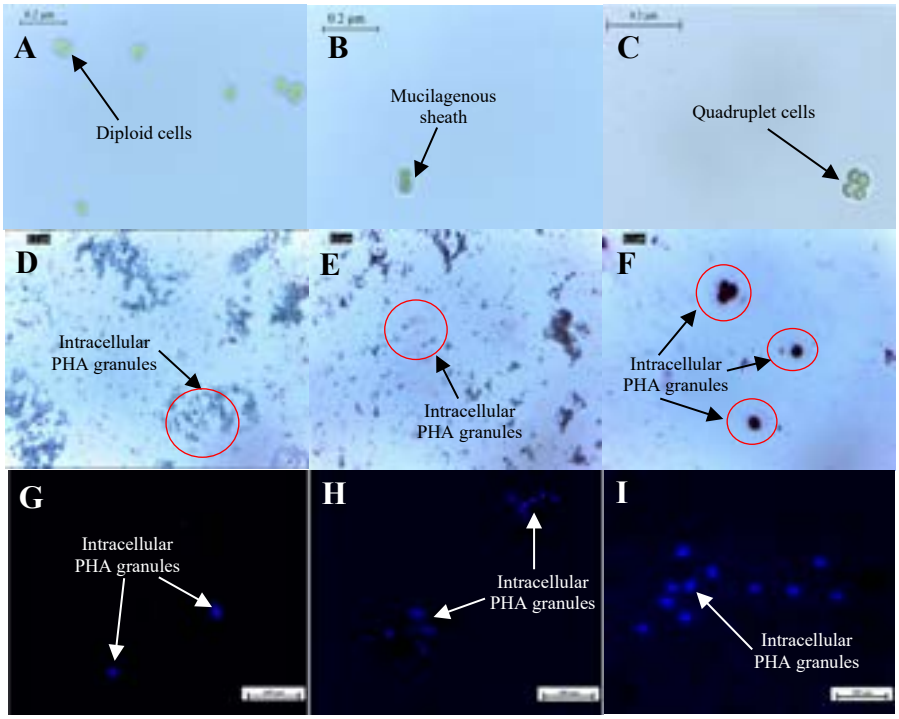

Figure 1. Morphology and PHA detection of thermophilic *Gloeocapsa* sp. strains; **A, B, C**: 2DL, Ci, and C samples, respectively at 1000× magnification using light microscopy; **D, E, F**: SBB stained 2DL, Ci, and C samples at 100x magnification, respectively at 100x magnification; and **G, H, I**: Fluorescence microscopy visualization of Nile Blue stained 2DL, Ci, and C samples at 40x magnification and UV (405nm).

The effect of different carbon sources on *Gloeocapsa* sp. cell biomass

All *Gloeocapsa* sp. strains recorded the highest DCW when they were cultivated in basic BG11 media (Figure 2). Noteworthy, the least growth were recorded for all *Gloeocapsa* sp. strains (2DL, Ci, and C) when they were cultured in BG11 added with flue gas. This might be due to the high toxicity of flue gas which contains the reaction products of fuel and combustion air and residual substances such as particulate matter (dust), sulfur oxides, nitrogen oxides, and carbon monoxide (Singh et al., 2016). Sample C showed the greatest DCW in all cultivation except for FGW supplied BG11 media, this is because high CO_2 concentration might slow down the cell growth. However, only Sample 2DL grew well in the FGW supplied BG11 media, which shows that 2DL cells were able to utilize nitrate and sulphate as their nutrient source (Chou et al., 2021). Comparably, all *Gloeocapsa* sp. strains were able yield higher biomass in pineapple skin extract supplied BG11 media cultivation than FGW supplied BG11 media cultivation. This is due to the presence of high lignocellulosic source (cellulose and hemicellulose) and complex sugar such as sucrose, fructose and glucose in PSE supplied BG11 media.

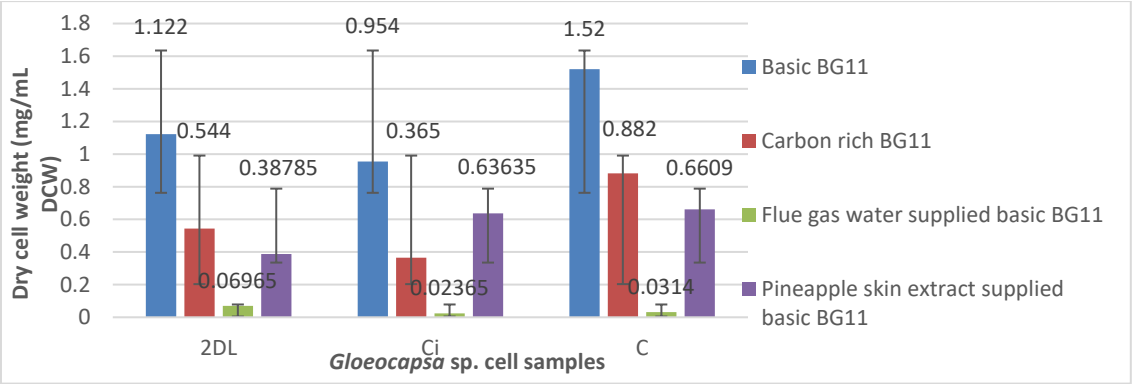

Figure 2. Dry cell weight (mg/mL DCW) of *Gloeocapsa* sp. samples (2DL, Ci, and C) cultivated in four different carbon sources. Reference: Abraham et al. (29 August 2024)

CONCLUSION

The thermophilic *Gloeocapsa* sp. strains used in this study were able to accumulate intracellular PHA granules as the SBB and NBA stained smeared cells have demonstated PHA granules upon imaging. Besides that, all thermophilic *Gloeocapsa* sp. strains have shown their respective biomass production in DCW from different carbon sources. Noteworthy, basic BG11 media was the best carbon source for the thermophilic *Gloeocapsa* sp. to grow as all strains have recorded the greatest DCW compared to other carbon source cultivations. In future, optimization of growth media and conditions can provide a significant impact on the cyanobacterial metabolism to produce higher cell biomass which will eventually help in increasing PHA production.

REFERENCES

Balakrishna Pillai, A., Jaya Kumar, A., & Kumarapillai, H. (2018). Enhanced production of poly(3-hydroxybutyrate) in recombinant *Escherichia coli* and EDTA–microwave-assisted cell lysis for polymer recovery. AMB Express, 8(1). https://doi.org/10.1186/s13568-018-0672-6

Chaudhry, W. N., Jamil, N., Ali, I., Ayaz, M. H., & Hasnain, S. (2011). Screening for polyhydroxyalkanoate (PHA)-producing bacterial strains and comparison of PHA production from various inexpensive carbon sources. Annals of Microbiology, 61(3), 623–629. https://doi.org/10.1007/s13213-010-0181-6

Chou, H. H., Su, H. Y., Chow, T. J., Lee, T. M., Cheng, W. H., Chang, J. S., & Chen, H. J. (2021). Engineering cyanobacteria with enhanced growth in simulated flue gases for high-yield bioethanol production. Biochemical Engineering Journal, 165. https://doi.org/10.1016/j.bej.2020.107823

Hai, T., Hein, S., & Steinbu $ Chel, A. (2001). Multiple evidence for widespread and general occurrence of type-III PHA synthases in cyanobacteria and molecular characterization of the PHA synthases from two thermophilic cyanobacteria : *Chlorogloeopsis fritschii* PCC 6912 and *Synechococcus* sp. strain MA19 (Vol. 147). www.sgmjournals.org

Koller, M., & Rodríguez-Contreras, A. (2015). Techniques for tracing PHA-producing organisms and for qualitative and quantitative analysis of intra- and extracellular PHA. In Engineering in Life Sciences (Vol. 15, Issue 6, pp. 558–581). Wiley-VCH Verlag. https://doi.org/10.1002/elsc.201400228

Kumar, K., Mella-Herrera, R. A., & Golden, J. W. (2010). Cyanobacterial heterocysts. Cold Spring Harbor Perspectives in Biology, 2(4). https://doi.org/10.1101/cshperspect.a000315

Legat, A., Gruber, C., Zangger, K., Wanner, G., & Stan-Lotter, H. (2010). Identification of polyhydroxyalkanoates in *Halococcus* and other *haloarchaeal* species. Applied Microbiology and Biotechnology, 87(3), 1119–1127. https://doi.org/10.1007/s00253-010-2611-6

Mohammed, S., & Ray, L. (2022). Polyhydroxyalkanoate recovery from newly screened *Bacillus* sp. LPPI-18 using various methods of extraction from Loktak Lake sediment sample. Journal of Genetic Engineering and Biotechnology, 20(1). https://doi.org/10.1186/s43141-022-00392-7

Ratnaningrum, D., Saraswaty, V., Priatni, S., Lisdiyanti, P., Purnomo, A., & Pudjiraharti, S. (2019). Screening of polyhydroxyalkanoates (PHA)-producing bacteria from soil bacteria strains. IOP Conference Series: Earth and Environmental Science, 277(1). https://doi.org/10.1088/1755-1315/277/1/012003

Singh, A. K., & Mallick, N. (2017). Advances in cyanobacterial polyhydroxyalkanoates production. In FEMS Microbiology Letters (Vol. 364, Issue 20). Oxford University Press. https://doi.org/10.1093/femsle/fnx189

Singh, J. S., Kumar, A., Rai, A. N., & Singh, D. P. (2016). Cyanobacteria: A precious bio-resource in agriculture, ecosystem, and environmental sustainability. In Frontiers in Microbiology (Vol. 7, Issue APR). Frontiers Research Foundation. https://doi.org/10.3389/fmicb.2016.00529

Souza, M. de J., Mercadante-Simões, M. O., & Ribeiro, L. M. (2020). Secondary-cell-wall release: a particular pattern of secretion in the mucilaginous seed coat of *Magonia pubescens*. American Journal of Botany, 107(1), 31–44. https://doi.org/10.1002/ajb2.1415

Zili, F., Mezhoud, N., Trabelsi, L., Chreif, I., Hatem, &, & Ouada, B. (n.d.). Fatty acid composition of the thermophilic *Gloeocapsa gelatinosa* under different combinations of temperature, light intensity, and NaNO 3 concentration. https://doi.org/10.1007/s10811-014-0296-4/Published

EXPLORING THE SYNERGISTIC EFFECTS OF ASTAXANTHIN AND TOCOTRIENOLS ON LPS-INDUCED INFLAMMATION IN HUMAN LUNG CELLS (CALU-3)

Muhamad Helmi Husaini Rusmidi[1], Maliya Azilah Mohamad Aini[2], Khairul Adzfa Radzun[1*], Nabiha Iran[2], Asmida Ismail[1], Faezah Pardi[1], Wan Razarinah Wan Abdul Razak[1], Sitti Rahma Abd Hafid[2*]

[1] *Universiti Teknologi MARA40450 Shah Alam, Selangor, MALAYSIA.*

[2]*Malaysian Palm Oil Board, No.6 Persiaran Institusi, Bandar Baru Bangi, Kajang Selangor D.E.*

**khairuladzfa@uitm.edu.my , ctrahma@mpob.gov.my*

ABSTRACT

This work aims at determining the synergistic effects of astaxanthin and tocotrienols in reducing inflammation in CALU-3 cell line. Lipopolysaccharide (LPS) was used to cause inflammation and isobologram analysis using Chou-Talalay method applied to evaluate synergism. Preliminary optimization experiments reveal that the best conditions for inflammation induction were 10,000 cells/well and 10ng/mL LPS, measured over 72h with the iCelligence system. Essentially, the synergistic effects of both compounds in moderating the inflammatory markers were established and some interaction combinations had highest decrease in NO levels. Specifically, positive synergy can be observed in all time points with the mixture of 2.0 µg/mL astaxanthin and 1.0 µg/mL tocotrienols. Taken together, this research points to the efficacy of astaxanthin and tocotrienols as a therapeutic option for inflammatory respiratory diseases and emphasizes the necessity of further investigation of the combined anti-inflammatory action in CALU-3 cells.

Keywords: Astaxanthin, Tocotrienols, CALU-3 cells, Inflammation, LPS, Synergism, Isobologram

INTRODUCTION

Inflammation is involved in numerous respiratory diseases and thus, the continued hunt for effective anti-inflammatory agents. Carotenoid, astaxanthin and tocotrienols, a form of vitamin E have been reported to exert anti- inflammatory effects [1], [2]. This present study aims to investigate the joint impact of these two drugs on inflamed CALU-3 cells, a human airway epithelial cell line using isobologram analysis for synergy. There is a significant lack of experimental studies employing LPS to stimulate inflammation in CALU-3 cells, which in leads to limited studies on the potential of astaxanthin and tocotrienols to alleviate inflammation.

Astaxanthin has been described as a powerful antioxidant that exhibits a strong ability to scavenge singlet oxygen and superoxide radicals [1]. It has been reported to have synergistic effects with tocotrienols, another potent antioxidant in several studies. For example, Kogure [1] described how astaxanthin and tocotrienols have a synergistic effect to eliminate singlet oxygen and hydroxyl radicals.

Tocotrienols, a form of vitamin E, are known to be better antioxidants and anti-inflammatory compounds compared to tocopherols. Research has established that tocotrienols effective in decreasing oxidative stress and inflammatory biomarkers [2], [3]. Additionally, synergistic effects have also been illustrated through combined treatments of astaxanthin and tocotrienols in various experiments, especially involving human diet with these two compounds [4], [5].

Isobologram analysis is used in various research to assess the synergistic effects of drugs when they are mixed. The Chou-Talalay method is the most impact approach for the accurate arithmetic in calculating combination indices, which algebraically describe the interrelationships of the compounds [6], [7]. This approach has been applied in previous studies to demonstrate the improved effectiveness of combined antioxidants in different biological models [8], [9].

However, there is still a deficiency of experimental studies using LPS to cause inflammation in CALU-3 cells exclusively. Furthermore, there is a lack of evidence regarding the ability of astaxanthin and tocotrienols to synergistically decrease inflammation in this cell line.

METHODOLOGY

Cell Culture and Inflammation Induction

CALU-3 cells were grown under regular media conditions using Gibco™ RPMI 1640 Medium with GlutaMAX™ Supplement, supplemented with 10% Gibco™ FBS, and 1.0 mM Gibco™ Sodium Pyruvate. The cells were maintained in T-75 flasks and passaged every 3-4 days using Gibco™ TrypLE™ dissociation reagent to prevent senescence. For cell counting, standard trypan blue exclusion was used to ensure >90% viability and 80% confluence on the day of the experiment.

Lipopolysaccharides (LPS) were added at various concentrations (10 ng/mL, 100 ng/mL, 200 ng/mL, 500 ng/mL, and 1000 ng/mL) to induce inflammation, with the optimal conditions determined through experimental optimization described in section 3.2.

Optimization of Cell Count and LPS Concentration

Before running the actual tests, several preliminary experiments were conducted to establish the optimal cell density and LPS concentration needed to trigger a strong inflammatory response in CALU-3 cells. The cells were seeded at densities of 5,000, 10,000, 15,000, 20,000, and 40,000 cells per well, and LPS was added at concentrations of 10 ng/mL, 100 ng/mL, 200 ng/mL, 500 ng/mL, and 1000 ng/mL.

Cells were first counted using a cell counter with trypan blue exclusion to ensure accurate cell densities. These conditions were monitored over 72 hours using the iCELLigence system to characterize the maximum cell index.

Treatment with Astaxanthin and Tocotrienols

The cells that were inflamed with LPS after the optimization experiment (3.2), treated with different concentrations of astaxanthin and tocotrienols, separately as well as in different combination ratios. First, the cells were incubated with astaxanthin at 1, 4, 7, 10, 13, 16, 19, 22 and 25 µg/ml and tocotrienols 1, 4, 7, 10, 13, 16, 19, 22 and 25 µg/ml, and negative and positive controls of each compound [13], Negative controls involved cells only without any treatment to account for the baseline cell response. Positive controls involved cells treated with 10 ng/mL LPS only without any additional treatment to validate the inflammatory response. For achieving almost 50% inhibition, the maximum concentration of both astaxanthin and tocotrienols was set to 4 µg/mL based on the observed Nitric Oxide (NO) reduction. Afterwards, 15 mixtures were prepared by mixing 1, 2 and 4 µg/mL of astaxanthin and tocotrienols to determine their synergistic effects in minimizing inflammation in CALU-3 cells.

Isobologram Analysis

The interaction between astaxanthin and tocotrienols was assessed by the Chou-Talalay method for isobologram analysis on synergistic effects. In this method, combination index (CI) values are determined such that the value of CI < 1 is synergistic, CI = 1 is additive and CI > 1 is antagonistic [13]. The combination index (CI) is calculated using the below formula [13]:

$$C1 = \frac{(D)_1}{(Dx)_1} + \frac{(D)_2}{(Dx)_2}$$

$(D)_1$ and $(D)_2$ are the doses of drug 1 and drug 2 in combination that achieve a given effect, and $(Dx)_1$ and $(Dx)_2$ are the doses of drug 1 and drug 2 alone that achieve the same effect.

In this study, the two bioactive compounds, astaxanthin and tocotrienols were mixed in different ratios. CI values were estimated from the NO reduction data obtained in the experiments-presented in Table 1-3 for 24, 48, and 72 hours, respectively. A CI value less than 1 was an indication that astaxanthin and tocotrienols had a synergistic effect in the CALU-3 cells, thus; helped to magnify the anti-inflammatory activity [13], [14].

RESULTS

Optimization Results

Optimal conditions for inducing inflammation in CALU-3 cells were determined to be at a density of 10,000 cells per well and 10 ng/mL of LPS. Figure1 and 2 illustrate the optimization results.

Figure 1 illustrates the growth of CALU-3 cells over 72 hours at different initial seeding densities (5,000, 10,000, 15,000, 20,000, and 40,000 cells per well). The graph shows that higher initial cell densities lead to a faster

increase in cell index, with 40,000 cells per well reaching the highest growth. The optimal seeding density for further experiments was determined to be 10,000 cells per well, balancing rapid growth without risking over-confluence.

Figure 2 illustrates the response of CALU-3 cells to different concentrations of Lipopolysaccharides (LPS) over 72 hours. The y-axis represents the Cell Index, which measures cell proliferation and response, while the x-axis represents time in hours. The concentrations tested were 0 ng/mL, 10 ng/mL, 100 ng/mL, 200 ng/mL, 500 ng/mL, and 1000 ng/mL. The graph shows that as the concentration of LPS increases, the Cell Index also increases, indicating a stronger inflammatory response. Among the tested concentrations, 1000 ng/mL produced the highest cell index, suggesting the most significant inflammatory effect. However, for subsequent experiments, a concentration of 10 ng/mL was chosen as it provided a strong yet manageable inflammatory response, suitable for assessing the effects of astaxanthin and tocotrienols without overwhelming the system.

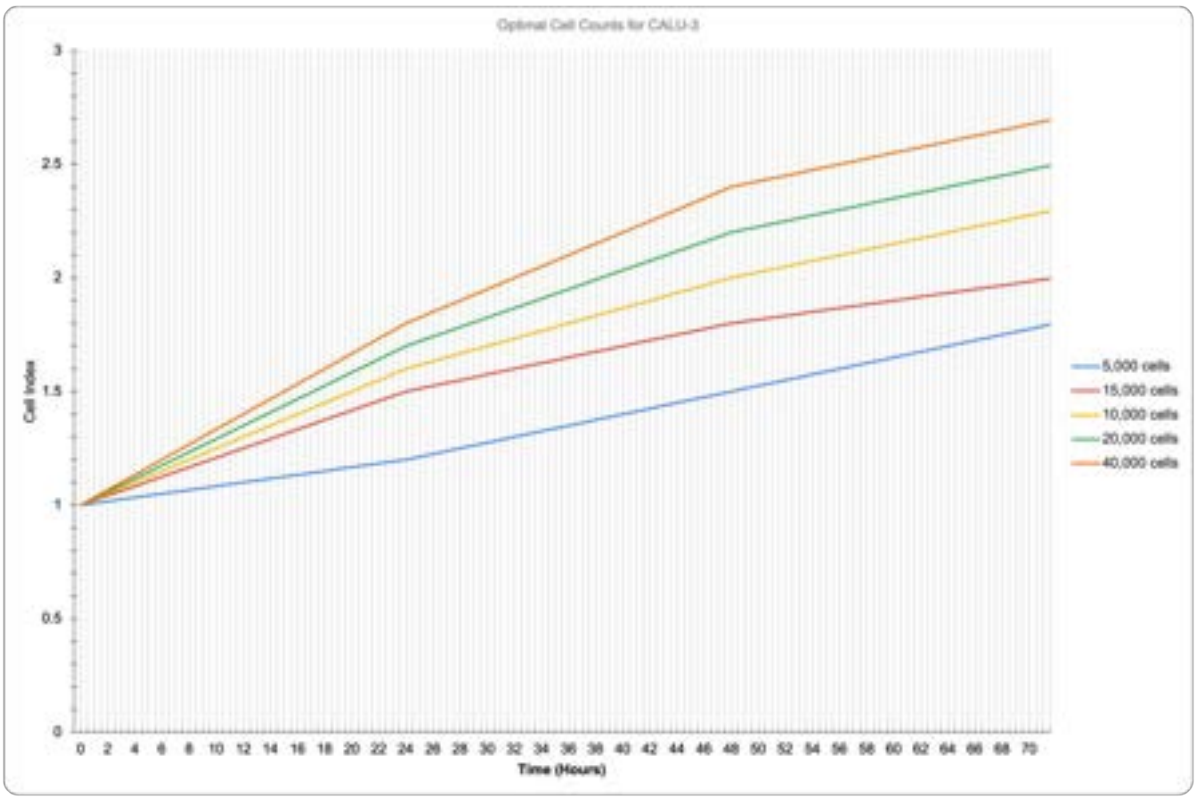

Figure 1. Optimal Cell Counts for CALU-3

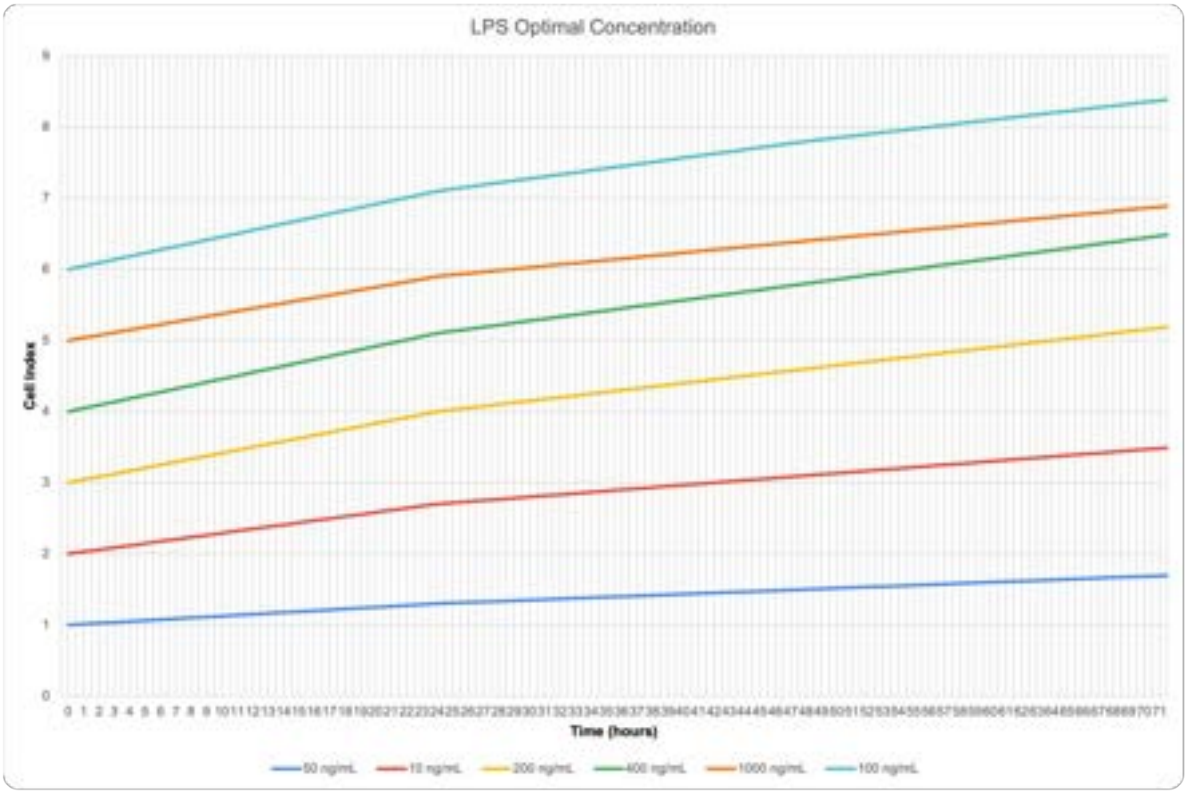

Figure 2. LPS Optimal Concentration

Synergistic Effects

Isobologram analysis revealed a significant synergistic effect between astaxanthin and tocotrienols at specific concentrations, which indicated by a combination index of less than 1 (see Figure 3-5).

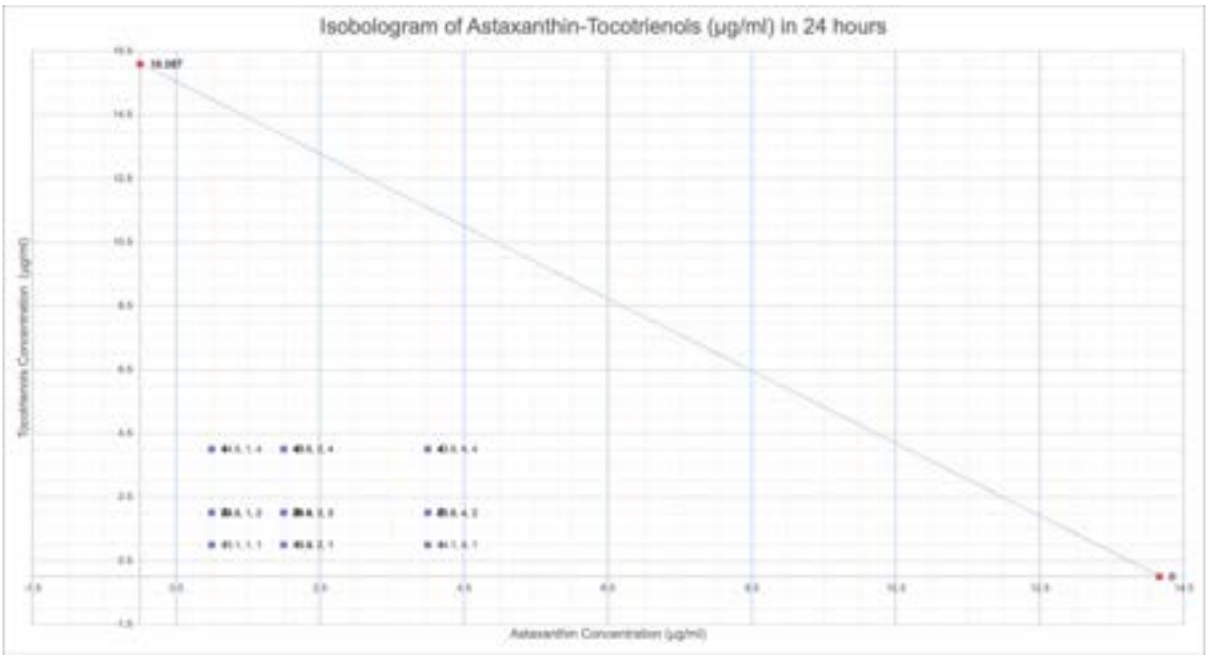

Figure 3. Isobologram of Astaxanthin-Tocotrienols (24 hours)

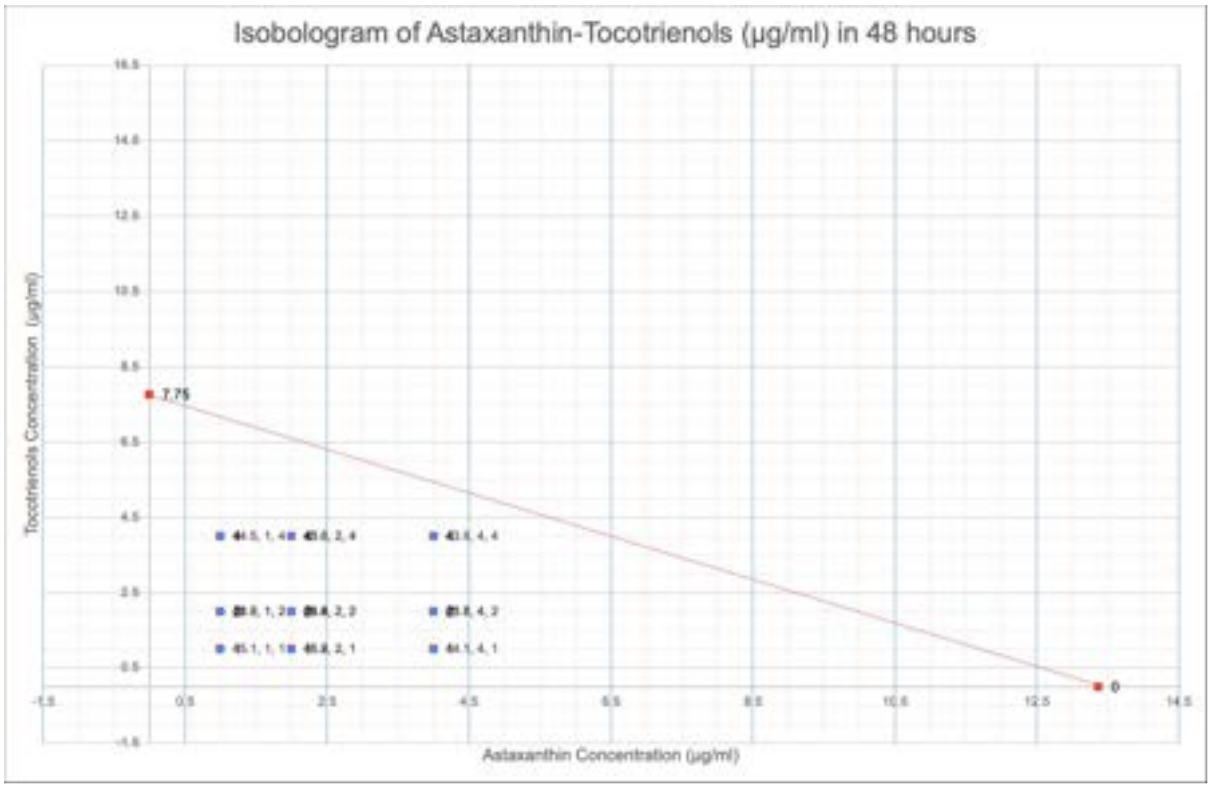

Figure 4. Isobologram of Astaxanthin-Tocotrienols (48 hours)

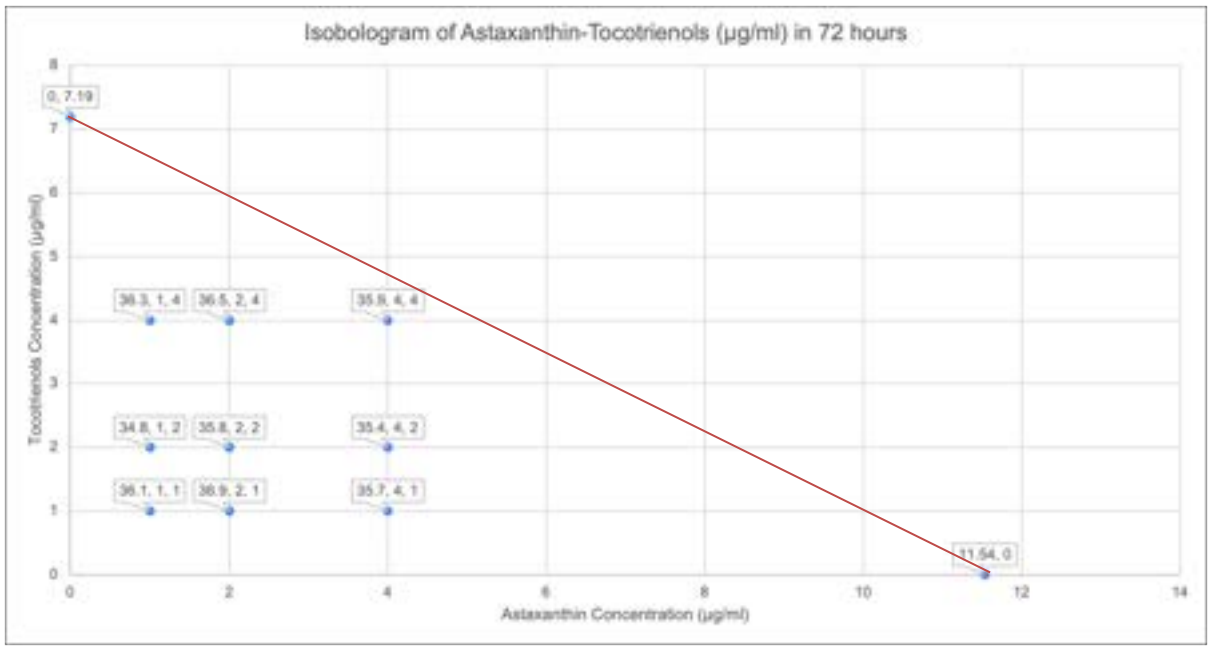

Figure 5. Isobologram of Astaxanthin-Tocotrienols (72 hours)

The concentration and observed NO reduction percentage with combination index (CI) values are shown in Tables 1 to 3 for 24, 48, and 72 hours, respectively.

Table 1. Concentrations and Observed NO Reduction at 24 hours

Astaxanthin Concentration (µg/ml)	Tocotrienols Concentration (µg/ml)	Observed NO Reduction (%)	Combination Index (CI)
4	4	43.9	0.531
2	1	46.2	0.203
1	2	44.8	0.195
4	2	45.7	0.407
2	4	43.6	0.39
1	4	44.5	0.32
4	2	43.5	0.407
1	2	42.8	0.195
2	2	45.9	0.266
2	2	45.3	0.266
4	1	44.1	0.345
1	1	45.1	0.133
2	2	44.4	0.266
2	1	45.8	0.203
2	4	45.6	0.39

Table 2. Concentrations and Observed NO Reduction at 48 hours

Astaxanthin Concentration (µg/ml)	Tocotrienols Concentration (µg/ml)	Observed NO Reduction (%)	Combination Index (CI)
4	4	39.8	0.815
2	1	41.6	0.279
1	2	40.3	0.333
4	2	41.21	0.557
2	4	39.3	0.666
1	4	40.1	0.591
4	2	39.2	0.557
1	2	38.5	0.333
2	2	40.9	0.408
2	2	40.6	0.408
4	1	39.1	0.428
1	1	40.2	0.204
2	2	39.7	0.408
2	1	40.8	0.279
2	4	40.5	0.666

Table 3. Concentrations and Observed NO Reduction at 72 hours

Astaxanthin Concentration (µg/ml)	Tocotrienols Concentration (µg/ml)	Observed NO Reduction (%)	Combination Index (CI)
4	4	35.9	0.903
2	1	37.3	0.312
1	2	36.1	0.365
4	2	36.9	0.625
2	4	35.5	0.73
1	4	36.3	0.643
4	2	35.4	0.625
1	2	34.8	0.365
2	2	36.8	0.451
2	2	36.6	0.451
4	1	35.7	0.486
1	1	36.1	0.226
2	2	35.8	0.451
2	1	36.9	0.312
2	4	36.5	0.73

DISCUSSION

The findings of this research show that there were a strong synergistic interaction between astaxanthin and tocotrienols in the suppression of inflammation in CALU-3 cells. The most effective concentrations for activating inflammation were identified to be 10,000 cells per well and 10 ng/mL of LPS using the iCelligence system for 72 hours [11]. Chou-Talalay isobologram analysis showed that some combinations of astaxanthin and tocotrienols exhibited synergistic effects at CI values less than one [13], [14]. From the data obtained at 24 hours, it could be seen that the significant synergistic effect for 2 µg/mL astaxanthin and 1 µg/mL tocotrienols, with a CI value of 0.203 and an observed NO reduction of 46.2%. Likewise, at 48 hrs, the same agents showed extreme synergistic effect since the CI value equal to 0.279 and an observed NO reduction of 41. 6%. At 72 hours, this combination was still potent with a CI of 0.312 and an observed NO reduction of 37.3%.

Moreover, a combination of astaxanthin (1 µg/mL) with tocotrienols at 2 µg/mL has also shown synergistic effect in all time points, which suggested this compound pair as a promising inflammation suppressor. These results indicated that the synergistic therapy of astaxanthin and tocotrienols could be potentially beneficial in treating inflammatory respiratory disorders, as a lower dose of each compound administrated resulted in increased anti-inflammatory activity, therefore can reduce potential side effects caused by a higher dose [15], [16]. Further research should be addressed to explain the molecular basis of this synergistic effect and validate these observations in *vivo*.

CONCLUSION

This study supports the possibility of a synergetic therapeutic application of astaxanthin and tocotrienols in treating inflammatory respiratory diseases. More elaborate work, however, must be done to explicate the specifics of how the synergism mentioned has been achieved.

ACKNOWLEDGEMENT

The authors would like to thank the Ministry of Higher Education Malaysia (MOHE), Universiti Teknologi MARA (UiTM) and Malaysian Palm Oil Board (MPOB) for the support of the research. This work was supported under Fundamental Grant Scheme (FRGS), MOHE – (600-RMC/GIP 5/3 (046/2022)) and UiTM Grant 600-RMC/FRGS 5/3 (060/2022).

REFERENCES

[1] K. Kogure, "Novel Antioxidative Activity of Astaxanthin and Its Synergistic Effect with Vitamin E," *Journal of Nutritional Science and Vitaminology*, vol. 65, no. Supplement, pp. S109-S112, 2019. https://doi.org/10.3177/jnsv.65.s109

[2] A. Donoso, J. González, A. Muñoz, P. González, and C. Agurto-Muñoz, "Therapeutic uses of natural astaxanthin: An evidence-based review focused on human clinical trials," *Pharmacological Research*, vol. 105479, 2021. https://doi.org/10.1016/j.phrs.2021.105479

[3] R. Huang et al., "Isobologram Analysis: A Comprehensive Review of Methodology and Current Research," *Frontiers in Pharmacology*, vol. 10, 2019. https://doi.org/10.3389/fphar.2019.01222

[4] J. Łuszczki and A. Wlaź, "Isobolographic analysis of interactions – a pre-clinical perspective," *Journal of Pre-Clinical and Clinical Research*, 2023. https://doi.org/10.26444/jpccr/177246

[5] M. Chang and F. Xiong, "Astaxanthin and its Effects in Inflammatory Responses and Inflammation-Associated Diseases: Recent Advances and Future Directions," *Molecules*, vol. 25, 2020. https://doi.org/10.3390/molecules25225342

[6] F. Wan et al., "Protective effects of astaxanthin on lipopolysaccharide-induced inflammation in bovine endometrial epithelial cells," *Biology of Reproduction*, vol. 102, pp. 339-347, 2019. https://doi.org/10.1093/biolre/ioz187

[7] C. Yang et al., "Anti-Inflammatory Effects of Different Astaxanthin Isomers and the Roles of Lipid Transporters in the Cellular Transport of Astaxanthin Isomers in Caco-2 Cell Monolayers," *Journal of Agricultural and Food Chemistry*, vol. 67, no. 22, pp. 6222-6231, 2019. https://doi.org/10.1021/acs.jafc.9b02102

[8] A. Brodzikowska et al., "Role of Lipopolysaccharide, Derived from Various Bacterial Species, in Pulpitis—A Systematic Review," *Biomolecules*, vol. 12, 2022. https://doi.org/10.3390/biom12010138

[9] O. Ajuwon et al., "Red Palm Oil Ameliorates Oxidative Challenge and Inflammatory Responses Associated with Lipopolysaccharide-Induced Hepatic Injury by Modulating NF-κβ and Nrf2/GCL/HO-1 Signaling Pathways in Rats," *Antioxidants*, vol. 11, 2022. https://doi.org/10.3390/antiox11081629

[10] C. Seiler et al., "Epigenetic Changes in Alveolar Type II Lung Cells of A/J Mice Following Intranasal Treatment with Lipopolysaccharide," *Chemical Research in Toxicology*, vol. 32, no. 5, pp. 831-839, 2019. https://doi.org/10.1021/acs.chemrestox.9b00015

[11] N. Sibinovska et al., "Suitability and functional characterization of two Calu-3 cell models for prediction of drug permeability across the airway epithelial barrier," *International Journal of Pharmaceutics*, 2020. https://doi.org/10.1016/j.ijpharm.2020.119484

[12] X. Ji et al., "Evaluation of Calu-3 cell lines as an in vitro model to study the inhalation toxicity of flavoring extracts," *Toxicology Mechanisms and Methods*, vol. 32, pp. 171-179, 2021. https://doi.org/10.1080/15376516.2021.1977880

[13] Q. Gong et al., "Comparison of the TLR4/NFκB and NLRP3 signalling pathways in major organs of the mouse after intravenous injection of lipopolysaccharide," *Pharmaceutical Biology*, vol. 57, pp. 555-563, 2019. https://doi.org/10.1080/13880209.2019.1653326

[14] H. Zhang et al., "Echinacea polysaccharide alleviates LPS-induced lung injury via inhibiting inflammation, apoptosis and activation of the TLR4/NF-κB signal pathway," *International Immunopharmacology*, vol. 88, 2020. https://doi.org/10.1016/J.INTIMP.2020.106974

[15] J. Davino-Chiovatto et al., "Montelukast, Leukotriene Inhibitor, Reduces LPS-Induced Acute Lung Inflammation and Human Neutrophil Activation," *Archivos de Bronconeumologia*, 2019. https://doi.org/10.1016/j.arbres.2019.05.003

[16] T. Fukuta et al., "Enhancement of antioxidative activity of astaxanthin by combination with an antioxidant capable of forming intermolecular interactions," *Free Radical Research*, vol. 54, pp. 818-828, 2019. https://doi.org/10.1080/10715762.2019.1693042

OPTIMIZING HYDROGEN PEROXIDE CONCENTRATIONS DURING PRE-STERILIZATION OF *C. FRUTESCENS* AND *S. LYCOPERSİCUM* LEAF SAMPLES FOR MICROPROPAGATION

Nursuria Md setamam[1], Norrizah Jaafar Sidik[2]

[1]*Universiti Teknologi MARA, 26400 Jengka, Pahang, MALAYSIA*

nursuriasetamam@uitm.edu.my

[2]*Universiti Teknologi MARA, 40450 Shah Alam, Selangor, MALAYSIA*

norri536.uitm.edu.my

ABSTRACT

This study investigates the optimal hydrogen peroxide (H_2O_2) concentrations for pre-sterilizing leaf explants from Capsicum frutescens and Solanum lycopersicum to minimize contamination and necrosis in micropropagation. Ten concentrations (5%-50%) of H_2O_2 were tested with a one-minute application to determine their efficacy in reducing microbial contamination and preserving leaf explant viability via the foliar spray technique. Results indicated a linear increase in necrosis proportional to H_2O_2 concentration over 72 hours, with C. frutescens showing slightly lower necrosis than S. lycopersicum, likely due to its wax cuticle layer. The optimal concentration was found to be 15%, which effectively sterilizes explants with minimal necrosis, while higher concentrations (above 30%) caused significant tissue damage. These findings provide a valuable protocol for pre-sterilization in micropropagation practices, ensuring higher survival rates and reducing contamination.

Keywords: Hydrogen Peroxide, Pre-Sterilization, Leaf Explants, Micropropagation, Capsicum frutescens, Solanum lycopersicum

INTRODUCTION

Capsicum frutescens and *Solanum lycopersicum* are important crops within the Solanaceae family, known for their versatility in medicinal, cosmetic, and culinary applications [1;2]. These plants boast over 3,000 species and nearly 100,000 varieties, including the highly nurtured cherry tomato [2], which provides numerous beneficial properties for agriculture [3;4]. Due to high demand, micropropagation studies aim to enhance these plants, necessitating an efficient protocol for thriving *in-vitro* culture [4;5;6] using various plant organs [6]. However, in this study, the focus was on the leaves of *C. frutescens* and *S. lycopersicum* in which these leaves, waxy adaxial and trichome adaxial leaves, respectively, serve as ideal models due to their abundance and suitability for plant tissue culture [7;8;9]. Leaves are differentiated organs originating from pluripotent stem cells at the shoot apical meristem, offering advantages such as ease of handling, lower difficulty compared to other explants, and minimal destruction to the mother plant [5;9]. Despite these advantages, leaf explants are particularly susceptible to contamination, posing a significant challenge in PTC. High surface contamination can lead to necrosis and decreased viability of the leaf explants, hampering successful micropropagation [5;10;11]

Thus, this study investigates the application of hydrogen peroxide (H_2O_2) for leaf surface pre-sterilization, due to its broad-spectrum antimicrobial activity, low phytotoxicity, and affordability [12;13]. However, determining the optimal concentration and exposure time of H_2O_2 is crucial to balance effective decontamination with minimal necrosis of leaf [14, 15, 16]. The objective of this research is to optimize the concentration of H_2O_2 for pre-sterilization of leaf explants from *C. frutescens* and *S. lycopersicum*, enhancing the success of micropropagation, mainly when leaf sample collection requires storage before micropropagation begins. This study aims to identify an H_2O_2 concentration that effectively reduces surface contamination while maintaining explant viability by minimizing necrosis. The significance of this study lies in its potential to improve micropropagation practices by providing a reliable pre-sterilization protocol. Effective sterilization of leaf explants can lead to higher survival rates and more successful micropropagation outcomes, which are crucial for cultivating these economically and nutritionally essential crops. By addressing the challenge of surface contamination, this research contributes to the broader field of plant tissue culture, enhancing the efficiency and success of in vitro cultivation techniques.

LITERATURE REVIEW

Table 1. Comparison of Hydrogen Peroxide (H2O2) in Natural and Artificial Environments

Aspect	Natural Environment	Artificial Use (Surface Sterilization)
Formation	Produced naturally in biological processes	Synthetically produced and applied
Role	Signaling molecule, defense mechanisms	Disinfectant and sterilizing agent
Mechanism	Regulated by enzymatic breakdown	Oxidizes cellular components to destroy microbes
Application	Involved in plant stress responses	Used to sterilize surfaces and explants
Concentration	Low, tightly regulated by plants	Varied; needs optimization for effectiveness
Advantages	Essential for plant health and ecology	Broad-spectrum, environmentally friendly
Limitations	Potential for oxidative damage if unregulated	It can be corrosive and requires careful handling

This comparison highlights hydrogen peroxide's distinct roles and considerations in natural and artificial contexts, emphasizing its importance and versatility as both a natural signaling molecule and a powerful sterilizing agent for this research study [12, 13, 16, 17, 18, 19, 20].

METHODOLOGY

In this experiment, healthy leaf explants were selected: *C. frutescens* leaves exhibited a shiny, waxy layer and smooth surface, while S. *lycopersicum* leaves had abundant trichomes and a serrated shape. The shape, coloration, spots, lesions, and senescence of the leaves were noted during the selection process. during determine the optimum concentrations of H_2O_2, leaf explants were treated with foliar sprays of H_2O_2 at concentrations of 5%, 10%, 15%, 20%, 25%, 30%, 35%, 40%, 45%, and 50% on both the top and bottom surfaces. After treatment, samples were rinsed with distilled water, dried with sterile tissue paper, and stored in sealed bags. Leaf explants from the optimal H_2O_2 treatment were then cut to 3-4 cm and cultured in Murashige & Skoog (MS) medium with basic sterilization procedures. The MS medium was prepared by dissolving 4.4 g of powder in 1.0 L of sterile distilled water, adjusting the pH to 5.7-6.0, and adding 4.0 g of agar before autoclaving at 121°C and 15 psi for 20 minutes. After one week of observation, the emergence of necrosis and contaminants, including bacteria and fungi, was examined using a stereomicroscope and a compound microscope to assess their impact on leaf morphology.

RESULTS AND DISCUSSION

The results showed that at a high concentration of 30% H_2O_2, necrosis began to emerge along the veins within 24 hours, even though the leaf cells remained fresh and exhibited high durability, as evidenced by the opening stomata (Figure 1a, 1b,1c and 1d). This necrosis was likely due to the volatile bonds of H_2O_2, which easily break and initiate reactions [17]. It was noted that unattached leaves from the plant contained enzymatic catalases and peroxidases that acted against excessive H_2O_2 by transforming it into water and oxygen [21;22;23], thus preserving plant cells from necrosis effects. This protective mechanism was effective against both internal H_2O_2 secretion and external sources such as foliar sprays in agriculture [17;21]. However, once the plant was collected and the sampling procedure was performed, these enzymes no longer provided protection, leading to eventual necrosis when external H_2O_2 was introduced [24]. Depending on the type of plant, explant samples exhibited delayed reactions to H_2O_2 and varying degrees of necrosis due to the breakdown of H_2O_2 bonds. Previous studies showed that a short contact time with a high concentration of H_2O_2 for surface sterilization was optimal [20;23], while another study found that a low concentration of H_2O_2 with a longer contact time of about 20 minutes resulted in the highest explant survival rate during *in vitro* culture [18;20;21]. In terms of the durability of *C. frutescens* and *S. lycopersicum leaf sample*s, the optimal pre-sterilization needed to withstand the actual sterilization and IVC culture by showing a low level of necrosis with no spike in browning [14;24]. Standard IVC testing showed that the pre-sterilization treatment of 15% H_2O_2 for one minute allowed leaf explant morphology to maintain green

coloration with minimal necrosis, compared to 30% H_2O_2, which resulted in browning and necrosis after two days for both species.

In these micropropagation experiments, two contaminants were identified for *C. frutescens* and *S. lycopersicum*: bacteria and fungi (Figure 1e, 1f, 1g, and 1h). The condition of contaminant emergence varied. Although bacterial-fungal co-infections can exhibit antagonistic, synergistic, or cohabitant effects in explants [25], the variety of contaminants in each plate indicated high contamination density and rapid emergence. Some of these "environmental microorganisms" became latent due to the high nutrient availability in MS media, but most bloomed due to the various nutrient content in the MS media [26]. Bacterial colonization tended to prompt cell death, with necrosis appearing as soon as the infection occurred [25;26]. Fungus infections, meanwhile, delayed necrosis [25] of explants by a few days but eventually contaminated entire plates. Within less than three days, all plates exhibited contamination; however, plates with prior sterilization using 15% H_2O_2 showed green explants with a lack of both types of contaminants, especially bacteria, compared to those without 15% H_2O_2, which showed both bacterial and fungal emergence within three days, indicating a high microbial population density on the leaf explant surface. Without prior optimal pre-sterilization, the explants also rotted faster and turned brown, regardless of species.

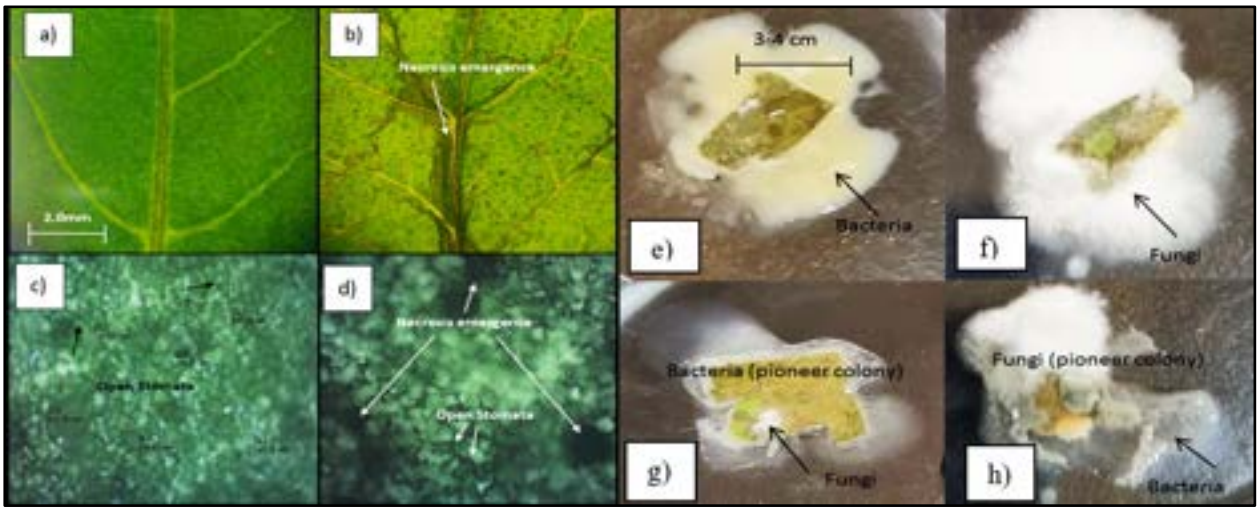

Figure 1. Necrosis and contaminant emergences a) 40x stereomicroscope within 6 hours, b) 40x stereomicroscope within 24 hours; c) 400x stereomicroscope within 6 hours of d) 400 x stereomicroscope within 24 hours, e) bacteria, f) fungi g) bacteria (pioneer colony) with fungi h) fungi (pioneer colony) with bacteria.

CONCLUSION

This study explored the optimal concentration of hydrogen peroxide (H_2O_2) for pre-sterilizing leaf explants from *Capsicum frutescens* and *Solanum lycopersicum* to improve micropropagation success. The optimal pre-sterilization was a 15% H_2O_2 treatment for one minute, which maintained the green color of the leaves and minimized necrosis while effectively reducing high density contamination population from bacteria and fungi. In contrast, explants without prior sterilization showed rapid contamination and browning. Future research should focus on long-term contamination control, sustainable sterilization methods, and testing the effectiveness of the 15% H_2O_2 concentration across different plant species.

ACKNOWLEDGEMENT

The authors would like to thank the staff of the Biology Laboratory at UiTM Jengka Pahang for their support and contribution to the research.

REFERENCES

[1] Sanatombi, K., & Sharma, G. (2008). In vitro plant regeneration in six cultivars of Capsicum spp. Using different explants. Biologia Plantarum, 52(1), 141-145. https://doi.org/10.1007/s10535-008-0029-0.

[2] Peralta, I. E., Spooner, D. M., & Knapp, S. (2008). Taxonomy of wild tomatoes and their relatives (Solanum sect. Lycopersicoides, sect. Juglandifolia, sect. Lycopersicon; Solanaceae). Systematic Botany Monographs, The American Society of Plant Taxonomists, Vol. 84, pp. 186.

[3] Sakthivel, & Manivannan, K. (2021). Effect of foliar application of biostimulants on chili's growth, yield, and quality parameters (Capsicum annuum L). *Research Journal of Agricultural Sciences, 12*(2), 466-469.

[4] Ahmed, S., Wan Azizan, W. A. S., Akhond, M. A. Y., Juraimi, A. S., Ismail, S. I., Ahmed, R., & Md Hatta, M. A. (2023). Optimization of in vitro regeneration protocol of tomato cv. MT1 for genetic transformation. *Horticulturae, 9*(7), 800. https://doi.org/10.3390/horticulturae9070800.

[5] Abdalla, N., El-Ramady, H., Seliem, M., El-Mahrouk, M., Taha, N., Bayoumi, Y., Shalaby, T., & Dobránszki, J. (2022). An academic and technical overview of plant micropropagation challenges. *Horticulturae, 8*(8), 677. https://doi.org/10.3390/horticulturae8080677.

[6] Ogra, S. (2023). Plant tissue culture industry in India: trends and scope. *International Journal of Advanced Biochemistry Research, 7*(1S), 28-33. https://doi.org/10.33545/26174693.2023.v7.i1sa.176.

[7] Hussain, A., Ahmed, I., Nazir, H., & Ullah, I. (2012). Plant tissue culture: Current status and opportunities. *InTech*. https://doi.org/10.5772/50568.

[8] Wijerathna-Yapa, A., & Hiti-Bandaralage, J. (2023). Tissue culture—a sustainable approach to explore plant stresses. *Life, 13*(3), 780. https://doi.org/10.3390/life13030780.

[9] Cardoso, J. C., Sheng, G. L. T., & Teixeira da Silva, J. A. (2018). Micropropagation in the twenty-first century. *Methods in Molecular Biology, 1815*, 17-46. https://doi.org/10.1007/978-1-4939-8594-4_2.

[10] Leifert, C., & Cassells, A. C. (2001). Microbial hazards in plant tissue and cell cultures. *In Vitro Cellular & Developmental Biology - Plant, 37*(2), 133-138. https://doi.org/10.1007/s11627-001-0025-y.

[11] Moreno-Vázquez, S., Larrañaga, N., Uberhuaga, E., Braga, E., & Pérez-Ruíz, C. (2014). Bacterial contamination of in vitro plant cultures: confounding effects on somaclonal variation and detection of contamination in plant tissues. *Plant Cell Tissue and Organ Culture (PCTOC), 119*(3), 533-541. https://doi.org/10.1007/s11240-014-0553-x.

[12] Chihara, R., Kitajima, H., Ogawa, Y., Nakamura, H., Tsutsui, S., Mizutani, M., Kino-Oka, M., & Ezoe, S. (2018). Effects of residual H_2O_2 on the growth of MSCs after decontamination. *Regenerative Therapy, 9*, 111-115. https://doi.org/10.1016/j.reth.2018.08.003.

[13] Brudzynski, K., Abubaker, K., St-Martin, L., & Castle, A. (2011). Re-examining the role of hydrogen peroxide in bacteriostatic and bactericidal activities of honey. *Frontiers in Microbiology, 2*(1), 213.

[14] Zeisler-Diehl, V., Müller, Y., & Schreiber, L. (2018). Epicuticular wax on leaf cuticles does not establish the transpiration barrier, which is essentially formed by intracuticular wax. *Journal of Plant Physiology, 227*, 66-74. https://doi.org/10.1016/j.jplph.2018.03.018.

[15] Caponetti, J., Gray, D., & Trigiano, R. (2005). History of plant tissue and cell culture. In R. N. Trigiano & D. Gray (Eds.), *Plant Development and Biotechnology* (pp. 9-16). Boca Raton, London, New York, Washington DC: CRC Press.

[16] Yanagawa, H., et al. (1995). Hydrogen peroxide as a chemical sterilizer. *Journal of Plant Research, 108*(2), 113-120.

[17] Yoo, J. H. (2018). Review of disinfection and sterilization - Back to the basics. *Infection & Chemotherapy, 50*(2), 101-109. https://doi.org/10.3947/ic.2018.50.2.101.

[18] Linley, E., Denyer, S. P., McDonnell, G., Simons, C., & Maillard, J.-Y. (2012). Use of hydrogen peroxide as a biocide: New consideration of its mechanisms of biocidal action. *Journal of Antimicrobial Chemotherapy, 67*(7), 1589-1596. https://doi.org/10.1093/jac/dks129.

[19] McDonnell, G. (2014). The use of hydrogen peroxide for disinfection and sterilization applications. In Z. Rappoport (Ed.), *PATAI'S Chemistry of Functional Groups*.

[20] Metwaly, A., Salama, G. M., & Ali, G. A. (2018). Using hydrogen peroxide for reducing bacterial contamination in date palm tissue culture. *International Journal of Advances in Agricultural Science and Technology, 5*(4), 25-33.

[21] Curvetto, N. R., Marinangeli, P. A., & Mockel, G. C. (2006). Hydrogen peroxide in micropropagation of Lilium: A comparison with a traditional methodology. *Biocell, 30*(3), 497-500. https://doi.org/10.32604/biocell.2006.30.497.

[22] Finnegan, M., Linley, E., Denyer, S. P., McDonnell, G., Simons, C., & Maillard, J.-Y. (2010). Mode of action of hydrogen peroxide and other oxidizing agents: differences between liquid and gas forms. *Journal of Antimicrobial Chemotherapy, 65*(10), 2108-2115.

[23] Ikai, H., Nakamura, K., Shirato, M., Kanno, T., Iwasawa, A., Sasaki, K., Niwano, Y., & Kohno, M. (2010). Photolysis of hydrogen peroxide, an effective disinfection system via hydroxyl radical formation. *Antimicrobial Agents and Chemotherapy, 54*(1), 5086-5091.

[24] Permadi, N., Nurzaman, M., Alhasnawi, A., Doni, F., & Julaeha, E. (2023). Managing lethal browning and microbial contamination in Musa spp. Tissue culture: Synthesis and perspectives. *Horticulturae, 9*(4), 453. https://doi.org/10.3390/horticulturae9040453.

[25] Nogueira, F., Sharghi, S., Kuchler, K., & Lion, T. (2019). Pathogenetic impact of bacterial-fungal interactions. *Microorganisms, 7*(10), 459. https://doi.org/10.3390/microorganisms7100459.

[26] Ali, M., Boonerjee, S., Islam, M. N., Saha, M. L., Hoque, M. I., & Sarker, R. H. (2018). Endogenous bacterial contamination of plant tissue culture materials: Identification and control strategy. *Plant Tissue Culture and Biotechnology, 28*(1), 99-108.

SCREENING AND ANTIMICROBIAL SUSCEPTIBILITY OF COMMON PATHOGENIC BACTERIA IN COMMERCIALLY PREPARED BURGER PATTIES

Nur Husna Fatnin Mohd Lawi[1], Noorlis Ahmad[1*]

[1]*Faculty of Applied Sciences, UiTM Cawangan Negeri Sembilan, Kampus Kuala Pilah, 72000 Kuala Pilah, Negeri Sembilan*

**anorlis@uitm.edu.my*

ABSTRACT

Foodborne diseases or also known as food poisoning, are a major global public health concern that has been caused by consuming food or beverages that have been contaminated with pathogenic microorganisms. This study aimed to quantify the presence of common pathogenic bacteria and determine its antimicrobial susceptibility in commercially prepared beef burger patties. Various microbiology techniques such as sample collection, pre-enrichment, serial dilution, plate counting, identification methods and antimicrobial susceptibility test were applied. Out of fifteen (15) isolates obtained, four (4) of them were *Escherichia coli*, six (6) of them were *Shigella* sp. and five (5) of them were *Pseudomonas aeruginosa*. Overall, *Escherichia coli* isolates were highly resistant towards Neomycin, Streptomycin, Ampicillin, Chloramphenicol, Cephalothin, Ceftazidime, Erythromycin, Clindamycin, Doxycycline and Sulphamethoxazole. Additionally, *Shigella* sp. isolates were highly resistant towards Neomycin, Streptomycin, Ceftazidime, Erythromycin, Clindamycin and Sulphamethoxazole. Furthermore, *Pseudomonas aeruginosa* isolates were highly resistant towards Neomycin, Cephalothin, Ceftazidime, Erythromycin, Clindamycin, Furazolidone and Sulphamethoxazole. The multiple antibiotic resistance (MAR) index of all (15) isolates were more than 0.2 ranging from 0.50 to 0.93. The high MAR index values indicate an extensive antibiotic resistance that has frequent exposure to multiple antibiotics. Further research should be conducted to identify the resistant genes, virulence, and the whole genome sequencing.

***Keywords*:** Common pathogenic bacteria, beef burger patties, antibiotic susceptibility, MAR index

INTRODUCTION

Burger patties have been linked to several foodborne disease outbreaks. These patties, which are frequently made from ground meat, can act as a bacterial reservoir. This study aimed to quantify the presence of common pathogenic bacteria and determine its antimicrobial susceptibility in commercially prepared beef burger patties. Some burger patties are frequently consumed without further cooking, such as in rare or medium-rare burgers. Unless the burger patty is fully cooked, these bacteria can remain alive on the inside and pose a risk to any potential bacterial contamination. Commercially prepared burger patties are burger patties that are produced in a mass production to be commercialised in large quantities around the country. On the other hand, common pathogenic bacteria means that the bacteria caused the most illnesses, hospitalizations and even deaths and this include bacteria such as *Escherichia coli*, *Shigella* sp. and *Pseudomonas aeruginosa*. Various microbiological techniques such as sample collection, pre-enrichment, serial dilution, plate counting, identification methods such as biochemical tests were applied in this study. Antimicrobial susceptibility testing was carried out to determine the susceptibility patterns of isolated bacterial strains to commonly used antibiotics. Out of fifteen isolates obtained, four of them were *Escherichia coli*, six of them were *Shigella* sp. and five of them were *Pseudomonas aeruginosa*. Overall, *Escherichia coli* isolates were highly resistant towards Neomycin, Streptomycin, Ampicillin, Chloramphenicol, Cephalothin, Ceftazidime, Erythromycin, Clindamycin, Doxycycline and Sulphamethoxazole. Additionally, *Shigella* sp. isolates were highly resistant towards Neomycin, Streptomycin, Ceftazidime, Erythromycin, Clindamycin and Sulphamethoxazole. Furthermore, *Pseudomonas aeruginosa* isolates were highly resistant towards Neomycin, Cephalothin, Ceftazidime, Erythromycin, Clindamycin, Furazolidone and Sulphamethoxazole. The multiple antibiotic resistance (MAR) index of all 15 isolates were more than 0.2 ranging from 0.50 to 0.93.

MATERIALS AND METHODS

This study utilised nutrient broth, nutrient agar, MacConkey agar, Gram stain reagents, Methyl red indicator, MR-VP broth, Tryptophan broth, Kovac's reagent, Alpha-naphthol, Potassium hydroxide, Mueller Hinton agar, Simmons Citrate agar, distilled water, and a range of antibiotics such as Kanamycin, Gentamicin,

Neomycin, Streptomycin, Ampicillin, Imipenem, Chloramphenicol, Cephalothin, Ceftazidime, Erythromycin, Clindamycin, Doxycycline, Furazolidone and Sulphamethoxazole. Beef burger patties from three brands (Brand A, Brand B, Brand C) were purchased in Kuala Pilah, Negeri Sembilan and stored at 4°C in their original packaging until analysed. Each sample was weighed (10g) and homogenised in 90 mL of nutrient broth using a stomacher for 60 seconds to create a homogeneous mixture. The homogenised sample was incubated at 37°C overnight to promote bacterial growth (Ajourloo et al., 2021). Serial dilutions were performed by transferring 1 mL of the homogenised sample into 9 mL of nutrient broth and continued until it reaches the dilution factor of 10^{-9}. A 0.1 mL aliquot from each dilution was plated onto MacConkey agar and spread uniformly using a sterile spreader. Plates were incubated at 37°C overnight, allowing bacterial colonies to develop (Ben-David & Davidson, 2014). After that, the colonies were counted using the Plate Count Method. A single colony from each plate was isolated, purified on MacConkey agar, and then inoculated onto nutrient agar slants for further testing (O'Toole, 2016). Isolated bacterial colonies were subjected to Gram staining and the IMViC test (Indole test, Methyl Red test, Voges-Proskauer test, and Simmons Citrate test) to identify the bacteria (Aryal, 2022). The Kirby-Bauer disc diffusion method was utilised to assess the susceptibility of the bacterial isolates to 14 different antibiotics. The diameters of inhibition zones were measured after incubation and interpreted according to CLSI guidelines (Delgado, 2021). The MAR index of the isolated bacteria was calculated to assess the level of antibiotic resistance.

RESULTS AND DISCUSSION

Colonies on MacConkey agar

As illustrated in Figure 1, there are two types of colonies which are pink colonies and colourless colonies present on the MacConkey agar. The pink colonies indicate that the colonies are lactose-fermenting bacteria meanwhile the colourless colonies indicate that the colonies are non-lactose-fermenting bacteria.

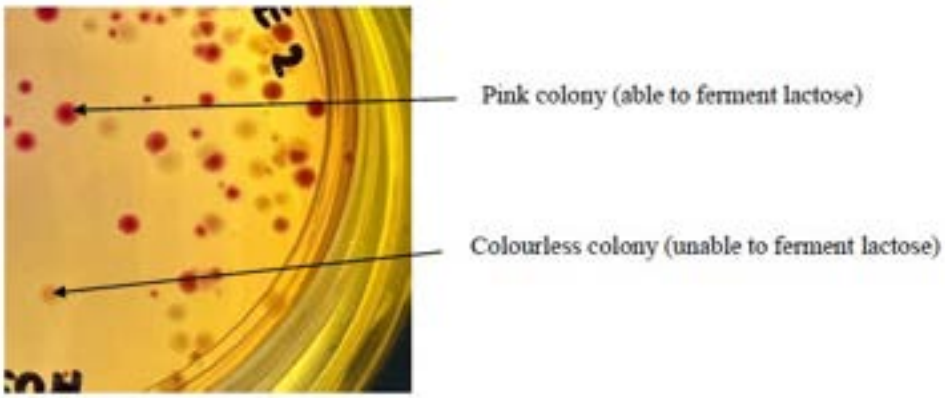

Figure 1. Characteristics of the growth on MacConkey agar

Plate count method in CFU/g of pink and colourless colonies

Brand A showed the highest bacterial load with the values of 1.27 x 10^8 CFU/g for pink colonies and 9.10 x 10^7 CFU/g for colourless colonies. On the other hand, Brand B showed the lowest bacterial load with the values of 1.02 x 10^6 CFU/g for pink colonies and 6.80 x 10^5 CFU/g for colourless colonies. Apart from that, Brand C also showed presence of pink and colourless colonies but they were not in countable range as they were Too Many to Count (TMTC) and Too Few to Count (TFTC). The high bacterial load showed significant contamination making the beef burger patties unsafe for consumption unless it is fully cooked to 75ºC for at least 30 seconds (Centre for Food Safety, 2022).

Biochemical test and Gram staining of the isolates

From three brands of beef burger patties, fifteen isolates were obtained. All of the isolates were Gram-negative. Brand A had three isolates and all of them identified as *Escherichia coli*. The presence of *E. coli* can be linked to contamination from faecal sources (Khan & Gupta, 2020). On the other hand, Brand B had seven isolates and six of them were identified as *Shigella* sp. meanwhile one of them was identified as *E. coli*. The presence of *Shigella* sp. can be linked to contamination from an infected food handler that practices poor hygiene while handling the raw materials in the production of burger patties (Bhutia et al., 2021). Apart from that, Brand C had five isolates and all of them identified as *Pseudomonas aeruginosa*. The presence of *P. aeruginosa* can be linked

to poor sanitation in meat shops, unhygienic processing practices, and a lack of awareness among meat retailers about essential requirements and guidelines for maintaining a clean meat shop (Elbehiry et al., 2022).

Antibiotic susceptibility test on *E. coli*, *Shigella* sp. and *P. aeruginosa* isolates

In this study, 4 isolates of *Escherichia coli*, 6 isolates of *Shigella* sp. and 5 isolates of *Pseudomonas aeruginosa* from three different brands of burger patties were tested with 14 types of antibiotics namely Kanamycin (K30), Gentamicin (CN10), Neomycin (N10), Streptomycin (S10), Ampicillin (AM10), Imipenem (IPM10), Chloramphenicol (C30), Cephalothin (KF30), Ceftazidime (CAZ30), Erythromycin (E15), Clindamycin (DA2), Doxycycline (DO30), Furazolidone (FR100) and Sulphamethoxazole (RL25).

E. coli isolates were highly resistance to 10 different antibiotics namely Neomycin, Streptomycin, Ampicillin, Chloramphenicol, Cephalothin, Ceftazidime, Erythromycin, Clindamycin, Doxycycline and Sulphamethoxazole, with the percentage of resistance between 75% to 100%. This aligned with the previous study by Adzitey et al. (2020) with 71.67% of *E. coli* isolates being resistant towards Ampicillin and 85% of the isolates being resistant towards Erythromycin. On the other hand, only one type of antibiotic which is Gentamicin that *E.coli* isolates highly susceptible to with the percentage of susceptible of 75% and this also aligned with the previous study by Adzitey et al. (2020) with 88% of the *E. coli* isolates being susceptible to Gentamicin.

On the other hand, *Shigella* sp. isolates were highly resistant to 6 different antibiotics namely Neomycin, Streptomycin, Ceftazidime, Erythromycin, Clindamycin, and Sulphamethoxazole with the percentage of resistance of 100%. This aligned with the previous study by Pakbin et al. (2021) with 66.6% of *Shigella* sp. isolates being resistant towards Streptomycin and 50% of the isolates being resistant towards Ampicillin. On the other hand, there are 5 types of antibiotics which are Kanamycin, Gentamicin, Imipenem, Doxycycline and Furazolidone that *Shigella* sp. isolates were highly susceptible with the percentage between 67% to 100%. In the previous research by Pakbin et al. (2021) also reported the similar results with 100% of *Shigella* sp. isolates being susceptible towards Gentamicin.

Apart from that, *P. aeruginosa* isolates were highly resistant to 7 different antibiotics namely Neomycin, Cephalothin, Ceftazidime, Erythromycin, Clindamycin, Furazolidone and Sulphamethoxazole with the percentage of resistance between 80% to 100%. In the previous research by Arbab et al. (2023) also reported the similar results with 80% of *P. aeruginosa* isolates being resistant towards Erythromycin. On the other hand, there are 4 type of antibiotics which are Gentamicin, Ampicillin, Chloramphenicol and Doxycycline that *P. aeruginosa* isolates were highly susceptible with the percentage between 80% to 100%. In the previous research by Jauher & Hasan (2023) also reported similar results with 80% *P. aeruginosa* isolates susceptible towards Gentamicin.

Multiple Antibiotic Resistance (MAR) index and Antibiotic Resistance Pattern

Table 1 shows the antibiotics resistance patterns and multiple antibiotic resistance pattern (MAR) index of *Escherichia coli*, *Shigella* sp. and *P. aeruginosa* isolates. The number of resistance patterns for 4 of the *E. coli* isolates were in between 9 to 13 with MAR index values ranging from 0.64 to 0.93. This aligns with findings from Adzitey et al. in 2020 with the MAR index of 0.63 and 0.60 in the raw beef samples. Similarly, a study conducted by Datok et al. (2021) reported the MAR index of 0.5 to 1.0 in the kebab samples sold in a Nigerian city. Datok et al. (2021) and Adzitey et al. (2020) also stated that a MAR index of 0.4 and above is associated with human faecal source contamination and a MAR index of less than 0.4 is associated with nonhuman faecal contamination. On the other hand, the number of resistance patterns for 6 of the *Shigella* sp. isolates were in between 7 to 8 with MAR index values ranging from 0.50 to 0.57. This aligns with findings from Arbab et al. (2023) with the MAR index ranging from 0.6 to 0.9 from healthy cattle samples. On the other hand, the number of resistance patterns for 5 of the *Pseudomonas aeruginosa* isolates were in between 9 to 11 with MAR index values ranging from 0.64 to 0.79. This aligns with findings from a study conducted by Badawy et al. (2023) with the MAR index ranging from 0.44 to 0.77 in the samples originating from cows and their drinking water. The high MAR index values for *E.* coli, *Shigella* sp. and *P. aeruginosa* isolates indicate an extensive antibiotic resistance that has frequent exposure to multiple antibiotics. This is also highly likely due to improper use or overuse of antibiotics in the food production environment.

Table 1. Antibiotics resistance patterns and multiple antibiotic resistance pattern (MAR) index of *E.coli*, *Shigella* sp. and *P. aeruginosa* isolates

Bacteria	Isolate no.	[a]Resistance Pattern	No of Resistance patterns	[b]MAR Index
E. coli	A1	AmCCazDaDoEFrIpmKKfNRlS	13	0.93
	A2	AmCCazDaDoEFrIpmKKfNRlS	13	0.93
	A3	AmCCazCnDaDoEFrIpmKfNRlS	13	0.93
	B7	AmCazDaEFrKfNRlS	9	0.64
Shigella sp.	B1	AmCazDaEKfNRlS	8	0.57
	B2	AmCazDaEFrNRlS	8	0.57
	B3	AmCazDaEKfNRlS	8	0.57
	B4	AmCazDaEKfNRlS	8	0.57
	B5	AmCazDaENRlS	7	0.50
	B6	AmCazDaEFrNRlS	8	0.57
P. aeruginosa	C1	AmCazDaEFrIpmKKfNRlS	11	0.79
	C2	CazDaEFrIpmKfNRlS	9	0.64
	C3	CazDaEIpmKKfNRlS	9	0.64
	C4	CCazDaEFrIpmKfNRlS	10	0.71
	C5	AmCazDaEFrIpmKKfNRlS	11	0.79

[a]Tested for Kanamycin (K30), Gentamicin (CN10), Neomycin (N10), Ampicilin (AM10), Imipenem (IPM10), Chloramphenicol (C30), Cephalothin (KF30), Ceftazidime (CAZ30), Erythromycin (E15), Clindamycin (DA2), Doxycycline (DO30), Furazolidone (FR100), Streptomycin (S10) and Sulphamethoxazole (RL25).

[b]MAR index = $\frac{\text{The number of antibiotics to which isolates was resistant (a)}}{\text{Total number of antibiotics to which isolates was exposed (b)}}$

CONCLUSION

To conclude, from three different brands, Brand A has the highest plate count value in CFU/g in both pink and colourless colonies. Furthermore, there are three bacteria that can be found in beef burger patties which are *Escherichia coli*, *Shigella* sp. and *Pseudomonas aeruginosa*. Apart from that, there are significant resistance to multiple antibiotics observed and *E. coli* showed the highest range of MAR index. The high resistance of these common pathogenic bacteria emphasises the importance of farmers using fewer antibiotics in livestock production and relying on good management practices to prevent diseases that require the use of antibiotics. Moreover, it is crucial to properly handle the burger patties such as cooking them thoroughly rather than consuming them medium or medium-rare. In addition, more extensive sampling are required to understand any potential variation in the screening of these common pathogenic bacteria as well as their antibiotic resistance profiles. Further research involving the molecular characterization of resistant strains and identification of resistance mechanisms are also highly recommended to determine the resistant genes, virulence, and the whole genome sequencing.

REFERENCES

Adzitey, F., Assoah-Peprah, P., Teye, G. A., Somboro, A. M., Kumalo, H. M., & Amoako, D. G. (2020). Prevalence and Antimicrobial Resistance of Escherichia coli Isolated from Various Meat Types in the Tamale Metropolis of Ghana. *International Journal of Food Science*, *2020*, 1–7. Retrieved from https://doi.org/10.1155/2020/8877196

Ajourloo, M., Khanjari, A., Misaghi, A., Basti, A. A., Kamkar, A., Yadegar, F., Gholami, F., Khansavar, F., & Fallah, F. (2021). Combined effects of Ziziphora clinopodioides essential oil and lysozyme to extend shelf life and control *Listeria monocytogenes* in Balkan-style fresh sausage. *Food Science and Nutrition*, *9*(3), 1665–1675. Retrieved from https://doi.org/10.1002/fsn3.2141

Arbab, S., Ullah, H., Wei, X., Wang, W., Ahmad, S. U., & Zhang, J. (2023). Drug resistance and susceptibility testing of Gram-negative bacterial isolates from healthy cattle with different β – Lactam resistance Phenotypes from Shandong province China. *Brazilian Journal of Biology*, *83*. Retrieved from https://doi.org/10.1590/1519- 6984.247061

Aryal, S. (2022, September 7). *IMVIC Test- Principle, Result Chart, Examples, Uses*. Microbe Notes. Retrieved February 2, 2024, from https://microbenotes.com/imvic-tests/

Badawy, B., Moustafa, S., Shata, R., Sayed-Ahmed, M. Z., Alqahtani, S. S., Ali, M. S., Alam, N., Ahmad, S., Kasem,

N., Elbaz, E., El-Bahkiry, H. S., Radwan, R. M., El-Gohary, A., & Elsayed, M. M. (2023). Prevalence of Multidrug-Resistant Pseudomonas aeruginosa Isolated from Dairy Cattle, Milk, Environment, and Workers' Hands. *Microorganisms*, *11*(11), 2775. Retrieved from https://doi.org/10.3390/microorganisms11112775

Ben-David, A., & Davidson, C. E. (2014). Estimation method for serial dilution experiments. *Journal of Microbiological Methods*, *107*, 214–221. Retrieved from https://doi.org/10.1016/j.mimet.2014.08.023

Bhutia, M. O., Thapa, N., & Tamang, J. P. (2021). Molecular characterization of bacteria, detection of enterotoxin genes, and screening of antibiotic susceptibility patterns in traditionally processed meat products of Sikkim, India. *Frontiers in Microbiology*, *11*. Retrieved from https://doi.org/10.3389/fmicb.2020.599606Centers for Food Safety. (2022, March). *Beef Burgers Food Safety Guidelines for Food Businesses*. Retrieved July 20, 2024, from https://www.cfs.gov.hk/english/whatsnew/whatsnew_fst/files/Beef_e.pdf

Datok, D. W., Ishaleku, D., Tsaku, P. A., Agya, E. O., & Adoga, M. P. (2021). Multidrug resistance to commonly prescribed antibiotics in Escherichia coli isolated from barbecued beef (Suya) sold in a Nigerian City. *˜ the oe Pan African Medical Journal*, *39*. Retrieved from https://doi.org/10.11604/pamj.2021.39.50.25502

Delgado, E. (2021, May 6). *Salmonella spp. antibiotic susceptibility testing by the Kirby-Bauer disk diffusion method*. protocols.io. Retrieved December 17, 2023, from https://www.protocols.io/view/*Salmonella*-spp- antibiotic-susceptibility- testing-b-n92ld9p1og5b/v1

Elbehiry, A., Marzouk, E., Aldubaib, M., Moussa, I., Abalkhail, A., Ibrahem, M., Hamada, M., Sindi, W., Alzaben, F., Almuzaini, A. M., Algammal, A. M., & Rawway, M. (2022). Pseudomonas species prevalence, protein analysis, and antibiotic resistance: an evolving public health challenge. *AMB Express*, *12*(1). Retrieved from https://doi.org/10.1186/s13568-022-01390-1

Jawher, I. M., & Hasan, M. G. (2023). Antibiotics resistance patterns of Pseudomonas aeruginosa isolated from meat at Mosul city retails. *˜ Al-oe Mağallaẗ Al- 'irāqiyyaẗ Li-l-'ulūm Al-bayṭariyyaẗ/Iraqi Journal of Veterinary Sciences*, *37*(2), 363–367. Retrieved from https://doi.org/10.33899/ijvs.2022.133961.2322

Khan, F. M., & Gupta, R. (2020). Escherichia coli (E. coli) as an Indicator of Fecal Contamination in Groundwater: A Review. *Environmental Science and Engineering*, 225–235. Retrieved from https://doi.org/10.1007/978-3-030- 45263-6_21

O'Toole, G. A. (2016). Classic Spotlight: Plate Counting you can count on. *Journal of Bacteriology*, *198*(23), 3127. Retrieved from https://doi.org/10.1128/jb.00711-16

Pakbin, B., Amani, Z., Allahyari, S., Mousavi, S., Mahmoudi, R., Brück, W. M., & Peymani, A. (2021). Genetic

diversity and antibiotic resistance of Shigella spp. isolates from food products. *Food* https://doi.org/10.1002/fsn3.2603

FATTY ACID PROFILES OF URINARY EXTRACELLULAR VESICLES USING GAS CHROMATOGRAPHY

Nur Nazira Nabila Amiszan [1], Nur Fatinah Adenan [2], Iqbal Jalaludin[3], Mohd Aizuddin Mohd Lazaldin[4]

[1,2,3]*Department of Chemistry, Faculty of Science, Universiti Teknologi Malaysia*
81310 Johor Bahru, Johor, MALAYSIA
[4]*Department of Bioscience, Faculty of Science, Universiti Teknologi Malaysia*
81310 Johor Bahru, Johor, MALAYSIA

[1]*nazira1999@graduate.utm.my,*[2]*nurfatinahadenan@gmail.com,* [3] *muhamadiqbal.j@utm.my,*
[4]*mohdaizuddin@utm.my*

ABSTRACT

Extracellular vesicles (EVs) are membrane-bound nanoparticles released by cells to facilitate intercellular communication. They can potentially be used in medicine for diagnosis, prognosis and drug delivery systems. Ultracentrifugation is the current gold standard for isolating EVs, but the constantly changing parameters to maximize yield and purity highlight the research gap in achieving an optimal isolation method. This study aims to optimize the EV isolation method from urine using ultracentrifugation. The number of centrifugation cycles was first determined prior to optimization. As a result, particle size analysis (PSA) revealed that the one-cycle centrifugation EV showed more monodispersed particles than the two-cycles centrifugation. The size distribution for one-and two-cycle centrifugation were 93.1167 and 177.3333 respectively. of the particles. Furthermore, the bicinchoninic acid (BCA) protein assay showed that the two-cycles centrifugation EVs contained fewer proteins than the one-cycle centrifugation EVs. This implies the elimination of non-EV proteins, resulting in highly pure EVs. The findings of these investigations can help develop a more efficient and reliable technique for ensuring higher purity and yields of EVs, which is critical for downstream applications.
Keywords: Extracellular Vesicles, Isolation, Ultracentrifugation

INTRODUCTION

Extracellular vesicles (EVs) are nanosized vesicles released by cells in eukaryotes and prokaryotes organisms that act as communication tools with another cell (1). EVs that are released by their parent cell carries cargo and information from their parent cell to the recipient cell. In human, among the cargo that EVs carries include protein, lipid, glycan and genome information (1). Parent cell release EV into extracellular environment of the body and can be found in biofluid secretion such as urine, saliva and blood (1). Over the decade, massive research has been done to explore many metabolites in EV especially protein, mRNA and lipid (3). Hence, EVs have attracted the attention of many researchers from various fields, prompting further exploration. For instance, the metabolomic analysis has been proven to differentiate between healthy and sick population in variety of disease, such as cancer (1), autoimmune disease and inflammatory disease (2). Thus, EVs possess potential to be engineered as disease biomarker and drug delivery agents.

Although there has been a significant amount of study conducted on EVs, there are still some necessary processes that must be taken in order to obtain accurate and precise analytical results for EVs. The steps involved in this process are sample collection, isolation, characterisation, and EV analysis. Out of all these steps, the isolation stage is the most critical. An optimal isolation process is crucial for achieving both high production and purity of EVs. Ultracentrifugation (UC) is the most commonly employed method for isolation (4). The simplicity and time efficiency of UC have made it a favoured choice among researchers, contributing to its convenience and popularity compared to alternative methodologies. Nevertheless, there is currently no established process for UC that ensures the utmost efficiency and cleanliness of EVs (4). Various investigations have employed different ultracentrifugation speeds and durations, hence confounding the ability to compare the obtained results. Hence, this study aims to optimize the method of isolating EVs in order to establish a universally accepted protocol for EV isolation.

METHODOLOGY

Urine sample collection

Midstream, morning urine from six healthy volunteers aged 21-51 were pooled. The urine samples were treated with dithiothreitol to make the concentration of 4.05×10-3 M to release entrapped EV by uromodulin protein.

EV Isolation

Samples were centrifuged using Beckman Coulter Allegra X-15GR Centrifuge at 2,000 xg (30 minutes), 17,000 xg (15 minutes), and ultracentrifuged with Thermo Scientific WX Ultra Series Centrifuge at 200,000 xg for 2 hours, all at 4°C. To investigate the optimized method of EV isolation, another cycle of ultracentrifugation is introduced after the first cycle of ultracentrifugation, at the same speed, time, and temperature. At the end of ultracentrifugation, the white pellet suspended at the bottom of the tube that is expected to be EV is carefully collected, added with 100µL PBS, and stored at -80°C to avoid EV degradation.

Characterization of EV

Isolated EV sample was then characterized by BCA Protein Assay to determine the protein concentration in both cycles and urine control. The protocol on purchased BCA Protein Assay was followed and the absorbance was determined with microplate reader BMG Labtech Spectrostar Nano Microplate Reader for absorbance reading. Another characterization done in this research is a Particle Size Analyzer (PSA) to determine the size of vesicles isolated in 1-cycle and 2-cycles by using Malvern Mastersizer 3000 instrument. The sample was diluted with 10 mL PBS at a ratio 1:300 for suitability in the instrument. The purity and yield was observed by looking at the PSA and BCA protein Assay result.

RESULTS

Bicinchoninic Acid (BCA) Protein Assay

Standard working solution with known protein concentration was prepared according to the instructed protocol. From the absorbance, a standard curve of concentration against absorbance was plotted. The correlation coefficient, R^2 was calculated, giving value of 0.9954, indicating a well-fit regression of known concentration to the absorbance. Hence, the linear equation can be used to calculate the protein concentration of sample. From linear equation $y= 1.0185x – 0.0006$, the concentration of protein is calculated and depicted in Figure 2 to test whether there is significant loss of protein between sample and control, t-test statistical test was carried out. At significant difference 95% ($\alpha= 0.05$), p-value is lower than α, null hypothesis is rejected, hence there is significant difference of protein concentration between control and sample. There are few reasons that may explain lower protein concentration as cycle increase. As the cycle increase, As the cycle increase, we were able to remove higher density protein that retained in the sample. The protein removed was suspected to be non tetraspanins, such as albumin and uromodulin. Hence, non tetraspanin protein was successfully removed from sample in two-cycle. Hence, optimization of EV isolation by two-cycles of ultracentrifugation is successfully achieved.

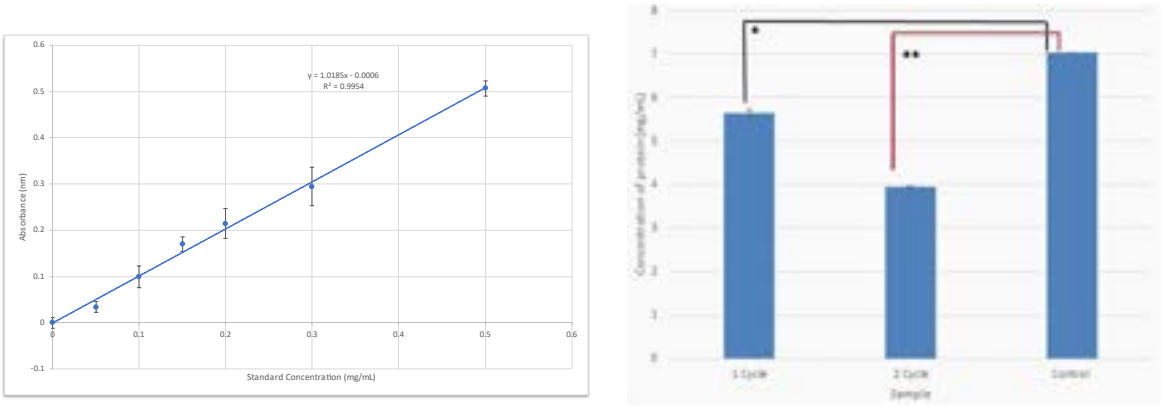

(a) (b)

Figure 2. (a) Standard curve of protein concentration of EV against UV absorbance (b) protein concentration of the EV between centrifugation cycles and control

Particle Size Analyzer

Average size (d.nm) for both cycles were determined by Malvern Mastersizer 3000. From the analysis, it is found that one cycle has smaller average size compared to two cycle sample with 93.7767 d.nm and 177.3333 d.nm respectively. There is also a difference in Pdi value between the samples. For one cycle, the Pdi value obtain was 0.4930 while for two cycles Pdi value was 0.6943 as also shown in figure below.

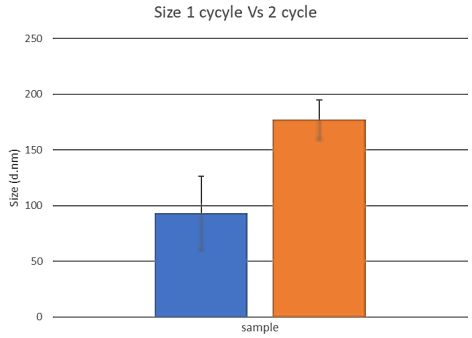

Sample	Average size (d.nm)	Pdi Value
1-cycle	93.1167	0.4930
2-cycle	177.3333	0.6943

Figure 3. (a) average size (d.nm) against type of sample (b) average size (d.nm) and Pdi value of samples

DISCUSSION

The isolated EV was analyzed by using the BCA protein assay in order to look at the protein concentration between the control, one cycle and two cycle sample. From the analysis, it can be seen that the concentration of the two-cycle sample was the lowest compared to the control and one cycle sample. This is due the difference in sample preparation before the analysis where the one cycle sample only undergo one time UC while two cycle sample undergo two time of UC. In other hand the control sample was the pure urine sample that has been treated first before the analysis. During the two cycles of UC, more of the protein and other component that abundance in the sample was remove compare to the one cycle of UC which made the concentration of protein in two cycle sample lower compare to others. According to the t-test that has been made with 95% confident interval, there is significant different between one cycle ($t(3) = 0.1653$, $p = 0.05$) and two cycle sample ($t(3) = 1.3691$, $p = 0.05$).

PSA was used in these studies to look at the size distribution of samples. From the result, it seems that the one cycle sample the smaller size average compared to the two cycle sample with 93.1167 d.nm and 177.3333 d.nm repectively. The one cycle sample average size was fall in to the range of the desired size of EV which around 30 until 150 nm. This is shows, that one cycle sample is the one that going to be use in further optimization method. This also can be proof by the Pdi value of the sample. The Pdi value obtain for the one cycle sample was 0.4930 and for the two-cycle sample was 0.6943. this show the Pdi value of one cycle sample was lower sample compared to two cycle sample. The lower Pdi value show that the sample has good monodispersed while the higher the Pdi

value shows that the sample indicate greater variation in sample. This may be due to the aggregation that happen to the sample during the two cycle UC.

CONCLUSION

In summary, the PSA results indicate that the one-cycle sample yields favorable outcomes, as the average sample size aligned with the reported EV size. The one-cycle sample also retains the majority of important proteins that are necessary for EV identification. Hence, the one-cycle sample will be chosen for subsequent refinement, with a specific emphasis on two factors, which are ultracentrifugation speed and time. Further investigations, including Scanning Electron Microscopy (SEM) and Transmission Electron Microscopy (TEM), will be carried out in the future to provide additional confirmation of the presence of aggregation in the two-cycle sample.

ACKNOWLEDGEMENT

This work is supported by the UTM-Encouragement Research Grant (UTM-ER) by award number PY/2023/01421.

REFERENCES

[1] Hadizadeh, N., Bagheri, D., Shamsara, M., Hamblin, M. R., Farmany, A., Xu, M., Liang, Z., Razi, F., & Hashemi, E. (2022). Extracellular vesicles biogenesis, isolation, manipulation and genetic engineering for potential in vitro and in vivo therapeutics: An overview. Frontiers in Bioengineering and Biotechnology, 10, 1019821

[2] Lu, M., DiBernardo, E., Parks, E., Fox, H., Zheng, S.-Y., & Wayne, E. (2021). The role of extracellular vesicles in the pathogenesis and treatment of autoimmune disorders. Frontiers in Immunology, 12, 566299

[3] Rosa-Fernandes, L., Rocha, V. B., Carregari, V. C., Urbani, A., & Palmisano, G. (2017). A perspective on extracellular vesicles proteomics. Frontiers in chemistry, 5, 102.

[4] Stam, J., Bartel, S., Bischoff, R., & Wolters, J. C. (2021). Isolation of extracellular vesicles with combined enrichment methods. J Chromatogr B Analyt Technol Biomed Life Sci, 1169, 122604. doi: 10.1016/j.jchromb.2021.122604

EVALUATION OF ANTICANCER EFFECTS OF BIOSYNTHESIZED CUO NPS AGAINST BREAST CARCINOMA CELLS

Norhafiza Mohd Arshad[1*], Devanthiran Letchumanan[1], Suriani Ibrahim[2], Noor Hasima Nagoor

[1]*Centre for Research in Biotechnology for Agriculture (CEBAR), Universiti Malaya, 50603 Kuala Lumpur*

[2]*Department of Mechanical Engineering, Faculty of Engineering, Universiti Malaya, 50603 Kuala Lumpur*

* *norhafiza@um.edu.my*

ABSTRACT

The increasing prevalence of breast carcinoma necessitates the development of novel and effective therapeutic agents. This study evaluates the anticancer potential of biogenically synthesized copper oxide nanoparticles (CuO NPs) using Camellia sinensis extract against human breast carcinoma cells. The synthesized nanoparticles were characterized using various techniques to confirm their crystalline structure, size, morphology, and functional groups involved in stabilization. The cytotoxic effects of these CuO NPs on MCF-7 breast cancer cells were assessed through MTT assay, revealing a dose-dependent reduction in cell viability with 50% inhibitory concentration (IC50) at 53.95 µg/ml. Further investigation into the mechanism of action was conducted using flow cytometry and apoptosis assays, which indicated that CuO NPs induced cell cycle arrest and apoptosis in cancer cells. Reactive oxygen species (ROS) generation, caspase activity assay and comet assay were also performed to elucidate the underlying pathways, suggesting that oxidative stress and DNA damage play pivotal roles in the cytotoxicity observed. Overall, our findings demonstrate that biogenic CuO NPs exhibit significant anticancer activity against human breast carcinoma cells with minimal effects on normal cells, highlighting their potential as a therapeutic agent due to their biocompatibility and lower toxicity. However, further validation of our data is required in *ex vivo* and *in vivo* models before this CuO NPs could be exploited for the treatment and management of human breast cancer.

Keywords: Biosynthesized, Copper oxide NPs, *Camellia sinensis,* Apoptosis, Breast cancer

INTRODUCTION

Cancer has become one of the most devastating diseases with more than 14 million new cases each year and is expected to continue rising. According to the statistics released by the World Health Organization (WHO), there were an estimated 20 million new cancer cases and 9.7 million deaths in 2022. With the advancement in nanotechnology, nanoparticles are gaining lots of significance due to their use in cancer therapy. Previous studies have reported that metal oxide nanoparticles can induce cytotoxicity in cancer cells with minimal side effects to the normal cells [2], poses anti-oxidant capacity that can decrease the rate of tumour cells progression [1] and induce generation of reactive oxygen species (ROS) oxidative stress which causes DNA damage and increases death receptor expression [3].

Copper oxide nanoparticles (CuO NPs) have garnered attention for their potent anticancer properties. Traditionally synthesized through chemical methods, CuO NPs have shown efficacy in inducing apoptosis and inhibiting the proliferation of various cancer cell lines. However, concerns regarding the environmental impact and biocompatibility of chemically synthesized nanoparticles necessitate the exploration of greener alternatives. In the present study, CuO NPs were synthesized using *Camellia sinensis* extracts. Biogenic synthesis of nanoparticles, utilizing plant extracts or other biological materials, offers a sustainable and eco-friendly approach. This method not only reduces the reliance on hazardous chemicals but also enhances the biocompatibility of the nanoparticles, making them more suitable for medical applications. Recent studies have highlighted the potential of biogenic CuO NPs in biomedical applications, however the specific anticancer mechanisms of CuO NPs synthesized from tea leaves extract remains underexplored.

Therefore, this study aims to evaluate the anticancer potential and their mechanisms of action of biosynthesized CuO NPs against against breast cancer cells. Through comprehensive in vitro analyses, including cytotoxicity assays, apoptosis evaluation, and mechanistic studies, we seek to elucidate the potential and therapeutic applications of these biosynthesized CuO NPs. This research could pave the way for developing novel, effective, and safe nanomedicine strategies for breast cancer treatment.

METHODOLOGY

Synthesis and Characterization of CuO NPs

The stock for copper nitrate solution was prepared using distilled water. Various concentrations of the tea extract solutions were used to measure the size of CuO NPs. The copper nitrate solution was stirred vigorously for 15 minutes at 350 rpm to get a well-mixed solution. Then, tea extracts were slowly added into the solution with constant stirring speed for about 1 hour. The color of the solution was changed from pale blue to pale yellow and finally to brown. The mixture was then cooled at room temperature for about 10 minutes. The precipitates were separated by filter paper and washed using distilled water and ethanol until reached pH 7. The precipitate obtained was dried in the oven at 100ºC for 2 hours to obtain black powdered particles. It is necessary to characterize the properties of the CuO NPs in order to understand the effect of experimental parameters and the physical and chemical nature of the NPs. Thus, various tests involving UV- vis, SEM, FESEM, HRTEM, EDS, FTIR and XRD were performed.

Cell culture

MCF- 7 breast cancer cells and RWPE-1 human prostate epithelial were used in this study. Both cell lines were cultured in growth medium supplemented with 10% FBS. Cells were allowed to grow as monolayer in a CO_2 incubator at 37 °C with 5% CO_2.

MTT assay

The cytotoxic activity of the CuO NPs compounds on the cells were assessed using the MTT cell viability assay. Briefly, the cell lines were seeded at approximately 10^4 cells/well in 96-well plate and were incubated overnight before treated with biosynthesized CuO NPs at various concentrations (0 -100 µg/mL) for 24 h. After incubation, 20 µL of MTT reagent (5 mg/mL) were added to each well of the microplate followed by incubation in the dark at 37ºC for 90 min. The spent media were then discarded, and purple formazan precipitates were dissolved in 200 µL DMSO. The optical density was measured with a microtiter plate reader (Tecan Sunrise, Switzerland). The assay was performed in triplicate and the half maximal inhibitory concentration (IC50) value was obtained.

Live/Dead assay

Fluorescence viability stains were enabled the visualization of cell appearance based on membrane integrity and differentially label live and dead cells. Qualitative assessment of cell viability upon treatment with CuO NPs was conducted using the LIVE/DEAD® Viability/Cytotoxicity Kit according to manufacturer's instructions. Visualization of samples were performed using a Nikon Eclipse TS-100 fluorescence microscope (Nikon, Tokyo, Japan) under 100× magnification.

Cell Cycle Assay

A total of 1.0×106 cells was grown as a monolayer and treated with CuO NPs incubated for 24h. Following treatment, the treated and untreated cells were collected through trypsinization, centrifuged and washed twice with ice-cold 1×PBS solution (cell harvesting). The cell pellets were re-suspended in 1 mL of 1×PBS solution and 3 mL of 70 % ethanol added dropwise by a continues vortex to fix the cells. The cells were left for 30 min at 40C for a complete fixation and were washed twice with 1×PBS solution at a high centrifugation speed (850xg) for 5 min. The cell pellets were stained with 200 µL of PI solution (stock: 50 µg/mL), 0.5 µL RNase (stock: 10000 µg/mL), and was incubated in the dark for 45 min. The samples were analyzed using MACSQuant® Analyzer 10 flow cytometry with MACSQuantify™ version 2.10 software (Miltenyi Biotec, Bergisch Gladbach, Germany).

Annexin V-FITC/ PI Flow Cytometry Assay

A total of 5.0×10^5 cells was cultured before treated with CuO NPs incubated for 24 h. Cells were then harvested from both floating and attached cells and were washed twice using 1× PBS solution and further was incubated for 15 min in the dark with 100.0 µL of binding buffer containing 5.0 µL of annexin V-FITC and PI, respectively. The samples were mixed with 400.0 µL binding buffer before being analyzed using MACSQuant® Analyzer 10 flow cytometry with MACSQuantify™ version 2.10 software (Miltenyi Biotec).

Caspase 3/7 Assay

A total of 0.3×106 cells of cancer cell lines was cultured and treated with CuO NPs and were incubated for 24h. Adherent cells were collected and centrifuged at 500xg for 5 min at 4℃. The cells were rinsed two times with PBS to remove the impurities or debris. The pellets were solubilized at 2×107 cell/mL in a chilled 1×cell extraction buffer PTR. Immediately the solution containing cells were incubated on ice for 20 min, followed by centrifugation at 18,000xg for 20 min at 4℃. The final supernatants were transferred into the clean tubes and the pellets were discarded. The samples were then tested using the assay immediately. A 50µL of sample was added into the 96-well, followed by adding a 50µL of antibody cocktail prepared. After 1 hour of incubation, the supernatants were aspirated and washed three times with 350µL 1×wash buffer PT. Then, 100µL TMB solution was added into each well and incubated for 10- 30 min. Immediately a 100µL stop solution was added to stop the reaction and OD reading was measured at 450 nm using TECAN microplate reader.

ROS Detection by Immunofluorescence Assay

ROS activity in the cancer cell lines treated with CuO NPs was studied using ROS assay kit purchased from Canvax, Spain. This assay kit uses the cell permeant reagent Dichlorodihydrofluorescein-diacetate (H2DCFDA), a fluorogenic dye that measures hydroxyl, peroxyl and other ROS activity within the cell. A total of 2.5×10^4 cells was grown in 96-well plates for 24 hours. Media was removed and the cells washed with 100µL ROS assay buffer (100µL/ well+PBS). The ROS buffer was removed and stain the cells by adding 100µL diluted H2DCFDA probe. Immediately, the cells were incubated with H2DCFDA probe for 45 min at 37°C in dark. Then, the H2DCFDA solution was removed by washing with 1×ROA buffer 100µL each well. The cells were treated with CuO NPs and incubated for 1-6 hours. H2O2 was used as the +ve control in this test. Immediately, the absorbance reading was measured at Ex/Em (485/530 nm) using TECAN microplate reader.

Comet Assay

A total of 1×10^4 cells were cultured on 6-well plates and treated with CuO NPs. After 24 h, the treated cells were placed in 1 mL of phosphate-buffered saline (PBS) containing 20 mM EDTA and 10% DMSO and then disintegrate by serial pipetting. Treatment with hydrogen peroxide was used as the positive control: H2O2 concentrations and the cells was spread onto microscope slides precoated with normal agarose and subjected to the alkaline comet assay. Viability was checked by trypan blue staining. The cells were lysed for 1 h in 10 mM Tris, 100 mM EDTA, 2.5 M NaCl, 10% DMSO, 1% Triton X-100 (pH 10). DNA unwinding was carried out for 20 min at 4oC in alkaline conditions (300 mM NaOH, 1 mM EDTA, pH ≥ 13). The electrophoresis was performed at 4°C under an electrical current of 400 mA (25 V) for 20 min. The slides were neutralized (Tris–HCl 0.4 M), dehydrated in 70% ethanol, stained with 50 L ethidium bromide (10 g L−1) and then analysed using a fluorescence microscope (400×magnification, Eclipse 50i, Nikon) and finally scored using Comet assay IV image analysis software (Perceptive Instrument, UK). The test parameter was considered as the % DNA in the tail (tail intensity). Comet assay results were analyzed for significance from negative control.

RESULTS AND DISCUSSION

The anticancer potential of biosynthesized CuO NPs against human breast carcinoma cells was evaluated through a series of in vitro experiments. X-ray diffraction analysis was performed to determine the crystal structure and phase of copper oxide nanoparticles. XRD results showed that the particles were highly crystalline and with monoclinic structure. Morphology of copper oxide nano particles confirmed by SEM, FESEM and TEM, which showed that the particles are spherical and are in 20- 60 nm range. The main composition of the CuO NPs were copper, oxygen and carbon from EDS result obtained. The presence of alcohol, aromatic hyroxyl and alkene from the FTIR spectroscopy results proves that the pytochemicals involved in the synthesis of CuO NPs and also acting as capping agent.

In this study, the cytotoxicity activity of CuO NPs were tested against MCF-7 breast cancer cells. The results showed CuO NPs treatment were able to suppress the growth of those cancer cells in dose-dependent manner. The percentage of viable cells were decreasing as the concentration of the CuO NPs increasing. The IC_{50} of CuO NPs in MCF-7 is 53.95±1.10 µg/mL. In addition, the CuO NPs treatment exhibited minimal cytotoxicity effects on the normal cell lines (RWPE-1). This result is in accordance to previous studies reported that the CuO NPs synthesized using *Pogestemon benghalensis* exhibit a half inhibitory effect on cell viability at 60.25 mg/L in human normal fibroblast HDF cell lines [4] and could be a potential anticancer agent as it does not induce significant cytotoxicity on normal cell lines. In addition, our finding through live/dead assay's result showed a large percentage of dead cells in MCF-7 cells treated with CuO NPs concentration in comparison to untreated cells. Whilst, we observed the MCF-7 cells undergo cell death by apoptosis. Using this assay, the cells can be recognized as viable (unstained), early apoptosis (annexin V-FITC stained only), late apoptosis (annexin V-FITC

and PI stained) and necrosis (PI stained only) across various dose of treatment to observe the shift of cells towards different stages of death.

Caspase cascades can be triggered through two major branches, either through cell surface TNF-superfamily death receptor and the pivotal adaptor protein Fas activated death domain (FADD) leading to activate of caspase- 8 and ultimately caspase- 3, or via the release of cytochrome C from mitochondria resulting in caspase-9 activity and subsequent caspase- 3 action. Caspase- 3, represents a convergence point between the two routes, and in turn induces PARP cleavage, chromosomal DNA breaks and finally the breakdown of the cell apoptotic bodies (J.-f. Zhao et al., 2009). In this study, we use human cleaved caspase 3/7 assay to evaluate the CuO NPs treated cells. We found that MCF-7 cell lines shows a higher expression caspase- 3/7 proteins in reference to the control cells, indicating the cells undergoing cell death via apoptosis.

Oxidative stress refers to the imbalance due to excess ROS or oxidants over the capability of the cell to overcome and response. Hence, oxidative stress leads to macromolecular damages and involves in various disease effects especially cancer. Generation of ROS, together with the release of pro- apoptotic proteins from the intermembrane space of mitochondria, trigger the activation of different modes of cell death. In this study, we observed a positive test towards the ROS assay where the florescence intensity in MCF-7 cell lines were relatively higher compared to the control cells. This conclude that the ROS generation in this cancer cell lines were higher, and this supports the results on the apoptotic and genotoxic effects as the result on comet assay shows a similar trend on the effects to the treated cells where the DNA double strand break is very clear using comet assay with scoring of the DNA.

CONCLUSION

Overall, our findings demonstrate that CuO NPs biosynthesized using *Camellia sinensis* extract exhibit significant anticancer activity against human breast carcinoma cells. The dose-dependent cytotoxicity, induction of apoptosis, and involvement of oxidative stress highlight the potential mechanisms through which these nanoparticles exert their effects. The biosynthesis approach not only enhances the biocompatibility of CuO NPs but also aligns with sustainable and eco-friendly practices. However, further in vivo studies and clinical trials are warranted to fully establish their therapeutic potential and safety profile. The integration of biogenic nanoparticle synthesis in cancer nanomedicine could pave the way for the development of novel, effective, and sustainable cancer treatments.

ACKNOWLEDGMENTS

This research was funded by Malaysia Ministry of Higher Education—Fundamental Research Grant Scheme FP027-2019A (FRGS/1/2019/STG05/UM/02/5) (N.M.A.)

REFERENCES

[1] Caputo, F., De Nicola, M., & Ghibelli, L. (2014). Pharmacological potential of bioactive engineered nanomaterials. Biochemical pharmacology, 92(1), 112-130.

[2] Vinardell, M., & Mitjans, M. (2015). Antitumor activities of metal oxide nanoparticles. Nanomaterials, 5(2), 10 04-1021.

[3] Yang H, Liu C, Yang DF, Zhang HS, Xi Z. (2009). Comparative study of cytotoxicity, oxidative stress and genotox icity induced by four typical nanomaterials: The role of particle size, shape and composition. J Appl Toxicol.29:69–78.

[4] Zou, X., Cheng, S., You, B., & Yang, C. (2020). Bio-mediated synthesis of copper oxide nanoparticles using Pogestemon benghalensis extract for treatment of the esophageal cancer in nursing care. *Journal of Drug Delivery Science and Technology, 58*, 101759. doi: https://doi.org/10.1016/j.jddst.2020.101759

[5] https://www.who.int/news/item/01-02-2024-global-cancer-burden-growing--amidst-mounting-need-for-services

INFAUNAL COMPOSITION IN THREE *NEPENTHES* SP. AT BRIS AREA IN MERANG, TERENGGANU

Rohani Shahrudin[1], Nabilah Naharuddin[1]

[1]*Faculty Science and Marine Environment, Universiti Malaysia Terengganu, 21030 Kuala Nerus, Terengganu.*

rohanishahrudin@umt.edu.my

ABSTRACT

Nepenthes, or pitcher plants, are carnivorous plants that attract and capture insect prey using modified leaves shaped like pitchers. This adaptation occurred because they lived in an environment deficient in nutrients, particularly nitrogen and phosphorus. We chose *Nepenthes ampullaria*, *Nepenthes gracilis*, and *Nepenthes rafflesiana* as the three species in this study. Human activities currently threaten the habitat of these plants, potentially leading to the decline of insects. Hence, the study aimed to identify the infaunal communities in each *Nepenthes* and investigate the relationship between the infaunal community and pitcher size. We collected the fluid content from ten pitchers in both the upper and lower pitcher water bodies of each *Nepenthes*, transferred it into plastic test tubes, and then stored it with 75% ethanol. The study revealed ten insect orders obtained from the pitchers of studied species, with hymenopterans being the most common prey. Other insects like mosquito larvae, flies, beetles, and unidentified arthropods were also present. The study further determined that pitcher shape influences the abundance of infaunal communities, with a positive and moderate correlation between pitcher volume and the number of insects. This study suggests that larger pitchers have a higher number of infaunal individuals in their water bodies.

***Keywords*:** Carnivorous plants, Inquilines, Ecological interactions, Forest disturbance.

INTRODUCTION

Nepenthes, commonly referred to as tropical pitcher plants, belong to the Nepenthaceae family, which is exclusively composed of the *Nepenthes* genus. Tropical pitcher plants' unusual pitchers simplify their feeding processes and make them clearly identified. This is in sharp contrast to typical plants, whose roots absorb nutrients from the earth (Dezhi & Aili, 2010). Nepenthes leaves have evolved into a pitcher structure with lubricating wax crystals on the inner wall and 'insect aquaplaning' on the peristome (Bauer et al. 2012). This structure traps insects in the carnivorous *Nepenthes* and collects desiccated leaves in the omnivore *Nepenthes*. This phenomenon results from the fact that pitcher plants thrive in nutrient-deficient soils, particularly those lacking nitrogen, which inhibit the growth of other plants. As a result, the pitchers are essential to *Nepenthes'* survival.

The infaunal communities found in the phytotelmata of *Nepenthes* play a significant ecological role, contributing to the production of nutrients, particularly nitrogen (Miller & Kneitel, 2005). In return, the pitcher plants provide a safe haven for inquilines from predators and serve as food sources for Nepenthephiles. Thus, the infaunal communities and Nepenthes establish a symbiotic relationship, demonstrating mutual interaction, as demonstrated by Lam et al. (2018). They assert that an inquiline can assist in sequestering nutrients within the phytotelma where it resides. **Beach Ridges Interspersed with Swales (BRIS) are coastal plains characterized by sandy soils, common in eastern Peninsular Malaysia.** However, rapid urbanization threatens their existence, leading to habitat destruction and biodiversity loss. Insects, crucial for ecosystem functioning, are particularly vulnerable to habitat loss. Therefore, this study **aims to investigate the infaunal diversity within** *Nepenthes* **pitchers in a BRIS ecosystem, in Merang, Terengganu.**

MATERIALS AND METHODS

The sampling of infaunal communities was carried out in the BRIS ecosystem at Kampung Rhu Tapai, Merang Terengganu (5°31'02"N, 102°58'16"E). Three *Nepenthes* species, *N. ampullaria*, *N. gracilis*, and *N. rafflesiana*, were selected for this study. A total of 20 pitchers were collected from each species, comprising 10 upper pitchers and 10 lower pitchers. Pitcher maturity, determined by size, was a key criterion for selection. While most pitchers were from different individuals, some were collected from the same plant due to their clustered growth pattern.

Infaunal communities and pitcher fluid were extracted using a syringe-based inhalation/exhalation technique. Larger insects were manually removed using a dissecting spatula. Samples were preserved in 75%

ethanol and sealed with parafilm. The phylum, class, order, and relationships to the *Nepenthes* spp. were used to identify and classify the inquilines species number within each pitcher plant species.

Pitcher volume was calculated based on measurements of peristome width and length using a vernier caliper. Peristome length was measured from the opening of the pitcher to the base of the tendrils, while width was measured at the widest point of the peristome. The collected data on pitcher length and peristome width were used to analyze the relationship between pitcher morphology and infaunal community abundance. Correlation and regression analyses were employed to examine the association between the size of Nepenthes and the infaunal communities.

RESULTS AND DISCUSSION

A total of 3,187 infaunal individuals, representing ten orders of arthropods (Insecta and Arachnida), were captured in pitchers of three *Nepenthes* species: *N. ampullaria*, *N. gracilis*, and *N. rafflesiana (Table 1)*. The order richness found in this study is comparable with previous studies. A study in Sarawak found ten insects order in five *Nepenthes* sp. at Setiam Hill Sarawak (Marina et al., 2018), while six insects order and one non insects order were encountered in five *Nepenthes* sp. at heath forest of Brunei (Gaume et al., 2016), and seven insects order from *N. rafflesiana* at Central Catchment Nature Reserve (CCNR) in Singapore (Lam et al, 2020).

The abundance of infauna varied significantly among species, with *N. rafflesiana* hosting the highest number of individuals (1,152), followed by *N. gracilis* (1,407) and *N. ampullaria* (278). The diversity of prey captured by these *Nepenthes* species also differed. *N. rafflesiana* attracted a wider range of insect orders, including flying insects like Blattodea, Diptera, Coleoptera, Orthoptera and Mantodea (Figure 1). In contrast, *N. gracilis* primarily captured crawling insects such as ants and mites. *Nepenthes ampullaria* predominantly contained insect larvae, particularly those of flies. Overall, ants, mites, insect larvae, and flying insects were the most common infaunal groups found in *Nepenthes* pitchers. While arachnids (Araneae) were present, they constituted a smaller proportion of the infaunal community. Hymenopterans especially ants were observed as the common infaunas found in each *Nepenthes* pitchers, which was the same as the study by Adlassnig et al. (2011). Meanwhile, ants were found mostly in lower pitchers of each *Nepenthes*, since they are epigeic foragers that build nest on the ground (Lam et al., 2020).

Table 1. The abundance of infaunal communities that can be found in three *Nepenthes* species sampled from BRIS area in Merang, Terengganu.

	Phylum	Arthropoda												Total
	Class	Insecta										Arachnida		
Taxon	Order	Hymenoptera	Diptera larvae	Blattodea	Coleoptera	Diptera	Lepidoptera	Orthoptera	Lepidoptera larvae	Mantodea	Odonata	Acari	Araneae	
N. ampullaria														
(Upper pitchers)		51	5	0	1	3	1	0	0	0	0	20	2	83
(Lower pitchers)		101	77	0	13	0	0	0	0	0	0	4	0	195
N. gracilis														
(Upper pitchers)		368	6	4	0	0	0	0	1	0	0	50	4	433
(Lower pitchers)		898	16	1	0	5	0	0	0	0	1	46	7	974
N. rafflesiana														
(Upper pitchers)		302	0	48	17	16	8	2	0	0	0	0	8	401
(Lower pitchers)		962	6	55	5	12	0	2	1	1	0	38	19	1101
Total		2682	110	108	36	36	9	4	2	1	1	158	40	3187
Relative abundance (%)		84.15	3.45	3.39	1.13	1.13	0.28	0.13	0.06	0.03	0.03	4.96	1.26	100

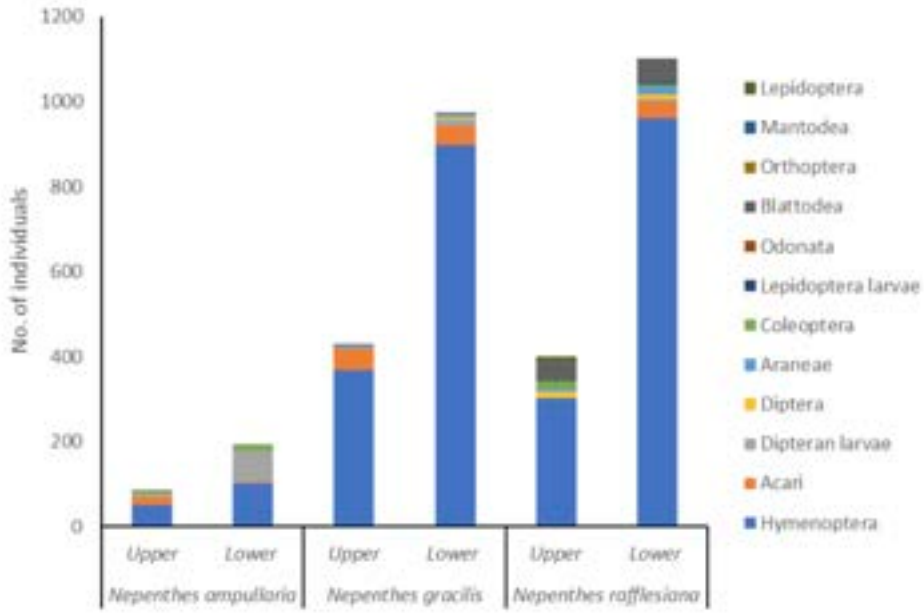

Figure 1. The infaunal assemblages in three Nepenthes species sampled from BRIS area in Merang, Terengganu.

Our analysis of pitcher size (length and width) revealed that *N. rafflesiana* had the largest pitchers, followed by *N. gracilis* and *N. ampullaria*. Consistent with previous research (Cresswell, 1993; Gaume et al., 2019), we found a positive correlation between pitcher size and infaunal abundance. *Nepenthes rafflesiana* and *N. gracilis*, with their larger pitchers, captured a higher number of infaunal organisms. Correlation and regression analysis revealed a strong positive linear relationship between pitcher volume and the total number of infaunal individuals ($r = 0.776$, $p<0.05$). Pitcher size explains approximately 60.6% of the variation in infaunal abundance, which implies that pitcher size has a significant contribution on the captured infaunal. Larger pitchers with favorable conditions support greater infaunal diversity, reflecting the species-area relationship in ecology.

CONCLUSION

The pitchers of the three *Nepenthes* species contain ten orders of arthropods. The trapped infaunas consist of ten insect orders (Hymenoptera, Blattodea, Diptera, Coleoptera, Orthoptera, Mantodea, and Odonata) and two noninsect orders (Araneae and Acari). The order of Hymenoptera, especially ants, are the most abundant infaunas that are found in each pitcher of every *Nepenthes* sp., especially in lower pitchers since they are foragers and have small sizes, which make it easier for them to be trapped. In addition, the study proved that the morphology of the pitchers influences the number of trapped infaunas, as evidenced by the strong and positive linear relationship between the number of infaunas and pitcher volume. Therefore, the higher the pitcher volume, the higher the number of infaunal communities trapped. For more research into the ecological dynamics of *Nepenthes* pitcher plants and the animals that live with them, future studies could look at how the diversity and make-up of these animal communities change throughout the year as a result of changes in temperature, rainfall, and plant growth. This would provide insights into the seasonal dynamics of these ecosystems.

REFERENCES

Adlassnig, W., Peroutka, M., & Lendl, T. (2011). Traps of carnivorous pitcher plants as a habitat: Composition of the fluid, biodiversity and mutualistic activities. *Annals of Botany*, 107(2), 181–194.

Bauer, U., Giusto, B. D., Skepper, J., Grafe, T. U., & Federle, W. (2012). With a Flick of the Lid: A Novel Trapping Mechanism in *Nepenthes gracilis* Pitcher Plants. *PLOS ONE*, 7(6), e38951.

Dezhi, L., & Aili, Q. (2010). "Pitcher Plants of the Old World" by Stewart McPherson. 2009. [Book review]. The Canadian Field-Naturalist, 124(2), Article 2.

Gaume L., Bazile V., Bonhomme V., Huguin M. & Bonhomme V. (2016) Different pitcher shapes and trapping syndromes explain resource partitioning in *Nepenthes* species. *Ecology and Evolution*, 6(5): 1378–1392.

Lam, W. N., Lim, R. J. Y., Wong, S. H., & Tan, H. T. W. (2018). Predatory dipteran larva contributes to nutrient sequestration in a carnivorous pitcher plant. *Biology Letters*, 14(3), 20170716.

Lam, W. N., Yeo, H., Lim, R. J. Y., Wong, S. H., Lam-Phua, S. G., Fashing, N. J., Neo, L., Wang, W. Y., Cheong, L. F., Ng, P. Y. C., & Tan, H. T. W. (2020). A comparative exploration of the inquiline and prey species of *Nepenthes rafflesiana* pitchers in contiguous and fragmented habitat patches in Singapore. *Raffles Bulletin of Zoology*, 68, 838–858.

Marina, M.T., Keen, C.J., Caroline, B.R., & Afsar, J. (2018). Fauna diversity in pitcher plants at Setiam Hill, Bintulu, Sarawak, Malaysia. *Sains Malaysiana*, 47(1), 19–25.

Miller, T.E., & Kneitel, J.M. (2005). Inquiline communities in pitcher plants as a prototypical metacommunity. In Holyoak, M., Leibold, M.A., & Holt, R.D. (Eds.) *Metacommunities: Spatial Dynamics and Ecological Communities*, (pp. 122–145). The University of Chicago Press.

EFFECTIVE EDNA PROTOCOL FOR BIODIVERSITY MONITORING

Ghazanfer Ali[1*], Subha Bhassu[1*], Thenmoli Govindasamy[1], Danish Zikry[1], Alya Batrisyia[1] and Muhamad Afiq Aziz[1] and Norhafiza Mohd Arshad[2]

[1] *Animal Genetics and Genome Evolutionary Biology Lab, Institute of Biological Sciences, Faculty of Science, Universiti Malaya, 50603 Kuala Lumpur, Malaysia*

s2125068@siswa.um.edu.my and subhabhassu@um.edu.my

[2]*Centre for Research in Biotechnology for Agriculture, Universiti Malaya, 50603 Kuala Lumpur, Malaysia; norhafiza@um.edu.my*

ABSTRACT

This study evaluates eDNA extraction techniques to improve aquatic biodiversity monitoring by comparing two filtration methods: single and multiple filter protocols, using various filters. Results indicate that a multiple filter protocol using 0.45 µm cellulose nitrate (CN) membranes yields the highest eDNA. Among extraction methods, the Phenol Chloroform Isoamyl alcohol (PCI) method significantly outperformed commercial kits in eDNA yield. PCR amplification and Illumina MiSeq sequencing identified 14 families and 21 fish species. The study recommends the CN 0.45 µm filter and PCI method for efficient, cost-effective eDNA extraction in aquatic biodiversity research, particularly benefiting resource-limited settings.

***Keywords*:** Environmental DNA; single filter; multiple filter; high yield; cost-effective; aquatic biodiversity.

INTRODUCTION

Environmental DNA (eDNA) analysis has emerged as a highly promising tool for the monitoring of aquatic biodiversity (Andres et al., 2023). However, due to sample degradation during sampling and processing, the standardized eDNA extraction protocol still presents a challenge to obtaining accurate and repeatable results (Bowers et al., 2021; Beng & Corlett 2020). This study aimed to examine two filtration techniques for eDNA extraction from water samples by employing four different filter types to increase eDNA yield.

MATERIALS AND METHODS

In this present study we reported two filtration techniques: a single filter protocol and a multiple filter protocol. We used cellulose nitrate (CN) membranes with pore size of 0.22 µm and 0.45 µm, polyvinylidene difluoride (PVDF) membrane with pore size of 0.45 µm and common filter (CF) membrane to filter the sample water. eDNA was extracted by a NucleoSpin eDNA water kit and Phenol Chloroform Isoamyl alcohol (PCI) method. The eDNA extracted from each method was assessed for quantity and quality using a Nanodrop spectrophotometer and agarose gel electrophoresis, respectively. PCR amplification was done using 12S RNA gene. Some eDNA samples were sequenced using Illumina MiSeq platform to result validation.

RESULTS AND DISCUSSION

Using multiple filter protocol high eDNA yield was obtained. Comparison of all filter membranes showed that CN membrane with pore size of 0.45 µm can capture more eDNA than other filter membranes (Figure 1). Between the extraction methods, PCI with multiple filter protocol could isolate five times more eDNA compared to commercial DNA extraction kit method (Figure 2). Increasing the initial filter volume can increase the eDNA yield. eDNA extracts were amplified using PCR primers for 12S rRNA gene to validate the results. Agarose gel electrophoresis for assessing the quality of eDNA found all the same. 9 orders, 14 families, 18 genera and 21 species of fish were obtained using the Illumina MiSeq platform (Illumina, San Diego, CA, USA) (Figure 3). Our findings align with those of Capo et al. (2020) and Hunter et al. (2019), who demonstrated that a multiple filter protocol enhances eDNA yield, making it suitable for detecting species, even those present at low abundance. Moreover, Ruan et al. (2022) evaluated various sampling, filtration, and extraction methods for monitoring fish diversity via eDNA. They compared direct filtration and filtration-based precipitation, alongside three DNA extraction techniques: DNeasy Power-Water Kit, DNeasy Blood & Tissue Kit, and conventional phenol/chloroform. Analyzing water volumes of 500, 1,000, and 2,000 ml, they concluded that increasing filtration

volume effectively enhances eDNA yield, aiding fish community structure characterization in complex ecosystems.

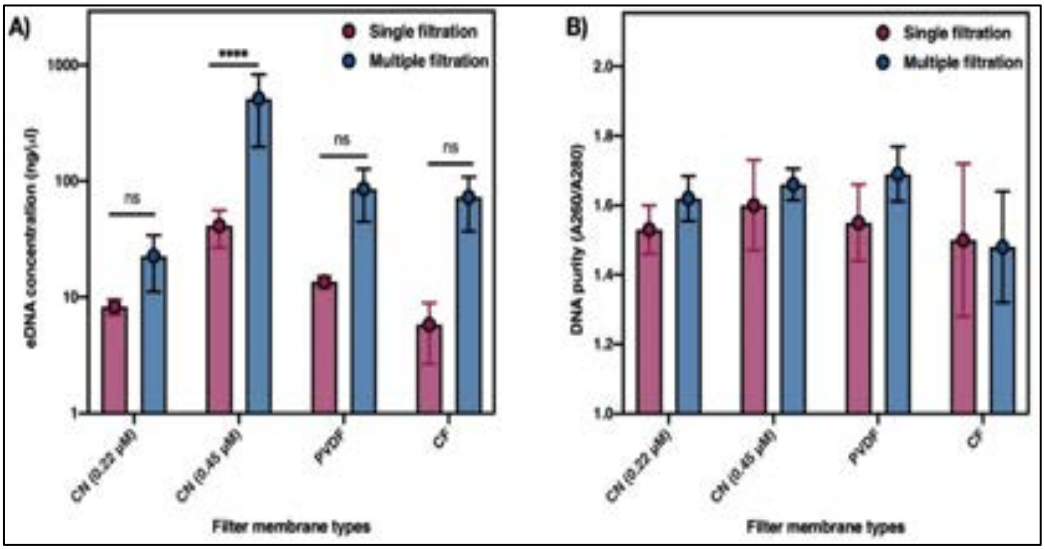

Figure 1. Comparison between single filter and multiple filter method. A) Average concentration of eDNA extracted using PCI method with single filter (red columns) and from multiple filters (blue columns). B) Average absorbance ratio of A260/A280 of DNA extracted following PCI method using single filter (red columns) and multiple filters (blue columns). Error bars indicate standard deviation of the mean. Value represents average of at least three technical replicates, ns denotes not significant with ($P > 0.05$); **, $P<0.01$; ****, $P<0.0001$.

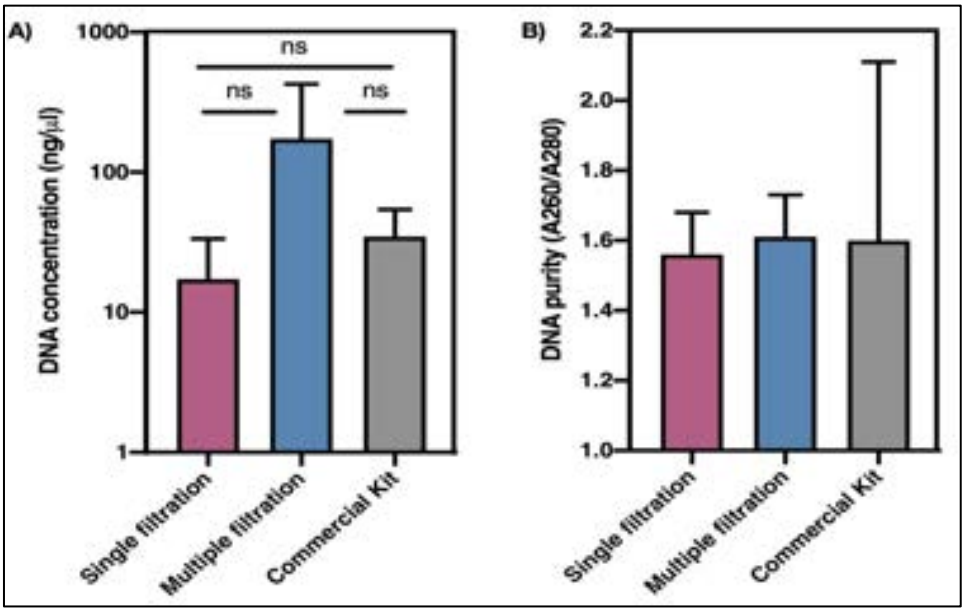

Figure 2. Comparison of eDNA extraction method. A) Efficiency of PCI method with single and multiple filters and kit method. B) A260/A280 ratios of eDNA extraction methods. Value represents average of at least three technical replicates, ns denotes not significant with ($P > 0.05$); **, $P<0.01$; ****, $P<0.0001$. Statistical analysis was performed using two-way ANOVA with Tukey multiple comparison test.

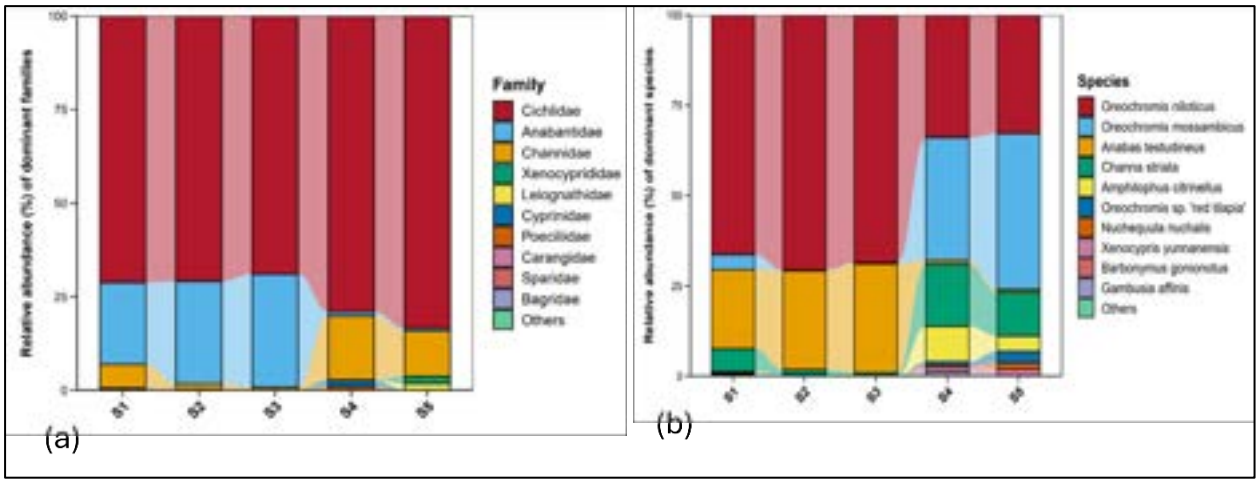

Figure 3. Fish families and species obtained by eDNA metabarcod

CONCLUSION

For water filtration, CN 0.45 µm pore size membrane has advantages over others. PCI is recommended as the best method for eDNA extraction with multiple filter protocol from aquatic samples with the least cost and appropriate purity. The commercial eDNA extraction kit takes the shortest time; however, it is costly and so not suggested for developing nations. We recommend the CN membrane pore size (0.45 µm) and PCI extraction with multiple filter protocol for rapid assessment of aquatic biodiversity. The presented protocol will be helpful for developing countries and will open new insights into research especially assessing biodiversity at an advanced level.

REFERENCES

[1] Andres, K. J., Lodge, D. M., & Andrés, J. (2023). Environmental DNA reveals the genetic diversity and population structure of an invasive species in the Laurentian Great Lakes. Proceedings of the National Academy of Sciences, 120(37), e2307345120.

[2] Beng, K. C., & Corlett, R. T. (2020). Applications of environmental DNA (eDNA) in ecology and conservation: opportunities, challenges and prospects. *Biodiversity and conservation*, *29*(7), 2089-212.

[3] Bowers, H. A., Pochon, X., von Ammon, U., Gemmell, N., Stanton, J. A. L., Jeunen, G. J., ... & Zaiko, A. (2021). Towards the optimization of eDNA/eRNA sampling technologies for marine biosecurity surveillance. *Water*, *13*(8), 1113.

[4] Capo, E., Spong, G., Königsson, H., & Byström, P. (2020). Effects of filtration methods and water volume on the quantification of brown trout (Salmo trutta) and Arctic char (Salvelinus alpinus) eDNA concentrations via droplet digital PCR. Environmental DNA, 2(2), 152-160.

[5] Hunter, M. E., Ferrante, J. A., Meigs-Friend, G., & Ulmer, A. (2019). Improving eDNA yield and inhibitor reduction through increased water volumes and multi-filter isolation techniques. Scientific Reports, 9(1), 5259.

[6] Ruan, H. T., Wang, R. L., Li, H. T., Liu, L., Kuang, T. X., Li, M., & Zou, K. S. (2022). Effects of sampling strategies and DNA extraction methods on eDNA metabarcoding: A case study of estuarine fish diversity monitoring. Zoological Research, 43(2), 192.

EFFECTS OF FEED SUPPLEMENTED WITH FUCOIDAN AND CURCUMIN ON THE GROWTH AND FEED UTILIZATION IN RED NILE TILAPIA (*OREOCHROMİS NİLOTİCUS*) JUVENILES

Nur Anissa Ainnina Md Daud[1], Nadiatul Hafiza Hassan[1*], Mohammad Noor Amal Azmai[1,2], Dania Aziz[3]

[1]*Department of Biology, Faculty of Science, Universiti Putra Malaysia, 43400 Serdang UPM, Selangor, Malaysia*

nadiahafiza@upm.edu.my

[2] *Aquatic Animal Health and Therapeutics Laboratory, Institute of Bioscience, Universiti Putra Malaysia, 43400 Serdang UPM, Selangor, Malaysia*

mnamal@upm.edu.my

[3]*Department of Aquaculture, Faculty of Agriculture, Universiti Putra Malaysia, 43400 Serdang UPM, Selangor, Malaysia*

dania@upm.edu.my

ABSTRACT

A 44-day feeding trial was conducted to evaluate the effects of feed supplemented with fucoidan and curcumin on the growth performance and feed utilization of juvenile red Nile tilapia (1.98 ± 0.46g). Four experimental diets were tested; Control, 1.5 g/kg fucoidan (FD), 0.05 g/kg curcumin (CR), and 1.5 g/kg fucoidan with 0.05 g/kg curcumin (FDR). A total of two hundred (n=200) homogenous tilapia juveniles were fed with the experimental diets for 44 days, where each replicate was stocked with 10 fish. The study demonstrated no significant difference in the specific growth rate, SGR ($p>0.05$). Protein efficiency ratio (PER) showed a significant difference for fish in CR ($p<0.05$). While feed conversion ratio (FCR) and average daily weight gain (ADWG) in CR were enhanced by 21% and 1.83%, respectively. This finding is contradicted by the results of the SGR that demonstrated no significant difference between the treatment and control groups. Overall, the inclusion of fucoidan and curcumin with the concentration of 1.5 g/kg and 0.05 g/kg, respectively, do not improve the overall growth performance parameter of the red Nile tilapia however, PER, FCR, and ADWG was observed to have positive significant difference in CR compared to the control group. The current study found that dietary supplementation with fucoidan (FD) at a dose of 1.5 g/kg did not lead to significant improvements in growth rate or intestinal histological profile. In contrast, curcumin (CR) at a dose of 0.05 g/kg successfully improved the PER, FCR, and ADWG of the fish. This information is of increasing interest in fish nutrition that will affect the overall growth factor to provide a healthy and sustainable feed formulation.

***Keywords*:** curcumin, fucoidan, growth performance, feed utilization, tilapia

INTRODUCTION

Nowadays, with a continuously expanding global population, the food sector is growing rapidly, particularly, aquaculture which continues to supply protein sources for human consumption. Aquaculture fish, especially tilapias, have been seen to be a potential species to combat poverty, malnutrition, and food insecurity due to their ability to survive in harsh environments, easy to culture, and marketability (Prabu et al., 2019). However, due to high demand, the sustainability of the fish remains a significant concern. The major challenge comes from feeding the farmed fish with an economically sustainable yet nutritious feed. At present, antibiotics and other chemical drugs are used to promote the growth and health of the fish (Reda et al., 2013). The overuse of these substances causes negative effects on the environment and the health of animals including humans. For example, it contributes to the emergence of antimicrobial resistance of strains of bacteria (Akinnawo, 2023). Hence, numerous studies have been conducted to find alternatives to antibiotics. Environmentally sustainable feed additives such as immunostimulants, probiotics, and prebiotics have been introduced and practiced in the aquaculture farm to increase the growth rate and health status of the aquatic animals

Fucoidans and curcumin have recently been highlighted in several aquaculture research as multifunctional feed additives. Fucoidan which originates from brown seaweed can enhance growth performances, maintain a healthy intestinal lining, and boost immunity in both fish and shrimp (Yang & Lim, 2021). Curcumin has been acknowledged as a powerful immunomodulator as it has substantial pharmacological and biological properties including antioxidant, anti-inflammatory, and anti-microbial which are also involved in the growth promotion of fish (Amer et al., 2022; Mahmoud et al., 2017). Previous studies have been conducted to examine the effects of

fucoidan and curcumin on the growth, gut microbiome, and intestine profile of aquatic organisms (Ji et al., 2021; Mahgoub et al., 2020). However, the combination of both fucoidan and curcumin in the diets is not well studied in growth performance and feed utilization in fish. Furthermore, there is still little information on whether curcumin can improve the effect of fucoidan on the growth performance and feed utilization of the fish.

Thus, the present study was conducted to evaluate the effects of the combination of fucoidan and curcumin supplemented diets on the growth performance and feed utilization in red Nile tilapia (*Oreochromis niloticus*) juveniles.

MATERIALS AND METHODS

Experimental Diets and Feeding Trials

The feeding trials were conducted at the SATREPS-COSMOS Demo Site, Faculty of Agriculture, Universiti Putra Malaysia, UPM, and were performed following the rule of the Institutional Animal Care and Use Committee of Universiti Putra Malaysia (UPM) (IACUC/AUP-R007/2023). The basal diets used in this study were modified from sources of the diets that have been documented to fulfill the nutrient requirements of tilapia (*O. niloticus*) diets. The feeding diets were prepared by the inclusion of fucoidan (MANIS, UKM) and curcumin (Bio Basic, Sangon Biotech) as follows; 0 (Control), 1.5 g/kg of fucoidan (FD) as described in a previous study (Fabrini et al., 2017), 0.05 g/kg of curcumin (CR) as described in a previous study (Amer et al., 2022), 1.5 g/kg and 0.05 g/kg of fucoidan and curcumin (FDR), respectively.

Experimental Designs and Growth Performance Parameter

A total of 200 red Nile tilapia juveniles were purchased (1.98 ± 0.46 g) and distributed randomly into four experimental groups. Each group had 5 replicates of 10 fish (n=50/group). The fish were acclimatized in 20 tanks (30 cm x 19 cm x 18 cm) a week before the experiment. The water quality was maintained at a temperature, 25.0 ± 1.5°C; dissolved oxygen, 5.0 ± 0.1 mg/l; pH, 7.0 ± 0.5; ammonia, less than 0.02 mg/l, and nitrite, less than 0.5 mg/l as described in previous studies (Van Doan et al., 2014). For 44 days, each of the four experimental groups was fed according to the prepared feed; Control, FD, CR, and FDR. At the end of the feeding trial, the final weight of randomly selected fish was weighed from each replicate (n=15) to calculate the growth parameters such as average daily weight gain (ADWG), specific growth rate (SGR), protein efficiency ratio (PER), and feed conversion ratio (FCR)

Average daily weight gain (ADWG) = total weight gain (g) / experimental days

Specific growth rate (SGR) = 100 x (ln final weight – ln initial weight) / total period of experiment (days)

Protein efficiency ratio (PER) = total weight gain (g) / protein intake (g) x 100

Feed conversion ratio (FCR) = total feed intake (g) / total weight gain (g)

Statistical analysis

Collected data were statistically analyzed using ANOVA (SPSS Version 29 for MacOS SPSS Inc., Chicago, IL, USA). Post hoc Duncan test was used to assess differences among means; the variation in the data was expressed as pooled SEM, and the significance level was set at $p<0.05$.

RESULTS AND DISCUSSIONS

Growth performance parameters

The study showed no significant difference in the SGR ($p>0.05$) between fish in different experiment groups. However, PER showed a significant increase for fish in CR ($p<0.05$), while FCR and ADWG in CR were enhanced by 21% and 1.83%, respectively (Table 1). This finding is contradicted by the results of the SGR that demonstrated no significant difference between the treatment and control groups. The results showing an improvement of PER, FCR, and ADWG are consistent with previous studies in red Nile tilapia (*O. niloticus*) (Amer et al., 2022; Mahmoud et al., 2017), grass carp (*Ctenopharyngodon idella)* (Ming et al., 2020), and large yellow croaker (*Pseudosciaene crocea*) (Ji et al., 2021). The enhanced PER, FCR, and ADWG while no significant increase was observed on SGR could be linked to several factors. Firstly, balanced nutrition has long been recognized as a key factor in supporting growth performance, resulting in optimal body and flesh quality and, at

the same time sustaining the health of the fish (Adewumi, 2018). For example, the lack of essential nutrients such as lipids, carbohydrates, minerals, and vitamins could affect the overall growth of the fish. The current studies have focused only on the efficiency with which protein in the diet is converted into body mass instead of the overall nutrients in the diet. Secondly, despite the increase in ADWG, there is no change in SGR, which suggests that the starting weight of the fish was large enough for the SGR to remain stable and the fish have reached a size where absolute growth (in grams per day) has improved making the ADWG have a significant increase.

At present, curcumin showed a positive increase in the PER, FCR, and ADWG compared to the control groups. This is consistent with the information that stated that curcumin could boost nutrient utilization remarkably (Jiang et al., 2016). The increased ADWG of the fish in CR could be due to the properties of curcumin in improving digestion by increasing the trypsin and lipase activities leading to faster growth (Yang et al., 2022). The lowest FCR was also observed in the curcumin group (CR), which was improved by 21% compared to the control groups. Curcumin has a unique flavor that has been used in many local delicacies, which may increase the palatability of feed resulting in increasing of feed intake (Alagawany et al., 2021). Thus, the feed was utilized more efficiently by the fish which improved the feed efficiency. Curcumin's anti-inflammatory properties reduce the inflammation in the gut lining which improves the digestive efficiency and nutrient uptake, overall leading to a better growth performance and lower FCR (Giri et al., 2019). Lower FCR indicates better efficiency in converting feed into body mass making it to be desirable in achieving sustainable aquaculture practices. Less feed is needed to achieve optimum growth which can minimize the cost and environmental effects. This study suggests that curcumin can reduce the feed conversion ratio which leads to an increase in ADWG. Next, PER in the CR groups showed an improvement compared to control groups ($p<0.05$). This could be due to the role of curcumin in increasing the intestinal microbiota and digestive enzyme activities of the fish (Jiang et al., 2016). Meanwhile, fucoidan in this study does not show any significance in growth performance parameters. Similar results related to the growth performance parameter in the fingerlings of *O. niloticus*, were observed in a study by Fabrini et al., (2017), who investigated the effect of different concentrations (0%, 0.5%, 1.0%, and 1.5%) of sulfated polysaccharides, fucoidan extracted from brown algae.

Table 1. Growth performance and feed utilization of juvenile Nile tilapia fed with different diets containing fucoidan and curcumin (n=60).

	IW (g)	FW (g)	ADWG (g/day)	SGR (%)	PER (g/g)	FCR (g)
Control	1.953 ± 0.145^{a}	2.201 ± 0.151^{a}	0.006 ± 0.001^{a}	0.276 ± 0.063^{a}	9.313 ± 1.992^{a}	1.576 ± 0.126^{b}
FD	2.013 ± 0.062^{a}	2.439 ± 0.099^{ab}	0.010 ± 0.002^{ab}	0.433 ± 0.100^{a}	14.539 ± 3.458^{ab}	1.378 ± 0.108^{ab}
CR	2.009 ± 0.218^{a}	2.760 ± 0.116^{b}	0.017 ± 0.006^{b}	0.781 ± 0.328^{a}	31.189 ± 11.075^{b}	1.116 ± 0.179^{a}
FDR	1.945 ± 0.104^{a}	2.445 ± 0.191^{ab}	0.011 ± 0.002^{ab}	0.506 ± 0.078^{a}	19.194 ± 4.010^{ab}	1.242 ± 0.088^{ab}

Values within the same column having different superscripts are significantly different ($P<0.05$). Data were presented as mean ± SE.
IW, initial weight; FW, final weight; ADWG, average daily weight gain; SGR, specific growth rate; PER, protein efficiency ratio; FCR, feed conversion ratio

CONCLUSION

The inclusion of 1.5 g/kg of fucoidan has not improved the growth performance and feed utilization of the red Nile tilapia while the inclusion of 0.05 g/kg of curcumin leads to significant improvement in growth performance and lower FCR. The present study showed that a combination of fucoidan and curcumin with the stated dose was not effective in increasing the growth performance and feed utilization of *O. niloticus*. The study could direct future research on the optimum dose of fucoidan to be included in the diet for the significant effects on the growth performance and feed utilization of *O. niloticus*.

REFERENCES

A.A., Adewumi. (2018). The impact of nutrition on fish development, growth and health. *International Journal of Scientific and Research Publications (IJSRP)*, 8(6). https://doi.org/10.29322/ijsrp.8.6.2018.p7822

Akinnawo, S. O. (2023). Eutrophication: Causes, consequences, physical, chemical and biological techniques for mitigation strategies. *In Environmental Challenges (Vol. 12*). Elsevier B.V. https://doi.org/10.1016/j.envc.2023.100733

Alagawany, M., Farag, M. R., Abdelnour, S. A., Dawood, M. A. O., Elnesr, S. S., & Dhama, K. (2021). Curcumin and its different forms: A review on fish nutrition. *In Aquaculture (Vol. 532)*. Elsevier B.V. https://doi.org/10.1016/j.aquaculture.2020.736030

Amer, S. A., El-Araby, D. A., Tartor, H., Farahat, M., Goda, N. I. A., Farag, M. F. M., Fahmy, E. M., Hassan, A. M., Abo El-Maati, M. F., & Osman, A. (2022). Long-Term Feeding with Curcumin Affects the Growth, Antioxidant Capacity, Immune Status, Tissue Histoarchitecture, Immune Expression of Proinflammatory Cytokines, and Apoptosis Indicators in Nile Tilapia, *Oreochromis niloticus*. *Antioxidants*, 11(5). https://doi.org/10.3390/antiox11050937

Fabrini, B. C., Fernandes Braga, W., Souza Andrade, E., de Jesus Paula, D. A., Paulino, R. R., Carvalho Costa, A., Paiva, L. V., Lelis da Silva, F., & Solis Murgas, L. D. (2017). Sulfated Polysaccharides in Diets for Nile tilapia (*Oreochromis niloticus*) in the Initial Growth Phase. *Journal of Aquaculture Research & Development*, 08(04). https://doi.org/10.4172/2155-9546.1000477

Giri, S. S., Sukumaran, V., & Park, S. C. (2019). Effects of bioactive substance from turmeric on growth, skin mucosal immunity and antioxidant factors in common carp, *Cyprinus carpio*. *Fish and Shellfish Immunology*, 92, 612–620. https://doi.org/10.1016/j.fsi.2019.06.053

Ji, R., Xiang, X., Li, X., Mai, K., & Ai, Q. (2021). Effects of dietary curcumin on growth, antioxidant capacity, fatty acid composition and expression of lipid metabolism-related genes of large yellow croaker fed a high-fat diet. *British Journal of Nutrition*, 126(3), 345–354. https://doi.org/10.1017/S0007114520004171

Jiang, J., Wu, X. Y., Zhou, X. Q., Feng, L., Liu, Y., Jiang, W. D., Wu, P., & Zhao, Y. (2016). Effects of dietary curcumin supplementation on growth performance, intestinal digestive enzyme activities and antioxidant capacity of crucian carp *Carassius auratus*. *Aquaculture*, 463, 174–180. https://doi.org/10.1016/j.aquaculture.2016.05.040

Mahgoub, H. A., El-Adl, M. A. M., Ghanem, H. M., & Martyniuk, C. J. (2020). The effect of fucoidan or potassium permanganate on growth performance, intestinal pathology, and antioxidant status in Nile tilapia (*Oreochromis niloticus*). *Fish Physiology and Biochemistry*, 46(6), 2109–2131. https://doi.org/10.1007/s10695-020-00858-w

Mahmoud, H. K., Al-Sagheer, A. A., Reda, F. M., Mahgoub, S. A., & Ayyat, M. S. (2017). Dietary curcumin supplement influence on growth, immunity, antioxidant status, and resistance to *Aeromonas hydrophila* in *Oreochromis niloticus*. *Aquaculture*, 475, 16–23. https://doi.org/10.1016/j.aquaculture.2017.03.043

Prabu, E., Rajagopalsamy, C. B. T., Ahilan, B., Jeevagan, I. J. M. A., & Renuhadevi, M. (2019). Tilapia – An Excellent Candidate Species for World Aquaculture: A Review. *Annual Research & Review in Biology*, 1–14. https://doi.org/10.9734/arrb/2019/v31i330052

Purbomartono, C., Emawati, R., Mulia, D. S., & Haryanto, H. (2023). The Effectiveness of Dietary Fucoidan Compared to the Combination of Fucoidan with Turmeric on the Growth of African Catfish (*Clarias Gariepinus*). *Proceedings Series on Social Sciences & Humanities*, 8, 17–23. https://doi.org/10.30595/pssh.v8i.603

Van Doan, H., Doolgindachbaporn, S., & Suksri, A. (2014). Effects of low molecular weight agar and Lactobacillus plantarum on growth performance, immunity, and disease resistance of basa fish (*Pangasius bocourti*, Sauvage 1880). *Fish and Shellfish Immunology*, 41(2), 340–345. https://doi.org/10.1016/j.fsi.2014.09.015

Yang, J. Y., & Lim, S. Y. (2021). Fucoidans and bowel health. *In Marine Drugs* (Vol. 19, Issue 8). MDPI. https://doi.org/10.3390/md19080436

ANALYSIS OF LEAVES TRICHOME DENSITY IN RESPONSE TO WOUNDING ON CHILI PLANT, *CAPSİCUM ANNUUM* L.

Nur Fariza M. Shaipulah[1], Nurul Insyirah Zaidi[1], Salwa Shahimi[1]

[1]*Faculty of Science and Marine Environment, Universiti Malaysia Terengganu, 21030 Kuala Nerus, Terengganu, MALAYSIA*

fariza@umt.edu.my

ABSTRACT

Trichomes are hairlike structure on plant tissues. Trichomes play important role in plant defense against biotic and abiotic stress. The aim of this study is to determine the trichome density of chili leaves in response to mechanical wounding on Capsicum annuum L. Two months old of chili plants were used for the experiments. Leaves from nodes 7th and 9th were wounded using tweezer. All treatment were left for 12 days before trichome analysis. One way Analysis of Variance (ANOVA) showed a significant difference in mean density of trichomes between control, non-wounding, and wounding treatments on adaxial ($F_{(2,9)} = 53.49$, $p < 0.001$) and abaxial surfaces ($F_{(2,9)} = 25.84$, $p < 0.001$). Thus, this study suggested that the chili plants likely induced the formation of trichomes after the mechanical wounding.

Keywords: induced response, wounding, plant hair, plant stress

INTRODUCTION

Chili is an economically important crop and grown worldwide due to their marketable value that have been used in culinary, medicinal, and ornamental purposes [1,2]. *Capsicum* species belong to the Solanaceae family and the most well-known and actively farmed species are *C. annuum, C. frutescens, C. pubescens*, *C. chinense*, and *C. baccatum*, [3]. *Capsicum annuum* L. is a common domesticated chili and widely planted in Malaysia. Chili cultivation presents a few challenges, including pathogen and pest infestation, as well as abiotic stress [4]. Pests cause direct damage to plants, including yellowing of leaf tissue, stunted growth, reduced rate of photosynthesis, and vector for pathogenic viruses that can cause plant death [5,6]. The usage of pesticide as chemical control is less successful because pest have become more prominent, sprays only resistance towards certain species of pest [7].

Trichome is a small protrusion on the surface of the plant originating from the epidermis. Morphology of trichome study is often associated with plant defense. The occurrence of trichomes increase plant resistance against pest infestations [8]. Non-glandular trichomes inhibits the movement of pests on leaf epidermis [9] and glandular trichomes secretes the phenolic compounds that serve as chemical barriers on the epidermis by repelling the pest in contact with epidermis [10]. High density of non-glandular trichome coverage increase the physical coverage protection with fewer gaps prevent direct contact between cold air and leaf epidermis thus enhance cold resistance of plants [11].

Previous studies carried out on chili pepper were mainly focused on describing trichomes morphology of *Capsicum* sp. and discussed on the induction of leaves trichome density upon aphids infestation on *Capsicum frutescens* [12,13,14]. However, there is little documented studies on the specialization of trichomes as part of a plant stress. Thus, this project is aimed on the induction of trichomes in *C. annuum* in response to mechanical wounding. The density of trichomes of this species are compared between control and wounded plants. This information can be beneficial to plant breeders and agronomists in order to develop pest resistant crops, as well as to promote the concept of Integrated Plant Management (IPM) in Malaysia.

LITERATURE REVIEW

Trichomes

Trichomes are one of key defence mechanisms known to have constitutive and induced sites to produce chemical metabolites [15,16]. Trichomes are hair-like structures that can be found on the surface of various tissues on plants. Most of the leaves, herbaceous stems, fruits, and flowers often show multiple types of trichomes [17,18]. Trichomes are generally classified as unicellular or multicellular, branched or unbranched, and glandular or non-glandular. Trichomes vary in size, cell number, and shape. The morphology and density of trichomes vary among

individual, species, and plant population [19]. Kim et al. [13] observed unicellular, multicellular structures, non-glandular, and glandular trichomes on stems and leaves of *Capsicum* sp.

Function of Plant Trichomes

The trichomes can increase resistance by mechanically preventing herbivores from moving on the surface of the plant [25,26]. Trapping does have a direct impact on the individual adaptability and population of affected insects [27]. For instance, hooked tip non-glandular trichomes can reduce the lifespan and reproduction rate of aphids and increase death of nymphs [28]. On the other hand, glandular trichomes secrete viscous or fluids to trap arthropods or prevent herbivores from eating plants [29]. The glandular trichomes secrete sesquiterpenes and zingiberene as repellent compounds towards two-spotted spider mites in tomato [30,31]. Glandular trichomes also emit herbivore induced plant volatiles (HIPV) to attract the natural enemies of herbivores [32].

Trichome thickens the epidermis and contains slightly more long-chain fatty acids than other epidermal cells, which then aids in reducing evaporation and temperature regulation [33]. A higher trichome density will result in more visible wax coverage on the young leaves [33]. Leaf trichomes are thought to be an effective barrier to prevent CO2 and H2O diffusion by increasing the resistance of the leaf boundary layer [34]. Therefore, the thick trichome cover may be drought-resistant and can protect the plant to prevent excessive moisture loss [35].

Plant Response to Wounding

Wounding is a common damage to plants that is caused by abiotic stress such as strong wind, hail, or heavy rain, as well as biotic stress including feeding from herbivores [20]. Herbivores wound plant tissues via mouthpart and stylet by penetrating plant tissue and initiating plants to respond to the attacks. Physical damage by abiotic and biotic stress promotes water loss at the wound area that leads to osmotic stress. Scratching or puncturing the leaf surface is a common way to mimic herbivores feeding. However, plants can distinguish between herbivorous and environmental damage [21]. Plant defence responds to both abiotic and biotic stress differs in the amount of tissue removed, the spatial pattern of the wound, and the age of tissue. In addition, to tissues injury, plants also differentiate the damages by recognizing salivary protein from herbivores during tissues chewing or phloem sap sucking [22]. Herbivorous wounding could influence the response in induced plant defence [23]. This is due to artificial wounds and herbivores wounds leaves do not produce a similar mixture of volatile compounds [24].

METHODOLOGY

Two months old chili plants of *C. annuum* were used for the experiment. The experiments were conducted following treatments: i) control plants, ii) non-wounded plants, and iii) wounded plants. The leaves from nodes between the 7th and 9th of chili leaves were carefully wounded on the leaf surface with a tweezer [14]. Non-wounded leaves were collected from wounded plants, but from node 12 to 14. Healthy plants served as a control. The experiment was conducted in a laboratory at temperature 25°C to 27°C and relative humidity of 70%. The plant treatments were carried out for 12 days for four replicates. One-way Analysis of Variance (ANOVA) was used to compare mean density of trichomes between control, wounding, and non-wounding treatments.

RESULTS

The mean density of leaf trichomes on both adaxial and abaxial surfaces showed a significant difference, $F(2,9) = 53.49$, $p < 0.001$ and $F(2,9) = 25.84$, $p < 0.001$, respectively. One-way ANOVA was also conducted to compare the density of glandular and non-glandular trichomes between plant treatments on *C. annuum* leaves on adaxial leaf surfaces. The results revealed that there was a significant difference of glandular trichomes between treatments, $F(2,9) = 45.77$, $p < 0.001$ (Figure 1). The results demonstrated that glandular trichomes density on control leaves (18.02 ± 1.35 cm-2) were lowered compared with wounded leaves (32.26 ± 3.28 cm-2) and non-wounded leaves (31.27 ± 2.01 cm-2). However, the non-glandular trichomes density between control leaves (1.60 ± 0.62 cm-2), wounded leaves (1.74 ± 0.71 cm=2), and non-wounded leaves (2.05 ± 0.89 cm-2) were not differed, $F(2,9) = 0.38$, $p = 0.70$ (Figure 1).

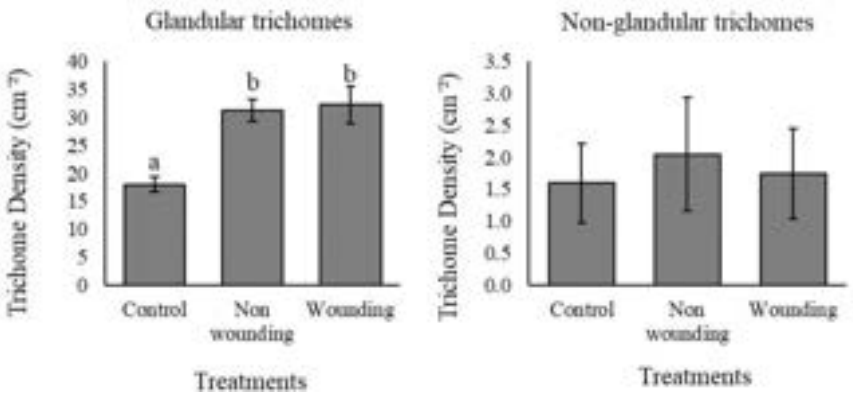

Figure 1. Mean density of trichomes on adaxial surfaces on chili leaves.

The comparison of mean density of glandular and non-glandular trichomes between plant treatments on abaxial is shown in Figure 2. The mean density of glandular trichomes were differed among treatments, $F(2.9) = 24.71$, $p < 0.001$, of which control, non-wounded, and wounded leaves recorded the mean density of trichomes as 17.13 ± 3.94 cm-2, 29.48 ± 2.90 cm-2, and 32.89 ± 3.08 cm-2 respectively. Non-glandular trichomes showed no significant difference on density between treatments, $F(2,9) = 1.27$, $p = 0.33$, of which control, non-wounded, and wounded leaves showed the mean density of non-glandular trichomes as 1.62 ± 0.71 cm-2, 2.15 ± 0.47 cm-2, and 1.58 ± 0.47 cm-2 , respectively.

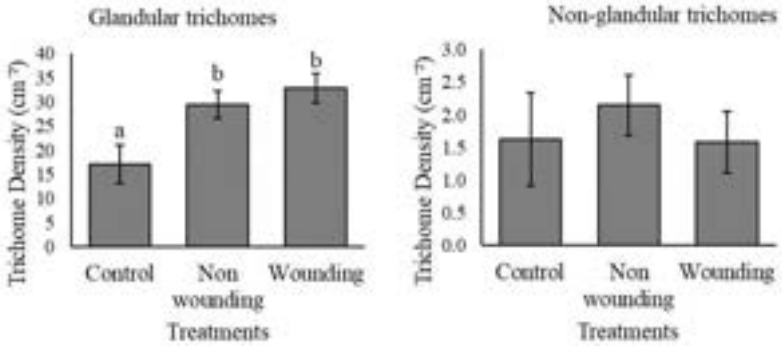

Figure 2. Mean density of trichomes on adaxial surfaces on chili leaves.

DISCUSSION

In this study revealed both glandular and non-glandular trichomes were present on the leaf surface of *C. annuum*. The density of leaf trichomes were increased on adaxial and abaxial surface of *C. annuum* upon mechanical wounding. The induction of trichomes was not only occurred around wounded tissues, but the trichomes number were increased in young and non-wounded leaves on the same plants. The results indicate that the occurrence of wound on leaf tissues able to induce the systemic response in *C. annuum*. Systemic response involves the activation of jasmonic acid (JA) and ethylene signalling pathway assisted by accumulation of protein inhibitors in response to mechanical wounding and transmitted the alarming signal from wounded leaves to the neighbouring non-wounded leaves [36]. The response leads to the long-distance responses by wounded leaves provide protection against future damage in non-wounded leaves.

As highlighted in the introduction, glandular and non-glandular trichomes play different roles in plant defence. Non-glandular are associated to mechanical defence, whereas glandular trichomes emitted chemical toxins and metabolites that regulate second line of defense in plants [37]. However, the present of non-glandular trichomes on *C. annuum* leaves were not affected after wounding, suggested that non-glandular trichomes mainly involve as constitutive defence. Abiotic stress like wind and strong hail can cause injury to the plant tissues. Even so, the resulting wound does not damage the entire plant tissue, but it is sufficient for the plant's defense system to activate signalling pathways. General signals of injury in plants involving the role of glandular trichomes which can be considered as a factory that stores and secretes secondary metabolites that activates signalling pathway resulting the induction of trichomes on undamaged leaves 38,39]. In addition, wound tissues may cause water loss

and consequently induce more glandular trichomes compared to non-glandular trichomes [40]. Non-glandular trichomes were only induced when they reached a certain degree of stress such as drought [41]. Therefore, in this study all plant treatments received a sufficient amount of water throughout 12 days of experiment. Thus, it is possible to suggest that formation of non-glandular trichomes were likely dependent on water shortage.

CONCLUSION

In summary, our results demonstrated that density of trichomes were higher on wounded plants than non-treated leaves on both abaxial and adaxial surfaces of *Capsicum annuum*. Only glandular trichomes were significantly increased after wounding, suggesting that glandular trichomes play important role in induced defence mechanism of *C. annuum*. In addition, *C. annuum* also showed more glandular trichomes on young, expanding leaves on wounding plants when compared to control, indicated systemic response on wounding plants was occurred. Further research is required to gain an insight into the distribution of trichome types in *C. annuum* and to understand how various types of glandular trichomes contain different organic compounds that affect plant resistance. Thus, the studies will provide more proven evidence on the roles of glandular and non-glandular trichomes in plant defence mechanisms that are beneficial in controlling aphid colonization on chili plants especially in biological control.

REFERENCES

[1] Agrawal, A. A. (1998). Induced responses to herbivory and increased plant performance. Science, 279(5354), 1201-1202.

[2] Barroso, P. A., Rêgo, E. R., Rêgo, M. M., Nascimento, K. S., Nascimento, N. F. F., Nascimento, M. F., Soares, W. S., Ferreira, K. T. C., & Otoni, W. C. (2012). Analysis of segregating generation for components of seedling and plant height of pepper (*Capsicum annuum* L.) for medicinal and ornamental purposes. In XXIV International Eucarpia Symposium Section Ornamentals: Ornamental Breeding Worldwide 953. pp. 269-275.

[3] Sudré, C.P., Gonçalves, L.S.A., Rodrigues, R., Amaral Júnior, A.D., Riva-Souza, E.M. & Bento, C.D.S. (2010). Genetic variability in domesticated *Capsicum* spp. as assessed by morphological and agronomic data in mixed statistical analysis. Genetics and Molecular Research, 9(1): 283-294.

[4] Frantz, J. D., Gardner, J., Hoffmann, M. P., & Jahn, M. M. (2004). Greenhouse screening of capsicum accessions for resistance to green peach aphid (*Myzus persicae*). HortScience, 39(6), 1332-1335.

[5] Blackman, R. L., & Eastop, V. F. (2000). Aphids on the World's Crops: An Identification and Information Guide (No. Ed. 2). John Wiley & Sons Ltd.

[6] Mureithi, D. M., Fiaboe, K. K. M., Ekesi, S., & Meyhöfer, R. (2017). Important arthropod pests on leafy amaranth (*Amaranthus viridis*, *A. tricolor* and *A. blitum*) and broadleafed African nightshade (*Solanum scabrum*) with a special focus on host-plant ranges. African Journal Horticultural Science, 11, 1-17.

[7] Zeb, Q., Naeem, M., Khan, S. A., & Ahmad, S. (2016). Effect of insecticides on the population of aphids, natural enemies and yield components of wheat. Pakistan Journal of Zoology, 48(6), 1839-1848.

[8] Kang, J.-H., Liu, G., Shi, F., Jones, A.D., Beaudry, R.M., & Howe, G. A. (2010). The tomato odorless-2 mutant is defective in trichome-based production of diverse specialized metabolites and broad-spectrum resistance to insect herbivores. Plant Physiology, 154(1), 262– 272.

[9] Szyndler, M. W., Haynes, K. F., Potter, M, F., Corn, R. M., & Loudon, C. (2013). Entrapment of bed bugs by leaf trichomes inspires microfabrication of biomimetic surfaces. Journal of the Royal Society Interface, 10(83), 1-9.

[10] Karabourniotis, G., Liakopoulos, G., Nikolopoulos, D., & Bresta, P. (2019). Protective and defensive roles of non-glandular trichomes against multiple stresses: structure–function coordination. Journal of Forestry Research, 31(4), 1-12.

[11] Zhang, Y., Song, H., Wang, X., Zhou, X. Zhang, K., Chen, X., Liu, J., Han, J., & Wang, A. (2020). The roles of different types of trichomes in tomato resistance to cold, drought, whiteflies, and botrytis. Agronomy, 10(3), 411.

[12] Adedeji, O., Ajuwon, O. Y., & Babawale, O. O. (2007). Foliar epidermal studies, organographic distribution and taxonomic importance of trichomes in the family Solanaceae. International Journal of Botany, 3(3), 276-282.

[13] Kim, H. J., Seo, E. Y., Kim, J. H., Cheong, H. J., Kang, B. C., & Choi, D. I. (2012). Morphological classification of trichomes associated with possible biotic stress resistance in the genus *Capsicum*. The Plant Pathology Journal, 28(1), 107-113.

[14] Abu Bakar N. S. (2020). The induction of leaves trichomes by aphids infestation on chili plant, *Capsicum frutescens* L. Undergraduate thesis. Bachelor of Applied Science (Biodiversity Conservation and Management), School of Marine and Environmental Science, Universiti Malaysia Terengganu, Terengganu. 31 pp.
[15] Holeski, L. M., Chase-Alone, R., & Kelly, J. K. (2010). The genetics of phenotypic plasticity in plant defense: trichome production in *Mimulus guttatus*. The American Naturalist, *175*(4), 391-400.
[16] Tissier, A. (2012). Glandular trichomes: What comes after expressed sequence tags? The Plant Journal, 70(1), 51-68.
[17] Telfer, A., Bollman, K. M., & Poethig, R. S. (1997). Phase change and the regulation of trichome distribution in *Arabidopsis thaliana*. Development, 124(3), 645-654.
[18] Chen, C., Liu, M., Jiang, L., Liu, X., Zhao, J., Yan, S., Yang, S., Ren, H., Liu, R., & Zhang, X. (2014). Transcriptome profiling reveals roles of meristem regulators and polarity genes during fruit trichome development in cucumber (*Cucumis sativus* L.). Journal of Experimental Botany, 65(17), 4943-4958.
[19] Dalin, P., Ågren, J., Björkman, C., Huttunen, P., & Kärkkäinen, K. (2008). Leaf trichome formation and plant resistance to herbivory. In: Induced Plant Resistance to Herbivory. Springer, Dordrecht pp. 89-105.
[20] Cheong, Y. H., Chang, H. S., Gupta, R., Wang, X., Zhu, T., & Luan, S. (2002). Transcriptional profiling reveals novel interactions between wounding, pathogen, abiotic stress, and hormonal responses in Arabidopsis. Plant Physiology, 129(2), 661677.
[21] Bruinsma, M., & Dicke, M. (2008). Herbivore-induced indirect defense: from induction mechanisms to community ecology. In Induced plant resistance to herbivory. pp. 31-60.
[22] Mithöfer, A., Wanner, G., & Boland, W. (2005). Effects of feeding *Spodoptera littoralis* on lima bean leaves. II. Continuous mechanical wounding resembling insect feeding is sufficient to elicit herbivory-related volatile emission. *Plant Physiology*, 137(3), 1160–1168.
[23] Schoonhoven, L. M., Van Loon, B., van Loon, J. J., & Dicke, M. (2005). Insect-plant Biology. 2nd eds. Oxford University Press on Demand. 440 pp.
[24] Van Poecke, R. M., Roosjen, M., Pumarino, L., & Dicke, M. (2003). Attraction of the specialist parasitoid *Cotesia rubecula* to *Arabidopsis thaliana* infested by host or non-host herbivore species. Entomologia Experimentalis et Applicata, 107(3), 229-236.
[25] Kennedy, G. G. (2003). Tomato, pests, parasitoids, and predators: tritrophic interactions involving the genus Lycopersicon. Annual Review of Entomology, 48(1), 51-72.
[26] Simmons, A. T., McGrath, D., & Gurr, G. M. (2005). Trichome characteristics of F1 *Lycopersicon esculentum* × *L. cheesmanii* f. *minor* and *L. esculentum* × *L. pennellii* hybrids and effects on *Myzus persicae*. Euphytica, 144(3), 313-320.
[27] Peterson, J. A., Ode, P. J., Oliveira-Hofman, C., & Harwood, J. D. (2016). Integration of plant defense traits with biological control of arthropod pests: challenges and opportunities. Frontiers in Plant Science, 7, 1794.
[28] Johnson, B. (1953). The injurious effects of the hooked epidermal hairs of french beans (*Phaseolus vulgaris* L.) on *Aphis craccivora* Koch. Bulletin of Entomological Research, 44(4), 779-788.
[29] Wheeler, A. G., & Krimmel, B. A. (2015). Mirid (Hemiptera: Heteroptera) specialists of sticky plants: adaptations, interactions, and ecological implications. Annual Review of Entomology, 60, 393–414.
[30] Xu, J., van Herwijnen, Z. O., Dräger, D. B., Sui, C., Haring, M. A., & Schuurink, R. C. (2018). SlMYC1 regulates type VI glandular trichome formation and terpene biosynthesis in tomato glandular cells. The Plant Cell, 30(12), 2988–3005.
[31] Dawood, M. H., & Synder, J. C. (2020). The alcohol and epoxy alcohol of zingiberene, produced in trichomes of wild tomato, are more repellent to spider mites than zingiberene. Frontiers in Plant Science, 11, 35.
[32] Dicke, M., & Baldwin, I. (2010). The evolutionary context for herbivore-induced plant volatiles: beyond the 'cry for help'. Trends in Plant Science, 15(3), 167-175.
[33] Busta, L., Hegebarth, D., Kroc, E., & Jetter, R. (2017). Changes in cuticular wax coverage and composition on developing Arabidopsis leaves are influenced by wax biosynthesis gene expression levels and trichome density. Planta, 245(2), 297–311.
[34] Guerfel, M., Baccouri, O., Boujnah, D., Chaibi, W., & Zarrouk, M. (2009). Impacts of water stress on gas exchange, water relations, chlorophyll content and leaf structure in the two main Tunisian olive (*Olea europaea* L.) cultivars. Scientia Horticulturae, 119(3), 257–263.
[35] Mo, Y., Yang, R., Liu, L., Gu, X., Yang, X., Wang, Y., Zhang, X., & Li, H. (2016). Growth, photosynthesis and adaptive responses of wild and domesticated watermelon genotypes to drought stress and subsequent re-watering. *Plant Growth Regulation*, 79(2), 229–241.
[36] García, T., Gutiérrez, J., Veloso, J., Gago-Fuentes, R., & Díaz, J. (2015). Wounding induces local resistance but systemic susceptibility to *Botrytis cinerea* in pepper plants. Journal of Plant Physiology, 176, 202-209.

[37] Wahyuni, D. S., Choi, Y. H., Leiss, K. A., & Klinkhamer, P. G. (2021). Morphological and chemical factors related to western flower thrips resistance in the ornamental gladiolus. Plants, 10(7), 1384.
[38] Glas, J. J., Schimmel, B. C., Alba, J. M., Escobar-Bravo, R., Schuurink, R. C., & Kant, M. R. (2012). Plant glandular trichomes as targets for breeding or engineering of resistance to herbivores. International Journal of Molecular Sciences, 13(12), 17077–17103.
[39] Ruan, J., Zhou, Y., Zhou, M., Khurshid, M., Weng, W., Cheng, J., & Zhang, K. (2019). Jasmonic acid signaling pathway. International Journal of Molecular Science, 20(10), 2479-2494.
[40] León, J., Rojo, E., & Sánchez-Serrano, J. J. (2001). Wound signalling in plants. Journal of Experimental Botany, 52(354), 1-9.
[41] Gonzales, W. L., Negritto, M. A., Suarez, L. H., & Gianoli, E. (2008). Induction of glandular and non-glandular trichomes by damage in leaves of *Madia sativa* under contrasting water regimes. Acta Oecologica, 33(1), 128-132.

THE DIVERSITY OF AIRBORNE BACTERIA AND ANTIBIOTIC RESISTANCE PROFILES AT URBAN KINDERGARTEN

Nabil Alias[1], Nurkhalida Khalil[1], Baderin Osman[2], Wan Syaidatul Aqma[1*]

[1]*Department of Biological Sciences and Biotechnology, Faculty of Science and Technology, Universiti Kebangsaan Malaysia, 43600 UKM Bangi, Malaysia*

[2]*Consultation Research Development Department, National Institute of Occupational Safety and Health (NIOSH), 43650 Bandar Baru Bangi, Malaysia*

syaidatul@ukm.edu.my

ABSTRACT

Indoor air quality (IAQ) issues in school buildings can affect students' academic performance because children are more vulnerable to dangerous risks such as sick building syndrome than adults. The purpose of this study is to isolate and identify airborne bacteria in an urban kindergarten, Bangi, Malaysia and determine the antibiotic resistance. Sampling was done in eight sampling rooms through an active sampling method and the colony forming units CFU/m3 of bacteria were recorded, identified and correlated with indoor air physicochemical parameters. Bacteria with a high Multiple Antibiotic Resistance Index (MAR) were identified and selected for 16S rRNA sequencing. The results showed that the colony formation unit in the evening was 343 CFU/m3 higher than in the morning which was 320 CFU/m3. The identified bacterial strains are Acinetobacter sp., Pseudomonas stutzeri, Leclercia sp. and Mixta calida. Total colony forming unit of bacterial formation were at safe levels and all physicochemical parameters met the established standards, showed the space is at a safe level for habitation.
***Keywords*:** Indoor air quality (IAQ), bioaerosols, airborne bacteria, antibiotic resistance

INTRODUCTION

Indoor air quality (IAQ) resulting from high levels of bacterial concentration is a critical global issue because individuals spend approximately 90 percent of their time at home, in the office, or at other workplaces, exposing them to various types of pathogens (Mannan and Al-Ghamdi 2021). IAQ is important because it involves chemicals like carbon monoxide, carbon dioxide, and smoke haze, as well as factors like temperature, humidity, and air movement. It also includes aerosol pollutants, which can harm the health, comfort, and performance of building occupants. Exposure to bioaerosols containing airborne microorganisms can result in respiratory distress and other adverse health effects such as respiratory-related infections, pneumonitis, hypersensitivity and toxic reactions (Wei et al. 2021). The study of indoor air quality should not be limited to measuring abiotic physicochemical parameters but should also include aerosol pollutants (bioaerosols) due to their adverse effects on health.

LITERATURE REVIEW

Bioaerosols are defined as airborne particles originating from biological sources such as bacteria, viruses, protozoa, plants and animals or non-living organisms such as dust. Because of its small size and mass, it is easily moved from one place to another and stays in the air for a long time. *Staphylococcus, Micrococcus, Streptococcus, Bacillus* are *Neisseria* are the most dominant bacterial genera in indoor air while fungi are *Cladosporium* sp., *Alternia* sp., *Penicillium* sp. and *Aspergillus* sp. (Kumar, Singh and Singh 2022). Antimicrobial resistance to antibiotics occurs when microorganisms such as bacteria and fungi develop the ability to resist resistance from antimicrobial agents and continue to multiply in the presence of antimicrobial agents. Many factors influence the results of antibiotic resistance tests, including environmental factors including temperature, osmotic pressure, drying, and ions from electricity while biotic factors are among the factors found in the bacteria. The growing use of antibiotics for personal care is thought to be the cause of the spread of antibiotic resistance in indoor environments even though there are several sources of indoor antibiotic resistance bacteria (Lee and Yoo 2022). The objective of this study is to explore the comprehensive effects of air quality on airborne bacteria and provide a scientific basis for mitigating human exposure risks in indoor building of a nursery and pre-school. Poor indoor air quality affects the productivity and health of students and employees, with the health of students, especially children, being a particular concern due to their susceptibility to airborne microorganisms and weaker immune systems. IAQ problems in school buildings may be more serious than in other building categories due to higher occupant density, inadequate classroom sanitation, and inadequate outdoor air supply, lack of construction and frequent maintenance of school buildings. Poor indoor air quality can also affect academic performance and

student attendance because children are more exposed to health risks and exposure to environmental hazards than adults. According to the Occupational Health and Safety Department, indoor air pollution has received little attention compared to air pollution in the outdoor environment. Now, it has become a matter of public concern which is partly driven by the emergence of new indoor air pollutants.

METHODOLOGY

Sampling of indoor air and airborne bacteria using the active sampling method at an urban kindergarten in Bangi, Malaysia (2°55' 31.8" N 101°46' 32.7" E). Air sampling was taken from 12 rooms where six rooms from pre-school (children aged 4-6 years), four bedrooms, library and isolation room. In-situ parameters were taken during indoor air sampling by recording the number of individuals present, temperature, air movement, humidity percentage and concentration of aerosol pollutants such as dust and fumes (Di Giulio et al. 2010). Active sampling of airborne bacteria was performed using the MicroBio MB2 400 Hole Bioaerosol Air Sampler supplied by Cantium Scientific. A total of 100 liters of air is taken for one minute and triplicated each time the sampling is carried out. Tryptone Soya Agar (TSA) and Buffered Charcoal-Yeast Extract (BCYE) agar. Petri dishes were incubated at a temperature of 37°C for 48 hours while BCYE petri dishes incubated at 35°C for 72 hours. The density of bacteria in the air was determined through the calculation of the number of colony forming units per cubic meter (CFU/m^3) on agar plates. Antibiotic resistance tests were performed on bacterial isolates through the Kirby-Bauer disk diffusion method by referring to the Clinical Laboratory Standard Institute (CLSI) protocol. Genomic DNA isolation from bacterial samples was carried out according to the protocol from the Bacterial Genomic DNA Isolation Kit (ab288102) (Abcam) and the genomic DNA extract was used as a template to amplify the gene by PCR. Bacterial samples were isolated and purified using the Bacterial Genome DNA Isolation Kit (ab288102). Purified PCR amplicon samples were sent to Apical Scientific Company (Malaysia) for 16S rRNA sequencing and analysis.

RESULTS

Indoor air physicochemical parameters and Identification of Bacteria

Physicochemical parameters of indoor air were recorded and compared. Readings were taken in triplicate for each parameter in all sampling rooms conducted using a Q-Trak 7575 Indoor Air Quality Monitor connected to a 964 Straight Probe Thermoanemometer and a DustTrak™ DRX 8534 Aerosol Monitor supplied by TSI Incorporated. Colony forming units (CFU) of bacterial isolates on TSA agar from air samples were recorded and compared using units (CFU /m^3). For each sampling room, isolation was performed in triplicate. The record of bacterial CFU in the evening is higher than in the morning. The average range of bacterial CFU in the evening was 343 CFU /m^3. The average number of bacterial CFU in the evening was recorded the highest in 4 Betik, 5 Nenas and 6 Tembikai. The average total evening bacterial CFU recorded for these three rooms was 665 CFU/m^3, 517 CFU/m^3 and 435 CFU/m^3. The lowest average amount of bacterial CFU in the evening was in the Library which was 48 CFU/m^3. In the morning, the average range of bacterial CFU was 320 CFU/m^3 where 6 Mangga recorded the highest bacterial CFU (894 CFU/m^3) and the Isolation Room and Library recorded the lowest average CFU of 123 and 30 CFU/m^3. Based on the data recorded where class 6 Mangga were sampled next to be used as a control room to compare the level of cleanliness in each room with a reading of 41 CFU/m^3.

Antibiotic Resistance

All bacterial isolates are resistant to Ampicillin (96.55%) except bacterial isolate 15 which has an inhibition zone diameter of 14 mm while all bacterial isolates are susceptible to the antibiotics Amikacin and Kanamycin (0%). The percentage of Tobramycin antibiotic disc resistance was 24.14% representing 7 isolates out of 29. Amikacin is in the group of aminoglycosides used to treat infections caused by more resistant strains of Gram-negative bacteria and some Gram-positive bacteria. Seven bacterial isolates gave the highest MAR index reading of 0.5 where bacterial isolates (1, 4, 9, 12, 16, 17 and 18) resistance to Tobramycin and Ampicillin. There is one bacterial isolate with a MAR index of 0, bacterial isolate 15 which is susceptible to the four types of antibiotics used. Result of BLAST N analysis for bacterial isolates 1 and 16 have the same genus (*Acinetobacter*). Bacteria isolates 4 and 12 have the same description except that bacterium 12 has a difference in the description of *Enterobacter* sp. strain Dg-N11. *Leclercia* is a bacillus-shaped Gram-negative bacterium belonging to the Enterobacteriaceae family and can be isolated from environmental specimens. *L. adecarboxylata* as an emerging opportunistic pathogen with the potential to cause severe infections in immunocompromised patients. Bacterial isolates 9 and 18 were identified as *Pseudomonas stutzeri*, a bacillus-shaped Gram-negative bacterium that is motile because it has a single flagellum and has been categorized as an opportunistic pathogen of humans and

frequently isolated from clinical settings. Immunocompromised patients are also susceptible to this *P. stutzeri* (Alwazzeh et al. 2020). *Mixta calida* is a bacillus-shaped Gram-negative bacterium from the Enterobacteriaceae family. It used to be known as *Pantoea calida*. This bacterium has been reported to cause postoperative meningitis and bacteremia (Bhopalwala et al. 2022).

DISCUSSION

The increase in average bacterial CFU of air isolates for the eight sampling rooms can be related to physicochemical parameters such as the number of individuals, relative humidity and temperature which play an important role. The high number of occupants contributes to the concentration of microorganisms present in the room. The results of microscopic observations show that most of the bacteria that have been successfully isolated are Gram positive bacteria that have the form of cocci and rod.

CONCLUSION

The reading of physiochemical parameters and the formation of indoor air quality bacteria in the kindergarten is below the accepted standard limits, indicating that it is at a safe level to be occupied but the maintenance of indoor air quality needs to be improved due to the presence of opportunistic pathogens. Further studies by surface sampling can be done following the presence of non-airborne bacteria to obtain more accurate results.

ACKNOWLEDGEMENT

This study is supported by Faculty of Science and Technology, Universiti Kebangsaan Malaysia.

REFERENCES

Alwazzeh, M. J., Alkuwaiti, F. A., Alqasim, M., Alwarthan, S., & El-ghoneimy, Y. 2020. Infective Endocarditis Caused by Pseudomonas stutzeri: A Case Report and Literature Review. *Infectious Disease Reports*, *12*(3), 105–109.

Bhopalwala, H., Mishra, V., Dewaswala, N., Villegas-Galaviz.J., Arshad, S., Ganti, S. S., Bhopalwala, A., & Vaidya, G. 2022. Indolent course of *Mixta calida* bacteremia mimicking decompensated heart failure. *Cardiovascular Disease CHEST Journal.* Vol. 162 Issue 4:160-161.

Kumar, P., Singh, A. B., & Singh, R. 2022. Comprehensive health risk assessment of microbial indoor air quality in microenvironments. *PLoS ONE* 17(2)

Lee, G., Yoo, K. 2022. A review of the emergence of antibiotic resistance in bioaerosols and its monitoring methods. *Review Environmental Science Biotechnology*. 21:799-827.

Mannan, M., & Al-Ghamdi, S. G. (2021). Indoor Air Quality in Buildings: A Comprehensive Review on the Factors Influencing Air Pollution in Residential and Commercial Structure. *International journal of environmental research and public health*, *18*(6), 3276.

Wei, D., J, Liu, W., T., Chin, H., T., Lin, C., H., Chen, I., C & Chang, Y., T. 2021. An Investigation of Airborne Bioaerosols and Endotoxins Present in Indoor Traditional Wet Markets before and after Operation in Taiwan: A Case Study. *International Journal Environmental Research Public Health*. 13;18(6):2945.

DIVERSITY AND SPECIES COMPOSITION OF SMALL MAMMALS IN CHEMERONG RECREATIONAL FOREST AND KENYIR, TERENGGANU

Muhammad Syimir Nur Azim Azhar[1], Mohammad Izuan Mohd Zamri[1], Aini Hasanah Abd Mutalib2, and Nur Juliani Shafie[1]*

[1]*Faculty of Science and Marine Environment, Universiti Malaysia Terengganu, 21030 Kuala Nerus Terengganu, MALAYSIA*

syimirazim97@gmail.com, izizuan97@gmail.com, nur.shafie@umt.edu.my

[2]*Institute of Tropical Biodiversity and Sustainable Development, Universiti Malaysia Terengganu, 21030 Kuala Nerus Terengganu, MALAYSIA*

a.hasanah@umt.edu.my

ABSTRACT

Malaysia comprises large number of mammals species, and most of which are small mammals. The diversity and species composition of small mammals is still understudy, especially in east-coast of Peninsular Malaysia. This study aimed to determine the diversity and species composition of small mammals in Chemerong Recreational Forest and Kenyir. Ten sampling sessions with a total of 3000 sampling efforts, were conducted between November 2021 and October 2022. Hundreds of collapsible wire mesh live traps were used in each sampling session. In Chemerong Recreational Forest, 50 individuals were identified from 11 species, which is dominated by Rattus rattus (n = 14), followed by Maxomys whiteheadi and Tupaia glis with nine individuals, respectively. In Kenyir, 62 individuals were captured from nine species and mostly comprised of Sundamys muelleri (n = 15), followed by Maxomys rajah (n = 14), and Rattus rattus (n = 13). Data from this study showed the diversity and species composition varied between both study areas. Chemerong Recreational Forest shows higher diversity of small mammals while Kenyir shows high dominance. The data recorded from this study can be used as baseline data for further study and conservations effort for small mammal species.
Keywords: Diversity, species composition, small mammals, recreational forest, Terengganu

INTRODUCTION

Malaysia indeed stands out as a biodiversity hotspot (Von Rintelen *et al*., 2017), renowned for its rich variety of flora and fauna. a This record includes diverse array of small mammal species, many of which weigh below 5 kilograms when they reach maturity (Bourliere, 1975). In Peninsular Malaysia, there are about 205 small mammal species, which comprise families such as Chiroptera, Muridae, Sciuridae, Scandentia, and Insectivora, from more than 360 species of mammals (Department of Wildlife and National Parks (DWNP), 2023). They can be found in diverse habitats, including high montane forests, coastal mangroves, swamp forests, and many more (Laurent & Inza, 2020). Thus, with a huge range of habitats, they thrive occupying various niches and are important for the survival of many ecosystems. Small mammals are important as they act as seed dispersal agents which help in maintaining forest health, and their excrement contains seeds that promote the growth of new trees (Acharya., 2001; Wells & Bagchi, 2005; Zwolak *et al*., 2010). Additionally, they also act as prey for animals higher up the food chain (Nadchatram, 2008; Chaisiri *et al*., 2010).

Some species of small mammals can also be found in built-up areas such as agricultural land, housing, and urban areas. Certain species have become very adaptable in thriving in man-made areas and becoming dominant species. Species that are known to be dominant in these areas such as House rat (*Rattus rattus)*, Brown rat (*Rattus norvegicus)*, and Asian house shrew (*Suncus murinus)* as they are highly adaptable to various habitats and are considered habitat generalists (Rhim *et al*., 2007; Bernard *et al*., 2009; Benacer *et al*., 2013). Ihe study of small mammal diversity in Terengganu is indeed an area that has received relatively less attention compared to other regions, especially in forested areas. To date, previous studies have only focused on a few districts, such as in Hulu Terengganu and several islands within the state (Noor *et al*., 2016; Nor Zalipah *et al*., 2019; Baqi *et al*., 2021). Past literatures have also shown that there are about 74 species of small mammals in Hulu Terengganu and 56 species of small mammals in both Pulau Perhentian Besar and Pulau Perhentian Kecil (Baqi *et al*., 2021). Although only a few areas have been studied, a large diversity of small mammals has been found, with about 30% of small mammals in Malaysia found in Terengganu (Rahim *et al*., 2016). The high level of small mammal diversity is related to the relative density of intact forest areas in Terengganu, which provide a suitable habitat for small mammals to thrive. Terengganu is one of the states in Malaysia and has the largest forest cover behind Sabah,

Sarawak, and Pahang. More than 95750 ha of land in Terengganu are forested areas and are known as important tourist hotspots (Terengganu Forestry, 2016). Therefore, this study aimed to determine the diversity and species composition of small mammal species in Chemerong Recreational Forest and Kenyir in Terengganu.

METHODOLOGY

Study Area

The study was conducted at two recreational areas, the Chemerong Recreational Forest, and Kenyir (Figure 1). The Chemerong Recreational Forest is located in the Pasir Raja forest reserve in Dungun. The area of this recreational area is about 292 hectares and about 30km from the nearest city. The main attraction is the waterfalls and hiking trails to camp at the mountain top. The second study area was conducted in Kenyir. Kenyir is located in Hulu Terengganu, which is known as the second-largest man-made lake in Southeast Asia (Zainol *et al*., 2020). It has a total landmass of 38,000 hectares and Lake Kenyir offers many recreational spots around the vast lake area which are accessible by speed boats and houseboats. Some of the famous are the Saok and Lasir rivers which have many waterfalls, the Kelah Sanctuary, Bewah Cave, and the Belunak hiking trail.

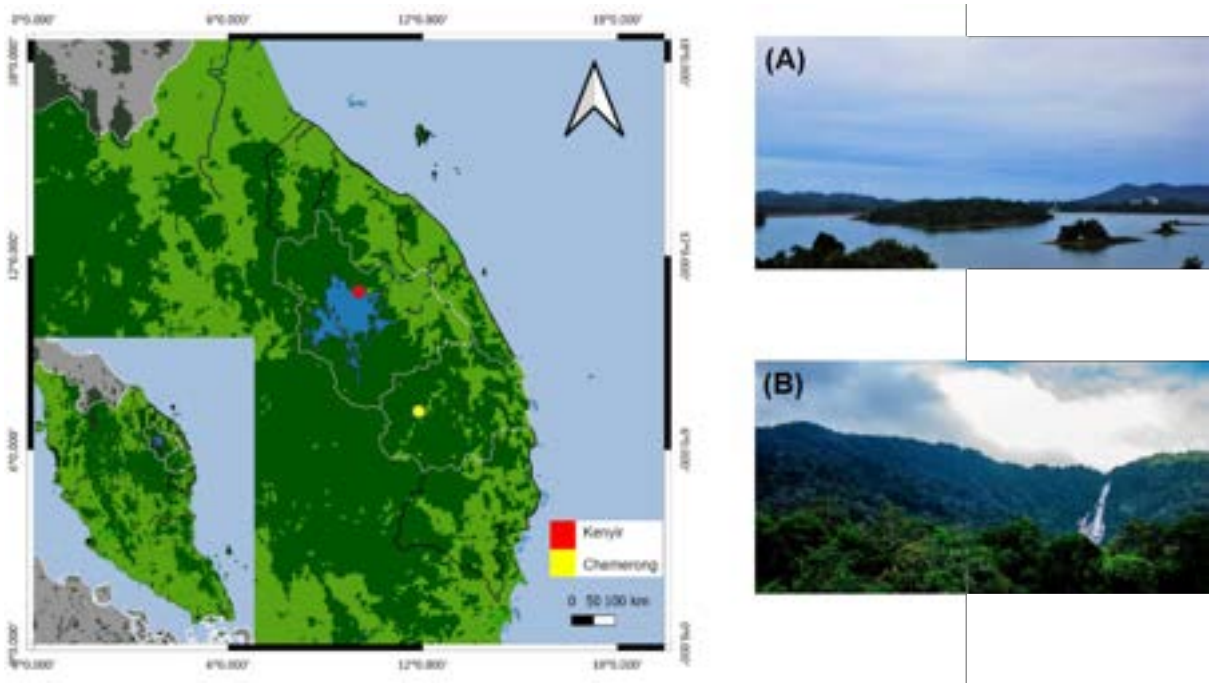

Figure 1. Map showing the location of the study areas in Peninsular Malaysia and within Terengganu state. (A) View of Tasik Kenyir, (B) View of Chemerong Recreational Forest.

Ethical and Permit Approvals

This study was conducted with ethical approval from the UMT Animal Ethics committee (UMT/JKEPHMK/2021/60)), permits for entering the study site from the Forestry Department (JH/100Jld.29(76) and PHNT.100/58/2/33Bhg.3(6)), Development Authority of Terengganu Tengah (LKTT:060/1/4/3/5Jld.3-(28)) and also permit to capture animal from the Department of Wildlife and National Park (UMT/JPHLTn.600-6/1/4JLD2(83)/210922).

Animal Trapping

The animal trapping sessions were conducted between May and November 2022. Four days and three nights were allocated for each trapping session. Ten trapping sessions were conducted in the Chemerong Recreational Forest and Kenyir respectively. A hundred wire-mesh live traps with dimensions of 25 cm X 15 cm X 12 cm were used in each trapping session with a total of 300 trapping efforts per session. The traps were randomly deployed along forest trails and river edges with a distance of 10m between each trap (Figure 2). Ripe banana, oil palm fruit and sausages were used as baits and the traps were set during late evening and checked each

day. The bait was replaced each day and traps that managed to capture specimens were brought back to the Universiti Malaysia Terengganu (UMT) laboratory for further morphometric measurements and species identification.

Figure 2. (A) Wire-mesh live traps with dimensions of 25 cm X 15 cm X 12 cm were used in each trapping session (B) Traps were randomly deployed along forest trails and river edges with a distance of 10m between each trap and (C) All captured individuals were brought back to the Universiti Malaysia Terengganu (UMT) lab for further laboratory work and species identification.

Species identification

The morphometric measurements that were taken (Figure 3) such as the head-body length (from nose tip to the anus), tail length (from anus to the tail tip), ear length (from external opening to the tip), hindfoot length (from the tip of the longest toe to the heel), and the specimen bodyweight (Islam et al. 2021). The specimen sexes also were recorded. All captured animals were identified until species level based on Francis (2019).

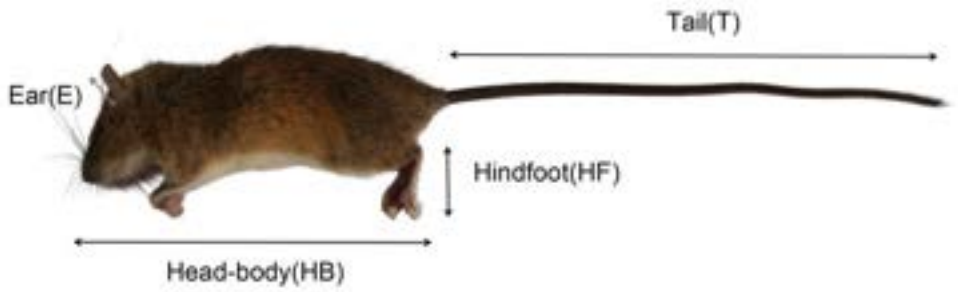

Figure 3. The morphometric measurement (Olayemi et al. 2008): Head-body (HB), 2) Tail (T), 3) Ear (E), 4) Hindfoot (HF)

DATA ANALYSIS

Analysis was conducted on the diversity and abundance of small mammal species, using diversity indices, species rank-abundance, species richness estimator, and rarefaction. The analysis of diversity was carried out using PAST software version 4.11 (Hammer *et al*., 2001), iNEXT online latest version Aug. 2022 (Chao *et al*., 2014) and Excel version 2310.

RESULTS AND DISCUSSION

Species Composition of Small Mammals

A total number of 112 individuals were caught from both study sites, comprising 12 species from three families, namely Tupaiidae, Sciuridae, and Muridae (Table 1). Kenyir recorded 62 individuals from 9 species and Chemerong Recreational Forest with 50 and 11 respectively. The most dominant family caught was Muridae with 93 individuals, followed by Tupaiidae with 17 individuals, and Sciuridae with 2 individuals (Figure 4). In Chemerong Recreational Forest, the most common species were *Rattus rattus* with 14 individuals, followed by *Maxomys whiteheadi* with 9 individuals. As for Kenyir, the most dominant species were *Maxomys rajah* and *Sundamys muelleri* with 15 and 14 individuals respectively (Figure 5). In both study sites, the presence of rare species was recorded with one individual respectively. Chemerong Recreational Forest recorded 2 species while Kenyir with one species, which is *Sundamys muelleri* and *Maxomys surifer* in Chemerong, and *Chiropodomys gliroides*.

Table 1. Checklist of small mammals captured based on the study sites in family order.

Species	Common name	IUCN	Chemerong	Kenyir	Total individual
Order Scandentia					
Family Tupaiidae					
Tupaia glis	Common Treeshrew	LC	9	8	17
Order Rodentia					
Family Sciuridae					
Callosciurus notatus	Plantain Squirrel	LC	2	0	2
Family Muridae					
Rattus rattus	House Rat	LC	14	13	27
Rattus tiomanicus	Malaysian Field Rat	LC	2	0	2
Sundamys muelleri	Muller's Giant Sunda Rat	LC	1	14	15
Niviventer cremoriventer	Dark-tailed Niviventer	LC	4	4	8
Leopoldamys sabanus	Long-tailed Giant Rat	LC	3	3	6
Leopoldamys ciliatus	Sundaic Mountain Leopoldamys	LC	0	2	2
Maxomys rajah	Rajah Spiny Rat	VU	2	15	17
Maxomys surifer	Red Spiny Rat	LC	1	2	3
Maxomys whiteheadi	Whitehead's Spiny Rat	VU	9	0	9
Chiropodomys gliroides	Indomalayan Pencil-tailed Tree-mouse	LC	3	1	4
Total no. of individuals			50	62	112
No. of species			11	9	12
No. of family			3	2	3
Sampling effort			3000	3000	6000
Capture rate			1.7%	2.0%	1.9%

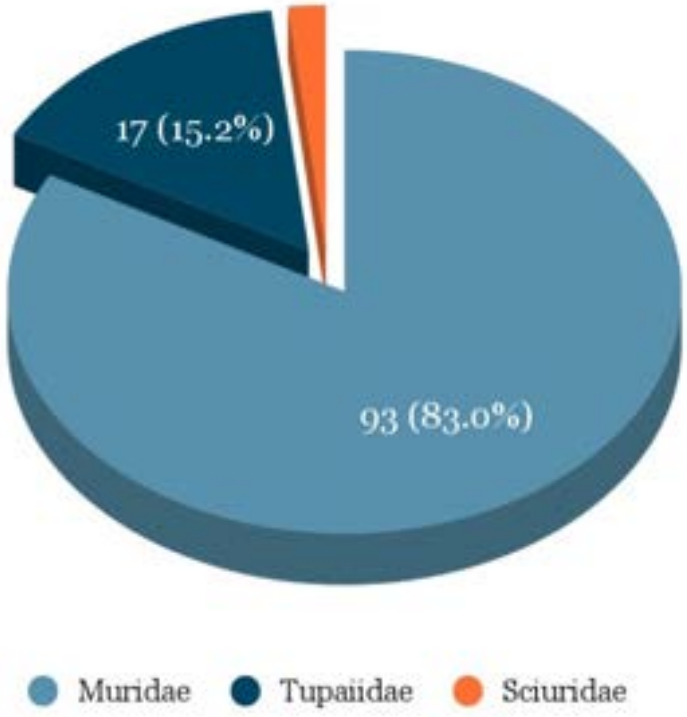

Figure 4. Abundance of small mammals according to family.

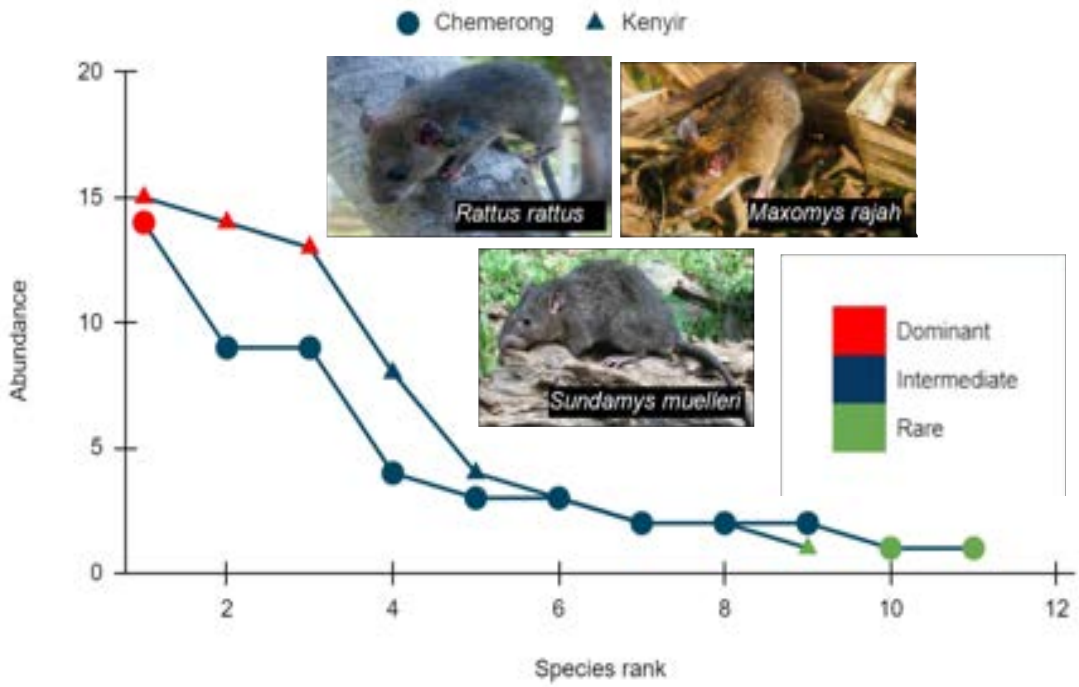

Figure 5. Rank abundance curve of small mammals captured from Chemerong Recreational Forest, and Kenyir.

This study showed that Family Muridae with more than 83% capture rate resulting in being the most abundant in both study sites. The high abundance of this family group was expected as Family Muridae are known to be the most abundant rodent with more than 120 genera (William-Dee *et al*., 2019; Department of Wildlife and

National Parks, 2023). The nature of the study sites also contributes to the number of species abundance, as forest habitats are known to have high abundance compared to urban and suburban areas according to data from previous studies (Rhim *et al*., 2007; Bernard *et al*., 2009; Benacer *et al*., 2013). The complexity of forest habitat creates more niches for many species to cohabitate rather than generalise habitats in urban and suburban areas.

Besides, trapping methods by deploying cage traps on the forest floor have been shown to capture more Family Muridae compared to other families of rodents. The theory revolves around the feeding behavior of each family. Members of the Family Muridae, mostly comprised of rats and mice, are known to prefer floor foraging, as they are not an excellent climber; they forage for seeds and fruits on bushes and also insects that crawl on the ground (Wolton, 1985; Corbalán & Debandi, 2006). While most of the Family Muridae are known to be nocturnal, both families, Tupaiidae and Sciuridae, have similar characteristics which are diurnal and known to be active during the morning and before dusk (Gould, 1978; Kvartalnov, 2022). Furthermore, these two rodent families were known for their adaptation to climb trees and canopy (Wells *et al*., 2006). They have strong hind legs and slender bodies that help them to move from one branch to another. They also prefer eating fruits and seeds, they mostly forage food on trees and rarely go to the ground (Corlett, 2017).

The dominant species in this study contrasts with a previous study that has been conducted in the Sekayu Recreational Forest (Shafie *et al*., 2021). The data from the previous study shows that the Sekayu recreational forest was dominated by *Rattus tiomanicus* while the data from this study shows that Chemerong Recreational Forest and Kenyir were dominated by *Rattus rattus* and *Sundamys muelleri* respectively. These differences in dominated species were probably due to the geographical differences between habitats. Sekayu recreational forest was surrounded by oil palm plantations, orchards, , and human settlements. Chemerong Recreational Forest has similar surroundings as Sekayu, but it is located more profoundly in the forest area and near a mountain. In contrast, Kenyir is distinct from the other two sites with large water bodies, and it is known for the biggest man-made lake in Southeast Asia (Zainol *et al*., 2020). The differences in the dominant species are closely related to the animal ecology and its adaptability to human-dominated areas (Rhim *et al*., 2007; Bernard *et al*., 2009; Benacer *et al*., 2013). *Rattus rattus* can be predominantly found in human settlements where it has adapted to be reliable to humans for food. Although the Sekayu recreational forest is near to human settlements, the sampling point for the conducted study was further from houses. Sekayu recreational forest are surrounded by grassy habitat oil palm, and abandoned wood structure that were known to be primary habitat for *Rattus tiomanicus* (Saufi *et al.,* 2020). This explains the dominance of *Rattus tiomanicus* in Sekayu. *Sundamys muelleri* is known to inhabit the area near water bodies such as in Kenyir, since this species is a strong swimmer (Pimsai *et al*., 2014).

Diversity Indices of Small Mammals

The diversity indices that were used for the estimation of diversity are Dominance (D'), Simpson (1-D), Shannon (H'), and Evenness (E'). Out of these four indices, three indices showed that Chemerong Recreational Forest has higher values, while Kenyir has higher value in D'. This shows that Chemerong Recreational Forest has higher diversity, while Kenyir has higher dominance (Table 2). Figure 6 shows the individual-based rarefaction curve of both study sites. This graph showed that Chemerong Recreational Forest has higher diversity compared to Kenyir and the line was extrapolated (dotted line) until it reaches asymptomatic.

Table 2. The diversity indices for both study sites.

	Chemerong	Kenyir
No. of species	11	9
No. of individuals	50	62
Dominance (D')	0.1453	0.1655
Simpson (1-D)	0.8547	0.8345
Shannon (H')	2.156	1.947
Evenness (E')	0.7853	0.7787

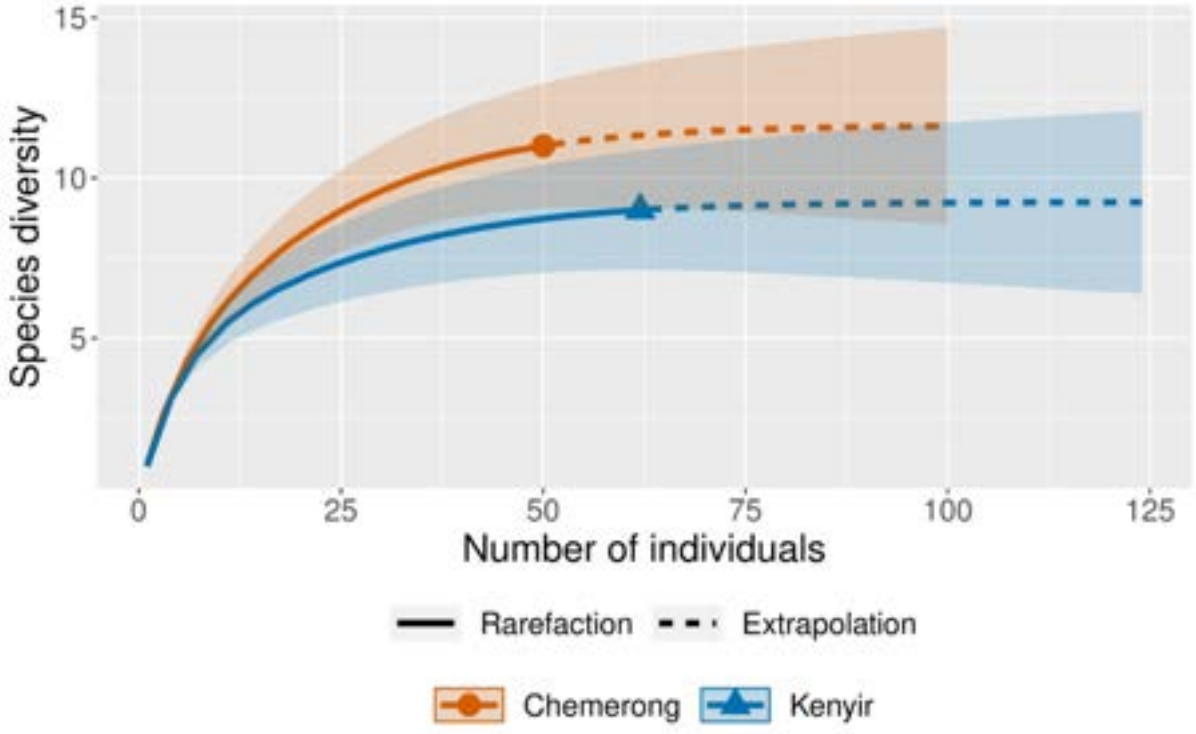

Figure 6. The extrapolated graph of individual-based rarefaction for both study sites.

The individual-based rarefaction and extrapolation curves showed that both study areas nearly achieve asymptote (Chao *et al*., 2014). The asymptote line on the graph gives general indication on the data collected were enough to represent the study sites (Chao *et al.,* 2009). Therefore, to help estimating the actual number of individuals in the study sites, the extrapolated value was used, which is visualised as a dotted line on the graph that has shown the graph achieved asymptote when the individual was doubled to 100.

CONCLUSION

In conclusion, this study provided useful information about the diversity and species composition of small mammals in Chemerong Recreational Forest and Kenyir, Terengganu. Our results illustrate that Chemerong Recreational Forest has higher diversity, while Kenyir has higher dominance. Although, the data from this study showed that both study area have similar small mammal species. Thus, further study in multiple forested area were recommended to understand the diversity and species composition in east-coast of Peninsular Malaysia.

ACKNOWLEDGEMENTS

The work presented in the study was funded by the SEAOHUN Small Grant Program with the generous support of the American people through US Agency for International Development (USAID) One Health Workforce - Next Generation (OHW-NG) Award 7200AA19CA00018. The contents of the manuscript are the responsibility of the authors and do not necessarily reflect the views of USAID or the US Government. We would like to thank Universiti Malaysia Terengganu for approval to conduct this study and special thanks to Khairul Ikhwan, Adam Ibrahim, Muhammad Fatihah Syafiq, Shahril Ridhuan, final year students for helping during the data collection.

REFERENCES

Acharya, P. R. (2001). Small mammals: viable conservation issues. *Life Science Journo-Magazine, 2*(1), 15-20.

Benacer, D., Woh, P. Y., Zain, S. N. M., Amran, F., & Thong, K. L. (2013). Pathogenic and saprophytic Leptospira species in water and soils from selected urban sites in peninsular Malaysia. *Microbes and Environments*, *28*(1), 135-140.

Baqi, A., Azhar, I., Chen, E. W., Khan, F. A. A., Lian, C. J., Nelson, B. R., & Kumaran, J. V. (2021). The diversity of small mammals in Pulau Perhentian Kecil, Terengganu, Malaysia. *Journal of Threatened Taxa*, *13*(6), 18427-18440.

Bourliere, F. (1975). Mammals, Small and Large: The ecological implications of size. *Small Mammals: Their Productivity and Population Dynamics.* Cambridge University Press, London, 1-9.

Bernard, H., Fjeldsa, J., & Maryati, M. (2009). A case study on the effects of disturbance and conversion of tropical lowland rain forest on the non-volant small mammals in North Borneo: Management implications. *Mammal Study 34*(2), 85-96.

Chaisiri, K., W. Chaeychomsri, J. Siruntawineti, F. Bordes, V. Herbreteau & Morand, S. (2010). Human-dominated habitats and helminth parasitism in Southeast Asian murids. *Parasitology Research*, 107, 931-937.

Chao, A., Colwell, R. K., Lin, C. W., & Gotelli, N. J. (2009). Sufficient sampling for asymptotic minimum species richness estimators. *Ecology*, *90*(4), 1125-1133.

Chao, A., Gotelli, N. J., Hsieh, T. C., Sander, E. L., Ma, K. H., Colwell, R. K., & Ellison, A. M. (2014). Rarefaction and extrapolation with Hill numbers: a framework for sampling and estimation in species diversity studies. *Ecological Monographs*, *84*(1), 45-67.

Corbalán, V., & Debandi, G. (2006). Microhabitat use by Eligmodontia typus (Rodentia: muridae) in the Monte Desert (Argentina). *Mammalian Biology*, *71*(2), 124-127.

Corlett, R. T. (2017). Frugivory and seed dispersal by vertebrates in tropical and subtropical Asia: An update. *Global Ecology and Conservation*, *11*, 1-22. Department of Wildlife and National Parks. (2023) Field, A. (2013). Discovering statistics using IBM SPSS statistics (4th ed.). SAGE Publications.

Francis, C. (2019). *Field guide to the mammals of South-east Asia* (2nd ed). Bloomsbury Publishing.

Gould, E. (1978). The behavior of the moonrat, Echinosorex gymnurus (Erinaceidae) and the pentail shrew, Ptilocercus lowi (Tupaiidae) with comments on the behavior of other Insectivora. *Zeitschrift für Tierpsychologie*, *48*(1), 1-27.

Hammer Ø., Harper D. A. T., Ryan P. D. (2001). PAST: Paleontological Statistics Software Package for Education and Data Analysis. *Palaeontologia Electronica 4*(1): 1-9.

Kvartalnov, P. V. (2022). Ecology and Behavior of the Slender-Tailed Tree Shrew (Dendrogale murina, Scandentia). *Biology Bulletin*, *49*(7), 915-923.

Nadchatram, M. (2008). The beneficial rain forest ecosystem with environmental effects on zoonoses involving ticks and mites (Acari), a Malaysian perspective and review. *Tropical Bio Medical*., 25(2), 1-92.

Noor Aisyah, A. R., Nur Izzah Izzati, A., Amirah Azizah, Z., Elizabeth, P., Muhammad Razali, S., Mazrul Aswady, M., & Mohd Tajuddin, A. (2016). Brief survey of non-volant small mammals on Pulau Perhentian Besar, Terengganu, Malaysia.

Nor Zalipah, M., Roslan, A., Senawi, J., Jayaraj, V. K., Azhar, M. I., Abdullah, M. T., & Lim, B. L. (2019). Checklist of small mammals of Hulu Terengganu, Terengganu. *Greater Kenyir Landscapes: Social Development and Environmental Sustainability: From Ridge to Reef*, 191-200.

Pimsai, U., Pearch, M. J., Satasook, C., Bumrungsri, S., & Bates, P. J. (2014). Murine rodents (Rodentia: Murinae) of the Myanmar-Thai-Malaysian peninsula and Singapore: taxonomy, distribution, ecology, conservation status, and illustrated identification keys. *Bonn Zoological Bulletin*, *63*(1), 15-114.

Rahim, N. A. A., Ahmad, N. I. I., Zakaria, A. A., Pesiu, E., Salam, M. R., Mamat, M. A., & Abdullah, M. T. (2016). Brief survey of non-volant small mammals on Pulau Perhentian Besar, Terengganu, Malaysia. *The International Seminar on the Straits of Malacca and the South China Sea 2016*.

Rhim, S. J., Lee, J. Y., Kim, M. J., Park, S. J., Lee, E. J., & Lee, W. S. (2007). Differences in small rodent populations between forest and forest road areas. *Journal of Korean Society of Forest Science*, *96*(3), 245-250.

Saufi, S., Ravindran, S., Hamid, N. H., Zainal Abidin, C. M. R., Ahmad, H., Ahmad, A. H., & Salim, H. (2020). Diet composition of introduced Barn Owls (Tyto alba javanica) in urban area in comparison with agriculture settings. *Journal of Urban Ecology*, *6*(1).

Shafie, N. J., Halim, N. S. A., Zalipah, M. N., Amin, N. A. Z. M., Esa, S. M. A. S., Md-Nor, S., Casanovas-Massana, A., Ko, A. I., Palma, F., Souza, F. N., & Costa, F. (2021). Knowledge, Attitude, and Practices regarding Leptospirosis among Visitors to a Recreational Forest in Malaysia. *The American Journal of Tropical Medicine and Hygiene*, *104*(4), 1290.

Terengganu Forestry. (2016). Maklumat Perhutanan: Hutan Simpan Kekal. Retrieved from http://trgforestry.terengganu.gov.my/index.php?option=com_content&view=article&id=79&Itemid=321&lang=my.

Von Rintelen, K., Arida, E., & Häuser, C. (2017). A review of biodiversity-related issues and challenges in megadiverse Indonesia and other Southeast Asian countries. *Research Ideas and Outcomes*, *3*, e20860.

William-Dee, J., Khan, F. A. A., Rosli, Q., Morni, M. A., Azhar, I., Lim, L. S., Tingga, R. C. T., & Rahman, M. R. A. (2019). Comparative distribution of small mammals diversity in protected and non-protected area of Peninsular Malaysia. *Tropical Life Sciences Research*, *30*(2), 131-147.

Wells, K., & Bagchi, R. (2005). Eat in or take away – seed predation and removal by rats (Muridae) during a fruiting event in a dipterocarp rainforest. *The Raffles Bulletin of Zoology, 53*(2), 281-286.

Wells, K., Pfeiffer, M., Lakim, M. B., & Kalko, E. K. (2006). Movement trajectories and habitat partitioning of small mammals in logged and unlogged rain forests on Borneo. *Journal of Animal Ecology*, *75*(5), 1212-1223.

Wolton, R. J. (1985). The ranging and nesting behaviour of Wood mice, Apodemus sylvaticus (Rodentia: Muridae), as revealed by radio-tracking. *Journal of Zoology*, *206*(2), 203-222.

Zainol, N., Roshidi, A. N., Husin, S. M., Shukor, A. M., Ilias, R., & Nor, S. M. (2020). Impact of forest isolation on mammals diversity and distribution due to impoundment of Hulu Terengganu hydroelectric project, Terengganu, Peninsular Malaysia. In *ICDSME 2019: Proceedings of the 1st International Conference on Dam Safety Management and Engineering* (pp. 468-478).

Zwolak, R., Pearson, D. E., Ortega, Y. K., & Crone, E. E. (2010). Fire and mice: Seed predation moderates fire's influence on conifer recruitment. *Ecology*, *91*(4), 1124-1131.

COMPARATIVE STUDY OF LEAVES MICROMORPHOLOGY IN THE GENUS ZINGIBERACEAE

Nurul Nadhirah Mohd Faisal [1], Salwa Shahimi [2]

[1] *Universiti Malaysia Terengganu,Faculty of Science and Marine Environment,*

21030 Kuala Nerus, Terengganu, MALAYSIA

S62346@ocean.umt.edu.my

[2]*Universiti Malaysia Terengganu,Faculty of Science and Marine Environment,*

21030 Kuala Nerus, Terengganu, MALAYSIA

salwa.shahimi@umt.edu.my

ABSTRACT

Zingiberaceae is the largest family in order Zingiberales and commonly known as aromatic rhizomatous herbs. Leaf epidermal characteristics are important for phylogenetic and taxonomic studies of many plants In Zingiberaceae family, it is challenging to identify ginger species because of its large diversity and it can be difficult to identify based on vegetative or floral morphology only. The aimed of this study is to identify the leaf micromorphological characteristics and diagnostic characters that can be used in species identification in Zingiberaceae. The leaf epidermal micromorphology of 10 species in Zingiberaceae was investigated by light microscope. Based on the result, all nine ginger species leaves are amphistomatic type of stomata, except Globba patens which stomata only found on abaxial surface of the leaf. Tetracytic stomata found in all examined species except one anomocyctic type in Zingiber puberulum. Stomata mostly randomly distributed in both surfaces and are more common on the abaxial surface. Simple, unicellular and non-glandular trichome present in four species namely Globba sp. 1, Globba fragilis, Globba patens, and Zingiber puberulum. These morphological characteristics of the leaf can be used as an additional data for identification of species in ginger family.
Keywords: Ginger Family, Leaf epidermis, Light Microscope, Stomata, Trichomes

INTRODUCTION

Zingiberaceae also known as ginger family, classified under the order of Zingiberales [1,2] comprise of 53 genera and 1,500 species globally [3]. Zingiberaceae is a perennial, aromatic herb, and has sympodial branched of rhizome [4]. Although ginger is their most well-known spice, the family also contains other well-known favorites like cardamom, turmeric, and galangal. The plants in the Zingiberaceae family also display these typical traits of monocots: a single seed leaf, parallel veins, showy flowers, and a fibrous root system [5].

Leaf micromorphology provides a window into plant phylogeny taxonomy research activity. The characteristics and variation of leaf epidermal which include of stomatal types, surface ornamentation and trichome type can be useful as additional data for plant identification [6,7]. Specific plant species can be identified by certain micromorphological characteristics, such as the arrangement of stomata or the presence or absence of particular trichome types [7]. This is useful for identification, particularly for closely related species that may share a similar macroscopic appearance. Compared to methods requiring larger portions of the plant, micromorphological analysis is non-destructive because it often only requires a small sample of leaf tissue.

LITERATURE REVIEW

Zingiberaceae

The Zingiberaceae family, also known as the ginger family of flowering plants, is the largest family within the Zingiberales order, with roughly 1,500 species distributed across 56 genera, six tribes, and four subfamilies [8]. According to [9], Zingiberaceae is a family of rhizomatous plants that can be either annual or perennial. Distichous, typically ligulate leaves with a single, dithecal stamen and a petaloid labellum derived from two staminodes set the Zingiberaceae apart from related families of the Zingiberales [10].

More than 1,500 species of this family are distributed throughout tropical and subtropical regions, including Asia, Africa, and the Americas. Southeast Asia is home to the greatest diversity of species, nevertheless. The majority of its species are found in South and Southeast Asia. In Peninsular Malaysia, there are more than 160

Zingiberaceae species, divided into 18 genera [11,12]. Generally, Zingiberae, Alpiniaea, and Globbae tribes hold the most species diversity in Zingiberaceae family.

Leaf Micromorphology Zingiberaceae

The morphology of Zingiberaceae species and their ability to adapt to a variety of environments have been the subject of numerous studies. According to [5], the Zingiberaceae family has a single, symmetrical leaf blade, leaves arranged alternately in two opposing rows, and leaf sheaths that encircle the true stem to form a pseudo-stem. The study conducted by [13] examined how Zingiberaceae species modify their leaf morphology to accommodate varying light conditions.

Study by [7] stated that, for phylogenetic and taxonomic analyses of many plants, leaf epidermal is crucial. The epidermal cells shape, the anticlinal walls outline, type of stomata, surface ornamentation and trichome type that the researcher observed in *Zingiber* plants are now used to study phylogeny and taxonomy in many different plant species. It is reported that a robust correlation between the density of trichomes and the pressure exerted by herbivores [14]. Species that face greater herbivory tend to have more resilient trichomes. In order to differentiate between those families and genera where identification is difficult, leaf epidermal characteristics such as epidermal cell shape, stomatal type, size and distribution, and trichome type and distribution have proven crucial [15].

METHODOLOGY

Sampel Collection and Preservation

Fresh and mature leaves samples were obtained from Mount Liang, Kuala Behrang, Perak and Sekayu Recreational Forest, Kuala Berang, Terengganu. The leaves samples were cut and preserved in an AA solution (70% ethanol; 30% acetic acid) in ratio 3:1.

Epidermal Peeling

Epidermal peels were prepared by gently scraping on both leaf surfaces until a thin transparent layer was achieved [16,17]. The epidermal layers were washed with distilled water stained in 1% safranin before mounting on clean slide. Images were then captured using a light microscope and examined.

Stomata and Trichome Identification

The morphology of stomata and trichome for both adaxial and abaxial were identified based on their shape and type according to [18,19].

Stomata Density and Index

The stomatal index and stomatal density were obtained using the following formulae from [7]: stomata index = number of stomata/ (number of stomata + number of epidermal cells) x 100%.; stomata density = number of stomata/ area of view (mm^2).

RESULTS

Based on the results obtained in this study there were 10 species comprised of five genera observed for epidermis cell shapes, stomata type and the presence of trichomes. From all species observed, the stomata can be found in both the abaxial and adaxial surface of the leaf, known as an amphistomatic arrangement except for *Globba patens* which stomata only found on the abaxial surface. The trichomes can only be found in a few species (Table 1).

Epidermal Cells

The epidermal shape of all examined species were found to be mostly elongated or hexagonal, with the long axis usually perpendicular to the veins and arranged in rows parallel to the veins while the anticlinal walls were straight or slightly curved at the edge. Adaxial epidermal cells were always more regularly arranged than abaxial cells.

Stomata Morphology

All the species examined; the stomata are amphistomatic but are always more abundant on the abaxial than the adaxial leaf surface (Figure 1). The stomata are randomly distributed in all species. The sizes of the stomata are different in all species but constant on both surfaces. The stomata of all species studied are of tetracytic except for *Zingiber puberulum* which has anomocytic type stomata on the adaxial leaf surface (Table 1, Figure 1 (g)). The result from this study showed that the stomata index and densities are different in each species (Table 1). The stomatal index of the adaxial epidermis and the abaxial epidermis ranged from 0.26% (in *Globba fragilis*) to 1.80% (in *Alpinia* sp. 1) and from 1.50% (in *Alpinia* sp. 1) to 24.28% (in *Globba* sp. 1), respectively. The stomatal density of the adaxial epidermis and the abaxial epidermis ranged from 0.0011 (in *G. fragilis*) to 0.0064 (in *Alpinia* sp. 1) and from 0.0053 (in *Alpinia* sp. 1) to 0.0467 (in *Z. puberulum*), respectively.

Trichomes Morphology

Simple, unicellular and non-glandular trichomes were found in the four species studied (Table 1). The trichomes were more abundance on the abaxial epidermis. Figure 1 (h) and (i) present the type of trichomes in species examined.

Table 1. Comparable leaf epidermal characters of 10 species of Zingiberaceae

Species	Adaxial epidermis			Abaxial epidermis			Trichome
	Stomata type	Stomata density (mm^2)	Stomata index (100%)	Stomata type	Stomata density (mm^2)	Stomata index (100%)	
Alpinia sp. 1	Tetracyctic	0.0064	1.80	Tetracyctic	0.0053	1.50	-
Alpinia conchigera	Tetracyctic	0.0032	0.87	Tetracyctic	0.0393	7.69	-
Alpinia mutica	Tetracyctic	0.0032	0.86	Tetracyctic	0.0255	5.74	-
Boesenbergia sp. 1	Tetracyctic	0.0032	1.50	Tetracyctic	0.0149	5.65	-
Etlingera sp. 1	Tetracyctic	0.0042	1.38	Tetracyctic	0.0212	5.21	-
Globba sp. 1	Tetracyctic	0.0053	1.54	Tetracyctic	0.0287	24.28	Simple and unicellular
Globba fragilis	Tetracyctic	0.0011	0.26	Tetracyctic	0.0287	6.59	Simple and unicellular
Globba patens	-	-	-	Tetracyctic	0.0297	5.82	Simple and unicellular
Zingiber sp. 1	Tetracyctic	0.0032	0.85	Tetracyctic	0.0180	3.54	-
Zingiber puberulum	Anomocytic	0.0032	0.81	Tetracyctic	0.0467	8.42	Simple and unicellular

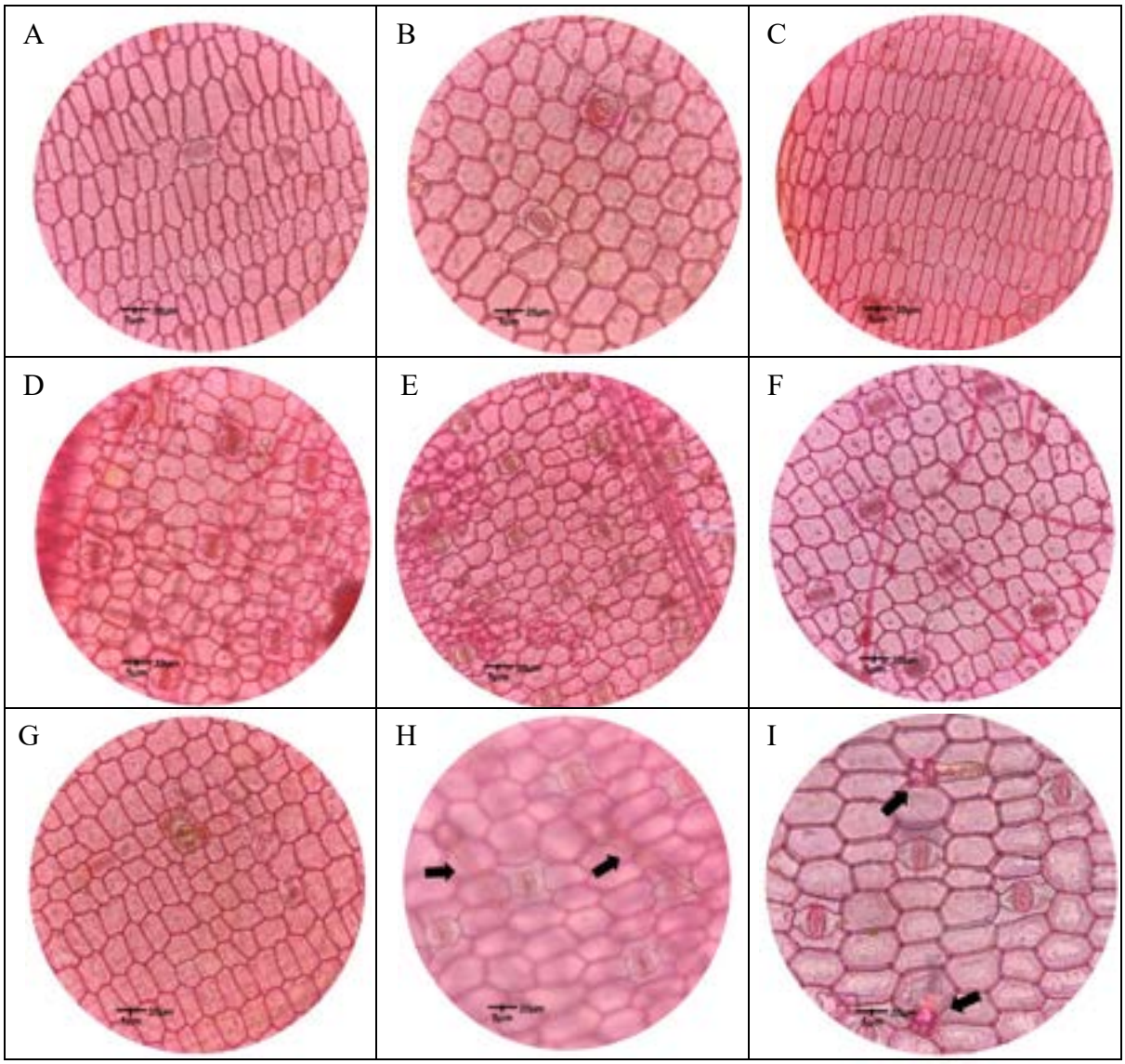

Figure 1. Leaf epidermis of studied specimens shown by light microscope. A-C Tetracytic stomata on adaxial surface of (A) *Alpinia conchigera,* (B) *Boesenbergia* sp. 1, (C) *Globba patens* (stomata absent). D-F Abaxial epidermis showing tetracytic stomata in (D) *Alpinia mutica,* (E) *Zingiber puberulum*, (F) *Etlingera* sp. 1. G Anomocytic stomata on adaxial surface of *Zingiber puberulum*. H-I Trichomes of simple, unicellular and non-glandular in *Globba fragilis* and *Globba patens* (arrow).

DISCUSSION

Our results show that the epidermal cells of all examined species are very similar in shape, i.e. elongated or hexagonal, while the anticlinal walls were straight or slightly curved at the edge. The findings were consistent with the reported characteristics in Zingiberaceae [7,20,21,22,23,24]

All the species examined in this study exhibit an amphistomatic leaf arrangement, where stomata are present on both surface (abaxial and adaxial) of the leaf except for Globba patens which stomata found on the abaxial surface only. Most of the stomata on both surfaces are tetracytic, specifically brachyparatetracytic type, which refer the guard cells are surrounded by four subsidiary cells (two on each lateral and terminal stomata) which corresponds to the reports by [25,26,27,5] except for Zingiber puberulum has anomocytic stomata on the adaxial leaf surface.

From this study, it was noted that the trichomes were simple, unicellular and non-glandular. This finding is consistent with the previous description publish by [17,20,24,28] yet for this study, trichomes were absent in Alpinia conchigera.

CONCLUSION

As a conclusion, the Zingiberaceae family displays a range in epidermal cell shape and arrangement. However, there are similarities in morphologies of stomata and trichomes. Tetracytic stomata are distributed on both surfaces. The results from this research showed the foliar epidermal features of the species were almost the same, yet some of these characters can be useful in identifying and classifying the studied taxa. The presence of anomocyctic stomata type on the adaxial surface in *Z. puberulum* and *G. patens* exhibit hypostomatic leaf arrangement high value have become a notable finding in this research. Although the overall epidermal morphology is similar among ginger species, stomata density, stomata index and trichome type can offer valuable systematic and taxonomic information as well as providing additional data for species identification.

ACKNOWLEDGEMENT

We would like to thank the Faculty of Science and Marine Environment, Universiti Malaysia Terengganu, for providing laboratory facilities.

REFERENCE

[1] Wohlmuth, H. (2008). Phytochemistry and pharmacology of plants from the ginger family, Zingiberaceae. PhD dissertation. Southern Cross University.
[2] Zahara, M. (2020). Identification of morphological and stomatal characteristics of Zingiberaceae as medicinal plants in Banda Aceh, Indonesia. The 1st International Conference on Agriculture and Bioindustry 2019. IOP Conference Series: Earth Environmental Science, 425: 012046.
[3] Furmuly, A. M., & Azemi, N. (2020). A review on golden species of Zingiberaceae family: Genus *Curcuma*. Journal of Critical Reviews, 7(16): 882-895.
[4] Larsen, K. (1980). Annotated key to the genera of Zingiberaceae of Thailand. Nat. Hist. Bull. Siam Soc, 28, 151-169.
[5] Windarsih, G., Riastiwi, I., Dewi, A. P., & Yuriyah, S. (2022). Stomatal and epidermal characteristics of Zingiberaceae in Serang District, Banten, Indonesia. Biodiversitas Journal of Biological Diversity, 23(10)
[6] Rahayu, S. E., Kartawinata, K., Chikmawati, T., & Hartana, A. (2012). Leaf anatomy of Pandanus species (Pandanaceae) from Java. Reinwardtia 13 (3): 305-313.
[7] Zhao, H., Xiao, M. H., Zhong, Y., & Wang, Y. Q. (2022). Leaf epidermal micromorphology of *Zingiber* (Zingiberaceae) from China and its systematic significance. PhytoKeys 190: 131-146.
[8] Holttum, Eric, R., Kress, & John, W. (2020). Zingiberales, Encyclopedia Britannica.
[9] Kaliyadasa, E., & Samarasinghe, B. (2023). A review on golden species of Zingiberaceae family around the world: Genus *Curcuma*. J Agric Res, 14(9), 519-531.
[10] Simpson, M. G. (2010). Diversity and Classification of Flowering Plants: Amborellales, Nymphaeales, Austrobaileyales, Magnoliids, Ceratophyllales, and Monocots (Plant Systematics (Second Edition) ed.). Academic Press.
[11] Larsen, K., H. Ibrahim, S.H. Khaw & L.G. Saw. (1999). Gingers of Peninsular Malaysia and Singapore. Natural History Publications (Borneo), Kota Kinabalu. 135 pp.
[12] Appalasamy, S., Arumugam, N., Zamri, N. S. A., Fadhlina, A., Kumaran, J. V., & Subramaniam, S. (2022). First report on wild ginger (Family: Zingiberaceae) species composition with new records in limestone forests of Kelantan, Peninsular Malaysia. Tropical Life Sciences Research, 33(3), 33.
[13] Chew, L. K. (2022). Leaf micromorphology reveals adaptation strategies to light availability in Zingiberaceae species. Frontiers in Plant Science, 13.
[14] Gomez, M. S. (2019). Trichome diversity and herbivory pressure in Zingiberaceae species from the Brazilian Atlantic Forest. Flora, 260.
[15] Qiu, J., Lin, M., & Tan, D. (2023). Taxonomic implications of leaf morphology and epidermal anatomy for 14 species of *Gagea* (Liliaceae) from Xinjiang, China. Botanical Studies, 64(1), 33.
[16] Hussin, K., H., Chua, T. S., Ibrahim, H., Wu, Q. G., Liao, J. P., & Liu, N. (2000). Comparative leaf anatomy of *Alpinia* Roxb. species (Zingiberaceae) from China. Botanical Journal of Linnean Society, 133(2): 161–180.

[17] Talip, N., Hussin, K. H., & Ibrahim, H. (2005). Comparative leaf anatomy of *Alpinia* species (Zingiberaceae) in Malaysia. Nordic Journal of Botany. 23: 463-483.
[18] Talip, N., Rahman, M. R. A. & Juhairi, M. A. A. A. (2019). Anatomi dan Mikroskopik Tumbuhan. Selangor: Universiti Kebangsaan Malaysia. 213pp.
[19] Amirul-Aiman, A. J., Noraini, T., & Nurul-Aini, C. A. C. (2017). Morfologi trikom pada petal dan sepal spesies terpilih Acanthaceae di Semenanjung Malaysia. Sains Malaysiana, 46(10), 1679–1685.
[20] Kajornjit, P., Saensouk, S., & Saensouk, P. (2018). Pollen morphology and leaf anatomy of genus *Globba* in Thailand. ScienceAsia, 44(3), 146-161.
[21] Salasiah, M., & Meekiong, K. (2018). Preliminary anatomical study on leaf surfaces of Bornean Zingiberaceae (tribe Alpinieae) from North East Sarawak. Malaysian Applied Biology, 47(5), 289-293.
[22] Martins M. B. G., Caravante A. L. C, Appezzato-Da-Glória B., Soares M. K. M., Moreira R. R. D., & Santos, L. E. (2010). Anatomical and phytochemical characterization of leaves and rhizomes from *Hedychium coronarium* J. König (Zingiberaceae). Revista Brasileira de Plantas Medicinais, 12(2): 179–187.
[23] Chen J., & Xia N. H. (2010). Chromosome cytology, leaf epidermal morphology and palynology *of Curcuma rubrobracteata* (Zingiberaceae). Nordic Journal of Botany, 28(2): 212–215.
[24] Hussin, K., H., Ibrahim H., Ali D. A. H. A., Liao J. P., Liu N. (2001). Anatomical variations in leaf of *Boesenbergia* O. Kuntze and *Kaempferia* L. species (Zingiberaceae). Redai Yaredai Zhiwu Xuebao, 9(1): 49–54.
[25] Tomlinson PB (1956) Studies in the systematic anatomy of the Zingiberaceae. Bot J Linn Soc 55,547–92..
[26] Tomlinson PB (1969) Anatomy of the Monocotyledons III Commelinales-Zingiberaceae, Clarendon Press, Oxford.
[27] Lakoet C (2004) Comparative anatomy of Zingiberaceae in Phu Phan National Park. MSc thesis, Khon Kaen Univ.
[28] Shahimi, S. (2024). Leaf micromorphology in genus Alpinia (Zingiberaceae). Universiti Malaysia Terengganu Journal of Undergraduate Research, 6(1).

TRACK B

APPLIED CHEMISTRY

CAFFEINE CONTENT VARIATION IN COFFEE BREWS BASED ON BEAN TYPES AND BREWING TECHNIQUES

Firus Musfirah Poli[1], Raden Izzati Aqilah[2], Nurain Johar[3]

[1]*Faculty of Applied Sciences, Universiti Teknologi MARA Sarawak, Samarahan 2 Campus, 94300 Kota Samarahan, Sarawak, Malaysia.*

musfirah4523@uitm.edu.my

[2] *Faculty of Applied Sciences, Universiti Teknologi MARA Sarawak, Samarahan 2 Campus, 94300 Kota Samarahan, Sarawak, Malaysia.*

radenizzati@gmail.com

[3] *Faculty of Applied Sciences, Universiti Teknologi MARA Sarawak, Mukah Campus, KM 7.5 Oya Road, 94600 Mukah, Sarawak, Malaysia.*

nurainjohar@uitm.edu.my

ABSTRACT

Coffee is the world's second most consumed beverage, and its popularity continues to rise. Made from dried and brewed beans, moderate coffee consumption offers various health benefits, including migraine relief, stress reduction, and an increase in antioxidants. However, understanding the caffeine content in locally available coffee drinks is crucial for consumer health and well-being. Excessive consumption can have adverse effects, such as anxiety, insomnia, digestive problems, and mental health issues. This study compared the caffeine content of hot Americano coffees made from Arabica and Liberica beans, sourced from local coffee shops in Kuching, Sarawak. Six samples were analyzed, with three brewed from Arabica beans (originating from Brazil, Costa Rica, and Indonesia) and three from Liberica beans cultivated in Sarawak. Liquid-liquid extraction using chloroform and Ultraviolet spectroscopy were employed for the analysis. The results showed that Arabica beans from Brazil had the highest caffeine concentration (948.506 ± 7.836 ppm), while Sarawak's Liberica beans had the lowest (579.595 ± 0.092 ppm). In order to study the effect of brewing techniques, brews prepared using an espresso machine and through the pour-over (V60) technique was compared for their caffeine concentration. The findings show the pour-over method yielded higher caffeine content for both Arabica and Liberica beans. This study highlights the influence of coffee bean types and origins, as well as brewing techniques on coffee's caffeine, offering valuable insights for coffee consumers and the local industry.

***Keywords*:** Coffee, caffeine content, Arabica bean, Liberica bean, UV-visible spectrophotometer.

INTRODUCTION

Coffee consumption has become a significant part of daily life globally and is especially popular in Malaysia, where both international and local coffee cultures thrive (Gaascht *et al*., 2015; Rahim *et al*., 2019). Coffee, the second-most consumed beverage worldwide, has more than 100 species, with Arabica and Robusta being the most common beans utilized in the coffee industry (Omar *et al*., 2022). Conversely, Liberica beans is a less common species of coffee. However, as global climate change, Liberica emerges as a resilient option as this species possesses adaptability to shifting climate patterns (Lee, 2023). Arabica coffee is originated in the high-altitude forests of Ethiopia and is highly regarded by its exceptional quality and delightful flavour (Cannon *et al*., 2010). Liberica beans are much larger than arabica and robusta beans, and they are distinguished by their unique jackfruit-like aroma (Insanu *et al*.,2021). In recent years, the national government and regional agricultural organizations in Sarawak have made intensive efforts to promote the cultivation of Liberica coffee, though there are still challenges that need to be addressed (Lee, 2023).

In Malaysia, coffee culture has evolved, with local coffee shops (Kopitiam) and international franchises such as Starbucks and Coffee Bean catering to an increasing demand for quality coffee products. Despite this, there is limited transparency regarding the nutritional content and active ingredients, such as caffeine, in the beverages offered by local coffee shops. Excessive caffeine consumption is linked to adverse health effects, including anxiety, insomnia, digestive disorders, and mental health issues (Fredholm *et al*., 2003; Lara, 2010). Therefore, understanding the caffeine content in various coffee drinks is essential for consumer awareness and

health considerations. However, more comprehensive studies are needed to focus on the caffeine content in locally brewed coffee drinks and the influence of different brewing techniques on this content.

This study aims to determine the caffeine content of various local coffee drinks sold in the local cafes and to examine how different bean types and origins, as well as brewing techniques affect the caffeine concentration. Six coffee samples were purchased from local coffee shops, and liquid-liquid extraction was employed using chloroform as the solvent to isolate the caffeine from the coffee samples. The extracts were subsequently analysed using Ultraviolet-Visible spectroscopy to quantify caffeine concentration. The findings from this will provide essential data for quality control, ensuring products meet demand and comply with health regulations, which consequently can enhance the reputation of coffee businesses.

MATERIALS AND METHODS

Materials

Caffeine standard, Chloroform. All chemicals were analytical-reagent grade. All solutions were prepared using deionized water.

Sample Collection

Hot Americano coffee samples were obtained from different coffee shops located in Kuching, Sarawak. The brewing technique used as well as the type and the origin of the coffee beans were recorded.

Extraction of Caffeine

Caffeine was extracted from the coffee samples according to the method by Miłek et al., (2021) with some modifications. Approximately 5.0 ml freshly brewed coffee sample was inserted in a separating funnel, followed by the addition of 0.50 mL of sodium hydroxide and 20 mL chloroform. The funnel was inverted three times and allowed to stratify for 5 minutes. The chloroform layer was removed in a clean 100 mL volumetric flask. The extraction was repeated twice more, each with a 20 mL chloroform addition. The combined extract was dissolved with chloroform up to the calibration mark. Each coffee samples were extracted according to the same procedure and prepared in triplicates.

Spectrophotometric determination of caffeine content

Quantitative analysis of caffeine was performed using a UV/Vis Spectrometer. The λ max was determined by scanning the standard caffeine solution from 190 - 400 nm and the obtained results gave an absorption spectrum, which was characterized by a single intensive absorption band located in the UV range at λ max at = 276 nm. The standard linear calibration curve was run to obtain the linear range of sample analysis, the correlation factor was with accepted value = 0.9923 and the standard calibration curve was linear with equation y = 0.0609x + 0.1618. The quantitative amount of caffeine in samples (ppm) was then determined using the standard calibration curve.

RESULTS AND DISCUSSION

Caffeine Content

The caffeine content in six coffee samples brewed from different coffee bean types and different origins is presented in Table 1. Based on the results, the highest caffeine concentration (948.506 ± 7.836 ppm) was found in a sample labeled as A2, which is coffee brewed from Arabica beans that originated from Brazil. In contrast, sample labeled as L1, coffee brewed from Sarawak's Liberica beans was found to contain the lowest caffeine content (579.595 ± 0.092 ppm). The finding of this analysis supports a study by Ling *et al*., (2001), which found that Arabica beans have a greater caffeine level (1.06 g/100g) compared to Liberica beans (0.86 g/100g).

Table 1. The caffeine content in coffee samples

Sample	Bean type	Origin	Caffeine content
A1	Arabica	Costa Rica	773.684 ± 3.907
A2		Brazil	948.506 ± 7.836
A3		Indonesia	751.571 ± 3.677
L1	Liberica	Sarawak	579.595 ± 0.092
L2		Sarawak	606.086 ± 1.092
L3		Sarawak	625.025 ± 2.343

For samples brewed from Arabica beans, a variation in the caffeine content can be observed based on the bean's geographical origin. A study conducted by Olechno *et al*. (2021) shows that Arabica beans grown in Kenya and Ethiopia have been discovered to have less caffeine than Arabica beans cultivated in Brazil. The difference in caffeine content of coffee beans with different origins is due to the overall amount of chemicals in the beans, which is also influenced by the surroundings, such as light and altitude above sea level. For instance, in a study by Ribeiro *et al*., (2016), the Arabica bean cultivated at an elevation of ≥1200 m above sea level has a greater caffeine concentration (13.39% to 12.35 g/kg of beans) compared to coffee bean grown at an elevation of less than 1000 m above sea level.

Effect of Different Brewing Techniques

Research has demonstrated that the brewing technique of coffee bean has an impact on its characteristics, in which the parameters involved significantly influence the extraction kinetics of the various chemical compounds found in the roasted bean (Cordoba *et al*., 2020). In order to assess how the brewing technique affected the composition of the brew, a pair of coffee drinks from each bean were prepared using different techniques; one brewed with an espresso machine and another using the pour-over (V60) technique. The samples then were analysed for the amount of caffeine using an ultraviolet/visible spectrophotometer. Figure 1 provides a summary of the findings.

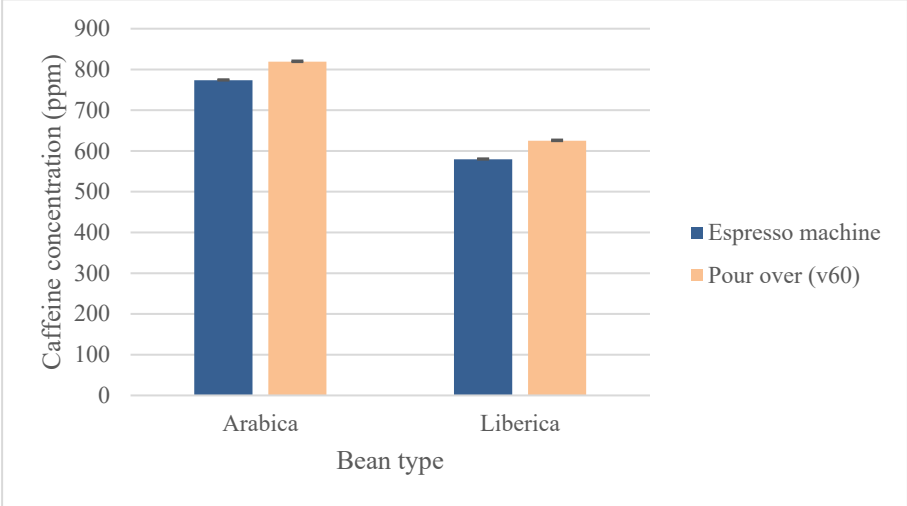

Figure 1. Comparison of caffeine concentration by different brewing techniques.

After examining the caffeine content of four particular coffee drinks prepared using two separate techniques, it is evident that the outcomes vary. A higher quantity of caffeine was found in both coffee beans when brewed using the pour-over method. The Arabica bean had a greater caffeine concentration at 819.004 ± 9.360 ppm, whereas the Liberica bean had a maximum of 625.025 ± 2.898 ppm. Falls under the infusion category

of extraction, pour over (V60) achieves the highest caffeine extraction rate because hot water can evenly pour over the ground coffee at a specific temperature, allowing for the rapid release of dissolved components within the first 2 minutes of extraction (Cordoba *et al*., 2020). In contrast, an espresso machine employs a driving force (high pressure) to rapidly push hot water through a compact bed of coffee grounds (Petracco, 2005). A study conducted by Herawati *et al*., (2024) also shows that coffee brews using the V60 technique exhibit the highest caffeine content when compared to Tubruk and cold brewing methods.

CONCLUSION

The findings of this study show that the bean types and origins, as well as brewing techniques, have a significant impact on the caffeine concentration of coffee brews. Generally, samples brewed from Arabica beans have greater caffeine content than those with Liberica beans. Additionally, the variation of geographical origins of the Arabica beans used in this study supports that the cultivation environment of the beans could influence the caffeine level in coffee. Further investigation on the impact of brewing techniques demonstrates that the pour-over (V60) method produced a higher quantity of caffeine for both Arabica and Liberica beans, compared to espresso machine brews. Liberica coffee presents an interesting subject for future research as Sarawak is an important region for the cultivation of Liberica beans. Conducting in-depth studies on Liberica beans could reveal the unique characteristics of these beans and contribute to a greater understanding of their potential in the coffee market.

REFERENCES

Cannon, R. J., Trinnaman, L., Grainger, B., & Trail, A. (2010). The key odorants of coffee from various geographical locations. In *Flavors in noncarbonated beverages* (pp. 77-90). American Chemical Society.

Cordoba, N., Fernandez-Alduenda, M., Moreno, F. L., & Ruiz, Y. (2020). Coffee extraction: A review of parameters and their influence on the physicochemical characteristics and flavour of coffee brews. *Trends in Food Science & Technology*, *96*, 45-60.

Fredholm, B. B., & Svenningsson, P. (2003). Adenosine-dopamine interactions: Development of a concept and some comments on therapeutic possibilities. *Neurology*, 61 (Issue 11, Supplement 6), 5–9.

Gaascht, F., Dicato, M., & Diederich, M. (2015). Coffee provides a natural multitarget pharmacopeia against the hallmarks of cancer. *Genes & Nutrition*, 10(6).

Herawati, D., Armawan, M. S., Nurhaliza, N., Mu'arij, F. A., Hunaefi, D., & Noviasari, S. (2024). Impact of bean origin and brewing methods on bioactive compounds, bioactivities, nutrition, and sensory perception in coffee brews: An Indonesian coffee gastronomy study. International Journal of Gastronomy and Food Science, 35, 100892.

Insanu, M., Fidrianny, I., Imtinan, N. H. H., & Kusmardiyani, S. (2021). Liberica coffee (Coffea liberica L.) from three different regions: In vitro antioxidant activities. *Biointerface Res. Appl. Chem*, *11*(5), 13031-13041.

Lara, D. R. (2010). Caffeine, mental health, and psychiatric disorders. *Journal of Alzheimer's Disease: JAD*, 20(1), S239-48.

Lee, K. W. T. (2023, August). Liberica Coffee Development and Refinement Project in Sarawak Malaysia. In *Proceedings* (Vol. 89, No. 1, p. 15). MDPI.

Ling, L. S., Daud, N. I. N., & Hassan, O. (2001). Determination of coffee content in coffee mixtures. *Malaysian Journal of Analytical Sciences*, *7*(2), 327-332.

Miłek, M., Młodecki, Ł., & Dżugan, M. (2021). Caffeine content and antioxidant activity of various brews of specialty grade coffee. *Acta Scientiarum Polonorum Technologia Alimentaria*, *20*(2), 179-188.

Omar, N. R. N., Ahmad, A. A., Nor, N. A. A. L. M., Abidin, A. Z. Z., Sulaiman, N. H., & Ahmad, B. (2022). Coffee industry in Malaysia: An overview and potential.

Petracco, M. (2005). The cup. *Espresso coffee: The science of quality*, 290-315.

Rahim, F. A., Jin, G. P., & Fong, C. L. (2019). Malaysian Coffee Culture: Attributes considered to purchase coffee beverages. *Journal of Marketing Advances and Practices*, 1(1), 50-62.

Ribeiro, D. E., Borem, F. M., Cirillo, M. A., Prado, M. V. B., Ferraz, V. P., Alves, H. M. R., & Taveira, J. D. S. (2016). Interaction of genotype, environment and processing in the chemical composition expression and sensorial quality of Arabica coffee.

CHARACTERIZATION OF PINEAPPLE CROWN LEAVES FOR EFFICIENT SORPTION OF POLLUTANTS

Rabuyah Ni[1], Abdul Somad Mustapha Kamal[2]

[1]*Universiti Teknologi MARA*

abuyani@uitm.edu.my

[2]*Universiti Teknologi MARA*

2022949879@student.uitm.edu.my

ABSTRACT

The unregulated discharge of pollutants into water bodies has created the development of enhanced adsorbent materials for on-site treatment applications to tackle water safety concerns. The utilization of agrowaste is widely used due to its availability and eco-friendly as sorbent. In this study, Pineapple Crown Leaves (PCL) was chemically (CPCL) and thermally modified (TPCL), and its characteristics were compared with the raw sample (RPCL). The elimination of non-cellulosic components at 1624 cm^{-1} in CPCL and TPCL was confirmed by FTIR spectra. The treatment resulted in an increased functional group through chemical and thermal alteration could facilitates the adsorption of pollutants. The thermal behavior of RPCL, CPCL, and TPCL were analyzed using Thermogravimetric Analysis (TGA). TGA results were in agreement with FTIR results where hemicellulose degraded first followed by cellulose and lignin at temperatures 206°C, 396°C, and 480°C respectively for RPCL. The degradation of hemicellulose, cellulose, and lignin is found at higher temperatures for chemically and thermally treated as compared with raw PCL, RPCL. The results presented and discussed in this study conclusively project the PCL as a potential sorbent material in water treatment. This paper highlights the characterization of the raw and modified PCL and their potential application in sorption processes.

***Keywords*:** pineapple crown, adsorption, agricultural biomass, carbonization

INTRODUCTION

The primary component found in the majority of agricultural waste or agrowaste is lignocellulose. It contains cellulose (40-50%), hemicellulose (20-30%), and lignin (10-25%), as well as trace levels of pectin, protein, and extractives (Deepa et al., 2015). The molecular structures of these parts have several functional groups that can adsorb pollution (Dai et al. 2018). Some functional groups are insulated or sterically inhibited within the bulk structure of the organic matrix, making them unavailable for direct interactions with contaminants, reducing adsorption efficacy. Modification modifies the nature of surface functional groups, with particular modification procedures chosen to optimize products for the intended use and chemical properties of the targeted pollutants (Liu et al., 2022). Physical and chemical methods can modify agrowaste. Chemical modification often improves adsorbents' physicochemical parameters, such as functional group composition and surface area. This enhancement leads to a greater improvement in adsorption performance compared to physical modification alteration (Aryee et al. 2021).

Alkaline treatment is one example of chemical modification. The reaction is often carried out by using NaOH or KOH. The treatment decreases the concentration of amorphous elements like lignin and hemicellulose, increasing surface area and exposing more functional groups in the treated agrowaste (Liu et al. 2022). Alkaline treatment enhances the mechanical characteristics and thermal stability of agricultural wastes, hence permitting improved removal of pollutants (Sahu and Gupta 2020). Conversely, carbonization refers to the process of transforming agrowaste into biochar. According to Divband Hafshejani et al. (2016), biochar products have a larger specific surface area, greater porosity, and more functional groups compared to the original agricultural wastes they were derived from. The characteristics of biochar made from agricultural waste are strongly influenced by the temperature of carbonization (Qiu et al. 2021). Typically, biochar made at temperatures below 500 °C has a higher amount of functional groups, while biochar made at temperatures between 500 and 700 °C has a more porous surface and greater total porosity (Oliveira et al. 2017).

Malaysia's rapid growth in agricultural industries, including palm oil, paddy, and pineapple, has led to high agrowaste production, with 1.6 million metric tons of agricultural waste dumped at landfills annually. Pineapple Crown Leaf (PCL) from pineapples, which contain 79-83% cellulose, is a suitable sorbent material due to its local availability. Malaysia is a leading pineapple producer, harvesting 400,000 to 600,000 metric tons per year with 16 varieties which include Nanas Sarawak, Maspine, Yankee, Gandul, Moris Gajah, Josapine, N36,

MD2, and Moris pineapple. Sarawak, the second largest pineapple producer in the state, has an area of 8,429 hectares, with Samarahan being the largest producer, covering 37% of the total planted areas (Matius et al., 2022). Thus, the objective of this research is to characterize raw PCL (RPCL), chemically treated PCL (CPCL) and thermally treated PCL (TPCL) using FTIR and TGA. The functional groups and thermal properties of each sample were evaluated for application as sorbent for the removal of pollutants.

MATERIALS AND METHODS

PCL is derived from Sarawak pineapple species obtained from local pineapple farm in Samarahan. The sample was prepared according to the method reported by Etanuro et al. (2023). The first step is to split the crowns into a single set of leaves. The leaves were oven-dried for 18 hours at 70°C to eliminate moisture and contaminants. The leaves were broken into powder and sieved through a British Standard Sieve (BSS Sieve) with a mesh size of 125-850 µm (20-120 mesh). This sample is known as raw PCL. Then, samples are further treated to obtain chemically treated (CPCL), and thermally treated (TPCL) samples. CPCL was prepared using 50 g of washed dried ground PCL and was treated for 1 hour with 500 mL of a 10% NaOH solution at 100 °C with stirring. The mixture was allowed to cool down at room temperature and then washed with deionized water until the pH was neutral (Li et al., 2012). While, TPCL was prepared by carbonizing the dried ground PCL in a muffle furnace at 300°C for an hour (Gheriany et al., 2020). Raw and modified PCL were characterized using FTIR and TGA. FTIR spectra analysis was performed within the wave number range 4000 – 600 cm–1 using ATR method on a Perkin-Elmer Frontier FTIR. Thermogravimetry Analysis (TGA) was executed using Thermogravimetric Analyser Pyris 1 TGA interfaced with a heated rate of 10 ◦C/min from 30 ◦C to 700 ◦C under the air atmosphere (Pham et al., 2022).

RESULTS AND DISCUSSION

Cellulose, hemicellulose, and lignin usually decompose at different temperatures. The removal of the majority of hemicellulose, cellulose, and, lignin from PCL after chemical and thermal treatment was attributed to the difference in TGA results (Figure 1). The thermogram showed four degradation steps which is loss of water and solvent, hemicellulose, cellulose, and lignin. In the first stage, it shows the mass loss at the temperature of approximately 100˚C, representing the loss of moisture and the release of weakly bonded water molecules. Next, the degradation of non-cellulose components such as hemicellulose and pectin occurred at the temperature of 206˚ C and 250˚C for RPCL and CPCL respectively. These results were in agreement with a study done by Pham et al. (2022). However, thermally treated samples showed the highest degradation temperature of hemicellulose at 304˚C as the degradation of hemicellulose begin between 220˚C to 310℃ (Emiola-Sadiq et al., 2021). The significant improvement in the degradation temperature of hemicellulose between raw, chemically, and thermally treated PCL could be explained by the absence of components degrading at a lower temperature such as hemicellulose in raw material.

The third stage is the loss of the most significant mass of samples which is loss of cellulose. In this stage, the degradation of cellulose would likely start at 300˚C to 450˚C (Reichert et al., 2021; Akubo et al., 2019). The degradation of cellulose ended at the high temperature of 396˚C, 394˚C, and 437˚C for the raw, chemically, and thermally treated samples respectively. The cellulose percentage for all the samples was found in the range 44 – 48%. Next stage, the degradation of lignin was found in between 400˚C to 600˚C (Lu & Gu, 2022). Based on the thermogram, the degradation of lignin ended at temperatures 480° C, 550° C, and 604° C for RPCL, CPCL, and TPCL respectively. The lignin content was found in between 8 – 10%. Finally, mass loss was recorded at high temperatures of 588 ℃ for raw samples, 550 ℃ for chemically treated samples, and 604.21℃ for thermally treated materials. The samples were combusted, and char formation resulted from the destruction of thermally stable structures in the compound severe heat (Gheriany et al., 2020).

In IR spectrum, the broad intense signal in the high energy region between 3600 and 3000 was attributed to the stretching vibration of hydroxyl groups. These were due to the free OH groups present in carbohydrates and phenolic groups present in PCL. The non-cellulose components specifically pectin in agrowaste samples could be found at 1628 cm^{-1} due to symmetrical stretching vibrations of the carboxylic acid group in pectin (Gheriany et al., 2020). These peaks are only present in RPCL but absent in CPCL and TPCL. Signals at 1602 cm^{-1} and 1580 cm^{-1} were assigned to the vibrations stretching of the C=O and C=C in aromatic rings, which indicated the existence of lignin and hemicellulose in RPCL and CPCL (Adapa et al., 2011). These findings were in agreement with the TGA result where thermal degradation of cellulose for TPCL is the highest compared to RPCL and CPCL This is due to the loss of the methoxy group and syringyl unit of lignin as a result of the elimination of hemicellulose and lignin by thermal alteration (Gaff et al., 2023). This condition suggests low

hemicellulose content in TPCL increases the thermal degradation of TPCL samples. The presence of a variety of functional groups from agrowaste would suggest it is a potential sorbent in the removal of pollutants through adsorption or sorption properties. A low hydroxyl group might suggest agrowaste as a potential sorbent to remove oil from the water system (AbdelWahab et al., 2016). The presence of hydroxyl, carbonyl, and ammine were significant in heavy metals and dyes removal (Liu et al., 2022).

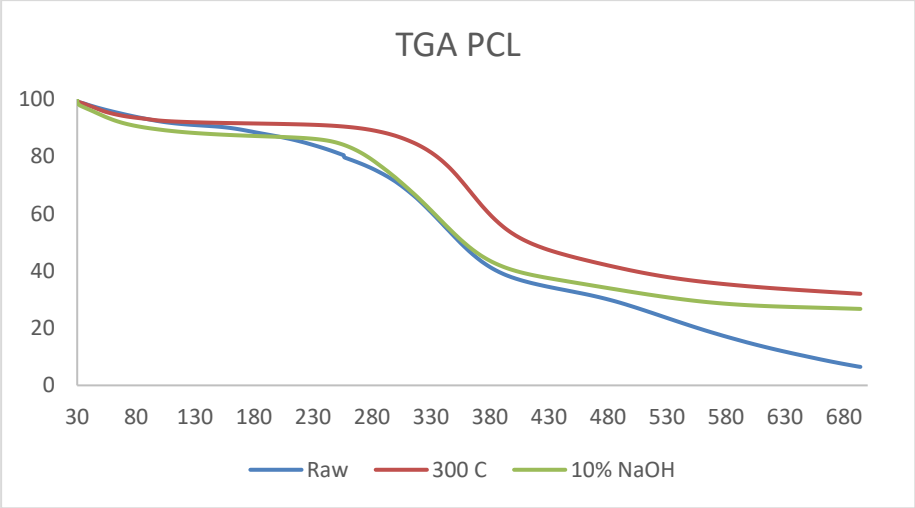

Figure 1. Comparison of TGA for raw, chemically, and thermally treated PCL samples

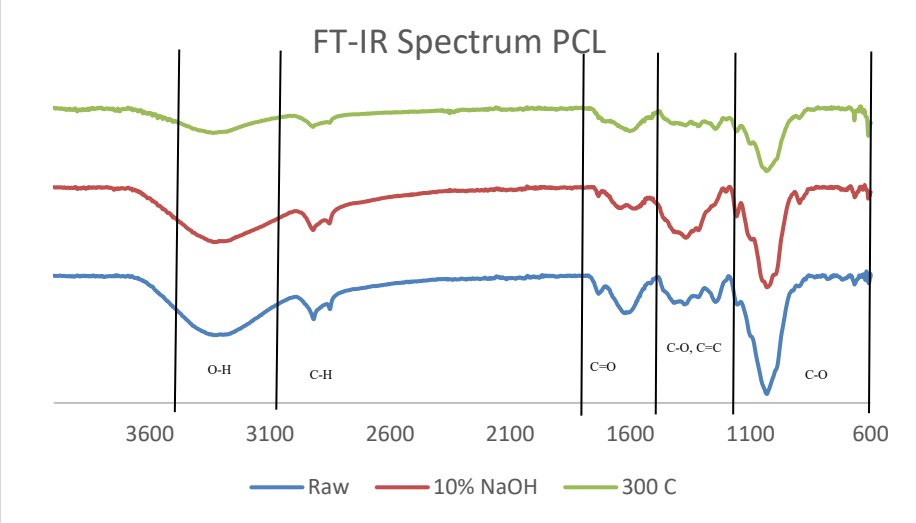

Figure 2. Comparison of FTIR spectrum for raw, chemically, and thermally treated PCL samples

CONCLUSION

The utilization of agricultural waste as sorbent in the removal of pollutants from water bodies offers a potential solution due to eco-friendly and cost effective as it only uses unwanted parts of plants which usually discarded. The high cellulose content in certain plants including the crown of pineapple (PCL) would be the best solution to adsorb the pollutant released into the water bodies. Modifying surface functional groups in organic materials optimize adsorption performance by altering their nature to suit the contaminants' intended application and chemical characteristics. Thus, chemically and thermally modified PCL would offer better pollutant removal since it has a higher surface area and having variety of functional groups.

REFERENCES

Abdelwahab, N., Shukry, N., & El-Kalyoubi, S. F. (2016). Preparation and characterization of polymer coated partially esterified sugarcane bagasse for separation of oil from seawater. Environmental Technology, 38(15), 1905–1914.

Akubo, K., Nahil, M. A., & Williams, P. T. (2019). Pyrolysis-catalytic steam reforming of agricultural biomass wastes and biomass components for production of hydrogen/syngas. Journal of the Energy Institute, 92(6), 1987–1996.

Adapa, P., Schonenau, L., Canam, T., & Dumonceaux, T. (2011). Quantitative analysis of lignocellulosic components of non-treated and steam exploded barley, canola, oat and wheat straw using Fourier transform infrared spectroscopy. *Journal of Agricultural Science and Technology*, 177.

Aryee AA, Mpatani FM, Kani AN, Dovi E, Han R, Li Z, Qu L (2021). A review on functionalized adsorbents based on peanut husk for the sequestration of pollutants in wastewater: modification methods and adsorption study. J Clean Prod 310:127502

Dai Y, Sun Q, Wang W, Lu L, Liu M, Li J, Yang S, Zhang K, Xu J, Zheng W, Hu Z, Yang Y, Gao Y, Chen Y, Zhang X, Gao F, Zhang Y (2018). Utilizations of agricultural waste as adsorbent for the removal of contaminants: a review. Chemosphere 211:235–253.

Deepa, B., Abraham, E., Cordeiro, N., Mozetič, M., Mathew, A. P., Oksman, K., Faria, M., Thomas, S., & Pothan, L. A. (2015). Utilization of various lignocellulosic biomass for the production of nanocellulose: a comparative study. Cellulose, 22(2), 1075–1090.

Divband Hafshejani L, Hooshmand A, Naseri AA, Mohammadi AS, Abbasi F, Bhatnagar A (2016). Removal of nitrate from aqueous solution by modified sugarcane bagasse biochar. Ecol Eng 95:101–111

Gheriany, I. a. E., Saqa, F. a. E., Amer, A. a. E. R., & Hussein, M. (2020). Oil spill sorption capacity of raw and thermally modified orange peel waste. Alexandria Engineering Journal, 59(2), 925–932.

Emiola-Sadiq, T., Zhang, L., & Dalai, A. K. (2021). Thermal and Kinetic studies on biomass degradation via thermogravimetric analysis: a combination of Model-Fitting and Model-Free approach. ACS Omega, 6(34), 22233–22247.

Etanuro, C., Doris, A., & Chidera, O. L. (2023). Adsorption study on the sorption of crude oil from water using raw/modified pineapple crown.

Fitriani, F., Aprilia, N. a. S., & Arahman, N. (2020). Properties of nanocrystalline cellulose from pineapple crown leaf waste. IOP Conference Series, 796(1), 012007.

Gaff, M., Kubovský, I., Síkora, A., Kačíková, D., Li, H., Kubovský, M., & Kačík, F. (2023). Impact of thermal modification on color and chemical changes of African padauk, merbau, mahogany, and iroko wood species. Reviews on Advanced Materials Science, 62(1).

Li, D., Zhu, F., Li, J. Y., Na, P., & Wang, N. (2013). Preparation and Characterization of Cellulose Fibers from Corn Straw as Natural Oil Sorbents. Industrial & Engineering Chemistry Research, 52(1), 516–524.

Lu, X., & Gu, X. (2022). A review on lignin pyrolysis: pyrolytic behavior, mechanism, and relevant upgrading for improving process efficiency. Biotechnology for Biofuels and Bioproducts, 15(1).

Matius, A., Saili, A. R., Hamzah, N., Fatah, F. A., Ramli, N. C., Hazwani, N., & Fatimah, S. (2022). Current practices and challenges of pineapple smallholder growers in managing the pineapple waste in Samarahan, Sarawak Malaysia. Food Research, 6(S1), 35–40.

Oliveira FR, Patel AK, Jaisi DP, Adhikari S, Lu H, Khanal SK (2017). Environmental application of biochar: current status and perspectives. Bioresource Technology 246:110–122

Pham, C. D., Vo, N. T., Do, N. H., Le, K. A., & Le, T. K. P. (2022). Investigation of bleaching stage in cellulose isolation from pineapple leaves for cellulose nanocrystals production. *VNUHCM Journal of Engineering and Technology, 5*(4), 1751-1758.

Qiu B, Tao X, Wang H, Li W, Ding X, Chu H (2021). Biochar as a low-cost adsorbent for aqueous heavy metal removal: a review. J Anal Appl Pyrolysis 155:105081

Reichert, A. A., Sá, M. R., De Freitas, T. C., Barbosa, R., Alves, T. S., Backes, E. H., Alano, J. H., & Oliveira, A. D. (2021). Barrier, Mechanical and Morphological Properties of Biodegradable Films Based on

Corn Starch Incorporated with Cellulose Obtained from Pineapple Crowns. Journal of Natural Fibers, 19(14), 8541–8554.

Sadi, T. (2021). The Challenges in Repurposing Food Wastes and Other Residuals for Agriculture. FFTC Agricultural Policy Platform (FFTC-AP).

Sahu P, Gupta MK (2020). A review on the properties of natural fibres and its bio-composites: effect of alkali treatment. Proceedings of the institution of mechanical engineers. P I Mech Eng L-j Mat 234(1):198–217

OPTIMISING ACTIVATED CARBON DERIVED FROM COUROUPITA GUIANENSIS KERNEL SHELLS FOR ENHANCED SUPERCAPACITOR PERFORMANCE: INSIGHTS FROM BET, SEM, AND FTIR ANALYSIS

N. J. Abdul Rahman1, M. R. Nurdik1, N. F. S. Nor Azmi1*, A. M. M. Ali2 & A. Lepit1*

[1]*Faculty of Applied Sciences, Universiti Teknologi MARA (UiTM), Cawangan Sabah, Campus Kota Kinabalu, Sabah 88997, Malaysia*

2022386987@student.uitm.edu.my, mohdruza@uitm.edu.my, faranaz@uitm.edu.my & ajis@sabah.uitm.edu.my

[2]*Faculty of Applied Sciences, Universiti Teknologi MARA (UiTM), 40450 Shah Alam, Selangor, Malaysia*

ammali@uitm.edu.my

ABSTRACT

This study explores the potential of activated carbon derived from Couroupita Guianensis kernel shells (CGKS) for use in supercapacitor applications, particularly electric double-layer capacitors (EDLCs). The activated carbon was synthesized and characterized to evaluate its structural, morphological, and functional properties crucial for energy storage. BET surface area analysis revealed a high specific surface area of 409.11 m^2/g with a significant micropore volume and an average pore diameter of 3.49 nm, indicating a predominance of mesopores—key attributes for enhancing the charge storage capacity in EDLCs. SEM analysis highlighted a porous morphology with macropores facilitating ion transport, critical for rapid charge/discharge cycles. FTIR analysis revealed the presence of functional groups and chemical bonds in CGKS, demonstrating that activated carbon has diverse surface functional groups. The EDLC demonstrated good performance through multiple charge-discharge cycles, with a loss in capacitance of less than 2%, demonstrating its potential for long cycle life. The combined insights from BET, SEM, and FTIR suggest that Couroupita Guianensis-derived activated carbon holds significant promise for high-performance supercapacitor applications, offering a sustainable and efficient alternative for energy storage technologies.

***Keywords*:** FTIR, SEM, BET, CGKS & material characterization.

INTRODUCTION

Activated carbon is a flexible, porous substance used for water, air, and industrial adsorption as well as energy storage. Traditionally, activated carbon was made from coal, coconut shells, and wood. However, biomass, particularly agricultural and forestry leftovers, is being used as raw materials for activated carbon synthesis due to the growing need for sustainable and eco-friendly alternatives (Marsh *et al*., 2006). Supercapacitors, also known as electrochemical capacitors, are energy storage devices with high power density, fast charge/discharge cycles, and long cycle life. Due to its high surface area, electrical conductivity, and porosity, activated carbon is the most used electrode material for supercapacitors (Yahya *et al*., 2015). In recent years, there has been a growing interest in developing sustainable and cost-effective sources of activated carbon for supercapacitor applications from fruit-based biomass wastes (Hadi *et al*., 2021). One such source is the Cannonball Tree (*Couroupita guianensis*), a tropical tree belonging to the family Lecythidaceae. It is native to Central and South American rainforests, particularly the Amazon Basin (Kumar et al., 2018). In Sabah, the cannonball tree had been found in Sabah Agricultural Park, Tenom. A lot of previous studies done by researchers on *Couroupita guianensis (CG)* are about its various applications in traditional medicine (Al-Dhabi *et al*., 2012). The investigation of CG fruit as activated carbon materials is still ongoing. Therefore, the waste material from this fruit needs to be exploited because it is an abundant and inexpensive natural supply. In this study, the *CG* fruit, particularly the fruit kernel shells, is a source of biomass for producing activated carbon. These shells, often considered waste, are abundant in regions where the tree is cultivated. Utilizing these shells not only provides a sustainable raw material for activated carbon production but also adds value to what would otherwise be discarded as organic waste. The production of activated carbon from *CGKS* involves two primary processes: carbonization and activation. During carbonization, the biomass is heated in a furnace at 350°C for an hour to produce char, which is then activated to increase its porosity and surface area. The activation process can be carried out chemically, using potassium hydroxide (KOH) as an activating agent. This study aims to investigate surface morphology including the surface area and size of porosity

of activated carbon produced by CGKS as well as charge and discharge analysis. This paper shows the surface morphology of activated carbon produced by *CGKS* has the potential and superior quality to be used as the active material for electrodes of supercapacitors.

MATERIALS AND METHODS

The CG fruit seed shells were broken into smaller pieces, submerged in water, dried, and carbonized in a fire at 350°C for an hour. The carbonized biomass was activated with a 1:3 mass KOH solution, filtered, rinsed, and heated in an oven.

Figure 1. Preparation of AC from CGKS

The electrode was created by mixing AC with casein and Polyethylene Glycol, using solvents like distilled water and acetone. Asymmetrical EDLC was created using an AC electrode for both the cathode and anode, separated by filter paper and 4.45 M KOH as the electrolyte. Physical characterisation of the activated carbon of CGKS was conducted using BET and SEM, while molecular analysis was conducted using FTIR. The EDLC's performance was assessed using a charge-discharge circuit connected to a 4.0 V power source.

RESULTS AND DISCUSSION

Table 1 shows the information regarding the activated carbon content of CGKS. BET theory calculates the specific surface area of solid materials of CGKS using gas adsorption data, providing crucial information on activated carbon material structure. The activated carbon of CGKS indicates a large surface area, including micropores and mesopores, makes it suitable for applications like adsorption, catalysis, and filtering, with detailed analysis revealing its porosity.

Table 1. BET of the activated carbon of CGKS

Specific Surface Area	Textural properties	Measured Value
Surface Area	Single point surface area at P/Po	0.302036194: 372.6396 m^2/g
	BET Surface Area	409.1105 m^2/g
	Langmuir Surface Area	539.4117 m^2/g
Pore Size	BJH Desorption average pore diameter (4V/A)	3.2290 - 3.4897 nm
DFT Pore Size	Volume in Pores	< 1.536 nm: 0.13215 cm^3/g
	Total Volume in Pores	≤ 100.008 nm: 0.18005 cm^3/g
	Total Area in Pores	≥ 1.536 nm: 93.574 m^2/g

Figure 2 shows an SEM image of micropores and mesopores in activated carbon. Smaller pores within macropore walls contribute to high surface area and adsorption capacity. The surface has a rough texture, suggesting activation. Small particles and debris suggest incomplete combustion or residuals from activation.

Cracks and fissures impact the structure's delicacy and adsorption capabilities. The irregular shape of activated carbon particles is common in materials with activation processes. These characteristics contribute to the material's adsorption capabilities.

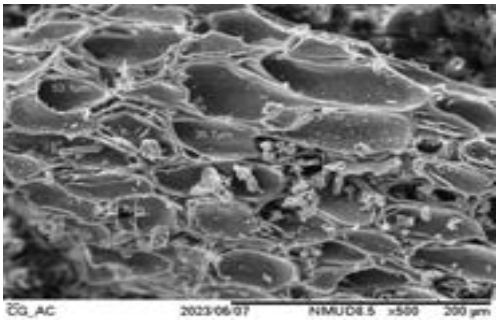

Figure 2. Surface morphology of AC of CGKS

The Fourier Transform Infrared (FTIR) spectra reveal the functionality and chemical composition of activated carbon, which can impact properties like adsorption capacity and affinity for different substances. The spectrum identifies several key peaks, including O–H stretching vibrations in hydroxyl groups or water molecules, nitrile groups, C=C stretching in aromatic rings, C–H bending in alkanes or phenolic O–H groups, ether or ester groups, and out-of-plane bending of C–H bonds in aromatic compounds. These peaks provide insight into the chemical composition and surface characteristics of activated carbon, which are crucial for its applications. The main peaks are 3227.33 cm^{-1}, 2214.81 cm^{-1}, 1574.15 cm^{-1}, 1366.57 cm^{-1}, 1231.55 cm^{-1}, and 800.08 cm^{-1}. These peaks provide valuable information about the surface chemistry and functional groups of activated carbon, which are essential for its applications.

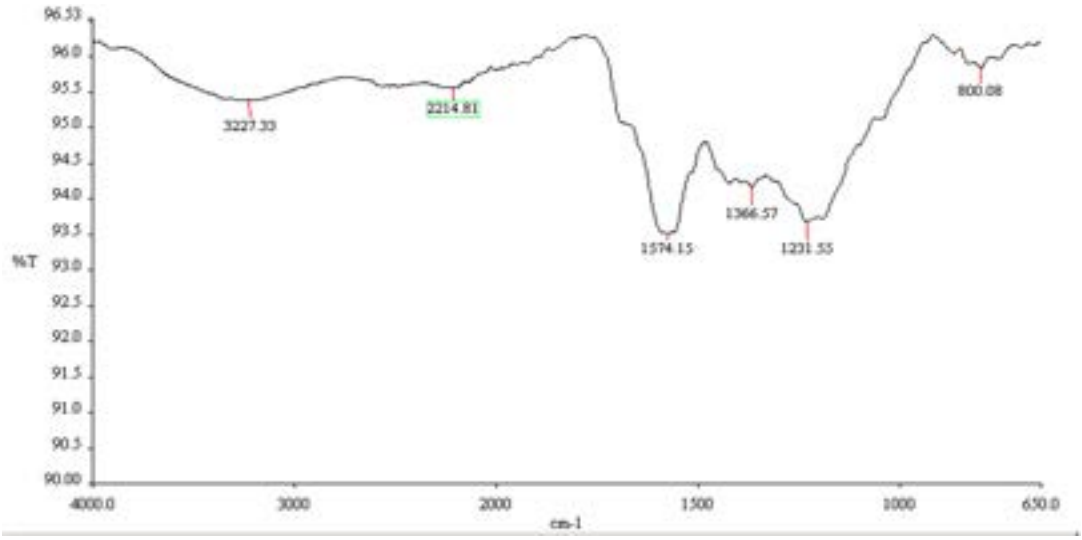

Figure 3. FTIR spectrum of AC of CGKS

The initial of ideal EDLC charge discharge graphs for the first tenth cycle have symmetric triangles (Figure 4). This typical AC electrode graph displays good capacitive behavior. This suggests CG electrode material conducts well. Over time, charge-discharge stability rises. This showed that the EDLC has good capacitive performance and high cycle life.

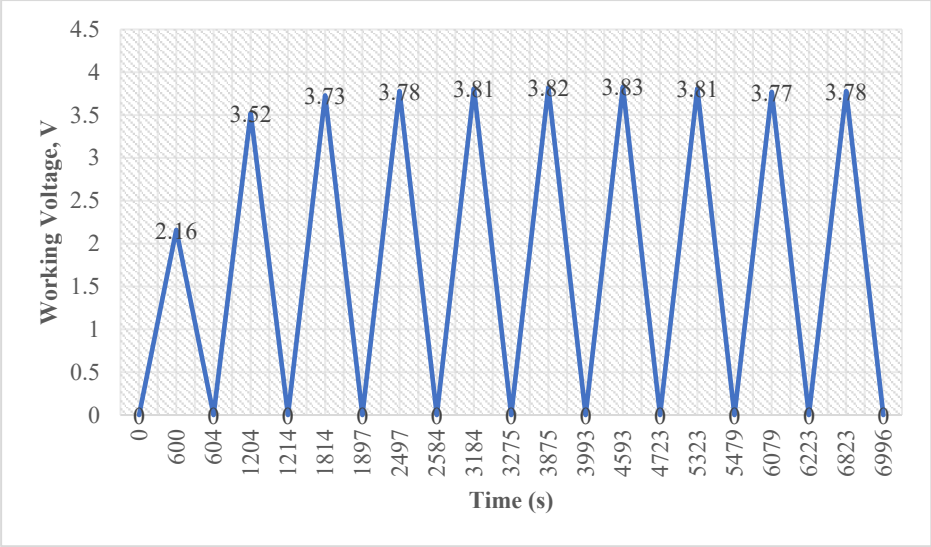

Figure 4: Voltage vs. time graph for 10 cycles of charge and discharge

CONCLUSION

Activated carbon, with its mechanical stability and macropores, is ideal for electrolyte and electrode applications due to its fluid flow and adsorption capacity. However, cracks and fissures can reduce stability. CGKS's large surface area and mix of micropores and mesopores make it suitable for adsorption, catalysis, and filtration. It can also be transformed into activated carbon, potentially used in energy storage devices like supercapacitors. The EDLC's charge-discharge graphs show good capacitive behavior, indicating good conductivity of the CG electrode material, and a high cycle life over time.

RECOMMENDATIONS

Investigating the enhancement of CGKS-based biomass predecessors with mixed media of other composite materials and their application at higher heating temperatures is being explored for various uses such as biocatalysts, electrodes, and energy storage.

REFERENCES

Al-Dhabi, N. A., Balachandran, C., Raj, M. K., Duraipandiyan, V., Muthukumar, C., Ignacimuthu, S., Rajput, V. S. (2012). Antimicrobial, antimycobacterial and antibiofilm properties of Couroupita guianensis Aubl. fruit extract. *BMC Complementary and Alternative Medicine*, *12*(1).

Hadi, N., Abu Seman, M., & Bermakai, M. (2021). Review on Activated Carbon from Fruit-Based Biomass for Supercapacitor. *Journal Of Academia, 9*(1), 117-126.

Kumar, P. S., & Vincent, C. (2018). "Preparation and Characterization of Activated Carbon from *Couroupita guianensis* Fruit Shells for Dye Adsorption." *Environmental Technology & Innovation*, 9, 100-110.

Marsh, H., & Rodríguez-Reinoso, F. (2006). *Activated Carbon*. Elsevier Science

Yahya, M. A., Al-Qodah, Z., & Ngah, C. W. Z. (2015). "Agricultural Bio-waste Materials as Potential Sustainable Precursors Used for Activated Carbon Production: A Review." *Renewable and Sustainable Energy Reviews*, 46, 218-235.

BIOLOGICAL AND PHYSIOCHEMICAL STUDIES OF OLEYL PALMITATE TO BE APPLIED AS AN ACTIVE AGENT IN COSMETIC FORMULATION

Nurul Fadhilah Abdul Halim [1], Salina Mat Radzi [1*], Maryam Mohd Rehan [1], Nor Amalina Mohd Amin [1] and Nurul Jannah Abdul Rahman [2]

[1] *Faculty of Science and Technology, Universiti Sains Islam Malaysia*

71800 Nilai, Negeri Sembilan, MALAYSIA

salina@usim.edu.my

[2]*Tamhidi Centre, Universiti Sains Islam Malaysia*

71800 Nilai, Negeri Sembilan, MALAYSIA

ABSTRACT

Oleyl palmitate, a wax ester widely used in various industries, including cosmetic formulation, is challenging to obtain naturally due to its high cost and limited availability. In this study, oleyl palmitate was synthesized through an esterification reaction using oleyl alcohol and palmitic acid. Verification of the synthesized wax ester was performed using Fourier Transform Infrared (FTIR) and Nuclear Magnetic Resonance (NMR) spectroscopy to confirm the presence of ester bonds in its molecular structure. The antimicrobial activity of oleyl palmitate was assessed against both Gram-positive and Gram-negative bacteria using the agar diffusion test. The Minimum Inhibition Concentration (MIC) value was determined through the microdilution method. Two biological activities, bactericidal effects (killing bacteria) and bacteriostatic effects (inhibiting bacterial growth), were determined by the Minimum Bactericidal Concentration (MBC) value. The synthesized oleyl palmitate exhibited a bactericidal effect against all Gram-positive bacteria studied, including Bacillus subtilis and Staphylococcus aureus. Additionally, physicochemical properties such as SPF values (15.0), peroxide values (18.0 mEq O_2/kg), saponification values (90.0 mg KOH/g), and iodine values (87.0 g I_2/100 g) were determined. The data obtained suggest that the synthesized oleyl palmitate holds potential as an active ingredient in cosmetic formulations.
Keywords: oleyl palmitate, biological, physicochemical, wax ester, cosmetic formulation

INTRODUCTION

Wax esters are esters with a chain length of 12 carbons or more, produced through the synthesis of fatty acids and alcohols. These compounds, derived from various plants, animals, fungi, and bacteria, serve diverse biological functions. In nature, wax esters play crucial roles such as protection, water resistance, and energy storage. For instance, in plants, wax esters form a protective layer on leaves, fruits, and stems, preventing water loss and shielding against external stresses. Additionally, animal sebum produced by sebaceous glands contains wax esters that serve as lubricants for the skin and hair.

Beeswax, sperm whale, and jojoba oil are instances of botanical and zoological sources from which wax esters can be obtained. Wax esters, also known as fat esters, are widely used in a variety of industries as lubricants, plasticizers, antifoaming agents, and coating materials in medical and food sectors, as well as raw materials in cosmetics and other chemical sectors [1]. In cosmetic formulations, due to their non-greasy, non-toxic and great emollient properties, wax esters are used to give the skin a smooth and soft texture [1].

The need for synthetic production of oleyl palmitate has risen due to the high cost and difficulty in obtaining naturally occurring wax esters. Both chemical and enzymatic processes have been successfully employed to synthesize wax esters [2]. These artificially produced wax esters offer similar qualities and benefits as their natural counterparts, such as emollience, moisturization and texture enhancement. Moreover, synthetic wax esters come with advantages such as regulated composition, increased stability and consistent quality, making them a preferred choice for cosmetic applications. In this investigation, oleyl palmitate will be synthesized through a straightforward esterification method involving palmitic acid and oleyl alcohol in the presence of hexane.

Therefore, this study aims to assess the biological properties by evaluating the Minimum Inhibitory Concentration (MIC) and Minimum Bactericidal Concentration (MBC) of the sample on the targeted bacteria. Additionally, the physicochemical properties of the synthesized oleyl palmitate, including peroxide value, saponification value, SPF value and iodine value, will be examined using a standard method.

The objectives of this study were to produce oleyl palmitate, a wax ester derived from the reaction of palmitic acid and oleyl alcohol in hexane via esterification reaction. The synthesized products underwent evaluation for both biological and physicochemical properties. To gauge their biological characteristics, a dilution process involving Gram-positive and Gram-negative bacteria such as *Bacillus subtilis* and *Escherichia coli* was employed to ascertain the Minimum Inhibitory Concentration (MIC) and Minimum Bactericidal Concentration (MBC) of the samples. Simultaneously, four parameters which are peroxide value, saponification value, SPF value, and iodine value were examined to determine the physicochemical properties of oleyl palmitate.

METHODOLOGY

The methodology was divided into three main components: the production of oleyl palmitate, the examination of antimicrobial properties, and the analysis of physicochemical characteristics, which illustrated in the experimental design depicted below (Figure 1).

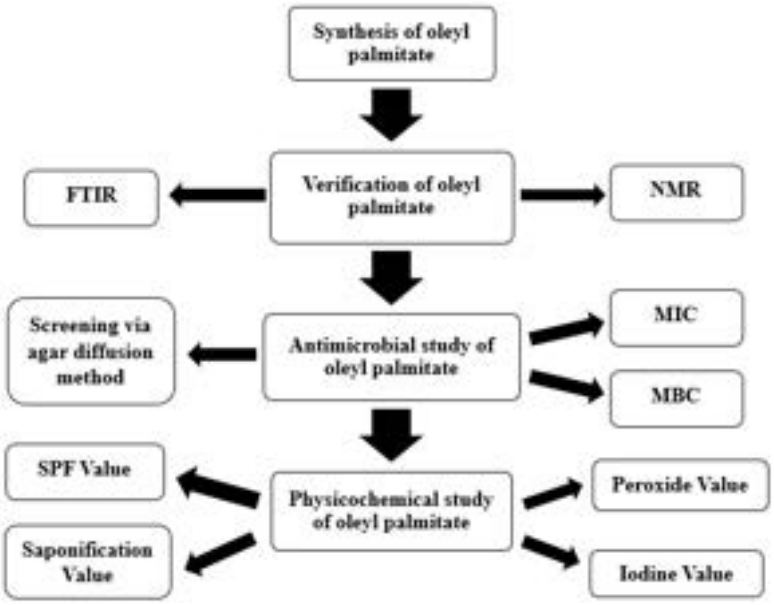

Figure 1. Experimental Design.

Synthesis of Oleyl Palmitate

Oleyl palmitate was synthesized by reacting palmitic acid with oleyl alcohol. In the initial stage, palmitic acid and oleyl alcohol were combined in a 250 mL universal bottle with n-hexane as the solvent, maintaining a molar ratio of 1:2. The mixture underwent a 5-hour incubation at a reaction temperature of 50°C in a water bath shaker set at 150 rpm [5].

Verification of Oleyl Palmitate

During the procedure, a sample (oleyl palmitate) from the reaction outcome underwent testing through thin-layer chromatography (TLC). Furthermore, the sample was analyzed using spectroscopic instruments such as Fourier Transform Infrared (FTIR) and Nuclear Magnetic Resonance (NMR). Prior to verification through FTIR and NMR, Thin Layer Chromatography (TLC) was employed as a preliminary step. For FTIR, to ascertain the functional group, the resulting product of the reaction was analyzed using Fourier Transform Infrared Spectroscopy (Perkin Elmer, model spectrometer 100, England). The absorption peaks corresponding to various functional groups are outlined in Table 1.

Table 1. FTIR Absorption Peaks for several Functional Groups.

Functional groups		Absorption peaks	
		Wavenumber (cm^{-1})	Wavelength (μm)
O-H	Aliphatic and aromatic	3600-3000	2.8-3.3
NH_2	Secondary and tertiary	3600-3100	2.8-3.2
C-H	Aromatic	3150-3000	3.2-3.3
C-H	Aliphatic	3000-2850	3.3-3.5
C≡N	Nitrile	2400-2200	4.2-4.6
C≡N-	Alkyne	2260-2100	4.4-4.8
COOR	Ester	1750-1700	5.7-2.9
COOH	Carboxylic acid	1740-1670	5.7-6.0
C=O	Aldehydes and ketones	1740-1660	5.7-6.0
$CONH_2$	Amides	1720-1640	5.8-6.1
C=C-	Alkene	1670-1610	6.0-6.2
Ø-O-R	Aromatic	1300-1180	7.7-8.5
R-O-R	Aliphatic	1160-1060	8.6-9.4

For NMR, the structure of the produced compound was subsequently established through NMR analysis of the ester sample using DMSO as the solvent. The chemical shift of the compound was gauged by employing H-NMR and C-NMR spectra for compound identification.

Table 2. The main signal present in ^{13}C-NMR functional groups of oleyl palmitate.

Functional groups	Chemical shifts, ppm
C=O	173.2
C=C	130.6
C-O	64.59
CH_2-COO-CH_2	32.82
CH_3	14.12

Table 3. The main signal present in ^{1}H-NMR functional groups of oleyl palmitate.

Functional groups	Chemical shifts, ppm
-CH_2-COO	2.26
-CH=CH-	5.32
CH_2-O-CO	4.02
C=C-C-H	1.85
CH_2	1.23-1.33
CH_3	0.85

Antimicrobial Study of Oleyl Palmitate

The effectiveness of the sample against microorganisms was assessed through an antimicrobial assay utilizing the agar diffusion method [6]. The MIC of the sample was established through the dilution method [7], and its MBC was also determined [7]. Microorganisms employed in this research were *Bacillus subtilis, Staphylococcus aureus, Salmonella typhimurium* and *Escherichia coli.* This is because, these organisms are well-characterized and widely used in laboratory settings, allowing for standardized experimental conditions and reproducibility.

Physicochemical Study of Oleyl Palmitate

Four parameters were selected for the physicochemical study of oleyl palmitate, including SPF value, peroxide value, saponification value and iodine value.

SPF value

The acronym "SPF" (Sun Protection Factor) refers to a product's efficacy in safeguarding the skin against the harmful effects of UV radiation. The SPF rating provides protection against UVB (ultraviolet B) rays, known for causing sunburn and skin damage. Elevated SPF numbers signify heightened levels of protection. The 12 determination of the SPF value involves employing specific techniques, either in vitro or in vivo testing [8]. The Mansur equation was employed to calculate the SPF value [9].

Mansur eq = CF × ∑ 320 290 × EE × I × Abs

Where, CF = correction factor

EE = an erythemal effect spectrum

I = the solar intensity spectrum

Abs = absorbance of the sample

Peroxide value

The quantification of reactive oxygen levels, expressed in milliequivalents (mEq) of free iodine per kilogram of fat, is known as the peroxide value (POV). This value can be assessed by titrating iodine released from potassium iodide with a sodium thiosulphate solution [10]. In cosmetic formulations, especially those incorporating oils like carrier oils, plant oils, or oils derived from organic sources, the peroxide value assumes a critical role. It provides insights into the stability and freshness of these oils, indicating potential levels of oxidation. Elevated peroxide values suggest heightened oxidation and potential degradation of the product. The equation below was applied to determine the peroxide value [11].

Peroxide value = [(B − S) x N x 1000]/W

Where, S = volume of titrant (mL) for the sample

B = volume of titrant (mL) for blank

N = normality of sodium thiosulphate solution (mmol/mL)

1000 = conversion of the unit (g/kg)

W = mass (g) of the sample (oleyl palmitate)

Saponification value

Saponification is the process of hydrolyzing an ester in an alkaline solution. The saponification value is a measure of the chain length of all fatty acids. It is determined by the quantity of potassium hydroxide required to neutralize the fatty acids produced through the complete hydrolysis of 1 g of the sample in oil or fat. Notably, long-chain fatty acids, characterized by fewer carboxylic functional groups, exhibit a low saponification value [12]. Equation 3.3 was then applied to calculate the saponification value [13].

Saponification value = [(B − S) x N x 56.1]/W

Where, B = volume of titrant (mL) for the blank

S = volume of titrant (mL) for the sample

N = normality of hydrochloric acid HCl (mmol/mL)

56.1 = the molecular weight of potassium hydroxide KOH (g/mol)

W = mass (g) of sample (oleyl palmitate)

Iodine value

The iodine value is a measure of the amount of unsaturation or double bonds present in fats and oils. It is also employed as one of the factors to evaluate the quality of olein. This value indicates the weight proportion of absorbed halogen, specifically iodine, under test conditions. The definition involves calculating the amount of iodine (in grams) absorbed by the fat (in 100 grams) during the test period. The iodine value is considered a significant constant that is easily calculable for fats and oils [14]. Equation below was employed to determine the iodine value [15].

$$\text{Iodine Value} = [(B - S) \times N \times 126.9]/W$$

Where, B = volume of titrant (mL) for the blank

S = volume of titrant (mL) for the sample

N = normality of sodium thiosulphate (mmol/mL)

126.9 = the molecular weight of iodine (g/mol)

W = mass of sample

RESULTS

Synthesis of Oleyl Palmitate

The esterification reaction mixtures of oleyl alcohol and palmitic acid were incubated in a water bath shaker (150 rpm) at 50°C reaction temperature and with 5 hours of reaction time in the presence of n-hexane that acts as solvent to help shift the reaction towards the products.

Verification of Oleyl Palmitate

To analyze the samples produced, oleyl palmitate was first isolated and purified before using FTIR and NMR. Thin layer chromatography (TLC) was used for this purpose.

For TLC results, the separation of mixtures was observed by exposing them to UV light at 254 nm. The chromatogram was characterized by the retention factor (Rf) of each analyte, which is the fractional distance where the analyte spot to solvent by moving along the plate. The distance for each substance spot is measured from the starting point of the substances, and the development distance for the substances is the distance to the center of the substance spot.

In this study, the FTIR spectrum of oleyl palmitate was analyzed, and the results are presented in Figure 2. Other than that, Figure 3 illustrates the ^{1}H-NMR spectrum and ^{12}C-NMR spectrum of oleyl palmitate.

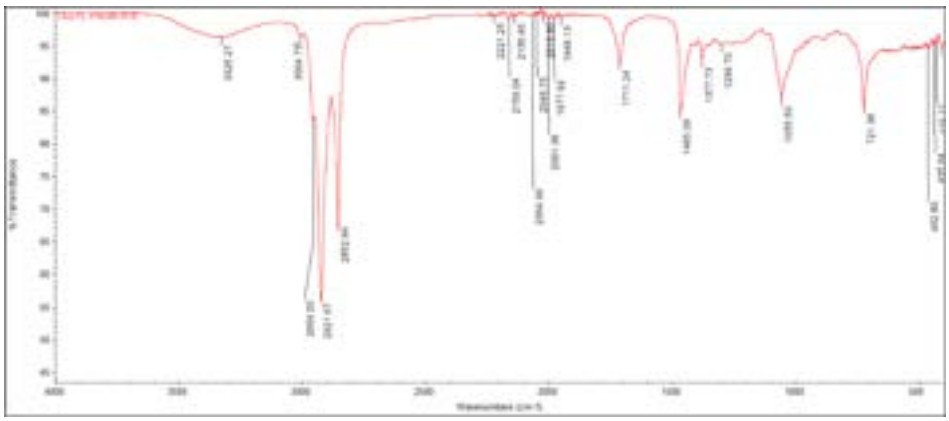

Figure 2. FTIR Absorption Spectra of Oleyl Palmitate.

The key peaks in the FTIR spectrum of oleyl palmitate are present in the range of peaks 2850-2950 cm^{-1} for the C-H stretching, 1700-1750 cm^{-1} for the C=O stretching, 1000-1300 cm^{-1} for the C-O stretching and 600-1500 cm^{-1} for fingerprint region. From figure 2 above, the presence of strong C-H stretching peaks at 2921.67 cm^{-1} confirms the long aliphatic chain, while the distinct C=O peak present at 1711.24 cm^{-1} indicates the ester functionality. The C-O stretching bands present at 1299.70-1055.50 cm^{-1} further support the identification of oleyl palmitate as an ester derived from oleyl alcohol and palmitic acid.

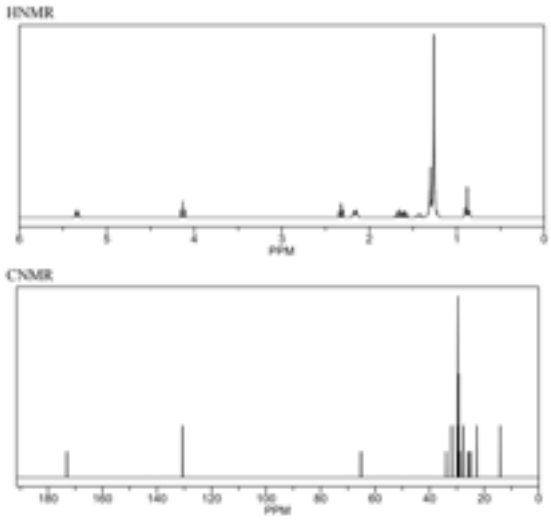

Figure 3. NMR Spectrum for ^{1}H-NMR and ^{12}C-NMR of Oleyl Palmitate.

The chemical shifts of the carbon atoms in the ester group of oleyl palmitate in the range of 160-185 ppm for the C=O and 20-30 ppm for the methyl group on the end of the ester. Based on the NMR results in figure 3 above, it shown that chemical shifts of the carbon atoms in the ester group of oleyl palmitate present at 173.2 ppm for C=O and the methyl group on the end of the ester which is oleyl palmitate present at 23.0 ppm.

Antimicrobial Assays of Oleyl Palmitate

The antimicrobial evaluation involved the utilization of agar-well diffusion and dilution methods. Within the dilution method, two distinct analyses were performed: MIC (Minimum Inhibitory Concentration) and MBC (Minimum Bactericidal Concentration).

According to the results of agar-well diffusion method, when assessed against Gram-positive bacteria *Bacillus subtilis* and *Staphylococcus aureus*, oleyl palmitate generated distinct clear zones on the agar plate. In contrast, there were no observable clear zones when the same compound was tested against Gram-negative bacteria *Salmonella typhimurium* and *Escherichia coli*.

In the dilution method, the MIC is defined as the lowest concentration (maximum dilution) of the antimicrobial agent that prevents turbidity growth, indicating that the agent is bacteriostatic, allowing some bacteria to remain alive [16]. The result for this technique shown that the MIC value for oleyl palmitate on *Bacillus subtilis* is at the second concentration (1:2 v/v) while on *Staphylococcus aureus* is at the third concentration (1:3 v/v). For Gram-negative bacteria which are *S. typhimurium* and *E. coli*, the MIC value for *S. typhimurium* cannot be obtained while the MIC value for *E. coli* is at the first concentration which is 1:1 v/v. The MIC value for *S. typhimurium* cannot be obtained might be because of the presence of other microbes could inhibit the growth of *S. typhimurium* and affect the accuracy of the MIC determination.

Table 4. The Minimum Inhibitory Concentration (MIC) Values of Oleyl Palmitate on Tested Bacteria.

Concentration of test samples (v/v)	Test Bacteria			
	Bacillus subtilis	*Staphylococcus aureus*	*Salmonella typhimurium*	*Escherichia coli*
1:1	-	-	+	-
1:2	-	-	+	+
1:3	+	-	+	+
1:4	+	+	+	+
Streptomycin sulfate	-	-	-	-

+: Presence of bacteria growth, -: Absence of the bacteria growth

Whereas, the Gram-positive and Gram-negative bacterial strains were evaluated for their Minimum Bactericidal Concentration (MBC) values. MBC is defined as the lowest concentration of an antimicrobial agent that eliminates more than 99.90% of the initial bacterial population, leading to no visible bacterial growth on the agar plates [17]. Table 5 presents the MBC values of oleyl palmitate against the tested bacteria. Streptomycin sulfate is an aminoglycoside antibiotic that primarily inhibits protein synthesis in bacteria. In MIC testing, streptomycin sulfate is used to establish the lowest concentration of the antibiotic that inhibits visible growth of the test organism.

Table 5. The Minimum Bactericidal Concentration (MBC) Values of Oleyl Palmitate on Tested Bacteria.

Concentration of test samples (v/v)	Test Bacteria			
	Bacillus subtilis	*Staphylococcus aureus*	*Salmonella typhimurium*	*Escherichia coli*
1:1	-	-	+	+
1:2	+	-	+	+
1:3	+	+	+	+
1:4	+	+	+	+
Streptomycin sulfate	-	-	-	-

+: Presence of bacteria growth, -: Absence of the bacteria growth

Physicochemical Study of Oleyl Palmitate

Following the determination of the antimicrobial properties of the created wax esters, their physicochemical properties, including SPF value, peroxide value, saponification value and iodine value were also assessed. Thus, table 6 provides a summary of the physicochemical properties of oleyl palmitate, the wax ester synthesized in this study.

Table 6. Summarize Physicochemical Properties for Oleyl Palmitate.

Physicochemical Properties	Oleyl Palmitate
SPF Value	15.0
Peroxide Value	18.0
Saponification Value	90.0
Iodine Value	87.0

DISCUSSION

In the current study, oleyl palmitate was produced through an esterification reaction involving palmitic acid and oleyl alcohol. It is expected that the products derived from the synthesis of wax esters would yield a high percentage, typically ranging from 70% to 90% or even exceeding these values [2]. The reaction was conducted with hexane serving as a solvent to dissolve the reactants and promote the formation of the desired product, namely oleyl palmitate.

In this study, FTIR and NMR instruments were used to verify the product. Thus, the function of FTIR is to detect the main functional group presence in the molecular structure and in FTIR, the ester bond (C=O) was detected present at 1711.24 cm^{-1}.

The antimicrobial activity of oleyl palmitate was assessed using agar diffusion tests against both Gram-positive and Gram-negative bacteria. The Minimum Inhibitory Concentration (MIC) and Minimum Bactericidal Concentration (MBC) values were determined using the microdilution method. The synthesized oleyl palmitate exhibited a bactericidal effect against all Gram-positive bacteria studied, including *Bacillus subtilis* and *Staphylococcus aureus*.

The physicochemical properties of the synthesized oleyl palmitate were evaluated by determining the SPF value, peroxide value, saponification value and iodine value. The SPF value was found to be 15.0, the peroxide value was 18.0 mEq O_2/kg, the saponification value was 90.0 mg KOH/g, and the iodine value was 87.0 g I_2/100 g. These results suggest that the synthesized oleyl palmitate holds promise as an active ingredient in cosmetic formulations.

CONCLUSION

The study successfully synthesized oleyl palmitate from palmitic acid and oleyl alcohol through an esterification reaction. The biological properties of the synthesized oleyl palmitate were evaluated using MIC and MBC methods, while its physicochemical properties assessed through SPF, peroxide, saponification and iodine values. The data obtained suggest that the synthesized oleyl palmitate holds potential as an active ingredient in cosmetic formulations, providing both biological and physicochemical benefits.

ACKNOWLEDGEMENT

This study is supported by Faculty Science and Technology (FST), USIM and Assoc Prof Dr Salina Binti Mat Radzi.

REFERENCES

[1] Abd Gani, S. S., Basri, M., Abdul Rahman, M. B., Kassim, A., Raja Abd Rahman, R. N. Z., Salleh, A. B., & Ismail, Z. (2011). Engkabang fat esters for cosmeceutical formulation. Journal of Surfactants and Detergents, 14(2), 227-233.

[2] Mat Radzi, S. M., Rosli, M. A., Noor, H. M., & Rehan, M. M. (2015, March 18-19). Optimization of Oleyl Ester using Statistical Approach of Response Surface Methodology. International Conference on Chemical, Environmental and Biological Sciences.

[3] Sánchez, M. A., Torres, G. C., Mazzieri, V. A., & Pieck, C. L. (2017). Selective hydrogenation of fatty acids and methyl esters of fatty acids to obtain fatty alcohols–a review. Journal of Chemical Technology & Biotechnology, 92(1), 27-42.

[4] Amira, P. O., Babalola, O. O., & Oyediran, A. M. (2014). Physicochemical properties of palm kernel oil. Current Research Journal of Biological Sciences, 6(5), 205-207.

[5] Gunawan, E. R., & Suhendra, D. (2010). Wax Esters Production by Alcoholysis of Palm Oil Fractions. Indonesian Journal of Chemistry, 8(3), 356–362.

[6] Balouiri, M., Sadiki, M., & Ibnsouda, S. K. (2016). Methods for in vitro evaluating antimicrobial activity: A review. Journal of Pharmaceutical Analysis, 6(2), 71–79.

[7] Bubonja-Šonje, M., Knežević, S., & Abram, M. (2020). Challenges to antimicrobial susceptibility testing of plant-derived polyphenolic compounds. Archives of Industrial Hygiene and Toxicology, 71(4), 300–311.
[8] Kaur, C. D., & Saraf, S. (2010). In vitro sun protection factor determination of herbal oils used in cosmetics. Pharmacognosy Research, 2(1), 22.
[9] Mansur JS, Breder MN, Mansur MC, Azulay RD (1986) Determination of Sun Protection Factor by Spectrophotometry. An Bras Dermatol 61: 121-124.
[10] Low, L., Kim, Ng, C., Siang, Low, L., & Ng, C. (2023). Analysis of oils: Determination of peroxide value. In H. Hasegawa (Ed.), Laboratory Manual on Analytical Methods and Procedures for Fish and Fish Products (pp. C-7). Marine Fisheries Research Department, Southeast Asian Fisheries Development Centre.
[11] American Oil Chemist's Society. *Official Methods and Recommended Practices of the American Oil Chemists' Society.* 4th ed. AOCS Press; Champaign, IL, USA: 1998. Method Cd 8b-90.
[12] Ivanova, M., Hanganu, A., Dumitriu, R., Tociu, M., Ivanov, G., Stavarache, C., Liliana Georgeta Popescu, Aliona Ghendov-Mosanu, Sturza, R., Calin Deleanu, & Chira, N. A. (2022). Saponification Value of Fats and Oils as Determined from 1H-NMR Data: The Case of Dairy Fats. Foods, 11(10), 1466.
[13] Turnbull, S., Bradshaw, L., & Yildiz, Y. (2019). Determination of Saponification Value in Carnuba Wax by USP/NF Residual Titration Method <541> *American Journal of Analytical Chemistry*, *10*(09), 423–427.
[14] Azmi, N., Radzi, S. M., Rehan, M. M., & Amin, N. A. M. (2022). A Review on Cosmetic Formulations and Physicochemical Characteristics of Emollient and Day Cream Using Vegetable Based-Wax Ester. Malaysian Journal of Science Health & Technology, 8(2), 38-45.
[15] Pulassery, S., Abraham, B., Ajikumar, N., Munnilath, A., & Yoosaf, K. (2022). Rapid iodine value estimation using a handheld Raman spectrometer for On-Site, Reagent-Free authentication of edible oils. *ACS Omega*, *7*(11), 9164–9171.
[16] Parvekar, P., Palaskar, J., Metgud, S., Maria, R., & Dutta, S. D. (2020). The minimum inhibitory concentration (MIC) and minimum bactericidal concentration (MBC) of silver nanoparticles against Staphylococcus aureus. Biomaterial Investigations in Dentistry, 7(1), 105–109.
[17] Petrus, E.M., Tinakumari, S., Chai, L., Tunung & Elexson, N., Chai, L. F. and Son, R., (2011). A study on the minimum inhibitory concentration and minimum 44 bactericidal concentration of Nano Colloidal Silver on food-borne pathogens. International Food Research Journal, 18, 55-66.

DECOMPOSITION OF LIGNOCELLULOSE MATERIAL FROM OIL PALM EMPTY FRUIT BUNCH (OPEFB) USING SULFATE-BASED IONIC LIQUID

Maizatul Liana Arshad[1], Nur Amalina Mohd Amin[2], Salina Mat Radzi[3]

[1,2,3] *Faculty of Science and Technology*

Universiti Sains Islam Malaysia

71800 Nilai, Negeri Sembilan, MALAYSIA

nuramalina@usim.edu.my

ABSTRACT

Ionic liquids are commonly employed as a green alternative to break down the recalcitrant structure of lignocellulose, an abundant material derived from agricultural crops like oil palm empty fruit bunch (OPEFB), and facilitating further product conversion. In this study, triethylammonium sulfate, [TEA][HSO_4] was synthesized from triethylamine (cation) and sulfuric acid (anion) achieving 71.2 % of percentage yield. Characterization was conducted through fourier-transform infrared spectroscopy (FTIR), nuclear magnetic resonance (NMR) spectroscopy, and thermogravimetric analysis (TGA) instruments that confirmed the successfulness of synthesis from the structural component of [TEA][HSO_4], molecular arrangement and its thermal stability. As sulfate-based ionic liquid can dissolve lignocellulosic components, the OPEFB subjecting the dissolution process to ionic liquid pretreatment with varying temperature (30, 80 and 130 °C) and mixing time (2h and 5h) to identify the optimum condition to achieve efficient decomposition. The characterization of untreated and treated OPEFB was done by performing FTIR and x-ray diffraction (XRD) showed a prominent reduction in structural crystallinity and lignin component of treated OPEFB. The field emission scanning electron microscopy (FESEM) illustrated the increases in porosity and distorted surface which showed the disruption on lignocellulose protective layer. The results indicate a significant breakdown of cellulose's hydrogen bond networks and recalcitrant structures, highlighting the effectiveness of ionic liquid in decomposing lignocellulose for potential value-added product such as fuels.

Keywords: triethylammonium sulfate, OPEFB, recalcitrant, optimum condition, decomposition

INTRODUCTION

Oil palm production is crucial in tropical regions for global vegetable oil supply but generates significant agricultural waste, like empty fruit bunches (EFBs). Biomass, including oil palm empty fruit bunches (OPEFB), is a key renewable energy source. Improper waste management can cause environmental issues. OPEFB is one of the lignocellulosic biomass mainly composed of of cellulose ($(C_6H_{10}O_5)_n$, hemicellulose ($C_5H_{10}O_5$)n and lignin ($C_{10}H_{11}O_{3.5}$) [1]. OPEFB can be converted into biofuels and other valuable products, but its complex structure poses a challenge.

In order to create new products from OPEFB, its lignocellulose material must be broken down its substituents by utilizing decomposition process from its native plant. Various pretreatment methods, like alkaline treatment and organosolv pulping [1], have been used, but they often require high energy, have low conversion rates, and can be harmful to the environment. Nowadays, researchers prone to seek simpler and environmental friendly decomposition process of lignocellulose biomass from OPEFB.

Ionic liquids (ILs) have become promising green solvents for breaking down OPEFB lignocellulose, offering an eco-friendly alternative to conventional methods. ILs can disrupt the strong bonds in lignocellulose, enhancing the extraction of cellulose, lignin, and hemicellulose. The higher selectivity of cationic and anionic structures of ionic liquid can enhance the extraction of lignin and hemicellulose for more cellulose accessibility from OPEFB lignocellulose since ILs have lower vapor pressure and are non-flammable [1].

Therefore, using ionic liquids (ILs) is suggested as an effective and cost-efficient green alternative for breaking down lignocellulose. This research focuses on synthesizing and characterizing ILs for decomposing lignocellulosic material from OPEFB. It examines the decomposition process, analyzes the properties of the products, and explores the optimum conditions, such as temperature and reaction time, to improve lignocellulose breakdown.

Importance of lignocellulose from OPEFB

The significant amount of waste produced from oil palm processing, particularly oil palm empty fruit bunches (OPEFB), holds potential for creating valuable new products. As a byproduct of palm oil milling, OPEFB is a fibrous material that could serve as a renewable biofuel alternative to fossil fuels [2]. Empty fruit bunches (EFB) in palm oil mills are abundant, fibrous materials of biological origin. These EFB fibers are strong, solid, and multicellular, featuring a central porous section called a lacuna. The fibers possess a polygonal cross-sectional shape, featuring a dense arrangement of cells that enclose a compact bundle or vascular packet. Empty fruit bunches (EFB) are devoid of chemical or mineral additives and may be free from foreign elements such as gravel, wood residues, nails, and other waste, contingent on the mill's handling practices [3].

OPEFB is primarily composed of cellulose $(C_6H_{10}O_5)_n$ (20-60% wt), hemicellulose $(C_5H_{10}O_5)_n$ (17-31% wt), and lignin $(C_{10}H_{11}O_{3.5})$ (18-50% wt) [1], with smaller amounts of organic compounds such as pectin and pigments [4]. This composition allows OPEFB to be an alternative resource for biofuel production, sugar extraction, and the creation of various bioconverted products [5]. As stated by Mohtar (2017), OPEFB lignocellulose, a crucial component of plant cell walls, is highly versatile for chemical modifications, making it valuable in industries such as food, pharmaceuticals, and medicine. Additionally, it can be used as a precursor for producing specialty chemicals, surfactants, herbicides, and solvents. Using alternative energy sources like this in internal combustion engines can reduce reliance on conventional fuels, significantly decreasing harmful emissions and contributing to the reduction of global energy and environmental issues [6].

Ionic liquid utilization in biomass decomposition

Using ILs to break down lignocellulosic biomass offers benefits over conventional methods by altering macromolecular structures, such as reducing cellulose crystallinity and extracting specific components like hemicellulose and lignin [7]. ILs also support various fractionation processes after pretreatment and can promote decrystallization by disrupting strong hydrogen bonds between cellulose fibers, which improves lignocellulose digestibility and increases surface area and porosity [8].

ILs' effectiveness in pretreating lignocellulosic biomass is linked to the basicity of the IL anion, which can weaken hydrogen bonds cross-link between hemicellulose, lignin, and cellulose [7]. The cationic and anionic parts of ionic liquids (ILs) help extract biopolymers from OPEFB lignocellulose [9]. Choosing specific cations and anions allows for tailoring ILs to better interact with biomass, improving the extraction process during lignocellulose breakdown. [10].

Decomposing OPEFB lignocellulose with ILs requires only a small amount of solvent, which is low in viscosity, recyclable, and reusable, while also shortening the processing time [9]. Compared to conventional methods, IL pretreatment is simpler, consumes less energy, and is more environmentally friendly [2]. ILs also helps to increase the surface area and reduce lignin content, making cellulose more accessible for hydrolysis, thereby promoting efficient decomposition [5].

While ionic liquids (ILs) are eco-friendly alternatives to traditional volatile solvents and can help reduce pollution, they can become more viscous during use [6]. This increased viscosity can lower their effectiveness by limiting their ability to penetrate lignocellulosic material, resulting in reduced yields of hemicellulose, cellulose, and lignin. Although some ILs can be costly, their recyclability allows them to perform almost as well as new ones [9]. However, some ILs are less effective for biomass decomposition due to their high cost, low thermal stability, poor humidity tolerance, and the need for low moisture during cellulose dissolution [11].

However, rather than to dissolve and pre-treat biomass, some ILs were found to be able to directly catalyze biomass conversion, mainly by hydrolyzing and processing the polysaccharides without any other catalyst [7]. Acidic ILs such as $[HSO_4]$- based ILs became an appealing option to be utilized in biomass pretreatment as the acidic properties selectively catalyze hemicellulose with a green and sustainable approach by allowing selective extraction of hemicellulose from processed biomass [7].

METHODOLOGY

Synthesis of IL [TEA][HSO_4]

The synthesis of [TEA][HSO_4] began by mixing 35 ml of triethylamine [TEA] with 25 ml of methanol in a round-bottom flask. Then, 125 ml of 2M sulfuric acid (98%) was slowly added to the flask while stirring it in an ice bath. Afterward, the flask was attached to a condenser for reflux, and the mixture was stirred at 70°C for 3 hours at 40 rpm to ensure the reaction was complete. The solution was then purified by washing it twice with 25 ml of diethyl ether and removing the solvent with a rotary evaporator at 55°C and 80 rpm. Finally, the [TEA][HSO_4] ionic liquid was analyzed using FTIR, NMR, and TGA techniques [11].

Decomposition of OPEFB lignocellulose in ionic liquids

Preparation of OPEFB biomass

In this study, the lignocellulosic biomass analyzed was oil palm empty fruit bunch (OPEFB) collected from Kg Banggol, Setiu, Terengganu. The raw material weighed between 3 and 5 kg. The OPEFB was first rinsed with tap water to remove dirt and sand, then cut into smaller pieces and dewaxed by soaking in acetonitrile overnight. Afterward, the OPEFB was filtered to remove the acetonitrile and washed with distilled water to eliminate any alcohol traces before being dried at 110°C for 16 hours. The dried OPEFB was then ground, shredded, and crushed in a high-speed mill to achieve a particle size of 0.4-1 µm [9], sieved to 250 µm, and stored in air-tight containers inside a desiccator for future use [4].

Decomposition of lignocellulose in ionic liquid

The sulfate-based OPEFB pretreatment process was conducted by examining two factors: temperature and mixing time. The ionic liquid (IL) used was triethylammonium sulfate [TEA][HSO4]. The temperatures tested were 30°C, 80°C, and 130°C, with mixing times of 2 hours and 5 hours. To perform the pretreatment, 27 ml of synthesized [TEA][HSO4] was mixed with 1 g of OPEFB pulp in a 250 ml beaker, using a ratio of 1:20 (OPEFB to IL). The mixture was stirred at 400 rpm for 2 hours while being heated to 30°C [11]. After treatment, the OPEFB was separated from the ILs using filter paper, rinsed with 25 ml of ethanol, and filtered using vacuum filtration. The filtrate was stored in glass vials, while the residue was dried in an oven at 80°C for 24 hours, cooled at room temperature for 20 minutes, and stored in an air-tight container for further analysis using FTIR, FESEM, and XRD.

RESULTS

Synthesis of triethylammonium sulfate [TEA][HSO_4]

The synthesis of triethylammonium sulfate [TEAS] was resulting ILs in yellowish color liquid. The yield of TEAS was approximately 71.2 % and the melting point is lower than 100°C.

Characterization of IL [TEA][HSO_4]

Fourier-transform infrared spectroscopy (FTIR)

The FTIR spectra for TEAS synthesis obtained with % transmittance plotted against wavenumbers (cm^{-1}) shows the peaks between 2660-2900 cm^{-1} are due to N-H stretching vibrations in TEAS, while CH bond stretching vibrations appear in the 3100-2900 cm^{-1} range [12]. In the FTIR spectrum of triethylamine, the CH bond stretching vibrations are found within this specific range. Additionally, during the synthesis of [TEA][HSO_4], a shift in the absorption peak occurs from 1400 (1453.73) cm^{-1} to 1500 (1477.25) cm^{-1}, indicating the CH_2 functional group, and from 1000 (1046.75) cm^{-1} to 1200 (1178.90) cm^{-1}, indicating the SO functional group. The absorption bands near 1250-1391 cm^{-1} are due to the vibration of CH_3 in the N-CH_2-CH_3 group of [TEA][HSO_4] [12].

Nuclear Magnetic Resonance (NMR)

^{1}H-NMR and ^{13}C-NMR analyses were conducted to confirm the CH_3CH_2- structure of the IL [TEA][HSO_4], indicating successful synthesis. In the ^{1}H-NMR spectrums, three distinctive peaks were observed. A small peak at 3.310 ppm was attributed to the reference solvent CD_3OD. A strong peak at 1.409 ppm corresponded to the nine protons in the CH_3 groups of $[TEA]^+$, showing a triplet pattern due to coupling with the CH_2 group. Another strong peak at 5.257 ppm was associated with the six protons in the CH_2 groups of $[TEA]^+$, expected to show a quadruplet but instead showed a single absorbance, possibly due to spin coupling effects. A small peak at 8.702 ppm indicated the proton attached to the nitrogen atom, confirming proton transfer from H_2SO_4 to TEA.

The ^{13}C-NMR spectrum also showed three distinct peaks. A small peak at 49.15 ppm was attributed to the reference solvent CD_3OD. A strong peak at 8.66 ppm was linked to the three methyl (CH_3) carbons in $[TEA]^+$. A prominent peak at 47.17 ppm corresponded to the three methylene (CH_2) carbons in the cation, with the downfield shift due to the electronegative effect of the nitrogen in CH_2-N, causing resonance in a higher energy region.

Thermogravimetric analysis (TGA)

The TGA analysis of IL [TEA][HSO_4] showed its thermal stability in relation to temperature and weight loss. The analysis started at 37 °C, and as the temperature increased to 150 °C, there was a significant drop in the weight, likely due to the evaporation of solvents like H_2O and ethanol. From 150 °C to 280 °C, the weight remained stable, indicating that the ionic liquid is thermally stable at high temperatures. This stability is beneficial for applications like biomass decomposition, where ILs is most effective at 150 °C to 170 °C [13]. However, the ionic liquid began to decompose when heated between 320 °C and 500 °C.

Decomposition of lignocellulosic from OPEFB in ionic liquid

The decomposition of lignocellulosic OPEFB was carried out on purpose to break down the recalcitrant structure for more accessible of cellulose. The IL [TEA][HSO_4] was chosen in this study for ionic liquid pretreatment. The structure of the cation and anion in an ionic liquid plays a significant role in determining the solvation chemistry, while the cation has a lesser effect [14]. Lignin, which contributes to hydrophobicity and structural rigidity, binds hemicelluloses to cellulose in the cell wall [15]. The OPEFB matrix dissolved in ionic liquids turns into a dark brown, thick, and sticky solution at 130 °C. The dark color comes from the removal of lignin and hemicellulose, which dissolve into the ionic liquid. Since lignin gives biomass its brown color, its removal affects both the color and thickness of the solution.

Characterization of treated and untreated OPEFB

Fourier-transform infrared spectroscopy (FTIR)

FTIR spectroscopy was used to study changes in the biomass surface during pretreatment to detect lignin deposition. Spectra of untreated OPEFB were compared with those of treated samples with IL[TEA][HSO_4] at different temperatures and mixing times.

The peak around 3300-3500 cm^{-1}, which indicates OH stretching, was reduced after treatment, suggesting that hydrogen bonds in cellulose were disrupted, making it more accessible to the reagent [2]. Peaks associated with aromatic C=C stretching (1500-1600 cm^{-1}) and alkyl-aryl C-O stretching (around 1250 cm^{-1}) showed that lignin content decreased with higher temperatures. The spectra for different temperatures and treatment times showed that at 30 °C, CO and OH stretching decreased slightly after 2 hours and more after 5 hours. Similar patterns were observed at 80 °C and 130 °C, with a slight increase in OH stretching transmittance after 5 hours at 130 °C compared to 2 hours.

Field emission scanning electron microscope (FESEM)

The FESEM images obtained depicting the morphology of treated and untreated lignocellulosic biomass. The images illustrate the changes resulting from the pretreatment process. Initially, the untreated pulps exhibit particles with a relatively high in fibrils, forming a thick and smooth surface to safeguard the enclosed cellulose [1]. A comparable images of raw OPEFB and treated OPEFB with IL [TEA][HSO_4] with 2000× magnification obtained via FESEM. The images highlight distinct variations in the morphology between the untreated OPEFB and the OPEFB subjected to IL-pretreatment, with variations in parameters including temperature and mixing

time. The differences proved the impact of the lignin disruption and cellulose crystallinity disruption during the pretreatment with ILs which interrupts the tissue system [5].

X-ray diffraction (XRD)

XRD profiles of biomass showed that untreated cellulose had peaks at around 16.6° and 22.2°, indicating its crystalline structure. Using these patterns, the Crystallinity Index (CrI) was calculated for untreated and pretreated OPEFB. For untreated OPEFB, the CrI was 35.61%. After 2 hours of pretreatment with IL at 30 °C, 80 °C, and 130 °C, the CrI values were 32.64%, 32.27%, and 34.85%, respectively. After 5 hours of pretreatment, the CrI dropped to 32.26% at 30 °C, 30.60% at 80 °C, and 18.39% at 130 °C. The OPEFB with 5-h pretreatment with ILs shows a significant decrease in CrI value from lower temperature 30 °C and 80 °C to higher temperature 130 °C.

DISCUSSION

In this research, the study aimed to synthesize green solvent Triethylammonium sulfate, [TEA][HSO_4] and explore the optimum condition of lignocellulosic decomposition evaluating two critical parameters: temperature and mixing time. This approach involved characterization of OPEFB lignocellulose through FTIR, FESEM and XRD.

According to FTIR analysis shows that as the temperature increases from 30°C to 130°C, there are noticeable changes in the OH stretching patterns. Higher temperatures seem to make lignin and hemicellulose more soluble in ionic liquids, which helps break down their structure and remove them more effectively [33]. The CO and OH stretching intensities decreased after 2 hours of pretreatment but became more noticeable after 5 hours at 80°C and 130°C. This suggests that longer exposure at higher temperatures affects the OH stretching bands. Overall, longer pretreatment times improve the dissolution of lignin and hemicellulose, which depends on how well the substance reacts with the ionic liquids [16].

FESEM analysis showed how the shape of the biomass changed before and after treatment. Pretreatment with IL made the biomass appear irregular, with a distorted surface and swollen structure, revealing more cellulose fibers [17]. As the temperature rose, the OPEFB structure degraded more, showing increased damage. At 30°C, OPEFB had noticeable pores, while untreated OPEFB was smooth. The most damage and open structure were seen at 130°C, indicating it is the best temperature for decomposition. Longer mixing times also affected the surface, with more peeling and deeper cracks after 5 hours compared to 2 hours. Longer pretreatment likely removes more lignin and weakens the cellulose layer.

XRD results showed that the Crystallinity Index (CrI) of the pretreated biomass changed slightly with different temperatures and mixing times, particularly after 5 hours. The CrI decreased in the treated OPEFB compared to the untreated sample, likely because removing lignin disrupted the cellulose structure. The ionic liquid (IL) helped extract crystalline components like hemicellulose and lignin, leading to peeling in the amorphous areas. However, OPEFB treated for 2 hours at 130°C had a slight increase in CrI, possibly due to the removal of amorphous regions which made the remaining cellulose more crystalline [34]. Higher temperatures and longer mixing times reduced the CrI because the IL caused the cellulose to swell, disrupting the plant cell walls and crystalline structure, turning the cellulose into an amorphous form [18].

CONCLUSION

In this study, we successfully synthesized and characterized the ionic liquid [TEA][HSO_4]. This liquid has triethylammonium as the cation and sulfate as the anion. We tested different temperatures and mixing times to find the best conditions for decomposing lignocellulose using ionic liquids. The ionic liquid had a 71.2% yield and was analyzed using FTIR, ^{1}H-NMR, ^{13}C-NMR, and TGA. FTIR confirmed the presence of functional groups, NMR provided details on chemical shifts, and TGA assessed thermal stability. The IL [TEA][HSO4] was stable from 150°C to 320°C and started to decompose above 500°C, making it suitable for high-temperature decomposition processes. The results showed that using high temperatures and longer mixing times, such as a 5-hour treatment at 130°C, improved the decomposition of lignocellulosic materials. This approach effectively removes lignin, disrupts the cell wall structure, and makes cellulose more accessible for further processing. Ionic liquids like [TEA][HSO_4] are effective and environmentally friendly solvents for this purpose.

ACKNOWLEDGEMENT

This study is supported by Universiti Sains Islam Malaysia grant.

REFERENCES

[1] Mohtar, S. S., Busu, T. N. Z. T. M., Noor, A. F. M., Shaari, N., & Mat, H. (2017). An ionic liquid treatment and fractionation of cellulose, hemicellulose and lignin from oil palm empty fruit bunch. *Carbohydrate Polymers*, *166*, 291–299. https://doi.org/10.1016/j.carbpol.2017.02.102

[2] Mudzakir, A., Rizky, K. M., Munawaroh, H. S. H., & Puspitasari, D. (2022). Oil palm empty fruit bunch waste pretreatment with benzotriazolium-based ionic liquids for cellulose conversion to glucose: Experiments with computational bibliometric analysis. *Indonesian Journal of Science and Technology*, *7*(2), 291-310.

[3] Jafri, N. J. S., Jimat, D. N., Azmin, N. F. M., Sulaiman, S., & Nor, Y. A. (2021). The potential of biomass waste in Malaysian palm oil industry: A case study of Boustead Plantation Berhad. *IOP Conference Series: Materials Science and Engineering*, *1192*(1), 012028. https://doi.org/10.1088/1757-899x/1192/1/012028

[4] Ngadi, N., & Lani, N. S. (2014). Extraction and Characterization of Cellulose from Empty Fruit Bunch (EFB) Fiber. *Jurnal Teknologi*, *68*(5). https://doi.org/10.11113/jt.v68.3028

[5] Elgharbawy, A. A., Alam, M. Z., Moniruzzaman, M., Kabbashi, N. A., & Jamal, P. (2018). Chemical and structural changes of pretreated empty fruit bunch (EFB) in ionic liquid-cellulase compatible system for fermentability to bioethanol. *3 Biotech*, *8*(5). https://doi.org/10.1007/s13205-018-1253-8

[6] Díaz-González, A., Luna, M. Y. P., Morales, E., Saldaña-Trinidad, S., Blanco, L. T. G., De La Cruz-Arreola, S., Pérez-Sariñana, B. Y., & Robles-Ocampo, J. B. (2022). Assessment of the Pretreatments and Bioconversion of Lignocellulosic Biomass Recovered from the Husk of the Cocoa Pod. Energies, 15(10), 3544. https://doi.org/10.3390/en15103544

[7] Carvalho, A. M., Costa, M. C., & Bogel-Łukasik, R. (2015). Relevance of the acidic 1-butyl-3-methylimidazolium hydrogen sulphate ionic liquid in the selective catalysis of the biomass hemicellulose fraction. *RSC Advances*, *5*(58), 47153–47164. https://doi.org/10.1039/c5ra07159c

[8] Diyanilla, R., Hamidon, T. S., Suryanegara, L., & Hussin, M. W. (2020). Overview of pretreatment methods employed on oil palm biomass in producing value-added products: A review. Bioresources, 15(4), 9935–9997. https://doi.org/10.15376/biores.15.4.diyanilla

[9] Sidik, D. a. B., Ngadi, N., & Amin, N. a. S. (2013). Optimization of lignin production from empty fruit bunch via liquefaction with ionic liquid. *Bioresource Technology*, *135*, 690–696. https://doi.org/10.1016/j.biortech.2012.09.041

[10] Tu, W., Weigand, L., Hummel, M., Sixta, H., Brandt, A., & Hallett, J. P. (2020). Characterisation of cellulose pulps isolated from Miscanthus using a low-cost acidic ionic liquid. *Cellulose*, *27*(8), 4745–4761. https://doi.org/10.1007/s10570-020-03073-1

[11] Nurdin, M., Abimanyu, H., Putriani, H. N., Setiawan, L. O. M. I., Maulidiyah, M., Wibowo, D., Ansharullah, A., Natsir, M. F., Salim, L. O. A., Arham, Z., & Mustapa, F. (2021). Optimization of OPEFB lignocellulose transformation process through ionic liquid [TEA][HSO4] based pretreatment. *Scientific Reports*, *11*(1). https://doi.org/10.1038/s41598-021-90891-3

[12] Khan, J., Muhammad, S., Shah, L. A., Ali, J., Ibrar, M., & Rehman, K. U. (2020). Synthesis, characterization and electrochemistry of triethyl ammonium sulphate ionic liquid. *Zeitschrift Für Physikalische Chemie*, *235*(9), 1099–1111. https://doi.org/10.1515/zpch-2020-1704

[13] Zahari, S. M. S. N. S., Azman, H. H., & Karim, L. (2018). Triethylammonium hydrogen sulfate ionic liquid as a low-cost solvent: A short review of synthesis, analysis and applications. *MATEC Web of Conferences*, *204*, 00006. https://doi.org/10.1051/matecconf/201820400006

[14] [14] Brandt, A., Gschwend, F. J. V., Fennell, P. S., Lammens, T. M., Tan, B., Weale, J., & Hallett, J. P. (2017). An economically viable ionic liquid for the fractionation of lignocellulosic biomass. *Green Chemistry*, *19*(13), 3078–3102. https://doi.org/10.1039/c7gc00705a

[15] [15] Zoghlami, A., & Paës, G. (2019). Lignocellulosic Biomass: Understanding Recalcitrance and Predicting Hydrolysis. *Frontiers in Chemistry*, *7*. https://doi.org/10.3389/fchem.2019.00874

[16] [16] Mansor, K. N., Halim, M. A., Ali, N., Rahman, W. Z. W. A., & Abdullah, S. (2019). Integrating ILS in dissolving palm fruit cellulose. *IOP Conference Series: Materials Science and Engineering*. https://doi.org/10.1088/1757-899x/702/1/012013

[17] [17] Singh, S. K., & Savoy, A. W. (2020). Ionic liquids synthesis and applications: An overview. *Journal of Molecular Liquids*, *297*, 112038. https://doi.org/10.1016/j.molliq.2019.112038

[18] Zhang, J., Wang, Y., Zhang, L., Zhang, R., Liu, G., & Cheng, G. (2014). Understanding changes in cellulose crystalline structure of lignocellulosic biomass during ionic liquid pretreatment by XRD. *Bioresource Technology*, *151*, 402–405. https://doi.org/10.1016/j.biortech.2013.10.009

LIQUID CHROMATOGRAPHY-MASS SPECTROMETRY (LC-MS) PROFILING OF *PHYSALİS ANGULATA* ETHANOLIC EXTRACT

Nurul Elisa Abd Samad[1,2], Salfarina Ramli[1,2], Michael Vin[3], Hannis Fadzillah Mohsin[2], Hasseri Halim[1,2], Donna Maretta Ariestanti[3], Richard Johari James[1,2]

[1] *Integrative Pharmacogenomics Institute, Universiti Teknologi MARA Cawangan Selangor, Puncak Alam, Selangor, MALAYSIA*

[2] *Faculty of Pharmacy, Universiti Teknologi MARA Cawangan Selangor, Puncak Alam, Selangor, MALAYSIA*

[3] *Faculty of Pharmacy, Universitas Indonesia, Depok, West Java, Indonesia*

**richard@uitm.edu.my*

ABSTRACT

Physalis angulata, known as cutleaf groundcherry or wild gooseberry, is a medicinal plant recognized for its health benefits due to its high concentration of bioactive compounds with pharmacological properties. Despite the recognized health benefits and traditional medicinal uses of Physalis angulata, there is limited scientific data on the bioactive compounds responsible for its pharmacological characteristics. Therefore, this research aims to identify compounds present in Physalis angulata ethanolic leaves extract. Liquid chromatography-Mass Spectrometry (LC-MS) Q-TOF analysis in positive ionization mode was carried out to profile the compounds in Physalis angulata ethanolic leaves extract. The identification of the compounds was done based on in-house database library and literature comparison. One compound from the flavonoid class and three compounds from the withanolide class were tentatively identified. Previous findings have shown that these compounds may contribute to anti-inflammatory, antioxidant, neuroprotective and anticancer effects of Physalis angulata extract. In summary, four compounds with bioactive properties were identified from the LC-MS profiling. Further research is needed to confirm the identified compounds.

***Keywords*:** *Physalis angulata*, LC-MS, Q-TOF, profiling.

INTRODUCTION

Plant extract profiling involves analytical techniques to characterise the complex composition of extracts. Liquid chromatography-mass spectrometry (LC-MS) has become a crucial method in phytochemical profiling due to its ability to identify and quantify compounds at trace levels (Jaberi et al., 2024). One of the most advanced hybrid mass spectrometer designs is the quadrupole time-of-flight (Q-TOF), which combines a TOF and a quadrupole instrument. This combination provides exact mass measurement for both precursor and product ions, as well as the ability to undertake fragmentation experiments (Taamalli et. al., 2015).

Physalis angulata belongs to the *Physalis* genus within the Solanaceae family, which includes over 120 species predominantly found in South and North America, with some species also occurring in Europe, Southeastern, and Central Asia (Tuan et al., 2020). The *Physalis* genus is commercially valuable not only as a food source but also for its abundant bioactive compounds (Sharma et al., 2015). However, there is limited scientific data on the bioactive compounds responsible for its pharmacological characteristics. Therefore, this study aims to identify the compounds in *Physalis angulata* ethanolic leaves extract using LC-MS Q-TOF. The findings could provide a foundation for further research into the therapeutic potential of this species.

MATERIALS AND METHODS

Sample extraction

The leaves of *Physalis angulata* were collected from Etalase Herbal in Bogor Regency, West Java, Indonesia. The leaves were thoroughly cleaned to remove any impurities. They were then dried in a drying cabinet set at 40°C for 5 days to ensure complete dehydration. The dried leaves were ground into a fine powder using a blender, and the powder was sieved and dissolved in ethanol with a solid-to-solvent ratio of 1:10. This mixture was sonicated using an ultrasonic bath at room temperature approximately 25°C for 1 hour. The resulting solution was then filtered through Whatman No. 1 filter paper to separate the plant debris, leaving an ethanolic filtrate containing the extracted compounds. The filtrate was concentrated using a rotary evaporator at 40°C until the

volume was significantly reduced. The concentrated extract was then further dried in a water bath at the same temperature to remove any remaining solvent, resulting in a semi-solid extract. The final semi-solid extract was stored in a 4°C refrigerator until further use.

Profiling of Physalis Angulata

The sample was reconstituted in ethanol and filtered using nonsterile hydrophobic PTFE Syringe Filters (0.22µm pore size). A total of 2 µg of sample was injected into the LC-MS Q-TOF (Agilent Technologies 6520, Santa Clara, CA, USA). Chromatographic separation was carried out using a ZORBAX Eclipse Plus C18 column (1.8 microns, 2.1 mm x 100 mm) from Agilent Technologies, SA, USA, which was maintained at 40°C in a column oven. The system operated at a flow rate of 0.25 mL/min, with mobile phase A consisting of 0.1% formic acid in water, and mobile phase B consisting of 0.1% formic acid in acetonitrile. The gradient was programmed to transition from 5% to 95% mobile phase B over 18 minutes, followed by a change from 95% to 5% over 12 minutes. Data were collected in positive electrospray ionization (ESI) mode. To ensure mass accuracy, continuous internal calibration was conducted during the analysis, using reference masses of m/z 121.0529 and m/z 922.0098.

Data analysis

The raw mass spectrometry (MS) data were processed and analyzed using Agilent Mass Hunter Qualitative Analysis (software version B.05.00) to convert .d files into .CEF files. The compounds were then identified by in-house database library (Personal Compound Database Library) and comparison with literature.

RESULTS AND DISCUSSION

The total ion chromatogram of the *Physalis angulata* leaves extract is presented in Figure 1. It represents the sum of all ion intensities detected at each time point throughout the 30-minute LC-MS run. The list of compounds detected between 9- to 18-minute is shown in Table 1. Nine compounds were detected using the in-house database library. However, compounds labeled as ND were those that the database could not identify.

In this analysis, a molecular ion $[M+H]^+$ of 611.1608 was detected and tentatively identified as robinetin 3-rutinoside according to the in-house database library. This finding was in accordance with fragment ion reported Rahim et al. (2022). Physalin E (*m/z* 545.2016) and physalin A (*m/z* 527.1912) were detected in this analysis, both of which were previously reported by Da Silva et al. (2015). A *m/z* of 511.1967 was identified as 25,27-dihydro-4,7-didehydro-7-deoxyphysalin A based on the in-house library. However, the fragment ion was not yet reported in literature.

Robinetin 3-rutinoside is a flavonoid that is known for its antioxidant properties that help to protect cells from oxidative stress and damage caused by free radicals (Sunday & Adeyemi, 2023). In addition, this LC/MS profiling of *Physalis angulata* leaves extract revealed the presence of withanolides including physalin E, physalin A, and 25,27-dihydro-4,7-didehydro-7-deoxyphysalin A, all of which are recognized for their anti-inflammatory effects and other health-promoting properties, such as immunomodulatory and anticancer activities (Novitasari et. al. 2024; Daltro et al., 2020).

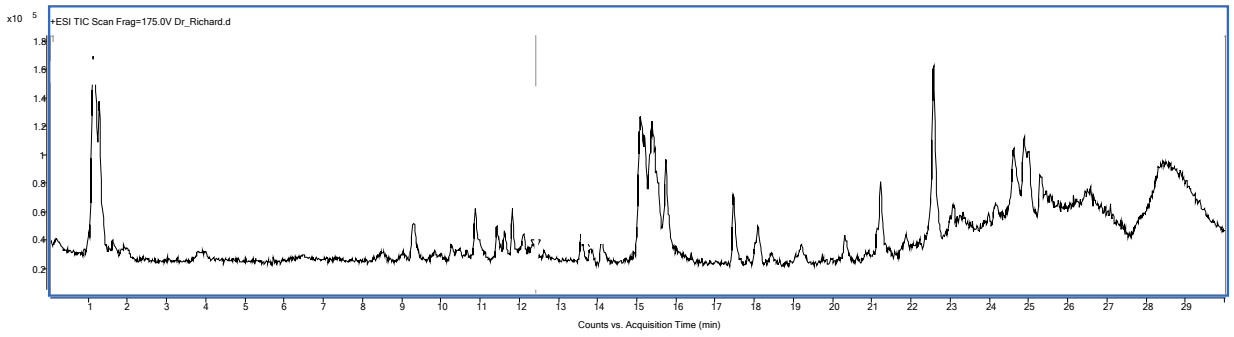

Figure 1. Total ion chromatogram of *Physalis angulata* ethanolic leaves extract.

Table 1. List of compounds identified from minute 9 to 18 of the LC-MS run.

RT (min) (library)	Compound name (library)	*m/z* (library)	Compound name (literature)	*m/z* (literature)
9.317	ND	215.1758	-	-
10.276	Robinetin 3-rutinoside	611.1608	Robinetin 3-rutinoside (Rahim et. al., 2022)	611.16 -
10.891	ND	328.2593	-	-
11.439	ND	679.5114	-	-
11.633	ND	441.3436	-	-
11.831	ND	396.8018	-	
13.582	Physalin E	545.2016	Physalin E (Da Silva et. al., 2015)	545.2023
15.748	Physalin A	527.1912	Physalin A (Da Silva et. al., 2015)	527.1917
17.477	25,27-Dihydro-4,7-didehydro-7-deoxyphysalin A	511.1967	-	-

CONCLUSION AND RECOMMENDATION

In conclusion, this LC-MS analysis of *Physalis angulata* leave extract has revealed four compounds from the group of flavonoids and withanolides. Further research is needed to properly confirm the identification of these compounds.

ACKNOWLEDGEMENT

Authors acknowledge the Ministry of Higher Education (MOHE) for funding under the Fundamental Research Grant Scheme (FRGS) (FRGS/1/2022/SKK05/UITM/02/3).

REFERENCES

Da Silva, R. R. P., Da Silva, B. J. M., Rodrigues, A. P. D., Farias, L. H. S., Da Silva, M. N., Alves, D. T. V., Bastos, G. N. T., Nascimento, J. L. M. D., & Silva, E. O. (2015). In vitro biological action of aqueous extract from roots of *Physalis angulata* against Leishmania (Leishmania) amazonensis. *BMC Complementary and Alternative Medicine*, *15*(1). https://doi.org/10.1186/s12906-015-0717-1

Daltro, S. R. T., Santos, I. P., Barros, P. L., Moreira, D. R. M., Tomassini, T. C. B., Ribeiro, I. M., Santos, R. R. D., Meira, C. S., & Soares, M. B. P. (2020). In vitro and In Vivo Immunomodulatory Activity of *Physalis angulata* Concentrated Ethanolic Extract. *Planta Medica*, *87*(01/02), 160–168. https://doi.org/10.1055/a-1237-4268

Iwansyah, A. C., Luthfiyanti, R., Ardiansyah, R. C. E., Rahman, N., Andriana, Y., & Hamid, H. A. (2022). Antidiabetic activity of *Physalis angulata L*. fruit juice on streptozotocin-induced diabetic rats. *South African Journal of Botany*, *145*, 313–319. https://doi.org/10.1016/j.sajb.2021.08.045

Jaberi, F. M. A., Alhawarri, M. B., Dewa, A., Zainal, Z., & Zakaria, F. (2024). Anti-obesity, Phytochemical Profiling and Acute Toxicity Study of Ethanolic Extract of Saffron *(Crocus sativus L.*). *Pharmacological Research - Modern Chinese Medicine*, *11*, 100420. https://doi.org/10.1016/j.prmcm.2024.100420

Nabavi, S. F., Nabavi, S. M., Sureda, A., Van Dongen, M., Daglia, M., & Devi, K. P. (2015). "Flavonoids: Antioxidant compounds with cytoprotective properties." *Asian Pacific Journal of Tropical Biomedicine*, 5(10), 805-814.

Novitasari, A., Rohmawaty, E., & Rosdianto, A. M. (2024). *Physalis angulata Linn*. as a medicinal plant (Review). Biomedical reports, 20(3), 47. https://doi.org/10.3892/br.2024.1735

Pan, Y., Wang, K., Huang, S., Wang, H., Mu, X., He, C., & Ji, X. (2011). "Antioxidant activity of microwave-assisted extract of longan (*Dimocarpus* longan Lour.) peel." Food Chemistry, 127(1), 214-220.

Rahim, N. A., Roslan, M. N. F., Muhamad, M., & Seeni, A. (2022). Antioxidant Activity, Total Phenolic and Flavonoid Content and LC–MS Profiling of Leaves Extracts of *Alstonia angustiloba*. *Separations*, *9*(9), 234. https://doi.org/10.3390/separations9090234

Sharma, N., Bano, A., Dhaliwal, H. S., & Sharma, V. (2015). A Pharmagological Comprehensive Review On 'Rassbhary' *Physalis angulata* (L.). *International Journal of Pharmacy and Pharmaceutical Sciences*, *8*(8), 30–34. https://innovareacademics.in/journals/index.php/ijpps/article/view/6657/6890

Sunday, R. M., & Adeyemi, O. I. (2023). Effect of *Physalis angulata L*. Leaves on Free Radicals: Antioxidant Study. *Trends in Medical Research*, *18*(1), 179–186. https://doi.org/10.3923/tmr.2023.179.186

Taamalli, A., Arráez-Román, D., Abaza, L., Iswaldi, I., Fernández-Gutiérrez, A., Zarrouk, M., & Segura-Carretero, A. (2015). LC-MS-based metabolite profiling of methanolic extracts from the medicinal and aromatic species *Mentha pulegium* and *Origanum majorana*. *Phytochemical Analysis*, *26*(5), 320–330. https://doi.org/10.1002/pca.2566

Tuan Anh, H. L., Le Ba, V., Do, T. T., Phan, V. K., Pham Thi, H. Y., Bach, L. G., Kim, Y. H. (2020). Bioactive compounds from *Physalis angulata* and their anti-inflammatory and cytotoxic activities. Journal of Asian Natural Products Research, 1–9. doi:10.1080/10286020.2020.1825390

Wu, J., Zhao, J., Zhang, T., Gu, Y., Khan, I. A., Zou, Z., & Xu, Q. (2021). Naturally occurring physalins from the genus Physalis: A review. *Phytochemistry*, *191*, 112925. https://doi.org/10.1016/j.phytochem.2021.112925

Wu, J., Zhao, J., Zhang, T., Gu, Y., Khan, I. A., Zou, Z., & Xu, Q. (2021b). Naturally occurring physalins from the genus Physalis: A review. *Phytochemistry*, *191*, 112925. https://doi.org/10.1016/j.phytochem.2021.112925

Xiao, J. F., Zhou, B., & Ressom, H. W. (2012). Metabolite identification and quantitation in LC-MS/MS-based metabolomics. Trends in analytical chemistry: TRAC, 32, 1–14. https://doi.org/10.1016/j.trac.2011.08.009

STUDIES OF MORPHOLOGY AND VIABILITY OF CANCER CELLS SPHEROID WITH ESSENTIAL OIL FROM *PIPER SARMENTOSUM*

Munira Shahbuddin[1], Firdaus Abdul Wahab[1], Bassam Jawahir[1] and Jahan Nazreen Yakath Ali[1]

[1]*Department of Chemical Engineering and Sustainability, Kulliyyah of Engineering,*

International Islamic University of Malaysia, 53100 Kuala Lumpur.

munirashah@iium.edu.my

ABSTRACT

Skin cancer victims have been increasing each year due to an increase in exposure to ultraviolet rays which increases the need for cancer research, The objectives of this project were to determine the optimal initial cell concentration and volume of cells for producing spheroid cells, to identify the suitable cell suspension media for producing spheroid cells and to study the effect of essential oil (EO) from *Piper sarmentosum* on spheroid cells' viability and morphology. The hanging drop method was used to form the spheroid. The spheroid cell viability and morphology were analyzed using MTT assay and ImageJ software. The morphology of melanoma and non-melanoma skin cancer show changes where the spheroid cells' spherical shape were broken, indicating disruption in cell-cell adhesion of spheroids however there were no changes for normal human fibroblast cell. The results showed that the MTT assay did not have any effect on all spheroids, indicating the presence of protective layers that prevent MTT reagent penetration however addition of EO from *Piper sarmentosum* increased the absorbance of MTT when given to spheroids in increasing dosage from 5 to 50 µl. All spheroids that were treated with 50 µl of essential oil gave the highest MTT absorbance reading. In conclusion, the effect of essential oil from *Piper sarmentosum* on spheroid cells can be used for further research on creating natural anti-cancer drugs.

***Keywords*:** spheroids, melanoma, non melanoma, essential oil and Piper sarmentosum

INTRODUCTION

Cancer is a disease where some of the body cells undergo mutation at a cellular level and grow uncontrollably. A normal cell will stop dividing at a certain point of growth and then die. However, a gene mutation causes the normal cell to stray away from its normal life cycle, keep on dividing and spread to other body parts. The cancerous cells can disrupt normal organ function because they are immature and cannot perform their specific function, disrupting oxygen and nutrient distribution to the normal cells and causing normal cells to die. If most of the normal cells that can perform their specific jobs die and only cancer cells that cannot their job remain, organ failure happens causing severe side effects for the cancer patient (Saini et al., 2020). Cancer victims have been increasing gradually each year with over 1 million cases estimated and over 600 thousand deaths estimated over the year 2020 (Siegel et al., 2020). Especially in skin cancer where one in every three cancer cases diagnosed is a form of skin cancer (Jeong et al., 2021). Melanoma also known as malignant melanoma is a rare type of skin cancer that is known for its high mortality rate, aggressiveness and persistence. The main cause of mutation that leads to melanoma skin cancer is overexposure to ultraviolet light or rays that mainly come from the sunlight. Opposite to melanoma skin cancer, non-melanoma skin cancer is more commonly diagnosed among cancer patients. The major difference between melanoma and non-melanoma skin cancer is that non-melanoma is a non-spreading skin cancer or has a very low chance of spreading to other body parts.

Anti-cancer drugs that only affect the cancerous cells need to be studied and developed such as using herbs. In this study, *Piper sarmentosum* is used in the form of essential oil to treat normal and cancer skin cells specifically fibroblast (HFF1), melanoma (A375) and non-melanoma (A431) cells. *Piper sarmentosum* is known for its medicinal effects such as anti-hypertension, anti-cancer and anti-diabetes due to its antioxidant characteristics (Ugusman, 2018). The main compounds of *Piper sarmentosum* that have anti-cancer properties are phytochemicals and amide alkaloids. Spheroid cancer cells are formed to be treated using essential oil extracted from *Piper sarmentosum*. Spheroid cells are formed because the 3D cell can mimic accurately the cancer cell structure, natural physiology, the resistance of cancer cells toward therapeutic strategies and the interactions among cells (Habanjar et al., 2021). A more accurate method can help produce accurate data at the end of this research.

MATERIALS AND METHODS

Cell Culture

Media Preparation (10% FBS)

45 ml of Dulbecco's Modified Eagles's Medium (DMEM) mixed with 5 ml Fetal Bovine Serum (FBS) (10% w/v) to make a total volume of 50 ml. The medium was stored in a refrigerator at 4°C. The needed amount for each subculture was transferred to a new bottle every time a subculture was done. The new bottle was heated in a water bath at 37°C before used.

Subculturing Monolayer Cells In T-Flask

Spent media was discarded from the 70 % confluent 75 cm2 T-flask into the waste beaker. T-flask was washed with 5 ml of Phosphate Buffer Saline (PBS) and discarded into a waste beaker. 1.5 ml of 0.025% trypsin was pipetted onto the monolayer cells and the flask was placed in a CO2 incubator for 10 minutes to detach the cells. 10 ml of fresh media was added to the flask. All contents of the flask consisting of cells, trypsin and media were transferred to a 15 ml centrifuge tube. The tube was centrifuged at 800 rpm for 5 minutes. The supernatant was discarded and cells resuspended in 10 ml of fresh medium. 1 ml of tube content and 14 ml of fresh media added into a new 75 cm2 T-flask. The flask was kept in the incubator for cell growth and the remaining 9 ml of cell solution in the centrifuge tube was used for spheroid formation.

Spheroid Formation

Spheroid cells with a concentration of 505,000 cell/ml, 815,000 cell/ml and 1,000,000 cell/ml for A375, A431 and HFF1 respectively was produced using the hanging drop method. The lids of each petri dish were removed and placed in a way the opening facing up. 50 µl of cell solution were pipetted from each cell and multiple doplets added onto the lids of each petri dish. 5 ml of PBS was added onto the bottom plate to create a hydration chamber to prevent the drying of cell solution media. The lids were flipped carefully to maintain the droplets' shape and the petri dishes were sealed with parafilm. Petri dishes were kept in an incubator for 7 days for production of compact spheroid cells.

Piper sarmentosum's Essential Oil Treatment

Transfer Spheroid Cells

The spheroids were formed on petri dish lids using the optimal initial cell concentration, volume of cell and suitable media as determined in previous experiments. After 7 days, the spheroids were transferred from petri dish lids into 96 well plate.

Essential Oil Addition

The media in each well plate were removed carefully without disrupting the spheroids. The essential oil from *Piper sarmentosum* was added into each well with increasing volume vertically from row B to F where no essential oil was added into the wells. The essential oil was diluted with a dilution factor of 2 using culture media. The well plate was sealed with parafilm and observed under a microscope for morphology analysis. Then, the well plate was kept in the incubator for 24 hours.

Morphology Observation & MTT Assay

After 24 hours, the well plate was observed under the microscope to record changes in morphology. Then MTT assay was done to analyse cell viability. The media was removed and 150 µl 5 µg/ml MTT reagent was added. The well plate was incubated for 4 hours. After 4 hours, media in all wells were removed and 100 µl Dimethyl sulfoxide was added into all wells from row B to row G. The plate was incubated for 10 minutes and the optical density reading at 570 nm was recorded.

RESULTS AND DISCUSSION

Results and discussion of the experiment to study the effect of essential oil from Piper sarmentosum on spheroid cells viability and morphology are shown below. This experiment also was done using three different types of cells such as melanoma skin cancer cell denoted as A375, non-melanoma skin cancer cell denoted as A431 and normal human fibroblast cell denoted as HFF1

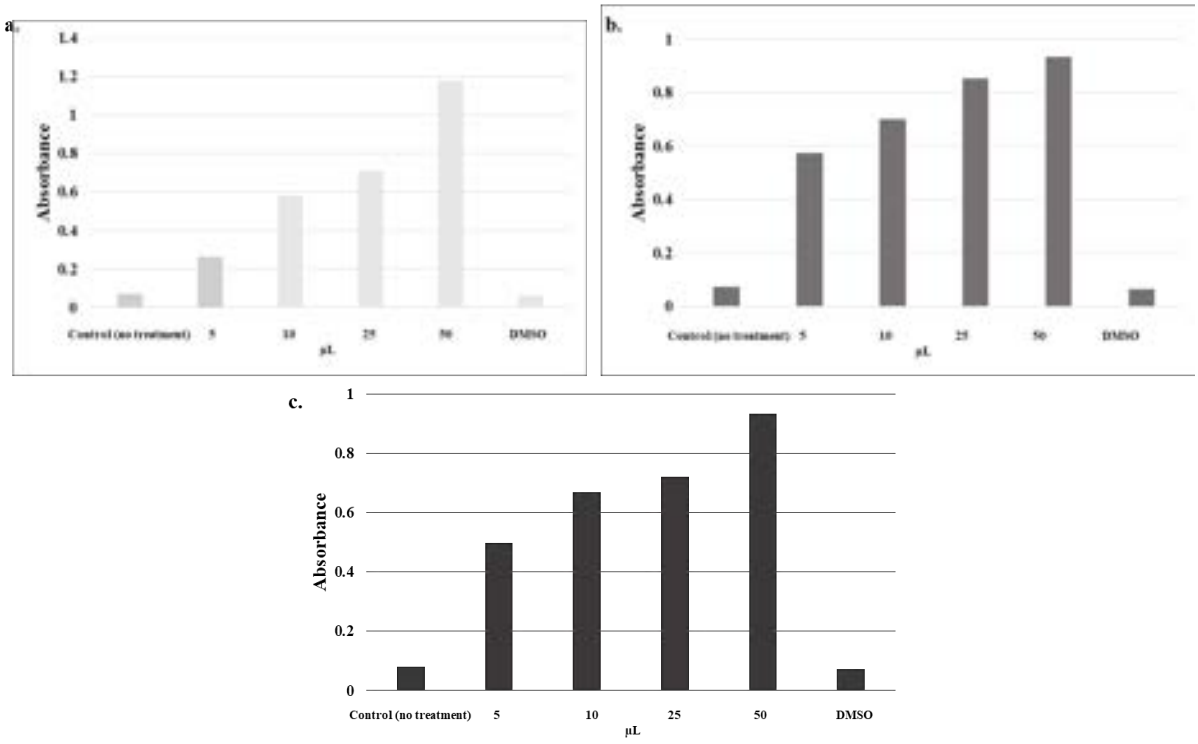

Figure 1. The effects of EO from *Piper sarmentosum* at varying concentrations onto the viability of a. melanoma b. non melanoma and c. human dermal fibroblast spheroids me asured by MTT assay

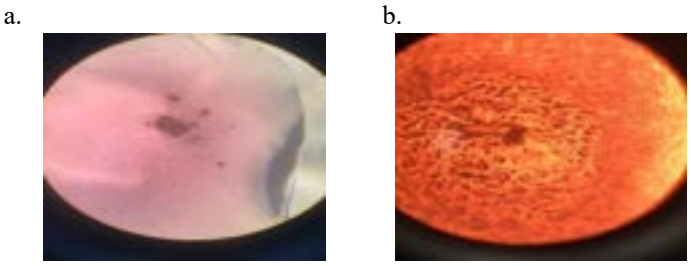

Figure 2. Microphotographs of melanoma cells (A431) a. before and b. after the treatment with 50 µL essential oil from *Piper sarmentosum*

Figure 1 shows the effects of EO from *Piper sarmentosum* at varying concentrations onto the viability of melanoma, non melanoma and human dermal fibroblast spheroids measured by MTT assay. From the result, the spheroids which were not treated with EOs did not give any reading for the MTT absorbance but not the spheroids treated with EOs. For negative control, we treated the spheroids with DMSO and could not get the MTT absorbance from the reading as well. Our observation onto these spheroid (result not disclosed) found that addition of MTT and DMSO did not break up the aggregation nor affecting the morphology of the spheroids. However, the value of MTT absorbance increased with the increase treatment of EOs for normal cells as well as both A431 and A471. This shows that EOs did not have cytotoxicity effect onto these cells and helped MTT assay to penetrate into the cell membrane to get into the mitochondria for staining. This result also proved that spheroids have protective mechanism to hinder chemicals or drugs from entering the cells which is interesting and yet to be discovered.

Spheroids are formed when cells attach using protein-based cell adhesion molecules such as integrins, cadherins, selectins and immunoglobulins. These cell adhesion molecules on the cell surface enabled the cells to gather in one place to attach and form a compact spheroid with a tight junction between each other (Janiszewska

et al., 2020). However, components in *Piper sarmentosum*'s essential oil have an effect on the cell adhesion molecules where it can reduce the effectiveness and amount of cell adhesion molecules by damaging and inhibiting the protein-based cell adhesion expression (Ekeuku et al., 2021). These explain the changes in A375 and A431 spheroids' morphology (Figure 2) after being exposed to *Piper sarmentosum*'s essential oil for 24 hours. The components in the essential oil damage the cell adhesion molecules and cause the spheroid to become loose and the cells were separated from each other. The higher volume of EO caused larger changes in spheroids morphology.

Hence, it can be concluded that EO from *Piper sarmentosum* affects the A375 and A431 spheroid cell morphology by breaking down the spherical shape of a spheroid through damaging cell adhesion molecule functions.

CONCLUSION

In conclusion, by carrying out the methodology, the objectives of this project were successfully achieved. There are morphology changes in A375 and A431 spheroids that were treated with essential oil from *Piper sarmentosum* where the spheroid cells' spherical shape is broken whereas no morphology changes in HFF1 spheroids. The viability effect of A375, A431 and HFF1 cannot be determined using MTT assay due to repelling effect and protective barrier of the spheroid cell but the spheroids treated with *Piper sarmentosum*'s essential oil show increasing absorbance of purple formazan with the increasing volume of essential oil because component in the essential oil increase cell permeability and reduce mitochondrial membrane potential. Hence, it can be concluded that *Piper sarmentosum*'s essential oil has more effect on cancerous cells than normal cells. Further research of this project with more suitable viability methods and changes in the form of essential oil used for treatment can help in creating an effective anti-cancer drug from natural herbs and depend less on chemical anti-cancer drugs

REFERENCES

Ekeuku, S. O., Azlina, M. F. N., & Chin, K. Y. (2021). Effects of piper sarmentosum on metabolic syndrome and its related complications: A review of preclinical evidence. In *Applied Sciences (Switzerland)* (Vol. 11, Issue 21). MDPI. https://doi.org/10.3390/app11219860

Habanjar, O., Diab-Assaf, M., Caldefie-Chezet, F., & Delort, L. (2021). 3D Cell Culture Systems: Tumor Application, Advantages, and Disadvantages. *International Journal of Molecular Sciences 2021, Vol. 22, Page 12200*, *22*(22), 12200. https://doi.org/10.3390/IJMS222212200

Hamil, M. S. R., Zakaria, F., Chong Yew, L., Pauzi, N., Mohd, K. S., & Saidan, N. H. (2023). Phenolics-Enhancing Piper sarmentosum (Roxburgh) Extracts Pre-Treated with Supercritical Carbon Dioxide and its Correlation with Cytotoxicity and α-Glucosidase Inhibitory Activities. *Pertanika Journal of Science and Technology*, *32*(1). https://doi.org/10.47836/pjst.32.1.18

Janiszewska, M., Primi, M. C., & Izard, T. (2020). Cell adhesion in cancer: Beyond the migration of single cells. *Journal of Biological Chemistry*, *295*(8), 2495–2505. https://doi.org/10.1074/jbc.REV119.007759

Jeong, W. Y., Kwon, M., Choi, H. E., & Kim, K. S. (2021). Recent advances in transdermal drug delivery systems: a review. *Biomaterials Research*, *25*(1), 1–15. https://doi.org/10.1186/S40824-021-00226-6/FIGURES/6

Kumar, P., Nagarajan, A., & Uchil, P. D. (2018). Analysis of cell viability by the MTT assay. *Cold Spring Harbor Protocols*, *2018*(6), 469–471. https://doi.org/10.1101/pdb.prot095505

Saini, A., Kumar, M., Bhatt, S., Saini, V., & Malik, A. (2020). CANCER CAUSES AND TREATMENTS. *International Journal of Pharmaceutical Sciences and Research*, *11*(7), 3121. https://doi.org/10.13040/IJPSR.0975-8232.11(7).3121-34

Siegel, R. L., Miller, K. D., & Jemal, A. (2020). Cancer statistics, 2020. *CA: A Cancer Journal for Clinicians*, *70*(1), 7–30. https://doi.org/10.3322/caac.2159

MONITORING THE API CONTENT OF AVONAC®, VOLTAREN®, DICLOTROY® AND DYFENAC® AVAILABLE IN LOCAL MARKET

Rossuriati Dol Hamid[1], Muhammad Zulhanif Noor Izhar[2]

[1,2]*Faculty of Applied Sciences, Universiti Teknologi MARA, 40450, Shah Alam, Malaysia*

[1] *rossuriati2996@uitm.edu.my*

ABSTRACT

This study focuses on the determination of active pharmaceutical ingredient (API) content of diclofenac sodium from four brands (Avonac®, Voltaren®, Diclotroy® and Dyfenac®) of the tablet drug. Diclofenac sodium, a non-steroidal anti-inflammatory drug (NSAID), is commonly used for its analgesic, anti-inflammatory, and antipyretic properties. Ensuring the accurate dosage of this medication is crucial as the drug does not require medical practitioner prescription. Overdoses of the drug associates with several adverse effects that even life-threatening. In addition, there is concern on the quality of the drug in local market considering the raise in counterfeit drug cases lately. Consumers can be attracted to the counterfeit drug as the drug usually at a lower price than its authentic ones. Thus, monitoring the quality of diclofenac sodium is essential. In this study the API content of diclofenac sodium in the chosen brands was determined using UV-VIS spectrophotometer. The absorbance at the λ_{max} was used for quantitative analysis. The external standard calibration curve was used to correlate the relationship between the absorbance at the λ_{max} and its corresponding concentration with strong correlation (R^2 value = 0.9988). The UV-VIS method used in this study was validated and found that the method can accurately (percent recovery: 90.7 – 107.8 %) and precisely (standard deviation less than 0.01) to determine the API content of the diclofenac sodium. All the API content of diclofenac sodium from all the brands were closed to its value claimed from their pharmaceutical companies. The percent assay obtained (95.37 – 99.27 %) also within the limit sets by British Pharmacopoeia standards. Thus, this indicates all the brands were authentic and safe to consume.

***Keywords*:** diclofenac sodium, UV-VIS, API content, quality

INTRODUCTION

Consuming counterfeit medications may pose unknown risks to consumers as the contents are not regulated. In Malaysia, about 5 % of medicine are counterfeit (Ng, 2014) and the percent is expected to increase in future (Nur Wahida et al., 2016). Even in Indonesia, our neighboring country, counterfeited drug has been reported sold in their local pharmacies (Rachmadi et al., 2017). This scenario is very alarming and highlight the necessity for monitoring the quality of drugs available in the Malaysian market. Since the physical appearance of counterfeit drugs similar as the authentic ones. In this study the quality of diclofenac sodium tablet from four brands (Avonac®, Voltaren®, Diclotroy® and Dyfenac®) were investigated by using UV-VIS spectrophotometer. The tablets samples were crushed into homogenized small powder using mortar and pestle prior dissolved in methanol. The solutions were sonicated, centrifuge and the supernatant were filtered prior use for UV-VIS measurement. The UV-VIS method was validated (in term of its accuracy, precision and linearity range) prior use for assessing the quality of the drug. The quality of the drug was assessed based on the active pharmaceutical ingredient (API) content and it's percent assay.

MATERIALS AND METHODS

Materials

Diclofenac sodium tablet samples were chosen from four brands, namely as Avonac®, Voltaren®, Diclotroy® and Dyfenac®). The value in ( ) refers to its active pharmaceutical ingredient (API) content. All the drugs were bought from several pharmacies in Shah Alam.

Preparation of diclofenac sodium sample solution

Preparation of sample solution followed Moreno et al. (2019). For each brand, 10 tablets were used. The tablets were taken out of their blister packs and weighed to determine the average weight per tablet. The tablets were then ground into a fine powder using a mortar. The amount of powder equivalent to one tablet was suspended in methanol in a 50 mL volumetric flask to prepare a 1000 mg/L sample solution. This solution was sonicated for

30 minutes and then centrifuged at 3000 rpm for 5 minutes. The resulting supernatant was collected and filtered through filter paper. From this, 20 mg/L sample solution was prepared.

Preparation of working standard solutions

1000 mg/L diclofenac sodium standard stock solution was prepared from diclofenac sodium powder (95% purity) in two different solvents: methanol and 0.1 M sodium hydroxide. Then, the stock solution was filtered prior prepared working standard solution.

UV-VIS measurement

All the blank, standard and sample solutions were measured by UV-VIS spectrophotometer at range 200 – 400 nm. The sequence for the measurement was as followed: blank, standard and sample solutions.

Validation study

The method used for quantification of diclofenac sodium in this study was validated based on linearity range of external standard calibration curve, accuracy and precision.

RESULTS AND DISCUSSION

The UV-VIS spectra of diclofenac sodium in standard solutions (Figure 1 (a)) displayed two prominent peaks with $\lambda_{max} \approx 220$ and 282 nm. The first prominent peak is not included in the study due to the shifting of the λ_{max} as the concentration increases. The second prominent peak at 282 nm is more stable and does not shift as the concentration increases, thus, this peak does follow the Beer-Lambert law. The observation in the current study was in line with previous studies that reported the prominent peak of diclofenac sodium to be at 282 nm (Mane et al., 2019; Hasan et al., 2017). Figure 1 (b) shows the spectra for four different brands of diclofenac sodium overlay with each other. The spectra feature of diclofenac sodium on these fours' brands have similar features observed in the standard solution, with the appearance of two prominent peaks at ≈ 220 and 282 nm. The first peaks were not chosen as the λ_{max} for Voltaren and Avonac were different from other brands. In contrast, the second peak the λ_{max} for all these four brands was constant. Therefore, the second peak was chosen for the quantification. The absorbance of the diclofenac sodium at 282 nm in the sample brands was almost the same, consistent with their theoretical concentrations prepared which were the same (i.e. 20 mg/L).

The absorbance at the λ_{max} was used as the y-axis to construct an external standard calibration curve. The calibration curve was used to find the relationship between the measured absorbance and its respective concentration. The curve showed a strong linear correlation between the absorbance and the concentration (R^2 value = 0.9988). This linearity range was valid for concentration range of 0 – 50 mg/L of diclofenac sodium. The accuracy of UV-VIS method used in this study was assessed by % recovery test that measured in triplicates for each sample brand (Table 1). The sample was spiked with 10 mg/L diclofenac sodium and all sample brands measured by UV spectrophotometer resulted with concentration closed to its spiked/added concentration with the % recovery lies between 90.7 and 107.8 %, which this range falls within the acceptable range (i.e. 80-110%) (Alquadeib, 2019). Therefore, the UV-VIS method used in this study can accurately quantify the diclofenac sodium in all sample brands. The precision of the method was assessed by its standard deviation showed in the column 3 of the table 1. The UV-VIS method used resulted with very good precision for triplicate measurements (with the largest standard deviation of 0.0088). The diclofenac sodium content per tablet (API) for all sample brands measured using in this study were closed to the content (API) claimed by their pharmaceutical companies (Table 2). This is evident from the % bias calculated (the measured API – API claimed by the pharmaceutical companies). The percent assay was calculated from UV spectra of standards and sample solution with 20 mg/L of diclofenac sodium. The percent assay obtained in this study was between 95.37 and 99.27 %, which this range is within the acceptable percent assay sets by British Pharmacopoeia standards for a drug (British Pharmacopoeia, 2004).

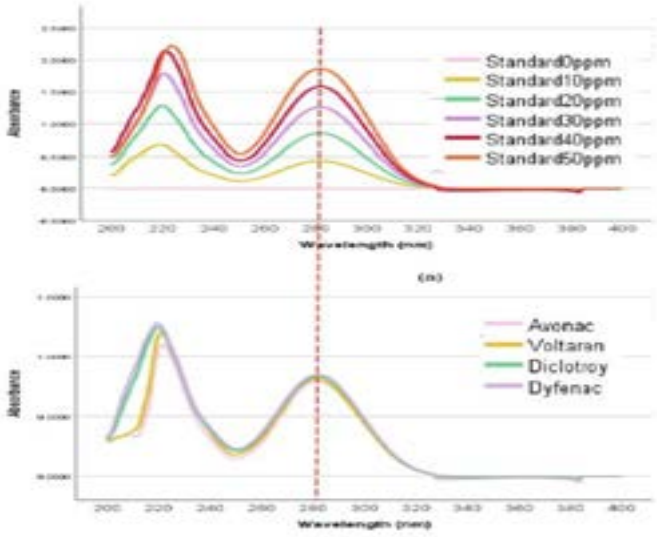

Figure 1. UV spectra of diclofenac sodium in (a) standards and (b) sample solutions.

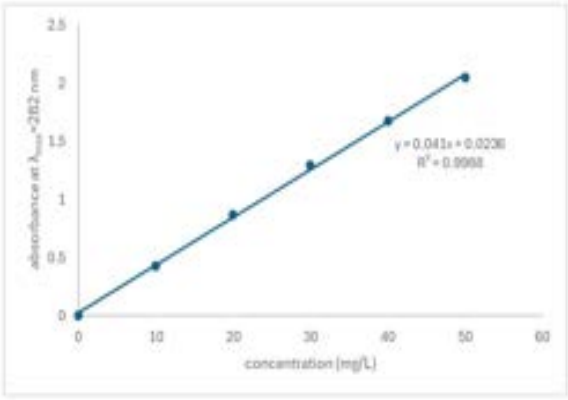

Figure 2. An external standard calibration curve for diclofenac sodium

Table 1. The accuracy and precision data for the UV-VIS method used

Brands	Concentration added (mg/L)	Concentration found (mg/L)	Range of Recovery (%)
Avonac	10	9.54±0.0088	93.50 – 97.72
Voltaren		10.24±0.0015	102.09 – 102.81
Diclotroy		9.14±0.0021	90.70 – 92.21
Dyfenac		10.77±0.0020	107.69 – 107.80

Table 2. The amount of diclofenac sodium and percent assay obtained in all sample brands

Sample Brands	Claimed amount per tablet by the manufacturer (mg)	Amounts obtain from each tablet (mg)	Percent Bias (%)	Percent Assay (%)
Avonac	100	99.85±0.0018	0.15	96.84 – 97.25
Voltaren		49.61±0.0084	0.78	95.37 – 97.24
Diclotroy	50	52.30±0.0020	4.60	98.72 – 99.19
Dyfenac		52.35±0.0018	4.70	98.85 – 99.27

CONCLUSION

The UV-VIS method used in this study are reliable for determination of API content in Avonac®, Voltaren®, Diclotroy® and Dyfenac®. This is supported by the validation study conducted that proven the UV-VIS method can accurately and precisely determined the API content of the four brands. All four brands were safe to consume as the API content close to the value claimed from the pharmaceutical companies. In addition, the percent assay of the drug in all brands was within the limit sets by the British Pharmacopoeia standards.

REFERENCES

Alquadeib, B. T. (2019). Development and validation of a new HPLC analytical method for the determination of diclofenac in tablets. *Saudi Pharmaceutical Journal*, *27*(1), 66–70.

British Pharmacopeia (2004). Diclofenac preparation. London: The Stationary office Vol.III., 2354-2355

Hasan, M., Hossain, M., Sultana, A., Shoeb, M., & Nahar, N. (2017). Evaluation of Diclofenac by UV-Vis Spectrophotometer in Some Locally Produced Tablets. *Dhaka University Journal of Science*, *65*(2), 163–165.

Mane, R. V., Patel, K., Sushmitha, G. S., & Vasantharaju, S. G. (2019). Development and Validation of Diclofenac sodium in tablets using Simple UV Spectrophotometric method. *Research Journal of Pharmacy and Technology*, *12*(2), 611.

Moreno, A., Barbosa, C., Souza, F. M. de, Guimarães, A., Vanderlei, A., Sousa, B. R., Fogaça, E. L., Rocha, G., Fernando, S., Duarte, P., & Matheus, C. (2019). Determination of 50MG sodium diclofenac content in generic and similar reference medicinal product by Ultraviolet-Visible spectrophotometry. *International Journal of Development Research*, *9*(11), 32069–32072.

Ng, C. (2014, November 12). *Five per cent of medicines in Malaysia are counterfeit - Pfizer*. Astro Awani. https://www.astroawani.com/berita-malaysia/five-cent-medicines-malaysia-are-counterfeit-pfizer-48197

Nur Wahida, Z., Noorizan, A. A., Yahaya, H., Mohamed Azmi, H., Nur Liyana, Z. B., & Azlan, A. (2016). Are we on the right track?: Overview of unregistered drugs in Malaysia. *Journal of Pharmacy Practice and Community Medicine*, *2*(4), 107–115.

Rachmadi, A., Lyrawati, D., & Danimayostu, A. A. (2017). Post marketing study of Ponstan®500 mg tablet under suspicion as counterfeit drug at pharmacies. *Research Journal of Pharmacy and Technology*, *10*(8), 2510–2516.

SYNTHESIS OF DIETHYLENETRIAMINE-MODIFIED POLY(ACRYLONITRILE-*CO*-ACRYLAMIDE) FOR THE ADSORPTION OF DOXYCYCLINE FROM AQUEOUS SOLUTION

Siti Nurul Ain Md Jamil[1,2*], Nur Ismahusna Azlee[1], Nur Nida Syamimi Subri[1]

[1]*Chemistry Department, Faculty of Science, Universiti Putra Malaysia, 43400 UPM Serdang, Selangor, Malaysia*

[2]*Centre for Foundation Studies in Science of Universiti Putra Malaysia, 43400 UPM Serdang, Selangor, Malaysia*

corresponding author: ctnurulain@upm.edu.my

ABSTRACT

Antibiotic residues have caused water pollution as it is consumed daily for the treatment of diseases. They are released to wastewater from the excretion by human bodies. This study explores the potential utilization of diethylenetriamine(DETA)-modified poly(AN/AM), as polymeric adsorbents for removal of doxycycline (DOX) from aqueous solutions. The FT-IR spectra revealed that the chemical modification of poly(AN/AM) with DETA was successful. The scanning electron microscopic (SEM) analysis showed that the poly(AN/AM) and DETA-modified poly(AN/AM) appear as agglomerated spherical beads with average particle size of 204 nm and 282 nm, respectively. The effect of pH, adsorbent dosage, contact time and initial concentration of DOX solution were investigated during the adsorption process. The adsorption isotherm studies are fitted well with Langmuir adsorption model with R^2 value of 0.9988 which indicates monolayer adsorption process. This study showed that a polymeric material; DETA-modified poly(AN/AM) is a promising adsorbent to capture DOX from aqueous systems.

Keywords: *adsorption, polymeric adsorbent, redox synthesis, pharmaceutical residues, chemical modification*

INTRODUCTION

One type of emerging pollutants in aquatic environment is antibiotics residues that was excreted in urine and faeces by human and animals. DOX was not fully metabolized by the body and still has strong activity even though has been released to water environment (Chen et al., 2023). DOX residue was detected in river water, sewage effluent and animal therapy where the highest concentration of DOX was found to be in the river water and animal therapy (~82.2 ng/L). The high levels of antibiotics are associated with the population densities because the river is located at the high populated areas. Hence, human activity is the main contributor to the existence of DOX in water (Deng et al., 2016). Many approaches had been conducted for the removal of antibiotics from water, but the high cost of operation impaired the effort of removal. Therefore, in this study, we proposed removal by using adsorption technique by using a polymeric material known as polyacrylonitrile (PAN). The adsorption process is arguably the most effective and efficient method due to its affordability and simplicity. Adsorption process is superior in the removal of a variety of pollutants like heavy metals, organic pollutants, and dyes due to their great adsorption properties as well as their economical method because it can be operated at low energy consumption (Sen et al., 2023). PAN was chosen by many researchers as an adsorbent to remove emerging pollutants because of the presence of nitrile group (-CN) that could be tailored with functional groups to selectively bind the pollutants (Adeyi et al., 2019). However, PAN homopolymer is not feasible to adsorb ions effectively due to the hydrophobicity of nitrile groups. Thus, acrylamide (AM) was integrated into the PAN system to enhance the effectiveness of the removal of heavy metal ions(Md Jamil et al., 2015). Polyacrylamide is commonly used as a water treatment component in wastewater flocculation and sludge dewatering. It is soluble in water and hydrophilic in nature due to its lengthy structure with charge amide groups. That being so, it was assigned for sweeping, bridging, and charge neutralization (Feng et al., 2020). Besides, the incorporation of AM into PAN lowered the nitrile-nitrile dipolar interactions and ease the chemical modification of nitrile groups by using amine-based reagent. Diethylenetriamine (DETA) was used as the amine-based chelating agent to chemically modified nitrile groups along the poly(AN/AM) polymer chain. In this work, the adsorption study was explored using DETA-modified poly(AN/AM) for the removal of DOX from water environment

MATERIALS AND METHODS

Poly(AN/AM) was prepared by using similar method that was reported before (Md Jamil et al., 2015). Chemical modification with diethylenetriamine (DETA) was carried out by adding 3 g of poly(AN/AM) to the mixture of 50 mL of methanol and 4.8 mL of diethylenetriamine (DETA) in a round bottom flask fitted with condenser. The mixture was stirred for 1 hour at room temperature. After that, 1 g of NaOH pellet and continued mixing for 6 hours at 70 °C. After completion of the reaction, the modified poly(AN/AM) was filtered and wash with deionized water. The chemically modified polymer was dried at 50 °C in a vacuum oven.

Characterizations

Fourier transforms infrared (FTIR) spectra was recorded on Spectrum 100 Perkin Elmer (U.S.A.) with Universal Attenuated Total Reflectance (UTAR) by using potassium bromide (KBr) pellets in a resolution range of 4000–500 cm^{-1} at room temperature (25 °C). Scanning electron microscopy (SEM) (JEOL JSM 6360 LA, Japan) was operated at 10.0 to 25.0 kV to observe the morphology of the polymer particles. Brunauer-Emmett-Teller (BET) analyser was used to evaluate the surface area and porosity of the sample.

Adsorption studies

0.01 g of DOX was dissolved in 100 mL of distilled water as a stock solution. It was then diluted serially to 20 mL of 100 ppm and added into a centrifuge tube mixed with each sorbent to carry out the adsorption capacity determination. The solution was shaken using Protech water bath shaker at room temperature (25 °C) for 240 min at 100 rpm. 3.00 mL aliquot of the supernatant was taken out and filtered using a 0.2 µm Millipore filter syringe and then centrifuged using DLAB DM0424 for 10 minutes to separate the adsorbent and supernatant. Dynamica HALODB-20 UV-Vis spectrometer was used to analysed them in the range of 200–400 nm of absorbance. The percentage removal of pharmaceuticals can be expressed as Equation 1.

$$\text{Percentage Removal } (\%) = \left(\frac{c_o - c_e}{c_o}\right) \times 100\ \% \qquad (1)$$

where C_o is expressed as the initial concentration (mg/L) and C_e is expressed as the equilibrium adsorbate concentration (mg/L). Then, the steps were repeated using variation of the following parameters: pH, adsorbent dosage, concentration of DOX and contact time.

RESULTS AND DISCUSSION

Fourier Transform Infrared (FT-IR) Analysis

As shown by the spectrum of poly(AN/AM) (Figure 1), there is appearance of absorption band at 2260 cm^{-1} that is assigned to the C≡N group absorption band. there is also appearance of an intense band that is assigned to C=O of secondary amide at the region of 1680 cm^{-1}. The peaks arising from N-H group of secondary amines was observed at region 3300-3400 cm^{-1} representing the presence of AM monomer integrated successfully into PAN structure. In the IR spectra of DETA-modified poly(AN/AM), there was an appearance of additional broad band at the region of 1640 cm^{-1} (due to the C=N stretching of imine group). The absorption band around 3400 cm^{-1} (due to the N-H stretching band) is also broader as compared to that of poly(AN/AM). These observations proved that the modification of poly(AN/AM) with DETA was successful.

Scanning Electron Microscope (SEM) Analysis

Figure 2 show the surface morphologies of poly(AN/AM) and DETA-modified poly(AN/AM). The particles appear as agglomation of spherical beads. The images were analyzed by using ImageJ software and it was found that the particle size of poly(AN/AM) and DETA-modified poly(AN/AM) are 204 nm and 282 nm, respectively.

Branauer-Emmett-Teller (BET) Surface Area Analysis

The surface are analysis revealed that the specific surface area of poly(AN/AM) and DETA-modified poly(AN/AM) are 51.54 m^2/g and 25.17 m^2/g, respectively. The average pore size of poly(AN/AM) and DETA-modified poly(AN/AM) are 19.30 nm and 29.95 nm, respectively. Meanwhile, the pore volume of poly(AN/AM) and DETA-modified poly(AN/AM) are 0.369 cm^3/g and 0.260 cm^3/g, respectively.

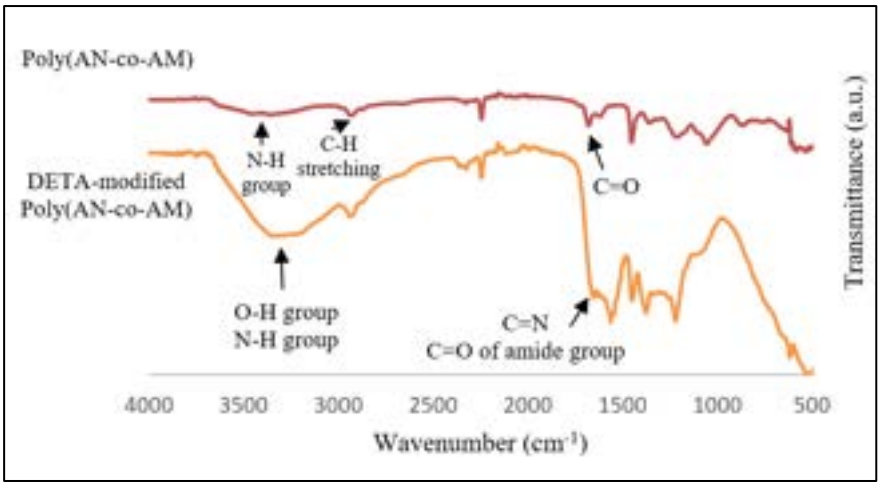

Figure 1. FT-IR spectra of poly(AN/AM) and DETA-modified poly(AN/AM)

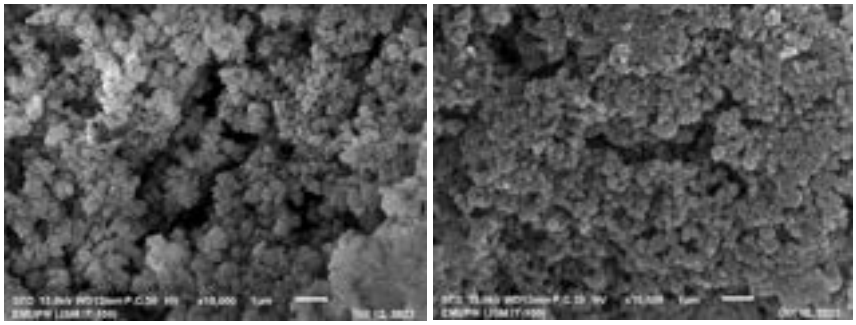

(a) **(b)**

Figure 2. SEM images of (a) poly(AN/AM) and (b) DETA-modified poly(AN/AM)

Point zero charge determination

pH_{PZC} of poly(AN/AM) and DETA-modified poly(AN/AM) was found to be 3.1 and 8.4, respectively. It is expected that at pH less than 3.1, poly(AN/AM) is positively charged which made it highly selective towards certain targeted drugs. In contrary, the pH_{PZC} of DETA-modified poly(AN/AM) is 8.4 which showed a basic character. The value is slightly near to neutrality thus it is more versatile adsorbent as compared to that of poly(AN/AM). DETA-modified poly(AN/AM) could be deduced as positively charged adsorbent when the pH less than 8.4 while pH beyond 8.4, it is negatively charged.

Batch Adsorption Studies

The percentage removal of DOX exhibited the highest with 81.2% (8.07 mg/g) at pH 5. DOX has three positions of ionizable functional groups (alcohol, phenol and amino) at different pKa values which are 3.02, 7.97 and 9.15 respectively. As a result, DOX display anion, cation, and zwitterion behaviour. It functions as a cation (DOX^+) at pH less than 3.02, a zwitterion (DOX^0) between pH 3.02 and 7.97, an anion (DOX^-) between pH 7.97 and 9.15, and beyond pH 9.15 (Aniagor et al., 2021). Besides, pH_{PZC} of DETA-modified poly(AN/AM) possessed a positively charged surface at pH. Due to this, the presence of zwitterion DOX showed the highest percentage removal when the positively charged DETA-modified poly(AN/AM) interacted with the anion. The study on the effect of initial concentration of DOX (at 100 ppm) showed that the adsorption capacity of DOX was 21 mg/g with the percentage removal of 47.6%. Meanwhile, the study on the effect of adsorption time demonstrated that

79.7% of DOX (3.91 mg/g) was removed at 150 min. The effect of adsorbent dosage showed that 82.3% of DOX was successfully removed by using 50 mg of adsorbent.

Adsorption isotherm studies

As shown in Table 1, adsorption of DOX is fitted well with the Langmuir adsorption isotherm model with R^2 value of 0.9988 with 39.53 mg/g of maximum adsorption capacity. The separation factor; R_L value is 0.1179 (smaller than 1) which indicates that the adsorbate prefers to bind to the adsorbent surface rather than remaining in the bulk solution (Al-Saeedi et al., 2023). The corelation coefficient, R^2 value for the models were arranged in the order of Langmuir > Temkin > Freundlich. The Temkin model showed the B_T value of 0.1172 J/mol; indicating that the adsorption process is relatively weak. This suggests that the adsorption of DOX onto DETA-modified poly(AN/AM) is likely to be a physical adsorption process, rather than a chemical one. Physical adsorption is typically characterized by weak intermolecular forces, such as van der Waals forces, between the adsorbate and the adsorbent.

Table 1. Adsorption isotherm model constants and correlation coefficients

Isotherm model					
Langmuir		Freundlich		Temkin	
q_{max} (mg/g)	39.53	K_F	3.130	B_T (J/mol)	0.1172
K_L (L/mg)	0.0530	n	1.706	K_T (L/g)	118.68234
R_L	0.1179	R^2	0.9622	R^2	0.9807
R^2	0.9988				

CONCLUSION

This study demonstrated that DETA-modified poly(AN/AM) is a promising polymeric adsorbent for the removal of DOX from aqueous solutions. The material showed high adsorption capacity and selectivity for DOX, and its surface properties can be tailored to optimize its performance. The results of this study provide valuable insights into the design and development of novel polymeric adsorbents for the removal of emerging pollutants from water environments.

REFERENCES

Adeyi, A. A., Jamil, S. N. A. M., Abdullah, L. C., & Choong, T. S. Y. (2019). Adsorption of malachite green dye from liquid phase using hydrophilic thiourea-modified poly(acrylonitrile- co -acrylic acid): Kinetic and isotherm studies. *Journal of Chemistry*, *2019*. https://doi.org/10.1155/2019/4321475

Al-Saeedi, S. I., Areej, A., Qamar, M. T., Alhujaily, A., Iqbal, S., Alotaibi, M. T., Aslam, M., Qayyum, M. A., Bahadur, A., Awwad, N. S., Jazaa, Y., & Elkaeed, E. B. (2023). Isotherm and kinetic studies for the adsorption of methylene blue onto a novel Mn3O4-Bi2O3 composite and their antifungal performance. *Frontiers in Environmental Science*, *11*. https://doi.org/10.3389/fenvs.2023.1156475

Aniagor, C. O., Igwegbe, C. A., Ighalo, J. O., & Oba, S. N. (2021). Adsorption of doxycycline from aqueous media: A review. In *Journal of Molecular Liquids* (Vol. 334). Elsevier B.V. https://doi.org/10.1016/j.molliq.2021.116124

Chen, J., Huang, Z., Wu, X., Jiaqiang, E., & Leng, E. (2023). Experimental investigation on decomposition characteristics of doxycycline in wastewater using hydrothermal treatment: Exploring the way to complete decomposition. *Journal of Environmental Chemical Engineering*, *11*(3). https://doi.org/10.1016/j.jece.2023.109849

Deng, W., Li, N., Zheng, H., & Lin, H. (2016). Occurrence and risk assessment of antibiotics in river water in Hong Kong. *Ecotoxicology and Environmental Safety*, *125*, 121–127. https://doi.org/10.1016/j.ecoenv.2015.12.002

Feng, X., Wan, J., Deng, J., Qin, W., Zhao, N., Luo, X., He, M., & Chen, X. (2020). Preparation of acrylamide and carboxymethyl cellulose graft copolymers and the effect of molecular weight on the flocculation properties in simulated dyeing wastewater under different pH conditions. *International Journal of Biological Macromolecules*, *155*, 1142–1156. https://doi.org/10.1016/j.ijbiomac.2019.11.081

Md Jamil, S. N. A., Khairuddin, M., & Daik, R. (2015). Preparation of acrylonitrile/acrylamide copolymer beads via a redox method and their adsorption properties after chemical modification. *E-Polymers*, *15*(1), 45–54. https://doi.org/10.1515/epoly-2014-0109

Sen, U., Esteves, B., Aguiar, T., & Pereira, H. (2023). Removal of Antibiotics by Biochars: A Critical Review. In *Applied Sciences (Switzerland)* (Vol. 13, Issue 21). Multidisciplinary Digital Publishing Institute (MDPI). https://doi.org/10.3390/app132111963

REVEALING MICROPLASTIC CONTAMINATION IN MANGROVE SEDIMENTS OF *RHIZOPHORA* SPECIES FROM SETIU WETLAND, MALAYSIA

Nur Syafiqah Mohd Maulana[1], Muhammad Shiddiq Zulkifli[1], Aina Arifah Khalid[1], Maisarah Jaafar[1]*, Rohani Shahrudin[1], Tuan Nurul Sabiqah Tuan Anuar[1]

[1] *Microplastics Research Interest Group (MRIG), Faculty of Science and Marine Environment, Universiti Malaysia Terengganu, 21030 Kuala Nerus, Malaysia*

* *maisarah@umt.edu.my*

ABSTRACT

The mangrove ecosystem, a vital land-sea interface, has been identified as a potential sink for microplastics originating from both marine and terrestrial sources. This study aimed to assess the presence of microplastics in the sediments of *Rhizophora apiculata* mangroves at Setiu Wetland. Surface sediments were collected from three stations (n=18) using a ponar grab and chemically extracted with a modified WESTPEC method, followed by manual sorting under a microscope. A total abundance of 2292 item/kg dry wt. were found across stations, with a mean abundance of 382±161 items/kg dry wt. The highest concentration was near a fish cage (Station 1), while the other stations had similar levels. Microplastics were predominantly fibers (≥80%), with fragments, films, and foams also present, but pellets were rare. Transparent and black microplastics were most common. SEM-EDS analysis revealed surface cracks and pits, indicating mechanical and chemical weathering, and attachment of toxic elements and biofilm. The microplastic polymers were made of polypropylene and polyvinyl chloride, which links the contamination to human activities in the surrounding area. Statistical analysis showed a correlation between microplastic abundance and sediment pH, but not with soil organic matter. These findings advance our understanding of microplastic pollution in mangroves and highlight the need for further research on its impacts on mangrove and aquatic ecosystems.

Keywords: *Microplastics, Mangrove sediment, Rhizophora, Setiu Wetland, Malaysia*

INTRODUCTION

Microplastics (MPs) are synthetic polymer particles smaller than 5 mm, classified as primary (originally manufactured) and secondary (broken down from larger plastics) (Dung et al., 2021). Mangrove ecosystems, situated at the land-sea interface, can accumulate MPs from both marine and terrestrial sources, including aquaculture waste and landfill runoff (Zhou et al., 2020). While mangroves typically exhibit lower levels of MPs contamination compared to other coastal areas, their distribution and characteristics in mangrove sediments remain poorly understood (Li et al., 2019). Mangrove sediments and roots play a crucial role in trapping contaminants, influenced by vegetation and tidal actions, which can increase microplastic prevalence (Zhang et al., 2021).

Globally, mangroves are critical for filtering sediments and providing habitats for diverse species, yet they face significant challenges from plastic pollution, with plastics making up 70% of marine waste in these areas (van Bijsterveldt et al., 2021). The aerial roots of mangrove trees are vital in reducing wave energy and limiting MPs accumulation (Duan et al., 2021). Recent studies have detected MPs in marine species from Setiu Wetland, Terengganu, underscoring the need for further investigation in Malaysia (Ibrahim et al., 2021). MPs enter mangrove ecosystems via runoff from urban, agricultural, aquaculture and industrial areas, posing risks to biota through direct ingestion or indirect consumption of contaminated prey (Bretas et al., 2020; Dung et al., 2021). Understanding microplastic pollution in mangroves is essential for managing these vital ecosystems, which cover just 0.5% of the world's coastlines (Maghsodian et al., 2022).

Setiu Wetland is the largest natural wetland on Peninsular Malaysia's East Coast, spans three river basins to form a 14 km continuous lagoon. This distinctive landscape includes nine interconnected ecosystems including mangroves forest that support a diversity of flora and fauna (Rahman et al., 2023). Thus, protecting this area from threats like microplastic pollution is crucial for maintaining the long-term health and benefits of its ecosystems. Therefore, this study aims to quantify and characterize microplastic in the mangrove sediments of Rhizophora species at Setiu Wetland, Terengganu. Microplastics can compromise the health of mangrove ecosystems by contaminating sediments and waters, posing risks to marine life and disrupting these critical habitats. The results will provide valuable insights for developing effective management strategies to address plastic pollution, ensuring the preservation of these essential ecosystems for coastal protection and biodiversity conservation.

MATERIAL AND METHODS

A total of 18 surface sediment samples were collected from three stations (ST01-ST03; Figure 1), each consisting of two *Rhizophora apiculata* plants spaced approximately 1 meter apart (coded as A and B). At each station, three replicate sediment samples were collected per mangrove plant using a Ponar grab. The samples were transferred to stainless-steel containers, covered with aluminum foil, labeled, and stored in an ice box for transport to Universiti Malaysia Terengganu. In the laboratory, samples were dried at 60°C for 72 hours, ground and sieved through 1 mm and 5 mm mesh. For microplastic extraction, 200 g of sediment underwent density separation with zinc chloride, followed by wet peroxide oxidation with hydrogen peroxide (WESTPAC, 2018). The samples were filtered through 47mm GF/C Whatman filter papers, placed in a cleaned petri dish, dried in a desiccator, and examined under a stereo microscope for microplastic abundance (item/kg dry wt.). Surface analysis was performed using a scanning electron microscope-energy- dispersive X-ray spectrometer (SEM-EDS), and polymer types were identified with ATR-FTIR (Ibrahim et al., 2021). The sediment pH was measured with a calibrated pH meter using a sediment-to-water ratio of 1:2.5. The organic matter content in the sediment was determined using the loss on ignition method, where it was heated in a muffle furnace at 450°C for 4 hours. For the quality control, blank samples throughout the study were included to ensure accuracy and prevent cross-contamination.

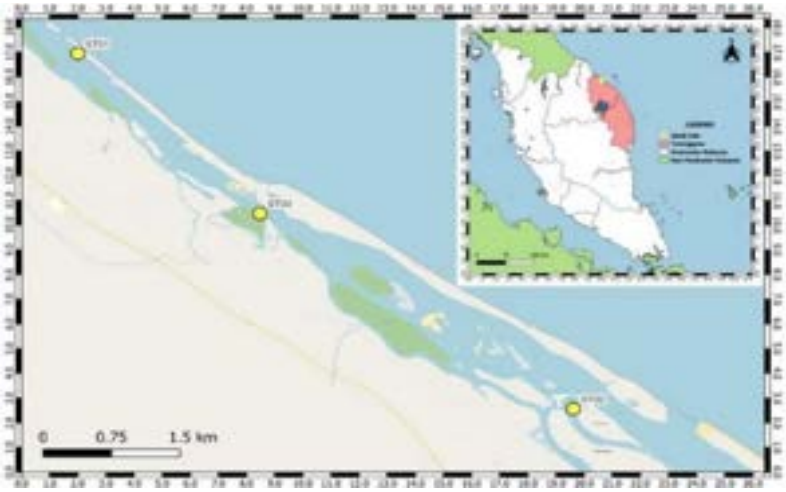

Figure 2. Map of sampling areas in Setiu Wetland, Terengganu

RESULTS AND DISCUSSIONS

Microplastics were observed at all sampling stations, with a total abundance of 2292 items/kg dry wt and a mean of 382±161 items/kg dry wt. Station 1 (ST01A and ST01B) had the highest abundance of MPs, followed by Station 2 and Station 3 (Table 1). The elevated levels at Station 1 may be due to nearby fish farms using plastic equipment like nets, cages, and foam buoys (Lin et al., 2022), which could contribute to MPs generation through degradation. Conversely, Stations 2 and 3 showed lower contamination, likely due to their locations, in which Station 2 is influenced by seawater intrusion, while Station 3 is near a jetty. The high disturbance at the jetty and the dilution from freshwater-seawater mixing possibly reduced MPs accumulation. In this study, MPs with small-sized (<1mm) were predominant compared to large-sized MPs (1-5 mm) (Table 1). This observation suggests that the generation of secondary microplastics is particularly favorable within mangrove sediments due the unique structural characteristics of mangrove ecosystems, including their complex root systems and sediment dynamics, enhance the efficiency of trapping and retention of smaller microplastics (Chaisanguansuk et al., 2023). The observed MPs were found in seven different colors, as illustrated in Figure 2, with transparent and black being the most common in the sediment samples. This suggests that plastic particles may subjected to degradation processes and have specific sources (Li et al., 2020). Fibers were the most prevalent, accounting for over 80% of the total MPs observed (Figure 3). Our results align with previous studies conducted in other Southeast Asian countries, which also identified microfibers as the dominant shape among the observed microplastics (Mohamed Nor &, 2014; Navarro et al., 2022; Chaisanguansuk et al., 2023; Vidayanti & Retnaningdyah, 2024).

Table 1. Total abundance of MPs based on sizes

Station	Total abundance of MPs based on size (item/kg dry wt.)				Total abundance (item/kg dry wt.)
	0.0-0.3 mm	0.3-0.5 mm	0.5-1.0 mm	1.0-5.0 mm	
ST01A	50	113±7.6	283±113	238±88	685±143
ST01B	43±11.5	63±11.5	173±11.5	165±13.2	445±161
ST02A	30±5.0	47±2.9	120±5.0	100	297±34
ST02B	17±2.9	37±2.9	132±2.9	118±2.9	303±33
ST03A	17±2.9	52±10.4	90±23	115±39	273±42
ST03B	25±5	42±7.6	110±10	112±7.6	288±91

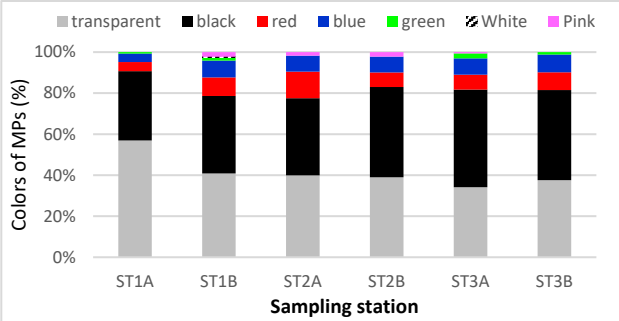

Figure 3. Colors of MPs across sampling stations

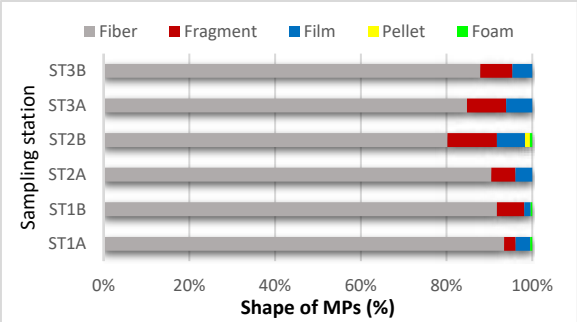

Figure 4. Shapes of MPs across sampling stations

Surface analysis of representative microplastics (MPs) using SEM-EDS revealed grooves, fractures, pit holes, and biofouling on their surfaces, indicating exposure to mechanical and oxidative weathering processes as well as microbial colonization. This might explain why more transparent microplastics were found in this study, as they aged over time. This increases the specific surface area of MPs, enhancing their capacity to adsorb toxic elements (Deng et al., 2020). The SEM-EDS results confirmed the presence of Cu, Fe, Ti, Ca, Zn, Al, and Ni on the MPs' surfaces, suggesting that metals can easily bind to MPs. This increases the risk of harmful impacts on aquatic organisms through bioaccumulation and biomagnification in the Setiu Wetland mangroves. Furthermore, the polymer types of the observed MPs were identified using ATR-FTIR, revealing that the fiber MPs were composed of polypropylene and polyvinyl chloride. Polypropylene fibers are commonly used in ropes, nonwoven fabrics, air filters, diapers, and fishing nets (Lin et al., 2022). Meanwhile, polyvinyl chloride fibers (vinyon) serve as bonding agents for nonwoven fabrics and products (Mohamed Nor & Obbard, 2014).

A negative correlation was observed between pH sediment and MPs abundance ($r = -0.94$, $p < 0.05$). Lower pH levels may alter the surface charge of both microplastics and sediment particles, enhancing microplastic adsorption. Additionally, acidic conditions can affect microbial activity, potentially reducing microplastic degradation rates and increasing their persistence (Maghsodian et al., 2022). However, no correlation was found between soil organic matter and microplastic abundance.

CONCLUSION

This study revealed a significant contamination of microplastics in the mangrove sediments of Setiu Wetland, with an overall abundance of 2292 items/kg dry wt. and an average of 382±161 items/kg. The highest concentrations were observed at Station 1, likely due to the proximity of fish farms that utilize plastic equipment, which contributes to microplastic generation through degradation. The small-sized MPs (<1 mm) were predominant, suggesting that mangrove ecosystems facilitate the trapping and retention of these particles. Fibers made up over 80% of the total observed MPs, with transparent and black being the most common colors. Surface analysis highlighted that these MPs are subjected to mechanical and oxidative weathering, increasing their potential to develop biofilm and adsorb toxic elements. Furthermore, the identified polymers were predominantly polypropylene and polyvinyl chloride, raising concerns regarding their impact on aquatic organisms through bioaccumulation and biomagnification. The negative correlation between sediment pH and microplastics suggests that the accumulation of MPs may be influenced by sediment characteristics. Regular monitoring programs should be implemented in Setiu Wetland to combat miroplastic pollution, particularly near fish farms, along with regulations to reduce plastic use in aquaculture, as MPs can be a vector for environmental pollutants. Further

research on sediment characteristics and mitigation strategies is needed to assess the effects of microplastics on ecosystem health and biodiversity.

REFERENCES

Bretas Alvim, C., Mendoza-Roca, J. A., & Bes-Piá, A. (2020). Wastewater treatment plant as microplastics release source – Quantification and identification techniques. *Journal of Environmental Management*, *255*, 109739. https://doi.org/10.1016/j.jenvman.2019.109739

Chaisanguansuk, P., Phantuwongraj, S., Jirapinyakul, A., & Assawincharoenkij, T. (2023). Preliminary study on microplastic abundance in mangrove sediment cores at Mae Klong River, upper Gulf of Thailand. *Frontiers in Environmental Science*, *11*(March), 1–12. https://doi.org/10.3389/fenvs.2023.1134988

Dung, L. V., Duc, T. H., Linh, L. T. K., Ly, T. T. D., Duong, H. A., & Hao, N. T. M. (2021). Depth profiles of microplastics in sediment cores from two mangrove forests in northern Vietnam. *Journal of Marine Science and Engineering, 9*(12), 1381. https://doi.org/10.3390/jmse9121381

Duan, J., Han, J., Cheung, S. G., Chong, R. K. Y., Lo, C. M., Lee, F. W. F., Xu, S. J. L., Tam, N. F. Y., & Zhou, H. C. (2021). How mangrove plants affect microplastic distribution in sediments of coastal wetlands: Case study in Shenzhen Bay, South China. *Science of the Total Environment*, *767*, 144695. https://doi.org/10.1016/j.scitotenv.2020.144695

Ibrahim, Y. S., Hamzah, S. R., Khalik, W. M. A. W. M., Ku Yusof, K. M. K., & Anuar, S. T. (2021). Spatiotemporal microplastic occurrence study of Setiu Wetland, South China Sea. *Science of the Total Environment*, *788*. https://doi.org/10.1016/j.scitotenv.2021.147809

Li, R., Zhang, L., Xue, B., & Wang, Y. (2019). Abundance and characteristics of microplastics in the mangrove sediment of the semi-enclosed Maowei Sea of the south China sea: New implications for location, rhizosphere, and sediment compositions. *Environmental Pollution*, *244*, 685–692. https://doi.org/10.1016/j.envpol.2018.10.089

Li, R., Yu, L., Chai, M., Wu, H., & Zhu, X. (2020). The distribution, characteristics and ecological risks of microplastics in the mangroves of Southern China. *Science of The Total Environment*, *708*, 135025. https://doi.org/10.1016/j.scitotenv.2019.135025.

Lin, L., Chen, C. C., Zhu, X., Pan, K., & Xu, X. (2022). Risk of aquaculture-derived microplastics in aquaculture areas: An overlooked issue or a non-issue? *Frontiers in Marine Science*, *9*, 923471. https://doi.org/10.3389/fmars.2022.923471

Maghsodian, Z., Sanati, A. M., Tahmasebi, S., Shahriari, M. H., & Ramavandi, B. (2022a). Study of microplastics pollution in sediments and organisms in mangrove forests: A review. *Environmental Research*, *208*, 45112725. https://doi.org/10.1016/j.envres.2022.112725

Mohamed Nor, N. H., & Obbard, J. P. (2014). Microplastics in Singapore's coastal mangrove ecosystems. *Marine Pollution Bulletin*, *79(1–2)*, 278–283. https://doi.org/10.1016/j.marpolbul.2013.11.025

Navarro, C. K. P., Gel, C., Arcadio, L. A., Similatan, K. M., Inocente, S. A. T., Banda, M. H. T., Capangpangan, R. Y., Torres, A. G., & Bacosa, H. P. (2022). Unraveling Microplastic Pollution in Mangrove Sediments of Butuan Bay, Philippines. *Sustainability*, *14*, 14469. https://doi.org/https://doi.org/10.3390/ su142114469

Rahman, A.F.M.A., Islam, M.A., Idrıs, M.H., Bhuıyan, M.K.A., Chowdhury, M.M., Abualreesh, M.H., & Kamal, A.H.M. (2023). Species Diversity and Assemblage of Mangroves at Setiu Wetland, Terengganu, Malaysia. *Borneo Journal of Resource Science and Technology 13*(1), 173-190. http://doi.org/10.33736/bjrst.5109.2023

van Bijsterveldt, C. E. J., van Wesenbeeck, B. K., Ramadhani, S., Raven, O. V., van Gool, F. E., Pribadi, R., & Bouma, T. J. (2021). Does plastic waste kill mangroves? A field experiment to assess the impact of macro plastics on mangrove growth, stress response and survival. *Science of the Total Environment*, *756*, 143826. https://doi.org/10.1016/j.scitotenv.2020.143826

Vidayanti, V., & Retnaningdyah, C. (2024). Microplastic pollution in the surface waters, sediments, and wild crabs of mangrove ecosystems of East Java, Indonesia. *Emerging Contaminants*, *10*(4), 100343. https://doi.org/10.1016/j.emcon.2024.100343

Zhang, S., Sun, Y., Liu, B., & Li, R. (2021). Full size microplastics in crab and fish collected from the mangrove wetland of Beibu Gulf: Evidences from Raman Tweezers (1–20 μm) and spectroscopy (20–5000 μm). *Science of the Total Environment*, *759*, 143504. https://doi.org/10.1016/j.scitotenv.2020.143504

Zhou, Q., Tu, C., Fu, C., Li, Y., Zhang, H., Xiong, K., Zhao, X., Li, L., Waniek, J. J., & Luo, Y. (2020). Characteristics and distribution of microplastics in the coastal mangrove sediments of China. *Science of the Total Environment*, *703*, 134807. https://doi.org/10.1016/j.scitotenv.2019.134807

DUAL-FUNCTIONAL METAL-DOPED ZIF-8 FOR PHOTODEGRADATION OF METHYLENE BLUE AND WATER SPLITTING IN A PHOTOELECTROCATALYTIC SYSTEM

Siti Nur Umairah Shikh Mohd Fauzi[1], Khairul Rijal Razali[1], Aishah Abdul Jalil[2],

Susilawati Toemen[1], Juan Matmin[1*]

[1]*Department of Chemistry, Faculty of Science, Universiti Teknologi Malaysia, 81310, UTM Skudai, Johor, Malaysia*

[2]*Centre of Hydrogen Energy, Institute of Future Energy, Universiti Teknologi Malaysia, 81310, UTM Skudai, Johor, Malaysia*

**juanmatmin@utm.my*

ABSTRACT

This study aims to prepare ZIF-8 incorporated with Ag and Ti as doped thin films showing dual functionalities as photocatalysts for methylene blue (MB) degradation and as photoelectrochemical (PEC) materials for water splitting. Based on the findings, the prepared Ag/ZIF-8 and Ti/ZIF-8 effectively narrowed the band gap, with ZIF-8 (3.60 eV) > Ag/ZIF-8 (3.55 eV) > Ti/ZIF-8 (3.50 eV). Moreover, the current density increased from 0.65 mA cm^{-2} for bare ZIF-8 to 1.50 mA cm^{-2} and 2.55 mA cm^{-2} for Ag/ZIF-8 and Ti/ZIF-8, respectively. The increased current facilitated efficient charge transfer and enhanced photocatalytic activity. Under optimal conditions, photodegradation of MB (10 mg L^{-1}) was achieved at more than 90% within 240 minutes, following the pseudo-first-order rate constants of 0.0103 min^{-1}, 0.0109 min^{-1}, and 0.0138 min^{-1} for ZIF-8, Ag/ZIF-8, and Ti/ZIF-8, respectively. The superior performance of Ti/ZIF-8 is attributed to its unique internal structure and the synergistic interactions between Ti and ZIF-8, which enhance light absorption and charge separation efficiency. This work highlights the potential of metal-doped ZIF-8, specifically Ti/ZIF-8 and Ag/ZIF-8 thin films, for dual-functional applications in photocatalytic water treatment and green energy production within a PEC system.

***Keywords*:** Dual-functional, metal-doped ZIF-8, dyes photodegradation, photoelectrochemical, water splitting

INTRODUCTION

Industrialization and population growth have led to severe environmental pollution and an energy crisis, largely due to inefficient wastewater treatment from industries like textiles that release harmful dyes. With the UN forecasting a 51% increase in wastewater by 2050, traditional methods struggle with dye removal and high energy consumption, exacerbating sustainability issues. This study seeks to address these challenges by exploring metal-doped Zeolite Imidazolate Framework-8 (ZIF-8) materials for dye degradation and hydrogen production through photocatalytic and photoelectrochemical processes. ZIFs, including ZIF-8, are promising for advanced photocatalytic applications due to their high surface area, tunable pore size, and chemical stability. However, ZIF-8's wide band gap limits its efficiency in visible light photocatalysis. Recent research has shown that doping ZIF-8 with metals can enhance its photocatalytic activity by narrowing the band gap and improving light absorption (Çelebi et al., 2022; Thamilselvan et al., 2023).

In this study, ZIF-8 and metal-doped variants (Ag/ZIF-8 and Ti/ZIF-8) were synthesized and evaluated for their photocatalytic and photoelectrochemical properties. Structural characterization was performed using X-ray diffraction (XRD), Fourier-transform infrared spectroscopy (FTIR), and energy-dispersive X-ray spectroscopy (EDX). Photocatalytic performance was assessed by degrading methylene blue (MB) under visible light, while photoelectrochemical performance was evaluated through hydrogen production using linear sweep voltammetry (LSV). The results revealed that metal-doped ZIF-8 catalysts exhibited superior efficiency in degrading MB compared to pure ZIF-8, with Ti/ZIF-8 demonstrating the highest photocatalytic performance and significant hydrogen production. These findings highlight the effectiveness of metal doping in enhancing both photocatalytic and photoelectrochemical activities, addressing critical issues of water pollution and energy production.

MATERIALS AND METHODS

Chemicals

Zinc nitrate hexahydrate ($Zn(NO_3)_2 \cdot 6H_2O$, 98%), 2-methylimidazole (2-MeIM, 99%), Triethylamine (TEA, 99.55%), Titanium isopropoxide (TTIP, 95%), silver nitrate ($AgNO_3$, 99%) and Methylene blue (MB) were purchased from Sigma-Aldrich (USA). All chemicals were used as received without any modification.

Synthesis of ZIF-8, Ag/ZIF-8 and Ti/ZIF-8

This synthesis procedure was adapted from the methodology developed by Naim et al. (2020) with some modifications. ZIF-8 was synthesized using a solventless method, employing $Zn(NO_3)_2 \cdot 6H_2O$ and 2-MeIM in a molar ratio of 1:6:500 with water as the solvent. The $Zn(NO_3)_2 \cdot 6H_2O$ was dissolved in deionized water, while 2-MeIM was prepared separately in deionized water with 3 mL of TEA added gradually. The two solutions were combined and stirred for 1.5 hours, resulting in the formation of ZIF-8. To synthesize Ti/ZIF-8 and Ag/ZIF-8, 0.0064 g of $AgNO_3$ and 760 μL TTIP was introduced into the ZIF-8 mixture. The resulting solids were isolated via centrifugation, washed, and dried at 60°C, followed by grinding and further drying at 80°C. Thin films of ZIF-8, Ag/ZIF-8 and Ti/ZIF-8 were then fabricated by compacting the dried powders onto Mylar substrates using epoxy resin, followed by natural air-drying.

RESULTS AND DISCUSSION

XRD analysis was conducted to understand the crystalline structures of ZIF-8, AgZIF-8 and Ti/ZIF-8. The obtained XRD patterns (Figure 1(i)) for ZIF-8 (a), AgZIF-8 (b) and Ti/ZIF-8 (c) displayed distinct and narrow peaks, indicating an ordered arrangements and confirming their crystalline ZIFs materials (Li et al., 2023; Yu et al., 2022). Furthermore, the diffraction peaks corresponding to ZIF-8, AgZIF-8 and Ti/ZIF-8 are clearly evident at 2θ angles of 7.20°, 10.34°, 12.60°, 14.56°, 16.34°, and 17.92°, which correspond to the (011), (002), (112), (022), (013), and (222) plane, respectively. These angles closely align with the JCPDS card no. 00-062-1030 for ZIF-8, as previously reported (Kim et al., 2023; Mohammadi & Nakhaei Pour, 2023). This result confirms that the ZIF-based photocatalyst was prepared successfully.

Table 1 displays the EDX spectra of ZIF-8 featuring peaks corresponding to Carbon (C), Zinc (Zn), Oxygen (O), and Nitrogen (N) with weight ratios of 55.8%, 17.3%, 6.0% and 21.0%, respectively. These findings serve as confirmation of the formation of ZIF-8. These weight ratios are in contrast to those documented in a previous study (Tuncel & Ökte, 2021) which reported weight percentages of 73.8% for C, 6.7% for Zn, 1.8% for O, and 17.6% for N. In this experiment, ZIF-8 exhibit higher abundance levels of C and Zn, indicative of the presence of zinc and organic components from 2-methylimidazole. The significant quantity of nitrogen underscores the formation of covalent bonds between zinc and 2-methylimidazole within the frameworks. Despite variations in the abundance ratios of ZIF-8 compared to the prior study, the presence of the elements remains consistent, confirming the synthesis of ZIF-8, Ag/ZIF-8 and Ti/ZIF-8. Furthermore, Ag/ZIF-8 and Ti/ZIF-8 also show the presence of Ag and Ti respectively in the EDX diagrams.

The FTIR spectrum was analyzed to verify the structural integrity of ZIF-8, Ag/ZIF-8, and Ti/ZIF-8 (Figure 1(ii)). In the spectrum of ZIF-8, an absorption peak was observed at 424 cm^{-1}, which corresponds to the stretching vibrations of Zn-N bonds (Narimbi et al., 2023; Rahaman et al., 2022; Santos et al., 2023). This peak indicates the chemical bonding of Zn with N atoms from the methylimidazole groups, confirming the formation of the imidazolate structure (Zhang et al., 2018), which in turn confirms the successful synthesis of the ZIF-8 compound.A broad peak between 2500 and 3700 cm^{-1} suggests the presence of hydroxyl groups (OH^-) (Wijaya et al., 2021; Zhang et al., 2018) and the N–H stretching mode (Rahim et al., 2021). According to Rahim and Majid (2023), the absence of peaks within the 3300–2200 cm^{-1} range in the ZIF-8 structure indicates the deprotonation of all hydrogen bonds. However, the N–H bending mode recorded at 3374, 3305, and 3315 cm^{-1} for ZIF-8 showed an increase in the area under the curve compared to 2-methylimidazole, suggesting a strong attachment of the imidazolate group to the Zn metal (Rahim et al., 2021).

Furthermore, when doped with metal, an additional increase in the area under the curve is observed, likely due to enhanced interaction between the doped metal ions and the imidazolate framework, which increases the density of vibrational states in the N–H bending region. This indicates that the doped metal ions are effectively incorporated into the ZIF-8 structure.The peaks at 3135 cm^{-1} and 2929 cm^{-1} were associated with aromatic and aliphatic C–H asymmetric stretching vibrations, respectively. A peak at 1676 cm^{-1}, corresponding to N-H, was observed only in 2-methylimidazole and not in ZIF-8, Ag/ZIF-8, or Ti/ZIF-8, which is attributed to the

deprotonation of the bond to facilitate metal-organic interactions in the ZIFs, as discussed by Zhang et al. (2018).The bands between 600 cm^{-1} to 1500 cm^{-1} were related to the stretching and bending modes of the imidazole ring (Khosravi, 2023).

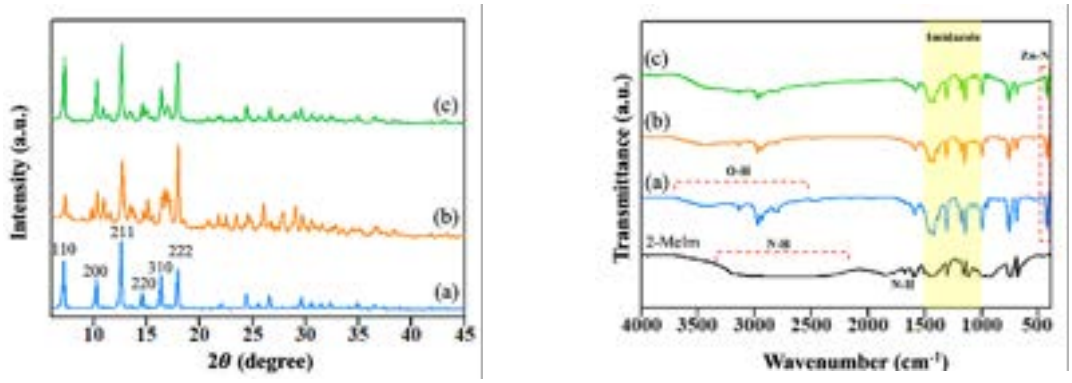

(i) (ii)

Figure 1 XRD spectra (i) and FTIR of 2-methylimidazole, (a) ZIF-8 , (b) Ag/ZIF-8, and (c) Ti/ZIF-8 (ii).

Table 1. The percentage of carbon,zinc,oxygen, nitrogen, silver and titanium for ZIF-8, Ag/ZIF-8 and Ti/ZIF-8.

Notation	Carbon (C)	Zinc (Zn)	Oxygen (O)	Nitrogen (N)	Silver (Ag)	Titanium (Ti)
ZIF-8	55.8 %	17.3 %	6.0 %	21.0 %	-	-
Ag/ZIF-8	50.8 %	17.1 %	3.3 %	28.1 %	0.7 %	-
Ti/ZIF-8	44.3%	15.2%	8.6%	18.8 %	-	13.0 %

The photocatalytic activity and degradation efficiency of MB are depicted in Figure 2(i). All the materials exhibit photocatalytic activity at varying levels, which may be influenced by the presence of the 2-methylimidazole ring. This ring, characterized by double bonds and lone pair electrons, behaves as an aromatic compound, allowing for potential π-π stacking interactions with the benzene ring of MB. Among the tested materials, Ti/ZIF-8 demonstrates superior photocatalytic performance compared to Ag/ZIF-8 and ZIF-8. The degradation efficiency of Ti/ZIF-8 reaches nearly 100% (96.35%) within 240 minutes under visible light irradiation, outperforming Ag/ZIF-8 (93.71%) and ZIF-8 (91.04%). The incorporation of Ag and Ti into the surface of ZIF-8, thereby enhancing photocatalytic performance. This improvement is corroborated by a narrower band gap and stronger absorption in the visible light region, as confirmed by the DR UV-Vis spectra.

To further explore the dual-functionality of ZIF-8-based photocatalysts, water splitting was analyzed using a PEC system. The efficiency of hydrogen generation was assessed through LSV, measured at 0.610 V versus Ag/AgCl, equivalent to 1.23 V for the normal hydrogen electrode (NHE) reference. Ti/ZIF-8 composite as photoanode exhibited the highest current density at 0.610 V, measuring 2.55 mA/cm², followed by Ag/ZIF-8 at 1.50 mA/cm², and ZIF-8 alone at 0.65 mA/cm². The enhanced hydrogen production in the PEC system was attributed to the charge carriers generated from the photoanode under photoelectrochemical excitation (Thamilselvan et al., 2023). In this context, Ti^{4+} ions, with their superior electron conductivity compared to Ag^{2+} ions, were more effective in transporting PEC-induced electrons to the counter electrode.

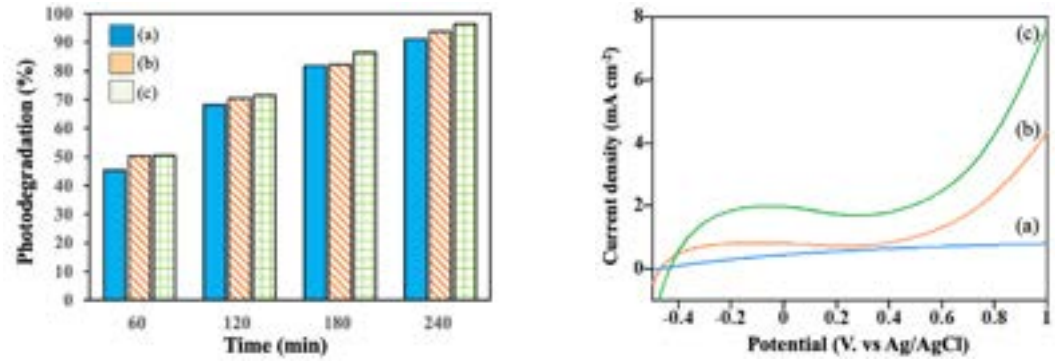

(i) (ii)

Figure 2 Photodegradation (i) and LSV (ii) of (a) ZIF-8 , (b) Ag/ZIF-8, and (c) Ti/ZIF-8

CONCLUSION

The study validates the successful synthesis of ZIF-8, Ag/ZIF-8, and Ti/ZIF-8, as confirmed by XRD, EDX, and FTIR analyses, which reveal their crystalline structures and elemental compositions. The strategic metal doping of ZIF-8 significantly enhances its photocatalytic and photoelectrochemical performance. In this advancement, Ag/ZIF-8 and Ti/ZIF-8 demonstrate higher efficiency in both MB degradation and hydrogen production compared to ZIF-8. Notably, Ti/ZIF-8 achieves the highest photodegradation efficiency at 96.35% over 240 minutes, surpassing Ag/ZIF-8 at 93.71% and ZIF-8 at 91.04%. LSV measurements further reveal that Ti/ZIF-8 achieves a current density of 2.55 mA/cm², outperforming Ag/ZIF-8 at 1.5 mA/cm² and ZIF-8 at 0.65 mA/cm². This superior performance is attributed to the enhanced electron conductivity of Ti^{4+} ions, which is more effective than Ag^{2+} ions in transporting PEC-induced electrons. Future research should explore bimetallic doping strategies to further enhance the performance and functionality of ZIF-based photocatalysts

REFERENCES

Çelebi, N., Soysal, F., & Salimi, K. (2022). Well-defined Core/shell pDA@Ni-MOF Heterostructures with Photostable Polydopamine as Electron-transfer-template for Efficient Photoelectrochemical H_2 Evolution. *International Journal of Hydrogen Energy, 47*(29), 13828-13837. https://doi.org/10.1016/j.ijhydene.2022.02.111

Khosravi, A., Randjbar, M., & Habibpour, R. (2023). Synthesis, Characterization, and Application of ZIF-8 for Removal of Cd, Ni, and Pb Ions from Aqueous Solutions: Optimization of the Process by Response Surface Methodology (RSM) based on Central Composite Design (CCD) Technique. *Journal of Metals, Materials and Minerals, 33*(2), 88-102. https://doi.org/10.55713/jmmm.v33i2.1668

Kim, E., Umar, A., Ameen, S., Kumar, R., Ibrahim, A. A., Alhamami, M. A. M., Akhtar, M. S., & Baskoutas, S. (2023). Synthesis and Characterizations of ZIF-8/GO and ZIF-8/rGO Composites for Highly Sensitive Detection of Cu^{2+} ions. *Surfaces and Interfaces, 41*. https://doi.org/10.1016/j.surfin.2023.103163

Li, S., Tu, L., Lu, Y., Lin, M., Ma, J., Bai, C., Gao, C., & Xue, L. (2023). Polyethyleneimine (PEI) Based Thin Film Nanocomposite (TFN) Total Heat Exchange Membranes (THEMs) Composed of Shaped ZIF-8 crystalline Micro-leaves (ZIF-L). *Separation and Purification Technology, 324*. https://doi.org/10.1016/j.seppur.2023.124435

Mohammadi, A., & Nakhaei Pour, A. (2023). Triethylenetetramine-Impregnated ZIF-8 Nanoparticles for CO_2 Adsorption. *Journal of CO_2 Utilization, 69*. https://doi.org/10.1016/j.jcou.2023.102424

Naim, R., Hazmo, N. H. W., Woei Jye, L., & Ismail, A. F. (2020). Effect of Composite Multi-Walled Carbon Nanotube and Zeolitic Imidazolate Framework-8 on the Performance and Fouling of PVDF Membranes. *Journal of Membrane Science and Research, 6*(4), 424-432. https://doi.org/10.22079/jmsr.2020.128313.1390

Rahim, A. H. A., & Majid, S. R. (2023). Ni/Co-based Zeolitic-Imidazolate Framework Pseudo Capacitance in Asymmetrical Cells. *Journal of Applied Electrochemistry, 53*(9), 1727-1737. https://doi.org/10.1007/s10800-023-01888-x

Rahim, A. H. A., Yusuf, S. N. F., Majid, S. R., & Osman, Z. (2021). One-Step Co-Precipitated B-Ni$(OH)_2$ at Different Ratios of Ni/2-Methylimidazole and Its Energy Storage Behaviour. *Journal of Applied Electrochemistry, 52*(1), 159-172. https://doi.org/10.1007/s10800-021-01627-0

Thamilselvan, A., Dang, V. D., & Doong, R. A. (2023, May 15). Ni-Co Bimetallic Decorated Dodecahedral ZIF as an Efficient Catalyst for Photoelectrochemical Degradation of Sulfamethoxazole Coupled with Hydrogen Production. *Science of the Total Environment, 873*, 162208. https://doi.org/10.1016/j.scitotenv.2023.162208

Tuncel, D., & Ökte, A. N. (2021). Improved Adsorption Capacity and Photoactivity of ZnO-ZIF-8 Nanocomposites. *Catalysis Today, 361*, 191-197. https://doi.org/10.1016/j.cattod.2020.04.014

Yu, C., Kim, Y. J., Kim, J., & Eum, K. (2022, Nov 27). ZIF-L to ZIF-8 Transformation: Morphology and Structure Controls. *Nanomaterials (Basel), 12*(23). https://doi.org/10.3390/nano12234224

NANOPARTICLE REINFORCED BIOSURFACTANT AND STUDY OF ADSORPTION BEHAVIOR, INTERFACIAL TENSION REDUCTION AND WETTABILITY ALTERATION

Umar Hassan [1], Mohammed Falalu Hamza [1,2*], Hassan Soleimani [3]

[1] *Department of Pure & Industrial Chemistry, Bayero University Kano, 3011 Kano, Nigeria*

Hassanumar218@gmail.com

[2]*School of Chemistry and Environment, Faculty of Applied Sciences, Universiti Teknologi MARA, 40450 Shah Alam, Selangor, Malaysia*

hamzafalal84@gmail.com

[3]*Institute of Hydrocarbon Recovery, Universiti Teknologi PETRONAS, 32610 Seri Iskandar, Perak Darul Ridzuan, Malaysia*

hassan.soleimani@utp.edu.my

ABSTRACT

Nanofluid is a promising technique for promoting crude oil displacement in reservoir through reduction of interfacial tension (IFT) and wettability. This study aims to evaluate the nanofluid capability of bio-surfactant synthesized from Palm kernel in synergy with SiO_2 NPs. The palm kernel surfactant (PS) combined with the SiO_2 NPs revealed significant adsorption at various operation conditions during nanofluid formulation (PSNP). The optimal adsorption parameters of PSNP were found to be at 120 minutes contact time, 0.2%wt SiO_2 NPs dosage, 40^{o}C temperature, pH 9, and 3% PS concentration. The adsorption isotherms data for PSNP experiment fitted with the Langmuir isotherm (R-squared value of 0.9). The nanofluid of PSNP was found to reduce the IFT of oil/brine system from 6.22 mN/m to a low level of 1 x 10^{-2} mN/m. Also, the nanofluid altered the wettability to water wet condition by 10%.

Keywords: Enhanced oil recovery (EOR), Surfactant, nanoparticles, and adsorption**.**

INTRODUCTION

Crude oil is a dominant primary source of energy and one of the developed marketplaces with the potential to address the global energy crisis [1-2]. The need for energy necessitates the application of diverse hydrocarbon recovery techniques including surfactant flooding[3]. Several factors are responsible for oil remaining in the reservoirs such as wettability, interfacial/surface tension and negative capillary force [4].

Surfactants

Surfactants play unprecedented roles in many EOR systems, including surfactant flooding, polymer-surfactant flooding, and foam flooding [5]. They have been considered as revolutionary agents with excellent EOR properties due to their surface acting capabilities, reduction of oil-water interfacial force and changing the rock wetting properties [6]. In recent years, there has been a surge of interest in the use of NPs in synergy with surfactants to overcome the limitation of surfactant-based EOR methods. This is mainly due to their nano size, thermal stability, and surface properties created by the electrostatic interaction of NPs with surfactant molecules [7]. Surfactant derives from plants are economically potential to oil industries due to their low toxicity, high biodegradability, multi-functionality, environmental capacity, and availability of resources [8].

Palm kernel oil (*Elaeis guineensis*)

Palm kernel oil (PKO) is an edible plant oil derived from the seeds of palm kernel tree (Elaeis guineensis). Palm oil is among few highly saturated vegetable fats containing 16-carbon atom saturated fatty acid (palmitic acid). The PKO is derived from the kernel, or the inner seed, of oil palm fruit and is widely used vegetable oil in various industries, including food, cosmetics, and personal care products [9-10].

METHODOLOGY

Synthesis & Adsorption Studies

For the synthesis, exactly 20 ml of PKO was separately heated around 80-90° C for 30 minutes to simmer the oils. 10 g NaOH was added by stiring, and the mixture was heated at 80° C for about 3 hours. The solid product was analyzed using Fourier transform infrared spectroscopy FTIR To determine the optimum concentration of PS adsorbed onto the SiO_2 NPs, various concentrations of the PS (1, 2, 3, 4, and 5%wt) each containing fixed amount of 0.2 % wt. SiO_2 NPs were prepared using 3 %wt. brine. Thereafter, the mixtures were agitated using orbital shaker at 300 rpm for 60 minutes at control temperature of 37 °C. All the filtrates were analyzed using UV-spectrophotometer. The adsorption at equilibrium of PS onto NPs was calculated.

IFT & Contact angle analysis

The IFT analysis was carried out using a SVT20 spinning drop at 80°C and 4000 rpm. The IFT tube was firstly filled with brine and placed in the chamber. After that, the tube was set under spinning at about 500 rpm, the rotation was able to keep the oil drop at the center of the tube. Subsequently, the rotation was increased to about 4000 rpm step-wise to ensure drop stabilization. At this stage the drop image was continuously captured by a camera attached to the equipment through which the IFT values were computed automatically using the principle of Young Laplace equation. Contact angle was performed by a drop shape analyzer instrument. At first, slices of reservoir sandstones were submerged in different formulations of PSNP and one sample as a control (in brine). Thereafter, they were allowed for 48 hours to ensure adequate saturation and then contact angles were analysed.

RESULTS

Physico-chemical Analysis

The physical and chemical properties of the oil and surfactant have are provided in Table 1. From the table there is an indication of successful synthesis of surfactant due to significant identified functional groups with shifts observation.

Table 1. Physico-chemical analysis results Palm kernel oil (PKO)

Physico-chemical Parameters	Oil properties	Func. groups	Oil FTIR (cm^{-1})	PS FTIR (cm^{-1})
State at room Temp.	Liquid	$-CH_2$ and $-CH_3$ st.	2921-2854	2921-2854
Color of oil	Dark brown	-C=O st.	1746	Shift 1550
Yield of oil	13%	$-CH_2$ and $-CH_3$ bend.	1466-1235	1400-1300
Moisture content	6.02%	-C-O	1163	Shift 950
Sap. mgKOH/g)	145.19	Long chain	729	729
Acid No. (mgKOH/g)	0.19			
Mass of PS (g)	24.15			

Adsorption studies

From the results in Figure 2a, the calibrations plot of absorbance against concentration have produced the R-squared value of 0.995. This data has demonstrate good correlation thatcan be used for subsequent adsorption studies.

Effects of PS concentration and SiO_2 NPs dosage on Adsorption capacity

In Figure 2b, the maximum adsorption capacity of PS was found to be 49.09% at 3%wt which indicates good efficiency of the PS in facilitating the adsorption onto NPs. This adsorption capacity demonstrates strong affinity of interaction with the SiO_2 NPs. The higher adsorption capacity implies a greater surface coverage of the SiO_2 NPs.

The results of SiO_2 NPs dosage on adsorption capacity can also be observed in Figure 2c, and has showed significant influence of the NPs dosage on adsorption capacity and depicting interesting trend. It was observed that the maximum adsorption of 86 % was achieved at a dosage of 0.2 %. This dosage exhibited the highest affinity between PS and the SiO_2 NPs, leading to a substantial adsorption capacity [11].

Effect of Contact Time on adsorption

From the result presented on Figure 2d, the PS exhibited a higher percentage of adsorption (61.1%) at 120 minutes. Economically, this suggests that the choice of surfactant and its interaction time significantly impact the adsorption process, and optimizing this parameter can enhance the overall efficiency of PS and SNPs interactions.

Effect of Temperature & pH on adsorption

Based on the data plot presented in Figure 2e the effects of temperature on adsorption capacity of the PS onto SiO_2 NPs have been demonstrated, it is observed that it exhibits a higher adsorption capacity at 40°C (54.7%). This result highlights the impact of temperature on the adsorption behavior of surfactants onto NPs under a constant operational conditions and optimized parameters such as dosage, contact time, concentration and others. In general, the adsorption isotherms data reveal that the PSNPs experiment fitted well with the Langmuir isotherm by respective R-squared value of 0.9417.

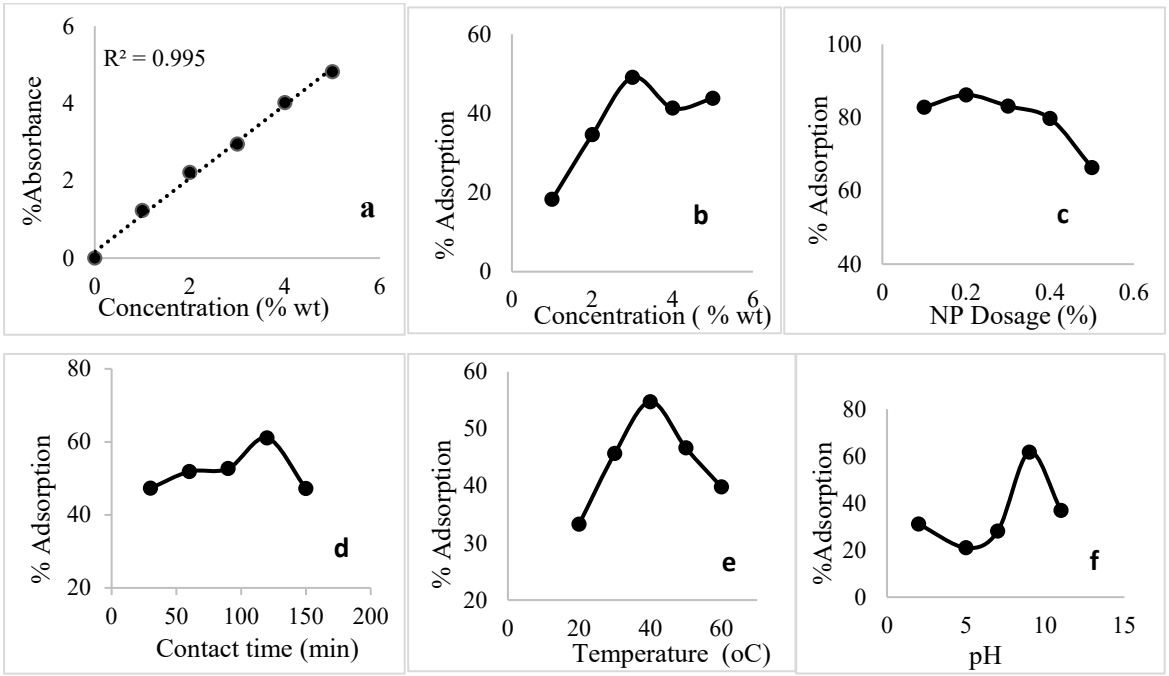

Figure 2. Results of (a) calibration curve to study the Effects of (b) PS concentration (c) dosage of SiO_2 NPs (d) Contact time of PSNP and (e) effect of temperature (f) pH of PSNP on the percent of adsorption capacity.

IFT & Contact angle Results

The average IFT value for oil/brine system was found to be 6.22mN/m as presented in Table 2, this represented the original interfacial force between the oil and brine which serves as a baseline for comparison. The average IFT values of PS and PSNP significantly showed tremendous IFT reduction effects to ultralow level of 4×10^{-3} and 1×10^{-2} mN/m, respectively. These further reductions are attributed to surface active properties of surfactant and NPs, respectively [10][1]. From the table 3 it can be seen that the original contact angle of the oil/brine system was found to be approximately 21 ± 5°. The control fluid exhibits the highest average contact angle, suggesting a relatively less wetting surface. When PS and PSNP were analyzed in comparison with the control, there were significant reductions from 20.58 ± 5° of a baseline to 14.09 ± 2° for PS and 18.47 ± 3° for PSNP, respectively. This has demonstrated that the PS and PSNP have abilities to alter the surface condition to more prefferred values due to wetting behaviours [14] as shown in figure 3.

Table 2. Average value of IFT

TIME	BRINE	PS	PSNP
20	6.2441	0.0032	0.0138
40	6.2445	0.0030	0.0140
60	6.3546	0.0042	0.0139
80	6.2440	0.0049	0.0143
100	6.0283	0.0049	0.0139
Average	**6.22 ± 0.1**	**4 × 10^{-3}**	**1.3 × 10^{-2}**

Table 3. Average values of contact angle

Parameters	Average (ca[°])	CA-Effect	Reduction (%)
BRINE	20.58 ± 5	-	-
PS	14.09 ± 2	6.49	32
PSNP	18.47 ± 3	2.11	10

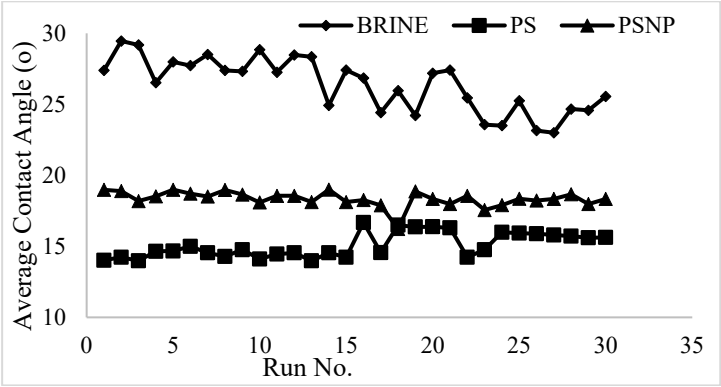

Figure 3. Contact Angle profile

CONCLUSION

From this study, there is a significant adsorption of PS onto the SNPs due to the van Waal and electrostatic attractions between the surface charges. The optimum adsorption conditions of the nanofluid were 3%wt of PS and 0.2 %wt SNPs at 40 oC and pH 9. These data fitted well with Langmuir isotherm having demonstrated R2 of 0.9417. The nanofluid PSNP demonstes good IFT reduction and wettability property. This hybrid material is anticipated to have numerous uses in EOR.

ACKNOWLEDGEMENT

The authors acknowledged Bayero University Kano, Nigeria, Universiti Teknologi MARA, Malaysia and Universiti Teknologi Petronas, Malaysia.

REFERENCES

[1] Hamza, M.F., Sinnathambi C.M., Zulkifli, M. Aljunid Merican, Soleimani, H., Karl D. Stephen, (2018). Effect of SiO2 on the foamability, thermal stability and interfacial tension of a novel nano-fluid hybrid surfactant. *International Journal of Advanced and Applied Sciences,* 5(1), Pages: 113-122

[2] Hamza, M.F., Hassan Soleimani, H., Zulkifi, M. Al, M Sinnathambi, C.M., Karl D.S., Abdelazeem A.A., (2020). Nano-fluid viscosity screening and study of in situ foam pressure buildup at high-temperature high-pressure conditions. *Journal of Petroleum Exploration and Production Technology* 10:1115–1126 https://doi.org/10.1007/s13202-019-00753-

[3] Alireza, B., Mojdeh Delshad. (2023) Strategy for Optimum Chemical Enhanced Oil Recovery Field Operation. *Journal Resource Recovery Volume 1, 100*

[4] Hamza, M.F., Sinnathambi, C.M., and Merican, Z.M., (2016): Recent advancement of hybrid materials used in chemical enhanced oil recovery (CEOR) A review 29th Symposium of Malaysian Chemical

Engineers (SOMChE). IOP Publishing IOP Conf. Series: *Materials Science and Engineering* 206 012007 doi:10.1088/1757-899X/206/1/012007

[5] Alanssari S, Ali M, Alajmi M, Akhondzadeh H, Khaksar Manshad A, Kalantariasl A, Iglauer S, Keshavarz A (2021) Synergistic effect of nanoparticles and polymers on the rheological properties of injection fluids: implications for enhanced oil recovery. Energy Fuels 35:6125–6135

[6] Kamal, M.S., Hussein, I.A., Sultan, A.S., (2017). Review on Surfactant Flooding: Phase Behavior, Retention, IFT, and Field Applications. *Energy Fuels*, 7701–7720. 10.1021/acs.energyfuels.7b00353

[7] Yekeen, N., Eswaran, P., Kamal, I., Syed M.I., (2019). Surfactant adsorption behaviors onto shale from Malaysian formations: Influence of silicon dioxide nanoparticles, surfactant type, temperature, salinity and shale lithology). *Journal of Petroleum Science and Engineering* 179 841-854.

[8] Ummusalma, S. M., and Hamza, M.F., (2022). Fenugreek surfactant: Extraction, Synthesis and Evaluation of Foam Properties for Application in Enhanced Oil Recovery. *Journal of Applied Science and Technology Express,* Article ID: ASTE-2211032112821.

[9] Apasee, N. D, David, A., Sabatini, B, Chantra Tongcumpoua, C, (2009). Microemulsion-Based Palm Kernel Oil Extraction Using Mixed Surfactant Solution. *Journal of Industrial Crops and Products*. Page 194–198.

[10] Davies, R.M. (2012). Physical and mechanical properties of palm fruit, kernel and nut. Journal of Agricultural Technology 8(7):2147-2156.

[11] Abooali, D., Soleimani, R. and Gholamreza-Ravi, S. (2020), Characterization of physico-chemical properties of biodiesel components using smart data mining approaches. *Journal of Fuel* 266, 117075 (2020).

[12] Zheng, H., Huang, F.K., and Jiming, H., (2004). Effect of Contact Time Adsorption of Rhodamine B, Methyl Orange and Methylene Blue Colors on Langsat Shell with Batch Methods J. Phys.: Conf. Ser. 1788 012008

[13] Hassan, Y. M.; Guan, B. H.; Chuan, L. K.; Hamza, M. F.; Khandaker, M. U.; Sikiru, S.; Adam, A. A.; Abdul Sani, S. F.; Abdulkadir, B. A.; Ayub, S. (2022). The influence of ZnO/SiO2 nanocomposite concentration on rheology, interfacial tension, and wettability for enhanced oil recovery. *Chem. Eng. Res. Des*, *179*, 452– 461, DOI: 10.1016/j.cherd.2022.01.033

[14] Li, S., Hendraningrat, L., Torsaeter, O., (2013). Improved oil recovery by hydrophilic silica nanoparticles suspension, *International Petroleum Technology Conference*, Beijing, China.

HIGH-SPEED STIRRING OPTIMIZATION IN CRAFTING UNIFORM SMMA NANOSPHERES

Syara Kassim [1,2*], Nur Aida Mohamed Shaul Hamid [1], Lee Oon Jew [1,2], Rozalina Zakaria [3]

[1] *Faculty of Science and Marine Environment, University Malaysia Terengganu, 21030 Kuala Nerus, Terengganu, Malaysia*

[2] *Advanced Nano Materials (AnoMa) Research Group, Nano Research Team, Faculty of Science and Marine Environment,*

Universiti Malaysia Terengganu, 21030 Kuala Nerus, Terengganu, Malaysia

[3] *Photonic Research Centre, University of Malaya, Lembah Pantai, 50603 Kuala Lumpur, Malaysia*

**syara.kassim@umt.edu.my*

ABSTRACT

This study explores a sustainable method for synthesizing monodisperse styrene methyl methacrylate (SMMA) copolymer nanospheres through free emulsifier approach and deionized water as the sole solvent. The impact of high-speed stirring which is 1000, 1250 and 1500 rpm on the particle size and dispersity of the SMMA nanospheres was systematically investigated. Notably, achieving monodisperse nanospheres with an average size of 154.6 nm without surfactants or stabilizers is significant. The results indicate that increasing stirring speed enhances uniformity and decreases particle size, with the highest stirring speed (1500 rpm) yielding the smallest and monodisperse nanoparticles. This environmentally friendly synthesis method holds promise for applications in drug delivery, coatings and nanocomposites. The optimized parameters and characterization insights from this study provide a foundation for future advancements in nanomaterials with tailored properties.

Keywords: SMMA copolymer, high-speed stirring, monodisperse nanospheres, free emulsifier method, environmental sustainability.

INTRODUCTION

Styrene methyl methacrylate (SMMA) copolymer combines the uniqueness of styrene, known for its high refractive index and optical properties along with methyl methacrylate, valued for its transparency and rigidity [1]. This copolymer exhibits low moisture absorption, high chemical resistance, transparency, stiffness and scratch resistance, making it suitable for diverse applications, including packaging, electrical appliances, automotive parts and medical equipment [2-5]. Traditional synthesis methods involving free radical polymerization often use hazardous solvents and surfactants, posing environmental and health risks [6]. This study seeks a greener alternative by employing high-speed stirring in a free emulsifier approach to produce monodisperse SMMA nanospheres, addressing the need for controlled particle size and minimizing environmental impact.

METHODOLOGY

SMMA copolymer nanospheres were synthesized via high-speed emulsion polymerization using styrene and methyl methacrylate monomers, potassium persulphate as the initiator, and deionized water as the solvent. The reaction was conducted in a 250 ml tri-neck round-bottom flask equipped with a magnetic stirrer and reflux condenser, with stirring speeds set at 1000, 1250, and 1500 rpm. The polymerization was carried out at 70°C under a nitrogen atmosphere for 8 hours. The resulting nanospheres were characterized using Malvern Nano Sizer for particle size and polydispersity index, Fourier Transform Infrared (FTIR) spectroscopy for molecular structure, and Scanning Electron Microscopy (SEM) for morphology.

RESULTS AND DISCUSSION

The study revealed that increasing the stirring speed significantly reduces the particle size of the SMMA nanospheres. At 1500 rpm, the particles reached an average size of 154.6 nm with a polydispersity index of 0.189, indicating a high level of uniformity. The FTIR analysis confirmed successful polymerization with the reduction of C=C absorption peaks and SEM images showed spherical and uniform nanospheres. These findings validate

the effectiveness of high-speed stirring in achieving monodisperse particles and highlight the potential of the free emulsifier method for environmentally friendly synthesis.

CONCLUSION

This research demonstrates the successful synthesis of monodisperse SMMA copolymer nanospheres using a green approach with high-speed stirring. The optimized parameters and resulting nanosphere characteristics underscore the method's potential for various applications, including drug delivery and coatings. This work contributes valuable insights into the synthesis of polymer nanomaterials and paves the way for further research and application development.

ACKNOWLEDGEMENT

This study is supported partially by Fundamental Research Grant Scheme (FRGS), Ministry of Education, Malaysia, Grant Number, 59630.

REFERENCES

[1] Maafa, I. M. (2021). Pyrolysis of Polystyrene Waste: A Review. Polymers, 13(2), 225. https://doi.org/10.3390/polym13020225.

[2] Tuğba Güngör Ertuğral, Merve Danışman, & Ayhan Oral. (2022). Microencapsulation of n-tridecane / n-tetradecane eutectic mixture with poly(methyl methacrylate) shell for candidate for food packaging thermal energy storage material. Polymer-Plastics Technology and Materials, 62(5), 554–562. https://doi.org/10.1080/25740881.2022.2124875.

[3] Hashim, A., & Abbas, B. (2019). Recent review on poly-methyl methacrylate (PMMA)- polystyrene (PS) blend doped with nanoparticles for modern applications. Research Journal of Agriculture and Biological Sciences, 14(3), 6–12. https://doi.org/10.22587/rjabs.2019.14.3.2.

[4] Wu, Y., Fei, M., Qiu, R., Liu, W., & Qiu, J. (2019). A review on Styrene substitutes in thermosets and their composites. Polymers, 11(11), 1815. https://doi.org/10.3390/polym11111815.

[5] Otto, D., Vosloo, H., Liebenberg, W., & Devilliers, M. (2008). Development of microporous drug-releasing films cast from artificial nanosized latexes of poly(styrene-co-methyl methacrylate) or poly(styrene-co-ethyl methacrylate). European Journal of Pharmaceutics and Biopharmaceutics, 69(3), 1121–1134. https://doi.org/10.1016/j.ejpb.2008.02.004.

[6] Göktaş, M. (2020). Copolymer Synthesis with Redox Polymerization and Free Radical Polymerization Systems. Redox. https://doi.org/10.5772/intechopen.88088.

SYNTHESIS AND CHARACTERIZATION OF *L*-TRYPTOPHAN IMPRINTED POLYMERS *VIA* BULK POLYMERIZATION FOR IMPROVED ADSORPTION EFFICIENCY

Faizatul Shimal binti Mehamod [1,2*], Nur Habibah Safiyah Jusoh[1], Nur Asyiqin Zulkefli[1]

[1] *Faculty of Science and Marine Environment,*

Universiti Malaysia Terengganu, 21030 Kuala Nerus, Terengganu, Malaysia

[2] *Advanced Nano Materials (AnoMa) Research Group, Nano Research Team,*

Faculty of Science and Marine Environment,

Universiti Malaysia Terengganu, 21030 Kuala Nerus, Terengganu, Malaysia

**fshimal@umt.edu.my*

ABSTRACT

A molecularly imprinted polymer (MIP) targeting L-tryptophan (L-Tryp) was synthesized using ethylene glycol dimethacrylate (EGDMA), methacrylic acid (MAA), and 2,2'-azobis(isobutyronitrile) (AIBN) with water and methanol as porogens. ATR-FTIR spectroscopy confirmed hydrogen bond formation between the polymer and L-Tryp. SEM and BET analyses characterized the surface morphology, area, and porosity of both non-imprinted (NIP) and L-Tryp-imprinted polymers (L-Tryp-IP). Adsorption studies demonstrated enhanced L-Tryp removal efficiency at pH 5 over 240 minutes, with the L-Tryp-IP showing a 90% removal rate compared to 67% for NIP. The adsorption followed the Langmuir model, and the pseudo-second-order model best described kinetics. The L-Tryp-IP showed high selectivity when tested against molecules similar in structure to L-Tryp and exhibited excellent sensitivity, stability, repeatability, and reusability.

***Keywords*:** L-tryptophan; imprinted polymer; adsorption study

INTRODUCTION

Cancer remains a global health concern, with mortality rates expected to rise due to demographic changes. Immune activation is crucial for cancer prevention, but advanced tumors often evade immune surveillance, creating an immunosuppressive environment [1]; [2]. *L*-Tryptophan (*L*-Tryp) metabolism significantly influences the tumor microenvironment, affecting both immunity and tumor progression [3]; [4]. Traditional *L*-Tryp analysis methods, such as UPLC-MS/MS and HPLC, are complex and costly [5]; [6]; [7].

Molecularly imprinted polymers (MIPs) offer a promising alternative for *L*-Tryp analysis due to their high specificity and selectivity [8]. Studies on *L*-Tryptophan-imprinted polymers (*L*-Tryp-IP) have used various techniques, including bulk polymerization, precipitation, and sol-gel methods [9]; [10]; [11].

Bulk polymerization for *L*-Tryp-IP synthesis faces challenges due to *L*-Tryp's insolubility in non-polar solvents. Researchers have improved adsorption by substrate coating or using novel monomers and solvents. This study explores *L*-Tryp-IP development using bulk polymerization without substrates to overcome solubility challenges and enhance detection, potentially improving the accuracy and reliability of *L*-Tryp analysis for cancer research and diagnostics.

METHODOLOGY

L-Tryp-IP and NIP were synthesized using a bulk free-radical polymerization method. Polymerization occurred in an oil bath at 60°C for 48 hours. NIP was prepared similarly, without *L*-Tryp. Post-polymerization, the polymers were ground into fine powder using a planetary ball mill and sieved to obtain 25-45 µm particles. These polymers were characterized via ATR-FTIR, SEM and BET. The adsorption studies were conducted by batch rebinding experiment, which was performed in an aqueous medium.

RESULTS AND DISCUSSION

The ATR-FTIR analysis of synthesized polymers, including MAA and EGDMA, revealed key insights into their functional groups. The IR spectra showed shifts in absorption peaks after the interaction with *L*-Tryptophan (*L*-Tryp) and its subsequent removal.

SEM images of *L*-Tryp-IP and NIP have cauliflower-shaped particles with irregular sizes. The use of a porogen solvent creates a porous structure. The cauliflower shape is due to phase separation in low-solvency media, which causes co-polymerization and pore filling. *L*-Tryp-IP has a rougher surface than NIP, signifying successful template removal and improved adsorption capacity. This particle morphology is characteristic of MIPs produced by bulk polymerization.

The BET analysis shows that *L*-Tryp-IP has a higher surface area (6.4127 m^2/g) and larger pore volume (0.0264 cm^3/g) compared to NIP (3.3041 m^2/g surface area, 0.0037 cm^3/g pore volume). *L*-Tryp-IP also has larger pores (22.99 nm) compared to NIP (8.41 nm), indicating better adsorption capacity and more recognition sites.

The adsorption studies showed that *L*-Tryp-IP has a greater removal percentage, selectivity, and stability than the NIP.

CONCLUSION

In conclusion, the synthesized *L*-Tryp-IP) demonstrated excellent adsorption properties, with high selectivity and efficiency in removing *L*-Tryp from analyte solutions. Various analyses, including IR spectra, SEM morphology, BET surface area measurements, and adsorption studies, confirmed that *L*-Tryp-IP possesses favorable adsorption kinetics, outstanding reusability, and stability across multiple cycles. Furthermore, selectivity experiments highlighted the specificity of *L*-Tryp-IP for *L*-Tryp, indicating its potential for practical applications in separation and purification processes. These findings suggest that *L*-Tryp-IP is a promising adsorbent for the efficient removal of *L*-Tryp from complex matrices.

ACKNOWLEDGEMENT

We would like to thank the Ministry of Higher Education Malaysia for the project funding support under Fundamental Research Grant Scheme (FRGS/1/2018/STG01/UMT/02/6 –Vot: 59493) and Universiti Malaysia Terengganu.

REFERENCES

[1] L. Lanser, K. Patricia, M. E. Eva, W. Wolfgang, F. Dietmar, W. Guenter and K. Katharina, "Inflammation-Induced Tryptophan Breakdown is Related With Anemia, Fatigue, and Depression in Cancer," Frontiers in Immunology, vol. 11, p. 249, 2020.

[2] F. Peyraud, J. P. Guegan, D. Bodet, S. Cousin, A. Bessede and A. Italiano, "Targeting Tryptophan Catabolism in Cancer Immunotherapy Era: Challenges and Perspectives," Frontiers in immunology, vol. 13, pp. -, 2022.

[3] M. Platten, E. A. A. Nollen, U. F. Röhrig, F. Fallarino and C. A. Opitz, "Tryptophan metabolism as a common therapeutic target in cancer, neurodegeneration and beyond," Nature Reviews Drug Discovery, vol. 18, no. 5, pp. 379-401, 2019.

[4] M. Friedman, "Analysis, nutrition, and health benefits of tryptophan," International Journal of Tryptophan Research, vol. 11, 2018.

[5] L. Whiley, L. C. Nye, I. Grant, N. Andreas, K. E. Chappell, M. H. Sarafian, R. Misra, R. S. Plumb, M. R. Lewis, J. K. Nicholson, E. Holmes, J. R. Swann and I. D. Wilson, "Ultrahigh-Performance Liquid Chromatography Tandem Mass Spectrometry with Electrospray Ionization Quantification of Tryptophan Metabolites and Markers of Gut Health in Serum and Plasma - Application to Clinical and Epidemiology Cohorts," Analytical Chemistry, vol. 91, no. 8, pp. 5207-5216, 2019.

[6] C. E. Onesti, F. Boemer, C. Josse, S. Leduc, V. Bours and G. Jerusalem, "Tryptophan catabolism increases in breast cancer patients compared to healthy controls without affecting the cancer outcome or response to chemotherapy," Journal of translational medicine, vol. 17, no. 1, pp. 1-11, 2019.

[7] C. A. Dailey, C. A. Dailey, C. A. Dailey and J. V. Sweedler, "Automated method for analysis of tryptophan and tyrosine metabolites using capillary electrophoresis with native," Analytical and bioanalytical chemistry, vol. 405, no. 8, p. 2451, 2013.
[8] N. B. Samarth, N. B. Samarth, P. A. Mahanwar, A. V. Rane and V. K. Abitha, "A historical perspective and the development of molecular imprinting polymer-A review," Chemistry International, vol. 1, no. 4, pp. 202-210, 2015.
[9] G. Vasapollo, R. D. Sole, L. Mergola, M. R. Lazzoi, A. Scardino, S. Scorrano and G. Mele, "Molecularly Imprinted Polymers: Present and Future Prospective," International Journal of Molecular Sciences, vol. 12, no. 9, pp. 5908-5945, 2011.
[10] Y. Jin, C. C. Liu, X. H. Sun, K. J. Lee, J. Y. and K. H. Row, "Adsorption Isotherms of Tryptophan Enantiomer on D-Tryptophan Molecular Imprinted Polymer," Asian Journal of Chemistry, vol. 24, no. 6, 2012.
[11] T. Alizadeh and S. Amjadi, "A tryptophan assay based on the glassy carbon electrode modified with a nano-sized tryptophan-imprinted polymer and multi-walled carbon nanotubes," New Journal of Chemistry, vol. 41, no. 11, pp. 4493-4502, 2017.

BIOMASS WASTE INTEGRATION IN $LA_{0.6}SR_{0.4}CO_{0.2}FE_{0.8}O_{3-A}$ - $BA(CE_{0.6}ZR_{0.4})_{0.9}Y_{0.1}O_{3-\Delta}$ COMPOSITE CATHODE: EFFECTS ON MICROSTRUCTURAL AND PHYSICAL PROPERTIES

Ismariza Ismail[1,4], Norizah Abd Karim[2,4], Shazlina Johari[3,4], Muhammad Mahyiddin Ramli[4]

[1]*Faculty of Chemical Engineering & Technology, Universiti Malaysia Perlis, 02600 Arau, Perlis, Malaysia.*

ismariza@unimap.edu.my

[2]*Faculty of Mechanical Engineering & Technology, Universiti Malaysia Perlis, 02600 Arau, Perlis, Malaysia.*

norizah@unimap.edu.my

[3]*Faculty of Electronic Engineering & Technology, Universiti Malaysia Perlis, 02600 Arau, Perlis, Malaysia.*

shazlinajohari@unimap.edu.my

[4]*Institute of Nano Electronic Engineering, Universiti Malaysia Perlis, 01000 Kangar, Perlis, Malaysia.*

mmahyiddin@unimap.edu.my

ABSTRACT

This study explores the integration of rice straw as a pore-forming agent in the fabrication of the $La_{0.6}Sr_{0.4}Co_{0.2}Fe_{0.8}O_{3-\alpha}$-$Ba(Ce_{0.6}Zr_{0.4})_{0.9}Y_{0.1}O_{3-\delta}$ (LSCF-BCZY) composite cathode for protonic ceramic fuel cells application. Rice straw was incorporated into the cathode matrix at different weight percentages, and the composite cathodes were sintered at 1000˚C. Their microstructural and physical properties were evaluated using X-ray diffraction, scanning electron microscopy, and densitometry. The results reveal that the inclusion of rice straw significantly enhances the porosity of the cathode, with porosity levels increasing proportionally with the amount of rice straw added. Notably, the crystalline structure of the LSCF-BCZY composite remained stable across all samples. The porosity increase, ranging from 5.53% to 27.74%, corresponded with a decrease in sample density from 1.3 to 0.9 g/cm3, indicating improved microstructural characteristics. The increased porosity improved reactant diffusion to active sites, potentially enhancing cell performance and operational stability. A comprehensive assessment of the modified cathode's mechanical and electrochemical properties would be beneficial for future studies, providing insights into how microstructural changes impact the composite cathode's structural integrity and phase conductivity.

***Keywords*:** Biomass waste, Pore former, Composite cathode, Microstructural properties, Protonic ceramic fuel cells.

INTRODUCTION

Protonic ceramic fuel cells (PCFCs) represent a significant advancement in electrochemical technology, converting hydrogen and low hydrocarbons into electrical energy with high efficiency and minimal environmental impact. PCFCs, utilizing proton-conducting ceramic electrolytes, offer several advantages over traditional solid oxide fuel cells (SOFCs) that use oxygen-ion-conducting electrolytes. These advantages include lower activation energy requirements and higher energy efficiency within the temperature range of 500-800°C, which also helps reduce operational costs and component degradation (Tahir et al., 2022). Additionally, PCFCs generate water at the cathode during the electrochemical reaction, thereby eliminating the need for further fuel recycling (Mather et al., 2021).

The performance of PCFCs is heavily dependent on the efficiency of the cathode, which plays a critical role in the electrochemical reduction of oxygen. An effective cathode must exhibit high electronic conductivity, compatibility with the electrolyte and interconnect materials, and adequate porosity to facilitate oxygen diffusion to the active sites (Tahir et al., 2022). Among the various materials used for cathodes, composite cathodes such as $La_{0.6}Sr_{0.4}Co_{0.2}Fe_{0.8}O_{3-\alpha}$-$Ba(Ce_{0.6}Zr_{0.4})_{0.9}Y_{0.1}O_{3-\delta}$ (LSCF-BCZY) have garnered attention for their enhanced performance due to improved ionic conductivities and expanded electrochemical activity (Abd Aziz et al., 2020).

Optimizing the microstructure of the cathode, particularly its porosity, is crucial for maximizing PCFCs performance. Porosity influences the accessibility of active sites and the diffusion of reactants, which are essential for efficient electrochemical reactions (Sun et al., 2010). Effective microstructure optimization often involves incorporating pore-forming agents into the cathode material to achieve desired porosity levels. Traditional pore

formers include graphite, starches, and polymers, which have been used to enhance the microstructural properties of cathodes (Nie et al., 2011; Abd Mutalib et al., 2016).

This study investigates the use of rice straw, a biomass waste, as a pore-forming agent in the fabrication of LSCF-BCZY composite cathodes. Rice straw was incorporated into the LSCF-BCZY cathode matrix at various weight percentages, and the composites were sintered at 1000°C. X-ray diffraction, scanning electron microscopy, and densitometry were used to evaluate the effects. The addition of rice straw increased the cathode porosity and reduced its density while preserving the crystalline structure of the composite. This enhanced porosity is expected to improve reactant diffusion and potentially enhance cell performance and stability.

MATERIALS AND METHODS

The LSCF ($La_{0.6}Sr_{0.4}Co_{0.2}Fe_{0.8}O_{3-\alpha}$) and BCZY ($Ba(Ce_{0.6}Zr_{0.4})_{0.9}Y_{0.1}O_{3-\delta}$) powders were prepared following the method outlined by Ismail et al. (2022). The powders were mixed in a 50:50 weight ratio and ground using an agate mortar to ensure a homogeneous distribution within the composite cathode.

Rice straw was collected from paddy fields in Perlis, cut into small pieces, and dried to remove moisture. The dried rice straw was then ground into a fine powder using a grinder and sieved through a 63 µm mesh. The sieved rice straw powder was stored in an airtight container for subsequent use.

The prepared LSCF-BCZY composite cathode powders were mixed with the rice straw powder at varying weight percentages (0%, 10%, 20%, 30%, and 40%). The mixture was then ground using an agate mortar to ensure uniform distribution of the pore former in the composite.

The resulting powder mixtures were pressed into pellets with a diameter of 13 mm using a hydraulic press under a pressure of 300 MPa for 5 minutes. This procedure was repeated for each concentration of rice straw powder to prepare composite cathodes with 10%, 20%, 30%, and 40% rice straw content.

RESULTS AND DISCUSSION

Figure 1 presents the X-ray diffraction (XRD) patterns of composite cathodes containing varying concentrations of rice straw (0%, 10%, 20%, 30%, and 40%). The analysis confirms that the characteristic diffraction peaks of LSCF and BCZY remain unchanged, indicating that rice straw is fully combusted during heat treatment and does not chemically interact with the composite. This absence of secondary phases underscores rice straw's suitability as a pore former. As noted by G. Ch. Kostogloudis et al. (2000), maintaining chemical compatibility between the cathode material and the electrolyte is crucial for optimal cell performance, as any reaction products at the cathode-electrolyte interface could adversely affect efficiency.

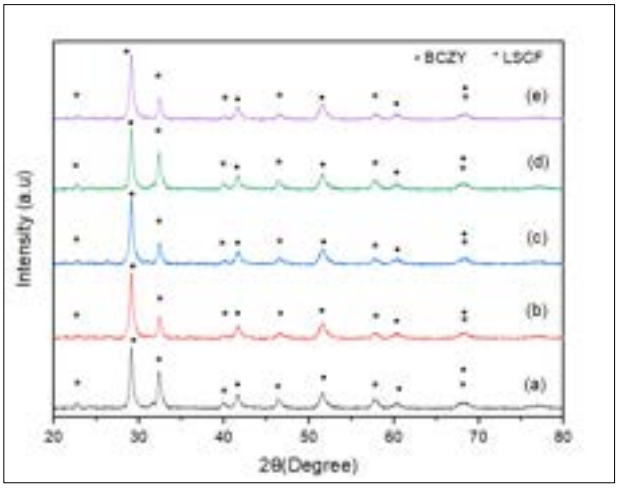

Figure 1. XRD patterns of the composite cathode with varying amounts of rice straw powder (a) 0wt.%, (b) 10wt.%, (c) 20wt.%, (d) 30wt.%, and (e) 40wt.%.

Figure 2 presents scanning electron microscopy (SEM) images of the composite cathodes with 0% and 40% rice straw concentrations. The images reveal a notable increase in porosity with the addition of 40% rice

straw, compared to the unmodified cathode. This enhancement in porosity is attributed to the decomposition of rice straw during heat treatment, which facilitates the formation of fine pores. The increased porosity improves gas diffusion and extends the triple-phase boundaries (TPB), which is essential for optimizing cathode performance. Table 1 summarizes the porosity levels of the composite cathode as determined by image analysis software. An increase in porosity is observed, starting from 8.44% at 10 wt.%, progressing to 12.33%, and further rising to 16.66% with the addition of 30 wt.% rice straw. The highest porosity of 20.94% is achieved at 40 wt.% rice straw, demonstrating a clear trend where higher pore former content correlates with increased porosity

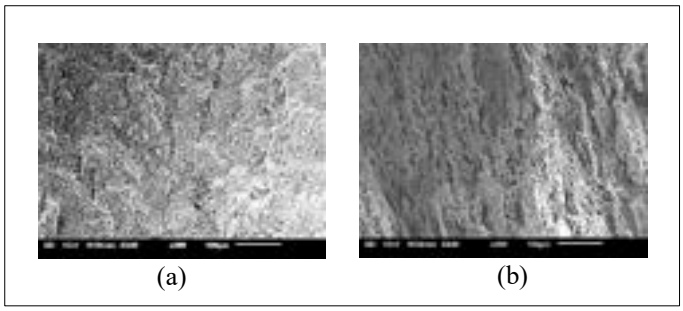

Figure 2. SEM Micrograph of the unmodified composite cathode (a) and the composite cathode modified with (b) 40 wt. %

Table 1. Porosity of LSCF-BCZY composite cathode with varying amounts of incorporated rice straw

Rice straw amount (wt. %)	Porosity (%)
0	5.53
10	13.33
20	15.47
30	20.07
40	27.74

Table 1 summarizes the density measurements of the composite cathodes after heat treatment at 1000°C. The density decreases from 1.33 g/cm³ at 0% rice straw to 0.93 g/cm³ at 40% rice straw, reflecting the increased porosity. While higher porosity enhances gas diffusion, excessive porosity may compromise structural integrity. Therefore, an optimal rice straw concentration, generally between 20% and 30%, is recommended to achieve a balance between performance and durability (Li et al., 2013; Abd Aziz et al., 2020; Nie et al., 2011).

Table 2. Density of LSCF-BCZY composite cathode with varying amounts of incorporated rice straw

Rice straw amount (wt. %)	Density (g/cm^3)
0	1.33
10	1.26
20	1.11
30	1.02
40	0.93

CONCLUSION

In conclusion, this study has demonstrated that rice straw is an effective pore-forming agent for fabricating LSCF-BCZY composite cathodes, significantly enhancing porosity while maintaining the original crystalline structure. The optimal porosity and density were achieved with 30 wt.% rice straw, balancing improved gas diffusion and mechanical stability. The absence of secondary phases confirms that rice straw does not chemically interact with the composite, ensuring reliable cathode performance. Future research should explore the mechanical and electrochemical properties of these modified cathodes to fully assess their potential in practical applications.

REFERENCES

Abd Aziz, A. J., Baharuddin, N. A., Somalu, M. R., & Muchtar, A. (2020). Review of composite cathodes for intermediate-temperature solid oxide fuel cell applications. In *Ceramics International* (Vol. 46, Issue 15). https://doi.org/10.1016/j.ceramint.2020.06.176

Abd Mutalib, M., Othman, M. H. D., Aziz, M., A. Rahman, M., Jaafar, J., Ismail, A. F., & Mohamed, M. A. (2016). The influence of PEEK as a pore former on the microstructure of brush-painted LSCF cathodes. *Journal of Solid State Electrochemistry*, *20*(10). https://doi.org/10.1007/s10008-016-3300-x

G.Ch. Kostogloudis, Ch. Ftikos, A. Ahmad-Khanlou, A. Naoumidis, & D. Stöver. (2000). Chemical compatibility of alternative perovskite oxide SOFC cathodes with doped lanthanum gallate solid electrolyte. *Solid State Ionics*, *134*(1-2), 127–138. https://doi.org/10.1016/s0167-2738(00)00721-9

Li, S., Wang, C. A., & Zhou, J. (2013). Effect of starch addition on microstructure and properties of highly porous alumina ceramics. *Ceramics International*, *39*(8). https://doi.org/10.1016/j.ceramint.2013.04.072

Ismail, I., Malek, N. I. A., Jani, A. M. M., Othman, M. H. D., & Osman, N. (2022). Optimization of $La_{0.6}Sr0.4Co0._2Fe_{0.8}O_{3-\alpha}$-$Ba(Ce_{0.6}Zr_{0.4})_{0.9}Y_{0.1}O_{3-\delta}$ cathode composition for proton ceramic fuel cell application. *Processing and Application of Ceramics*, *16*(4), 374-383. https://doi.org/10.2298/PAC2204374I

Mather, G. C., Muñoz-Gil, D., Zamudio-García, J., Porras-Vázquez, J. M., Marrero-López, D., & Pérez-Coll, D. (2021). Perspectives on cathodes for protonic ceramic fuel cells. In *Applied Sciences (Switzerland)* (Vol. 11, Issue 12). https://doi.org/10.3390/app11125363

Nie, L., Liu, J., Zhang, Y., & Liu, M. (2011). Effects of pore formers on microstructure and performance of cathode membranes for solid oxide fuel cells. *Journal of Power Sources*, *196*(23). https://doi.org/10.1016/j.jpowsour.2011.08.036

Sun, C., Hui, R., & Roller, J. (2010). Cathode materials for solid oxide fuel cells: A review. *Journal of Solid State Electrochemistry*, *14*(7). https://doi.org/10.1007/s10008-009-0932-0

Tahir, N. N. M., Baharuddin, N. A., Samat, A. A., Osman, N., & Somalu, M. R. (2022). A review on cathode materials for conventional and proton-conducting solid oxide fuel cells. In *Journal of Alloys and Compounds* (Vol. 894). https://doi.org/10.1016/j.jallcom.2021.162458

POLYPHENOLIC COMPOUND OF ORGANIC AND NON-ORGANIC SOLANUM LYCOPERSICUM IN MALAYSIA

Shah Christirani Azhar[1], Nur Farahaıen Natasya Ahmad Zaınal[2]

[1] *Centre For Foundatıon Studıes In Scıence,Universiti Putra Malaysia,*

43400 UPM, Serdang, Selangor, Malaysia

christirani@upm.edu.my

[2] *Faculty of Science, Universiti Putra Malaysia,*

43400 UPM, Serdang, Selangor, Malaysia

208091@student.upm.edu.my

ABSTRACT

A comparison between Solanum Lycopersicum or tomatoes grown organically and non-organically on the quantity of antioxidants, such as phenolic and flavonoid compounds and the total antioxidant activity was studied. The results based on the ultraviolet visible spectrophotometers revealed the organic tomato contained the highest total phenolic content with a value of 10.9 µg GAE /5 g and the highest total flavonoid content with a value of 1.693 µg QUE/5 g. The antioxidant activity of organic tomato evaluated by DPPH (2,2-diphenyl-1-picrylhydrazyl) free radical scavenging assay was higher (84.5%) than those of the non-organic tomato.While the inhibition concentration of 80% value for organic tomato was found to be lower (1.17 µg/ml) than non-organic tomato (1.71 µg/ml) indicating of better antioxidant properties in organic tomato. The results suggest that organic tomato could be a potential source of natural antioxidants that are worth the price. Therefore, further research to determine the overall antioxidant capacity of organic tomatoes is indispensable.

Keywords: Antioxidant activity, organic tomatoes, phenolic compound

INTRODUCTION

In Malaysia, market price of *organic Solanum Lycopersicum* or tomatoes is more expensive compared to non-organic tomatoes. Organic tomatoes are believed to have high antioxidant content and good for improving health. Since the 90's, an increasing number of consumers are willing to pay more for food produced by environmentally friendly and pesticide-free practices such as organic farming (Didier & Lucie, 2008). However, one question without a clear answer, whether the organic management system really improves the total antioxidant content in tomatoes.

Several studies have pointed out a better quality of organic foods compared to those from conventional production. For example, Vinha et al. (2014) reported the fruits grown using organic methods contain significantly more chemicals with estimation of 24% of total phenolics and 21% of flavonoids. Oliveira et al. (2013) discovered that organic tomatoes accumulate higher concentrations of vitamin C (55%) and phenolic compounds (139%) than those grown on conventional farms. In another study, Mitchell et al. (2007) had reported that organically grown tomatoes contained higher levels of flavonoids (quercetin and kaempferol aglycones) than conventional ones. Tomatoes fertilised organically have an ascorbic acid concentration that ranges between 29% and 31% (Caris-Veyrat et al., 2004; Toor et al., 2006), which is greater than the findings from tomatoes fertilised with mineral.

The present study conducted to compare the antioxidant potential of organic and non-organic tomatoes by analyzing phenolic and flavonoid compounds content in tomatoes and antioxidant activity. The outcomes of the research will assist the Malaysian consumers in planning and making decisions on buying right tomato that go towards achieving and sustaining a healthy life.

MATERIALS AND METHODS

Materials

Organic tomato brand of Suan Mokkh Gardens, harvested in Port Dickson, Negeri Sembilan and non-organic tomatoes brand of Segar2go, harvested in Kinta Highlands, Malaysia were purchased from Aeon Big Ampang. Folin-Ciocalteu reagent, sodium carbonate, gallic acid, distilled water, aluminium chloride, sodium

nitrate, sodium hydroxide, quercetin, DPPH (2,2-diphenyl-1-picrylhydrazyl), methanol and ascorbic acid were purchased from Sigma Aldrich.

Sampling

Convenience sampling was employed to get the sample for this study. Freshly harvested tomato organic brand of Suan Mokkh Gardens (Rm 7.99) and non-organic brand of Segar2go (RM 3.99) were purchased from local stall in Aeon Big Ampang. Samples were placed in air-tight plastic bags and immediately stored at 4 °C in laboratory, Faculty Sciences, UPM.

Sample preparation

Tomatoes were chopped into pieces and stored at -18 °C for a week. Then, the samples were freeze dried to remove the moisture content. After freeze-drying, the samples were powdered using a dry grinder.

Sample extraction

5 g of powdered tomatoes were extracted with 50 mL ethanol for 24 h at room temperature. The extracts were then evaporated in vacuum concentrator at 60 °C and stored in a 4 °C refrigerator (Robles-Ramírez et al., 2016).

Determination of total phenolic content

Total phenolic content (TPC) was determined according to the method of the FolinCiocalteu method (Singleton & Rossi, 1965). 1 ml of extract was mixed with 5 ml of distilled water and 1.5 ml of Folin Ciocalteau reagent. After the mixture was incubated at room temperature for 5 min, 4 ml of 20% w/v Na_2CO_3 solution was added, and the volume was made up to 25 ml with distilled water.The mixtures were vortexed and kept for 90 min in the dark at room temperature until blue colour develops.The samples were then observed on measuring absorbance at 765 nm using a spectrophotometer. Finally, absorbance values were compared with those of standard Gallic acid concentrations (20, 40, 60, 80, 100 µg/ml). The phenolic concentrations were expressed in terms of milligrams of Gallic acid equivalent per gram of fresh weight (mg GAE/g fresh matter.

Determination of total flavonoid content

The total flavonoids concentrations (TFC) were determined according to the method described by Koolen et al. (2013). 1 ml of extract (20,40,60,80,100 µg/ml) was mixed with 4 ml deionized water and 0.3 ml $NaNO_2$ (5%). After the mixture was incubated for 5 min, 0.3 ml of $AlCl_3$ (10%) were added followed by 2.0 ml of 1.0 M NaOH after one more minute. The volume was completed to 10 ml with distilled water. The mixture was stirred and kept at room temperature for 40 min. The absorbance was measured at 510 nm using a spectrophotometer. Total flavonoids were reported as milligrams of quercetin equivalent per gram of fresh weight.

IC_{80} of DPPH scavenging activity

The DPPH free radical scavenging assay described by Bouaziz et al. (2008). was used to evaluate the antioxidant capacity of organic and non-organic tomatoes. The mixture consisted of 2 ml of each sample methanol extract (25,50,75,100 µg/ml) was mixed with 2 ml of 0.004% DPPH methanolic solution. The mixture was kept in the dark at room temperature for 30 min and the absorbance was recorded at 517 nm using UV-VIS spectrophotometer. Ascorbic acid used as positive control references. The scavenging activity (SA) and the concentration of extract that could scavenge 80% of the DPPH radicals (IC_{80}) was calculated.

RESULTS AND DISCUSSION

Total phenolic content

Table 1 summarizes the results of total phenoliccontent in tomato, There are differences in the amounts of phenolic compounds in different tomato types. When compared to commercially cultivated tomato varieties, organic tomatoes typically have greater amounts (12.18 µg QUE/5 g) of TPC. These findings are consistent with the most recent research by Oliveira et al. (2013), which showed that compared to tomatoes grown on conventional farms, organic tomatoes acquire higher quantities of phenolic compounds (+139%) and vitamin C (+55%). Study

conducted by Oliveira et al. (2013) proposed that the higher concentrations of these compounds in organic tomatoes might be caused by the extra stress that organic farming exposed to the crops.

Table 1. Total phenolic and flavonoid content of organic and non-organic tomato

Tomato	Total phenolic (µg GAE /5 g)	Total Flavonoid (µg QUE /5 g)
Organic	12.18	1.693
Non-organic	5.93	1.578

Total flavonoid content

Table 1 summarizes the results of total flavonoid content in tomato . The result shows organic tomato possesses higher TFC with 1.693 µg QUE/5 g rather than non-organic tomato with only 1.578 µg QUE/5 g. Mitchell et al. (2007) have reported that organically grown tomatoes contain higher levels of flavonoids than conventional ones. Secondary metabolism of plants produces flavonoids to protect plants from bacteria and fungi withacts as a fungicide and antibiotic (Vickery & Vickery 1981). Therefore, the organic farming method, which does not utilise pesticides, accounts for the higher level of flavonoid compounds.

IC_{80} of DPPH scavenging activity

Calculation of IC_{80} based on the equation curve for organic tomato which is y =1.506x + 78.24 with R^2 = 0.9417 while for non-organic tomato is y = 1.635x + 77.21 with R^2 = 0.9639. According to Fitriansyah et al. (2017) the lowest IC_{80} means had the highest antioxidant capacity and a lower IC_{80} indicates higher potency, meaning the substance is effective at a lower concentration. Result IC_{80} value of organic tomato was 1.17 µg/ml lower than non-organic tomato with 1.71 µg/ml. Table 2 present the comparison of IC_{80} concentration which show that that organic tomato possesses the highest antioxidant activity since lower concentration needed to scavenge 80% of the initial DPPH radicals.

Table 2. % Radical inhibition of organic and non- organic tomato

Concentration (µg/ml)	% Radical Scavenging from DPPH Assay	
	Organic tomato	Non-organic tomato
25	79.61	78.46
50	81.76	80.96
75	82.15	82.31
100	84.50	83.46

CONCLUSION

A comparative study on the antioxidant potential of organic and non-organic tomatoes were conducted by analyzing phenolic and flavonoid compounds content in tomatoes and antioxidant activity. The organic tomatoes showed a relatively higher content of both phenolic compounds and flavonoid. The alcohol extracts from organic tomatoes presented higher antioxidant activity than the non-organic tomatoes. The results suggest that organic tomatoes contain rich sources of natural antioxidants and offer better health benefits. Therefore, the further research to determine antioxidant compounds such as lycopene, beta-carotene, ascorbic acid that contribute to the overall antioxidant capacity of tomatoes is indispensable.

REFERENCES

Bouaziz, M., Fki, I., Jemai, H., Ayadi, M., & Sayadi, S. (2008). Effect of storage on refined and husk olive oils composition: Stabilization by addition of natural antioxidants from from Chemlali olive leaves. *Food Chemistry, 108 (1),* 253-262.

Caris-Veyrat, C., Amiot, M.J., Tyssandier, V., Grasselly, D., Guilland, J.C., laude, G.J., Bouteloup - Demange, C., & Borel, P. (2004). Influence of organic versus conventional agriculture practice on antioxidant microconstituent content of tomatoes and derived purees; consequences on antioxidant plasma status in humans. *J. Agric. Food Chem*., *52,* 6503–6509.

Fitriansyah, S.N., Fidrianny,I., & Ruslan, K. (2017). Correlation of total phenolic, flavonoid and carotenoid content of Sesbania sesban (L. Merr) leaves extract with DPPH scavenging activities. *International Journal of Pharmacognosy.9(1),* 89-94.

Koolen, H.H.F., da Silva, F.M.A., Gozzo, F.C., de Souza, A.Q.L., & de Souza A.D.L. (2013). Antioxidant antimicrobial activities and characterization of phenolic compounds from buriti (Mauritia flexuosa L. f.) by UPLC–SI-MS/MS. *Food Res. Int., 51*, 467-473.

Mitchell, A.E., Hong, Y., Koh, E., Barrett, D.M., Bryant, D. E, Denison, R.F., & Kaffka, S. (2007). Ten-year comparison of the influence of organic and conventional crop management practices on the content of flavonoids in tomatoes. J. Agric. Food Chem., 55, 6154−6159.

Oliveira, A.B., Moura, C.F.H., Gomes-Filho, E., Marco, C.A., Urban, L., & Miranda, M.R.A. (2013). The impact of organic farming on quality of tomatoes is associated to increased oxidative stress during fruit development. Plos One, 8(2), e56354.

Robles-Ramírez, M. C., Monterrubio-López, R., Mora-Escobedo, R., & Beltrán-Orozco. M. C. (2016). Evaluation of extracts from potato and tomato wastes as natural antioxidant additives. Archivos Latinoamericanos de Nutrición, 66(1), 66-73.

Singleton, V. L. & Rossi, J.A. (1965).Colorimetry of total phenolics with phosphomolybdic-phosphotungstic acid reagents. Am J Enol Vitic, 16, 144-158.

Toor, R.K. and Savage, G.P. (2006). Antioxidant Activity in Different Fractions of Tomatoes. Food Research International, 38, 487-494.

Vickery, M.L., & Vickery, B. (1981). Secondary plant mechanism. Red Globe Press London.

Vinha, A.F., Barreira, S.V., Costa, A.S., Alves, R.C., Oliveira, M.B. (2014). Organic versus conventional tomatoes: influence on physicochemical parameter bioactive compounds and sensorial attributes. *Food Chem Toxicol*., *67,*139-144.

CHARACTERIZATION OF PDNİCO CATALYST ON UIO-66-NH_2BDC VS. PDNİCO-MOF-NH_2BDC

Noor Hayati Ridhwan[1], Najihah Syahbudin[1], Muhammad Shafie Norhisam[1], Norliza Dzakaria [1,2*], Nurul Auni Zainal Abidin[1]

[1]*Faculty of Applied Science, Universiti Teknologi MARA (UiTM), Cawangan Negeri Sembilan, Kampus Kuala Pilah, 72000 Kuala Pilah, Negeri Sembilan, Malaysia*

[2]*Advanced Material for Environmental Remediation (AMER) Research Group, Faculty of Applied Science, Universiti Teknologi MARA (UiTM), Cawangan Negeri Sembilan, Kampus Kuala Pilah, 72000 Kuala Pilah, Negeri Sembilan, Malaysia*

**norliza864@uitm.edu.my*

ABSTRACT

Developing efficient heterogeneous catalysts with high metal dispersion and good reusability is crucial to the catalytic activity. Herein, a metal organic framework (MOF) was used as an ideal support, like UiO-66-NH_2 to encapsulate PdNiCo nanoparticles via solvothermal methods. Most of the reported work is only focused on the single metal or two metal based MOFs and their application. This study aims to synthesis the PdNiCo-NH_2BDC and PdNiCo-UiO-66-NH_2BDC using the solvothermal method. The preparation of trimetallic, which is PdNiCo-NH_2BDC and PdNiCo-UiO-66-NH_2BDC, is characterized by using nitrogen adsorption-desorption analysis (Brunauer-Emmet-Teller, BET) and Fourier Transform Infrared Spectroscopy Attenuated Total Reflection (FTIR-ATR) spectroscopy. The result of FTIR-ATR shows the vibrational modes of molecules and can provide information about the functional group such as N-H stretching, O-H stretching, C-H stretching, C-O stretching, C-N stretching and CONH (DMF) stretching that are present in PdNiCo-UiO-66-NH_2BDC and PdNiCo-NH_2BDC, but the peak of Zr-O has present because the PdNiCo has embedded to UiO-66-NH_2BDC. Next, the result BET shows that PdNiCo-UiO-66- NH_2BDC has a larger surface area and pore volume compared to PdNiCo-NH_2BDC. As a result, PdNiCo-UiO-66-NH_2BDC shown the better characteristic due to the larger surface area compared to PdNiCo-NH_2BDC.

Keywords: Metal Organic Framework; PdNiCo-NH_2BDC; PdNiCo-UiO-66-NH_2BDC; FTIR-ATR; nitrogen adsorption-desorption analysis (Brunauer-Emmet-Teller, BET)

INTRODUCTION

Metal organic frameworks (MOFs), known as porous coordination polymers (PCPs), are materials. It is a novel permeable substance featuring a crystalline framework composed of three-dimensional structures formed through coordination bonds connecting metal ions or metal clusters with organic ligands. MOFs have open porous frameworks with periodic repetitive components, a large specific surface area, and a significant number of active sites [6]. MOFs are usually used as precursors for the annealing process to create materials based on transition metals or porous carbon nanomaterials, aiming to enhance the low conductivity of MOFs effectively [4}. However, monometallic MOFs explored as catalysts but face limitations like low catalytic activity and selectivity while bimetallic MOFs offer improvements over monometallic MOFs but still face challenges. Issues include suboptimal synergistic effects between the two metals, limited catalytic performance enhancement, and potential instability during prolonged use. While the metals that used were Pd, Ni and Co. The choice of these trimetallics which are PdNiCo-NH_2BDC and PdNiCo-UiO-66-NH_2BDC was made because Ni was selected due to its high electron transfer ability and larger electron occupancy [8], Pd has selective adsorption [2], and Co has various of versality of coordination [8]. Based on the distinct capabilities of each metal, this study will focus on the synthesis of a trimetallic MOF using a combination of Pd, Ni, and Co. In literature, the the synthesis of MOFs is reported using different methods which include solvothermal, microwave, ultrasonic, electrochemical, mechanochemical, solvent evaporation and ion thermal. Among the reported methods, solvothermal is mostly preferred due to its ease of operation, short reaction time, controllable reaction conditions and low-cost. In addition, the MOFs synthesized using the solvothermal method possess high-crystallinity, high-purity and superior properties compared to other methods of synthesis. In this work, we report that the preparation using the solvothermal method for the synthesis of PdNiCo-NH_2BDC and its comparison with PdNiCo-UiO-66-NH_2.

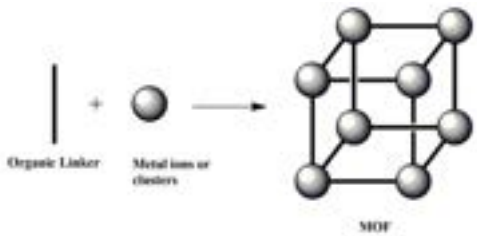

Figure 1. Structure of MOF

Sources: (Rafique, 2020)

MATERIALS AND METHODS

The study focuses on the synthesis of PdNiCo-NH_2BDC utilizing a modified technique from [1]. The synthesis used dissolved Ni $(NO_3)_2{\cdot}6H_2O$, Cobalt $(NO_3)2{\cdot}6H_2O$, Palladium $(NO_3)_2{\cdot}6H_2O$, 99% 2-aminoterephthalic acid ($C_8H_7NO_4$), and Zirconyl chloride octahydrate ($ZrOCl_2$) in a combination of Dimethylformamide (DMF), deionized water, and ethanol. The mixture was heated in a Teflon-lined autoclave for 48 hours before cooling, centrifugation, washing with DMF and ethanol, and drying in a hot air oven. The resulting black precipitate was collected, cleaned, and dried overnight. The resultant materials were identified as PdNiCo-NH_2-BDC. PdNiCo-UiO-66-NH_2BDC was the name given to the co-doped UiO-66-NH_2BDC containing Pd, Ni and Co. The precursor was dispersed in 15 mL of DMF solvent, then added to the solution while magnetically stirring. The mixture was transferred to a Teflon-lined autoclave and heated in a 90 ℃ oven for 48 hours. The synthesis material was identified as PdNiCo-UiO-66-NH_2-BDC.

Nitrogen adsorption desorption analysis (Brunauer-Emmet-Teller, BET) was used to investigate the surface area, pore volume and pore size of catalysts by using a Micromeritics ASAP 2020 instrument. Before the analysis is carried out, gaseous molecules that were chemically bound to the metal surface were removed by degassing at 300°C for 3 hours before analysing all samples under 77K liquid nitrogen environment to acquire adsorption isotherms. The surface chemistry of the PdNiCo-NH_2-BDC and PdNiCo-UiO-66-NH_2BDC was studied by using FTIR-ATR spectroscopy (Perkin Elmer Spectrum 400 FTIR-ATR Spectrometer). A small amount of the sample was added at the sample instrument. The IR spectrum was obtained at a resolution of 4 cm^{-1} over the range of 4000-600 cm^{-1} to observe the presence of functional groups.

RESULTS AND DISCUSSION

Nitrogen adsorption desorption analysis for textural properties.

The nitrogen adsorption-desorption isotherms and physical structural properties of PdNiCo-NH_2BDC and PdNiCo-UiO-66-NH_2BDC are presented in Table 1 and Figure 2, respectively. The adsorption isotherms refer to type IV according to IUPAC adsorption isotherms of classification, which indicate that PdNiCO-UiO-66-NH_2BDC and PdNiCo-NH_2BDC are mesoporous materials. PdNiCO-UiO-66-NH_2BDC and PdNiCo-NH_2BDC have BET surface areas of 14.6561 m^2/g and 459.7890 m^2/g, respectively. These values show that the addition of UiO-66 lead to an increase of BET surface area, the decreased of pore volume but for pore size there are insignificant change. Nevertheless, the direct NH_2BDC and UiO-66-NH_2BDC support cavities will have the typical pore diameter [2][7].

Table 1. BET surface area, pore size and pore volume of PdNiCO-UiO-66-NH_2BDC and PdNiCo-NH_2BDC.

MOF	BET surface area (m^2/g)	Pore Size (nm)	Pore Volume (m^2/g)
PdNiCo-NH_2BDC	14.6561	0.071109	18.2998
PdNiCo-UiO-66-NH_2BDC	459.7890	0.088553	9.5461

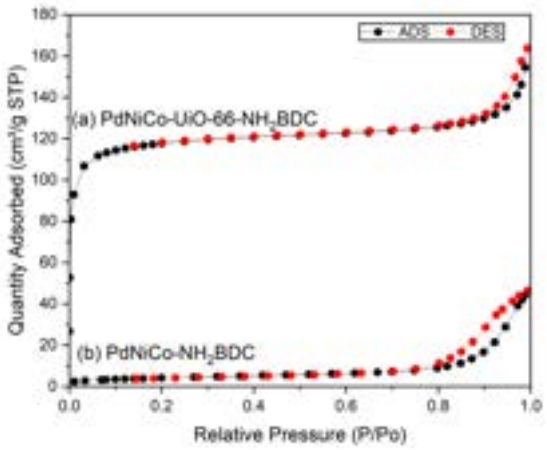

Figure 2. Nitrogen adsorption-desorption isotherm at 77K for (a) PdNiCo-UiO-66-NH_2BDC, (b) PdNiCo-UiO-66-NH_2BDC

FTIR analysis for determination of functional group.

FTIR analyses of PdNiCo-NH_2BDC and PdNiCo-UiO-66-NH_2BDC are presented in Figure 3 in the range of 650- 4000 cm^{-1}. The peaks appearing for PdNiCo-NH_2BDC and PdNiCo-UiO-66-NH_2BDC at 3284 to 3271 cm^{-1} and 3245 to 3267 cm^{-1} are related to the asymmetric and symmetric vibrations of amino groups. Generally, 2-aminoterephthalic acid (NH_2BDC) ligands exhibit broad peaks at 3390 cm^{-1} and 3479 cm^{-1} for both catalysts. The vibration peak of C-H assigned to the benzene ring for these two catalysts is the same, appearing at 768 cm^{-1}. Two peaks centered at 1571 and 1385 cm^{-1} correspond to the symmetric and asymmetric stretching of the C-O of the carboxylate group for PdNiCo- NH_2BDC, while the peaks appear at 1556 and 1385 cm^{-1} for PdNiCo-UiO-66-NH_2BDC. The bands at 1255 cm^{-1} and 1254 cm^{-1} can be assigned to the stretching vibrations of the C-N group, respectively. The presence of a peak related to CONH bands, resulting from coordinated DMF, is observed at around 1652 cm^{-1}. A distinguishing feature between PdNiCo-NH_2BDC and PdNiCo-UiO-66-NH_2BDC is the presence of a peak at 690 cm^{-1}, indicating the Zr-O signal [3][9].

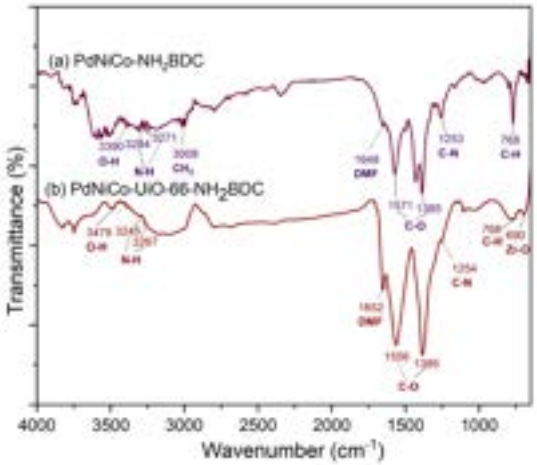

Figure 3. FTIR analysis of (a)PdNiCo-NH_2BDC (b)PdNiCo-UiO-66-NH_2BDC

CONCLUSION

PdNiCo-NH2BDC and PdNiCo-UiO-66-NH2BDC were synthesized using solvothermal synthesis. These materials were characterized by N2 adsorption-desorption isotherm analysis at 77K and FTIR-ATR analysis. The results indicate that PdNiCo was embedded into UiO-66-NH2 and fixed on the surface due to the presence of zirconium, which acts as a co-support for the metals. The FTIR spectra of PdNiCo-NH2BDC and PdNiCo-UiO-66-NH2BDC were almost identical, with the primary difference being the presence of Zr-O bands in PdNiCo-UiO-66-NH2BDC. Additionally, the surface area of PdNiCo-UiO-66-NH2BDC was observed to be higher compared to PdNiCo-NH2BDC. Surface morphology analysis indicated an enhancement in the porous structure of the material after PdNiCo was embedded into UiO-66-NH2. PdNiCo-UiO-66-NH2BDC exhibited higher activity due to its increased surface area, pore size, and pore volume compared to PdNiCo-NH2BDC.

REFERENCES

[1] Chen, C., Tuo, Y., Lu, Q., Lu, H., Zhang, S., Zhou, Y., Zhang, J., Liu, Z., Kang, Z., Feng, X., & Chen, D. (2021). Hierarchical trimetallic Co-Ni-Fe oxides derived from core-shell structured metal-organic frameworks for highly efficient oxygen evolution reaction. *Applied Catalysis. B, Environmental*, *287*, 119953.

[2] Guan, Q., Wang, B., Chai, X., Liu, J., Gu, J., & Ning, P. (2017b). Comparison of Pd-UiO-66 and Pd-UiO-66-NH 2 catalysts performance for phenol hydrogenation in aqueous medium. *Fuel*, *205*, 130–141.

[3] [Khosravi, F., Gholinejad, M., Sansano, J. M., & Luque, R. (2022). Low-amount palladium supported on Fe-Cu MOF: Synergetic effect between Pd, Cu and Fe in Sonogashira-Hagihara coupling reaction and reduction of organic dyes. *Molecular Catalysis*, *522*, 112199.

[4] Leng, X., Zeng, J., Yang, M., Li, C., Vattikuti, S. V. P., Chen, J., Li, S., Shim, J., Guo, T., & Ko,T. J. (2023). Bimetallic Ni–Co MOF@PAN modified electrospun separator enhances high- performance lithium–sulfur batteries. *Journal of Energy Chemistry*, *82*, 484–496.

[5] Liu, X., Yang, H., Diao, Y., He, Q., Lu, C., Singh, A., Kumar, A., Liu, J. & Lei, Q. (2022). Recent advances in the electrochemical applications of Ni-based metal organic frameworks (Ni-MOFs) and their derivatives. *Chemosphere*, *307*, 135729.

[6] Lv, W., Song, Y., Pei, H., & Mo, Z. (2023). Synthesis strategies and applications of metal–organic framework-quantum dot (MOF@QD) functional composites. *Journal of Industrial and Engineering Chemistry/Journal of Industrial and Engineering Chemistry - Korean Society of Industrial and Engineering Chemistry*, 128, 17–54.

[7] Rafique, M. M. (2020). Evaluation of metal–organic frameworks as potential adsorbents for solar cooling applications. *Applied System Innovation*, *3*(2), 1–20.

[8] Taherinia, D., Hatami, H., & Valadi, F. M. (2022). Trimetallic Co-Ni-Mn metal-organic framework as an efficient electrocatalyst for alkaline oxygen evolution reaction. *Journal of Electroanalytical Chemistry*, *922*, 116720.

[9] Zhu, P., Cao, H., Yang, H., Geng, M., Qin, S., Tan, L., Gao, X., & Wang, C. (2024). One-pot synthesis of Ni(II)-doped UiO-66-NH_2 for enhanced photocatalytic CO_2 reduction to CO with efficient charge transfer. *Applied Surface Science*, *652*, 159348.

DECOMPOSITION OF LIGNOCELLULOSE MATERIAL FROM COCONUT HUSK FIBER USING SULFATE-BASED IONIC LIQUID

Amni Husna Abdul Halim[1], Nur Amalina Mohd Amin[1], Salina Mat Radzi[1]

[1] *Faculty of Science and Technology, Universiti Sains Islam Malaysia, 71800 Nilai, Negeri Sembilan, MALAYSIA*

**nuramalina@usim.edu.my*

ABSTRACT

The increasing demand for sustainable agricultural practices has led to a rise in waste, particularly lignocellulose-rich biomass like coconut husk. The high lignin content and complex structure of lignocellulose materials pose significant challenges for efficient decomposition, making conventional technologies costly and environmentally impactful. To overcome these issues, ionic liquids (ILs), offer a promising solution due to their low vapour pressure, thermal stability, and high solubility. This research focuses on triethylammonium sulfate (TEAS), a sulfate-based IL synthesized with a 76% yield and characterized by Fourier Transform Infrared Spectroscopy (FTIR), Nuclear Magnetic Resonance Spectroscopy (NMR), and Thermogravimetric Analysis (TGA). TEAS was used to decompose coconut husk fibers at various temperatures (30, 80, and 130°C) and times (2 and 5 hours), analyzed using FTIR, X-ray Diffraction (XRD), and Field Emission Scanning Electron Microscopy (FESEM). Optimal decomposition conditions were found to be 80°C for 5 hours. The study demonstrates TEAS's effectiveness in lignocellulose breakdown, offering valuable insights into the structural changes in treated materials and presenting a sustainable solution for managing agricultural waste.

***Keywords*:** lignocellulose, coconut husk, ionic liquid, triethylammonium sulfate, decomposition

INTRODUCTION

Lignocellulose materials, also known as lignocellulose biomass, are abundant and cost-effective sources of biomass feedstock for the production of fuels and platform chemicals. These materials encompass a wide range of resources, including forestry waste such as forest cutting, reforestation, forest processing, and protection, as well as agricultural waste like crop straws, agricultural crops, and by-products. Additionally, lignocellulose biomass includes microalgae and urban solid wastes. Among the various lignocellulose materials, coconut husk fiber holds significant promise as a feedstock due to its abundant availability as a byproduct of the coconut industry.

Coconut husk fiber, also known as coir, forms the outermost coating of the coconut fruit and consists of lignocellulose components such as cellulose, hemicellulose, and lignin. Specifically, it contains 26.60% of cellulose $(C_6H_{10}O_5)_n$, 17.74% of hemicellulose $(C_5H_{10}O_5)_n$, and 41.18% of lignin $(C_{10}H_{11}O_{3.5})$ [16]. However, the high lignin content and complex structure of lignocellulose materials, including coconut husk fiber, present challenges in efficiently breaking down these materials into their constituent parts. Therefore, a crucial step in the process of lignocellulose biomass conversion is needed, known as decomposition.

Traditionally, various physical, chemical, and biological methods have been employed for lignocellulose decomposition. These methods include mechanical milling, pyrolysis, acid hydrolysis, alkaline treatment, enzymatic hydrolysis, and microbial fermentation. However, these conventional decomposition techniques often suffer from limitations such as high processing costs, process complexity, formation of degradation products, low selectivity, limited sugar release, and environmental impact [17].

Recently, the utilization of ionic liquids (ILs) as solvents for lignocellulose decomposition has emerged as a promising alternative. ILs are salts composed of organic cations and organic or inorganic anions that remain in a liquid state at room temperature. They possess unique properties, including low vapour pressure, good thermal stability, and high solubility for lignocellulose components. ILs are chemically inert and can effectively dissolve and disrupt the lignocellulose structure, facilitating the release of cellulose and hemicellulose for further conversion into valuable products [18].

Among the various IL types, sulfate-based ionic liquids have demonstrated significant potential in lignocellulose decomposition. These ILs typically consist of organic cations and sulfate anions, offering enhanced efficiency and selectivity compared to other ILs. The presence of sulfate anions improves product yield by separating it from the IL phase. Sulfate anions can interact with lignin, leading to its partial or complete dissolution, while the organic cations enhance the solubility of cellulose and hemicellulose.

METHODOLOGY

Biomass Preparation

Coconut husk sample as lignocellulose materials was obtained from hometown, Kg Banggol, Setiu, Terengganu. Coconut husk was washed, dried in the oven at 105 ºC for 2 to 3 days, and then ground into desired fine particles. Then, it was kept for further used.

Synthesis of Ionic Liquid

The synthesis of TEAS was conducted in a 250 ml round-bottomed flask immersed in an ice bath and fitted with a reflux condenser, following the method reported by [11]. 125 mL of 2M sulfuric acid (1 mol) and 25 mL methanol were added dropwise into 35 mL triethylamine (1 mol). The reaction mixture was stirred and heated at 70°C for 3 hours under a circulating water bath to ensure complete reaction. After cooling down, the mixture underwent a washing process with diethyl ether twice to remove impurities. Subsequently, the methanol content was evaporated by using a rotary evaporator. The synthesized TEAS was then characterized using FTIR, NMR, and TGA.

Decomposition of Lignocellulose Material

The dissolution of the coconut husk biomass in ILs was conducted following the procedure described in [12]. The dissolution process was performed in a 200 mL beaker, where 1g of coconut husk was introduced to 27 mL TEAS in a ratio of 1:20. This process was carried out for a duration of 2 hours. Subsequently, the beaker was placed on a heating block and stirred using a magnetic stirrer. The research involved varying the parameters of temperature and time, specifically exploring temperature ranges spanning from 30 to 80 °C and 130 °C, along with varying time intervals of 2 hours and 5 hours.

Upon completion of the dissolution process, the samples were removed from the heaters and allowed to cool down until they reached a room temperature of approximately 28-30 °C. The precipitated sample was rinsed three times with ethanol and filtered through vacuum filtration. Then, the samples were dried for approximately 24 hours at 110 °C in an oven.

RESULTS

Synthesis of triethylammonium sulfate [TEA][H_2SO_4]

The synthesized triethylammonium sulfate ionic liquid is yellowish in colour, exists in a liquid state, and exhibits an oily texture, with a percentage yield of 76 %.

Characterization of Ionic Liquids

Fourier Transform Infrared Spectroscopy (FTIR)

The FTIR spectrum of TEAS shows peaks beyond 2700 cm^{-1} appearing in the ranges of 3250-3450 cm^{-1} and 3100-2900 cm^{-1}. The CH stretching vibration in IL cation is described in the 3100-2900 cm^{-1} range but it has low intensity due to strong NH stretching in the 3250-3450 cm^{-1} range, as noted by [13]. An absorption band around 1650-1580 cm^{-1} indicates NH bending in amine groups. Further bands are seen at 1400-1500 cm^{-1} and 1250-1391 cm^{-1}, corresponding to ─CH_2 and ─CH_3 vibrations in the N─CH_2─CH_3 groups, respectively. Peaks at 1200-1185 cm^{-1} are linked to S-O stretching in sulfate ions, while those at 850-870 cm^{-1} denote SO_2 groups from sulfuric acid. Additionally, a medium-intensity peak in the 1250-1020 cm^{-1} range suggests CN stretching in amine groups. The observed peaks closely resemble those reported by [13] and [14].

Nuclear Magnetic Resonance Spectroscopy (NMR)

In the ^{1}H NMR spectrum, a peak at 8.702 ppm indicates the NH bond, while peaks between 5.2-5.4 ppm and 1.3-1.45 ppm correspond to hydrogen bonding in CH_2 and CH_3 groups, respectively. The solvent peak is at 3.31 ppm. In the ^{13}C NMR spectrum, three peaks are noted which are 49.15 ppm for the solvent CD_3OD, around 47 ppm for carbon in CH_2 groups, and 8.6 ppm for carbon in CH_3 groups.

Thermogravimetric Analysis (TGA)

At ambient temperature (30 °C), TEAS experiences slight weight loss, likely due to solvent evaporation. This weight loss continues until 130 °C as volatile components are removed. From 100 °C to 290 °C, TEAS remains stable with a constant weight percentage, indicating thermal resilience. However, significant weight loss and decomposition occur between 320 and 500 °C, indicating the breakdown of the compound.

Decomposition of Lignocellulose Material

At 30°C, the ionic liquid turned from yellow to reddish-yellow. At 80°C, it became a slightly darker red. At 130°C, the color changed significantly to dark brown or black, indicating intense reactions and breakdown of organic compounds. The husk became limp, black, and charred, suggesting excessive thermal degradation at the highest temperature. The decomposition of coconut husk was lowest at 6.93% at 30°C for 2 hours and highest at 26.16% at 80°C for 5 hours, indicating a significant increase in decomposition with higher temperature and longer duration.

Characterization of Untreated and Treated Lignocellulose Materials

Fourier Transform Infrared Spectroscopy (FTIR)

The untreated husk exhibits characteristic peaks indicating the presence of hydroxyl groups, aliphatic C-H bonds, carbonyl groups, aromatic skeletal vibrations, and C-H bending vibrations, associated with cellulose, hemicellulose, and lignin. Upon treatment at 30°C and 80°C for both durations, the spectra show a decrease in transmittance in the 3200-3500 cm^{-1} region, suggesting reduced hydroxyl groups linked to lignin, along with alterations in carbonyl groups, aromatic skeletal vibrations, and lignin structures, indicating the selective impact of the ionic liquid on lignin components.

However, at 130°C for a 2-hour treatment, an unexpected increase in the lignin peak at 3200-3500 cm^{-1} suggests incomplete lignin removal. While the 5-hour treatment at this temperature reduces the hydroxyl groups, it is not as effective as at 80°C. The optimal parameters for efficient lignocellulose decomposition using TEAS are determined to be 80°C for a 5-hour treatment, as this condition provides the most effective lignin modification and removal, aligning with the desired outcome for coconut husk decomposition.

X-ray Diffraction (XRD)

The XRD peaks decrease in intensity with increasing temperature and treatment duration, indicating a disruption in the crystalline arrangement. At 30 °C, a noticeable decrease in crystal intensity occurs, while at 80 °C, a significant reduction is observed, especially after 5 hours. At 130 °C, the decrease is less prominent than at 80 °C. The combined effect of higher temperatures and extended treatment times enhances the ionic liquid's impact, promoting the decomposition of lignocellulose and the formation of amorphous materials.

The decrease in crystallinity correlates with the reduction in lignin content in the treated samples. Ionic liquids effectively break down lignocellulose by targeting lignin, disrupting the ordered arrangement of cellulose and hemicellulose. According to [15], higher temperatures cause cellulose to swell, leading to a disordered structure and reduced crystallinity (CrI). The sample treated at 80°C for 5 hours shows a significant CrI reduction to 29.59%, aligning with the XRD peak decrease. This substantial modification in the lignocellulose structure demonstrates the potential of ionic liquid treatment for applications in biofuel production or other value-added products.

Field Emissions Scanning Electron Microscopy (FESEM)

The FESEM micrographs comparing untreated and TEAS-treated coconut husk for 2 and 5 hours at different temperatures. The untreated husk has a smooth, fibrillary surface due to intact lignin and hemicellulose. After 2 hours of treatment, minimal changes occur at 30 °C, while at 80 °C, pores form, indicating lignin removal. At 130 °C, the structure is significantly disrupted. For 5-hour treatment, pores appear at 30 °C and become more pronounced at 80 °C, with high temperature at 130 °C causing considerable structural destruction. The treatment induces pore formation, enhancing surface accessibility and reactivity for subsequent processes.

DISCUSSIONS

FTIR spectroscopy reveals specific absorption bands related to molecular vibrations, which help to identify functional groups and confirm the presence of triethylammonium and sulfate ions. The characteristic peaks corresponding to NH and CH stretching vibrations, as well as S-O and SO_2 stretching, indicate successful

incorporation of these groups into the ionic liquid structure. NMR spectroscopy further complements this by providing detailed information about the chemical environment of hydrogen and carbon atoms in TEAS. The observed chemical shifts confirm the presence of triethylammonium groups and validate the synthesis. TGA analysis assesses the thermal stability of TEAS by tracking weight loss as a function of temperature. This analysis is crucial for understanding the thermal resilience of the ionic liquid, which is important for its applications in high-temperature processes. The observed weight loss patterns help to identify the temperature ranges where the ionic liquid remains stable or undergoes decomposition, ensuring its suitability for various applications.

FTIR analysis of untreated and treated biomass provides insights into the chemical changes occurring during treatment with TEAS. Changes in the intensity of specific peaks related to cellulose, hemicellulose, and lignin reveal the impact of ionic liquid treatment on the biomass. Specifically, reductions in peaks associated with lignin suggest partial removal or modification of lignin, a key component in the lignocellulose matrix. XRD analysis complements this by showing changes in the crystalline structure of the biomass. The disruption of the crystalline arrangement, observed as decreased peak intensity, indicates the breakdown of the ordered cellulose and hemicellulose structures. This disruption correlates with the removal of lignin and the formation of more amorphous materials. FESEM micrographs provide a visual representation of these structural changes, showing the development of pores and surface disruptions. The increased porosity and structural modifications enhance the biomass's accessibility and reactivity, suggesting improved effectiveness of the ionic liquid treatment in altering the biomass's physical and chemical properties.

CONCLUSION

In summary, the synthesis of triethylammonium sulfate (TEAS) was successful, with its structure confirmed by FTIR and NMR analyses and thermal stability up to 320°C shown by TGA. TEAS effectively decomposed coconut husks, with the most efficient results obtained at 80°C for 5 hours. This treatment led to significant reductions in lignin content and crystallinity, as well as increased porosity, making the biomass more accessible that had been confirmed by FTIR, XRD and TGA analysis. These findings indicate that TEAS has promising potential for improving biomass processing, especially for biofuel production, and further research could enhance its effectiveness and sustainability in this field.

ACKNOWLEDGEMENT

This study is supported by Universiti Sains Islam Malaysia grant (PPPI/USIM/FST/USIM/111623).

REFERENCES

[1] Saini, J. K., Saini, R., & Tewari, L. (2015). Lignocellulosic agriculture wastes as biomass feedstocks for second-generation bioethanol production: concepts and recent developments. 3 Biotech., 5(4), 337–353. https://doi.org/10.1007/s13205-014- 0246-5

[2] Wei, H., YingTing, Y., JingJing, G., Wenshi, Y., & Jun-Hong, T. (2017). Lignocellulosic Biomass Valorization: Production of Ethanol. In Elsevier eBooks (pp. 601–604). https://doi.org/10.1016/b978-0-12-409548-9.10239-8

[3] Zoghlami, A., & Paës, G. (2019). Lignocellulosic Biomass: Understanding Recalcitrance and Predicting Hydrolysis. Frontiers in Chemistry, 7. https://doi.org/10.3389/fchem.2019.00874

[4] De Oliveira Santos, V. T., Siqueira, G., Milagres, A. M. F., & Ferraz, A. (2018). Role of hemicellulose removal during dilute acid pretreatment on the cellulose accessibility and enzymatic hydrolysis of compositionally diverse sugarcane hybrids. Industrial Crops and Products, 111, 722–730. https://doi.org/10.1016/j.indcrop.2017.11.053

[5] Liu, Q., Luo, L., & Zheng, L. (2018). Lignins: Biosynthesis and Biological Functions in Plants. International Journal of Molecular Sciences, 19(2), 335. https://doi.org/10.3390/ijms19020335

[6] Mishra, Leena & Basu, Gautam. (2020). Coconut Fibre: Its structure, properties and applications.

[7] Kianfar, E., & Mafi, S. (2020). Ionic Liquids: Properties, Application, and Synthesis. Fine Chemical Engineering, 22–31. https://doi.org/10.37256/fce.212021693

[8] Zhang, Z., Jia, Q., & Liao, W. (2015). Progress in the Separation Processes for Rare Earth Resources. In Handbook on The Physics and Chemistry of Rare Earths (pp. 287– 376). Elsevier BV. https://doi.org/10.1016/b978-0-444-63483-2.00004-1

[9] De Vos, N., Maton, C., & Stevens, C. V. (2014). Electrochemical Stability of Ionic Liquids: General Influences and Degradation Mechanisms. ChemElectroChem, 1(8), 1258–1270. https://doi.org/10.1002/celc.201402086

[10] Almeida, R., Moreira, A., Moreira, D., Pina, M. E., Ferriani, M. D. G. C., Rasteiro, M. G., & Gamelas, J. a. F. (2022). High-performance delignification of invasive tree species wood with ionic liquid and deep eutectic solvent for the production of cellulose-based polyelectrolytes. RSC Advances, 12(7), 3979–3989. https://doi.org/10.1039/d1ra08410k

[11] Ziaei-Rad, Z., Fooladi, J., Pazouki, M., & Gummadi, S. N. (2021). Lignocellulosic biomass pre-treatment using low-cost ionic liquid for bioethanol production: An economically viable method for wheat straw fractionation. Biomass & Bioenergy, 151, 106140. https://doi.org/10.1016/j.biombioe.2021.106140

[12] Zakaria, S. M., Idris, A., & Alias, Y. (2017). Lignin Extraction from Coconut Shell Using Aprotic Ionic Liquids. Bioresources, 12(3). https://doi.org/10.15376/biores.12.3.5749-5774

[13] Khan, J., Muhammad, S., Shah, L. A., Ali, J., Ibrar, M., & Rehman, K. U. (2021). Synthesis, characterization and electrochemistry of triethyl ammonium sulphate ionic liquid. Zeitschrift Für Physikalische Chemie, 235(9), 1099–1111. https://doi.org/10.1515/zpch-2020-1704

[14] Nurdin, M., Abimanyu, H., Putriani, H. N., Setiawan, L. O. M. I., Maulidiyah, M., Wibowo, D., Ansharullah, A., Natsir, M. F., Salim, L. O. A., Arham, Z., & Mustapa, F. (2021). Optimization of OPEFB lignocellulose transformation process through ionic liquid [TEA][HSO4] based pretreatment. Scientific Reports, 11(1). https://doi.org/10.1038/s41598-021-90891-3

[15] Zhang, J., Wang, Y., Zhang, L., Zhang, R., Liu, G., & Cheng, G. (2014). Understanding changes in cellulose crystalline structure of lignocellulosic biomass during ionic liquid pretreatment by XRD. Bioresource Technology, 151, 402–405. https://doi.org/10.1016/j.biortech.2013.10.009

[16] Sangian, H. F., & Widjaja, A. (2018). The Effect of Alkaline Concentration on Coconut Husk Crystallinity and the Yield of Sugars Released. IOP Conference Series: Materials Science and Engineering, 306, 012046. https://doi.org/10.1088/1757-899x/306/1/012046

[17] Chandel, H. K., Kumar, P., Chandel, A. K., & Verma, M. L. (2022). Biotechnological advances in biomass pretreatment for bio-renewable production through nanotechnological intervention. Biomass Conversion and Biorefinery. https://doi.org/10.1007/s13399-022-02746-0

[18] Rajan, K., Elder, T., Abdoulmoumine, N., Carrier, D. J., & Labbé, N. (2020). Understanding thein situstate of lignocellulosic biomass during ionic liquids-based engineering of renewable materials and chemicals. Green Chemistry, 22(20), 6748–6766. https://doi.org/10.1039/d0gc02582h

INVESTIGATION OF TWO NOVEL SYMMETRICAL AMIDE COMPOUNDS AS POTENTIAL MOLECULAR RECEPTORS FOR CHROMATE AND PHOSPHATE ANIONS

Maisara Abdul Kadir [1*], Putri Hebat Burhani Mustafar [1], Aina Zulaikha Assuhaimi [1]

[1]*Faculty of Science and Marine Environment, Universiti Malaysia Terengganu, 21030 Kuala Nerus, Terengganu, MALAYSIA*

**maisara@umt.edu.my, phbbm017@gmail.com, ainazulaikha32@gmail.com*

ABSTRACT

This study presents the outcomes of anion titration studies of two potential molecular recptors, namely 1,2-bis[N, N'-6-(3-pyridylmethylamido)pyridyl-2-carboxyamido]propane (L1) and 1,2-bis[N,N'-6-(3-pyridylmethylamido)pyridyl-2-carboxyamido]hexane (L2). These two novel compounds, L1 and L2 were synthesized from nucleophilic substitution reactions which combines n-diamine (n=5,6) with N-6-[(3-pyridylmethylamino) carbonyl]-pyridine-2-carboxylic acid methyl ester, respectively. Fourier Transform Infrared (FTIR), Nuclear Magnetic Resonance (NMR), and Ultraviolet-Visible (UV-Vis) were used to fully characterized the synthesized compounds. Important significant peaks were found in the infrared spectra, with corresponding to (N-H),(C-H),(C=O),(C-N) and (C=C) ranges from 3299-3301 cm^{-1}, 2857-2931 cm^{-1}, 1664-1526 cm^{-1}, 1431-1367 cm^{-1}, and 788-848 cm^{-1}. Meanwhile, ^{13}C NMR showed the resonances for the carbon of alkyl, pyridine, and carbonyl groups in range of 22.09-28.75 ppm, 50.79 ppm, and 121.66-161.65 ppm, respectively. In the ^{1}H NMR spectra, the protons of alkyl, pyridine, and amide groups were detected at 1.35-1.59 ppm, 3.34-4.62 ppm, and 7.34-8.58 ppm, respectively. Compounds L1 and L2 exhibit absorption band at λ_max = 224, 368, and 370 nm when titrated with chromate anion, and absorbance at 226 and 354 nm when titrated with phosphate.
Keywords: anion, analyte, chromate, phosphate, diamide

INTRODUCTION

Amide is a flexible functional group that is employed in a wide range of industrial processes and chemical reactions. However, amides' reactivity and limited reaction conditions make their synthesis and manipulation difficult. The harsh reaction conditions required by many current methods for synthesizing amides, such as high temperatures, potent acids, or toxic compounds, limit the spectrum of possible substrates and make the process challenging to scale and maintain. To enable amide synthesis under more favorable conditions while preserving high yields and selectivity, novel synthetic techniques are required.

Unlike amines, which are basic, amides are neutral chemicals. Despite the fact that the C-N bond is generally coupled by a single bond that allows for unrestricted rotation, the amide linkage is planar. Amide was chosen for this study because it can recognize both the counter anion and the entering molecule through hydrogen bonding contact. Anion binding receptors are classified into two types: those that bind anions only by hydrogen bonding or ion-dipole interactions, and those that coordinate anions in Lewis acidic centers.

By taking the advantages of amide NH functional group, several anion receptor molecules were created with a particular scaffold, such as a U-shaped structure, to facilitate anion binding via amide NH moieties. Through hydrogen bonding, an *in situ* anion's pocket will naturally operate as anion binding host by having inward oriented N-H fragments such as amine as the binding site. Thus, in this study, two novel diamide compounds, 1,2-bis[*N,N'*-6-(3-pyridylmethylamido)pyridyl-2-carboxyamido]propane (L1) and 1,2-bis[*N,N'*-6-(3-pyridylmethylamido)pyridyl-2-carboxyamido]hexane with amide NH pockets suitable for binding anions are proposed as molecular receptor for oxyanions such as chromate and phosphate (Figure 1).

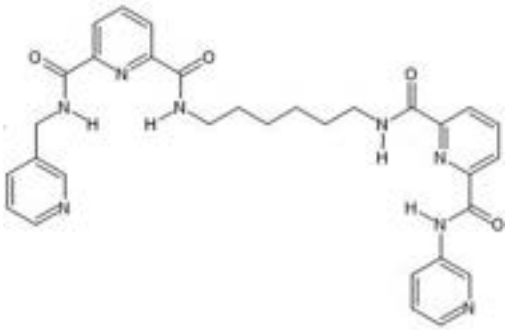

Figure 1. The structure of 1,2-bis[*N,N'*-6-(3-pyridylmethylamido) pyridyl-2-carboxyamido]hexane

Bis-pyridyl-amide ligands are excellent multi-N donor molecules and multi-O molecules, and they are a strong option for producing polyoxometalates-based metal-organic complexes (POM-based MOCs) because they can operate as both hydrogen bonding donors and acceptors (Wang et al., 2014). Their ability to meet metal ion coordination or anions requirements by bending their backbones for relevant twist angles and interacting with each other via hydrogen bonds between the amide groups. These flexible or semi-rigid bis-pyridyl–amide ligands have been tested as a great bridging ligand for constructing supramolecular networks and metal-organic frameworks.

Several ligands have structural and functional group similarities with bis-pyridyl-amide ligands and are frequently categorised accordingly. Bis-pyridyl ligands, or ligands having two pyridyl groups instead of an amide linker, can also bind to metal ions to create stable complexes. Bipyridine (2,2'-bipyridine), bis(pyridine), and phenanthroline are a few examples. A comparable ligand to bis-pyridyl-amide ligand is the bis-amine ligand, which has two amine groups and may likewise form stable complexes with metal ions. Bis(amine) ligands with different amine substituents are among them (Lee et al., 2022). Like bis-pyridyl-amide ligands, ligands with two oxazoline groups can bind with metal ions. One typical application for these ligands is in asymmetric catalysis (Satoh et al., 2012).

Due to their capacity to establish strong and specialised interactions with anions, amide ligands are extensively researched as anion receptors. They have a wide range of uses, including the detection of hazardous anions in aqueous solutions, biomedical diagnostics, and environmental monitoring. As anion transporters, amide-based substances can facilitate the flow of anions across membranes. These substances frequently have many amide groups, which interact with anions through hydrogen bonds to facilitate effective anion transport (Kaur et al., 2017).

METHODOLOGY

Toluene (40 mL) were mixed with *N*-6-[(3-pyridylmethyl amino)carbonyl]-pyridine-2-carboxylic acid methyl ester (0.4 g) and 1,5-pentadiamine/hexanediamine (1 M, 0.12 mL). They were refluxed in inert environment while being monitored using thin layer chromatography (TLC) until the reaction is completed. After that, the toluene was evaporated with a rotary evaporator, leaving the compound with a cream solid texture (Haris et al., 2021).

Anion Titration studies

The diamide compound and anions salt were dissolved in the solvent acetonitrile for anion recognition investigations. The product stock solution of 3 mL was placed into five volumetric flasks of 10 mL. In each volumetric flask (10µ L, 20 µL, 30 µL, 40 µL, and 50 µL), anions were titrated into the ligand. Each volumetric flask will have 10 µL of anions added.

RESULTS

UV-Vis titration studies were performed for L1.From the spectrum chromate anion, it shows that the C=O group of ligand undergoes n → π* at λ_{max} 240 nm and the pyridine group undergoes π → π* at λ_{max} 270 nm. From the spectrum phosphate anion, it shows that the C=O group of ligand undergoes n → π* at λ_{max} 240

nm and the pyridine groups undergoes $n \rightarrow \pi*$ at λ_{max} 285 nm. Electrons transferred from the benzene ring π-system to the C=O group triggered the electron transition in pyridine. In similar, the UV-Vis titration studies were performed for L2 with the corresponding set of anions in hexane to evaluate the binding interactions quantitatively. Molecular receptor in product shows an absorption band at λ_max = 224, 368, and 370 nm, with chromate respectively. The incremental addition of chromate ion to receptors resulted in a weakened adsorption which is hypochromic shift at 224 nm and an increase in the adsorption peak which is hyperchromic shift at 368 and 370 nm. Meanwhile, with phosphate, the molecular receptor in product shows an absorption band at λ_{max} = 222, 226, and 354 nm, respectively. The incremental addition of phosphate ion to receptor resulted in a hypochromic shift at 222 nm and increase in hyperchromic shift at 226 and 354 respectively.

CONCLUSION

In conclusion, the proposed molecular receptors displayed absorption bands with chromate anion at λ_{max} = 224, 368, and 370 nm, and absorbance with phosphate at λ_{max} = 222, 226, and 354 nm in UV spectra, that shown high potential to act as anion receptors for both chromate and phosphate.

ACKNOWLEDGEMENT

Authors would like to acknowledge Faculty of Science and Marine Environment for financial and scientific supports.

REFERENCES

[1] Wang, X., Luan, J., Lu, Q., Huang, L., Xu, C., & Liu, G. (2013). Four new metal–organic complexes by tuning the spacer length of flexible bis-pyridyl–bis-amide ligands: Assembly, structures and properties. Journal of Organometallic Chemistry, 740, 17–25. https://doi.org/10.1016/j.jorganchem.2013.04.040 [3]

[2] Lee, W., Liao, T., & Chen, J. (2022). Nickel (II) coordination polymers supported by bis-pyridyl-bis-amide and angular dicarboxylate ligands: Role of ligand flexibility in iodine adsorption. International Journal of Molecular Sciences, 23(7), 3603. https://doi.org/10.3390/ijms23073603

[3] Satoh, K., Kamigaito, M., & Sawamoto, M. (2012). Transition metal complexes for Metal-Catalyzed Atom Transfer Controlled/Living Radical Polymerization. In Elsevier eBooks (pp. 429–461). https://doi.org/10.1016/b978-0-444-53349-4.00072-8

[4] Kaur, N., Kaur, G., Fegade, U., Singh, A., Sahoo, S. K., Kuwar, A., & Singh, N. (2017). Anion sensing with chemosensors having multiple NH recognition units. TrAC Trends in Analytical Chemistry, 95, 86–109. https://doi.org/10.1016/j.trac.2017.08.003

POTENTIAL ANTI-OBESITY AND ANTIDIABETIC EFFECTS OF TURMERIC (*CURCUMA LONGA*) LEAF EXTRACTS

Yuswanie Md Yusof [1*], Nurul Syaza Rizuwan [1]

[1]*Faculty of Applied Sciences, Universiti Teknologi MARA Cawangan Perlis,*

Arau Campus, 02600 Arau, Perlis, MALAYSIA

**yuswanie824@uitm.edu.my*

ABSTRACT

The rising prevalence of obesity has been associated to the development of non-communicable diseases (NCDs), including stroke, cardiovascular disease, and diabetes. Despite available medications, there is an ongoing search for safe and cost-effective alternatives, and turmeric leaf (*Curcuma longa*) appears to be a promising candidate. This study aimed to evaluate the potential anti-obesity and antidiabetic properties of various extracts of turmeric leaf using *in vitro* procedures. The maceration extraction was employed by using solvents of different polarity viz. n-hexane, acetone and ethanol. Enzyme assay exhibited that the ethanolic extracts has significant activity against porcine pancreatic lipase at 500 µg/ml (IC_{50} = 123.16 µg/ml). Subsequently, the α-amylase inhibition assay revealed notable activities in all three extracts, with ethanolic extracts showed the highest inhibition (IC_{50} = 206.06 µg/ml), and was comparable to that of standard acarbose (IC_{50} = 128.91 µg/ml). In the reducing sugar content (RSC) assay, the ethanolic extracts exhibited the highest RSC value (304 ± 3.30 mg GE/g) than others. The dose-dependent relationship also proved that higher concentration of plant extracts resulted in increased inhibition. The findings of this study provide evidence that turmeric leaf possesses both anti-obesity and antidiabetic properties and could be developed as a natural remedy to combat chronic metabolic disorder like obesity and diabetes.

Keywords: pancreatic lipase, α-amylase, reducing sugar content, C. longa leaf

INTRODUCTION

Obesity is defined by abnormal or excessive fat build-up that can impair health. Reports from World Health Organization (WHO) has disclosed that the prevalence of obesity is an emerging problem globally, even in middle- and lower-income countries like Malaysia and is linked to several complications including stroke and cardiovascular diseases. Many obese also suffer from metabolic disorder such as type 2 diabetes mellitus (T2DM), which is characterized by upraised blood sugar levels (hyperglycemia) and abnormal lipid levels (dyslipidemia). This condition arises primarily due to insulin resistance, where the body's cells fail to respond effectively to insulin, a hormone crucial for regulating glucose and lipid metabolism (Abdella et al., 2024).

In recent years, preventive medicine has been integrated as one of the vital health strategies, and several reports have expressed that the ingestion of natural products with high polyphenol content can play a beneficial role in the prevention and amelioration of lifestyle-related diseases like obesity and diabetes (Núñez et al., 2023). Turmeric (*C. longa*) has gained a lot of interest for producing numerous complex compounds that are useful in foods such as spices, flavoring, and seasoning, as well as in the cosmetic and pharmaceutical industries (Sharma et al., 2022). Normally, utilization of turmeric is limited to rhizome, but the leaf part is also a rich source of bioactive compounds such as curcuminoids, flavonoids and terpenoids, which have potent anti-inflammatory, antioxidant, and antidiabetic properties (Fuloria et al., 2022). A study conducted by Zou et al., (2021) highlighted that dietary curcumin (natural flavonoids found in turmeric) could improve insulin sensitivity and reduced inflammation in rats with high-fat diet-induced obesity. Moreover, a study by Hodaei et al., (2019) has reported that curcumin supplement is effective in reducing blood glucose level and weight in T2DM patients.

Despite the reported biological properties and high nutritional values of turmeric leaf, the scientific research on its potential therapeutic effects in the management of obesity, diabetes, and related metabolic disorders is still limited. In this context, the purpose of this study was to evaluate the anti-obesity and antidiabetic properties of turmeric leaf extracts using *in vitro* method of enzymes inhibition of pancreatic lipase and α-amylase, as well as reducing sugar content analysis.

MATERIALS AND METHODS

Plant Material Preparation and Extraction

Fresh turmeric leaf was obtained from local market in Arau, Perlis. The plant sample was washed three times with distilled water to remove any impurities before being hot-air dried for 24 h at 60 °C in the oven. The dried leaf was then grounded into powder, sieved and stored at room temperature until further use. The extraction process was performed as previously reported by Kim et al. (2019), with slight modifications. Briefly, the powdered samples were macerated with n-hexane, acetone and warm ethanol in a separate beaker with ratio of 1:6 and left for 24 h at room temperature. The supernatant of each mixture was then be extracted and filtered through a 0.45 µm polyvinylidene difluoride (PVDF) filter.

Pancreatic Lipase Inhibitory Assay

The pancreatic lipase inhibitory effect of turmeric leaf was determined according to the method of Ngoh et al. (2017) using olive oil as a substrate. An aliquot of 500 µl of phosphate buffer, 100 µl of the plant extracts and 100 µl of olive oil were incubated at 37 °C for 10 min. Then, 100 µl of porcine pancreatic lipase solution was added and further incubated at 37 °C for 1 h. After placing in a boiling water bath for 10 min, the mixture was cooled with running water, and centrifuged at 2000 rpm for 10 min. The upper layer was discarded and titrated with 0.5 N NaOH, using phenolphthalein as an indicator.

α-amylase Inhibitory Assay

The inhibitory capacity of α-amylase was performed by reacting different concentrations of each of the plant extracts with α-amylase and starch solution, as described by Veena & Keshamma (2019) with slight modifications. The assay was carried out in an enzyme activity determination system of phosphate buffer saline (PBS) (0.1 M, pH 7.0). 500 µl of α-amylase (1 mg/ml) was pre-incubated for 10 min with varying concentrations of the plant extracts (100-500 µg/ml) and 500 µl of PBS. After pre-incubation, 500 µl of a 0.1% starch solution was added and further incubated at room temperature for 30 min and 1 ml of DNSA reagent was added to halt the reaction. The mixture was then incubated in a boiling water bath for 5 min before being cooled to room temperature and diluted to 10 ml with distilled water. The absorbance was recorded at 540 nm using UV-VIS. The results were presented as an inhibition percentage. The procedure was repeated using acarbose (1 mg/ml stock) as the positive control. The inhibitory activity was calculated using the following formula:

$$\%\ inhibition = \frac{\left(A_{control} - A_{sample}\right)}{A_{control}} \times 100$$

Reducing Sugar Content Assay

The 3,5-dinitrosalicylic acid (DNSA) method by Lam et al. (2021) was employed to determine the reducing sugar content (RSC), with minor modifications. The DNSA reagent was prepared by dissolving 1 g of DNSA and 30 g of sodium potassium tartrate in 80 ml of 0.5 N NaOH solution and heated until it was fully dissolved. The solution was cooled to room temperature and diluted to 100 ml with distilled water. For the analysis, 2 ml of DNSA reagent and 7 ml of distilled water were added to a test tube containing 1 ml of the plant extracts (1 mg/ml) and heated to 80 °C using water bath for 10 min. The mixture was then cooled using water bath for 20 min. The absorbance of the resulting solution was measured at 540 nm using UV-VIS. The RSC value was determined from the calibration curve of standard D-glucose (100-300 mg/l). The results were expressed as milligrams of D-glucose equivalent (GE) per gram of dry extract weight. A blank sample was prepared following the same procedure without the plant extracts.

Statistical Analysis

All experiments were conducted in triplicates and data obtained were analyzed by using standard deviation and mean wherever applicable.

RESULTS AND DISCUSSION

The capacity of extracts of turmeric leaf to mitigate complications implicated in obesity was assessed in the present study. It has been reported that inhibition of key digestive enzymes for lipids and carbohydrates can help in the management of obesity, diabetes, and other diseases linked to them (Magwaza et al., 2024). An enzyme called pancreatic lipase aids in the hydrolysis and digestion of fats to produce fatty acids and glycerols, which are absorbed into the blood stream and transported to various tissues. Another postprandial enzyme involved in the digestion of carbohydrates, α-amylase is essential for salivary and pancreatic secretions. Its inhibitors could decelerate food digestion and reduce post-meal blood sugar levels, making them a potential oral hypoglycemic agent for diabetes treatment (Guo et al., 2019). Furthermore, reducing sugars are a class of carbohydrates that could be oxidized and causes proteins, lipids and DNA to undergo glycation. This process leads to the gradual

cumulation of advanced glycation end products (AGEs) within cells and tissues, which are associated to the development of complications in diabetes. A study carried out by Al-Qarni, (2020) has found that the rise in amylase activity was correlated with higher levels of reducing sugars.

Thus, suppression of these enzymes' activity may prevent fat accumulation and hyperglycemia by impeding the digestion and absorption of lipids and carbohydrates, which produce absorbable fatty acids, triglycerides and glucose. In this study, turmeric leaf extracts significantly and dose-dependently inhibited the activities of porcine pancreatic lipase (PPL) (IC_{50} = ethanol: 123.16 µg/ml) and α-amylase (IC_{50} = ethanol: 206.06 µg/ml; acetone: 300.84 µg/ml; n-hexane: 250.14 µg/ml), respectively (Figure 1). The reducing sugar content (RSC) of turmeric leaf was found highest in the ethanolic extracts (304 ± 3.30 mg GE/g), compared to extracts of n-hexane (173.80 ± 3.27 mg GE/g) and acetone (128.73 ± 23.42 mg GE/g) (Figure 2). The RSC values in the turmeric leaf have not been reported till date. Nevertheless, these results could be improved through utilization of purified plant extracts instead of the crude samples.

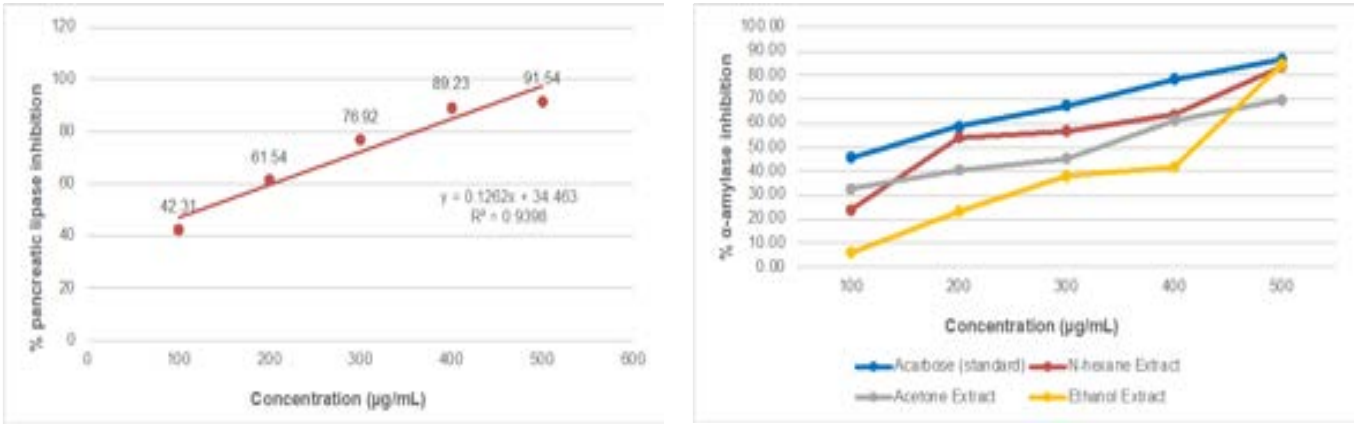

(a) (b)

Figure 1. (a) Inhibitory effects of ethanolic turmeric leaf extracts against porcine pancreatic lipase (PPL); (b) Inhibitory effects of turmeric leaf extracts against α-amylase

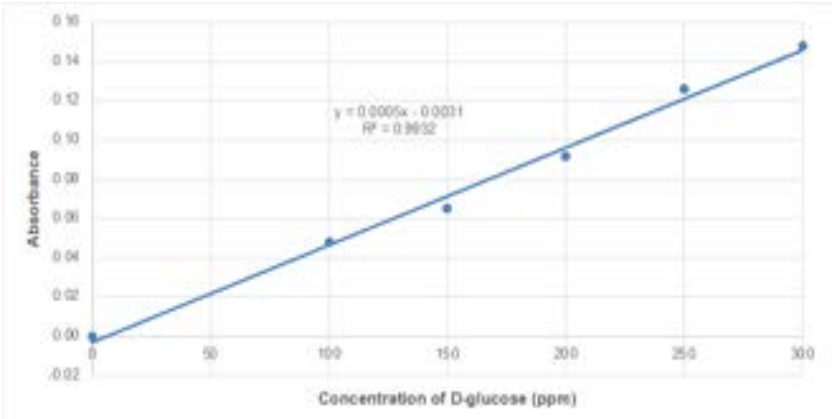

Figure 2. Calibration curve of standard D-glucose vs absorbance for reducing sugar content (RSC) analysis

Similar findings were observed in a previous study by Upreti et al., (2019), whereby the ethanolic extracts of *Eucalyptus camaladulensis* Dehnh leaves showed both PPL and α-amylase inhibition. The ability of turmeric leaf extracts to inhibit the activities of PPL and α-amylase indicates that they are potent inhibitors of lipids and carbohydrates hydrolyzing enzymes. Evidently, the inhibitory action of the ethanolic extracts against α-amylase was comparable to that of standard acarbose (IC_{50} = 128.91 µg/ml). These results also imply that turmeric leaf contains substances that are beneficial as a treatment for obesity and diabetes.

CONCLUSION

The present work concludes that the ethanolic extracts of turmeric leaf possess significant anti-obesity and antidiabetic properties. This was demonstrated by the ability to inhibit major digestive enzymes, which indicates its potential to suppress appetite and delay lipid and carbohydrate digestion and absorption. Further studies involving *in vivo* conditions are necessary to evaluate the effectiveness of the ethanolic extracts of turmeric leaf, which may be utilized as active ingredients in functional foods, food supplement, pharmaceuticals and natural therapies of obesity and diabetes.

REFERENCES

Abdella, F. I. A., Toumi, A., Boudriga, S., Alanazi, T. Y. A., Alshamari, A.K., Alrashdi, A. A. & Hamden, K. (2024). Antiobesity and antidiabetes effects of *Cyperus rotundus* rhizomes presenting protein tyrosine phosphatase, dipeptidyl peptidase 4, metabolic enzymes, stress oxidant and inflammation inhibitory potential. *Heliyon*, *10(2024)*, e27598.

Al-Qarni, S. S. (2020). Correlation between amylase activity & reducing sugar content in date fruits: A case of increased amylase activity with a proportional increase in reducing-sugar content of fruits. *Journal of Nutrition & Food Sciences*, *10*(*767*), 1-6.

Fuloria S., Mehta, J., Chandel, A., Sekar, M., Rani, N. N. I. M., Begum, M. Y., Subramaniyan, V., Chidambaram, K., Thangavelu, L., Nordin, R., Wu, Y. S., Sathasivam, K. V., Lum, P. T., Meenakshi, D. U., Kumarasamy, V., Azad, A. K. & Fuloria, N. K. (2022). A comprehensive review on the therapeutic potential of *Curcuma longa* Linn. in relation to its major active constituent curcumin. *Frontiers in Pharmacology*, *13*(*3*), 1–27.

Guo, Q., Chen, Z., Santhanam, R. K., Xu, L., Gao, X., Ma, Q., Xue, Z., & Chen, H. (2019). Hypoglycemic effects of polysaccharides from corn silk (Maydis stigma) and their beneficial roles via regulating the PI3K/Akt signaling pathway in L6 skeletal muscle myotubes. International Journal of Biological Macromolecules, 121, 981–988.

Hodaei H., Adibian, M., Nikpayam, O., Hedayati, M. & Sohrab, G. (2019). The effect of curcumin supplementation on anthropometric indices, insulin resistance and oxidative stress in patients with type 2 diabetes: A randomized, double-blind clinical trial. *Diabetology and Metabolic Syndrome*, *11*(*1*), 1–8.

Kim, S., Ko, S. C, Kim, Y. S, Ha, S. K, Park, H. Y, Park, Y. & Lee, S. H. (2019). Determination of *Curcuma longa* L. (Turmeric) leaf extraction conditions using response surface methodology to optimize extraction yield and antioxidant content. *Journal of Food Quality, 2019,* 1-8.

Lam, H. H., Nguyen, T. M. T., Do, T. A. S., Dinh, T. H. & Dang-Bao, T. (2021). Quantification of total sugars and reducing sugars of dragon fruit-derived sugar-samples by UV-Vis spectrophotometric method. *IOP Conference Series: Earth and Environmental Science*, *947*(*21*), 012041.

Magwaza, S. N., Erukainure, O. L., Olofinsan, K., Meriga, B. & Islam, M. S. (2024). Evaluation of the antidiabetic, antiobesity and antioxidant potential of *Anthophycus longifolius* ((Turner) Kützing). *Scientific African*, *23*(*2024*), e02051.

Ngoh, Y. Y., Choi, S. B. & Gan, C. Y. (2017). The potential roles of Pinto bean (*Phaseolus vulgaris* cv. Pinto) bioactive peptides in regulating physiological functions: Protease activating, lipase inhibiting and bile acid binding activities. *Journal of Functional Foods*, *33*, 67-75.

Núñez, S., Moliner, C., Valero, M. S., Mustafa, A. M., Maggi, F., Gómez-Rincón, C. & López, V. (2023). Antidiabetic and anti-obesity properties of a polyphenol-rich flower extract from *Tagetes erecta* L. and its effects on *Caenorhabditis elegans* fat storages. *Journal of Physiology and Biochemistry*, *79*, 427-440.

Sharma, N., Gupta, N., Orfali, R., Kumar, V., Patel, C. N., Peng, J. & Perveen, S. (2022). Evaluation of the antifungal, antioxidant, and anti-diabetic potential of the essential oil of *Curcuma longa* leaves from the North-Western Himalayas by *in vitro* and *in silico* analysis. *Molecules*, *27*(*22*), 7664.

Upreti, A., Byanju, B., Fuyal, M., Chhetri, A., Pandey, P., Ranjitkar, R., Bhatta, J. J. & Pandey, B. P. (2019). Evaluation of α-amylase, lipase inhibition and *in-vivo* pharmacological activities of *Eucalyptus camaladulensis* Dehnh leaf extract. *Journal of Traditional and Complementary Medicine*, *9*(*2019*), 312-318.

Veena, M. R., & Keshamma, E. (2019). Phytochemical analysis and evaluation of *in-vitro* alpha-amylase inhibition activity of rhizome extract of *Curcuma longa* (Turmeric). *International Journal of Current Microbiology and Applied Sciences*, *8*(*08*), 3130-3137.

Zou, T., Li, S., Wang, B., Wang, Z., Liu, Y., & You, J. (2021). Curcumin improves insulin sensitivity and increases energy expenditure in high-fat-diet–induced obese mice associated with activation of FNDC5/irisin. *Nutrition*, *90*, 111263.

TRACK C

APPLIED PHYSICS

CONVERGENCE CRITERIA FOR ITERATIVE VQE CALCULATIONS ON A QUANTUM COMPUTER

Ching-Hwa Wee[1], Meng-Hock Koh[1], Yung Szen Yap[1]

[1]*Universiti Teknologi Malaysia*

weechinghwa@gmail.com, kmhock@utm.my, yungszen@utm.my

ABSTRACT

In this study, we calculate the correlation energy in Helium-6 using Variational Quantum Eigensolver (VQE), with a full term unitary-paired-coupled-cluster-doubles ansatz (UpCCD) on various quantum computer simulators. We aimed to reduce the optimisation time steps involved in the VQE simulations. We implemented a set of termination criteria based on a fit of measured expectation value using a logarithmic function. One of the criteria that defines a proper termination involves using the fitted coefficients for two neighbouring fits, spaced 10 steps apart, where a small change in the fitting coefficient indicates termination. We showed that this set of termination criteria is effective at terminating non-converging and converging calculations, saving computing resources.

***Keywords*:** Nuclear pairing, Optimisation, Quantum Algorithm, VQE

INTRODUCTION

The revolutionary potential of quantum computers in quantum simulation has garnered significant attention as the field continues to mature. One area of research where this attention has notably increased is within the nuclear physics community, which has seen a growing application of quantum computing in nuclear structure. Quantum algorithms, particularly of variational quantum algorithms type such as VQE (Peruzzo et al., 2014), are especially attractive due to their relatively lower resource requirements and adaptability of the limitations of Noisy Intermidiate-scale quantum (NISQ) era hardware.

Despite the relatively lower resource requirements of VQE, implementation of deep quantum circuit depth necessary to prepare the ground state ansatz wavefunction is stifled. The constraints primarily lie in quantum hardware specification. To address these constraints, these nuclear structure studies were often limited to focus on either small nuclei (Kiss et al., 2022), toy models (Romero et al., 2022) or nuclear systems with small solution space. Otherwise, either simplifications of quantum circuits for ground state ansatz preparation were made (Dumitrescu et al., 2018) or state-vector simulations (Kiss et al., 2022) were carried out. We aimed to study the minimal quantum computer specifications required for nuclear structure calculations involving full-term ansatz. Full-term ansatz here refers to a unitary-paired-coupled-cluster-doubles (UpCCD) ansatz that consider first order trotterisation and full implementation of Jordan-Wigner mapping. Such study however, involve high calculation volumes. Here, we present a set of termination criteria based on a fit of mesured value using a logarithmic function to efficiently terminate calculations, saving computing resource.

THEORETICAL BACKGROUND

The hybrid quantum-classical VQE algorithm uses a quantum computer to compute the expectation value of a Hamiltonian, $\hat{H}$, with respect to a parameterised trial wavefunction $|\psi\rangle$; this expectation value is then to be minimsed by a classical computer. The expectation value is given by

$$E_{VQE} = \frac{\langle\psi\rangle}{\langle\psi\rangle} \geq E_0.$$

where the minimised E_{VQE} is an upper bound value of the actual ground-state energy E_0. In this study, we limit ourselves to solve a nuclear pairing problem in a ^{6}He nucleus, considering constant pairing matrix elements. The trial wavefunction used in this study is of type UpCCD, which composed of excitation operators that promote nucleons in pair. For optimisation, the Simultaneous Perturbation Stochastic Approximation (SPSA) optimiser (Spall, 1992) was employed in this study for its ability to tolerate moderate levels of noise.

The Hamiltonian to be solved is given by

$$\hat{H} = \sum_{i} \quad e_i \hat{a}_i^{\dagger} \hat{a}_i + \frac{1}{2} \sum_{ij} \quad V_{i\underline{i}j\underline{j}} \hat{a}_i^{\dagger} \hat{a}_{\underline{i}}^{\dagger} \hat{a}_{\underline{j}} \hat{a}_j,$$

where e_i is the one-body matrix representing single-particle energy and $V_{i\underline{i}j\underline{j}}$ is the two-body matrix elements that represents antisymmetrised pairing matrix elements. The single-particle energies were generated with a mean field description of the ^{6}He nucleus with nucleon-nucleon interaction of Skyrme (Beiner et al., 1975) type; and pairing is described by a constant pairing matrix elements generated by seniority force (Bonche et al., 1989) is given by

$$V_{i\underline{i}j\underline{j}} = \frac{G_q}{11 + N_q}$$

where G_q represents a pairing strength and N_q represents the nucleon number associated with the charge state $q \in \{n, p\}$ representing neutron and proton. We determine the correlation energy E_{corr}, defined by

$$E_{corr} = E - \sum_{i}^{A} \quad e_i \langle \hat{a}_i^{\dagger} \hat{a}_i \rangle$$

where E is the energy expectation value of the Hamiltonian, while the summation of the single-particle energy, e_i, involves the lowest occupied levels.

METHODS

The expectation value of the Hamiltonian operator was evaluated with respect to a unitary-paired-coupled-cluster-doubles (Lee et al., 2018) ansatz starting from a Hartree-Fock meanfield solution $|\Psi_0\rangle$. The ansatz is

$$|\psi_0\rangle = e^{\left(\hat{T}_2 - \hat{T}_2^{\dagger}\right)} |\Psi_0\rangle = e^{\sum_{ij} \quad \left(\theta_{i\underline{i}}^{j\underline{j}} \tau_{i\underline{i}}^{j\underline{j}}\right)} |\Psi_0\rangle.$$

where $\hat{T}_2$ (and its conjugate $\hat{T}_2^{\dagger}$) is a cluster operator that includes double excitation operators that promotes the nucleons in pairs. Assume real cluster amplitudes $\theta_{i\underline{i}}^{j\underline{j}} = \theta_{i\underline{i}}^{j\underline{j}*}$, the excitations operators and its conjugations can be rewritten as $\hat{T}_2 - \hat{T}_2^{\dagger} = \sum_{ij} \quad \left(\theta_{i\underline{i}}^{j\underline{j}} \tau_{i\underline{i}}^{j\underline{j}}\right)$, where $\tau_{i\underline{i}}^{j\underline{j}}$ composed of fermionic creation and annihilation operators. First order trotterisation and Jordan-Wigner (Jordan & Wigner, 1928) mapping were employed to convert the expectation value of the Hamiltonian with the ansatz into a circuit. This circuit ansatz is controlled by four parameters $\theta_{i\underline{i}}^{j\underline{j}}$ that represents all the possible pair excitations in a ^{6}He nucleus.

Next, optimisation of the set of parameters $\theta_{i\underline{i}}^{j\underline{j}}$ is done by configuring the classical optimiser SPSA with a learning rate given by a schedule as a function of iteration step k given by (Spall, 1992)

$$a_k = \frac{a}{(A + k + 1)^{\alpha}}$$

and the perturbation for each step was given by the function

$$c_k = \frac{c}{(k + 1)^{\gamma}}$$

where $\alpha = 0.602$, $\gamma = 0.101$, $A = 0$, $c = 0.1$ and a is calibrated to reduce the expectation value of the first iteration $k = 1$ by 1MeV.

All the calculations were started from the same excited state by setting all the initial parameters $\theta_{i\underline{i}}^{j\underline{j}}$ to zero except for $\theta_{1\underline{1}}^{3\underline{3}} = 1$ chosen arbitrarily, to mitigate barren plateaus as practised in (Kiss et al., 2022).

The set of termination criteria implemented were based on a fit of measured value using a logarithmic equation

$$y = m_k ln(x) + c_k$$

at specific optimisation step chosen such that $k = 10,20,30,\cdots,200$. The logarithmic fit takes into account all the preceding data up to the specific k-th step. The calculation were terminated whenever any of the following criteria is triggered:

Criterion 1: $m_k > 0$,

Criterion 2: $\|m_{10}\| < 0.1$,

Criterion 3: $\| \frac{m_k - m_{(k-10)}}{m_{(k-10)}} \| \leq \Delta m\%$.

The first criterion ensures that success iterations lead to a lower energy, ruling out cases with no obvious minimisation trend. In cases where the decrement in energy from $k = 1$ to $k = 10$ is rather small (defined as absolute value of m_{10} smaller than 0.1), calculation will be terminated. Calculations terminated with the first two criteria will be repeated.

Finally, the third criterion defines a proper way to terminate the calculation by comparing the change Δm, in the slope m_k between successive logarithmic fits (e.g. between m_{20} and m_{10} or between m_{60} and m_{50}). For Criterion 3, several values of $\Delta m \in \{5,8,10\}$ were examined and presented in the Results and Discussion section. Finally at termination, E_{corr} was extracted and an averaged value $\underline{E}_{corr}^{k}$ was obtained by taking an average of the 10 iterations from the last converged iteration.

Finally, the calculations described above were carried out on quantum computer simulators, hereforth called FakeJohors with various specifications, a state-vector simulator, and IBM 16-qubit FakeGuadalupe. FakeJohors utilised in calculations herein were modified from the FakeGuadalupe, a noisy quantum computer based on a real IBM 16-qubit quantum computer Guadalupe. We limited ourselves to modify only the coherence times and quantum errors of FakeJohors, while retaining other properties. Two FakeJohors are configured here, with coherence times of 5×10^{-3}ms and quantum errors of 10^{-3} for FakeJohor A; and 5×10^{1}ms and 10^{-7} for FakeJohor B.

RESULTS AND DISCUSSION

For the SPSA optimiser application, the convergence curve is characterised by a rapid decrease in the early iterations followed by a slower descent as it approaches convergence. The fitting function of $y = m_k ln(x) + c_k$ was chosen to capture such plateauing behaviour towards a convergence. Here, negative value of the coefficient m_k indicates a minimising trend and vice versa. In cases of intolerable noises, the convergence curve exhibits a fluctuating behaviour. The use of the logarithm fitting function takes in consideration the overall minimising trend, averaging out the fluctuating behaviour.

In Figure 1, the blue lines illustrate the extracted E_{corr} as a function of iterations for calculations simulated using FakeJohor A, FakeJohor B, a state-vector simulator and the IBM FakeGuadalupe. In Figure 1(a), a red solid line was fitted at $k = 10$, with the fitted coefficient $m_{10} = 1.346$. The red dash-dot line indicates the termination point at $k = 10$ triggered by the Criterion 1, where the positive m_{10} implies upward trend in the first 10 steps. Further iterations from iteration $k = 10$ show consistent fluctuations, where there is no obvious minimisation trend.

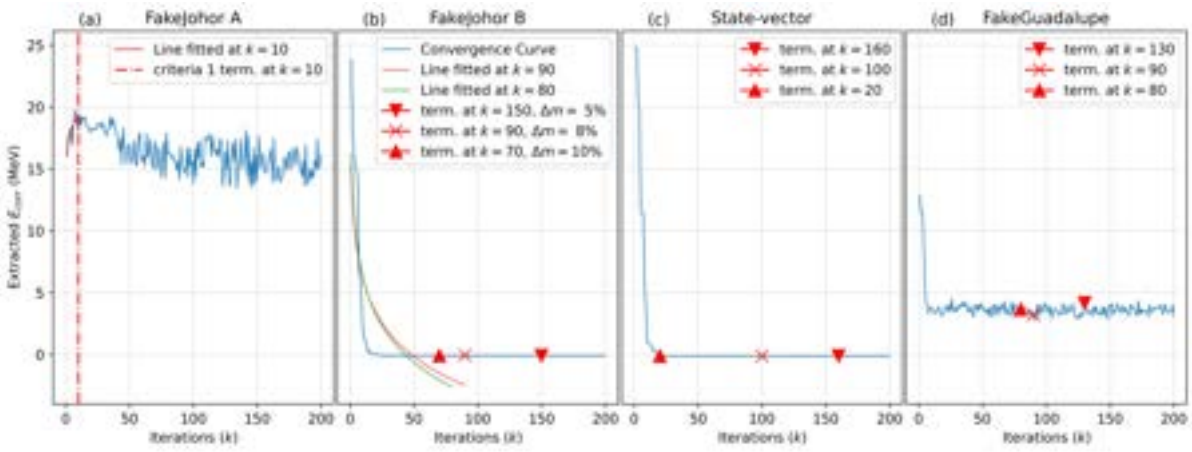

Figure 1. Convergence curve for VQE simulations using FakeJohorA with coherence times of 5×10^{-3}ms and quantum errors of 10^{-3}, FakeJohorB with 5×10^{1}ms and 10^{-7}, a state-vector simulator, and an IBM FakeGuadalupe. Termination Criterion 1 triggered is shown as a red verticle dash-dot line in (a). The markers ▲, x and ▼shows the termination triggered by Criterion 3 with $\Delta m = 10\%$, 8% and 5% respectively.

Meanwhile, the Criterion 2 was initially defined with the intention to terminate calculations with slow early descent, i.e. to consider only calculations with large decreases in the first 10 iterations. In many calculations where this set of termination criteria is applied, Criterion 2 was only triggered once.

In Figure 1(b) showing the convergence curve of simulation using FakeJohor B, two additional lines in green and red represent the fitted lines at iteration $k = 80$ and $k = 90$ respectively. The coefficients for the slopes at these two lines were fitted at $m_{80} = -2.868$ and $m_{90} = -2.725$. The relative difference in these 2 coefficient is less than 8%, and therefore marked by a marker, x, showing termination triggered by Criterion 3 with $\Delta m = 8\%$ at $k = 90$. The same process was also carried out for $\Delta m = 10\%$ and 5% in the same figure, and were marked by ▲ and ▼ respectively. The termination with a more a lenient $\Delta m = 10\%$ gives an earlier termination at $k = 70$, while the more stringent $\Delta m = 5\%$ terminates at later iteration at $k = 150$. Similar markings are noted for the simulations using state-vector and FakeGuadalupe in Figure 1(c) and 1(d), where they all showed earlier terminations than the maximum 200 iterations.

In Table 1, the values of $\underline{E}_{corr}^{k}$ terminated with Criterion 3 with different Δm are listed for the FakeJohor B and the state-vector simulation. The table also compares $\underline{E}_{corr}^{k}$ with the $\underline{E}_{corr}^{200}$, listing the absolute and relative differences. Despite being terminated in earlier iterations, all the results agree well within a small margin from the final $\underline{E}_{corr}^{200}$, with an exception to the state-vector simulation with the more lenient Criterion 3 ($\Delta m = 10\%$). The small margins for boths termination Criterion 3 with $\Delta m = 5\%$ and 8% reflect the good performance of the Criterion 3 employed.

Table 1. The values of $\underline{E}^{k}_{corr}$ at different $k_{term.}$ triggered by termination Criterion 3 with different Δm. These values are shown for FakeJohorB and state-vector simulations. At each termination, comparisons of $\underline{E}^{k}_{corr}$ with the $\underline{E}^{200}_{corr}$ at $k_{term.} = 200$ are listed as absolute and relative differences.

	Criterion 3 with	$k_{term.}$	$\underline{E}^{k}_{corr}$ (MeV)	$\underline{E}^{200}_{corr}$	$\underline{E}^{k}_{corr} - \underline{E}^{200}_{corr}$	Δ% from $\underline{E}^{200}_{corr}$
FakeJohor B	$\Delta m = 5\%$	150	-0.09487	-0.09190	-2.97E-03	3.23
	$\Delta m = 8\%$	90	-0.09548		-3.58E-03	3.90
	$\Delta m = 10\%$	70	-0.08996		1.94E-03	-2.11
State-vector	$\Delta m = 5\%$	160	-0.11713	-0.11717	4.00E-05	-0.03
	$\Delta m = 8\%$	100	-0.11705		1.20E-04	-0.10
	$\Delta m = 10\%$	20	0.33866		4.56E-01	-389.03

CONCLUSION

In calculations involving NISQ quantum computer with inherent noise, typical methods of comparing neighbouring values or simple moving averages no longer work. The termination criteria introduced mitigate this via a fit function, and terminates the calculation effectively, especially Criterion 1 that terminates fruitless calculations, and Criterion 3 that terminates converged calculations. In our work, using Criterion 3 with value of $\Delta m = 8\%$ is sufficient to balance the trade-off between computational resources and accuracy. With the set of termination criteria introduced, the calculations were successfully and consistently terminated at an earlier iterations, cutting the total number of iterations needed roughly in half.

REFERENCES

Peruzzo, A., McClean, J., Shadbolt, P., Yung, M.-H., Zhou, X.-Q., Love, P. J., Aspuru-Guzik, A., & O'Brien, J. L. (2014). A variational eigenvalue solver on a photonic quantum processor. *Nature Communications, 5(1)*.

Kiss, O., Grossi, M., Lougovski, P., Sanchez, F., Vallecorsa, S., & Papenbrock, T. (2022). Quantum computing of the 6Li nucleus via ordered unitary coupled clusters. *Physical Review C, 106(3)*.

Wee, Ching-Hwa, et al. "Quantum Computer Specification for Nuclear Structure Calculations." ArXiv.org, 2024, arxiv.org/abs/2406.16165.

Romero, A. M., Engel, J., Ho Lun Tang, & Economou, S. E. (2022). Solving nuclear structure problems with the adaptive variational quantum algorithm. *Physical Review. C, 105(6)*.

Dumitrescu, E. F., McCaskey, A. J., Hagen, G., Jansen, G. R., Morris, T. D., Papenbrock, T., Pooser, R. C., Dean, D. J., & Lougovski, P. (2018). Cloud Quantum Computing of an Atomic Nucleus. *Physical Review Letters, 120(21).*

Beiner, M., H. Flocard, Nguyen Van Giai, & Quentin, P. (1975). Nuclear ground-state properties and self-consistent calculations with the Skyrme interaction. *Nuclear Physics A, 238(1), 29–69*.

Spall, J. C. (1992). Multivariate stochastic approximation using a simultaneous perturbation gradient approximation. *IEEE Transactions on Automatic Control, 37(3), 332–341*.

Bonche, P., Krieger, S. J., Quentin, P., Weiss, M. S., Meyer, J., Meyer, M., Redon, N., Flocard, H., & Heenen, P.-H. . (1989). Superdeformation and shape isomerism at zero spin. *Nuclear Physics A, 500(2), 308–322*.

Lee, J., Huggins, W. J., Head-Gordon, M., & Whaley, K. B. (2018). Generalized unitary coupled cluster wave functions for quantum computation. *Journal of Chemical Theory and Computation*, *15*(1), 311–324.

Jordan, P., & Wigner, E. (1928). Über das Paulische ÄQuivalenzverbot. *Zeitschrift Für Physik, 47(9–10), 631–651*.

IMPACT OF NANOWIRE RADIUS ON BIOSENSOR PERFORMANCE: A SIMULATION STUDY USING NANOHUB'S BIOSENSOR LAB

Nur Sabrina Mohamad Zaini[1], Farah Liyana Muhammad Khir[1*]

[1]*School of Physics & Materials Studies, Faculty of Applied Sciences, Universiti Teknologi MARA (UiTM), Shah Alam*

*sbrnazni97@gmail.com, *farah668@uitm.edu.my*

ABSTRACT

This study investigates the reliability of NanoHub's BioLabSensor in simulating the performance of nanowire biosensors with varying radius. The primary objective is to systematically examine how nanowire radius impacts sensor efficiency and responsiveness. Using NanoHub's BioLabSensor, a series of simulations were conducted to evaluate the settling time of nanowire sensors across different analyte concentrations, maintaining consistent values for other parameters such as length, oxide thickness, and doping density. The findings reveal that smaller nanowire radius result in faster settling times, indicating higher sensitivity and responsiveness. Conversely, larger radius presented practical constraints, with non-finite and real function values at interval endpoints. The study highlights the importance of optimizing nanowire dimensions to enhance biosensor performance. Future research should focus on refining simulation tools and exploring the limitations observed in extreme cases to better accommodate a broader range of parameters.

Keywords: Nanowire biosensors, NanoHub BioLabSensor, radius size, settling time, simulation

INTRODUCTION

Nanowire biosensors, known for their high surface area-to-volume ratio and exceptional electrical properties, have garnered significant attention in biosensing. These sensors are crucial in applications such as medical diagnostics (He, et al., 2019)(Kumar et al., 2020), and biochemical research (Jadhav et al., 2021). According to Zhang et al. (2021), the sensitivity and efficiency of these sensors are heavily dependent on the radius of the nanowire.

This study focuses on the reliability of NanoHub's BioLabSensor in simulating the performance of nanowire sensors with varying radius. Sensor performance is evaluated by its settling time (duration for the sensor to stabilize and provide a reliable output in response to a change in input) across different analyte concentrations (Nair & Alam, 2006). The primary objective is to systematically examine key factors influencing nanowire sensor performance, focusing on the impact of nanowire radius on sensor efficiency and responsiveness. This research aims to enhance the understanding of nanowire biosensor efficiency and reliability by identifying optimal conditions through simulation.

Simulation results suggest that smaller radius results in faster settling times across all analyte concentrations, indicating higher sensitivity and responsiveness. However, simulations show limitations for large radius sizes, where interval endpoint function values were non-finite and real, suggesting practical constraints in the simulator's capability. The observations are important in pertaining to a knowledge of the nanowire structures design particularly with the aim to increase the sensitivity and responses of the biosensor.

MATERIALS AND METHODS

This study involves a comprehensive simulation approach using NanoHub's BioLabSensor to evaluate the performance of nanowire sensors with varying radius sizes. NanoHub's BioLabSensor was selected for its precise modeling capabilities.

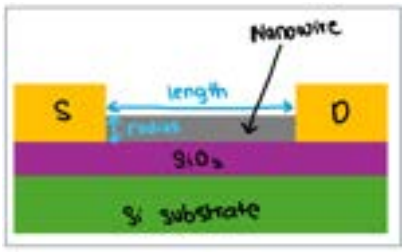

Figure 1. Structure of Nanowire Sensor

Table 1. Parameter of 6 nanowire sensor with different radius

	Radius	Length	Oxide Thickness	Doping Density
BioSensorLab	3.0×10^{-6} cm	5.0×10^{-4} cm	1×10^{-7} cm	1×10^{19} cC
My Study (1)	2.5×10^{-6} cm (Ryu, et al., 2010)			
My study (2)	3.5×10^{-6} cm (Spain, et al., 2015)			
My Study (3)	1.0×10^{-4} cm			
My Study (4)	1.0×10^{-5} cm			
My Study (5)	5.0×10^{-7} cm			

Each nanowire with mentioned radius was tested under the same environmental conditions. The simulator was configured to record the settling time of the sensor in response to analyte concentrations ranging from 1×10^{-15} M to 1×10^{-6} M. Settling time data were recorded and plotted to visualize the relationship between nanowire radius and sensor performance across these concentrations.

RESULTS AND DISCUSSION

An anomaly was noted during the simulation for My Study 3 with the radius of 1.0×10^{-4} cm, the largest radius, where the simulator failed to produce a finite and real function values, highlighting practical constraints in terms of the simulation capability.

Figure 2. Output of nanowire simulation for My Study (3)

Thus, My Study (4) with the radius of 1.0×10^{-5} cm was conducted, where now the sensor performance can be observed at range of 5.0×10^{-7} cm to 1.0×10-5 cm, as shown in Figure 3.

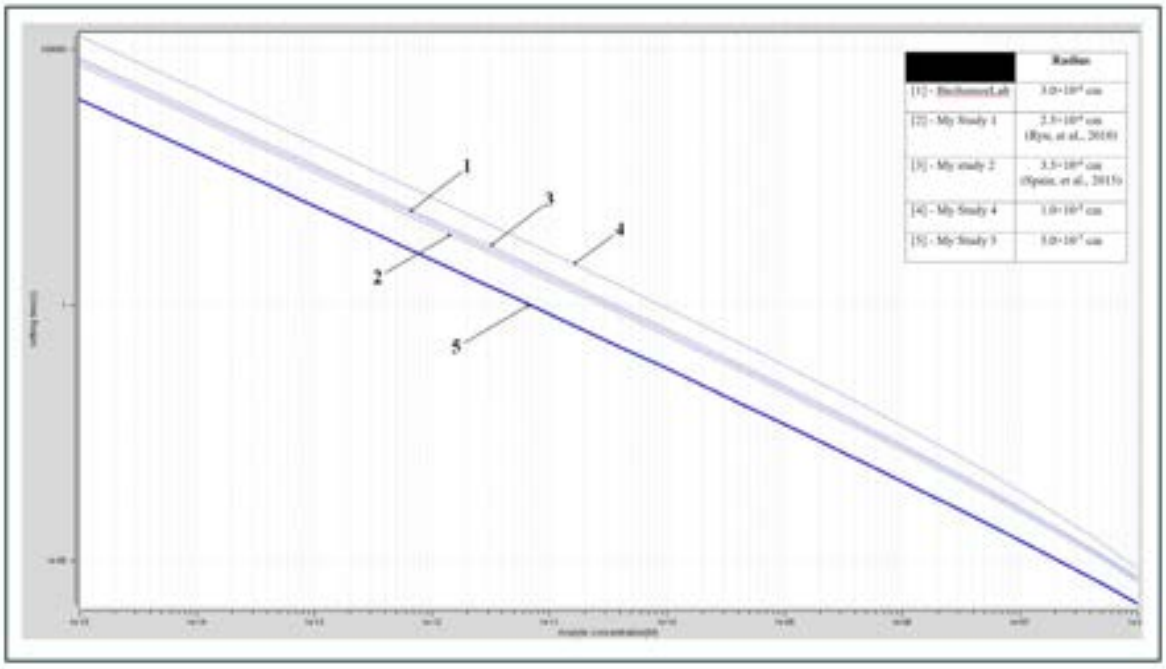

Figure 3. Graph of Settling time vs. Analyte Concentration for BioSensorLab, My Study (1), My Study (2), My Study (4), and My Study (5)

From Figure 3, a decreasing trend can be observed when the analyte concentration increases. It is suggested that the behavior indicates that the settling time of the nanowire biosensor decreases at higher concentrations of the analyte. From the results obtained, all the parameters used in this study (with various radius) exhibit a consistent downward trend, with slight variations between them. Here, the nanowire with radius of 5.0×10^{-7} cm as indicated by plot 5 in Figure 3 results in a faster settling time compared to the other studies. Meanwhile, the nanowire with radius of 1.0×10^{-5} cm as indicated in plot 4, results in a slowest settling time compared to the other studies. The settling time of a nanowire biosensor with a large radius is slower due to the increased conductance modulation achieved at higher target molecule densities with a larger radius of the silicon nanowire (Pawar, et al., 2019). Additionally, under flow conditions, the sensor length in the flow direction is a critical parameter limiting the concentration drop as the analyte flows past the sensor, affecting settling time (Jin, et al., 2019).

The detail from the plot can be seen from Table 2 below;

Table 2. Value of Settling Times at various analyte concentrations.

Analyte concentration (M)	Settling Time(s)				
	BioSensorLab	My Study (1)	My Study (2)	My Study (4)	My Study (5)
1e-15	59778.3	50210	69274	188820	10737.9
2.04336e-15	28345.5	23814.7	32840.7	89367.4	5103.91
2.21222e-11	1.51074	1.2774	1.74068	4.5465	0.287895
4.52035e-11	0.696769	0.589708	0.802154	2.08199	0.133866
4.8939e-07	1.22553e-05	1.09845e-05	1.3404e-05	2.2711e-05	3.66043e-06
1e-06	4.33613e-06	3.95007e-06	4.6748e-06	7.0871e-06	1.46527e-06

Based on Table 2, settling time for My Study (5) is the shortest among all the nanowires structure. The difference of settling time between BioSensorLab and My Study (5) at analyte concentration at1×10^{-6} M is 2.87086×10^{-6} seconds. Meanwhile at analyte concentration at 1×10^{-15} M, the difference is 49040.4 seconds. This proves that the radius of a nanowire significantly impacts the Settling Time when analyzing different target analyte concentrations in nanowire sensors. Miniaturizing biosensors into the nanoscale enhances signal-to-noise ratio by increasing signal density and reducing background signals, impacting the limit-of-detection and response time (Nair, & Alam, 2006). Yesayan's (2022) work underscores that thinner nanowires exhibit higher sensitivity to analyte concentrations, affecting the sensor's response time and overall performance.

CONCLUSION

In conclusion, this study has shown the capability and the limitation of the NanoHub BioLabSensor to simulate the performance of nanowire with various radius of sizes. The primary finding is that a decrease in nanowire radius correlates with a reduction in settling time, leading to faster sensor responses to varying analyte concentrations. This principle supports the notion that smaller nanowires enhance diffusion rates and sensitivity, thereby improving overall sensor performance. Specifically, the smallest radius which is 5.0×10^{-7} cm (as used in My Study 5) exhibited the shortest settling times across all analyte concentrations. It is recommended that future sensor designs should prioritize the optimization of nanowire dimensions within the identified effective range to maximize performance. Additionally, further study should explore the limitations observed in extreme cases and refine simulation tools to better accommodate a wider range of parameters.

REFERENCES

He, H., Dai, J., Dong, G., Shi, H., Wang, F., Qiu, Y., ... & Xiao, D. (2019). Self-replication-assisted rapid preparation of DNA nanowires at room temperature and its biosensing application. *Analytical chemistry*, *91*(4), 3043-3047.

Jadhav, M., Bhamare, S., Chauhan, V., Rao, S., Desai, N., & Subramaniam, S. (2021, October). Design Optimization and Implementation of Nanowire Based Biosensors. In *2021 2nd Global Conference for Advancement in Technology (GCAT)* (pp. 1-6). IEEE.

Jin, D. S., Brightbill, E. L., & Vogel, E. M. (2019). General model for mass transport to planar and nanowire biosensor surfaces. *Journal of Applied Physics*, *125*(11).

Kumar, H., Kuča, K., Bhatia, S. K., Saini, K., Kaushal, A., Verma, R., ... & Kumar, D. (2020). Applications of nanotechnology in sensor-based detection of foodborne pathogens. *Sensors*, *20*(7), 1966.

Nair, P. R., & Alam, M. A. (2006). Performance limits of nanobiosensors. *Applied physics letters*, *88*(23).

Pawar, A. V., Kanapally, S. S., Chougule, A. P., Waifalkar, P. P., More, K. V., Kamat, R. K., & Dongale, T. D. (2019). Simulation study of field-effect transistor based cylindrical silicon nanowire biosensor: effect of length and radius of the nanowire. *Журнал нано-та електронної фізики*, (11,№ 1), 01005-1.

Ryu, S. W., Kim, C. H., Han, J. W., Kim, C. J., Jung, C., Park, H. G., & Choi, Y. K. (2010). Gold nanoparticle embedded silicon nanowire biosensor for applications of label-free DNA detection. *Biosensors and Bioelectronics*, *25*(9), 2182-2185.

Spain, E., McCooey, A., Joyce, K., Keyes, T. E., & Forster, R. J. (2015). Gold nanowires and nanotubes for high sensitivity detection of pathogen DNA. *Sensors and Actuators B: Chemical*, *215*, 159-165.

Yesayan, A. (2022). Sensitivity Analysis of Nanowire FET Biosensor. *Armenian Journal of Physics*, *15*(4).

Zhang, G., Zeng, H., Liu, J., Nagashima, K., Takahashi, T., Hosomi, T., ... & Yanagida, T. (2021). Nanowire-based sensor electronics for chemical and biological applications. *Analyst*, *146*(22), 6684-6725.

FIRST-PRINCIPLES INSIGHTS INTO THE STRUCTURAL, ELECTRONIC AND LI-ION DIFFUSION PROPERTIES OF MN-DOPED LIFEPO$_4$ (LIFE$_{1-x}$MN$_x$PO$_4$) FOR X = 0.125, 0.25, AND 0.375

F.N. Sazman[1, a], F.W. Badrudin[2, b], N.H.M. Zaki[3, c], S.I. Ahmad[2, d], M.H. Samat[6, e], M.N.S. Saimin[3, f], O.H. Hassan[3, 4, h], M.Z.A Yahya[5, i], M.F.M. Taib[1, 3, j]*

[1]*Faculty of Applied Sciences, Universiti Teknologi MARA, 40450 Shah Alam, Selangor, Malaysia*

[2]*Centre for Defence Foundation Studies, Universiti Pertahanan Nasional Malaysia, Kem Sungai Besi, 57000 Kuala Lumpur, Malaysia*

[3]*Ionic Materials & Devices (iMADE) Research Laboratory, Institute of Science (IOS), Universiti Teknologi MARA, 40450 Shah Alam, Selangor, Malaysia*

[4]*Faculty of Arts and Design, Universiti Teknologi MARA, 40450 Shah Alam, Selangor, Malaysia*

[5]*Faculty of Defence Science & Technology, Universiti Pertahanan Nasional Malaysia, 57000 Kuala Lumpur, Malaysia*

[6]*Physics Section, School of Distance Education, Universiti Sains Malaysia, 1180 USM, Pulau Pinang, Malaysia*

[a]*fatinsazman29@gmail.com*, [b]*fadhlul@upnm.edu.my*, [c]*hamizahzaki@uitm.edu.my*, [d]*shahrulizwan@upnm.edu.my*, [e]*mohdhazrie@usm.edu.my*, [f]*syazwansaimin@ymail.com*, [g]*oskar@uitm.edu.my*, [h]*mzay@upnm.edu.my*, [i*]*mfariz@.uitm.edu.my*

ABSTRACT

This study investigates the structural, electronic, and Li-ion diffusion properties of Mn-doped $LiFePO_4$ ($LiFe_{1-x}Mn_xPO_4$, where x = 0.125, 0.25, 0.375) cathode materials for lithium-ion batteries using first-principles calculations with the GGA-PBE+U functional, as implemented in the CASTEP software package. The on-site Coulomb interactions were calculated with U values of 4.4 eV for Fe and 10.1 eV for Mn. The effects of varying Mn concentrations were systematically analyzed to identify the optimal doping level for enhancing the electrochemical properties of LFP. Results indicate that Mn substitution modifies the crystal structure and improves electronic conductivity by reducing the band gap, with $LiFe_{0.75}Mn_{0.25}PO_4$ showing the lowest band gap of 3.442 eV due to impurity energy levels from Mn 3d states observed in the density of states. Additionally, Mn doping enhances Li-ion diffusion by lowering the migration energy barrier, which is critical for high-rate performance. $LiFe_{0.875}Mn_{0.125}PO_4$ exhibited the lowest migration energy barrier of 0.68 eV, resulting in a significantly higher diffusion coefficient of 3.42×10-14 cm²/s compared to the pure $LiFePO_4$'s diffusion coefficient range of 10^{-14} to 10^{-13} cm²/s. Among the studied concentrations, $LiFe_{0.875}Mn_{0.125}PO_4$ demonstrated the best combination of structural stability, electronic conductivity, and Li-ion mobility, suggesting that Mn doping is an effective strategy for enhancing the performance of LFP-based cathodes. These findings provide valuable insights into the development of advanced cathode materials for next-generation lithium-ion batteries.

***Keywords*:** First-Principles, Cathode Materials, $LiFePO_4$, Manganese, Li-ion Diffusion

INTRODUCTION

The olivine-type $LiFePO_4$ (LFP) was first introduced by Padhi et al. [1] in 1997 as a potential cathode material for lithium-ion batteries. This material has garnered significant interest due to its high theoretical capacity, excellent stability and safety, cost-effectiveness and environmental friendliness [2]. The theoretical capacity of LFP is around 170 mAh/g which makes it a good choice for applications where long cycle life and safety are prioritized. The discharge voltage platform of LFP typically ranges from 3.4V to 3.5V which is lower than some other cathode materials like Nickel Manganese Cobalt (NMC) or Lithium Cobalt Oxide (LCO) but this is compensated by the excellent thermal stability and longer cycle life of LFP. Currently, LFP is primarily utilized in Electric Vehicles (EVs) and Hybrid Electric Vehicles (HEVs). However, despite its advantages, LFP cathode material is limited by low ionic and electronic conductivity. This results in reduced charge/discharge rates, lower energy density and diminished cycling performance, restricting its broader application in high-performance lithium-ion batteries [3]. To enhance its performance, various approaches have been explored including reducing particle size, applying carbon coatings and doping with different cations [4–6]. Among these methods, cation doping has emerged as particularly promising.

Recently, an increasing number of reports have emerged, documenting experimental studies focused on improving the electrochemical properties of LFP through the strategic doping of various elements. Moreover, the inherently poor electronic conductivity of LFP prevents the realization of its theoretical capacity. To address this challenge, Yamada et al. discovered that doping Fe ions in LFP with metal cations like Mn^{2+} can significantly enhance performance. Their research highlights that the most effective approach involves using $LiFe_{1-x}Mn_xPO_4$, which benefits from operating voltages in the optimal range of 3.5V to 4.1V [3]. Building on this, Guerfi et al. [7] state that $LiMnPO_4$ has a theoretical capacity (171 mAh/g) similar to LFP but offers about 20% higher energy density due to the higher redox potential of Mn^{3+}/Mn^{2+} (4.1 V versus 3.5 V for Fe^{3+}/Fe^{2+}). Hence, the selection of Mn as a cation dopant, owing to its ability to enhance energy density by leveraging the superior redox potential of the Mn^{3+}/Mn^{2+} couple, thus providing a strategic advantage over Fe^{3+}/Fe^{2+} in terms of voltage and overall electrochemical performance.

By using density functional theory (DFT) as implemented in computer code, the first-principles calculations on the physical and chemical properties of the solid materials can be performed. These include the properties such as structural, electronic as well as Li-ion diffusion properties [8–10]. The first-principles study of these properties on cation doping on LFP has been reported in previous research. For example, Wang et al. [11] demonstrated through both first-principles calculations and experimental work that doping with molybdenum (Mo) can improve the material's electronic conductivity. Similarly, Chung et al. [12] found that doping with niobium (Nb) enhanced the electrochemical properties of LFP. These studies suggest that doping can significantly improve certain performance aspects of the material. However, current research often overlooks how doping affects material stability which is crucial for battery performance. This research aims to provide a comprehensive view of how doping affects not only the electrochemical performance but also the atomic-scale structure and behavior of LFP materials with a particular focus on first-principles calculations of structural, electronic and Li-ion diffusion properties based on $LiFe_{1-x}Mn_xPO_4$ (x = 0,0.125,0.25,0.375). By integrating theoretical insights into Li-ion migration mechanisms, this study seeks to elucidate how dopants influence ion transport and contribute to performance enhancements at the atomic level.

COMPUTATIONAL METHOD

The first-principles calculations in this work are based on density functional theory (DFT) using exchange-correlation (XC) functional from generalized gradient approximation by Perdew-Burke-Ernzerhof [13]. The calculations were performed using Cambridge Serial Total Energy Package (CASTEP) computer code [14]. The pseudopotentials and plane-wave basis set were employed to calculate the structural, electronic and Li-ion diffusion properties of $LiFe_{1-x}Mn_xPO_4$ (x = 0,0.125,0.25,0.375). The configuration of Li-$1s^2$ $2s^1$, O-$2s^2$ $2p^4$, P-$3s^2$ $3p^3$, Fe-$3d^6$ $4s^2$ and Mn-$3d^5$ $4s^2$ are treated as the valence electrons for the Ultrasoft Pseudopotentials (USPP). Since using only the GGA-PBE generalization function would underestimate the electronic properties of LFP. Hence, the electronic properties show a substantial percentage percentage from the experimental data [15]. Therefore, the GGA+U method was used to describe the strongly localized electronic states of the transition metals in pure and doped compounds using the effective Hubbard U parameter with setting U = 4.4 eV to describe the Fe 3d state and U = 10.1 eV to describe Mn 4d state. This method is applicable to predict the properties of phosphate materials containing transition metals [16] The wave function for valence electrons was expended using a plane-wave basis set within a specified cut-off energy that was selected as 350 eV for pure LFP and $LiFeMnPO_4$. The Monkhorst-Pack scheme k-points were set as 5×6×7 for the pure LFP and 1×1×2 for the $LiFeMnPO_4$. For the geometrical optimization, the total energy was set using $5.0x10^{-6}$ eV/atom for total energy, 0.01 eV/Å for maximum force, 0.02 GPa for maximum stress and 5.0×10^{-4} Å for maximum displacement. As shown in **Figure 1** (a), the crystal structure of bulk LFP, depicted with an orthorhombic olivine structure in the *Pnma* space group was generated using Materials Studio 8.1 and consists of 28 atoms within its unit cells. The Mn doped LFP crystal structures with concentration of 0.125%, 0.25% and 0.375% as shown in **Figure 1** (b,c, and d) were illustrated by replacing Fe atom in 1×2×1 supercell consists of 56 atoms including 8 Li, 8 Fe, 8 P and 32 O.

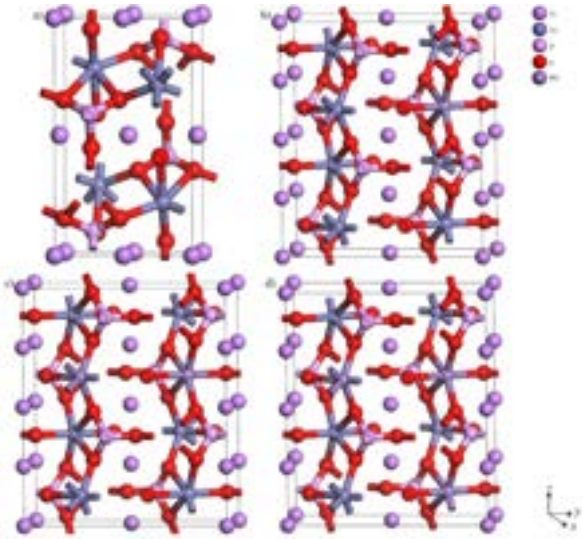

Figure 1. The crystal structures of (a) bulk $LiFePO_4$ (b) Mn doped $LiFePO_4$ with 0.125% concentration (c) Mn doped $LiFePO_4$ with 0.25% concentration and (d) Mn doped $LiFePO_4$ with 0.325% concentration

RESULTS AND DISCUSSION

Structural Properties

The calculated structural parameters of $LiFe_{0.875}Mn_{0.125}PO_4$, $LiFe_{0.75}Mn_{0.25}PO_4$, and $LiFe_{0.625}Mn_{0.375}PO_4$ are listed in **Table 1**. The obtained lattice parameters (a, b and c) and volume (V) from GGA-PBE functional are agreed with experimental reports and other theoretical calculations. Thus, the calculation method in this work is reasonable to be performed. To some extent, the structural parameters from LDA will be lower than the experimental values while GGA functional tends to overestimate the data. This shortcoming arises from the challenge of simulating the correlation interaction between electrons. As a result, the right electron density functional becomes difficult to calculate ref.

From **Table 1**, it can be seen that the Mn doping with different concentration does not destroy the original crystal structure of LFP, the lattice constant increases significantly and the cell volume increases. When Mn atoms are doped into the LFP with different concentration, the extra space is introduced and the change of ion radius leads to distortion of the crystal structure and expansion of the cell volume. On the one hand, the increase in the lattice constant caused by doping leads to lattice distortion of the crystal. This distortion may lead to changes in the interaction energy between atoms in the lattice which affects the electronic and energy band structure of the material. On the other hand, the increase in cell volume caused by doping can provide more space for the diffusion of lithium ions in the lattice. By expanding the cell volume, the movement path of lithium-ions in the lattice becomes longer, reducing the mutual collisions between ions thus lowering the migration energy barrier of ions and improving the mobility and conductivity of ions [17].

In summary, while Mn doping leads to structural changes such as increased lattice constants and cell volume, these modifications have positive effects on lithium-ion diffusion and battery performance. The reduced migration energy barrier and enhanced ion mobility can significantly improve charge/discharge rates and cycle stability making Mn-doped LFP materials more suitable for high-performance lithium-ion battery applications.

Table 1. Lattice parameters and volumes of $LiFe_{0.875}Mn_{0.125}PO_4$, $LiFe_{0.75}Mn_{0.25}PO_4$, and $LiFe_{0.625}Mn_{0.375}PO_4$ from theoretical and experimental data

Materials	Method	*a* (Å)	*b* (Å)	*c* (Å)	V (Å^3)
$LiFe_{0.875}Mn_{0.125}PO_4$	*This work* (GGA-PBE)	10.38	12.10	4.73	593.66
$LiFe_{0.75}Mn_{0.25}PO_4$		10.41	12.14	4.74	598.43
$LiFe_{0.625}Mn_{0.375}PO_4$		10.47	12.17	4.75	604.78
$LiFePO_4$	Exp [1]	10.33	6.011	4.69	291.40
		6.001	10.32	4.69	290.15
$LiFe_{0.99}Mn_{0.01}PO_4$		6.002	10.32	4.69	290.55
$LiFe_{0.97}Mn_{0.03}PO_4$	GGA-PBE [18]	6.004	10.32	4.69	290.76
$LiFe_{0.95}Mn_{0.05}PO_4$		6.01	10.32	4.69	290.93
$LiFe_{0.93}Mn_{0.07}PO_4$		6.01	10.33	4.69	291.21
$LiFe_{0.875}Mn_{0.125}PO_4$	GGA-PW91 [19]	10.36	12.10	4.73	593.48

Electronic Properties

The electronic properties of Mn-doped $LiFePO_4$ were investigated by examining the band structures of $LiFe_{0.875}Mn_{0.125}PO_4$, $LiFe_{0.75}Mn_{0.25}PO_4$, and $LiFe_{0.625}Mn_{0.375}PO_4$, as shown in **Figure 2** (a), (b), and (c), respectively. A common issue with density functional theory (DFT) calculations, particularly when using generalized gradient approximation (GGA) with PBE exchange-correlation functionals, is the underestimation of band gaps compared to experimental values. To address this, the GGA-PBE+U method was employed, which includes on-site Coulomb interactions and thus provides a more accurate representation of the electronic structure, yielding band gaps closer to the experimental range.The calculated band gaps for the Mn-doped compositions were found to be 3.625 eV for $LiFe_{0.875}Mn_{0.125}PO_4$, 3.442 eV for $LiFe_{0.75}Mn_{0.25}PO_4$, and 3.783 eV for $LiFe_{0.625}Mn_{0.375}PO_4$. These values are consistent with other theoretical works that report band gaps within the range of 3.4-4.0 eV, supporting the reliability of the GGA-PBE+U method in capturing the electronic behavior of these materials. Notably, the experimental band gap for undoped LFP is approximately 3.75 eV, which aligns closely with the calculated band gap for $LiFe_{0.625}Mn_{0.375}PO_4$, demonstrating the effectiveness of the GGA-PBE+U approach in replicating experimental results.

All three Mn-doped compositions exhibit a direct band gap with the valence band maximum and conduction band minimum occurring at the Q point, positioning the Fermi level at 0 eV on the energy axis. The introduction of Mn into the LFP lattice leads to the formation of impurity energy levels primarily from the Mn 3d states, which significantly influence the electronic properties of the material. These impurity levels reduce the band gap, thereby enhancing electronic conductivity by making it easier for electrons to be excited across the gap. Among the studied compositions, $LiFe_{0.75}Mn_{0.25}PO_4$ shows the lowest band gap of 3.442 eV, due to the pronounced presence of Mn impurity energy levels. This reduction in band gap facilitates improved electronic conductivity by providing additional pathways for charge carriers. The presence of these impurity energy levels not only narrows the band gap but also enhances the material's overall electronic properties, making Mn doping a viable strategy for enhancing the performance of $LiFePO_4$ in lithium-ion batteries. The improved conductivity resulting from Mn doping could lead to better battery efficiency and faster charge/discharge rates, making these materials more suitable for high-performance applications.

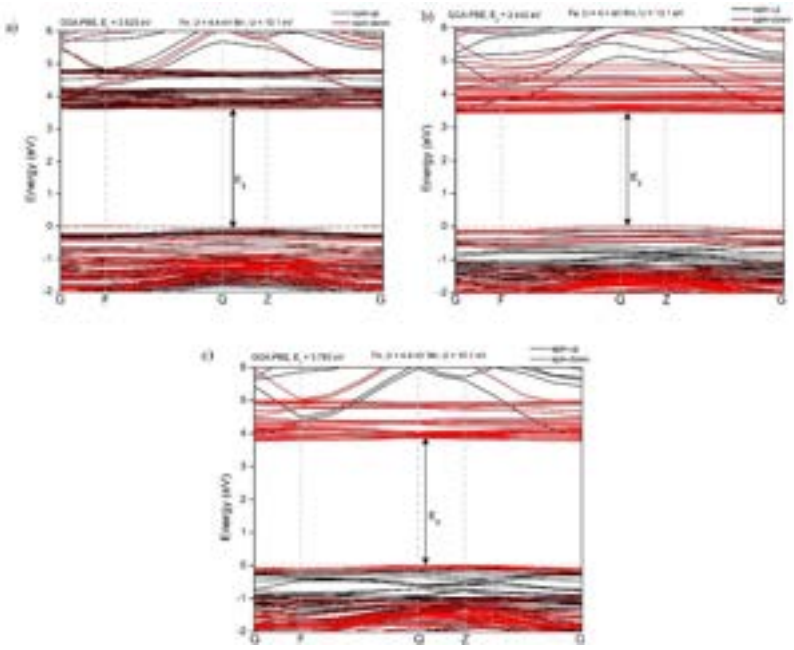

Figure 2. Calculated electronic band structures of (a) $LiFe_{0.875}Mn_{0.125}PO_4$ (b) $LiFe_{0.75}Mn_{0.25}PO_4$ and (c) $LiFe_{0.625}Mn_{0.375}PO_4$

The partial density of states (PDOS) analysis, as illustrated in **Figure 3**, provides a detailed understanding of how Mn doping affects the electronic structure of LFP. The PDOS for Mn 3*d* s, P 2*s*, P 2*p*, O 2*s* and O 2*p* states highlights the significant changes introduced by Mn doping. In undoped LFP, the electronic properties are primarily governed by the Fe 3*d* orbitals. However, upon introducing Mn, the Mn 3*d* states contribute new features to the band structure. This addition introduces impurity levels within the band gap, which are clearly visible in the PDOS. For instance, in $LiFe_{0.875}Mn_{0.125}PO_4$, the presence of Mn 3*d* states near the conduction band results in the lowest band gap of 3.442 eV. This reduction in the band gap is due to the pronounced Mn 3*d* states that enhance conductivity by facilitating easier electron transitions. Similarly, $LiFe_{0.75}Mn_{0.25}PO_4$ also exhibits a reduced band gap of 3.442 eV, attributed to substantial contributions from Mn 3*d* states, which improve the material's electronic conductivity. In contrast, $LiFe_{0.625}Mn_{0.375}PO_4$, although having a higher band gap of 3.783 eV, still shows significant Mn 3*d* effects. The higher band gap in this composition may result from increased scattering or localized states at higher Mn concentrations, which differently affect the electronic structure.

The PDOS analysis also provides insights into the contributions of the oxygen and phosphorus orbitals. The O 2*p* states, which are involved in bonding with Fe and P, interact significantly with Mn 3*d* states. These interactions are crucial in modifying the electronic properties of the material, as they influence the band structure and contribute to the observed reduction in the band gap. The O 2*p* states play a key role in the valence band and their alignment with Mn 3*d* states affects the electronic conductivity. Furthermore, the P 2*p* states, which interact with both the O 2*p* and *d* states, also impact the electronic behaviour. Although the P 2*s* states are involved in lattice bonding, have less direct influence on the band structure compared to the P 2*p* states.

Overall, the PDOS analysis underscores the impact of Mn doping on LFP electronic structure. The introduction of Mn 3*d* states results in a significant reduction in the band gap, enhancing the electronic conductivity. The interaction among Mn 3*d*, O 2*p*, and P 2*p* states plays a crucial role in this process, highlighting the effectiveness of Mn doping in improving the performance of LFP for lithium-ion batteries. This comprehensive understanding of the electronic changes induced by Mn doping demonstrates its potential to enhance the cathode materials suitability for high-performance applications.

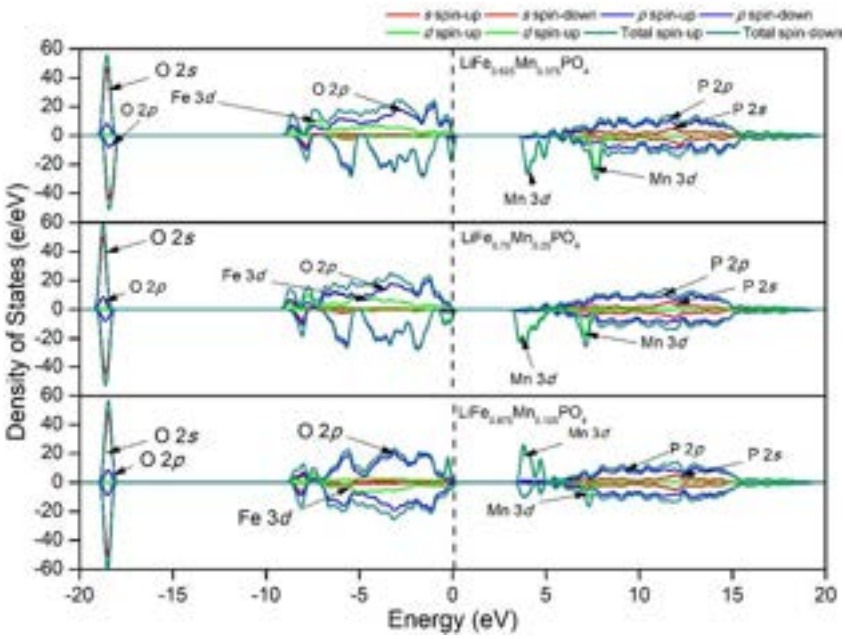

Figure 3. The calculated PDOS of (a) $LiFe_{0.875}Mn_{0.125}PO_4$ (b) $LiFe_{0.75}Mn_{0.25}PO_4$ and (c) $LiFe_{0.625}Mn_{0.375}PO_4$ obtained from DFT+U calculations

Li-İon Diffusion Properties

The multiplicity performance of lithium-ion batteries measures the performance of the battery when it is charged and discharged at high multiplicity over a short period of time, and this performance metric is influenced by the diffusion rate of lithium-ions [20]. In this paper, the search transition state theory was calculated to investigate and gain insight into the migration behavior of lithium ions in battery materials in order to provide more accurate guidance for optimizing the performance of lithium-ion batteries as shown in **Figure 4**. Experiments and theories show that the migration of lithium-ions in the (010) direction is a relatively stable direction. It is the main direction of lithium-ion insertion and extraction in the material [21]. To study the migration behavior of lithium ions in the doped system, the investigation focused on exploring the migration channels of lithium ions along the b-direction. By the transition state search method, we removed a lithium atom in the the doped supercell, constructed lithium vacancies and calculated the diffusion energy barrier of lithium-ions from the initial to the final state.

Zaki et al. states that the migration energy of pure LFP was 0.838 eV. Based on the data in **Figure 4**(a and b), the migration energy of lithium ions in the intrinsic of $LiFe_{0.875}Mn_{0.125}PO_4$ and $LiFe_{0.75}Mn_{0.25}PO_4$ are 0.68 eV and 0.69 eV which are lower than pure LFP which is consistent with the previous results [22]. Meanwhile, the migration energy of $LiFe_{0.625}Mn_{0.375}PO_4$ is higher than pure LFP which is 0.85 eV as shown in **Figure 4** (c) due to thet lithium-ions located in the b channel diffuse in an arc in the channel under the electrostatic repulsion with the neighboring Fe ions. The lowest migration energy in $LiFe_{0.875}Mn_{0.125}PO_4$ indicates that lithium ions can move more easily through the lattice, suggesting higher ionic conductivity compared to the other compositions. It has been shown that the diffusion constant of lithium-ions in doped LFP can be improved by decreasing the activation energy, thus improving its performance. To further investigate the effect of doping on the diffusion properties of lithium-ions, the diffusion coefficient of $LiFe_{0.875}Mn_{0.125}PO_4$, $LiFe_{0.75}Mn_{0.25}PO_4$ and $LiFe_{0.625}Mn_{0.375}PO_4$ have been calculated using equation (1).

$$D = a^2 \, exp \, exp \, (-\frac{E_{act}}{K_B T}) \quad (1)$$

Where a represents the distance between the $LiFe_{0.875}Mn_{0.125}PO_4$, $LiFe_{0.75}Mn_{0.25}PO_4$ and $LiFe_{0.625}Mn_{0.375}PO_4$ system bouncing along the b direction, ν is estimated to be 10^{13} Hz, K_B is the Boltzmann constant, T is the temperature of the system (300 K), and E_{act} represents the activation energy. After calculation, the diffusion coefficient of lithium-ions in the $LiFe_{0.875}Mn_{0.125}PO_4$, $LiFe_{0.75}Mn_{0.25}PO_4$ and $LiFe_{0.625}Mn_{0.375}PO_4$ are 3.42×10^{-14}, 2.27×10^{-14} and 2.30×10^{-15} cm^2/s. The diffusion coefficients of lithium ions were calculated for the Mn-doped $LiFePO_4$ systems, revealing significant differences in ion mobility among the various compositions. For $LiFe_{0.875}Mn_{0.125}PO_4$, the diffusion coefficient was found to be 3.42×10^{-14} cm^2/s, which is the highest among the studied compositions. This high diffusion coefficient is consistent with its lower migration energy barrier of

0.68 eV, indicating that lithium ions can migrate more easily within this material. In contrast, $LiFe_{0.75}Mn_{0.25}PO_4$ exhibited a diffusion coefficient of 2.27×10^{-14} cm²/s, slightly lower than that of $LiFe_{0.875}Mn_{0.125}PO_4$, corresponding to its slightly higher migration energy of 0.69 eV. Meanwhile, $LiFe_{0.625}Mn_{0.375}PO_4$ showed a significantly reduced diffusion coefficient of 2.30×10^{-15} cm²/s, which can be attributed to its higher migration energy of 0.85 eV. The decrease in the diffusion coefficient with increasing Mn content suggests that while Mn doping can enhance the electronic conductivity of $LiFePO_4$, excessive Mn concentrations may hinder lithium-ion mobility due to the increased migration barriers. Therefore, $LiFe_{0.875}Mn_{0.125}PO_4$ strikes the best balance between maintaining low migration energy and achieving a high diffusion coefficient, making it the most promising candidate among the studied compositions for enhancing lithium-ion transport in cathode materials.

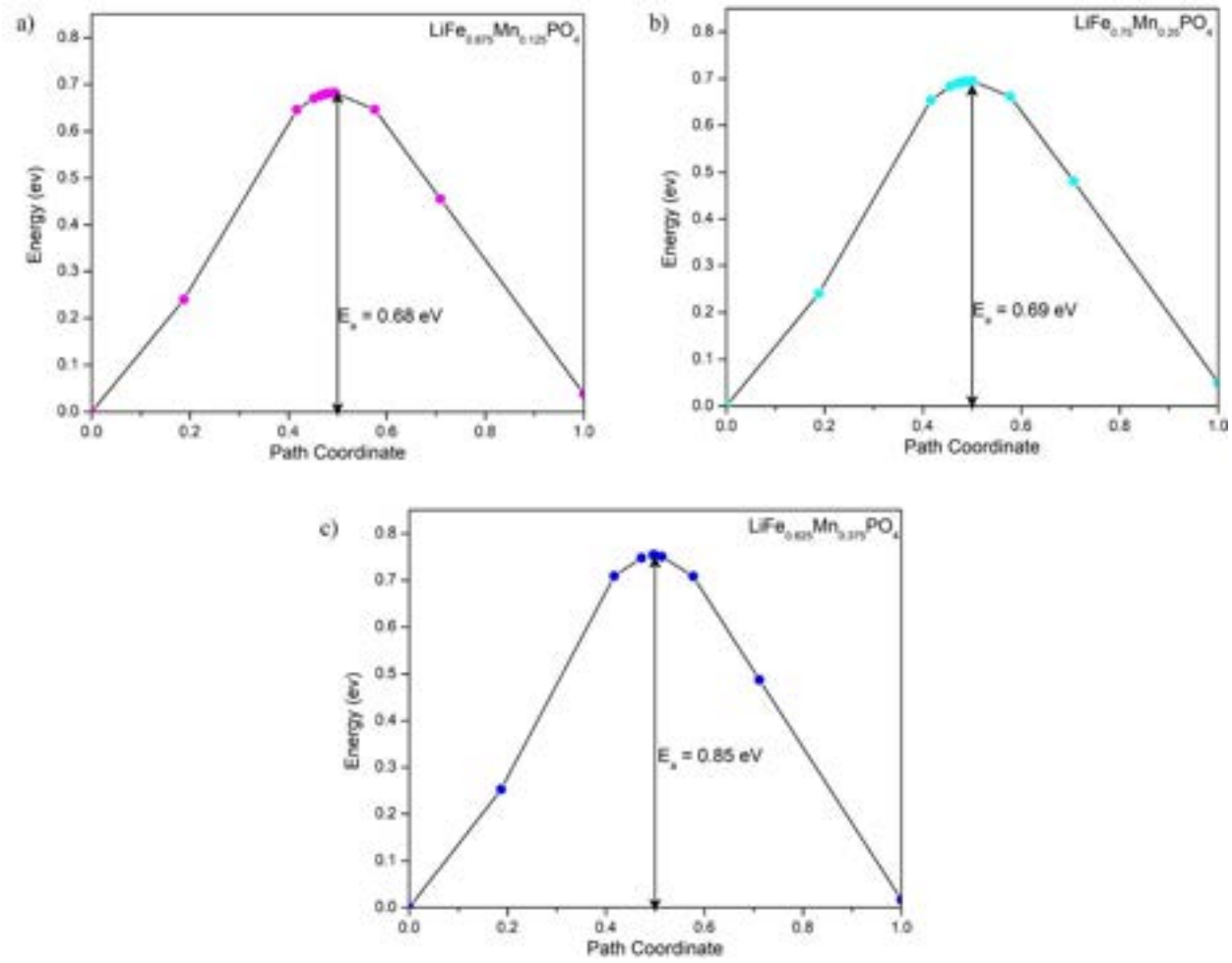

Figure 4. Energy profiles of the ion migration and its migration energy for (a)$LiFe_{0.875}Mn_{0.125}PO_4$, (b) $LiFe_{0.75}Mn_{0.25}PO_4$ and(c) $LiFe_{0.625}Mn_{0.375}PO_4$

CONCLUSION

In conclusion, this study provides a thorough evaluation of Mn-doped $LiFePO_4$ cathode materials, focusing on their structural, electronic, and Li-ion diffusion properties. The results reveal that Mn doping significantly influences these aspects, with $LiFe_{0.875}Mn_{0.125}PO_4$ emerging as the most advantageous composition. The structural analysis indicates that Mn doping expands the lattice and cell volume without compromising the crystal structure, thanks to the different ionic radii of Mn and Fe. This expansion improves Li-ion diffusion by reducing migration energy barriers. Electronically, Mn doping introduces impurity levels from Mn 3*d* states, leading to a substantial reduction in the band gap, with $LiFe_{0.875}Mn_{0.125}PO_4$ achieving the lowest band gap of 3.442 eV. This reduction enhances electronic conductivity, making the material more efficient for charge transfer. The highest diffusion coefficient of 3.42×10^{-14} cm²/s observed for $LiFe_{0.875}Mn_{0.125}PO_4$ underscores its superior Li-ion mobility. Overall, $LiFe_{0.875}Mn_{0.125}PO_4$ presents an optimal combination of reduced band gap, improved electronic

conductivity and enhanced Li-ion diffusion, making it the best candidate for high-performance lithium-ion battery applications.

ACKNOWLEDGEMENT

Appreciation to Ionic Materials & Devices (iMADE) Research Laboratory, Institute of Science, Universiti Teknologi MARA (UiTM) for the facilities provided. This work was supported by Universiti Teknologi MARA (UiTM) under 600-RMC/YTR/5/3(009/2022) grant.

REFERENCES

A. K. Padhi, K. S. Nanjundaswamy, and J. B. Goodenough, "Phospho-olivines as Positive-Electrode Materials for Rechargeable Lithium Batteries," *J. Electrochem. Soc.*, vol. 144, no. 4, pp. 1188–1194, Apr. 1997, doi: 10.1149/1.1837571.

Z. Ahsan, B. Ding, Z. Cai, C. Wen, W. Yang, Y. Ma, S. Zhang, G. Song, and M. S. Javed, "Recent Progress in Capacity Enhancement of LiFePO4 Cathode for Li-Ion Batteries," *J. Electrochem. Energy Convers. Storage*, vol. 18, no. 1, pp. 1–18, Feb. 2021, doi: 10.1115/1.4047222.

A. Yamada and S.-C. Chung, "Crystal Chemistry of the Olivine-Type Li(Mn[sub y]Fe[sub 1−y])PO[sub 4] and (Mn[sub y]Fe[sub 1−y])PO[sub 4] as Possible 4 V Cathode Materials for Lithium Batteries," *J. Electrochem. Soc.*, vol. 148, no. 8, p. A960, 2001, doi: 10.1149/1.1385377.

X. Ouyang, M. Lei, S. Shi, C. Luo, D. Liu, D. Jiang, Z. Ye, and M. Lei, "First-principles studies on surface electronic structure and stability of LiFePO4," *J. Alloys Compd.*, vol. 476, no. 1–2, pp. 462–465, May 2009, doi: 10.1016/j.jallcom.2008.09.028.

A. Tomaszewska *et al.*, "Lithium-ion battery fast charging: A review," *eTransportation*, vol. 1, p. 100011, Aug. 2019, doi: 10.1016/j.etran.2019.100011.

Y.-H. Zhu, X. Yang, T. Sun, S. Wang, Y.-L. Zhao, J.-M. Yan, and X.-B. Zhang, "Recent Progresses and Prospects of Cathode Materials for Non-aqueous Potassium-Ion Batteries," *Electrochem. Energy Rev.*, vol. 1, no. 4, pp. 548–566, 2018, doi: 10.1007/s41918-018-0019-7.

A. Guerfi, J.-F. Labrecque, P. Charest, W. Zhu, M. Dontigny, and K. Zaghib, "Nano-LiMnPO 4 Cathode Material Prepared by Combination Hydrothermal-Wet Mill Processes," *ECS Meet. Abstr.*, vol. MA2010-03, no. 1, pp. 399–399, May 2010, doi: 10.1149/MA2010-03/1/399.

T. Chen and R. Lin, "Effects of Metal Doping on Properties of LiFePO 4 Cathode Material by First-Principle Calculation," vol. 5, no. 5, pp. 121–124, 2015, doi: 10.5923/j.ijme.20150505.03.

J. Jyoti, B. P. Singh, and S. K. Tripathi, "Recent advancements in development of different cathode materials for rechargeable lithium ion batteries," *J. Energy Storage*, vol. 43, no. January, p. 103112, 2021, doi: 10.1016/j.est.2021.103112.

Y. Lyu, Y. Liu, Z. E. Yu, N. Su, Y. Liu, W. Li, Q. Li, B. Guo, and B. Liu, "Recent advances in high energy-density cathode materials for sodium-ion batteries," *Sustain. Mater. Technol.*, vol. 21, p. e00098, Sep. 2019, doi: 10.1016/j.susmat.2019.e00098.

Z. Wang, S. Sun, D. Xia, W. Chu, S. Zhang, and Z. Wu, "Investigation of electronic conductivity and occupancy sites of Mo doped into LiFePO4 by ab initio calculation and X-ray absorption spectroscopy," *J. Phys. Chem. C*, vol. 112, no. 44, pp. 17450–17455, 2008, doi: 10.1021/jp801497z.

S.-Y. Chung and Y.-M. Chiang, "Microscale Measurements of the Electrical Conductivity of Doped LiFePO[sub 4]," *Electrochem. Solid-State Lett.*, vol. 6, no. 12, p. A278, 2003, doi: 10.1149/1.1621289.

J. P. Perdew, K. Burke, and M. Ernzerhof, "Generalized Gradient Approximation Made Simple," *Phys. Rev. Lett.*, vol. 77, no. 18, pp. 3865–3868, Oct. 1996, doi: 10.1103/PhysRevLett.77.3865.

S. J. Clark, M. D. Segall, C. J. Pickard, P. J. Hasnip, M. I. J. Probert, K. Refson, and M. C. Payne, "First principles methods using CASTEP," *Zeitschrift für Krist. - Cryst. Mater.*, vol. 220, no. 5–6, pp. 567–570, May 2005, doi: 10.1524/zkri.220.5.567.65075.

Y. Zhang, J. A. Alarco, A. S. Best, G. A. Snook, P. C. Talbot, and J. Y. Nerkar, “Re-evaluation of experimental measurements for the validation of electronic band structure calculations for LiFePO 4 and FePO 4,” *RSC Adv.*, vol. 9, no. 2, pp. 1134–1146, 2019, doi: 10.1039/C8RA09154D.

F. Zhou, M. Cococcioni, C. A. Marianetti, D. Morgan, and G. Ceder, “First-principles prediction of redox potentials in transition-metal compounds with LDA+U,” *Phys. Rev. B*, vol. 70, no. 23, p. 235121, Dec. 2004, doi: 10.1103/PhysRevB.70.235121.

S. Wang, F. Wang, Z. Chen, T. Li, C. Yao, M. Wang, H. Wang, and H. Wu, “First-principles investigation of the electronic and Li-ion diffusion properties of LiFePO4 by graphene surface modification,” *Mol. Phys.*, 2023, doi: 10.1080/00268976.2023.2239380.

Y. Wang, Z. S. Feng, L. L. Wang, L. Yu, J. J. Chen, Z. Liang, and R. Wang, “A joint experimental and theoretical study on the effect of manganese doping on the structural, electrochemical and physical properties of lithium iron phosphate,” *RSC Adv.*, vol. 4, no. 93, pp. 51609–51614, 2014, doi: 10.1039/c4ra11366g.

D. Zhang, J. Wang, K. Dong, and A. Hao, “First principles investigation on the elastic and electronic properties of Mn, Co, Nb, Mo doped LiFePO4,” *Comput. Mater. Sci.*, vol. 155, no. August, pp. 410–415, Dec. 2018, doi: 10.1016/j.commatsci.2018.09.010.

G. Henkelman, B. P. Uberuaga, and H. Jónsson, “A climbing image nudged elastic band method for finding saddle points and minimum energy paths,” *J. Chem. Phys.*, vol. 113, no. 22, pp. 9901–9904, Dec. 2000, doi: 10.1063/1.1329672.

S. I. Nishimura, G. Kobayashi, K. Ohoyama, R. Kanno, M. Yashima, and A. Yamada, “Experimental visualization of lithium diffusion in LixFePO 4,” *Nat. Mater.*, vol. 7, no. 9, pp. 707–711, 2008, doi: 10.1038/nmat2251.

N. H. M. Zaki, S. I. Ahmad, F. N. Sazman, F. W. Badrudin, A. L. A. Abdullah, M. F. M. Taib, O. H. Hassan, and M. Z. A. Yahya, “The influence of Cl doping on the structural, electronic properties and Li-ion migration of LiFePO4: A DFT study,” *Comput. Theor. Chem.*, vol. 1221, no. January, p. 114029, Mar. 2023, doi: 10.1016/j.comptc.2023.114029.

REINFORCEMENT EFFECT OF GRAPHENE NANOPLATELETS ON POLYLACTIC ACID/KENAF BIOCOMPOSITE FOAMS

Ruey Shan Chen[1*], Justin Wong Jia Min[2]

[1]*Department of Applied Physics, Faculty of Science and Technology, Universiti Kebangsaan Malaysia, 43600 UKM Bangi, Selangor, Malaysia*

**chen@ukm.edu.my*

[2]*Materials Science Program, Faculty of Science and Technology, Universiti Kebangsaan Malaysia, 43600 UKM Bangi, Selangor, Malaysia*

A161099@siswa.ukm.edu.my

ABSTRACT

This research investigated the effect of graphene nanoplatelets (GNP) on the properties of polylactic acid (PLA)/kenaf fibre (KF) biocomposite foams. Azodicarbonamide (ADC) was used as blowing agent for the PLA composites, while zinc oxide (ZnO) was used as activator for ADC. Biocomposite foams of PLA/KF/GNP/ADC/ZnO were prepared using a twin-screw extruder and compression molding. Different loadings of GNP were used: 0.05, 0.10 and 0.15 phr. The sample without GNP served as the control sample. The tensile, thermal, water absorption and morphological properties of the samples were examined. The inclusion of 0.05 phr GNP optimally increased tensile properties and water absorption resistance compared to the control sample. However, the thermal stability of the nanocomposites showed insignificant changes with the small amount of GNP nanofiller. Scanning electron microscope micrograph demonstrated good interfacial interaction between the polymer and the filler. This finding concluded that 0.05 phr GNP could enhance the mechanical tensile properties of biocomposite foam. Future recommendations include exploring surface treatments or coupling agent to achieve improvements in other aspects.

***Keywords*:** Biopolymer; blowing agent; tensile properties; TGA; water absorption

INTRODUCTION

Researchers are increasingly directing their efforts toward combating pressing environmental concerns by developing a new category of eco-friendly composites known as bio-composites. These materials, fully biodegradable, incorporate natural fibers alongside recycled polymer resins. Kenaf, a widely utilized natural fiber, stands out for its appealing mechanical and physical attributes, which are yet to be fully explored. Moreover, kenaf's rapid growth rate ensures its ready availability (Arjmandi et al., 2021). Thermoplastics filled with kenaf fiber are gaining traction as bio-composites, particularly in Malaysia, given the country's favorable climate for kenaf cultivation (Mustafa et al., 2015).

In 2019, global plastic production reached 370 million tons, with a mere 9% undergoing recycled, 12% incineration, and the remainder persisting in the environment or landfills. Plastics poses significant challenges to aquatic ecosystems, where organisms readily ingest small plastic particles that subsequently permeate the food chain, endangering both animals and humans (Kumar et al., 2021). Hence, employing polylactic acid (PLA) polymers presents a viable solution to environmental challenges. As outlined in Marra et al. (Marra, Silvestre, Duraccio, & Cimmino, 2016), PLA production offers numerous benefits, such as recyclability into lactic acid via hydrolysis, the capability to manufacture biodegradable hybrid paper-plastic packaging, waste reduction in landfills, and the potential to tailor physical properties through material modification. Consequently, blending kenaf fiber with PLA yields an eco-friendly composite material.

Reducing weight not only lessens resource use during manufacturing but also decreases energy needed for transportation, thereby conserving resources and lowering CO_2 emissions. The is particularly in mobility applications. However, achieving weight reduction without sacrificing performance, poses a significant challenge in producing lightweight structural components. Methods must be devised to achieve substantial weight reduction with minimal impact on mechanical performance, all while maintaining high productivity and keeping costs low (Mihalic, Pretschuh, Lummerstorfer, & Unterweger, 2023). Incorporating graphene nanoplatelets (GNP) as nano-reinforcements in polymers offers significant enhancements in mechanical performance owing to their planar structure and extremely high aspect ratio. Graphene boasts notably higher tensile modulus (1 TPa) and ultimate tensile strength (130 GPa) compared to other nano-reinforcements. Its high specific surface area facilitates the effective transfer of stress across the interface, providing superior reinforcement compared to carbon nanotubes (Mohammed, Tcherbi-Narteh, & Jeelani, 2020).

In this work, the objective was to investigate the effect of GNP at small loading on the mechanical tensile, thermal stability and water resistance of PLA/kenaf fibre composite foams.

MATERIALS AND METHODS

Raw Materials

Poly(lactic acid) (PLA), with a melting temperature of 165°C and graded as 3251D Natureworks Ingeo™ Biopolymer, was sourced from Unic Technology Ltd, China. This PLA has a density of 1.24 g/cm³ and a melt flow index of 80 g/10 min (190°C/2.6 kg). Kenaf fiber (KF) powder, ranging from 100 to 150 µm in size, was used to reinforce the PLA matrix and was provided by Kenaf and Tobacco State. Azodicarbonamide (ADC), an exothermic foaming agent with a decomposition temperature of 200-210°C, along with zinc oxide (ZnO), a foaming agent decomposition stabilizer, were obtained from Sigma Aldrich.

Sample Preparation and Characterization

The preparation process for the PLA/kenaf fiber/GNP bio-composite foam samples was divided into two stages: extrusion and compression molding. Before starting the melt-blending process, kenaf fibers and PLA were dried in an oven at 65°C for 24 hours. In the first stage, all the materials were melt-blended using a co-rotating twin-screw extruder (Thermo Prism THE 16PC). The PLA/kenaf fiber was fixed at 70/30 (wt/wt), while 2 phr azodicarbonamide (ADC) and 2 phr zinc oxide were used as chemical blowing agent and activator. The temperature profile was set for each barrel from the feed zone to the die zone at 165°C, 170°C, 175°C, and 165°C, with a screw speed of 40 revolutions per minute (rpm). In the second stage, the extruded pellets were compressed via a hot and cold pressing process (model LP50 machine) at 180°C for 13 minutes to form bio-composite samples.

For the characterization tests, dumbbell-shaped samples were used for tensile testing. This test was conducted at room temperature using a Universal Testing Machine Model Testometric M350-10CT with a load of 1000 N and a speed of 5 mm/min. Thermogravimetric analysis (TGA) was run from room temperature to 600 °C, at the heating rate of 10 °C/min under nitrogen atmosphere. The water absorption test was conducted to determine the percentage of water absorbed by the sample at room temperature in tap water. The percentage of water absorption was computed using the formula SA (%) = 100 [(Bt – B0) / B0], where Bt is the weight of the sample at time t and B0 is the weight of the sample before immersion in tap water. Scanning electron microscope (SEM) was run to observe the surface morphologies of tensile fractured composite specimen after coating with gold.

RESULTS AND DISCUSSION

Table 1 describes the tensile properties of PLA/kenaf fiber bio-composite with various small loadings of GNP. When GNP was incorporated at 0.05 phr, the tensile strength, Youngs modulus and elongation of nanocomposite increased to maximum values of 8.28 MPa, 1248.7 MPa and 1.06 %, respectively. The 0.05 phr of GNP is considered as the optimum loading, promoting good compatibility between the PLA matrix and filler component. This could be attributed to the good dispersion of GNP within PLA/kenaf fiber composite, which prevents agglomeration (Mohd Amran et al., 2021; Shahdan, Ahmad, Chen, Ali, & Zailan, 2016), as observed in Figure 2 (b) with uniform morphology. When GNP loading increased, the tensile properties gradually decreased, but the tensile strength and modulus for the nanocomposite at 0.1 phr were still higher than those of the control sample (without GNP). The decreasing trend at higher GNP content can be explained by the tendency of GNP agglomeration in the bio-composite samples, which acts as initiation or propagation points for cracks (Naveen, Jawaid, Zainudin, Thariq Hameed Sultan, & Yahaya, 2019). Meanwhile, the nanocomposite with the presence of GNP, irrespective of its loading, exhibited higher elongation, which is probably correlated to the increased crystallinity induced by GNP nanofiller (Mistretta, Botta, Vinci, Ceraulo, & La Mantia, 2019).

Table 1. Tensile properties of PLA/kenaf fiber/GNP foamed bio-composite samples

GNP content (phr)	Tensile strength (MPa)	Youngs modulus (MPa)	Elongation (%)
0	6.22 ± 0.74	1131.36 ± 78	0.94 ± 0.05
0.05	8.28 ± 0.60	1248.68 ± 211	1.06 ± 0.10
0.1	6.37 ± 0.53	1196.21 ± 80	1.03 ± 0.09
0.15	1.40 ± 0.05	696 ± 200	1.03 ± 0.08

Figure 1 shows the effect of GNP loading on the TGA curves of PLA/kenaf fiber foamed bio-composites. Generally, the weight loss curves of the composites exhibited insignificant shifts, suggesting that the GNP loading used in this study is too small to improve thermal stability. The decomposition temperature recorded around 300 °C, which is consistent with previous study on PLA/kenaf fiber composite (Abu Hassan, Ahmad, Chen, & Natarajan, 2022).

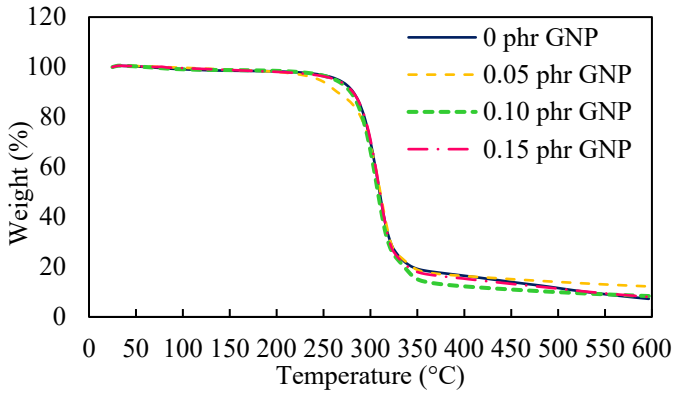

Figure 1. TGA thermogram of PLA/kenaf fiber/GNP foamed bio-composite samples

Table 2 lists the water absorption and thickness swelling of PLA/kenaf fiber foamed samples containing different GNP loading after short-term (24 h) water immersion. The neat PLA/kenaf fiber foamed sample exhibited the water absorption and thickness swelling for 12.43% and 4.32%, respectively. The water absorption of 12.43% was higher when compared to a previous study on PLA reinforced with 20 wt% kenaf fiber (<5% for 24 h) (Abu Hassan, Ahmad, Chen, & Shahdan, 2020), due to the higher kenaf loading used in this study. Interestingly, the water absorption and swelling values decreased in the nanocomposites with 0.05 phr GNP. This could be attributed to the GNP acting as an effective barrier, preventing water molecules from penetrating the PLA matrix (Naveen et al., 2019). Beyond 0.05 phr GNP, the water resistance effect is lesser due to non-uniform distribution of GNP.

Table 2. Water absorption of PLA/kenaf fiber/GNP foamed bio-composite samples

GNP content (phr)	24 h water absorption (%)	24 h thickness swelling (%)
0	12.43	4.32
0.05	8.32	3.67
0.1	13.13	5.18
0.15	9.37	5.11

Figure 2 shows the SEM micrograph of PLA/kenaf fiber foamed bio-composites (a) without and (b) with 0.05 phr GNP. As observed in Figure 2 (a), some holes are present, and the foam cells are bigger in size. In contrast, Figure 2 (b) illustrates a more uniform microstructure with no large gaps, showing well interfacial interaction. With the presence GNP, smaller and perfect round shape foam cells were formed in the nanocomposite. This observation supports the increased tensile properties results as shown in Table 1.

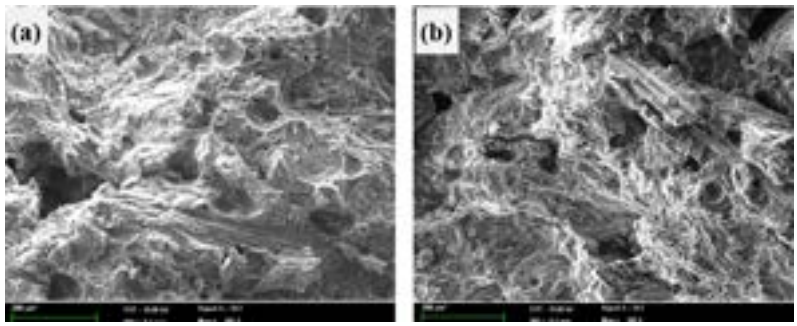

Figure 2. SEM micrograph of PLA/kenaf fiber foamed bio-composites

(a) without and (b) with 0.05 phr GNP

CONCLUSION

Bio-composite foams made from PLA, kenaf fiber and GNP were prepared via melt-blending technique. The inclusion of GNP at 0.05 phr increased the tensile properties and improved the water resistance of PLA/kenaf fiber bio-composites. However, a small loading of GNP did not significantly affect thermal stability. Future recommendations include surface modification or treatment and optimization of processing techniques to further enhance the developed bio-composite foam.

REFERENCES

Abu Hassan, N. A., Ahmad, S., Chen, R. S., & Natarajan, V. D. (2022). Synergistically enhanced mechanical, combustion and acoustic properties of biopolymer composite foams reinforcement by kenaf fibre. *Composites Part A: Applied Science and Manufacturing, 155*, 106826. doi:https://doi.org/10.1016/j.compositesa.2022.106826

Abu Hassan, N. A., Ahmad, S., Chen, R. S., & Shahdan, D. (2020). Cells analyses, mechanical and thermal stability of extruded polylactic acid/kenaf bio-composite foams. *Construction and Building Materials, 240*, 117884. doi:https://doi.org/10.1016/j.conbuildmat.2019.117884

Arjmandi, R., Yıldırım, I., Hatton, F., Hassan, A., Jefferies, C., Mohamad, Z., & Othman, N. (2021). Kenaf fibers reinforced unsaturated polyester composites: A review. *Journal of Engineered Fibers and Fabrics, 16*, 15589250211040184. doi:10.1177/15589250211040184

Kumar, R., Verma, A., Shome, A., Sinha, R., Sinha, S., Jha, P. K., . . . Vara Prasad, P. V. (2021). Impacts of Plastic Pollution on Ecosystem Services, Sustainable Development Goals, and Need to Focus on Circular Economy and Policy Interventions. *Sustainability, 13*(17), 9963. Retrieved from https://www.mdpi.com/2071-1050/13/17/9963

Marra, A., Silvestre, C., Duraccio, D., & Cimmino, S. (2016). Polylactic acid/zinc oxide biocomposite films for food packaging application. *International journal of biological macromolecules, 88*, 254-262. doi:https://doi.org/10.1016/j.ijbiomac.2016.03.039

Mihalic, M., Pretschuh, C., Lummerstorfer, T., & Unterweger, C. (2023). Physical and Chemical Foam Injection Moulding of Natural-Fibre-Reinforced Polypropylene—Assessment of Weight-Reduction Potential and Mechanical Properties. *Journal of Composites Science, 7*(4), 144. Retrieved from https://www.mdpi.com/2504-477X/7/4/144

Mistretta, M., Botta, L., Vinci, A., Ceraulo, M., & La Mantia, F. (2019). Photo-oxidation of polypropylene/graphene nanoplatelets composites. *Polymer Degradation and Stability, 160*, 35-43.

Mohammed, Z., Tcherbi-Narteh, A., & Jeelani, S. (2020). Effect of graphene nanoplatelets and montmorillonite nanoclay on mechanical and thermal properties of polymer nanocomposites and carbon fiber reinforced composites. *SN Applied Sciences, 2*(12), 1959. doi:10.1007/s42452-020-03780-1

Mohd Amran, N. A., Ahmad, S., Chen, R. S., Shahdan, D., Flaifel, M. H., & Omar, A. (2021). Assessment of Mechanical and Electrical Performances of Polylactic Acid/Liquid Natural Rubber/Graphene Platelets Nanocomposites in the Light of Different Graphene Platelets Functionalization Routes. *Macromolecular Chemistry and Physics, 222*(19), 2100185. doi:https://doi.org/10.1002/macp.202100185

Mustafa, A. e., Abdollah, M. F. B., Shuhimi, F. F., Ismail, N., Amiruddin, H., & Umehara, N. (2015). Selection and verification of kenaf fibres as an alternative friction material using Weighted Decision Matrix method. *Materials & Design, 67*, 577-582. doi:https://doi.org/10.1016/j.matdes.2014.10.091

Naveen, J., Jawaid, M., Zainudin, E. S., Thariq Hameed Sultan, M., & Yahaya, R. (2019). Improved mechanical and moisture-resistant properties of woven hybrid epoxy composites by graphene nanoplatelets (GNP). *Materials, 12*(8), 1249.

Shahdan, D., Ahmad, S. H., Chen, R. S., Ali, A. M., & Zailan, F. D. (2016). Optimization of processing parameter for fabrication of polylactic acid/liquid natural rubber/graphene nanoplatelet by tensile properties. Paper presented at the AIP Conference Proceedings.

EXPLORING THE STRUCTURAL CHARACTERISTICS OF $LA_2CUTİO_6$ DOUBLE PEROVSKITE

M. S. M. Rafie[1], S. S. S. A. Aziz[2], N. A. Amaran[1], N. A. Hamdan[3], Z. Mohamed[1] and N. Ibrahim[1]

[1]*Department of Physics, Faculty of Applied Sciences, Universiti Teknologi MARA, 40450 Shah Alam, Selangor, Malaysia.*

syaabanirafie@gmail.com, norasmiraamaran@gmail.com, zakiah626@gmail.com, noraz954@uitm.edu.my

[2]*Faculty of Applied Sciences, Universiti Teknologi MARA, Cawangan Perak, Kampus Tapah, 35400 Tapah Road, Perak, Malaysia.*

sumaiyahaziz@uitm.edu.my

[3]*Center of Foundation Studies, Universiti Teknologi MARA, UiTM Dengkil, 43800, Selangor, Malaysia.*

ainhamdan@uitm.edu.my

ABSTRACT

This research investigates the structural and microstructural characteristics of the undoped double perovskite La2CuTiO6 (LCTO) utilize X-ray diffraction (XRD), Fourier-transform infrared spectroscopy (FTIR), and field-emission scanning electron microscopy (FESEM). XRD results confirmed the phase purity and crystal structure of LCTO, offering detailed insights into its lattice parameters and overall crystallinity. FESEM analysis provided a detailed view of the material's microstructure, showing a consistent grain size and morphology, which are important for determining its physical properties. FTIR spectroscopy was utilized to identify vibrational modes and bonding configurations, providing a deeper understanding of the local structural features of LCTO. These comprehensive analyses establish a foundational understanding of the undoped compound's structural stability and microstructural attributes, which are crucial for its potential use in electronic and dielectric applications.
***Keywords*:** Double perovskite, X-ray diffraction (XRD), Fourier-transform infrared spectroscopy (FTIR), Field-emission scanning electron microscopy (FESEM)

INTRODUCTION

This research focuses on the structural and microstructural characteristics of undoped La_2CuTiO_6 (LCTO), aiming to explore its potential for dielectric applications, an area with limited existing research. The study addresses the lack of comprehensive understanding of LCTO's crystallinity, grain morphology, and bonding structures. While perovskites, including double perovskites, have been extensively studied for various technological applications, there is limited exploration of La-based perovskites with Cu and Ti (Tsvetkov et al., 2019). Past studies have emphasized the role of B-site cations in influencing the stability and performance of perovskite materials (Agarwal et al., 2022), often using X-ray diffraction (XRD) to analyze phase purity (Liu et al., 2017), field-emission scanning electron microscopy (FESEM) to assess grain size (Sahoo et al., 2023), and Fourier-transform infrared spectroscopy (FTIR) to investigate bonding configurations and vibrational modes (Neenu Lekshmi et al., 2014). In this study, XRD, FESEM, and FTIR were utilized to examine the structural and microstructural properties of LCTO. The findings confirm a well-ordered crystal structure, uniform grain size, and stable bonding configurations, underscoring LCTO's potential in electronic and dielectric applications. These results enhance the understanding of perovskite materials and their future optimization in advanced technologies.

MATERIALS AND METHODS

La_2CuTiO_6 (LCTO) was synthesized using high-purity starting materials, including Lanthanum (III) oxide (La_2O_3) from Sigma Aldrich (99.99% purity), and Titanium dioxide (TiO_2) and Copper (II) oxide (CuO) from Alfa Aesar (each 99.99% purity). The powders were carefully weighed according to the required stoichiometric ratios and then mixed thoroughly. This mixture underwent a solid-state reaction process: initially, it was ground for 1 to 2 hours to ensure a uniform blend. The powders were then calcined at 900°C for 24 hours. Afterward, the material was ground again and subjected to a second calcination at 1100°C for an additional 24 hours to facilitate phase development. For the characterization of LCTO, X-ray diffraction (XRD) was performed out utilizing a PAN-analytical Xpert PRO MPD diffractometer with Cu-Kα radiation (wavelength of 1.5418 Å) in the 2θ range from 18 to 90 degrees. Fourier-transform infrared (FTIR) spectroscopy, carried out with a Thermo

Fisher Nicolet 6700 spectrometer, measured infrared absorption spectra between 400 and 1500 cm^{-1} to investigate bonding characteristics. Additionally, field-emission scanning electron microscopy (FESEM) with a Hitachi SU 8000 was used to capture high-resolution images of the material's microstructure and surface features.

RESULTS AND DISCUSSIONS

The study of LCTO identifies it as having a single-phase orthorhombic structure with P*nma* symmetry, supported by X-ray diffraction (XRD) results that display clearly defined peaks, indicating excellent crystalline quality (Li et al., 2023). The lattice parameters are determined as a = 5.616 Å, b = 7.860 Å, and c = 5.575 Å, resulting in a unit cell volume of 246.112 $Å^3$. Although the lattice parameters are largely consistent, there is a significant increase in the b parameter due to distortion in the TiO_6 octahedra (Yang et al., 2010). Additionally, the study observes that bond lengths and angles within the B-site octahedral structure are distorted, with Ti–O bonds showing variations in length that reflect both elongation and compression. Figure 1 shows the XRD pattern of LCTO.

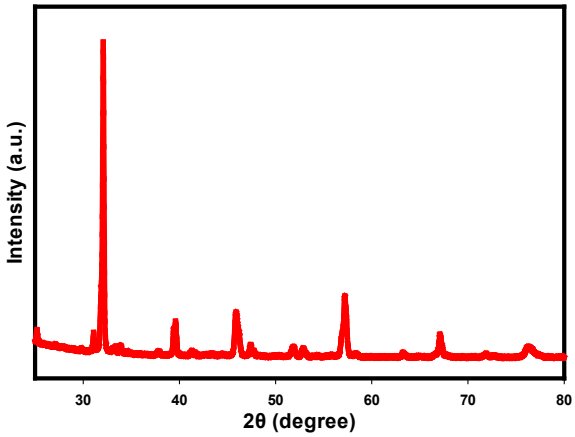

Figure 1. X-ray diffraction (XRD) pattern of LCTO

In the FTIR spectrum of LCTO, a significant absorption peak is observed around 590.14 cm^{-1}. This peak is linked to the symmetric stretching vibrations of the CuO_6 and TiO_6 octahedra. The peak's position is affected by the higher oxidation states of Cu^{2+} and Ti^{4+}, which alter the vibrational frequencies of these octahedral units within the perovskite lattice (Parida et al., 2019). The detection of this peak supports the presence of these octahedra in the material and aligns with the expected FTIR features of perovskite compounds, confirming that LCTO retains its perovskite structure.

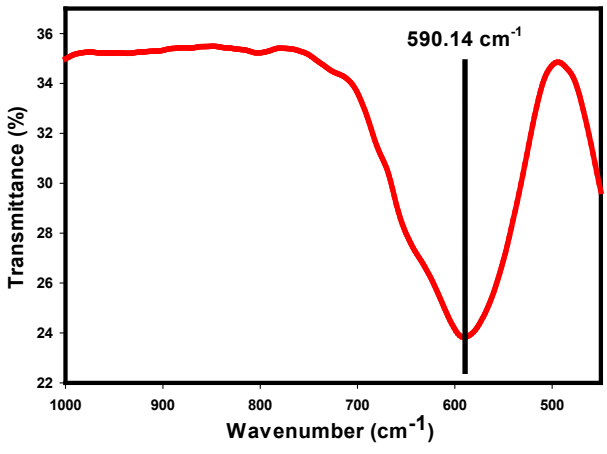

Figure 2. Fourier-transform infrared (FTIR) pattern of LCTO

The FESEM examination of LCTO indicates that the particles are irregular and vary in size, often clustering together, which is likely due to the high preparation temperature. The grain size of LCTO is relatively small, possibly related to reduced structural distortion and lower grain boundary energy. These characteristics can affect nucleation rates and enhance diffusion, making the material suitable for applications requiring efficient ion or electron transport, such as solid oxide fuel cells. Figure 3 shows the FESEM image of LCTO.

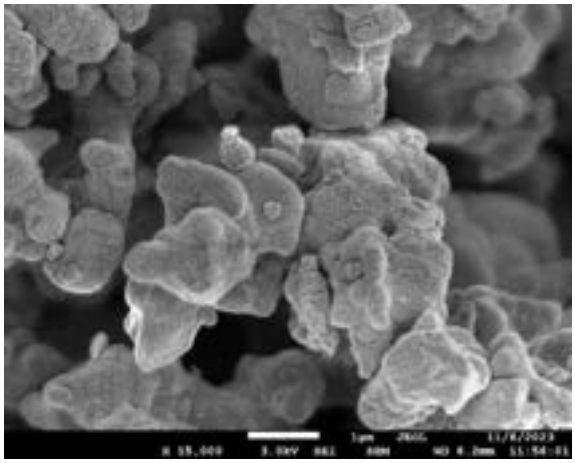

Figure 3. FESEM image of LCTO

CONCLUSION

The examination of LCTO confirms that it maintains a perovskite structure with lattice parameters of a = 5.616 Å, b = 7.860 Å, and c = 5.575 Å, and identifies CuO_6 and TiO_6 octahedra through an FTIR peak at 590.14 cm^{-1}. However, FESEM analysis reveals problems with small grain sizes and particle aggregation, which are likely due to high preparation temperatures. While the structural stability aligns with theoretical expectations, these practical issues may impact the material's performance. To improve the effectiveness of La_2CuTiO_6 in applications such as solid oxide fuel cells, it is advisable to adjust the synthesis conditions to better manage grain size and reduce clustering.

REFERENCES

Agarwal, C., Mittal, H., Bano, T., Kumar, J., Gora, M., & Kumar, A. (2022). A Review on Recent Advancements in Rare-Earth based Double Perovskite Compounds. *Indian J. Pure Appl. Phys.*, *10*(3), 1–16. https://doi.org/10.4172/2320-2459.10.3.004

Li, C., Zheng, S., Qiu, Y., Lei, Q., Wang, C., Lu, Y., Yang, Y., Yan, H., & Luo, Y. (2023). Effect of Ti substitution on structural, magnetic and magnetocaloric properties in double perovskites Gd2NiMn1-xTixO6 ($0 \leq x \leq 1$). *Ceramics International*, *49*(4), 6891–6898. https://doi.org/10.1016/j.ceramint.2022.10.091

Liu, Q., Wang, L., Huang, W., Zhang, L., Yu, M., & Zhang, Q. (2017). Enhanced luminescence properties of double perovskite (Ba, Sr) LaMgSbO 6 : Eu 3 þ phosphors based on composition modulation. 717, 156–163.

Neenu Lekshmi, P., Vasundhara, M., Varma, M. R., Suresh, K. G., & Valant, M. (2014). Structural, magnetic and dielectric properties of rare earth based double perovskites RE2NiMnO6 (RE=La, pr, Sm, Tb). *Physica B: Condensed Matter*, *448*, 285–289. https://doi.org/10.1016/j.physb.2014.04.057

Parida, R. K., Pattanayak, D. K., Mohanty, B., Parida, B. N., & Nayak, N. C. (2019). Dielectric and ferroelectric investigations of barium doped double perovskite Pb2BiVO6 for electronic and optical devices. *Materials Chemistry and Physics*, *231*, 372–381. https://doi.org/10.1016/j.matchemphys.2019.04.051

Sahoo, L., Parida, R., & Nanda, B. (2023). Materials Today: Proceedings polycrystalline double perovskite. 74, 688–692.

Tsvetkov, D. S., Ivanov, I. L., Malyshkin, D. A., Sednev, A. L., Sereda, V. V, & Zuev, A. Y. (2019). Conference paper (RE = La, Pr , Nd , Eu , Gd , Y ; M = Fe , Mn) as energy-related materials : an overview.

Yang, W. Z., Mao, M. M., Liu, X. Q., & Chen, X. M. (2010). Structure and dielectric relaxation of double perovskite La 2CuTiO6 ceramics. *Journal of Applied Physics*, *107*(12), 4–8. https://doi.org/10.1063/1.3446846

ORGANIC FIBERS ALTER THE MECHANICAL PROPERTIES OF COMPOSITE GYPSUM

Asmahani Awang[1,*], Farmizan Pirman[2]

[1,*]*Industrial Physics Programme, Faculty of Science and Natural Resources, Universiti Malaysia Sabah, 88400 Kota Kinabalu, Sabah*

asmahani_awang@ums.edu.my

[2]*Pure Physics Programme, School of Physics, Universiti Sains Malaysia, 11800 UMS Penang, Malaysia*

ijampirman@gmail.com

ABSTRACT

In the present study, a series of composite gypsum were fabricated using a conventional method by incorporating different sizes of banana trunk fibers with sizes of 38 µm, 63 µm, 125 µm, and 250 µm into the gypsum matrix. The elemental traces and compressive strength of gypsum containing different sizes of banana trunk fibers were determined using a Scanning Electron Microscopy equipped with Energy-dispersive X-ray (EDX) Spectroscopy and a Universal Mechanical Testing machine. The EDX spectra reveal the emergence of C (carbon), O (oxygen), S (sulfur), Ca (calcium), Mg (magnesium), Si (silicon), P (phosphorus), K (potassium), and Na (sodium) elements. Meanwhile, the mechanical testing shows the compressive strength of composite gypsum varied from 1.771 MPa to 11.278 MPa. Variation in compressive strength of composite gypsum was affected by the size of banana trunk fiber modified the fiber spacings and load transfer mechanism in the gypsum matrix.
***Keywords*:** Gypsum, banana trunk, organic fibers, compressive strength, cracks

INTRODUCTION

Nowadays, composite materials utilize raw materials to extract lignocellulosic fibers from various sources such as fruits, seeds, stems, leaves, lianas, pseudo-trunks, and roots [1]. A banana plant is categorized as a colossal herb that arises from an underground stem to form a trunk with a certain height of approximately 3- to 6-meters. It is composed of several main parts such as a stem or trunk, fruits, and leaves. The banana trunk is also known as pseudostem, in which the formation is facilitated by tightly packed overlapping leaf sheats [2]. The mass production of bananas yields a vast amount of pseudo-stem waste and generates a major agro-waste problem and an environmental issue. Therefore, an alternative to manage the arising issues related to banana pseudo-stem is vital to pursue [3]. Composite is a type of material that is made of two or more constituent materials consisting of matrix and reinforcement that exhibit different physical or chemical properties that generates new material with significant features that are different from the individual component [2].

The development of industrial sectors expanding the application of various fiber-reinforced composites. The possible applications of fibers become wide due to the generation of new fibers that possess high performance, low-cost production, and beneficial features that can enhance the properties of existing composites. Organic fibers attract attention among researchers due to their advantages of being environmentally friendly, renewable resources, recyclable, and satisfying the requirement of green building rating systems that enable them to be used as construction materials [4]. Gypsum products are unique and are based chemically on calcium sulfate hemihydrate $CaSO_4.2H_2O$. However, the strength of gypsum products depends on several factors such as the water/powder ratio, additive materials, mixing time et cetera [6]. Developing gypsum composites containing natural fibers emerges as an alternative to address environmental issues related to carbon dioxide emissions from synthetic fiber production contributing to the positive aspects since it can enhance the mechanical, thermal, and acoustic properties [5]. Therefore, the aim of this study is to use banana trunk fibers as reinforcement agents in gypsum to enhance the mechanical properties of final products.

MATERIALS AND METHODS

Extraction of Fibers

Banana trunks were obtained from Kota Kinabalu, Sabah, Malaysia. At the initial stage, the banana trunks were cut into a specific dimension of 30 cm · 15 cm (length x width). Then, the outer cortical region of the banana trunks was removed manually. This process was followed with the removal of the flesh part of the banana

trunks using a semi-sharp knife to obtain banana trunk fibers in a bulk form. Next, sodium hydroxide (4 wt% NaOH) was used for alkaline treatment to facilitate the removal of lignin and hemicellulose. The chemical treatment was performed in a round bottom flask and subject to the stirring process for a duration of two hours. After that, the banana trunk bulk fibers were subjected to the drying process. Then, the banana trunk bulk fibers were rinsed using distilled water several times and subjected to the drying process under sunlight. Finally, the banana trunk bulk fibers were subjected to a milling and sieving process (Sieving set/ RX-29 (Tyler USA)) to obtain distinctive sizes of fine fibers in the range of 38 µm, 63 µm, 125 µm, and 250 µm.

Fabrication and Characterization of Samples

The sample without banana trunk fibers was prepared using 25 g gypsum powder (Sigma Aldrich) and 15 ml distilled water. Meanwhile, the sample with banana trunk fibers was prepared using 24.25 g gypsum powder, 0.75 g banana trunk fibers, and 15 ml distilled water. The weight of all constituent powders was measured by using analytical balance. All the ingredients and distilled water were mixed and stirred to attain homogeneous mixtures. After that, the mixtures were poured into the mould and subjected to a drying process with a duration of 4 hours under the sunlight. Then, the samples were subjected to structural and mechanical testing. The elemental traces were performed using HITACHI S-3400. The mechanical properties of samples were determined by using a Universal Mechanical Testing Machine (Gotech/ai-7000I-10/fritsch/pulversette14). The compressive strength of each sample was evaluated by using the following equation [7];

$$Compressive\ strength = \frac{Load\ (N)}{Surface\ area\ (mm^2)} \tag{1}$$

The compressive strength enhancement factor was calculated as follows.

$$Enhancement\ factor = \frac{Compressive\ strength\ of\ gypsum\ with\ organic\ fibers}{Compressive\ strength\ of\ gypsum\ without\ organic\ fibers} \tag{2}$$

RESULTS AND DISCUSSION

Structural Properties

Figure 1 shows EDX spectra of gypsum containing banana trunk fibers with a size of 125 µm reflecting the emergence of C (carbon), O (oxygen), S (sulfur), Ca (calcium), Mg (magnesium), Si (silicon), P (phosphorus), K (potassium), and Na (sodium). All elements detected from EDX and their respective weight percentages and atomic percentages are summarized in Table 1. The inset in Figure 1 manifests gypsum containing banana trunk fibers in powder form. The gypsum crystals exhibit a tabular cleavage making it to appear like a fine slivers [10].

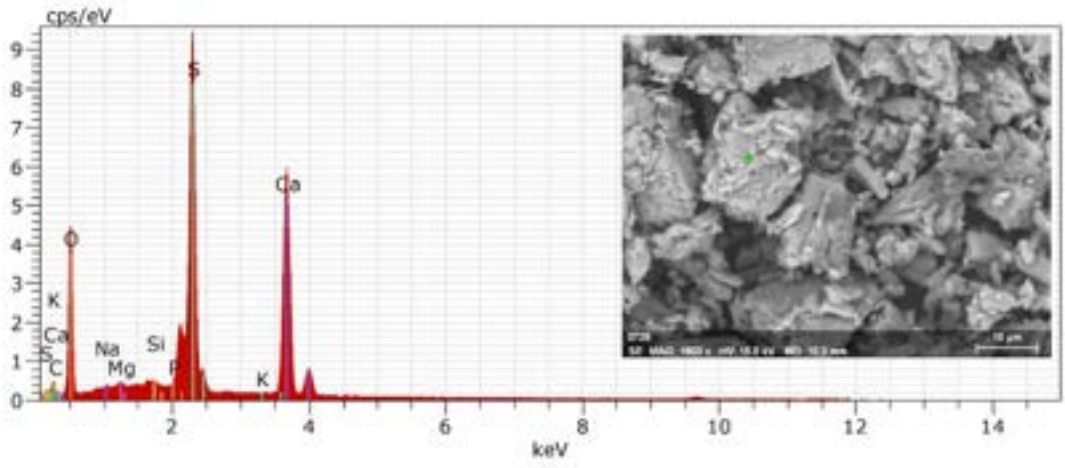

Figure 1. EDX spectra of gypsum plaster containing banana trunk fibers. Inset shows the SEM image of gypsum plaster containing banana trunk fibers

Table 1. EDX elemental traces of gypsum containing organic fibers

Element	Series	Weight (%)	Atomic (%)
Carbon	K-series	1.64	3.11
Oxygen	K-series	44.01	62.66
Sulfur	K-series	21.59	15.34
Calcium	K-series	31.55	17.93
Magnesium	K-series	0.16	0.15
Silicon	K-series	0.22	0.18
Phosphorus	K-series	0.54	0.40
Potassium	K-series	0.11	0.07
Sodium	K-series	0.17	0.17

Mechanical Properties

Table 2 shows variations in the compressive strength of gypsum containing different sizes of banana trunk fibers. It can be observed that the incorporation of a smaller size of banana trunk fibers with a size of 38 µm and 63 µm (PPBT38 and PPBT63 samples) into the gypsum matrix decreases the compressive strength from 5.498 MPa to 1.771 MPa and 4.838 MPa. The decrease in compressive is due to the large fiber spacing that lowers the transferring loads efficiency. In addition, the small size of banana trunk fibers causes impairment to the crystal lap structure inside the gypsum matrix and reduces the gypsum strength [9].

Meanwhile, the incorporation of a bigger size of banana trunk fibers with a size of 125 µm and 250 µm (PPBT125 and PPBT250 samples) into the gypsum matrix elevates the compressive strength to 11.278 MPa and 10.762 MPa with a significant enhancement factor of 2.05 and 1.96, respectively. A significant increase in compressive strength of gypsum with the incorporation of bigger size of banana trunk fibers due to the short distance between fibers and even distribution of fibers in the gypsum matrix. In this view, the applied force was transferred to the fibers and distributed to the matrix between the fibers. Therefore, stress concentration can be reduced [9].

Table 2. Compressive strength of gypsum with varying sizes of banana trunk fibers

Sample code	Compressive strength (MPa)	Enhancement factor
PP	5.498	1.00
PPBT38	1.771	0.32
PPBT63	4.838	0.88
PPBT125	11.278	2.05
PPBT250	10.762	1.96

CONCLUSION

The incorporation of banana trunk fibers with distinct sizes into the gypsum matrix significantly alters the compressive strength of composite gypsum. The current findings show that the tiny banana trunk fibers of sizes 38 µm and 63 µm weakened the gypsum structure due to the generation of larger fiber spacing. Meanwhile, the incorporation of bigger banana trunk fibers of sizes 125 µm and 250 µm strengthened the gypsum structure.

REFERENCES

L. Libog, F. Biyeme, A.D.O. Betene, A.B. Biwole, B. Ndiwe, J.P.E. Mbang, T. Claude, J.A. Mbey, J.R.L. Meva'a. Influence of the extraction location on the physical and mechanical properties of the psedo-trunk banana fibers. Journal of Natural Fibers. 20 (2023) 2204451.

M.I. Ishak, C.N. Ismail, C.Y. Khor, M.U. Rosli, M.R. Jamalludin, M.H.M. Hazwan, M.A.M. Nawi, M. Syafiq A.K. Investigation on the mechanical properties of banana trunk fibre-reinforced polymer composites for furniture making application. IOP Conf. Series: Materials Science and Engineering. 551 (2019) 012107.

L.H. Ho, A.A. Noor Aziah, R. Bhat. Mineral composition and pasting properties of banana pseudo-stem flour from *Musa acuminata* X *balbisiana* cv. Awak grown locally in Perak, Malaysia. International Food Research Journal. 19 (2012) 1479−1485.

A.P. Fantilli, D. Jozwiak-Niedzwiedzka, P. Denis. Bio-fibres as a reinforcement of gypsum composites. Materials. 14 (2021) 4830.

M.T. Esan. Review of gypsum reinforced composites as building materials. Discover Civil Engineering. 1 (2024)

F.A. Kati, I.N. Yassin, W.A. Razak. Effect of adding some additives and drying method on compressive strength of gypsum products. Tikrit Journal for Dental Sciences. 5 (2017) 25−32.

M. Hostalkova, N. Vavrinova, V. Longauerova. Mechanical properties of the gypsum composite reinforcement with wooden fibers. Int. Rev. Appl. Sci. Eng. 10 (2019) 15−21.

D-E. Aizi, M. Kaid-Harche. Mechanical behavior of gypsum composites reinforced with *Retama monosperma* fibers. 63 (2021) 40.

Y. Ye, Q. Huang, X. Li. Effect of fiber loading on mechanical and flame-retardant properties of poplar-fiber-reinforced gypsum composites. Molecules. 29 (2024) 2674.

Oliveira, M., 2013. Study of the degradation of 18th century alabaster sculptures through accelerated aging on test samples. CeROArt. [online] Aviable at: <http://ceroart.revues.org/3187> [Accessed 16 August 2024].

SQUEEZED LIGHT GENERATION ACROSS DUAL OCTAVE MULTICHANNEL WAVEGUIDES WITH CAVITY MIRROR

Mohammad Zulkarnain Khan Zulkifpeli[1*] and Rafael Julius[1]

Faculty of Applied Sciences, Universiti Teknologi MARA (UiTM) Perak,

Tapah Campus, 35400, Tapah Road, Perak, Malaysia.

**Corresponding author: zulkarnainsmkbg@gmail.com*

ABSTRACT

This study explores the potential to amplify and extend the generation of intracavity-squeezed light across the fourth harmonic frequency using a dual-octave system composed of multichannel nonlinear waveguides. The Hamiltonian of the model is solved using the phase space P representation. The results demonstrate that the model successfully amplifies and extends the frequency range of the squeezed light. This highlights the potential of dual-octave multichannel waveguides as a promising candidate for advancements in quantum optics and photonic technology.

Keywords: quantum optics; squeezed light; quantum noise; harmonic generation; positive-P representation.

INTRODUCTION

The application of squeezed light is immensely significant in quantum optics, with various applications such as quantum imaging [1], gravitational wave detector [2, 3], optical communication [4], and quantum teleportation [5]. One of the simplest yet most effective sources for generating squeezed light involves the use of nonlinear waveguides in various configurations and interactions [6]. In this paper, we explore the potential for extending the range of squeezing to the fourth harmonic frequency using multichannel nonlinear waveguides *a*, *b*, *c*, and *d* operating under second-order nonlinearity to facilitate harmonic generation. These waveguides are designed as a dual octave system, each comprising multichannel waveguides with similar properties enhanced by cavity mirrors.

MATHEMATICAL ASPECT

The Hamiltonian describing our proposed model can be written as,

$$\hat{H} = i\hbar\sum_{j=1}^{3}\left\{\hat{H}_{\Omega} + \hat{H}_{\chi} + \hat{H}_{k} + \hat{H}_{\varepsilon} + \hat{H}_{\Gamma}\right\} \tag{1}$$

$$\hat{H}_{\Omega} = \Omega_n\left(\hat{a}_n^{\dagger}\hat{a}_n + \hat{b}_n^{\dagger}\hat{b}_n + \hat{c}_n^{\dagger}\hat{c}_n + \hat{d}_n^{\dagger}\hat{d}_n\right) \tag{2}$$

$$\hat{H}_{\chi} = \frac{1}{2}\left[\chi\left(\hat{a}_n^{\dagger 2}\hat{a}_{n+1} - \hat{a}_n^{2}\hat{a}_{n+1}^{\dagger}\right) + \left(\hat{b}_n^{\dagger 2}\hat{b}_{n+1} - \hat{b}_n^{2}\hat{b}_{n+1}^{\dagger}\right) + \left(\hat{c}_n^{\dagger 2}\hat{c}_{n+1} - \hat{c}_n^{2}\hat{c}_{n+1}^{\dagger}\right) + \left(\hat{d}_n^{\dagger 2}\hat{d}_{n+1} - \hat{d}_n^{2}\hat{d}_{n+1}^{\dagger}\right)\right] \tag{3}$$

$$\hat{H}_{k} = k_n\left(\hat{a}_n\hat{b}_n^{\dagger} + \hat{b}_n\hat{a}_n^{\dagger} + \hat{a}_n\hat{c}_n^{\dagger} + \hat{c}_n\hat{a}_n^{\dagger} + \hat{a}_n\hat{d}_n^{\dagger} + \hat{d}_n\hat{a}_n^{\dagger}\right) \tag{4}$$

$$\hat{H}_{\varepsilon} = \left(\varepsilon_n\hat{a}_n^{\dagger} - \varepsilon_n^{*}\hat{a}_n\right) + \left(\varepsilon_n\hat{b}_n^{\dagger} - \varepsilon_n^{*}\hat{b}_n\right) + \left(\varepsilon_n\hat{c}_n^{\dagger} - \varepsilon_n^{*}\hat{c}_n\right) + \left(\varepsilon_n\hat{d}_n^{\dagger} - \varepsilon_n^{*}\hat{d}_n\right) \tag{5}$$

$$\hat{H}_{\Gamma} = \left(\hat{a}_n\Gamma_n^{\dagger} + \hat{a}_n^{\dagger}\Gamma_n\right) + \left(\hat{b}_n\Gamma_n^{\dagger} + \hat{b}_n^{\dagger}\Gamma_n\right) + \left(\hat{c}_n\Gamma_n^{\dagger} + \hat{c}_n^{\dagger}\Gamma_n\right) + \left(\hat{d}_n\Gamma_n^{\dagger} + \hat{d}_n^{\dagger}\Gamma_n\right) \tag{6}$$

where $\hbar$ denoted the reduced Planck constant. $\hat{H}_{\Omega}$ describe the free Hamiltonian with coefficient $\hat{a}_n^{\dagger}\hat{a}_n, \hat{b}_n^{\dagger}\hat{b}_n, \hat{c}_n^{\dagger}\hat{c}_n, \hat{d}_n^{\dagger}\hat{d}_n$ being the bosonic operator for the input fields in the channels *a*, *b*, *c*, and *d*, where *n* = 1, 2, 3 represent the field at the first Ω_1, second Ω_2, and fourth Ω_3 harmonic frequencies. $\hat{H}_{\chi}$ describe the nonlinear Hamiltonian with χ denoted the nonlinear coupling of the quadratic nonlinearity $\chi^{(2)}$. Furthermore, $\hat{H}_{\chi}$ gives the coupling Hamiltonian between the channel waveguides respectively. The external pumping fields from

the cavity mirror and cavity lose are modelled through Hamiltonian $\hat{H}_{\varepsilon}$ and $\hat{H}_{\Gamma}$. We obtain the master equation of the Hamiltonian following the Von-Neumann equation of motion by the application of the positive *P* representation, the Fokker-Planck Equation (FPE) is derived. In the positive *P* representation, the resulting FPE can be directly converted to its corresponding Stochastic Differential Equation (SDE) using Ito Calculus. We develop a program using the fourth-order Runge Kutta method to solve the SDE over 10^3 stochastic trajectories in MATLAB. Accordingly, the squeezing of the system is investigated by using;

$$S_X = 4\left\langle \left(\Delta\hat{X}\right)^2 \right\rangle - 1 \le 0 \quad ; \quad S_Y = 4\left\langle \left(\Delta\hat{Y}\right)^2 \right\rangle - 1 \le 0 \tag{7}$$

where,

$$\hat{X} = \left(\hat{A} + \hat{A}^{\dagger}\right)/2 \quad ; \quad \hat{Y} = \left(\hat{A} - \hat{A}^{\dagger}\right)/2i \tag{8}$$

and $\hat{A}^{\dagger}\hat{A} \Leftrightarrow \hat{a}_n^{\dagger}\hat{a}_n, \hat{b}_n^{\dagger}\hat{b}_n, \hat{c}_n^{\dagger}\hat{c}_n, \hat{d}_n^{\dagger}\hat{d}_n$.

RESULTS

Figure 1 shows the generation of the squeezed light in the system. The squeezing effects are observed in both the X and Y quadrature, labelled as S_X and S_Y in Figure 1, respectively. The generation scheme involves coherent initialization in channel *a* and vacuum initialization in the other channels. Figure 1(a) shows strong squeezing in the Y quadrature. While strong squeezing is only observed in the Y quadrature for the first harmonic, both quadrature variances exhibit squeezing in the second (Figure 1(b)) and fourth (Figure 1(c)) harmonic generations. For the first and second harmonics, squeezing appears early in the quadrature evolution, while it takes more time for the fourth harmonic fields to develop stronger squeezing. With cavity support, we observed that both the first and second harmonics undergo amplitude squeezing magnification by a factor of 10^3, while the fourth harmonic achieves up to 10^4 squeezing amplification.

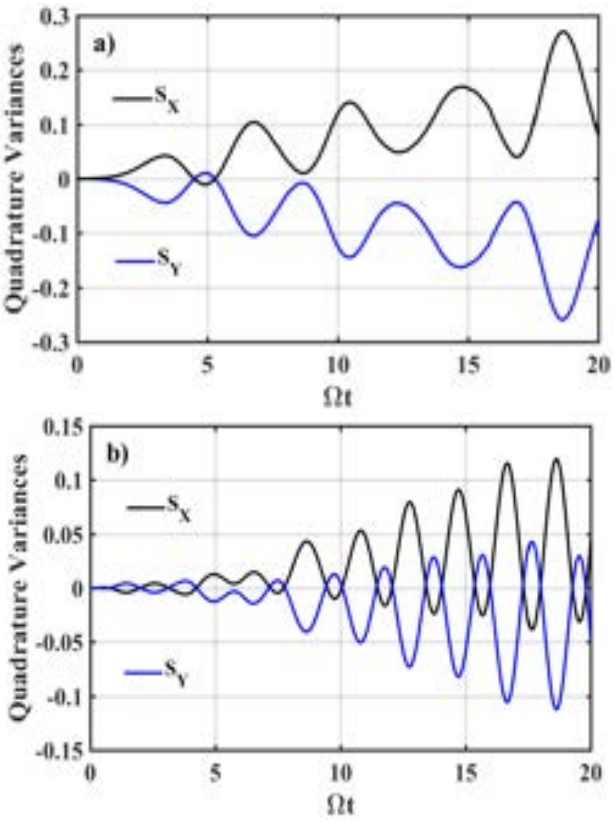

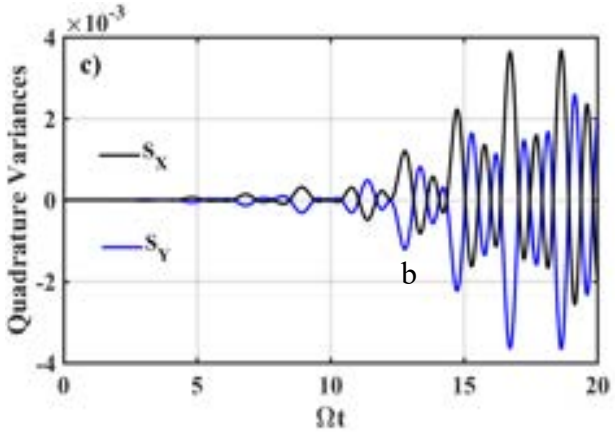

Figure 1. Squeezed light in channel a. (a) First Harmonic, (b) Second Harmonic, and (c) Fourth Harmonic frequencies.

CONCLUSION

The possibility of amplifying and extending intracavity-squeezed light generation across the fourth harmonic frequency using a dual-octave system of multichannel nonlinear waveguides has been studied. The system can generate strong squeezed light in the first, second, and fourth harmonic frequencies. The first and second harmonics showed squeezing amplification by a factor of 10^3, while the fourth harmonic reached up to 10^4. This system shows promise for enhancing quantum optical applications.

ACKNOWLEDGEMENT

This study was funded by a Fundamental Research Grant Scheme (FRGS/1/2021/STG07/02/4) from the Ministry of Higher Education Malaysia.

REFERENCES

J. L. O. Brien and J. L. O. Brien, "Optical Quantum Computing," vol. 1567, no. 2007, 2014, doi: 10.1126/science.1142892.

M. S. M. Hanafi, A.-A. M. A. Ibrahim, R. Julius, and P. K. Choudhury, "Squeezed Light Generation in Three-Channel Nonlinear Coupler with Second-Harmonic Generation and Frequency Mismatch," *J. Phys. Conf. Ser.*, 2022, doi: 10.1088/1742-6596/2411/1/012021.

R. Julius and A. B. M. A. Ibrahim, "Squeezing over Two Octaves of Frequency Difference with Second Harmonic" *J. Phys. Conf. Ser.*, 2022, doi: 10.1088/1742-6596/2411/1/012022.

R. Julius *et al.*, "Single- and compound-mode squeezing in nonlinear coupler with frequency mismatch," *J. Electromagn. Waves Appl.*, vol. 0, no. 0, pp. 1–15, 2019, doi: 10.1080/09205071.2019.1702591.

M. K. Olsen, "Entanglement and asymmetric steering over two octaves of frequency difference," vol. 063839, pp. 1–6, 2017, doi: 10.1103/PhysRevA.96.063839.

R. Julius *et al.*, "Sub-Poissonian photon squeezing and entanglement in optical chain second harmonic generation," *J. Mod. Opt.*, 2019, doi: 10.1080/09500340.2019.1603408.

INVESTIGATION OF NEMS CARBON NANOTUBE BASED FIXED-FIXED BEAM STRUCTURE BY USING NANOHUB SIMULATION

Wan Nur Shamila Binti Wan Saimi[1], Farah Liyana Binti Muhammad Khir[2*]

[1]*School of Physics & Materials Studies, Faculty of Applied Sciences, Universiti Teknologi MARA (UiTM), Shah Alam*

shamilasaimi01@gmail.com, farah668@uitm.edu.my*

ABSTRACT

This study aims to simulate the pull-in voltage behavior of fixed-fixed beams for NEMS applications in switch by using NanoHUB Simulation. The simulation focuses on parameters such as beam length to observe the pull-in voltage behavior and to investigate the influence of van der Waals forces on the pull-in voltage of these beams. In order to validate the results, we compare the bending behavior with findings from previous research. We have found that the simulation is successful where we can see the bending behavior when we increase the beam length, but the simulation is not successful for the lowest and highest beam length as there is no bending behavior. For future recommendations, we suggest that other parameters such as initial gap can be used to investigate the pull-in voltage behavior of fixed-fixed beams for NEMS applications in switch.

***Keywords*:** Fixed-fixed beam, carbon nanotube NEMS, pull-in voltage

INTRODUCTION

Nanoelectromechanical systems (NEMS) include nanometer-sized switches, actuators, and sensors. This paper focuses only on carbon nanotubes-based NEMS switches, which are essential for designing random access memory and communication networks with high frequency and fast switching speed (Dequesnes, 2002). Pull-in voltage characteristics of nanostructures in different working conditions affect device performance and reliability. Nano structures experience an attractive force that can cause mechanical instability near their pull-in voltage. Understanding this behavior optimizes design parameters, prevents failure, and boosts the NEMS efficiency. Researchers can develop more robust and efficient NEMS by studying pull-in voltage with parameter changes. In this study, we propose a varying beam parameter focusing on beam length for the simulation of fixed–fixed beam for carbon nanotubes-based NEMS switches.

The carbon nanotubes-based NEMS switches structure consists of a beam and ground plane. The beam will be deflected once a voltage is applied between the beam and ground plane. When the beam has been deflected, there would be a reaction on the existing electric field that exists between the beam and ground plane enhancing the distribution of charges (Sankar et al., 2013). Van der Waals forces would deflect the beam aside from the applied voltage, but the effect of this force depends on the gap between the beam and the ground plane. The deflection forces are countered by elastic forces that try to return the beam to its original position, in agreement with the Newton 3rd Law. When the potential difference between the beam and the ground plane exceeds a critical value, the beam becomes unstable and collapses onto the ground plane (Yang et al., 2008). The potential which causes the beam to collapse onto the ground plane is defined as pull-in voltage. After applying the pull-in voltage, the beam and ground plane make a contact and result to be turned ON (Mahdi et al., 2021). However, if the beam and ground plane are no longer in contact, this indicates that the device is OFF (here, pull-in voltage is not applied to the beam).

In this study, we focus on the simulation via NanoHUB software. Here, we investigate the pull-in behavior of a fixed-fixed beam as a carbon nanotubes-based NEMS switches. The results obtained from varying the beam length by comparing it with other research work were analyzed systematically. From the simulation, a basic finding regarding the simulated carbon nanotubes-based NEMS switches will be used to understand the effect of pull-in behavior exhibited by the device.

MATERIALS AND METHODS

The study involved a simulation performed by using a freeware known as NanoHUB. The selection of the carbon nanotube-based NEMS switches for fixed-fixed beam can be found under “Carbon nanotube based fixed-fixed NEMS". The structure of carbon nanotube-based NEMS switch is shown as in Figure 1.

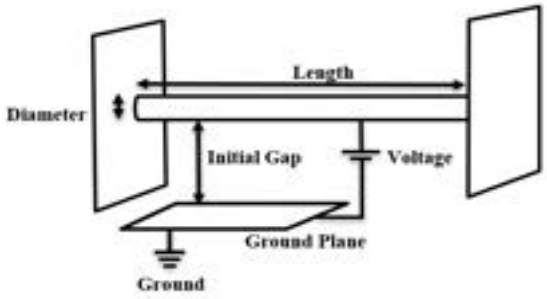

Figure 1. Carbon nanotube-based NEMS switch structure

Here, the simulations were repeated four times with various beam lengths as shown in Table 1.

Table 1. Parameters of carbon nanotube-based NEMS switch for fixed-fixed beam

Length (nm)	Diameter (nm)	Initial Gap (nm)	References
50.00	2.00	4.00	Dequesnes et al., 2002
80.00	2.00	4.00	Dequesnes et al., 2002
1.00	2.00	4.00	My work
3000.00	2.00	4.00	My work

RESULTS AND DISCUSSION

The fixed-fixed beam of the carbon nanotubes-based NEMS switches was investigated with applied voltage range between 0-20V. Table 2 shows the simulation results based on the parameters mentioned previously in the methodology section.

Table 2. Pull-in voltage of carbon nanotube-based NEMS switches for fixed-fixed beam

Length (nm)	Diameter(nm)	Initial Gap (nm)	Pull-in Voltage (with vdw) (V)	Pull-in Voltage obtained from simulation (with vdw) (V)	Pull-in Voltage (without vdw) (V)	Pull-in Voltage obtained from simulation (without vdw) (V)	References
50.00	2.00	4.00	6.20*	6.75	6.30*	6.95	Dequesnes et al., 2002
80.00	2.00	4.00	2.20*	2.20	Not stated	2.70	Dequesnes et al., 2002
1.00	2.00	4.00		Not in range		Not in range	My work
3000.00	2.00	4.00		Not in range		Not in range	My work

*Results obtained from (Dequesnes et al., 2002)

For the simulation of 50 nm beam length, our observation shows that the pull-in voltage with van der Waals forces is 6.75 V in comparison with (Dequesnes et al., 2002) where the pull-in voltage obtained was 6.20 V. It is suggested that the discrepancy between these works may result from different simulation tools with different commands in terms of parameters. Interestingly, the pull-in voltage without van der Waals forces increase to 6.95 V in comparison with (Dequesnes et al., 2002) where the pull-in voltage value was 6.30 V. From our observation, both pull-in voltage with and without van der Waals forces resulted in significant amounts of differences in voltage.

The simulation for 80 nm length shows that the pull-in voltage with van der Waals forces obtained was 2.20V, in agreement with the results performed by (Dequesnes et al., 2002) study. However, the pull-in voltage without van der Waals forces from previous study was not stated in their study. Thus, for future work, it is recommended to further investigate the effect of length by referencing more work from other researchers.

The simulation of 1 nm length was conducted since to further investigate the pull-in voltage for the smallest length of the structure. Here, the pull-in voltage with and without van der Waals were not obtained. The simulation was also conducted for the highest value of length (3000 nm) that can be included in NanoHUB simulation. The results shows that there was no pull-in voltage from the simulation. We suggest that the NanoHUB simulation has limitations in terms of length. Table 2 systematically shows a visualization of a deflected beams obtained from our simulation results.

Table 2. The pull-in behavior of carbon nanotubes based fixed-fixed NEMS switches

Parameter	Simulation result	Pull-in Voltage (V)	Reference
Length = 50 nm Diameter = 2 nm Initial gap = 4 nm	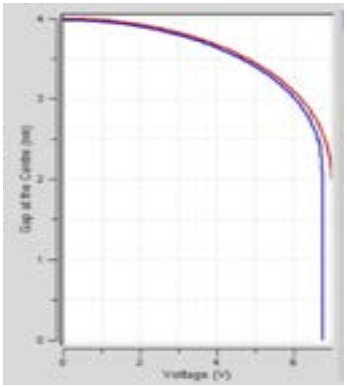 (a)	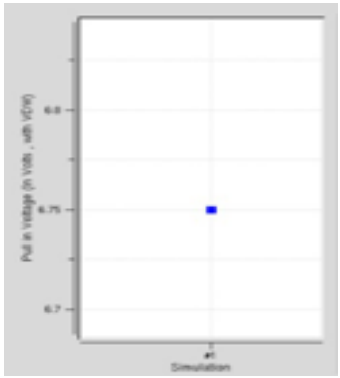 (b)	Dequesnes et al., 2002
Length = 80 nm Diameter = 2 nm Initial gap = 4 nm	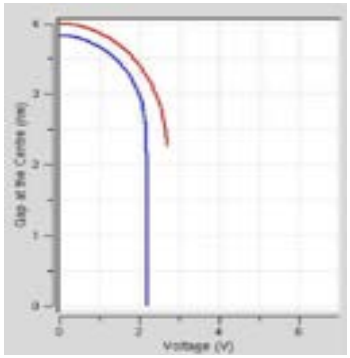 (c)	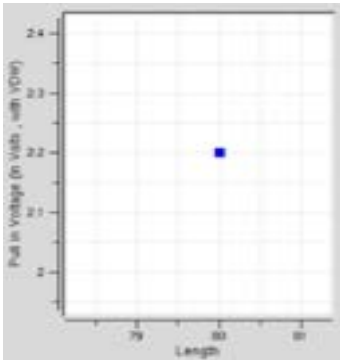 (d)	Dequesnes et al., 2002

Length = 1 nm Diameter = 2 nm Initial gap = 4 nm	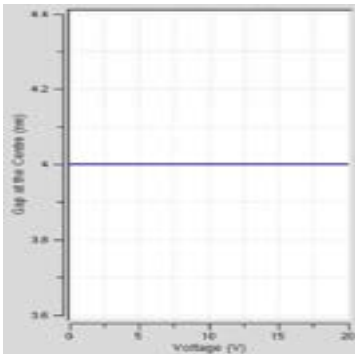 (e)	 (f)	My work
Length = 3000 nm Diameter = 2 nm Initial gap = 4 nm	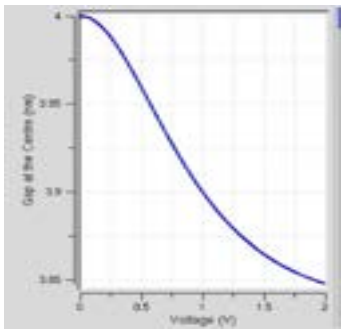 (g)	 (h)	My work

CONCLUSION

In this paper the pull-in behavior of the carbon nanotubes based fixed-fixed NEMS switches is presented. The result is successful when compare with other research work. Here, when the length is increased to an optimum value, the pull-in voltage will decrease. However, the simulation is not successful for the lowest and highest beam length as there is no bending behavior observed via the simulation plot. Thus, NanoHUB simulation software is capable of investigating the pull-in behavior of a fixed-fixed beam but with a limitation in terms of the length value. Further investigation is suggested to monitor the effect of length by referencing more work from other researchers.

REFERENCES

Dequesnes, M., Rotkin, S. V., & Aluru, N. R. (2002). Calculation of pull-in voltages for carbon-nanotube-based nanoelectromechanical switches. Nanotechnology, 13(1), 120.

Mahdi, L., & Al-Gayem, Q. (2021). Design, simulation and testing of an array of nano electromechanical switches (NEMS). Indonesian Journal of Electrical Engineering and Computer Science, 22(1), 113-120.

Sankar, P. G., & Udhayakumar, K. (2013). Pull-in Voltage Analysis of Carbon Nanotube based Electrostatic Actuators by using the ANSYS Software. Advanced Materials Research, 818, 117-123.

Yang, J., Jia, X. L., & Kitipornchai, S. (2008). Pull-in instability of nano-switches using nonlocal elasticity theory. Journal of Physics D: Applied Physics, 41(3), 035103.

ERBIUM-DOPED BOROTELLURITE GLASS-CERAMIC DIELECTRIC RESONATOR FOR ELECTRON SPIN RESONANCE AT X BAND

Yu Hui Lua[1], Syazana Othman[1,2], Yung Szen Yap[1,3], Ezza Syuhada Sazali[1,2]

[1] *Department of Physics, Faculty of Science, Universiti Teknologi Malaysia,*

81310 Johor Bahru, Johor, MALAYSIA.

yhlua0304@gmail.com, yungszen@utm.my

[2] *Advanced Optical Materials Research Group,*

Department of Physics, Faculty of Science, MALAYSIA.

[3] *Centre for Quantum Technologies, National University of Singapore, 3 Science Drive 2,*

Singapore 117543, SINGAPORE.

ABSTRACT

Electron Spin Resonance (ESR) spectroscopy is a technique employed to investigate molecules that contain unpaired electrons and a resonator is used for excitation and detection of the ESR signals. Here, the design for a cylindrical dielectric resonator (DR) based on erbium-doped borotellurite glass-ceramics enclosed in an aluminium cylindrical conducting cavity is simulated for X band ESR experiments. To that end, we have measured the dielectric constant and dielectric loss and based on the measurement, we simulated the DR design for operation at around 9 GHz.

Keywords: Dielectric resonator, erbium-doped borotellurite, microwave, X band, dielectric constant, dielectric loss, resonant cavity perturbation, quality factor

INTRODUCTION

Electron Spin Resonance (ESR) or Electron Paramagnetic Resonance (EPR) involves the excitation of unpaired electrons, with an energy splitting caused by the Zeeman effect. ESR spectroscopy uses resonators to detect and excite such paramagnetic substances, i.e. radical species in an external magnetic field, via microwave absorption. Applications of ESR include tracking electrical transport changes in quantum tunneling/interactions, spin-dependent photoluminescence for spin dynamics, and scanning probe techniques for materials science and biology [1]. Quantum computing also uses resonators to couple qubits, enhance readout sensitivity, and control the qubit quantum state. Some of the commonly used resonator designs are cylindrical cavity, rectangular cavity or re-entrant, stripline [2] and dielectric resonator (DR), where the microwave magnetic component aligns perpendicularly to the externally applied field.

ESR spectrometers are typically used in X band and higher frequencies, such as Q band (34 GHz) [3] and W band (95 GHz) [4]. Researches show resonant frequencies of DR are determined by their dimensions and dielectric properties [5-7], e.g. for a specific frequency, the resonator can be designed to have different dimensions depending on its dielectric constant [6,7]. Small DRs based on materials with high dielectric constant have an added benefit for small-sized applications, e.g. mobile communications and satellites. Typical dielectric materials used for resonators are rexolite (ϵ^* = 2.53 and tan δ = 6.0 × 10^{-4} measured at 10 GHz), ease for machining/fabrication [8], rutile (ϵ^* = 80 to 100) [9], and alumina (ϵ^* = 9.8 to 10.2), which offers good dielectric constant performance.

In this work, we investigate erbium-doped borotellurite glass-ceramics as the dielectric material for an ESR resonator at X band frequency, housed in a cylindrical aluminium conducting cavity and coupled with iris holes to facilitate microwave signal propagation. A through hole at the top of DR accommodates a quartz tube sample holder, ensuring precise sample placement at the highest induced microwave magnetic field. In the following sections, we explained the experimental works and simulation results.

DIELECTRIC PROPERTIES MEASUREMENT OF ERBIUM-DOPED BOROTELLURITE GLASS-CERAMICS

There are several techniques to measure the dielectric properties. Reference [10] proposed transmission-reflection technique that requires full S-parameter measurement for waveguides or coaxial lines. The free-space technique involved the use of wide-open spaces in the experimental setup [11], and the open-probe technique used flattened and solidified samples [12]. For cylindrical rod samples, the resonant cavity perturbation technique is typically used [13-15].

To determine the dielectric properties, $\epsilon^* = \epsilon' - i\epsilon''$ [16], we employed the resonant cavity perturbation technique using Q-factor extraction method by taking in account the shifts in resonant frequencies, Δf, and inverse of quality factors, $\Delta\left(\frac{1}{Q}\right)$ for real part, ϵ' and imaginary part, ϵ'' of complex permittivities [17]:

$$\epsilon' = \frac{V_c(f_c - f_s)}{2V_s f_s} + 1 \quad [1]$$

$$\epsilon'' = \left(\frac{\epsilon' - 1}{2\epsilon'}\right)\frac{f_s}{(f_c - f_s)}\left(\frac{1}{Q_s} - \frac{1}{Q_c}\right) \quad [2]$$

where f_c, f_s, Q_c, Q_s, V_c, and V_s are resonant frequencies, quality factors, and volumes for unloaded and loaded cavities, respectively.

For our TE_{101} mode cavity resonator, we designed WR-90 waveguide with 8 mm iris holes placed at both ends to create standing waves at resonant frequency, f_o = 8.12 GHz for the unloaded cavity (see Fig. 1). The Fig. 2 cavity resonator shows the dimension of the resonator: 22.86 mm (width) × 10.16 mm (height) × 30 mm (length). A 2 mm sample hole at the cavity's center was drilled to ensure the interactions onto sample at the maximum concentrated electric field [18]. Finite Element Method (FEM) simulation (Ansys HFSS) was used to simulate the cavity resonators, as shown in Fig. 1. Measurements are conducted using scalar network analyzer, (Signal Hound USB-TG124A and USB-SA124B) to measure the insertion loss.

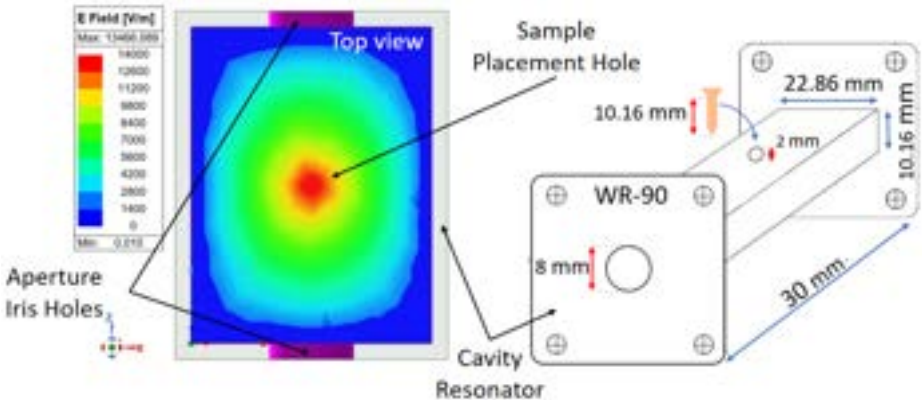

Figure. 1. Simulation design for rectangular cavity resonator, with a = 22.86 mm, b = 10.16 mm and d = 30 mm.

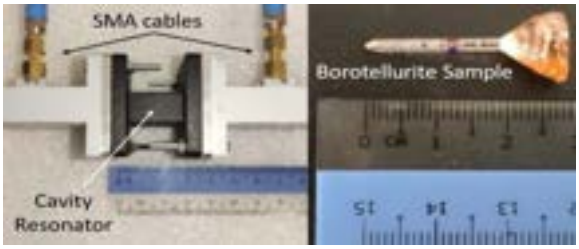

Figure. 2. Rectangular cavity resonator (left) and borotellurite sample (right).

To verify the perturbation technique is accurate, simulation was done and the results was used with Eqn. (1) and (2). The result shows a 6.22 % error for dielectric constant of an alumina sample compared to the reference values in the simulation. The contributing factors are most likely due to the Q-factor extraction method and

simulation accuracy. Hence, the alumina sample is determined to have a dielectric constant, $\epsilon^* = 8.59 \pm 6$ %. The dielectric loss of the sample is tan $\delta = 9.504 \times 10^{-4} \pm 17$ %.

For erbium-doped borotellurite glass-ceramics, the resonant frequency for unloaded cavity, $f_o = 8.12$ GHz shifted to $f_o = 7.039$ GHz after the insertion of the sample. Thus, the dielectric constant was determined using Eqn. 1 where $\epsilon^* = 17.73 \pm 6$ %. Fig. 3 also shows the S_{21} peak of -17.12 dB for unloaded cavity with a narrow linewidth of 15.7 MHz. After the sample insertion, the S_{21} peak reduced to -36.60 dB with a broader linewidth of 20.7 MHz. Consequently, the Q-factor decreased from 517.6 (unloaded) to 339.9 (loaded), resulting in the dielectric loss, tan $\delta = 2.289 \times 10^{-4} \pm 17$ %, which is significantly determined by its quality factors, as expressed in Eqn. 2 [19].

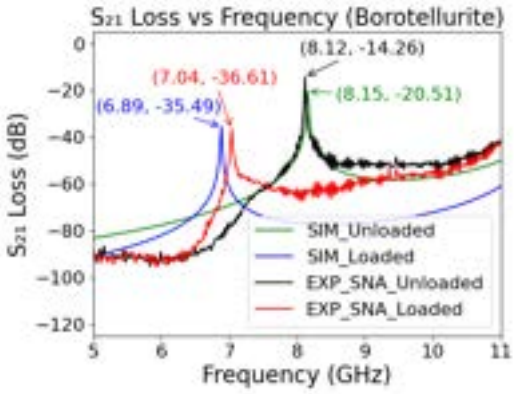

Figure. 3. Unloaded and loaded cavities between SNA experimental results with simulated results.

DESIGN AND SIMULATION OF DIELECTRIC RESONATOR USING ERBIUM-DOPED BOROTELLURITE GLASS-CERAMICS

A cylindrical DR made of borotellurite ($\epsilon^* = 17.73 \pm 6$ %, tan $\delta = 2.289 \times 10^{-4} \pm 17$ %) with dimensions: 6 mm (radius) × 7.2 mm (height), operating at $f_o = 8.395$ GHz, being placed inside an aluminium cavity (25 mm radius × 30 mm height). *TEM* mode was confirmed to be TE_{011} mode using FEM simulation. A 4 mm diameter quartz tube holds the sample to provide a high filling factor. The simulated results in Fig. 4, shows waveguide adapters of X band dimensions 22.86 mm (width) × 10.16 mm (height) connecting on both sides, directing the electromagnetic waves into and out of the cavity. Fig. 4 also shows the S_{21} peak of -6.076 dB for unloaded cavity, reduced to -7.578 dB after the sample insertion.

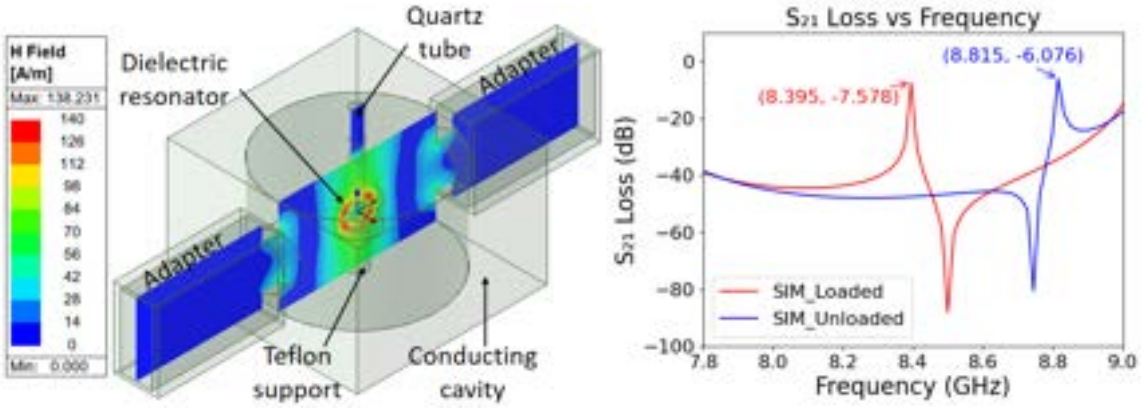

Figure. 4. Proposed simulation design for cylindrical DR (left) and simulated results for loaded and unloaded cavities (right).

CONCLUSION

This project aims to design a DR using erbium-doped borotellurite glass ceramics, with higher dielectric constant than alumina, in order to enhance the concentration of the induced magnetic field for ESR signal detection at X band frequencies while also reducing the overall size of the DR. A comparative study of dielectric

properties between alumina and borotellurite was conducted. We found that alumina has $\epsilon^* = 8.59 \pm 6$ % and tan $\delta = 9.504 \times 10^{-4} \pm 17$ %, determined through the resonant cavity perturbation technique with Q-factor extraction, whereas borotellurite has a dielectric constant of 17.73 ± 6 % and a dielectric loss of $2.289 \times 10^{-4} \pm 17$ %. Using borotellurite, we have designed and simulated the DR and it was found to resonate at 8.395 GHz. The next phase of the project involves fabricating designs and conducting cavity for ESR signal detection.

ACKNOWLEDGEMENT

The author acknowledges the Fundamental Research Grant Scheme (FRGS), grant number FRGS/1/2021/STG0//UTM/03/1 funded by the Ministry of Higher Education (MOHE)

REFERENCES

[1] Wang, Z., Balembois, L., Ranciˇ c, M.´ *et al.* Single-electron spin resonance detection by microwave photon counting. *Nature*, 2023. 619: 276–281. doi:10.1038/ s41586-023-06097-2.

[2] Yap, Y.S., Precise control and initialization of electron spin qubits, 2013.

[3] Guilarte, V., Trompier, F. and Duval, M. Evaluating the Potential of Q-Band ESR Spectroscopy for Dose Reconstruction of Fossil Tooth Enamel. *PLOS ONE*, 2016. 11: e0150346. doi:10.1371/journal.pone.0150346.

[4] Konkin, A., Popov, A., Ritter, U., Orlinskii, S., Mamin, G., Aganov, A., Konkin, A. and Scharff, P. Combined W-Band Light-Induced ESR/ENDOR/TRIPLE and DFT Study of PPVtype/PC 61 BM Ion Radicals. *The Journal of Physical Chemistry C*, 2016. 120. doi:10.1021/acs.jpcc.6b08034.

[5] Boe, P., Miek, D., Kamrath, F. and Hoft, M.¨ Hybrid Inline TE/TM Mode Dielectric Resonator Filters with Wide Spurious Free Range and Controllable Transmission Zeros. 2021. 555–58. doi:10.23919/EuMC48046.2021.9338165.

[6] Breeze, J., Aupi, X. and Alford, N. Ultra-Low Loss Polycrystalline Alumina. *Applied Physics Letters*, 2002. 81: 5021–5023.doi:10.1063/1.1532553.

[7] Friedlander, S., Ovchar, O., Voigt, H., B¨ ottcher, R., Belous, A.and P¨ oppl, A.¨ Dielectric Ceramic EPR Resonators for Low Temperature Spectroscopy at Xband Frequencies. *Applied Magnetic Resonance*, 2014. 46: 33–48. doi:10.1007/ s00723-014-0611-x.

[8] Sienkiewicz, A., Vileno, B., Garaj, S., Jaworski, M. and Forro, L. Dielectric resonator-´ based resonant structure for sensitive ESR measurements at high-hydrostatic pressures. *Journal of Magnetic Resonance*, 2005. 177(2): 261–273. doi:10.1016/j. jmr.2005.08.002. Epub 2005 Sep 15.

[9] Torokhtii, K., Pompeo, N. and Silva, E. A rectangular dielectric resonator for measurements of the anisotropic microwave properties in planar conductors. *Measurement Science and Technology*, 2013. 25. doi:10.1088/0957-0233/25/2/ 025601.

[10] Roberts, S. and Von Hippel, A. A New Method for Measuring Dielectric Constant and Loss in the Range of Centimeter Waves. *Journal of Applied Physics*, 1946. 17(7): 610–616.

[11] Trabelsi, S., Kraszewski, A. and Nelson, S. A New Density-Independent Function For Microwave Moisture Content Determination in Particulate Materials. 1997.

[12] You, K. Y., Esa, F. and Abbas, Z. Macroscopic characterization of materials using microwave measurement methods — A survey. 2017. 194–204. doi:10.1109/ PIERS-FALL.2017.8293135.

[13] Meda, V. and Raghavan, V. An Overview of Dielectric Properties Measuring Techniques. *Canadian Biosystems Engineering / Le Genie des biosystems au Canada*, 2005. 47: 15–30.

[14] Sheen, J. Amendment of Cavity Perturbation Technique for Loss Tangent Measurement at Microwave Frequencies. *Journalof Applied Physics - J APPL PHYS*, 2007. 102. doi:10.1063/1.2751484.

[15] Yang, R., Tsay, C.-Y., Hung, D., Liang, W., Yao, Y. and Lin, C.-K. Complex permittivity and permeability of iron-based composite absorbers measured by cavity perturbation method in X-band frequency range. *Journal of Applied Physics*, 2009. 105: 07A528 – 07A528. doi:10.1063/1.3088882.

[16]Rubinger, C. and Costa, L. Building a resonant cavity for the measurement of microwave dielectric permittivity of high oss materials. *Microwave and Optical Technology Letters*, 2007. 49: 1687 – 1690. doi:10.1002/mop.22506.

[17] Pompeo, N., Torokhtii, K., Leccese, F., Scorza, A., Sciuto, S. and Silva, E. Fitting strategy of resonance curves from microwave resonators with non-idealities. 2017. 1–6. doi: 10.1109/I2MTC.2017.7969903.

[18] Kim, C.-K., Minz, L. and Park, S.-O. Improved Measurement Method of Material Properties Using Continuous Cavity Perturbation Without Relocation. *IEEE Transactions on Instrumentation and Measurement*, 2020. PP: 1–1. doi:10.1109/ TIM.2020.2966358.

[19] Sebastian, Mailadil & Silva, M. A. S. & Sombra, Sergio. (2017). Measurement of Microwave Dielectric Properties and Factors Affecting Them. 10.1002/9781119208549.ch1.

THE PERFORMANCE OF LITHIUM-ION CAPACITOR BY USING ASYMMETRIC AND SYMMETRIC ELECTRODE.

Nor Faranaz Shamin[1], Nor Fadhlin Jaafar[2], Nurul Nazwa Mohammad[3], and Norha Abdul Hadi[4]

[1]*Faculty of Applied Sciences, Universiti Teknologi MARA, Cawangan Sabah, Kampus Kota Kinabalu*

faranaz@uitm.edu.my

[2]*Faculty of Applied Sciences, Universiti Teknologi MARA, Cawangan Negeri Sembilan, Kampus Kuala Pilah*

norfadhlin543@uitm.edu.my

[3]*Faculty of Applied Sciences, Universiti Teknologi MARA, Cawangan Perak, Kampus Tapah*

nurul.nazwa@uitm.edu.my

[4]*Faculty of Applied Sciences, Universiti Teknologi MARA, Cawangan Perlis, Kampus Arau*

norha.hadi@uitm.edu.my

ABSTRACT

Lithium-ion capacitors (LICs) are hybrid energy storage devices that merge the high energy density of lithium-ion batteries with the high-power density and long cycle life of supercapacitors. This study investigates the electrochemical performance of LICs using both asymmetric and symmetric electrode configurations. In asymmetric LICs, different materials are used for the anode and cathode, typically pairing a battery-type anode like MCMB with a capacitor-type cathode such as activated carbon. In contrast, symmetric LICs use the same material for both electrodes; in this study, Nano Fiber Graphene (PGNF) and activated carbon (AC) were utilized. The research involved preparing positive and negative electrodes using various carbon-based materials and assembling LICs with four different combinations of these electrodes. The samples were labeled as follows: sample I (MCMB and AC), sample II (AC and AC), sample III (PGNF and AC), and sample IV (PGNF and PGNF). All samples underwent cyclic voltammetry to assess their electrochemical properties. The results showed that sample III exhibited the highest capacitance and energy density, with values of 50.3 F/g and 15.72 Wh/kg, respectively, outperforming the other samples. Additionally, the study found that asymmetric LICs generally provide higher energy density than symmetric LICs. These results suggest that combining PGNF as an anode with AC as a cathode in an asymmetric configuration can significantly enhance the energy storage capacity of LICs while maintaining a reasonable power density.

***Keywords*:** Lithium-ion capacitors, asymmetric electrode, symmetric electrode, energy density, Nano Fiber Graphene (PGNF)

INTRODUCTION

Lithium-ion capacitors (LICs) are hybrid energy storage devices that combine the high energy density of lithium-ion batteries with the high-power density and long cycle life of supercapacitors (Naoi & Simon, 2008). This unique combination makes LICs suitable for various applications, including electric vehicles, portable electronics, and renewable energy systems. The performance of LICs is heavily influenced by the configuration of their electrodes, which can be either asymmetric or symmetric.In an asymmetric configuration, different materials are used for the anode and cathode, typically combining a battery-type anode, such as mesocarbon microbeads (MCMB), with a capacitor-type cathode, like activated carbon (Amatucci & Badway, 2003). This setup is designed to optimize energy density by leveraging the strengths of both materials. On the other hand, a symmetric LIC uses the same material for both electrodes, often resulting in better power density and cycle stability (Miller & Simon, 2008). Materials such as activated carbon (AC) are commonly used in symmetric configurations to maintain balance and uniformity in the electrochemical processes (Pandolfo & Hollenkamp, 2006). This study focuses on evaluating the electrochemical performance of LICs using both asymmetric and symmetric electrode configurations. For asymmetric LICs, different materials were selected for the anode and cathode, specifically using MCMB as the anode material, which allows for lithium-ion intercalation, and AC as the cathode material, which offers a high surface area for electrostatic charge storage. To explore symmetric configurations, materials such as PGNF and AC were employed. The study compares the performance of these LICs by preparing four distinct electrode combinations: Sample I (MCMB and AC), Sample II (AC and AC), Sample III (PGNF and AC), and Sample IV (PGNF and PGNF). The results of the study showed that Sample III (PGNF and AC) exhibited the highest performance. Furthermore, the study confirmed that asymmetric LICs generally provide higher energy density compared to symmetric LICs. However, symmetric LICs demonstrated superior power density and cycle

stability, making them more suitable for applications requiring rapid charge/discharge cycles and long-term durability. The findings of this study will contribute to the ongoing development of optimized LIC designs tailored for specific energy storage applications (Zhang & Zhao, 2009).

MATERIALS AND METHODS

This research aims to examine how changes in cathode and anode materials affect the electrochemical properties of lithium-ion capacitors. Typically, commercial lithium-ion capacitors use MCMB for the negative electrode and activated carbon for the positive electrode. This standard combination will serve as a reference sample. To enhance the capacitance of the cell, 20% by weight of Lithium Iron Phosphate ($LiFePO_4$) will be added to the positive electrode. The experiment begins by preparing the positive and negative electrodes. Table 1 helps in understanding how variations in electrode materials and their masses might affect the performance of lithium-ion capacitors.

Table 1. Mass and composition of material for positive and negative electrode

Sample	I		II		III		IV	
	Negative electrode material	Positive electrode material	Negative electrode material	Positive electrode material	Negative electrode material	Positive electrode material	Negative electrode material	Positive electrode material
Material	MCMB	AC + $LiFePO_4$	AC	AC + $LiFePO_4$	PGNF	AC + $LiFePO_4$	PGNF	PGNF+ $LiFePO_4$
Mass	0.0245	0.0286	0.0255	0.0309	0.0254	0.0319	0.0251	0.0298

This column lists the identifiers for each sample, labeled as I, II, III and IV. All samples use activated carbon (AC) or pristine graphene nanoflakes (PGNF) as positive electrodes. Meanwhile, negative electrode materials vary between Mesocarbon Microbeads (MCMB) and PGNF across different samples.

Each electrode was assembled into Teflon cells inside a glove box, utilizing a 1M $LiPF_6$ electrolyte (Ethylene Carbonate-Dimethyl Carbonate EC-DMC) and a polypropylene (PP) separator. This setup was then replicated by incorporating 20% $LiFePO_4$ into the positive electrode of each sample. Negative electrodes include a range of materials such as MCMB, AC, and PGNF. By changing the negative electrode materials and the amount of $LiFePO_4$, the table aims to assess the impact of these variations on the performance of the energy density lithium-ion capacitors.

RESULTS AND DISCUSSION

Figure 1 below shows a combination of cyclic voltammetry curves for four samples of Lithium-ion capacitors by using a different combination of positive and negative material. $LiFePO_4$ is added to the positive electrode in each sample to assess their electrochemical properties. From this CV curve, sample III (red color) gets a wider curve compared to other samples.

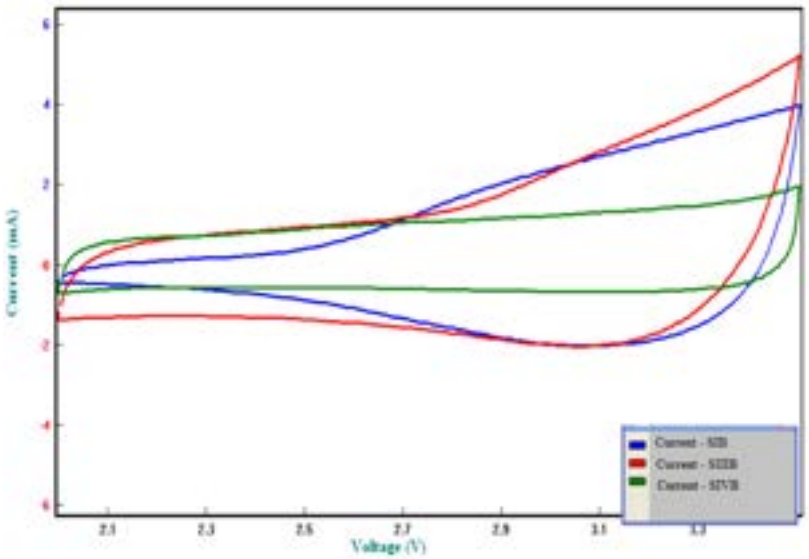

Figure 1. Cyclic Voltammetry curve for (Sample I) SIB, (Sample III) SIIIB and (Sample IV) SIVB. The scan rate for each sample is 5mV/s with cut of potential 2-3.5V

Table 2. Data Analysis for sample adding 20% of LiFePO4

Sample	MCMB_AC I	AC_AC II	PGNF_AC III	PGNF_PGNF IV
Scan Rate	5mV/s	5mV/s	5mV/s	5mV/s
Current (50mA/g)	0.00237	0.0006	0.0036	0.00091
Capacitance (F)	0.4741	0.1098	0.72036	0.18279
Total Mass LIC (g)	0.0531	0.0564	0.0573	0.0549
Specific Capacitance (F/g)	35.71406	7.7844	50.2869	13.31818
Energy Density (Wh/g)	11.16065	2.4326	15.7147	4.16193

Table 2 shows that sample III obtains the higher result of energy density which is 15.7147 Wh/kg compared to other samples. This result may be considered as a higher energy density because the value is more than 10Wh/kg. This is because of the unique structural atom of PGNF (asad ali et.al, 2022). It helps to improve the Solid Electrolyte Interface (SEI) layer that may usually occur during the first cycle of the cell. Next, the second higher energy density is obtained by Sample I which is 11.16Wh/kg. This combination is more convenient to use as a commercial LIC because the material of MCMB is cheaper compared to PGNF.

CONCLUSION

The experimental results demonstrated that asymmetric LICs, particularly the combination of Nano Fiber Graphene (PGNF) as the anode and Activated Carbon (AC) as the cathode, outperform other configurations in terms of energy density, achieving 15.72 Wh/kg with a capacitance of 50.3 F/g. This configuration optimizes energy storage while maintaining a satisfactory power density, making it a promising option for applications that require high energy storage capabilities.

On the other hand, symmetric LICs, which utilized the same materials for both electrodes, showed better power density and cycle stability. This makes symmetric configurations more suitable for applications demanding rapid charge/discharge cycles and long-term durability.

In summary, the research findings underscore the importance of selecting appropriate electrode materials based on the specific energy and power requirements of LIC applications. Future work should explore the integration of these materials in practical energy storage systems and further investigate the long-term stability of these configurations.

REFERENCES

Naoi, K., & Simon, P. (2008). "New Materials and New Configurations for Advanced Electrochemical Capacitors." *The Electrochemical Society Interface*, 17(1), 34-37.

Amatucci, G. G., & Badway, F. (2003). "Lithium-ion Capacitors: Hybrid Electrochemical Energy Storage Devices." *Journal of the Electrochemical Society*, 150(6), A745-A752.

Miller, J. R., & Simon, P. (2008). "Electrochemical Capacitors for Energy Management." *Science*, 321(5889), 651-652.

Pandolfo, A. G., & Hollenkamp, A. F. (2006). "Carbon Properties and Their Role in Supercapacitors." *Journal of Power Sources*, 157(1), 11-27.

Zhang, L., & Zhao, X. S. (2009). "Carbon-based Materials as Supercapacitor Electrodes." *Chemical Society Reviews*, 38(9), 2520-2531.

Ali, A., Liang, F., Zhu, J., & Shen, P. K. (2022). The role of graphene in rechargeable lithium batteries: Synthesis, functionalisation, and perspectives. *Nano Material Sciences*. https://doi.org/10.1016/j.nanoms.2022.07.004

TRACK D

OTHER APPLIED SCIENCES

EVALUATION OF STABILITY, TANNIN CONTENT, ANTIOXIDANT ACTIVITY, AND ANTIMICROBIAL PROPERTIES OF *MELASTOMA MALABATHRICUM L.* LEAF EXTRACT IN A WATER-BASED EMULSION

Amira Liyana binti Azri Sani [1], Norashikin binti Ahmad Zamanhuri ,[1,2]

[1]*School of Chemical Engineering, College of Engineering, Universiti Teknologi MARA, Selangor, Malaysia*

amiraliyana2001@gmail.com

[2]*Surface Coating Research Group, School of Chemical Engineering, College of Engineering, Universiti Teknologi MARA, Selangor, Malaysia*

shikin.zamanhuri@uitm.edu.my

ABSTRACT

Melastoma Malabathricum Linn (MML) is a small tree that grows wildly on wastelands and roadsides of Southeast Asia. It is known to traditionally treat various ailments including haemorrhoids and confinement wounds from childbirth. The many phytochemical constituents in its leaf like tannins exerts a great source of antimicrobial and antioxidant properties that may change the face of medicine that is in threat due to pathogens resistant to antibiotics, for example *Staphylococcus Aureus.* In folks medicine, the M. *malabathricum* L. leaves are chopped up and made into a paste to apply to wounds. This method was found to be impractical and hence a more conventional approach is applied where the leaf extract is added to topical preparations in the form of lotion. The study serves as a purpose to evaluate the emulsion based on tannin contents, antimicrobial and antioxidant assays, and stability tests on three different concentrations of the crude leaf extract oil –3.0%, 5.0%, and 7.0% of 10 grams of water-based emulsion. The leaves extract was obtained by Soxhlet and Cold extraction methods in a ratio of solvent combinations (70:20:10) of ethanol, methanol, and water. 3.62 and 4.98 grams of crude extract was obtained from cold and Soxhlet extraction methods respectively after undergoing rotary evaporation. The results have indicated that Cold extraction method extracts more tannins from MML with 31.63% difference to Soxhlet extract. Nonetheless, more antioxidant activity was exhibited in Soxhlet extract with 66.94% difference. The stability test results indicated that this water-based emulsion must be kept at 30ºC to avoid it from dissociating. From the presented study, 7% emulsion was proven to be most effective in antimicrobial agent.

***Keywords*:** Melastoma, leaves, extraction, medicinal, water-based emulsion

INTRODUCTION

Traditional herbal medicine, derived from plants, is widely embraced in various nations, including Malaysia, owing to the rich pharmacological properties of medicinal plants. Over 80% of the global population turns to plants for fundamental healthcare needs, driven by a growing scepticism towards modern medicine due to its high expenses, restricted availability, and potential adverse effects. Consequently, researchers are proactively seeking cost-effective, safe, and sustainable medicinal alternatives with fewer side effects and an extended duration before resistance development (Mhatre, Nagaral, & Kulkarni, 2014)

Multidrug resistance manifests when bacteria, fungi, or other microorganisms undergo evolutionary changes, developing mechanisms to resist the impact of antibiotics – e.g., *Staphylococcus aureus*. This development poses a substantial global health risk, potentially causing antibiotic treatments to falter, complicating infection control, and heightening the likelihood of contagion (de Kraker, Stewardson, & Harbarth, 2016). In response to this challenge, the scientific community has sought to counteract multidrug resistance by developing new antibiotics over the years.

A shrub native to Southeast Asia, *Melastoma malabathricum* is also known by the names Senduduk, Singapore Rhododendron, Indian Rhododendron, and Malabar Gooseberry. This small tree is native to the China, Australia, Singapore, Indonesia, Malaysia, and other tropical and monsoonal climate countries. The leaves, flowers, and fruits of *M. malabathricum* are the main features of its ethnobotany; nevertheless, this study focuses mostly on its herbal leaves due to it being available in a larger quantity. Leucorrhoea, dysentery, haemorrhoids, diarrhoea, and confinement wounds from birth are among several ailments that these leaves have a long history of treating in Indonesia, Malaysia, and India (Idris, Purnomo, Martak, & Fatmawati, 2022).

In addition, (Joffry et al., 2012) discussed that in folks' medicine, the leaves of Melastoma malabathricum was used to be applied as paste onto wounds to prevent them from scarring. Despite the long history of traditional

use of *M. malabathricum L.* for a variety of illnesses, there is currently little scientific evidence to support the herb's potential as a source of antioxidant and antimicrobial agents. The development and application of *M. malabathricum* leaves for therapeutic purposes is severely hampered by this knowledge gap.

Furthermore, *M. malabathricum L.* leaves were proven to contain phytochemical constituents like tannins, flavonoids, and alkaloids (Isnaini, Permatasari, Mintaroem, & Widodo, 2018)(Thatoi, Panda, Rath, & Dutta, 2008). According to (Nortjie, Basitere, Moyo, & Nyamukamba, 2022), tannins consist of polymeric phenols like ellagitannin which exerts antidiarrheal, and antimicrobial activities. Other than that, though much research has proven saponins to exhibit antioxidant activities, tannins were also said to mimic antioxidant properties (Amarowicz, 2007).

The possibility to extract tannins alone from the leaf allows for a more focused exploration of their specific properties, unmasking their full therapeutic potential. To the best of our knowledge, there were no studies focusing on optimizing the leaf's antimicrobial and antioxidant efficacy from tannins. As stated by Maria Elvina Tresia Butar-Butar et al (2021), deciphering the antimicrobial and antioxidant efficacy in Melastoma malabathricum leaves may help develop a strong, stable, and effective water-based emulsion. This emulsion is also easier to apply to the skin as compared to the traditional paste.

In this work, the antimicrobial properties and stability of *M. malabathricum L.* leaves extract from the developed water-based emulsion will be investigated. It will also measure the tannin content and antioxidant activity of the leaves extract. The combinations of antimicrobial properties, stability assessment, tannin content measurement, and antioxidant activity evaluation will provide a comprehensive understanding of the potential medicinal and functional properties of the *M. malabathricum L.* leaves extract in the form of the developed water-based emulsion, lotion

MATERIALS AND METHODS

Apparatus and Materials

The apparatus needed in this study is a laboratory grinder, glass beaker, aluminium foil, filter paper (Whatman No.1), UV-Visible Spectrophotometer, Soxhlet Apparatus, analytical balance, petri dish, mini centrifuge, rotary evaporator, sterile swab, and an incubator. The materials needed in this research are the Melastoma malabathricum leaves, water-based emulsion, 300 mL of 99% methanol, 600 mL of 99% ethanol, water, 2,2-diphenyl-1-picrylhydrazyl (DPPH), nutrient agar, mannitol salt agar, Folin Ciocalteau reagent, tryptone soya broth, and sodium carbonate (Na_2CO_3). All chemicals used are analytical reagent grade chemicals to ensure this study meets research standard, enhancing the credibility of this study.

Pre-treatment of M. malabathricum L. leaves

The leaves were collected from Selangor, Malaysia. It was then washed thoroughly in running water and distilled water to remove any dirt and unwanted contaminants. Next, the leaves will be dried in a confined air-conditioned space of 18 °C for cold extraction method (Abah & Egwari, 2011), whereas for the conventional method Soxhlet, the leaves were air-dried at room temperature. The air-dried leaves were blended into powder to increase its surface area for extraction.

Extraction of Leaves

Two methods of extraction were implied in this study – Soxhlet extraction and Cold Extraction methods. Both methods imply the same amount of ethanol, methanol, and water solvents in ratio of 70:20:10 (Abah & Egwari, 2011).

The powder was placed in a thimble-holder and filled with fresh solvent from a distillation flask. When the vapor rises, the solvent was condensed and filled up the thimble (Nortjie et al., 2022). The soxhlation of M. *malabathricum* leaves were performed using 99% ethanol, 99% methanol and water as solvent, in the ratio of 70:20:10 respectively. 10 grams powdered leaves were wrapped in filter paper, tied at both ends with thread and inserted into the Soxhlet apparatus. Then, 300 mL of the solvent were poured into the round bottom flask of the Soxhlet apparatus (Septiani et al., 2021). The soxhlation were conducted at 80°C for 6 hours until the cycle droplets are colourless.

The powdered leaves were soaked with solvent and kept in an enclosed jar for 72 hours for cold extraction method. The contents were shaken before filtering using filter paper (Whatman No. 1). The part of filtered content was concentrated using a rotary evaporator at 40°C (Abah & Egwari, 2011)(Rajkumar, Panambara, &

Sanmugarajah, 2022). The crude leaf extract from this method were tested against tannin content and antioxidant assay and were compared to the Soxhlet Extraction Method.

Water-based emulsion characterizations

The extracted leaves were infused with the water-based emulsion and were tested against two categories, which were antimicrobial assay and stability tests. These tests were done to three different concentrations of the leaf extract incorporated in 10 grams of emulsion, which were 3%, 5% and 7%.

Quantitative Assay of Tannin Content

Total tannin compounds will be determined calorimetrically using saturated Na_2CO_3 and Folin Ciocalteu reagent. UV-Visible spectrophotometer will be used to measure the compounds at a modified maximum wavelength of 750 nm (Suharni P. Sinaga et al., 2023). Standard solutions of tannic acid were prepared at 2%, 4%, 6% and 8%. 10 mL of sodium carbonate was added to each concentration along with 5 mL of Folin-Ciocalteu reagent. After that, distilled water was added until the solution reached 100 mL. The mixture was then transferred into labelled test tubes and left for forty minutes. Finally, a blank solution was prepared by adding 10 mL of sodium carbonate and 5 mL of Folin-Ciocalteu reagent to 85 mL of distilled water. The absorption of standard tannin solutions was measured under identical conditions and a standard curve was constructed (Antasionasti, Datu, Lestari, Abdullah, & Jayanto, 2021).

Antimicrobial Assay

The pathogens used for the antimicrobial assay were Staphylococcus Aureus and Escherichia Coli (Nortjie et al., 2022). The Kirby-Bauer agar disk diffusion approach was followed in the qualitative assessment of antibacterial activity. In summary, every bacterium was initially cultivated for 24 hours at 37 °C in Tryptone Soya Broth. Next, a 1000 µL micropipette was used to inoculate the bacterium solution onto Mannitol Salt Agar (MSA) and Mueller Hinton Agar plates.

The infected plates were given a little period of time to dry. The inoculated plates were then covered with disks that contained water-based emulsion at different sample concentrations (3%,5%,7%). The plates were incubated for 24 hours at 37 °C. Following this time, the inhibition zone's diameter was measured, and after an additional four days of incubation, the diameter of the inhibition zone was evaluated once more (Colucci et al., 2020). Figure 1 shows MSA agar before incubation.

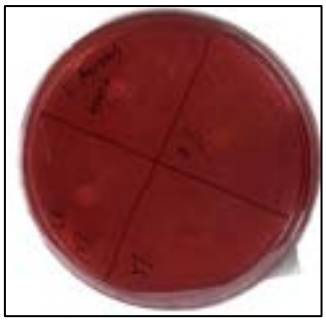

Figure 1. MSA agar before incubation

Antioxidant Assay

24 mg of 2,2-diphenyl-1-picrylhydrazyl (DPPH) powder was added to 100 mL of methanol to produce a 0.6 mM solution of DPPH in methanol, resulting in a dark violet solution (Baliyan et al., 2022). The samples must be diluted into a series of concentration, which are 2%, 4%, 6%, 8%, and 10% in 10 mL solvent. 2 mL of each concentration were set aside for dilution to serve as blank samples. 8 mL of DPPH solution was added to the remaining volume of each concentration for UV-Visible Spectrophotometer reading. The tested samples were then fully covered with aluminum foil and incubated at 37°C in a dark room for 30 minutes. At 515 nm, the absorbance of the reaction solution was determined using the UV-Visible Spectrophotometer. The percentage of the antioxidant activity were calculated using the formula in Eq. (1): (Colucci et al., 2020).

$$\%\ Scavenging\ Activity = \frac{A\ (control) - A\ (sample)}{A\ (control)} \times\ 100\%\ \ (1)$$

where: A symbolizes absorbance reading from the UV-Visible Spectrophotometer.

Stability Test

The base emulsion and three other emulsions incorporated with different extract concentrations (3%, 5%, and 7%) were submitted to two stability tests, which are thermal test and colour test. The thermal test was conducted in a water bath. The samples were heated in duplicate over three different temperatures, which were 30ºC, 50ºC, and 70ºC. The emulsion was visually observed if there were any changes in texture or colour (Colucci et al., 2020). A colour test was conducted to further analyse the changes quantitatively. A colorimeter was used to measure the colour changes in the water-based emulsion after undergoing various temperature tests. The L*, a*, and b* of the emulsions were recorded and discussed (Ly et al., 2020).

RESULTS AND DISCUSSION

The extraction of 10 grams of leaves using 300 mL of combined and ratioed polar solvents gave different results from two different methods. The Soxhlet extraction method managed to yield about 4.98 grams of dark green extract while cold extraction method yielded 3.62 grams of sage green extract. Further analyses are discussed below.

Both extraction techniques used a ratio of three polar solvents to extract plant leaves, and these solvents were combined and found to be soluble. The extraction method can affect the physical properties of the crude leaf extract. According to Abah and Egwari (2011), the heat in the Soxhlet extraction method can influence solubility. Therefore, choosing the right solvent is crucial. Figure 2 shows the results of crude leaf extract from the Soxhlet and Cold Extraction Methods.

The Soxhlet Extraction Method yielded more extract (4.98 grams) compared to the Cold Extraction Method (3.62 grams), with a yield difference of approximately 31.63%. This suggests that Soxhlet extraction is more efficient for obtaining components from leaves and is considered the most effective method for extracting crude oil from leaves (Nortjie et al., 2022). However, further analysis is needed to determine the phytochemical constituents, such as tannins, in both methods.

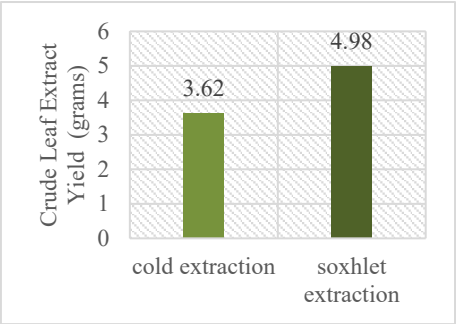

Figure 2. Yield of Different Extraction Methods

Tannin Content Analysis

This study shows a positive presence of tannin in M. *malabathricum* leaf extract. The type of extraction matters in deciding the best methods to extract tannins from herbal leaves (Kumar et al., 2023). As such, a standard curve was constructed with a linear regression line (y=16.05x+0.2954) as shown in Figure 3 (a) with a value of R^2 of 0.9942, indicating a high reliability of data to be used when comparing two types of extraction methods. From the equation, the tannin contents in the samples were calculated where y is the absorbance of sample and x is the Tannic Acid Equivalent (TAE). Figure 3(b) shows the number of tannins present in cold extraction method and Soxhlet extraction method.

The cold method extracts more tannins than the Soxhlet extraction method. However, the percentage difference between these two methods is only about 3.05%. Since the percentage difference is less than 5%, the significance might be questionable. Abah & Egwari (2011) suggested that the amount of tannins in cold extraction

were found to be more than Soxhlet extraction method. This finding is also backed up by Sankeshwari et al. (2018) where it was stated that cold extraction proved to be better than Soxhlet for extraction of tannins and saponins that contributes to the antibacterial activity of the extracts.

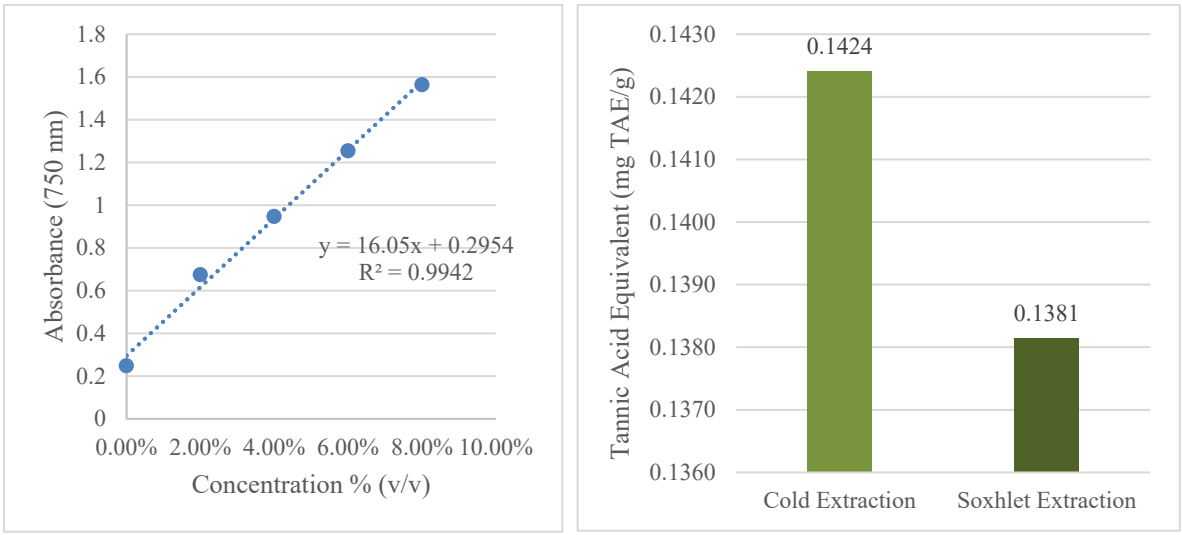

(a) (b)

Figure 3. (a) Tannic Acid Standard Curve and (b)Tannin Content of Each Extraction Methods

DPPH Radical Scavenging Activity (%RSA)

The findings of this analysis focus on the antioxidant potential of each extraction method. The results of the analysis are tabulated in Table 1 whereas the graph is constructed in Figure 4. The highest amount of scavenging activity in Soxhlet method was 99.01% whereas highest for cold method was 49.36%. A percentage difference of antioxidant activity between cold and Soxhlet is 54.65%. This value holds a very high significance in validating the obtained data as differences in scavenging activity indicates varying antioxidant capacities.

Based on Figure 4**,** the cold extraction method demonstrated a lower radical scavenging activity than the Soxhlet extraction method. The trend of the graph in cold extraction method indicated that there was a significant increase in the antioxidant activity in between 2% to 4% and 6% to 8%. While in Soxhlet extraction method, the %RSA increases rapidly at 2% and then steadily increase from 4% to 8%. This indicated that as the concentration of extract increases, the percentage of radical scavenging activity also increases (Fatiha & Abdelkader, 2019).

Fai-Chu Wong (2012) have studied different types of medicinal plants in Malaysia and found the highest scavenging activity to be 99.6% in *S. Barbata*, a plant indigenous to Malaysia, validating that it is possible to get a significantly high %RSA. Additionally, even though the number of tannins extracted from cold method is higher, other phenolic contents like flavonoids and alkaloids might be contributing to the high %RSA in Soxhlet method.

Abah & Egwari (2011) found that the total amount of phenolic content in Soxhlet method is higher than cold method due to the amount of alkaloids present in Soxhlet method is higher. This study is also backed up by (Dalimunthe et al., 2022) where the Soxhlet extraction procedure employing DPPH method yielded the highest amount of antioxidant activity and phenolic content.

Table 1. Soxhlet extraction and Cold extraction Radical Scavenging Activity %RSA data

Concentration (% v/v)	Absorbance @ 515 nm	% RSA
Soxhlet extraction		
0	0.5943	0.0000
2	0.0776	0.8694
4	0.0415	0.9301
6	0.0378	0.9364
8	0.0059	0.9901
Concentration (% v/v)	Absorbance @ 515 nm	% RSA

Cold extraction		
0	1.1082	0.0000
2	1.0305	7.0114
4	0.7161	35.3817
6	0.6825	38.4136
8	0.5612	49.3593

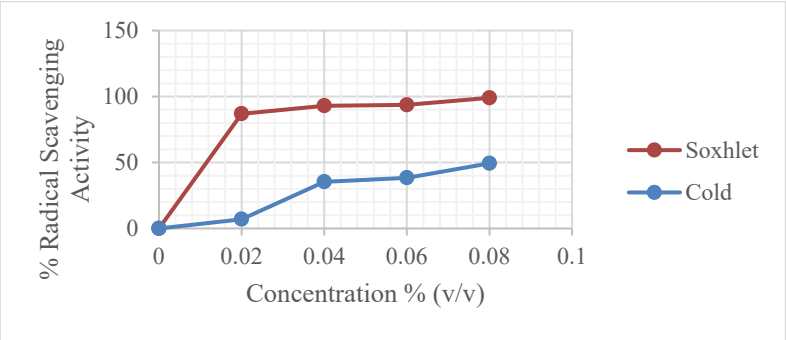

Figure 4. DPPH Radical Scavenging Activity on Different Extraction Method

Thermal and Colour Stability

This test focuses on the stability of the emulsion in terms of colour degradation due to thermal changes and how methods of extraction affect thermal behaviour of emulsions. The thermal test was conducted on all six different emulsions, with two distinct methods having 3 different concentrations. Figure 5 (a) shows the emulsion of cold extract while Figure 5(b) shows the emulsion of Soxhlet extract. Table 2 shows the physical data of emulsion before thermal test. After undergoing thermal test, the colour analysis was made and the results of L*, a*, and b* are differentiated.

Table 2. Data before thermal test

Properties	Cold Method	Soxhlet Method
Temperature	25ºC	25ºC
Colour (7%)	Dark green	Pale Green

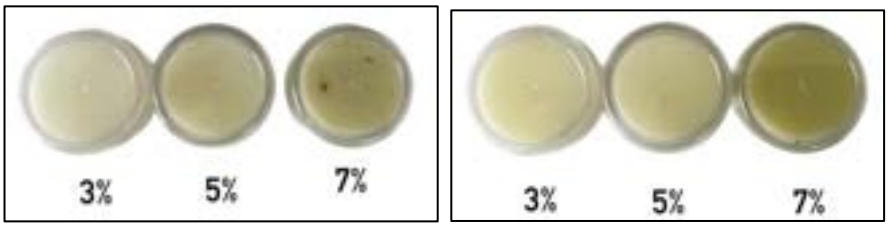

(a) **(b)**

Figure 5. Extract Emulsion (a) Soxhlet Method and (b) Cold Extract

Antimicrobial Analysis

This test focuses on the microbial susceptibility of cold and Soxhlet extract at different emulsion concentrations. It is seen in that the MSA agar have turned from red to yellow (Fig. 7a – 7b), indicating the presence of *Staphylococcus Aureus* (Mamay, 2022). Table 3 shows the data of results. After 24 hours, lower inhibition zones are observed at Soxhlet extraction method (SEM) (Fig. 7a & Fig. 7c) as compared to cold extraction method (CEM) (Fig. 7b & Fig 7d).

This is probably due to the presence of tannins being higher in cold extract than Soxhlet extract (Indriaty et al., 2023). This finding is supported by Abah & Egwari (2011) where they found that cold extraction exhibits a higher bacterial resistance than Soxhlet extract. This consistency across studies reinforces the idea that extraction

methods significantly impact the antimicrobial efficacy of plant extracts. The control disc containing only water-based emulsion did not exhibit any resistance toward both pathogens, just as expected.

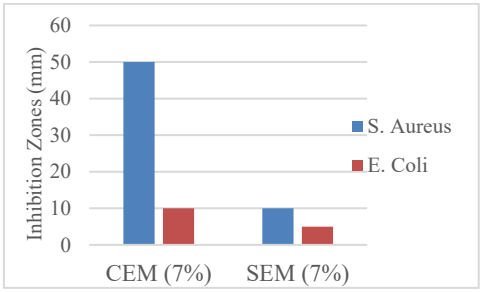

Figure 6. Inhibition zones of 7% Extracts

Based of Figure 6, the highest inhibition zone is obtained from pathogen *S.Aureus* (±50 mm) at 7% cold extract whereas the highest inhibition zone for Soxhlet extract is ±10 mm from *S. Aureus.* Additionally, for pathogen *E.Coli*, ±10 mm of inhibition region was recorded for cold extract, and ±5 mm for Soxhlet extract. This indicates that gram-negative pathogen exhibits more resistant towards the plant extract compared gram-positive (Sulaiman et al., 2011). The Soxhlet extract shows a 43.33% less inhibitory region than cold extract. This means that in gram-positive pathogen, the tannin activity is high (Fai-Chu Wong, 2012). This finding is crucial in developing natural antimicrobial agents for pharmaceutical or food preservation purposes. From this finding, it can be concluded that at higher concentrations of cold extract, a higher resistance to pathogens is built

Table 3. Data before thermal test

Extract	Pathogens	Inhibition Zones (mm)			
		Control	3% Extract	5% Extract	7% Extract
Cold Extraction Method	*Staphylococcus Aureus*	±0	±0	±20	±50
	Escherichia Coli	±0	±0	±10	±10
Soxhlet Extraction Method	*Staphylococcus Aureus*	±0	±0	±10	±10
	Escherichia Coli	±0	±0	±0	±5

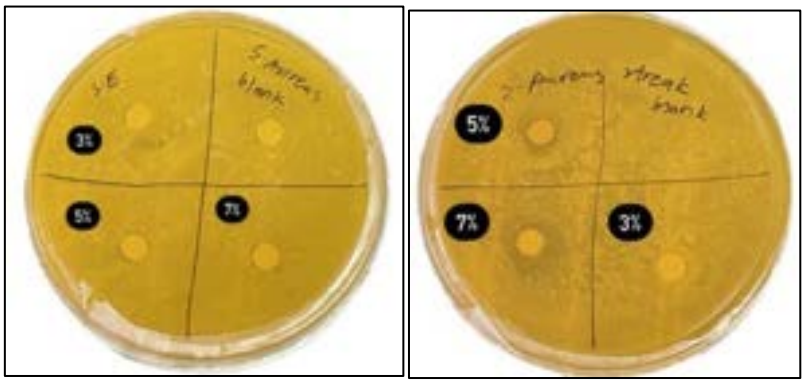

(a) **(b)**

Figure. 7(a-b). *S. Aureus* Inhibitory region of SEM **(a)** and CEM **(b)**

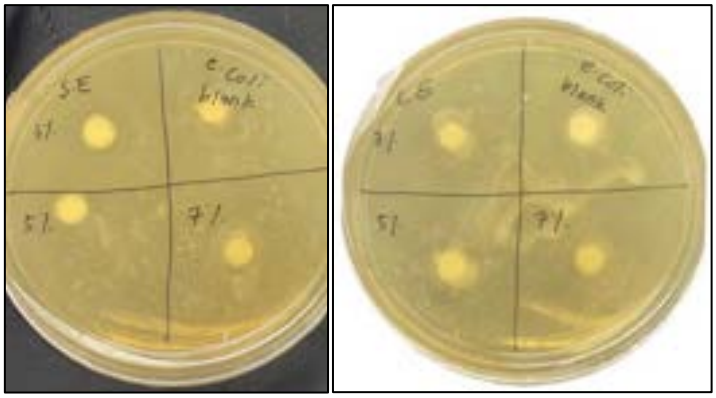

(c) **(d)**

Figure. 7(c-d). *E.coli* Inhibitory region of SEM **(c)** and CEM **(d)**

CONCLUSION

The study concludes that Soxhlet extraction is superior in yield and antioxidant activity, whereas cold extraction is more effective for antimicrobial applications due to higher tannin content. These findings highlight the need to select extraction methods based on specific bioactive properties desired for different applications, such as pharmaceuticals. Further research is recommended to explore the mechanisms behind these differences and the broader applications of *Melastoma malabathricum*, integrating traditional knowledge with modern scientific methods to unlock the plant's full potential for innovative and sustainable herbal medicine solutions.

REFERENCES

Abah, S. E., & Egwari, L. O. (2011). Methods of Extraction and Antimicrobial Susceptibility Testing of Plant Extracts, 3(5), 205–209.

Antasionasti, I., Datu, O. S., Lestari, U. S., Abdullah, S. S., & Jayanto, I. (2021). Correlation Analysis of Antioxidant Activities with Tannin, Total Flavonoid, and Total Phenolic Contents of Nutmeg (Myristica fragrans Houtt) Fruit Precipitated by Egg white. Borneo Journal of Pharmacy, 4(4), 301–310. https://doi.org/10.33084/bjop.v4i4.2497

Colucci, G., Santamaria-Echart, A., Silva, S. C., Fernandes, I. P. M., Sipoli, C. C., & Barreiro, M. F. (2020). Development of water-in-oil emulsions as delivery vehicles and testing with a natural antimicrobial extract. Molecules, 25(9), 5–7. https://doi.org/10.3390/molecules25092105

de Kraker, M. E. A., Stewardson, A. J., & Harbarth, S. (2016). Will 10 Million People Die a Year due to Antimicrobial Resistance by 2050? PLoS Medicine, 13(11), 1–6. https://doi.org/10.1371/journal.pmed.1002184

Idris, M., Purnomo, A. S., Martak, F., & Fatmawati, S. (2022). Antioxidant and Antidiabetic Activities of Melastoma Malabathricum Leaves Extracts. Journal of Hunan University Natural Sciences, 49(7), 144–153. https://doi.org/10.55463/issn.1674-2974.49.7.16

Isnaini, Permatasari, N., Mintaroem, K., & Widodo, M. A. (2018). Analysis of quercetin and kaempferol levels in various phase of flowers melastoma malabathricum L. International Journal of Plant Biology, 9(1), 1–4. https://doi.org/10.4081/pb.2018.6846

Joffry, S. M., Yob, N. J., Rofiee, M. S., Affandi, M. M. R. M. M., Suhaili, Z., Othman, F., … Zakaria, Z. A. (2012). Melastoma malabathricum (L.) smith ethnomedicinal uses, chemical constituents, and pharmacological properties: A review. Evidence-Based Complementary and Alternative Medicine, 2012(Table 1), 6–20. https://doi.org/10.1155/2012/258434

Mhatre, J., Nagaral, S., & Kulkarni, S. (2014). Formulation and evaluation of antibacterial activity of a herbal ointment prepared from crude extracts of Aegle Marmelos, (Bael). International Journal of Pharmacy and Pharmaceutical Sciences, 6(SUPPL. 2), 575–579.

Nortjie, E., Basitere, M., Moyo, D., & Nyamukamba, P. (2022). Extraction Methods, Quantitative and Qualitative Phytochemical Screening of Medicinal Plants for Antimicrobial Textiles: A Review. Plants, 11(15). https://doi.org/10.3390/plants11152011

Rajkumar, G., Panambara, P. A. H. R., & Sanmugarajah, V. (2022). Comparative Analysis of Qualitative and Quantitative Phytochemical Evaluation of Selected Leaves of Medicinal Plants in Jaffna, Sri Lanka. Borneo Journal of Pharmacy, 5(2), 93–103. https://doi.org/10.33084/bjop.v5i2.3091

Thatoi, H. N., Panda, S. K., Rath, S. K., & Dutta, S. K. (2008). Antimicrobial activity and ethnomedicinal uses of some medicinal plants from Similipal Biosphere Reserve, Orissa. Asian Journal of Plant Sciences, 7(3), 260–267. https://doi.org/10.3923/ajps.2008.260.267

POLYETHERSULFONE (PES) ULTRAFILTRATION MEMBRANE FOR WATER TREATMENT APPLICATIONS BY USING POLYVINYLPYRROLIDONE (PVP) AS PORE FORMING AGENT

Maimunah Villiamor [1], Chiam Chel Ken [1], Akhtar Razul Razali [2], Noor Maizura Ismail [1]

[1]*Chemical Engineering Programme, Faculty of Engineering,*

Universiti Malaysia Sabah Jln UMS 88400 Kota Kinabalu Sabah, MALAYSIA

maizura@ums.edu.my

[2]*Fakulti Teknologi Kejuruteraan Mekanikal & Automotif,*

Universiti Malaysia Pahang Al-Sultan Abdullah (UMPSA), Pahang, Malaysia

ABSTRACT

Porous polymeric membranes are produced from polyethersulfone (PES) for water treatment due to their excellent thermal, chemical, hydraulic and mechanical stability. However, the hydrophobicity of PES has led to fouling and reduced the membrane lifetime as high forces are required to move the water through the pores. Polyvinylpyrrolidone (PVP) as an additive adds to PES to relatively increase the PES membrane hydrophilicity and enhance pore-forming. Therefore, this work aims to determine the effect of the PVP-to-polymer ratio (0wt% to 32wt%) on the functional groups, morphologies, and hydrophilicity of the membrane. The PES membrane modification was carried out by blending method meanwhile the membrane preparation was accomplished through non-solvent induced phase inversion (NIPS). The successful fabrication of the PES membrane with PVP has been unequivocally demonstrated through the FTIR results. In addition, the scanning electron microscopy (SEM) images further confirmed as the PVP ratio increased, the porosity of enhanced as the membrane morphology (cross section) will change from the macro-void structures to spongier structure and denser compared to neat PES membrane. The addition of PVP enhances the membrane's hydrophilicity which the optimum hydrophilicity obtained through 16wt% of PVP. In conclusion the addition of PVP in the PES matrix has improved the pore formation and hydrophilicity of the membrane. For future research, the next generation of PES/PVP membranes modification should focus on addressing the mechanical properties of modified PES membrane in which will enhance the membrane hydrophilicity and permeability without altering the mechanical properties.

Keywords: Polyethersulfone, polyvinylpyrrolidone, membrane, water treatment, pore-forming

INTRODUCTION

The continuously rising demand of cleaned potable water is one of the current huge issues for the 21st century due to the few aspects that reducing the accessible of cleaned water such as expanded growing of industrialization and overpopulation (1). To resolve the increasing demand, it is vital for the contaminated water to undergo water treatment prior to domestic consumption. Water treatment process is technically involved separating and filtering all the biological, chemical and physical contaminants that are potentially harmful to domestic consumption throughout water supply (2). The properties and quality of water are influenced by contaminants such as pathogens and harmful chemicals. Water can be treated through physical, chemical, biological, radioactive and electrical methods to eliminate contaminants. Physical conventional technologies of water treatment, namely screening flocculation, sedimentation, flotation and filtration are utilized. In 2030, the access water is aimed to be consumable for all according to the Nations' Sustainable Development Goal 6 (SDG 6) (3). Therefore, concerning the clean water supply, improved and advanced technology should be implemented worldwide to produce high water quality. Membrane filtration, specifically ultrafiltration, is a developed technology of water treatment that has proven to be more effective than conventional ones. Membrane filtration capable of removing fine particulates (suspended and dissolved solid) from water under pressure or vacuum in which sedimentation is not capable, although they are similar.

Membranes are illustrated as thin layer material which is capable of particle separation according to their physical and chemical properties when a driving force is applied across the membrane. The main advantages of low-pressure UF membrane processes compare with conventional clarification and disinfection (post chlorination) processes are inessential for chemicals, size-exclusion filtration as opposed to media depth filtration, provide a good and consistent quality of treated water in terms of particle and microbial removal regardless of raw feed water quality (4).

Polyethersulfone (PES)-based membranes have been widely implemented in the separation process as they exhibit excellent oxidative, thermal and hydrolytic stability as well as distinguish mechanical properties (5).

Nevertheless, PES is relatively hydrophobic. Hence, according to Kourde-Hanafi et al. (6), PES is mixed with additives such as polyvinylpyrrolidone (PVP) to enhance the membrane hydrophilicity and to initiate the pore-forming during membrane synthesis by phase inversion. The morphologies (pore structure) and hydrophobicity of the membrane depending on the ratio of the additive-to-polymer utilized (7-8). Therefore, this work aims to fill the previous research gap by determining and studying the role of PVP addition with different ratios in affecting the membrane performance, morphologies, mechanical properties, porosity, and pore size.

LITERATURE REVIEW

Membrane Filtration

Separation through membrane filtration promises high efficiency of pollutants removal along with economically and environmentally safe as none of chemical utilized during the filtration process. Membrane can be either synthetic or non-synthetic (natural) based. The synthetic-based include of polyethersulfone (PES), polysulfone (PSF), cellulose acetate (CA) etc. Meanwhile, natural-based is usually produced from cellulose, chitin, starch, and alginate which is mostly used to fabricate fully or semi-biodegradable membranes (9). The main concern of membrane filtration utilization is the hydrophilicity and morphology of the membranes as it highly influences the effectiveness of pollutants removal in water treatment. The effectiveness of the membrane performance is dependent on membrane rejection, antifouling and permeability (10). Figure 1.0 depicts the general mechanism of membrane filtration. Membrane filtration mechanism required driving force to move the water molecules between two sides. The driving force could be in terms of pressure, concentration and electric potential gradient. The molecules that can permeate through membrane layer are determined by the membrane pore sizes.

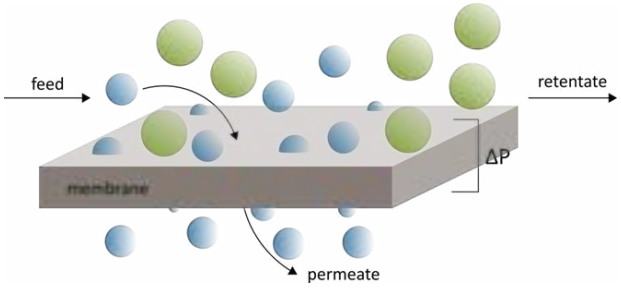

Figure 1. General mechanism of membrane filtration

Membrane separation filtration has been widely applied in industrial water treatment processes as it promotes clean technology with efficient energy consumption. In future prospects, membrane filtration can be fully replaced by conventional processes such as filtration, distillation, ion exchange, and chemical treatment systems. The advantages of membrane filtration utilization are the flexibility where it can be operated even in mild conditions, enables an easy upscaling hybrid processing, and the membrane physical and chemical characteristics can be also modified to the desired end-result. However, this particular technology has some drawbacks in which it is easily prone to membrane fouling consequently reducing the membrane life-span and low selectivity and flux. Fortunately, the issues can be resolved by fabricating membranes with different types of morphologies depending on the type of application. The modification is achievable by modifying and optimizing the material and its ratio utilized during membrane fabrication (11-14).

PVP as an Additive to PES Membrane

Despite the advantages offered by PES membrane, consistency of contaminants removal in water difficult to accomplished due to its relatively hydrophobic characteristics that reducing the water flux permeate through it (13). Hydrophobicity can lead to fouling as high forces are required to transfer and move the water molecules from different regions of membrane (14). Consequently, fouling reduces membrane flux and lowers the stability and life span of the membrane (15). One of the resolutions suggested is by adding the additive into the PES to enhance the membrane's hydrophilicity while maintaining good performance. Example of additives are polyethylene glycol (PEG), lithium chloride (LiCl), polyvinylpyrrolidone (PVP), Pluronic and tetronic copolymers, surfactants- like cetyl trimethylammonium bromide (CTAB), Triton-X 100 and sodium dodecyl sulfate (SDS) (16). Among the hydrophilic additives mentioned, polyvinylpyrrolidone (PVP) has been a standout due to its biocompatibility, non-toxicity, resistance to thermal degradation and cost-effectiveness (17-18).

Polyvinylpyrrolidone (PVP), or its often addressed as polyvidone or povidone is categorized as water-soluble polymer created from the monomer N-vinylpyrrolidone (19). Additionally, PVP provides excellent permeability and readily forms films. Figure 2.0 illustrates the PVP formation through free-radical polymerization of the monomer N-vinylpyrrolidone in the presence of initiator (AIBN). Figure 2. depicts the physical mechanism of PVP added into PES membrane to increase the hydrophilicity, permeation, and rejection. The hydrophilic component of PVP is anticipated to be dissolved away in water during the phase inversion process (NIPS), causing PVP-containing locations to become micropores (20). Also, the pore size formed depends on the molecular weight of PVP utilized as more PVP or larger PVP molecular size is introduced, the pores formed became larger (21).

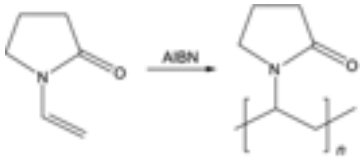

Figure 2. Synthesis of PVP through free-radical polymerization (Kariduraganavar et al., 2014).

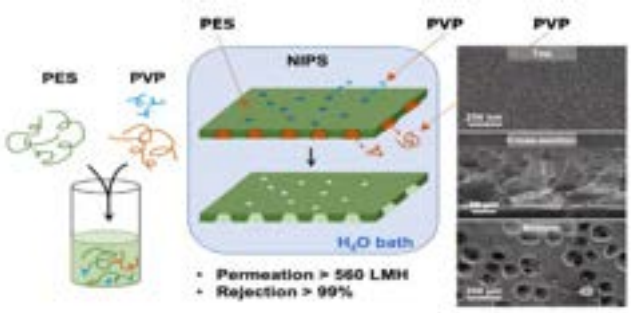

Figure 2.1. Physical mechanism of PVP addition into PES membrane (Ho & Su, 2022b).

METHODOLOGY

PES/PVP membrane fabrication was adapted from the literature with different variation of ratio (6). The neat PES and PES/PVP membrane fabrication was done through blending modification and prepared through non-solvent phase inversion (NIPS) procedure as shown in Figure 3.

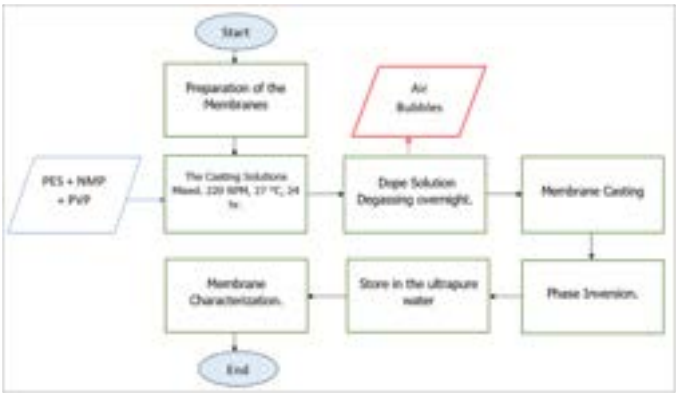

Figure 3. Process flowchart for the methodology proposed.

Materials and Membrane Synthesis

Polyethersulfone (PES, Kornchen, MW=58,000 g/mol) supplied by GoodFellow Cambridge Limited Huntingdon PE29 6WR (England) and N-Methyl-2- pyrrolidone (NMP, purity of 99.5% and MW of 99 g/mol which was purchased from Sigma-Aldrich, Germany) were used to prepare casting solutions for membrane preparation. Polyvinylpyrrolidone (average MW=1, 300, 000 g/mol and was purchased from Sigma-Aldrich, Germany) was used as a hydrophilic additive and pore former agent.

The preparation of the membranes with different composition of additives are shown in Table 3.0 as the PVP/PES range ratios utilized varied from 0wt% to 32wt%. The first membrane will not add any additive (PVP) as this membrane will act as a control parameter and to observe membrane morphology without PVP addition. The casting solutions are prepared by incorporating the stated number of PES (polymer), NMP (solvent) and PVP (additive) in Table 3.0. The PES/PVP fabricated by remaining the same value of PES and NMP while varied the PVP value (0% to 32%). The casting solutions are mixed in a sample bottle under continuous stirring (200RPM) at room temperature of (25±2 °C) for at least 12 hours until the polymer solution is completely dissolved using Motor Stirrer (IKA RW Digital) (22).

Subsequently, the polymer solution is degassed overnight to remove air bubbles trapped in it prior to casting. Then, after the membrane casting procedure is done in a rigid supporting layer such as glass plate and glass rod to flatten the casting solution evenly in a two layer of masking tape of thickness. After that, the polymer is immersed in the water bath for phase inversion. The Non-Solvent Induced Phase Inversion (NIPS) method implemented for phase inversion in which an equilibrium dope solution is transformed from liquid to solid phase in a few milliseconds with the water as the drive mechanism under crucial thermodynamic and kinetic aspects (23). Consequently, a flat membrane formed through this process as the cast polymer on a rigid supporting material dissolved in the solvent (polymer solution). The polymer membrane is kept in ultrapure water before usage.

Table 3. Polymeric solution composition for PVP-polymer blends membrane.

SAMPLE NAME	PES (wt%)	NMP (wt%)	PVP/PES Ratio (wt%)
PES	25.0	75.0	0
PES/4PVP	25.0	75.0	4
PES/8PVP	25.0	75.0	8
PES/16PVP	25.0	75.0	16
PES/32PVP	25.0	75.0	32

Membrane Characterizations

a) Membrane functional group: ATR-FTIR spectroscopy

According to Milescu et al. (24) the membrane has to undergo a dynamical vacuum drying for 2 days prior to characterized using a 400 FT-IR/FT-NIR (Fourier Transform Infrared Spectrometer) brand Perkin Elmer Spectrum IR Version 10.6.2. The FTIR-ATR is equipped with a ZnSe crystal ATR element with single reflection and incidence angle of 45°. The spectra will be collected from 650 〖cm〗^(-1) to 4000 〖cm〗^(-1) at 2 〖cm〗^(-1)resolution and each spectrum accomplished from average 4 scans after background recording carry out at ambient air.

b) Membrane morphology: Scanning Electron Microscope (SEM) micrographs.

For membrane morphology specifically in cross section analysis, Field Emission Scanning Electron Microscope (Carl Zeiss EVO MA 10) will be utilized to record and analyses the images at 20 kV and magnification ranging from 200× to 20,000× as suggested in the literature (25) in which will be done at the Centre for Instrumentation and Science Services (PIPS) at University Malaysia Sabah to determine the morphology and structure of the membranes after they were frozen and fractured in liquid nitrogen followed by Au/Pd coating.

c) Surface wetting property: Contact angle

The contact angle is determined by using Biolin Scientific contact angle instrument and a sessile drop method following a procedure that similar to (23). A water drop (5 microliter) was slowly and carefully placed onto membrane surface using a needle tips. The image of the droplet was generated with One Attension Version 4.1.1 (r9486). The contact angle of the droplet on the membrane surface was automatically measured at room temperature (22 Degree Celsius). The static contact angle will be determined by automated software. The contact angle will be taken of 3 different points to generate an average data (24).

According to Bolong et al. (26) due to the evaporation effect, it is suggested to conduct measurements as quickly as possible (within 10 seconds) to minimize the disturbance caused by evaporation. Furthermore, Mu and Zhao (2009) also noted that the contact angle decreases over time, with the water contact angle for the original PES membrane declining from approximately 89° at the start to 66° at 185 seconds. They attribute this phenomenon to water drop penetration into the membrane pores. Additionally, it is important to note that due to variations in pore sizes and porosities among different PES membranes, contact angle measurements of modified PES membranes from various studies are not directly comparable.

RESULTS AND DISCUSSIONS

Membrane functional group: ATR-FTIR spectroscopy

Polyvinylpyrrolidone (PVP) can be detected and identified using FTIR spectroscopy. These characteristic absorption peaks can serve as diagnostic markers for the presence of PVP in a sample during FTIR analysis. By comparing the observed peaks in the sample's FTIR spectrum with known reference spectra or databases, the presence and identity of PVP can be confirmed. In an FTIR analysis of a sample containing PVP, characteristic absorption peaks corresponding to the functional groups present in PVP can be observed in the infrared spectrum. By referring to Figure 4. 0, the PVP functional groups (C=O stretch) can be detected as there are absorption peaks in the FTIR spectrum which range 1660 〖cm〗^(-1) to 1670 〖cm〗^(-1).

Milescu et al. reported that residual PVP indicated by a C=O stretch at 1667 to 1662 〖cm〗^(-1), pyrrolidinyl radical at 1462 and 1423 〖cm〗^(-1) (24). A medium to strong peak is observed around 〖1072 cm〗^(-1), representing the stretching vibration of the carbon-nitrogen bond (C-N) in the pyrrolidone ring. And the C-H asymmetric stretch at 2950 〖cm〗^(-1). During the membrane precipitation process, a portion of the PES and the water-soluble polymer is removed from the membrane's surface, but a sufficient amount of PVP remains, therefore, there will be C=O stretch at 〖1667 cm〗^(-1). This residual PVP contributes to the hydrophilicity of the polymer surface, making it more hydrophilic compared to the surface of PES alone.

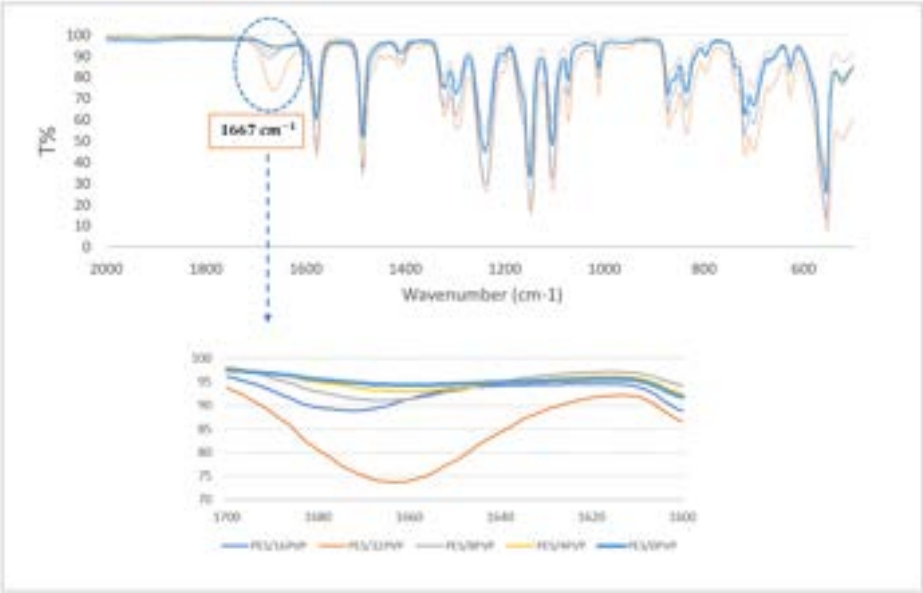

Figure 4. FTIR/ATR spectra of neat PES membrane and PES/PVP membranes.

Vatsha et al. studied the PES membrane modification with the addition of PVP and the FTIR spectrum showed a new absorption peak at 1677.5〖cm〗^(-1), which highly indicate the PVP existence in the PES membranes while the rest of the spectrum remained constant (27). The PVP carbonyl is responsible for this new band. As a result, the polymer surface is more hydrophilic than the surface of neat PES, indicating that PVP is trapped in the PES network and forms a crucial component of the polymeric structure. Therefore, the expected result for ATR-FTIR, is that the peak spectrum at around 1677.5 〖cm〗^(-1) which gives the indication of PVP existence in the PES membranes.

Additionally, Kourde-Hanafi et al. stated that the spectrum region about 1673〖cm〗^(-1) that can be attributed to the C=O oscillation of PVP is where the two spectra highly diverge (6). Meanwhile, the spectrum at around 1440〖cm〗^(-1) in which this band is attributed to the CH2C=O group of PVP's C-H vibration. The study also determines and analyze the ratio of the bands at 1673〖cm〗^(-1) and 1235〖cm〗^(-1) for each membrane sample to mainly examine the impact of the amount of PVP in the PES membrane. These bands were chosen because they can be attributed to the C-O bond in PES and the C-O vibration in PVP, respectively. Therefore, the expected result for ATR-FTIR, is that the peak spectrum at around 1673 〖cm〗^(-1) which indicates the O=C bond vibration of PVP molecules.

In conclusion, the successful fabrication of the membrane with Polyvinylpyrrolidone (PVP) has been unequivocally demonstrated through the compelling FTIR results. The FTIR analysis served as a crucial tool in verifying the chemical composition and structural integrity of the membrane. The distinctive absorption peaks observed in the FTIR spectra provided concrete evidence of the presence of PVP and its interaction with other components of the membrane.

Membrane morphology: Field Emission Scanning Electron Microscope (FESEM) micrographs.

In Figure 4.1 and Figure 4.2, the imaging of the synthesized membrane's top view and cross-section through SEM was used to determine the structure of the membrane with the PVP concentration of 0%, 4%, 8%, 16% and 32%. By referring to Figure 4.1, the illustration of the membrane active layer is at the top of the PES and PES/PVP membranes which display a typical characteristic structure of a microfiltration membrane, featuring a porous surface. The pore distribution of modified PES membranes increases as the PVP concentration contained in the PES membranes increased, therefore, indicates the porosity increment as well. Luque-Alled et al. validate the trend observed in the SEM images, which confirmed that the addition of pore-forming agents to the casting solutions leads to an increase in porosity (28). The highly dense pore size was associated with the PES/16PVP and PES/32PVP membrane which indicates higher porosity compared to other synthesized membranes.

Figure 4.2 displays the cross-sectional SEM micrographs of both the PES membrane and the PES/PVP membranes. For all the membranes, a distinct morphology was observed, characterized by a dense top layer and a

porous sublayer with a finger-like and a network-like cross-section. However, the porous sublayer of the PES/PVP membranes exhibited greater irregularity and prominence compared to that of the neat PES membrane.

The top-layer layer of PVP/PES membrane was observed and recorded to have several tens of micrometers thick and fairly dense. This could be attributed to the dope solution containing high amount of PES content (25 g for 75 g of NMP) as a result, produced a solution with a high viscosity and promotes fabrication of membranes with fewer macrovoids (6). As the concentration of pore-forming additive (PVP) increased, the structure of the macro-voids undergoes a transformation from a large, finger-like shape to a teardrop shape.

Additionally, Figure 4.2 (e) shows the sponge-like appearance of the membrane cross-sectional porous structure of (membrane sublayer). This occurs due to the elevated viscosity of the dope solution, which hinders the diffusion exchange between the solvent (NMP) and the non-solvent (water) within the membrane sublayer. Consequently, leading to a deceleration in de-mixing kinetics and affect the diffusion exchange process.

As a result, the membrane morphology undergoes a transition towards a spongier (tear drop) structure (29). Subsequently, rapid phase separation takes place at the skin layer, while the precipitation rate slows down in the membrane sublayer. Therefore, the scanning electron microscopy (SEM) images further confirmed that as the PVP ratio increased, the membrane morphology (cross section) will change from the macro-void structures to spongier structure and denser compared to pure PES membrane.

Nonetheless, the cross-sectional image of the membrane lacks clarity due to being cut with scissors rather than fractured using liquid nitrogen. Consequently, the resulting fracturing was uneven. To ensure the generation of accurate data in the future, it is recommended to adhere to the characterization technique outlined in prior research. This is particularly crucial for determining the morphology and structure of the membranes subsequent to their freezing and fracturing in liquid nitrogen, followed by Au/Pd coating.

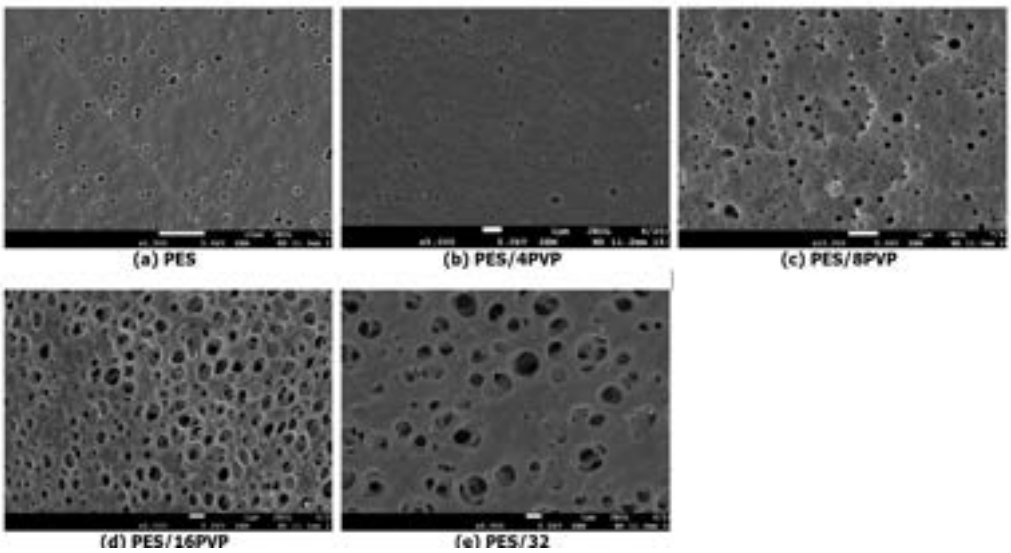

Figure 4.1. SEM images of top view of neat PES membrane and PES/PVP membranes.

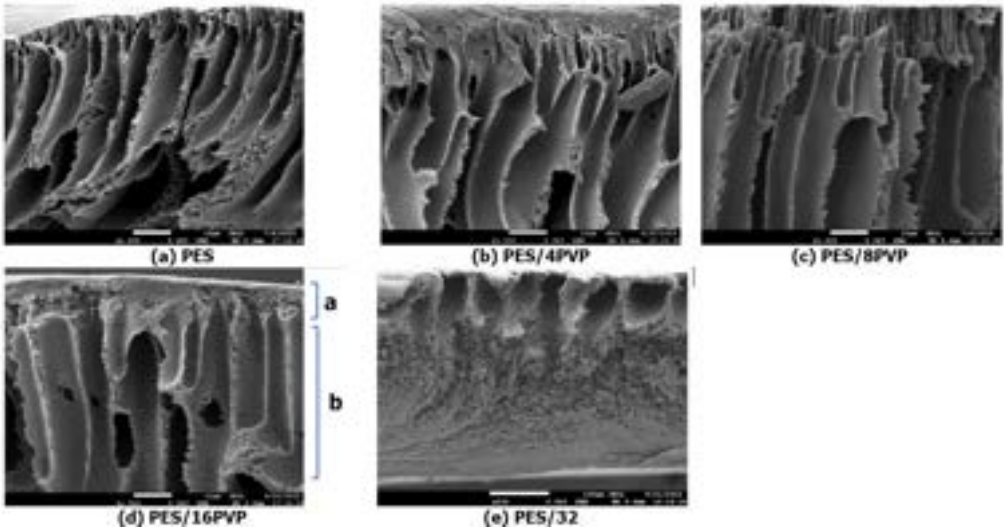

Figure 4.2. SEM images of cross-section view of neat PES membrane and PES/PVP membranes, a: Dense top layer, b: porous sublayer.

Surface wetting property: Contact Angle (Sessile Method)

The measurement of contact angle is a widely used method to assess the wettability of a surface or material. The contact angle, which is the angle formed by the liquid in contact with the solid or liquid, is a key parameter in determining wetting. The contact angle of a membrane surface is used to determine its hydrophilic (contact angle < 90 degrees) or hydrophobic (contact angle > 90 degrees) nature. The traditional definition of contact angle is the angle formed by the liquid when it is deposited on a solid or liquid substrate (30).

An unsurprising and distinct inverse relationship has been observed between the contact angle (CA) values and the concentration of pore forming agents (PVP) of the hand-made PES membranes (as shown in Figure 4.3). The increment of PVP concentration from 0% to 16% by weight resulted in a decrease in the contact angle (CA) of the membranes from 76.90° to 36.14° respectively. Nevertheless, a further increase in the PVP concentration led to a slight increase in the contact angle (CA) value, reaching 47.86° for the PES/32PVP membrane. By referring to the results obtained, the maximum hydrophilicity of PES/PVP membrane, reaching 36.14°, was associated with the PES/16PVP membrane (16% by weight) among the other synthesized membranes in this study. The study results are aligned with previous research findings as discovered that incorporating PVP into PES membranes significantly enhances the membrane's permeability up to a certain point (31). However, at higher concentrations of PVP, the top layer of the membrane becomes denser, leading to a decrease in water permeability and increase water contact angle (CA). Therefore, this study revealed that adding PVP to the casting solution significantly enhances the membrane's permeability up to a certain point.

According to Kurakula & Rao, the presence of a pyrrolidone ring with highly apolar amide components, as well as apolar methylene and methine groups along its structure, enabled PVP to dissolve in both water and non-aqueous solvents, contributing to the formation of pores within the membrane's structure, therefore, increasing the hydrophilicity and reducing the contact angle (CA) (32). Additionally, the hydrophilicity of the PES membrane was found to increase due to the inclusion of certain substances that reduced surface abrasion and density. This, in turn, facilitated the formation of a hydration layer on the surface, effectively preventing the adsorption or deposition of hydrophobic pollutants.

The effect of adding PVP on membrane pore size was studied by (Marchese et al., 2003). The results revealed that addition of PVP leading to significant modifications in fouling or molecule adsorption on the membrane's pore surface as well as increase the hydrophilicity and the permeability of the membranes as long as the additive remained entrapped.

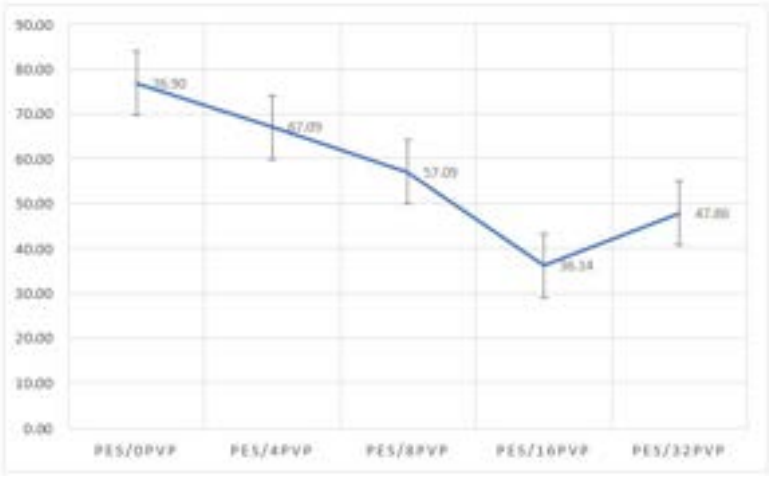

Figure 4.3. Contact Angle Measurement of neat PES membrane and PES/PVP membranes.

According to the findings of Wang et al., the inclusion of PVP in PES membranes result in increased water flux and water adsorption, as well as a decrease in water contact angle (CA) compared to pure PES membranes which promotes high hydrophilicity of membrane (33). Specifically, when the PVP content in the dope solution was 10 wt.%, the contact angle decreased by 16 wt.%. Additionally, Milescu et al. (2019), reported that the water contact angle decreased of the newly produced PES films using PVP. This CA decrease indicates that the membrane's hydrophilicity increased as the residual PVP content increased.

In most instances, modifying PES membranes tends to increase their hydrophilicity by exhibiting lower contact angle (CA<90°). As a result, researchers commonly rely on measuring the water contact angles on PES membranes before and after modification (34). The preferred techniques for such measurements are typically the statistical sessile drop method and the captive air bubble technique (35-36). Reported data are usually obtained by averaging multiple measurements taken at different locations to ensure accuracy. All studies confirm that incorporating hydrophilic components into PES membranes leads to a decrease in water contact angles. However, researchers have observed that the water contact angles continue to change even after water is dropped onto the PES membrane surface.

Luque-Alled et al. evaluate the membrane surface hydrophilicity through the static water contact angle (CA) measurements (28). The results demonstrate that the unmodified PES membrane exhibited a CA value of approximately 72°. When membranes are produced using casting solutions that include pore formers, the water contact angle (CA) values decrease significantly to a range of 52° to 63°. The inclusion of pore formers in the casting solutions appears to have a greater impact on the ultimate hydrophilic properties of the membranes. This effect can be linked not only to the hydrophilic nature of the pore formers but also to the increased surface roughness they introduce. Similarly, PES membrane added with PVP through modification method, will demonstrate a decrease in contact angle (CA) values.

Rahimpour et al. have studied the contact angles (CA) of membranes, which were measured to assess their hydrophobicity and reported that pure PES membranes CA relatively falls in range of above 60° (37). In addition, the membrane surface characteristics dissimilarity, such as pore size, pore size distribution and roughness parameters can potentially influence the contact angle values (38). These findings align with previous literature that reported similar results (39). Therefore, this study revealed that adding PVP to the casting solution significantly enhances the membrane's permeability up to a certain point.

CONCLUSION

Polyethersulfone (PES)-based membranes have been widely implemented in the separation process as they exhibit excellent oxidative, thermal, and hydrolytic stability as well as distinguish mechanical properties. Nevertheless, PES is relatively hydrophobic. Hence, PES is mixed with additives such as polyvinylpyrrolidone (PVP) to enhance the membrane hydrophilicity and to initiate the pore-forming during membrane synthesis by phase inversion. Therefore, this work helps to determine and study the role of PVP addition with different ratios in affecting the membrane performance, morphologies, mechanical properties, porosity, and pore size.

Based on the findings, the successful fabrication of the PES membrane with Polyvinylpyrrolidone (PVP) has been unequivocally demonstrated through the compelling FTIR results. In addition, the scanning electron microscopy (SEM) images further confirmed that as the PVP ratio increased, the porosity of enhanced as the membrane morphology (cross section) will change from the macro-void structures to spongier structure and denser compared to pure PES membrane. Further, the contact angle (CA) results discovered that incorporating PVP into PES membranes significantly enhances the membrane's hydrophilicity up to a certain point. However, at higher concentrations of PVP, the top layer of the membrane becomes denser, leading to a decrease in water permeability and increase water contact angle (CA).

In this study, it can be concluded that, with the addition of PVP (additive) to the PES membrane will membrane's hydrophilicity up to a certain point and enhance the membrane's porosity, nevertheless, will results in decreasing of membrane mechanical strength. Therefore, a relation between membrane morphology and mechanical properties was proved and the objectives were achieved.

ACKNOWLEDGEMENT

This study is supported partially by University Sains Malaysia grant (304/PPSK/6315498).

REFERENCE

[1] Ahmad, A., Sarif, M., Desalination, S. I.-, & 2005, undefined. (n.d.). Development of an integrally skinned ultrafiltration membrane for wastewater treatment: effect of different formulations of PSf/NMP/PVP on flux and rejection. Elsevier. Retrieved January 16, 2023, from https://www.sciencedirect.com/science/article/pii/S0011916405002894

[2] al Aani, S., Wright, C. J., & Hilal, N. (2018). Investigation of UF membranes fouling and potentials as pre-treatment step in desalination and surface water applications. Desalination, 432, 115–127. https://doi.org/10.1016/J.DESAL.2018.01.017

[3] Al Malek, S. A., Abu Seman, M. N., Johnson, D., & Hilal, N. (2012). Formation and characterization of polyethersulfone membranes using different concentrations of polyvinylpyrrolidone. Desalination, 288, 31–39. https://doi.org/10.1016/J.DESAL.2011.12.006

[4] Alardhi, S. M., Alrubaye, J. M., & Albayati, T. M. (2018). IOP Conference Series: Earth and Environmental Science Application of Ultrafiltration Technology in Water Treatment . https://doi.org/10.1088/1755-1315/186/3/012009

[5] Amin, P. D., Bhanushali, V., & Joshi, S. (2018). Role of Polyvinlyppyrrolidone in Membrane Technologies. International Journal of ChemTech Research, 11, 247–259. https://doi.org/10.20902/IJCTR.2018.110932

[6] Amirilargani, M., Saljoughi, E., Mohammadi, T., & Moghbeli, M. R. (2010). Effects of coagulation bath temperature and polyvinylpyrrolidone content on flat sheet asymmetric polyethersulfone membranes. Polymer Engineering & Science, 50(5), 885–893. https://doi.org/10.1002/PEN.21603

[7] Bell, K. Y., Bandy, J., Beck, S., Keen, O., Kolankowsky, N., Parker, A. M., Linden, K., & Smith, C. (2012). Emerging Pollutants – Part II: Treatment. Water Environment Research, 84(10), 1909–1940. https://doi.org/10.2175/106143012X13407275695832

[8] Bellie, P. N. (n.d.). (PDF) Waste Water Treatment by Coagulation and Flocculation. Retrieved January 18, 2023, from https://www.researchgate.net/publication/273638362_Waste_Water_Treatment_by_Coagulation_and_Flocculation

[9] Boom, R. M., Wienk, I. M., van den Boomgaard, T., & Smolders, C. A. (1992a). Microstructures in phase inversion membranes. Part 2. The role of a polymeric additive. Journal of Membrane Science, 73(2–3), 277–292. https://doi.org/10.1016/0376-7388(92)80135-7

[10] Boom, R. M., Wienk, I. M., van den Boomgaard, T., & Smolders, C. A. (1992b). Microstructures in phase inversion membranes. Part 2. The role of a polymeric additive. Journal of Membrane Science, 73(2–3), 277–292. https://doi.org/10.1016/0376-7388(92)80135-7

[11] Cabasso, I., Klein, E., & Smith, J. K. (1976). Polysulfone hollow fibers. I. Spinning and properties. Journal of Applied Polymer Science, 20(9), 2377–2394. https://doi.org/10.1002/APP.1976.070200908

[12] Cheng, N., Wang, B., Wu, P., Lee, X., Xing, Y., Chen, M., & Gao, B. (2021). Adsorption of emerging contaminants from water and wastewater by modified biochar: A review. Environmental Pollution (Barking, Essex : 1987), 273. https://doi.org/10.1016/J.ENVPOL.2021.116448

[13] Chuang, W. Y., Young, T. H., Chiu, W. Y., & Lin, C. Y. (2000). The effect of polymeric additives on the structure and permeability of poly(vinyl alcohol) asymmetric membranes. Polymer, 41(15), 5633–5641. https://doi.org/10.1016/S0032-3861(99)00818-6

[14] Delgado, N., Capparelli, A., Navarro, A., & Marino, D. (2019). Pharmaceutical emerging pollutants removal from water using powdered activated carbon: Study of kinetics and adsorption equilibrium. Journal of Environmental Management, 236, 301–308. https://doi.org/10.1016/J.JENVMAN.2019.01.116

[15] Dwivedi, C., Pandey, I., Pandey, H., Ramteke, P. W., Pandey, A. C., Mishra, S. B., & Patil, S. (2017). Electrospun Nanofibrous Scaffold as a Potential Carrier of Antimicrobial Therapeutics for Diabetic Wound Healing and Tissue Regeneration. Nano- and Microscale Drug Delivery Systems: Design and Fabrication, 147–164. https://doi.org/10.1016/B978-0-323-52727-9.00009-1

[16] Ezugbe, E. O., & Rathilal, S. (2020). Membrane Technologies in Wastewater Treatment: A Review. Membranes 2020, Vol. 10, Page 89, 10(5), 89. https://doi.org/10.3390/MEMBRANES10050089

[17] Foroutan, R., Mohammadi, R., Farjadfard, S., Esmaeili, H., Saberi, M., Sahebi, S., Dobaradaran, S., & Ramavandi, B. (2019). Characteristics and performance of Cd, Ni, and Pb bio-adsorption using Callinectes sapidus biomass: real wastewater treatment. Environmental Science and Pollution Research International, 26(7), 6336–6347. https://doi.org/10.1007/S11356-018-04108-8

[18] Freger, V. (2003). Nanoscale Heterogeneity of Polyamide Membranes Formed by Interfacial Polymerization. Langmuir, 19(11), 4791–4797. https://doi.org/10.1021/LA020920Q

[19] Gonçalves Lemos, J., Stefanello, A., Olivier Bernardi, A., Valle Garcia, M., Nicoloso Magrini, L., Cichoski, A. J., Wagner, R., & Venturini Copetti, M. (2020). Antifungal efficacy of sanitizers and electrolyzed waters against toxigenic Aspergillus. Food Research International, 137, 109451. https://doi.org/10.1016/J.FOODRES.2020.109451

[20] Guo, W., Ngo, H. H., & Li, J. (2012). A mini-review on membrane fouling. Bioresource Technology, 122, 27–34. https://doi.org/10.1016/J.BIORTECH.2012.04.089

[21] Hamza, A., Pham, V. A., Matsuura, T., & Santerre, J. P. (1997). Development of membranes with low surface energy to reduce the fouling in ultrafiltration applications. Journal of Membrane Science, 131(1–2), 217–227. https://doi.org/10.1016/S0376-7388(97)00050-1

[22] Han, D., E, J., Deng, Y., Chen, J., Leng, E., Liao, G., Zhao, X., Feng, C., & Zhang, F. (2021). A review of studies using hydrocarbon adsorption material for reducing hydrocarbon emissions from cold start of gasoline engine. Renewable and Sustainable Energy Reviews, 135, 110079. https://doi.org/10.1016/J.RSER.2020.110079

[23] Heras, I. de las, Molina, R., Segura, Y., … T. H.-J. of hazardous, & 2020, undefined. (n.d.). Contamination of N-poor wastewater with emerging pollutants does not affect the performance of purple phototrophic bacteria and the subsequent resource recovery. Elsevier. Retrieved January 15, 2023, from https://www.sciencedirect.com/science/article/pii/S0304389419315717

[24] Ho, C. C., & Su, J. F. (2022a). Boosting permeation and separation characteristics of polyethersulfone ultrafiltration membranes by structure modification via dual-PVP pore formers. Polymer, 241, 124560. https://doi.org/10.1016/J.POLYMER.2022.124560

[25] Ho, C. C., & Su, J. F. (2022b). Boosting permeation and separation characteristics of polyethersulfone ultrafiltration membranes by structure modification via dual-PVP pore formers. Polymer, 241, 124560. https://doi.org/10.1016/J.POLYMER.2022.124560

[26] Hołda, A. K., Aernouts, B., Saeys, W., & Vankelecom, I. F. J. (2013). Study of polymer concentration and evaporation time as phase inversion parameters for polysulfone-based SRNF membranes. Journal of Membrane Science, 442, 196–205. https://doi.org/10.1016/J.MEMSCI.2013.04.017

[27] Ismail, N. M., Ismail, A. F., & Mustafa, A. (2015). Sustainability in Petrochemical Industry: Mixed Matrix Membranes from Polyethersulfone/Cloisite15a® for the Removal of Carbon Dioxide. Procedia CIRP, 26, 461–466. https://doi.org/10.1016/J.PROCIR.2015.03.005

[28] Issaoui, M., Jellali, S., Zorpas, A. A., & Dutournie, P. (2022). Membrane technology for sustainable water resources management: Challenges and future projections. Sustainable Chemistry and Pharmacy, 25, 100590. https://doi.org/10.1016/J.SCP.2021.100590

[29] J. Brandrup, E. H. I. and E. A. G. (1999). Polymer Handbook 2 Volumes Set. 2366. https://www.wiley.com/en-us/Polymer+Handbook%2C+2+Volumes+Set%2C+4th+Edition-p-9780471479369

[30] Jagini, S., Thaduri, S., Konda, S., Saranga, V. K., Dheeravath, B., & Vurimindi, H. (2021). Emerging contaminant (Triclosan) removal by adsorption and oxidation process: comparative study. Modeling Earth Systems and Environment, 7(4), 2431–2438. https://doi.org/10.1007/S40808-020-01020-4

[31] Jeong, S., & Kim, H.-W. (2023). In situ real-time monitoring technologies for fouling detection in membrane processes. Current Developments in Biotechnology and Bioengineering, 43–64. https://doi.org/10.1016/B978-0-443-19180-0.00008-0

[32] Kariduraganavar, M. Y., Kittur, A. A., & Kamble, R. R. (2014). Polymer Synthesis and Processing. Natural and Synthetic Biomedical Polymers, 1–31. https://doi.org/10.1016/B978-0-12-396983-5.00001-6

[33] Karimi-Maleh, H., Ayati, A., Davoodi, R., … B. T.-J. of C., & 2021, undefined. (n.d.). Recent advances in using of chitosan-based adsorbents for removal of pharmaceutical contaminants: A review. Elsevier. Retrieved January 14, 2023, from https://www.sciencedirect.com/science/article/pii/S0959652621001001

[34] Karimi-Maleh, H., Ayati, A., Ghanbari, S., … Y. O.-J. of molecular, & 2021, undefined. (n.d.). Recent advances in removal techniques of Cr (VI) toxic ion from aqueous solution: A comprehensive review. Elsevier. Retrieved January 14, 2023, from https://www.sciencedirect.com/science/article/pii/S0167732220373049

[35] Karimi-Maleh, H., Ranjbari, S., Tanhaei, B., Ayati, A., Orooji, Y., Alizadeh, M., Karimi, F., Salmanpour, S., Rouhi, J., Sillanpää, M., & Sen, F. (2021). Novel 1-butyl-3-methylimidazolium bromide impregnated chitosan hydrogel beads nanostructure as an efficient nanobio-adsorbent for cationic dye removal: Kinetic study. Environmental Research, 195, 110809. https://doi.org/10.1016/J.ENVRES.2021.110809

[36] Khayet, M., & García-Payo, M. C. (2009). X-Ray diffraction study of polyethersulfone polymer, flat-sheet and hollow fibers prepared from the same under different gas-gaps. Desalination, 245(1–3), 494–500. https://doi.org/10.1016/J.DESAL.2009.02.013

[37] Koh, M., Clark, M. M., & Howe, K. J. (2005). Filtration of lake natural organic matter: Adsorption capacity of a polypropylene microfilter. Article in Journal of Membrane Science. https://doi.org/10.1016/j.memsci.2005.02.016

[38] Kourde-Hanafi, Y., Loulergue, P., Szymczyk, A., Van Der Bruggen, B., Nachtnebel, M., Rabiller-Baudry, M., Audic, J.-L., Pölt, P., & Baddari, K. (2017). Influence of PVP content on degradation of PES/PVP membranes: insights from characterization of membranes with controlled composition. Journal of Membrane Science. https://doi.org/10.1016/j.memsci.2017.03.050

[39] Kim, I. C., Choi, J. G., & Tak, T. M. (1999). Sulfonated polyethersulfone by heterogeneous method and its membrane performances - Kim - 1999 - Journal of Applied Polymer Science - Wiley Online Library. Applied Polymer, 2046–2055. https://onlinelibrary.wiley.com/doi/abs/10.1002/%28SICI%291097-4628%2819991121%2974%3A8%3C2046%3A%3AAID-APP20%3E3.0.CO%3B2-3

PRELIMINARY ANALYSIS OF BIOFOULING GROWTH AND ADHESION - A FIELD STUDY OF OCEAN THERMAL ENERGY CONVERSION FACILITY

Mohd Zaki Bin Zainal Abidin[1], Jay Jackreson Bin Josrin[2], Ronaldo Basik Anak Ignatius Stoper[3], Muhammad Syazwan Afiq Bin Shauki[4], Zaquan Bin Zakaria[5]

[1]*School of Chemical Engineering, College of Engineering,*

Universiti Teknologi Mara (UiTM) Shah Alam, Malaysia

zakizainal@uitm.edu.my

ABSTRACT

Ocean Thermal Energy Conversion (OTEC) is a renewable energy technology that exploits temperature differences between warm surface ocean waters and cold deep ocean water to generate energy based on the principle of thermodynamic heat engine systems. Due to the system's direct contact with seawater, it has a high potential for unwanted accumulation and growth of biofouling such as microorganisms, plants, algae, or turnips on wet surfaces. Hence, it is required to conduct a study on the growth rate of the biofouling to know the severity for different periods of time. This was conducted by designing a cage that contains plastic board that has an HDPE pipe coupon attached to it for biofouling to growth. Through this study, the results indicated that biofouling formation could occur after 3 weeks after the cages were immersed in the sea. This was proven through the data, where the average weight percent of the coupon for cage 2 Plate B increased up to 14 percent of its originally weight. As this study was conducted based on the weight and area of the coupons, another method can be done for future continuation of the works.

Keywords: Ocean thermal energy conversion (OTEC), biofouling, environmental science

INTRODUCTION

Ocean Thermal Energy Conversion (OTEC) is a renewable energy technology that exploits the temperature difference between warm surface ocean waters and cold deep ocean waters to generate energy based on the principle of thermodynamic heat engine systems. Unlike other renewable energy generation sources, OTEC offers a large and consistent source of energy, where the technology is suitable for its implementation in remote tropical regions. The application of OTEC in Malaysian coastal area is promising, given that strategic location of Malaysian which is within tropical climate condition and the presence of deep seawater region near to Sabah's east coast section. Currently, a laboratory-scale OTEC facility has been built at Teluk Kemang, Port Dickson, Negri Sembilan where the facility houses hybrid-OTEC (H-OTEC) processing facility which is capable in generating energy and producing desalinated water (Azam et al., 2022).

As the system uses seawater for its main fluid, it has direct contact to the surface of the equipment and increases the chance for unwanted accumulation and growth of biofouling such as microorganisms, plants, algae, or tunicle on wetted surface. It poses significant concern for marine industries due to its impact on material integrity and performance. A comprehensive study for assessing biofouling is crucial since different physicochemical and biological properties of seawater produces different potential biofouling growth and deposition mechanism. The field sampling method is the best approach in assessing biofouling as it offers realistic and representable conditions of biofouling sample. In this study, focus will be on potential biofouling threat in the H-OTEC facility at Port Dickson, Negeri Sembilan, where there is an urgent need to conduct preliminary assessment of potential biofouling growth and adhesion profile near to the facility particularly for period. The assessment allows early predictive evaluation of biofouling and effective approaches in managing potential biofouling growth and adhesion profile (Gu, 2005).

Therefore, the paper focuses on assessing biofouling on OTEC facility by deploying a biofouling sampling device at Port Dickson. The objective is to measure the extent of biofouling, particularly focusing on weight and dimensional changes of the materials used, and to evaluate the impact of time on biofouling accumulation. Previous studies have explored various methods for assessing and mitigating biofouling, including the use of different materials and coatings.

MATERIALS AND METHODS

This work was conducted by designing a cage, which contains three plastic boards with a set of polyethylene (HDPE) pipe coupons attached to the plastic board using Velcro straps. The cages were immersed in the shallow coastal area of the site where the observation of the coupons was done every two or three weeks. A total of six cages were placed and immersed in seawater at Port Dickson Beach, which is located at Teluk Kemang, Negeri Sembilan. The cages were immersed in seawater, where the coordinates of the cages placed are (2.46, 101.84).

The analysis of this experiment focuses on the idea to determine time required for visible, macrofouling sample growth and accumulated since it has greater threat to OTEC facility. In this case, the attached coupons were collected and analysed based on accumulated weight sampling analysis and the area covered by biofouling was analysed using J-Image software in each visit conducted. In addition, basic observation analysis was done to identify potential biological or non-biological elements that could accumulate on the coupons.

RESULTS AND DISCUSSION

Figure. 1(a) displays the cage made of baskets that will be used to position the coupons, while Figure 1(b) illustrates the high-density polyethylene (HDPE) pipe coupons that will serve as a medium for biofouling adherence.

Figure 1. Cage for positioning the coupon (a) and high-density polyethylene (HDPE) pipe coupons as the medium for the adhesion of biofouling (b)

Figure 2 indicates that the average percentage of weight differences in the coupons showed no significant changes during the second and third visits, with values ranging from a maximum of 82% to a minimum of 11%. However, an increase in the average percentage of weight differences was noted during the fourth visit for samples collected from cage 2, plates B and C. This increase may be attributed to various factors, including elevated temperatures, nutrient availability, or increased seawater salinity, all of which could enhance biofouling (Arndt et al., 2021).

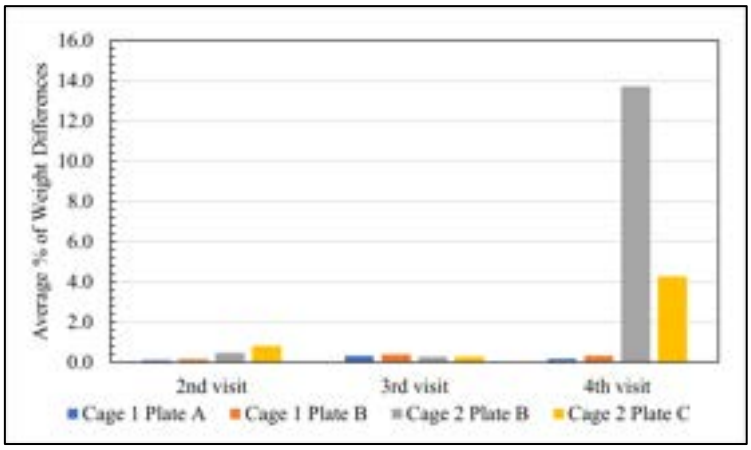

Figure 2. Graph of average percentage of weight differences vs the number of visits

Table 1 presented above is set of data obtained from ImageJ software, which indicates the area and percentage of biofouling coverage on different coupons during the 3rd and 4th visits. During the 3rd visit, biofouling coverage was minimal, with the area ranging from 3.32 mm² to 8.31 mm² and coverage percentages between 0.53% and 1.28% for plates B and C, respectively. By the 4th visit, biofouling had significantly increased, particularly on the control plate (Plate A), where coupon A3 showed the highest coverage at 438.81 mm² (67.51%). Plate B and Plate C also experienced moderate biofouling, with the highest coverage being 55.52% on Coupon B6 and 20.57% on Coupon C6. This data suggests a substantial increase in biofouling over time, with the control plate being the most affected.

The highest coverage area was found at Coupon A3, which is 438.81 mm² with 67.51% biofouling, is significant in the context of biofouling because it is indicator of severe biofouling. The extensive coverage on Coupon A3 suggests that the material or treatment used on this coupon is highly susceptible to biofouling. This level of biofouling can lead to significant operational and maintenance challenges in real-world applications, such as in marine environments or industrial systems where biofouling is a concern.

Table 1. Area of coupon covered by the biofouling for plate A cage 2

Cage	Plate	Coupon	Area of Biofouling Coverage (mm^2)	Percentage of Biofouling Coverage (%)
2	A (Control Plate)	A1	27.76	4.63
		A2	252.87	40.46
		A3	438.81	67.51
		A4	16.26	2.40
		A5	13.31	2.05
		A6	260.28	41.64

The findings from this study indicate a significant potential for macrofouling growth on contact surfaces immersed in seawater, even within a relatively short period. Over the course of just three weeks, substantial biofouling is observed, evident through both the visible accumulation of macrofouling organisms and a significant increase in the weight of the affected surfaces. This rapid growth suggests that the marine environment is highly conducive to the proliferation of fouling species, such as Balanus Glandula (US Department of Commerce, 2016) and Uruchordata, (Ghiselin, 2024) which are known to colonize surfaces aggressively. The accelerated rate of macrofouling within such a brief timeframe highlights the urgency of implementing effective preventive strategies. Without these measures, the surfaces are likely to experience even more extensive fouling over time, leading to potential operational challenges and increased maintenance costs. The three-week assessment period has proven to be sufficient for observing notable fouling, underscoring the need for early intervention to minimize the extent of biofouling (Affandy et al., 2019).

CONCLUSION

This work has proven that macrofouling growth has a high possibility of occurring at the surface of a system that was immersed in seawater for a minimum of 3 weeks. This was proven from the average percentage of weight difference data that was obtained from this work, and the data that was obtained from the fourth visit show that the average weight percentage of cage 2 Plate B has increased up to 14 percent. However, there is no significant difference in average weight percentage for the second and third visits. This show a suitable time of visit to obtain a macrofouling formation sample are after the 3 weeks the surface of the system been immersed. Besides that, the challenges in obtain the result are the condition of the sea, which it may cause the system that was immersed being brought to the shore due to the wave. Other than that, through this work it has contributing on the identified the potential species that growth on the surface such as tunicate, barnacles and oyster shell. This led to the finding the suitable way on controlling the growth of macrofouling formation on a surface of a system.

REFERENCES

Affandy, M. A. M., Madin, J., Jakobsen, K. P., & Auluck, M. (2019). Development and succession of sessile macrofouling organisms on the artificial structure in the Shallow Coastal Waters of Sabah, Malaysia. *IOP Conference Series: Earth and Environmental Science*, *236*(1). https://doi.org/10.1088/1755-1315/236/1/012046

Arndt, E., Robinson, A., Hester, S., Woodham, B., Wilkinson, P., & Gorgula, S. (2021). Factors that influence vessel biofouling and its prevention and management. *Final Report for CEBRA Project*, *190803*.

Azam, K. H. K., Abidin, M. Z. Z., Husain, M. K. A., Jaafar, A. B., Zaki, N. I. M., & Aziz, F. N. A. A. (2022). Evaluation of hybrid ocean thermal energy conversion system plantwide performance. *Journal of Physics: Conference Series*, *2259*(1). https://doi.org/10.1088/1742-6596/2259/1/012030

Ghiselin, M. T. (2024, August 27). *Tunicate*. Encyclopædia Britannica.

https://www.britannica.com/animal/tunicate

Gu, J. D. (2005). Biofouling and prevention. Corrosion, biodeterioration and biodegradation of materials. In *Handbook of Environmental Degradation of Materials* (pp. 179–206). Elsevier Inc. https://doi.org/10.1016/B978-081551500-5.50011-2

US Department of Commerce, N. O. and A. A. (2016, March 30). *What are barnacles?*. NOAA's

National Ocean Service.
https://oceanservice.noaa.gov/facts/barnacles.html#:~:text=Barnacles%20(Balanus%20glandula)%20are%20sticky,to%20crabs%2C%20lobsters%2C%20and%20shrimps

SLEEP DURATION AND BLOOD PRESSURE : A CROSS-SECTIONAL PRELIMINARY STUDY OF BOARDING SCHOOL STUDENTS

Adriana Khairin Khairuddin[1], Siti Hazizah Adnan[1], Puteri Hazwarnur Syida Zazali[1], Muhammad, Nur Fazidah Asmuje[1]

[1]*Kolej PERMATA Insan, Universiti Sains Islam Malaysia*

Adrianakhairin123@gmail.com, hazizahadnan07@gmail.com, puteri.hazwanur@raudah.usim.edu.my, nurfazidah@usim.edu.my

ABSTRACT

Sleep duration is recognized as a significant risk factor for cardiometabolic health, influenced substantially by daily activities and lifestyle. While numerous studies have explored the relationship between sleep and blood pressure (BP) among adults, research on this association among school students remains limited. Therefore, this study aimed to evaluate the impact of sleep duration on BP among Muslim gifted and talented students residing in a boarding school. This cross-sectional study included 109 first and second-year students from Kolej PERMATA Insan. Systolic, diastolic BP, and heart rate were measured using the home blood pressure monitoring device HEM 7142T, with sleep duration self-reported by participants. Demographic data, including gender, height, weight, and body mass index (BMI), were analysed using independent t-tests. Linear regression was then used to assess the relationship between sleep duration and BP based on the academic year. Results showed that 53 first-year students slept significantly longer, with a mean (SD) of 5 hours 10 minutes (1 hour 1 minute), compared to 56 second-year students, who slept on average 4 hours 25 minutes (57 minutes) (p=0.01). Additionally, second-year students had a significantly higher heart rate (83.45 (11.91) bpm) compared to first-year students (77.17 (10.26) bpm). Despite these differences, there was no significant relationship found between sleep duration and BP among either group of students. This suggests that variations in sleep duration did not translate into measurable differences in BP, possibly due to the early adulthood stage where blood vessels are more elastic and baroreceptors highly sensitive in both groups. Future studies could explore the effects of sleep duration on BP among students in higher academic years, considering potential differences in academic workload, extracurricular activities, and social factors.
***Keywords*:** Blood Pressure, Sleep, Sleep duration, Heart rate, Muslim Gifted Education

INTRODUCTION

Insufficient sleep is widely recognized as a public health concern, leading to myriad diseases including cardiometabolic disease. These disease which include cardiovascular disease, stroke and diabetes have seen an increase in prevalence and are significant contributors to mortality and quality of life(Cappuccio & Miller, 2017). According to National Health and Morbidity Survey 2023 (NHMS), the prevalence of diabetes has shown an upward trend among adults, increasing the risk of heart disease and stroke (Institute for Public Health, 2024).

While, these cardiometabolic disease not only have serious implication for the individual health, it also a considerable burden on public healthcare system and the global economy. In the U.S. alone, approximately 70 million suffer from sleep disorders, contributing to $16 billion in healthcare costs and $50 billion in lost productivity annually (U.S. Department of Health and Human Services & National Institutes of Health, 2011).

Hypertension (high blood pressure) or hypotension (low blood pressure) are global risk factor for cardiometabolic disease (Asmuje et al., 2022). Both condition are often referred to as “silent killer” as they rarely show symptom. Hypertension may damage blood vessels and vital organs such as heart, kidneys, and brain while hypotension may cause inadequate blood flow to these organs, leading to dysfunction(Asmuje et al., 2022, 2023). Controlling blood pressure (BP) within 120/80 mmHg is essential in reducing the risk of these diseases.

Sleep issues including sleep deprivation, disrupted sleep, or sleep disorders such as sleep apnea, has consistently been linked to an increased risk of blood pressure problems. Report show that 38% of adults in Malaysia do not get enough sleep, defined as less than seven hours on average within a 24-hour period (Institute for Public Health, 2024). However, the requirement for sleep duration varies across the lifespan and may decreases with age (Chaput et al., 2020). Optimal sleep duration as recommended by American Academy of Sleep Foundation, range 14 to 17 hours for newborn, 11 to 14 hours for toddlers, 9 to 11 hours for school-aged children, 8 to 10 hours for teenagers and 7 to 9 hours adults (Hirshkowitz et al., 2015).

Adequate sleep duration is an effective method to control the BP hence preventing the cardiometabolic disease. While numerous studies on sleep and BP have been conducted among adults (Makarem et al., 2021; Ogugu

et al., 2022; Sajjadieh et al., 2020), data among students, particularly those in boarding school students, remains limited. Therefore, this study aims to investigate the sleep duration among Muslim gifted and talented students residing in a boarding school and its association with BP.

MATERIALS AND METHODS

A total of 109 first and second-year students from Kolej PERMATA Insan (KPI), Universiti Sains Islam Malysia were called to gather in a school's hall to complete the survey in March 2024. Informed consent were obtained before data is collected.

Kolej PERMATA Insan is a boarding school which utilized the Muslim gifted and talented (IGEd) curriculum. The school week includes all these curriculum components, with the school day running from 6:00 am to 4:30 pm. Additionally, students attend Al-Quran classes from 7:30 pm to 9:30 pm, followed by a self-study period. Students typically go to bed at 11:00 pm.

The self-reported sleep questionnaire used in this study was adapted from Sleep Questionnaire for Adults by Sleep Disorders Clinic Department of Clinical Neurophysiology. The data was collected using responses to the questions "What time do you usually go to sleep?" and What time do you usually get up?". The duration of sleep was defined as the difference between the time participants went to sleep and the time woke up, calculated separately for weekday and weekends. The average hour of sleep per week were then used in this study. Meanwhile, systolic, diastolic BP, and heart rate were measured using the home blood pressure monitoring device HEM 7142T.

Demographic data, including gender, height, weight, and body mass index (BMI), were analysed using independent t-tests. Linear regression was then used to assess the relationship between sleep duration and BP based on the academic year.

RESULTS AND DISCUSSION

Among the 109 participants, 53 (48.6%) were first-year students. As shown in Table 1, first-year students had significantly lower weight, height and body mass index (BMI) than second-year students. According to the (World Health Organization, (2024) BMI-for-age percentile chart, both cohort were within normal weight ranges; from 15.4 to 20.8 for male and 15.6 to 21.8 for females.

Regarding non-invasive cardiovascular assessment, there were no significant differences is systolic and diastolic blood pressure measurements between among both cohorts. However, second-year students had a significantly higher heart rate (83.45 (11.91) bpm) compared to first-year students (77.17 (10.26) bpm). Both groups also reported insufficients sleep duration as was suggested by Hirshkowitz et al., (2015) and Chaput et al., (2020), 8 to 10 hours for teenagers. Notably, second-year students experienced shorter sleep duration than first-year students which possibly due to their packed schedule, late-night studying or completing assignments.

Table 1. Participant's Demographic based on Groups

	First-Year (n=53)	Second-Year (n=56)	p-value
Gender, n (%)			0.44
Male	24 (45.3%)	21 (37.5%)	
Female	29 (54.7%)	35 (64.5%)	
Weight (kg), mean (SD)	41.92 (11.78)	48.69 (10.08)	<0.01*
Height (cm), mean (SD)	151.23 (6.76)	155.00 (5.87)	<0.01*
Body Mass Index mean (SD)	18.60 (3.89)	20.25 (3.97)	0.03*
Sleep duration mean (SD)	5 hrs 10 min (1 hr 1 min)	4 hrs 25 min (57 min)	<0.01*
Systolic BP, mmHg mean (SD)	99.64 (11.21)	101.93 (10.81)	0.28
Diastolic BP, mmHg mean (SD)	63.70 (8.51)	65.19 (8.29)	0.36
Heart Rate (bpm) mean (SD)	77.17 (10.27)	83.45 (11.91)	<0.01*

hrs= hours; min = minutes; * p-value = < 0.05

While several studies suggest a link between insufficient sleep and increased blood pressure (Zhao et al., 2023), this study did not identify a significant relationship between sleep duration and BP among first-and second-year students. Similar findings were reported in a study on Thai students (Pirojsakul et al., 2022).

This discrepancy could be attribute to the significant changes associated with adolescence, which may mitigate the influence of sleep pattern on blood pressure. Blood pressure in adolescence is known to fluctuate due to rapid growth and hormonal changes, but adolescents probably show resilience to BP increases. This resilience is linked to the autonomic balance in adolescents, as their blood vessels are more elastic and baroreceptors more sensitive (Makarem et al., 2021; Pirojsakul et al., 2022). Sun et al., (2020) also highlighted that diet may mediate the relationship between sleep duration and blood pressure, although it was not measured in this study.

Table 2. Association between Sleep and Cardiovascular Assessment based on Cohort

	First-Year Students β (95%CI)	Second-Year Students β (95%CI)
Systolic BP	0.03 (-0.02,0.08)	0.03 (-0.03,0.08)
Diastolic BP	-0.01 (-0.04,0.04)	-0.03 (-0.06,0.01)
Heart Rate	-0.05 (-0.09,-0.01)*	-0.04 (-0.09,-0.02)*

* Indicates P<0.05

Meanwhile, insufficient sleep was associated with a significant increase in heart rate in both first-and second year students as hypothesized. As this study relied on a single measurement rather than repeated assessment, the increased heart rate may be linked to activation of the sympathetic nervous system, which elevated stress hormone such as adrenaline and cortisol. This response is short-term period as the body becomes alert when fatigue due to sleep deprivation (Gómez-García et al., 2021; Sajjadieh et al., 2020).

In addition, KPI is a boarding school where students have more structured daily routines, and engage in consistent physical activities. The structured hostel environment promotes a healthy lifestyle, with proper nutrition controlled by the school leads to prevention of cardiovascular risk factors. These factors, likely contribute to improve autonomic balance and suggest that sleep deprivation may not affected the BP in this population.

CONCLUSION

The present study examined the sleep duration among Muslim gifted and talented students and its relationship with blood pressure. The findings indicate that participants had insufficient sleep, averaging less than 5 hours and 30 minutes. However, this sleep deprivation did not show a significant association with systolic and diastolic blood pressure. This may be attributed to the natural resilience of adolescents to BP changes, likely due

to growth hormone fluctuation and improved autonomic balance. On the other hand, second-year students had a significantly higher heart rate compared to first year students, which could be linked to the sleep deprivation. The elevated stress hormones resulting from sleep deprivation likely activated the sympathetic nervous system, contributing to the increase heart rate.

This study has its limitation. As a cross sectional study, cause-effect relationship between sleep duration and blood pressure cannot be established. Moreover, variation in heart rate should be considered, as anxiety during data collection could have influenced the results. Additionally, since the participants are adolescent residing in a controlled school environment, longitudinal assessments would be beneficial to better understand the long-term effect of sleep duration on BP in future study.

REFERENCES

Asmuje, N. F., Mat, S., Goh, C. H., Myint, P., & Tan, M. P. (2023). Reduced beat-to-beat blood pressure variability is associated with cognitive decline over six years in the Malaysian Elders Longitudinal Research (MELoR) study. *Alzheimer's & Dementia*, *19*(S4). https://doi.org/10.1002/alz.067683

Asmuje, N. F., Mat, S., Myint, P. K., & Tan, M. P. (2022). Blood Pressure Variability and Cognitive Function: a Scoping Review. In *Current Hypertension Reports* (Vol. 24, Issue 10, pp. 375–383). Springer.

Cappuccio, F. P., & Miller, M. A. (2017). Sleep and Cardio-Metabolic Disease. In *Current Cardiology Reports* (Vol. 19, Issue 11). Current Medicine Group LLC 1. https://doi.org/10.1007/s11886-017-0916-0

Chaput, J. P., Dutil, C., Featherstone, R., Ross, R., Giangregorio, L., Saunders, T. J., Janssen, I., Poitras, V. J., Kho, M. E., Ross-White, A., Zankar, S., & Carrier, J. (2020). Sleep timing, sleep consistency, and health in adults: a systematic review. *Applied Physiology, Nutrition, and Metabolism = Physiologie Appliquee, Nutrition et Metabolisme*, *45*(10), S232–S247. https://doi.org/10.1139/apnm-2020-0032

Gómez-García, M., Bia, D., & Zócalo, Y. (2021). Physical activity, sedentary behavior and sleep time: Association with cardiovascular hemodynamic parameters, blood pressure and structural and functional arterial properties in childhood. *Journal of Cardiovascular Development and Disease*, *8*(6). https://doi.org/10.3390/jcdd8060062

Hirshkowitz, M., Whiton, K., Albert, S. M., Alessi, C., Bruni, O., DonCarlos, L., Hazen, N., Herman, J., Katz, E. S., Kheirandish-Gozal, L., Neubauer, D. N., O'Donnell, A. E., Ohayon, M., Peever, J., Rawding, R., Sachdeva, R. C., Setters, B., Vitiello, M. V., Ware, J. C., & Adams Hillard, P. J. (2015). National Sleep Foundation's sleep time duration recommendations: methodology and results summary. *Sleep Health*, *1*(1), 40–43.

Institute for Public Health. (2024). *National Health and Morbidity Survey (NHMS) 2023: Non-communicable Diseases and Healthcare Demand - Key Findings*.

Makarem, N., Alcántara, C., Williams, N., Bello, N. A., & Abdalla, M. (2021). Effect of Sleep Disturbances on Blood Pressure. In *Hypertension* (Vol. 77, Issue 4, pp. 1036–1046). Lippincott Williams and Wilkins.

Ogugu, E. G., Catz, S. L., Bell, J. F., Drake, C., Bidwell, J. T., & Gangwisch, J. E. (2022). The Association Between Habitual Sleep Duration and Blood Pressure Control in United States (US) Adults with Hypertension. *Integrated Blood Pressure Control*, *15*, 53–66. https://doi.org/10.2147/IBPC.S359444

Pirojsakul, K., Aekplakorn, W., Siwarom, S., Paksi, W., Kessomboon, P., Neelapaichit, N., Chariyalertsak, S., Assanangkornchai, S., & Taneepanichskul, S. (2022). Sleep duration and risk of high blood pressure in Thai adolescents: the Thai National Health Examination Survey V, 2014 (NHES-V). *BMC Public Health*, *22*(1).

Sajjadieh, A., Shahsavari, A., Safaei, A., Penzel, T., Schoebel, C., Fietze, I., Mozafarian, N., Amra, B., & Kelishadi, R. (2020). The Association of Sleep Duration and Quality with Heart Rate Variability and Blood Pressure. *Tanaffos*, *19*(2), 135–143.

Sun, J., Wang, M., Yang, L., Zhao, M., Bovet, P., & Xi, B. (2020). Sleep duration and cardiovascular risk factors in children and adolescents: A systematic review. In *Sleep Medicine Reviews* (Vol. 53). W.B. Saunders Ltd.

World Health Organization. (2024). *BMI-for-age (5-19 years)*.

Zhao, Q., He, M., Zhang, M., Chu, Y., & Ban, B. (2023). Non-linear relationship between sleep duration and blood pressure in children with short stature. *Frontiers in Pediatrics*, *11*. https://doi.org/10.3389/fped.2023.1302750

EVALUATION OF BIOPLASTICS PRODUCED FROM BANANA PEELS AND CHITOSAN

Nur Idayu Idris[1], Maryam Mohamed Rehan[1], Salina Mat Radzi[1]

[1]*Faculty of Science and Technology, Universiti Sains Islam Malaysia*

aayuidris@gmail.com

maryam@usim.edu.my, salina@usim.edu.my

ABSTRACT

The conventional production of plastics from non-renewable fossil fuels contributes to significant environmental issues, including pollution and resource depletion. This study explores the development of sustainable bioplastics utilizing banana peels (Musa acuminata) and chitosan, both of which are abundant and biodegradable resources. The bioplastics were produced by integrating chitosan into banana peel-based formulations, and their properties were compared with bioplastics without chitosan incorporation. Fourier-transform infrared spectroscopy (FTIR) analysis confirmed the presence of functional groups indicative of successful bioplastic formation. Mechanical properties, including tensile strength and toughness, were assessed using a Texture Analyzer, revealing no significant differences between formulations with and without chitosan. A significantly higher water activity of bioplastics made from banana peels with chitosan (0.6498±0.05) compared to those without chitosan incorporation (0.4824±0.02) were also observed. Field Emission Scanning Electron Microscopy (FESEM) demonstrated good cohesion between the fibers and chitosan, while biodegradability tests indicated that the chitosan-enhanced bioplastic degraded more effectively than the banana peel-only formulation, with a significant difference in degradation rates ($P<0.05$). The results suggest that banana peels and chitosan hold promise as viable materials for sustainable bioplastic production, offering a potential alternative to conventional plastics.

Keywords: Bioplastics, biodegradable, banana peels, chitosan.

INTRODUCTION

The conventional production of plastic materials from non-renewable fossil fuels poses significant environmental challenges, including pollution, waste generation, and resource depletion. Additionally, large quantities of agricultural waste, such as banana peels, are often discarded without being utilized effectively. To mitigate these issues, there is a need for the development of sustainable alternatives, such as bioplastics derived from renewable sources. Bioplastics are biodegradable and do not contribute to pollution, thereby addressing environmental concerns associated with conventional plastics (Ribadiya et al., 2021). Banana peels and chitosan are abundant natural resources that offer considerable potential for sustainable bioplastic production due to their biodegradable properties. Banana peels contain cellulose, hemicellulose, and amino acids, making them an excellent renewable source for bioplastic materials (Misran et al., 2020). Chitosan, derived from crustacean exoskeletons, is known for its biodegradability, biocompatibility, and antimicrobial properties, which can enhance the functionality of bioplastics (Erna et al., 2022). The integration of these natural components for bioplastics productions may improve their mechanical and thermal properties, offering a sustainable alternative to traditional plastics (Ramadhan et al., 2020).

This study aimed to explore the feasibility of using banana peels from Musa Acuminata and chitosan to develop an effective and environmentally friendly process for bioplastic production. The objectives of this study are to determine the surface structure of the produced bioplastics using Field Emission Scanning Electron Microscopy (FESEM), to evaluate their functional groups and mechanical properties through Fourier-transform infrared spectroscopy (FTIR) and a Texture Analyzer, and to quantify the percentage of biodegradability of the bioplastics incorporating banana peels and chitosan. The findings from this research could contribute to the advancement of sustainable materials and the reduction of environmental impact from plastic waste.

MATERIALS AND METHODS

Raw Materials: 2 kg of *Musa Acuminata* Lady Finger bananas from Pasar Malam Nilai, Negeri Sembilan, and 500g prawn shells from Haris Johan Tomyam Restaurant, Nilai, Negeri Sembilan, were used.

Materials: Chemicals included Sodium hydroxide, Sodium metabisulphite, Hydrochloric acid, Acetic acid, Acetone, Ethanol, and Glycerol.

Preparation of Banana Peels: 200g of banana peels were cut, treated with sodium metabisulphite (0.2M) for 45 mins, boiled, dried, and blended into a paste (Deepika, 2020).

Preparation of Chitosan: Chitosan was extracted from prawn shells through demineralization with 4% HCl, followed by deproteinization and deacetylation using NaOH (4% and 50% respectively). 100 ml of acetone for decolorization (Gibson et al., 2022).

Bioplastic Production: 25g of the banana peel paste was mixed with 0.5M HCl, 2 ml glycerol, 0.5M NaOH, and chitosan, spread on silicon paper, and dried at 60°C for 24 hours (Deepika, 2020).

Characterization: Bioplastics were analyzed using FTIR for chemical composition (Lutfi et al., 2017), Texture Analyser for tensile strength (Sofiah, 2018), Field Emission Scanning Electron Microscopy (FESEM) for structural analysis. Water activity was assessed with Aqua Lab and biodegradability via Soil Burial Test.

Statistical Analysis: All tests were performed in triplicate with results analyzed using ANOVA in MINITAB 21.4.2 to ensure significance and reliability.

RESULTS AND DISCUSSION

Production of Bioplastics

Bioplastic produced from banana peels without chitosan exhibited a flexible and smooth texture (Figure 1). The inclusion of chitosan in the banana peels-derived bioplastic formulation enhances its strength and rigidity, giving it a firmer texture and unique crystal-like appearance (Figure 2) compared to bioplastics made solely from banana peels.

Figure 1. Bioplastics from banana peels

Figure 2. Bioplastics from banana peels and chitosan

Surface topography analysis of bioplastics by FESEM

The bioplastic surface was characterized using Field Emission Scanning Electron Microscopy (FESEM) at 3kV with scale bars of 10µm, 5µm, and 1µm. FESEM images revealed distinct surface topography differences between bioplastic from banana peels and those with added chitosan. Chitosan showed a well-dispersed structure bonded with cellulose, although weak interfacial adhesion was noted. Glycerol improved bonding, enhancing the overall adhesion between fibers and natural additives.

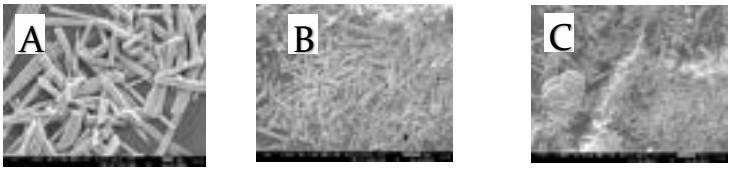

Figure 3. FESEM microphotographs of the bioplastic from banana peels at 3kV resolution. The images are under 1 µm (A), 5 µm (B) and 10 µm (C).

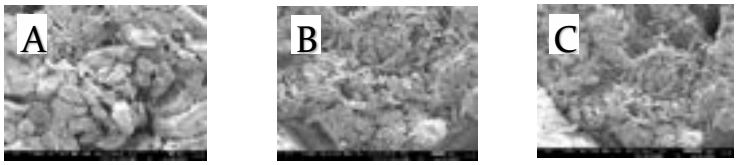

Figure 4. FESEM microphotographs of the bioplastic from banana peels added with chitosan at 3kV resolution. The images are under 1 µm (A), 5 µm (B) and 10 µm (C).

Texture Profile Analysis of Bioplastics

Tensile strength, breaking strain and toughness of the different bioplastic formulations were analyzed using Texture Profile Analysis. No significant differences ($P>0.05$) were observed between the bioplastic produced solely from banana peels and those incorporating chitosan, which could be attributed to the shared chemical characteristics between banana peels and chitosan. Both materials contain polysaccharides, which may contribute to comparable mechanical properties. Nevertheless, chitosan is known for its ability to maintain structural integrity and resist moisture, which might be beneficial in certain applications (Lutfi, 2017).

Table 1. Mechanical properties of bioplastics, including tensile strength, breaking strain, and toughness, analyzed using Texture Profile Analyzer (mean ± standard deviation)

Analysis	Bioplastics from banana peels	Bioplastics from banana peels and chitosan
Strength	(0.02 ± 0.01) MPa	(0.03 ± 0.01) MPa
Breaking Strain	(108.63 ± 8.20) %	(115.91 ± 1.43) %
Toughness	(0.001 ± 0.001) MJ/m^3	(0.002 ± 0.001) MJ/m^3

Water activity of Bioplastics

Water activity, which impacts bioplastic quality and shelf-life, was measured using an Aqualab 4TE meter. The results indicated a significantly higher water activity of bioplastics made from banana peels with chitosan (0.6498±0.05) compared to those without chitosan incorporation (0.4824±0.02). This elevated water activity in chitosan-enriched bioplastics suggests a greater potential for microbial growth, although both bioplastic types generally have low enough water activity to inhibit most microbial activity, thereby extending shelf life. Most bacteria and molds require a minimum water activity level of approximately 0.91 to 0.95 for growth, while yeasts may grow at levels as low as 0.88 (Fontana, 2020). Furthermore, the water activity of bioplastics can also be influenced by the presence of plasticizers, fillers, and other additives (Maura et al., 2022).

Table 2. Water activity of bioplastics (mean ± standard deviation)

Bioplastics from banana peels	Bioplastics from banana peels and chitosan
(0.4824±0.02) aw	(0.6498±0.05) aw

Analysis of Fourier-transform infrared spectroscopy (FTIR) on Bioplastic

FTIR analysis revealed distinct functional groups in bioplastics from banana peels and those with chitosan. The banana peel bioplastic shows peaks for cellulose, hemicellulose, and lignin, while the composite bioplastic with chitosan features additional peaks for amine groups and amide bands, indicating chitosan's presence. These findings align with a previous research on bioplastics FTIR spectra, showing characteristic peaks for hydroxyl, carboxylic, and amine groups (Agusman et al., 2022).

Table 3. Functional Group in Bioplastics

Bioplastics from banana peels		Bioplastics from banana peels and chitosan	
Functional Group	**Peaks**	**Functional Group**	**Peaks**
C-H	2900-3000 cm^{-1}	N-H	3300 cm^{-1}
O-H	3300 cm^{-1}	amide I	1650 cm^{-1}
C=O	1630 cm^{-1}	amide II	1550 cm^{-1}
C-O	1450 cm^{-1}	C=O	1720 cm^{-1}
H-C-H	1450 cm^{-1}	C-O-C	1150 cm^{-1}

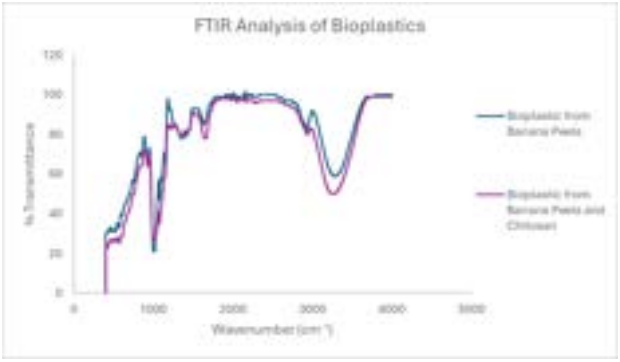

Figure 5. FTIR Spectra for Bioplastics

Test for Biodegradation of Synthesised Bioplastics

The biodegradability test buried in soil for both bioplastics from banana peels and those added with chitosan provides insights into the environmental fate of these materials. The test, conducted over 21 days, revealed that bioplastics from banana peels with chitosan (58.91%) exhibited a higher degree of biodegradation compared to those made solely from banana peels (45.92%), as shown in Table 4. The addition of chitosan significantly enhanced biodegradability ($P<0.05$), potentially by promoting microbial activity or altering the degradation rate due to chitosan's properties (Erna et al., 2023). Moreover, chitosan may modify the chemical structure of the bioplastic, increasing its susceptibility to microbial attack and enzymatic degradation (Marta et al., 2023).

Table 4. Percentage of biodegradability for bioplastics (mean ± standard deviation)

Bioplastics from banana peels	Bioplastics from banana peels and chitosan
(45.92 ± 0.72) %	(58.91 ± 0.16) %

CONCLUSION

This study demonstrated the potential of bioplastics made from banana peels and chitosan as sustainable alternatives to conventional plastics. The addition of chitosan significantly enhanced the bioplastics' properties, as evidenced by FESEM analysis showing strong fiber-chitosan cohesion, and mechanical tests indicating improved resilience and flexibility. Significant differences ($P<0.05$) in biodegradability, water activity, surface topography, and FTIR spectra were observed between bioplastics with and without chitosan. FTIR analysis confirmed effective bonding of the components, and biodegradability tests showed that chitosan-enhanced bioplastics decompose more efficiently. Future research should focus on optimizing formulations, conducting long-term environmental impact assessments, and exploring cost-effective production methods to support the broader adoption of these sustainable materials.

REFERENCES

Agusman, D Fransiska, Murdinah, T Wahyuni, H E Irianto, P Priambudi, Fateha, A H D Abdullah, R D Nissa, B Firdiana and Nurhayati. Physical properties of bioplastic agar/chitosanblend. Retrieved from https://www.researchgate.net/publication/358745002_Physical_properties_of_bioplastic_agarchitosan_blend

Aranaz, I., Alcántara, A. R., Civera, M. C., Arias, C., Elorza, B., Heras Caballero, A., & Acosta, N. (2021). Chitosan: An overview of its properties and applications. Polymers, 13(19), 3256. Retrieved fromhttps://doi.org/10.3390/polym13193256

Erna Rusliana, Muhamad Saleh and Sri Utami (2022). Characteristics of biodegradable plastic from Mulu Bebe banana peel starch with the addition of chitosan and glycerol plasticizer. IOP Conference Series: Earth and Environmental Science, 1177(1), 012047. https://doi.org/10.1088/1755-1315/1177/1/012047

Kevin, Narancic, T., Cerrone, F., Beagan, N., & O'Connor. (2020). Recent advances in Bioplastics: Application and biodegradation. Polymers, 12(4), 920. Retrieved from https://doi.org/10.3390/polym12040920

Kevin, Narancic, T., Cerrone, F., Beagan, N., & O'Connor. (2020). Recent advances in Bioplastics: Application and biodegradation. Polymers, 12(4), 920. Retrieved from https://doi.org/10.3390/polym12040920

Marta, M & Natalia. W. (2023) Biodegradable Chitosan-Based Films as an Alternative to Plastic Packaging. Retrieved from https://www.mdpi.com/2304-8158/12/18/3519

Maura, L, Katiuska, L. (2022) Development of a Bioplastic from Banana Peel. Retrieved from https://dialnet.unirioja.es/descarga/articulo/8613002.pdf

Misran, A Amirul & S Z Othman (2020). Mechanical and Morphology Studies of Bioplastic-Based Banana Peels. Retrieved from https://iopscience.iop.org/article/10.1088/1742-6596/1529/3/032091/pdf

Ponmozhi M (2022). Synthesis and characterization of banana peel starch-based bioplastic for intravenous tubes preparation. *Materials Today Communications*, *33*, 104464. Retrieved from https://doi.org/10.1016/j.mtcomm.2022.104464

Pradeepa Duraisamy, Aswani Ram Vinod, Keerthika S, Dhana Rangesh Kumar V (2022) Extraction, Characterization, Antimicrobial Activity of Chitosan Extracted From Crab Shell And Preparation Of Chitosan-Based Bioplastic Film For Food Packaging. Retrieved from http://sciensage.info/index.php/JASR/article/view/797/455

Ribadiya, Upadhayay,D, Marchawala F , Bhattacharya I, and Andhare P. (2021) Bioplastic: Production of bioplastic from Banana Peels.International Journal of Biology, Pharmacy and Allied Sciences, 10(4). Retrieved from https://doi.org/10.31032/ijbpas/2021/10.4.1015

Sofiah, Yuniar, Aznury, M., & Melianti. (2019). Mechanical properties of bioplastics product from Musa paradisica formatypica concentrate with plasticizer variables. Journal of Physics: Conference Series, 1167, 012048. Retrieved from https://doi.org/10.1088/1742-6596/1167/1/012048

CORRELATES OF DEPRESSIVE AND ANXIETY SYMPTOMS AMONG PRIVATE AND PUBLIC UNIVERSITY STUDENTS IN THE KLANG VALLEY, MALAYSIA

Ching Sin Siau [1], Lei Hum Wee [2*], Norhayati Ibrahim [3], Caryn Mei Hsien Chan[1], Meng Chuan Ho[4], Muhamad Nur Fariduddin[5]

[1] *Centre for Community Health Studies, Faculty of Health Sciences, Universiti Kebangsaan Malaysia 50300 Kuala Lumpur, MALAYSIA*

chingsin.siau@ukm.edu.my

caryn@ukm.edu.my

[2] *School of Medicine,Faculty of Medicine and Health Sciences,Taylor's University, 47500 Selangor, MALAYSIA*

LeiHum.Wee@taylors.edu.my

[3] *Centre for Healthy Ageing and Wellness,Faculty of Health Sciences, Universiti Kebangsaan Malaysia 50300 Kuala Lumpur, MALAYSIA*

yatieibra@ukm.edu.my

[4] *UCSI University, Taman Connaught, 56000 Kuala Lumpur, MALAYSIA*

homc@ucsiuniversity.edu.my

[5] *Faculty of Education, Universiti Teknologi MARA, 40450 Shah Alam, Selangor, MALAYSIA*

fariduddin@uitm.edu.my

ABSTRACT

There has been a lack of studies investigating depressive and anxiety symptoms in university students after the COVID-19 pandemic. This study aimed to examine factors associated with depressive symptoms among public and private university students in the Klang Valley, Malaysia. Participants filled out questionnaires containing a demographic sheet and scales measuring depression, anxiety, psychological strains, purpose in life and religious commitment. A total of 603 participants were recruited (Mean age = 21.13, SD = 2.08; Female = 66%), of which 54.6% and 66.5% screened positive for depression and anxiety symptoms respectively. Private university students had higher scores in depressive and anxiety symptoms. Depressive symptoms were significantly associated with psychological strain ($\beta = 0.519$, $p < 0.001$), purpose in life ($\beta = -0.290$, $p < 0.001$) and religious commitment ($\beta = 0.082$, $p = 0.008$), whilst anxiety was significantly associated with psychological strain ($\beta = 0.540$, $p < 0.001$), purpose in life ($\beta = -0.198$, $p < 0.001$). There is a need to address depression and anxiety among university students, especially in private universities in the Klang Valley post-COVID-19.

Keywords: Depression, Anxiety, University Students, Klang Valley

INTRODUCTION

After the COVID-19 pandemic becomes endemic, universities reopen and university students readjust to a post-pandemic life. This readjustment is stressful for many and about one-fifths of individuals who were asymptomatic during the pandemic developed psychological distress symptoms post-pandemic (Lin et al., 2022). Some educators who returned to work in face-to-face classes suffered from higher burnout and psychological distress (Estrada-Araoz et al., 2023).Other studies, however, found an overall increase in mental health after the pandemic (Reutter et al., 2024). In Malaysia, the mental health of university students remains largely unknown.

LITERATURE REVIEW

Past studies have shown that depressive and anxiety symptoms among university students is high. A meta-analysis of university students in Lower- and Middle-Income Countries found that an estimated 24.4% of university students had depressive symptoms (Akhtar et al., 2020). Another meta-analysis found that the pooled depression prevalence of China university students was 28.4% (Gao et al., 2020). In Malaysia, during the COVID-19 pandemic, a study found that the prevalence of depression was 53.9% (Wong et al., 2023). On the other hand,

the same study found that anxiety was detected in 66.2% of the participants (Wong et al., 2023). Globally, however, a meta-analysis found that anxiety was present in 39.0% of the university students surveyed (Li et al., 2022).

A number of factors have been associated with depressive and anxiety symptoms among university students. Factors predicting depressive symptoms were various, among which is psychological strains (Zhang & Lv, 2014). Psychological strains may cause an individual to be pulled apart by two conflicting stressors (Zhang & Lv, 2014). Among university students, higher strains have been a significant predictor for depression and anxiety (Sun et al., 2020). On the other hand, purpose in life has been identified as a protective factor against depression among adolescents (Barcaccia et al., 2023). Finally, religious commitment has been negatively associated with depression and anxiety (Koenig et al., 2012). This may be due to religiosity providing a sense of meaning in life for university students. However, another study has found that religiosity may work against mental wellbeing if the individual perceived the religion as a threat rather than as a source of comfort (Malinakova et al., 2020).

METHODOLOGY

Study Design: This is a quantitative study involving undergraduate students in public and private universities. Also, this study will be utilising cross-sectional survey for data collection among participants.

Study Location: Three universities in Malaysia; Taylor's University, UCSI University, National University of Malaysia (UKM) were selected.

Measures: The following questionnaires will be self-administered to undergraduate students:

1. Demographic information

   Demographics to be collected include gender, ethnicity, date of birth, sexual orientation, perceived academic achievement, parents' marital harmony, belief in God's existence, believe in karma, life after death, and attendance at religious services.

2. Psychological strain.

   Psychological Strain Scale (PSS) is a 40-item self-reporting scale developed by Zhang et al (2012) to measure psychological strain in four dimensions: value strain, aspiration strain, deprivation strain, and coping strain. Participants answered on a five-point Likert scale ranging from 1="Never" to 5="Always". A total higher score indicates higher levels of strain in the individual. This instrument yielded high reliability with Cronbach's alpha value of .96 among large sample of university students in China (Zhang et al., 2020). However, the scale needs to be validated in Malaysia. As this is a new scale in Malaysia, its psychometric properties will be further explored.

3. Perceived meaning and life purpose.

   Purpose in life test-short form (PIL-SF) is a 4-item instrument developed by Schulenberg, Schnetzer, and Buchanan (2011), designed to assess an individual's meaning and life purpose. Participants answer on a 7-point Likert scale to indicate various degrees of feelings about life purpose, from the lowest (1="no plan", "empty and meaningless", "no progress", and "meaningless goal") to the greatest (7="very clear goals", "meaningful and objective", "fully completed my life goals", "satusfying goal"). The scale shown excellent psychometric properties, with Cronbach's alpha coefficients of .92 among university students in China (Lew et al., 2020). However, the scale needs to be validated in Malaysia. As this is a new scale in Malaysia, its psychometric properties will be further explored.

4. Religious commitment.

   Religiosity will be measured using the Centrality of Religiosity Scale Interreligious-7 (CRSi-7). The questionnaire has 7 questions in which the participants respond to a 5-point Likert scale ranging from 1=Never/Not at all to 5=Very often/Very much so. In the calculation of the CRS score, the item sum score is divided through the number of scored scale items. This allows for a range of the CRS score between 1.0 and 5.0. For the categorization of the groups of the "highly religious", "religious", and "non-religious" we propose the following thresholds: 1.0 to 2.0: not-religious, 2.1 to 3.9: religious, 4.0 to 5.0: highly-religious (Huber & Huber, 2012). This questionnaire will be validated separately in the Malay language in another project.

5. Depression and anxiety.

Automated Readability Index (ARI)

The Automated Readability Index test is another readability test that was used in the research. The ARI, a formidable tool in readability assessment, scrutinizes word and sentence complexity [6]. It translates these complexities into an age-based estimate of text comprehension. A lower ARI score underscores enhanced accessibility, while a higher score suggests elevated complexity. The factor relating to sentence structure (average number of words per sentence) is identical to that found in most currently used indices, such as the Coleman-Liau Index, so no verification was required.

The formula for the Automated Readability Index is [7]: *4.71 / (Character / word) + 0.5 (words / sentence) – 21.43*

Table 2. Automated Readability Index grade level and age range

Score School Level	Age range (years old)
Kindergarten	5-6
1st & 2nd Grade	6-7
3rd Grade	7-9
4th Grade	9-10
5th Grade	10-11
6th Grade	11-12
7th Grade	12-13
8th Grade	13-14
9th Grade	14-15
10th Grade	15-16
11th Grade	16-17
12th Grade	17-18
College student	18-24
Professor	24+

The ARI outputs a number that approximates the age needed to understand the text. As a rough guide, US grade level 1 corresponds to ages 6 to 8. Reading level grade 8 corresponds to the typical reading level of a 14-year-old US child. Grade 12, the highest US secondary school grade before college, corresponds to the reading level of a 17-year-old.

The Gunning Fox Index

The Gunning Fog Index measures readability based on word and sentence characteristics [8]. It aims to simplify text for better comprehension. We aim for a FOG index between 7 and 8, indicating moderate readability.

The index's purpose is to simplify text for seamless comprehension. In our endeavor, we target a FOG index score that positions the RAIQ between moderate and highly readable, ensuring that it resonates with IOs.

The formula for the FOG index is given by [9]:

Gunning Fox Index = 0.4 [amount of words / number of sentences) + Percentage of Hard Words]

Words having three or more syllables, such as comparable, fortunate, and necessary, are considered hard words. The FOG index should typically measure tool readability between 7 and 8. The FOG index is considered challenging if it is greater than 12. The FOG index provides ways to make written material simpler for better comprehension. However, the FOG index also promotes poor writing habits, which could unintentionally lead to the creation of dry and uninspiring material.

Cronbach Alpha reliability test

Cronbach's alpha test is an important and more useful test for internal reliability of questionnaire [10]. The researcher decided that Cronbach's alpha would be used as an indicator of internal consistency and would serve as the dependent variable in this research work. Cronbach's alpha test is an important and more useful test for internal reliability of a questionnaire. Normally the researcher uses Cronbach's alpha when designing and testing a new survey or assessment instrument. This statistic helps them evaluate the quality of the tool during the design phase before deploying it fully [11]. It is a measure of reliability. The mathematical formulae to calculate Cronbach Alpha as follows: - [12]:

RESULTS

Readability test

Using various readability test methodologies, we designed the questionnaire and analyzed the test findings. The questionnaire consists of 20 questions, totaling 754 words and 4993 characters. It includes 57 sentences with an average of 6.6 characters per word and an average of 13.2 words per sentence. We received responses from 25 Investigation Officers (IOs) who participated in the study, with 16 of them being men and the remaining 14 women, with an average age of 34.6. The overall response rate was an impressive 89.7%.

Table 4 provides an overview of readability tests. The New Dale Chall Readability Test, assessing the reading grade level for this questionnaire, yielded a score of 8.6, equivalent to an 11th and 12th-grade reading level. This suggests that individuals around 17 or 18 years old should comfortably comprehend the questionnaire. The Automated Readability Index (ARI) scored the questionnaire at 17.2, corresponding to a standard 12th-grade reading level and indicating individuals above 19 should easily understand it. The higher ARI score suggests a relatively higher level of complexity, better suited for those with advanced education. The Gunning Fog Index, with a score of 11.6, places the questionnaire in the range of moderate readability, making it accessible and understandable to a broad audience, including those without advanced education.

In summary, the results of the readability tests provide a nuanced understanding of the questionnaire's readability. The New Dale Chall score and the Gunning Fog Index suggest that the questionnaire is likely to be comprehensible to individuals with varying education levels. However, the higher ARI score indicates that the questionnaire may be more suitable for individuals above the age of 19 or those with a higher level of education and literacy. These results underscore the questionnaire's versatility in catering to a diverse audience while also indicating its potential suitability for individuals with more advanced educational backgrounds.

Reliability test

There were 25 Investigation Officers from the Criminal Investigation Department that consented to being part of this study, of which 15 of the officers are on probation while the rest have more than 3 years of working experience. The reliability of the questionnaire was calculated through Cronbach's alpha which generated an alpha level of 0.96 ($\alpha = .96$). When the score is more than 0.7, it means it has high internal reliability, hence rendering the findings consistent.

In summary, the results of the readability tests indicate that the questionnaire is highly readable and comprehensible for the target sample of IOs. Additionally, the Cronbach's alpha reliability test shows that the questionnaire has a high level of internal reliability, making it a dependable tool for assessing crime risk perceptions among Investigation Officers in the Royal Malaysian Police. These findings validate the efforts made to enhance the validity, reliability, and user-friendliness of the Risk Appetite Index Questionnaire (RAIQ) and confirm its suitability as a robust and accessible tool for gathering actionable insights.

DISCUSSION

In this research, the authors have undertaken a comprehensive analysis of the Risk Appetite Index Questionnaire (RAIQ) designed for Investigation Officers (IOs) in the Royal Malaysian Police (RMP). The study aimed to enhance the questionnaire's usability and effectiveness, addressing two critical dimensions: readability and reliability. Their approach involved a series of readability tests to evaluate how well the RAIQ could be understood by the target audience. The New Dale Chall Score, Automated Readability Index (ARI), and Gunning Fog Index collectively provide valuable insights into the questionnaire's accessibility. While these tests suggested

varying degrees of readability, they collectively positioned the RAIQ as an instrument that could cater to a broad range of educational backgrounds while potentially requiring a higher level of education for comprehensive understanding, as indicated by the ARI.

Furthermore, the assessment of reliability through Cronbach's alpha yielded a substantial result of 0.96, indicating a high level of internal consistency in the responses generated by the questionnaire. This strong reliability underscores the questionnaire's dependability, making it a trustworthy tool for assessing crime risk perceptions among IOs in the RMP. This validation is particularly crucial in the context of law enforcement, where the accuracy and consistency of data are paramount for decision-making and policy formulation.

Additionally, it is important to acknowledge certain limitations of this study, notably the relatively small sample size of 25 IOs. Future research endeavors could consider expanding the sample size to enhance the generalizability of the findings. Moreover, the study primarily focused on the questionnaire's readability and reliability in a controlled research setting. To further establish its practical utility, future investigations could explore how the RAIQ performs in real law enforcement scenarios. By doing so, it would be possible to ascertain whether the questionnaire effectively translates into actionable insights and contributes to more informed decision-making within the dynamic and challenging realm of crime risk management. In conclusion, this research makes a valuable contribution by emphasizing the significance of both readability and reliability in questionnaire development and validation, offering a robust approach to strengthening the RAIQ as a powerful tool for IOs in the RMP.

CONCLUSION

The research work is to identify the knowledge of crime risk management towards the Investigation Officer in Royal Malaysian Police. In order to measure it, the questionnaire was developed. In this work, various aspects of tool development have been thoroughly explored. There have been significant attempts made to gather all the data. The research instrument has demonstrated its reliability through validity, reliability, and readability test. Additionally, the research tool has proved its credibility. Thus, Cronbach's alpha shows that an alpha score of 0.9 indicates that the questionnaire set has a good level of internal reliability and provides consistent results (refer table 3). Since the investigation officers had at least a diploma and all of the questions can be answered by a student who is 19 years old (refer Table 4), it has been proven that they were able to complete the questionnaires.

This paper also demonstrates the importance of developing questionnaires that are both reliable and readable to gather accurate and valuable data for informed decision-making in law enforcement and organizational research. The authors have used a combination of readability tests and reliability measures to ensure the effectiveness of their questionnaire.

ACKNOWLEDGEMENT

This study is supported partially by university Sains Malaysia grant (304/PPSK/6315498).

REFERENCES

[40] Pfeffer, J., & Salancik, G. R. (2003). The external control of organizations: A resource dependence perspective. Stanford University Press.

[41] Kojaie-Bidgoli, A., Fadayevatan, R., Sharifi, F., Alizadeh-Khoei, M., Vahabi, Z., & Aminalroaya, R. (2022). Applicability of SPMSQ in illiterate outpatients in clinics: The validity and reliability of the Short Portable Mental Status Questionnaire. Applied Neuropsychology: Adult, 29(4), 591-597.

[42] Tahir, M., Usman, M., Muhammad, F., Rehman, S. U., Khan, I., Idrees, M., ... & Glowacz, A. (2020). Evaluation of quality and readability of online health information on high blood pressure using DISCERN and Flesch-Kincaid tools. Applied Sciences, 10(9), 3214.

[43] Zhou, S., Jeong, H., & Green, P. A. (2017). How consistent are the best-known readability equations in estimating the readability of design standards. IEEE Transactions on Professional Communication, 60(1), 97-111.

[44] Singh, A., Kachway, D. S., Kuschi, V. S., Vikas, G., Kaushal, N., & Sigh, A. (2017). Edible oil coatings prolong shelf life and improve quality of guava (Psidium guajava L.). International Journal of Pure & Applied Bioscience, 5(3), 837- 843.

[45] Bailin, A., & Grafstein, A. (2016). Readability: Text and context. Springer.

[46] De Franco, G., Hope, O. K., Vyas, D., & Zhou, Y. (2015). Analyst report readability. Contemporary Accounting Research, 32(1), 76-104.
[47] Balz, T. (2022). Scientometric Full-Text Analysis of Papers Published in Remote Sensing between 2009 and 2021. Remote Sensing, 14(17), 4285.
[48] Gabitov, A. I., Solnyshkina, M. I., Shayakhmetova, L. K., Ilyasova, L. G., & Adobarova, S. (2017). Text complexity in Russian textbooks on social studies. Revista Publicando, 4(13), 2.
[49] Zhou, S., Jeong, H., & Green, P. A. (2017). How consistent are the best-known readability equations in estimating the readability of design standards. IEEE Transactions on Professional Communication, 60(1), 97-111.
[50] Brigo, F., Otte, W. M., Igwe, S. C., Tezzon, F., & Nardone, R. (2015). Clearly written, easily comprehended? The readability of websites providing information on epilepsy. Epilepsy & Behavior, 44, 35-39.
[51] Plotnikov, A. V. (2020, August). Gunning fog-index measurement of customer reviews of the Russian Agricultural Bank. In IOP Conference Series: Earth and Environmental Science (Vol. 548, No. 2, p. 022046). IOP Publishing.
[52] Mohamad Fahmi Hussin, Bin Wang, Ramani Hipnie, The reliability and validity of Basic Offshore Safety and Emergency Training knowledge test, Journal of King Saud University - Engineering Sciences, Volume 24, Issue 2, 2012, Pages 95-105
[53] Bujang, M. A., Omar, E. D., & Baharum, N. A. (2018). A review on sample size determination for Cronbach's alpha test: a simple guide for researchers. The Malaysian journal of medical sciences: MJMS, 25(6), 85.
[54] Vaske, J. J., Beaman, J., & Sponarski, C. C. (2017). Rethinking internal consistency in Cronbach's alpha. Leisure sciences, 39(2), 163-173.
[55] Heo, M., Kim, N., & Faith, M. S. (2015). Statistical power as a function of Cronbach alpha of instrument questionnaire items. BMC medical research methodology, 15(1), 1-9.

CHARACTERIZATION OF *MUSA PARADISIACA* PEEL AND IT'S DERIVED PAPER

Ibtisam Abu Bakar[1], Wahida Abdul Rahman[2*]and Nur Hanim Aqilla Suhaimi[3]

[1,2*]*Faculty of Applied Sciences, Universiti Teknologi MARA Perlis Branch, Arau Campus, 02600 Arau, Perlis*

[2*]*wahida811@uitm.edu.my*

ABSTRACT

Musa Paradisiaca is a variety of bananas used mainly for cooking instead of being consumed fresh. The skin, frequently seen as a by-product, holds valuable nutritional and industrial potential. This research aimed to determine the nutritional content of the banana peel of *Musa Paradisiaca* and produce paper from it. The banana peel was analyzed for its nutritional content across different ripening stages. The results showed that the nutritional content in the banana peel varies depending on the maturity stages with unripe peels having the highest dry matter and fat content, ripe peels having the highest moisture, crude fiber, and protein content, and overripe peels having the highest ash content. Moreover, the total phenolic content of the ripe peel is at 7.93 mg GAE/g, indicating strong antioxidant properties in the peel. Ripe banana peels were identified as the best for paper production due to their higher moisture content, which is essential for the pulping process, and their abundant fiber content that provides structural integrity for paper formation. The paper made from the peel is pale yellow with a rough texture and moderate flexibility compared to regular paper. Furthermore, the Attenuated Total Reflectance-Fourier Transform Infrared Spectroscopy (ATR-FTIR) analysis of the paper indicates that the presence of functional groups contributes to the paper's structural integrity. Additionally, the paper exhibited moderate tensile strength and rigidity, and a soil burial experiment showed a 36.43% decrease in weight over 10 days, indicating rapid biodegradation.

***Keywords*:** Musa Paradisiaca; phenolic content; ripening stages; Gallic Acid

INTRODUCTION

Banana is a tropical fruit crop that is widely farmed and consumed. The average consumption of bananas per person is 12 kg, thus making it the world's fourth most important food crop after rice, wheat, and maize. Over the past 20 years, the production of bananas has continuously grown. In 2019, the production of bananas was about 117 million tonnes, a 50% increase compared to 1999 which was only 70 million tonnes. Recently, in 2021, almost 125 million tons of the bananas produced globally (Zaini et al., 2022). The banana fruit's flesh is the part that is used the most while the outer skin or peels is solely used as organic fertilizer and animal feed. It shows that the banana peel waste is still not fully optimized (Agustina & Susanti, 2018a). *Musa paradisiaca* is one of the species of banana that is hybrid from *Musa acuminata* and *Musa balbisiana*. It is an edible banana and tasty yellow banana with ripe fruit that is sweet, juicy, and full of seeds (Issara et al., 2024). The banana peel makes up about a third of the weight of a banana. The chemical compounds in banana peel are rich with antioxidant and antimicrobial activities such as phenolic compounds, alkaloids, flavonoids, tannins, saponins, glycosides, and carotenoids (Hikal et al., 2022). Banana peel waste includes more fine fibers compared to wood. It contains with high cellulose content (60-65%), hemicellulose (6-8%), and lignin (5-10%). Currently, paper is typically made from softwood, which comprises just cellulose (41%), hemicellulose (24%), and lignin (27.8%). The cellulose content in banana peel is significantly higher than in softwood. Banana peel contains just 5-10% lignin, making cellulose separation easier. Banana peels can be used to make paper, reducing the need for wood (decreased deforestation) as a raw material for packaging application such as wrapping paper (Agustina & Susanti, 2018b). This research aims to analyze the proximate composition and its nutritional value (total fat content, protein content, moisture content, ash content, crude fiber content, cellulose content, dry matter, total sugar analysis, color analysis) and total phenolic compound such as Gallic Acid that acts as important role in ripening stages for banana peel waste of *Musa paradisiaca*. Besides, papers derived from ripe banana peel of *Musa paradisiaca* have been fabricated. Finally, physical and mechanical properties of the derived papers have been analyzed using FTIR analysis, sensory evaluation test, biodegradability test, pH test and tensile test.

MATERIALS AND METHODS

Unripe, ripe, and overripe banana peels of *Musa paradisiaca* were collected from local vendor in Arau, Perlis. Determination of nutritional content (total fat content, protein content, moisture content, ash content, crude fiber content, cellulose content, dry matter, total sugar analysis, color analysis) have been analyzed using various method with slight modification (Agustina & Susanti, 2018b; Arul Marcel Moshi et al., 2019; Ruwali et al., 2022; Sojinu et al., 2021a; Turker et al., 2022). The total phenolic content was determined based on the Folin-Ciocalteu method. The amount of total phenolic content (TPC) (mg GAE/g DM) was calculated based on the Gallic acid (0–200 μM) calibration curve (R2 = 0.9976) (Islam et al., 2023). Paper from ripe banana peel of *Musa paradisiaca* has been fabricated based on method by Alasalvar et al., 2023 with few modifications. Finally, the derived paper was then characterized via FTIR and tensile instruments in order to determine the functional groups existed and the mechanical properties including Young's Modulus, tensile strength and elongation at break (Alasalvar et al., 2023; Chandrasekar et al., 2023). The physical properties such as pH and biodegradability of the derived papers have been analyzed via other few analysis and tests (Sojinu et al., 2021b; Verma et al., 2024).

RESULTS AND DISCUSSION

The proximate compositions and nutritional content of the banana peel of *Musa paradisiaca* across different ripening stages are presented in Table 1. From the table, the dry matter of the ripe peel is 13.64 % which is less compared to the unripe and overripe peel with 26.48 % and 23.45 % respectively. The ripe peel has 89.19 % moisture content compared to unripe and overripe peel with 89.41 % and 85.1 %, respectively. The ash content in banana peel for unripe, ripe and overripe are 4.37 %, 2.16 % and 5.22 %. Ripe peel has the least ash content as the moisture in the peel has been converted into sugar (Koni et al., 2023). The ripe peel has the highest crude fiber content, 24.57 % compared to unripe and overripe peel with 20.37 % and 22.13 %, respectively. The cellulose content in the ripe peel (1.07 %) was lower than the unripe peel (1.75 %) and slightly higher than the overripe peel (1.06 %). The fat content in the peel was found to be higher for unripe peel (7.55 %) compared to the ripe (4.79 %) and overripe peel (4.88 %). The ripe peel has the highest protein content which is 4.07 % while the overripe peel has the lowest, 0.82 % and the unripe peel is 1.74 %.

Table 1. Proximate composition of banana peel of *Musa paradisiaca* at different ripening stages

Ripening Stage	Dry matter (%)	Moisture Content (%)	Ash Content (%)	Crude fiber Content (%)	Cellulose Content (%)	Fat Content (%)	Protein Content (%)
Unripe	26.48	89.19	4.37	20.37	1.75	7.55	1.74
Ripe	13.64	89.41	2.16	24.57	1.07	4.79	4.07
Overripe	23.45	85.1	5.22	22.13	1.06	4.88	0.82

Table 2 below illustrates the results of the banana peel of *Musa paradisiaca* color test, showcasing the changes in day, color, and physical characteristics at each ripening stage. The color of banana peel is significantly related to banana maturity. The results show that the color change of banana peel from green to brown speckles as the banana matured.

Table 2. Color analysis of banana peel of *Musa paradisiaca*

	Duration of Ripening Stages (Day)			
	1 (Unripe)	**3 (Unripe)**	**7 (Ripe)**	**10 (Overripe)**
Physical Appearance of raw *Musa paradisiaca* peel (based on different ripening stages)	 Hard green	 More green than yellow	 Fully yellow	 Fully yellow with brown speckles
Color Index	1	3	6	7

The total phenolic content compound was determined in the banana peel of *Musa paradisiaca* by the Folin-Ciocalteu method. Based on the linear equation obtained i.e. y = 0.0051x + 0.0018, R^2= 0.9993 approaching linearity where R2= 1 as shown in Figure 1. The total phenol of the peel can be calculated with the resulting sample absorbance value of 0.305. This indicates that the banana peel of *Musa paradisiaca* contains a total phenol content of 7.93 mg GAE/g of powder. According to Vu et al., 2018,the total phenolic content in banana peel ranges from 4.95 to 47 mg gallic acid equivalent/g dry matter (mg GAE/g DM). Thus, the banana peel of *Musa paradisiaca* is rich in dietary fiber and phenolic compounds with high antioxidant and antimicrobial activities. Figure 2 shows the FTIR results for both raw ripe *Musa paradisiaca* peel and its derived paper. The FTIR spectra of paper derived from banana peel and raw banana peel overlap significantly, demonstrating that essential functional groups are retained during the papermaking process.

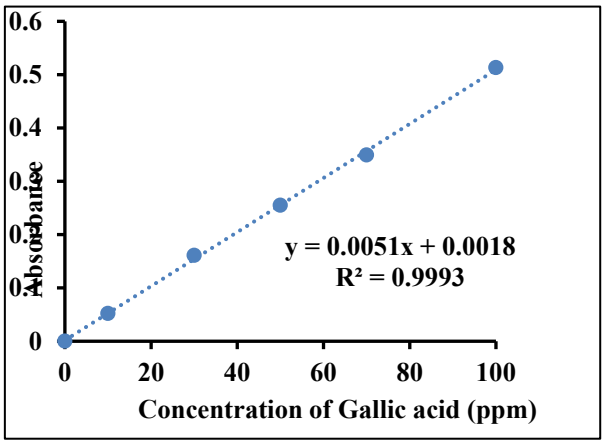

Figure 1. Calibration Curve of Gallic Acid Standard

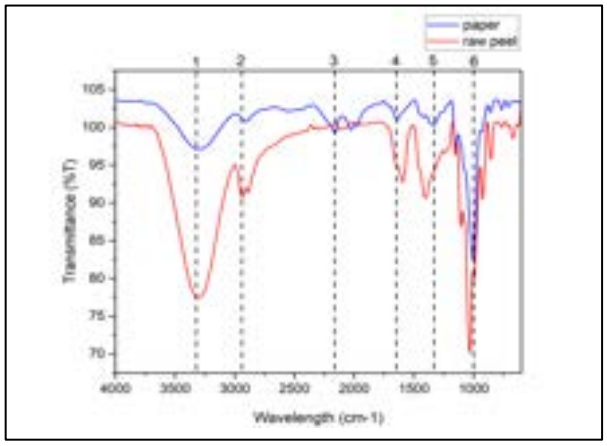

Figure 2. FTIR spectra comparison between the derived paper from the banana peel and the raw peel

Table 3. Sensory evaluation characteristics and observation, FTIR analysis of several functional groups and mechanical properties of paper made from the ripe peel of *Musa paradisiaca*

Characteristics & Observation	Tensile Test
 Exhibits pale yellow color with slightly flexible paper strength, has neutral smell and a slightly rough surface texture. pH of the paper is 7.08.	• Tensile stress at Maximum Load (0.33MPa) • Elongation at break (1.03 %) • Young's Modulus (41.68 MPa) • Maximum Load (4.05 MPa)

Table 3 shows the result of the paper made from the banana peel of *Musa paradisiaca*. From the figure in Table 3, it can be seen that the color of derived paper is in pale yellow. The colors indicates that the banana peel's natural pigmentation has been retained to some extent during the papermaking process. Besides that, the paper shows flexibility and can be torn off. The smell of the paper is neutral, not have a strong odor or scent. The neutral smell of the paper is a favorable characteristic, indicating that there are no strong or unpleasant odors associated with the banana peel fibers. Due to its odorless nature, the paper can be used in a greater variety of applications, including those where smell sensitivity might be a concern, such as food packaging or stationary goods. Thus, it shows that banana peel has potential industrial applications in sanitary pads, textiles, pulp and paper, food, and reinforced composite materials. Lastly, the texture of the paper is a little bit rough compared to regular paper. The rough texture of the paper suggests that the fibers from banana peels are rougher than those found in regular paper. This roughness is due to the natural structure of banana peel fibers and the processing method used (Balda et al., 2021). The pH of the paper obtained is 7.08, which is close to neutral. This neutral pH indicates that the paper is either too acidic nor too alkaline, making it suitable for a variety of uses without the risk of damaging sensitive materials or reacting with other substances. The tensile stress at the maximum load of the paper was found to be at 0.33018 MPa. It shows that the paper able to bear moderate stress at maximum load before failure. Additionally, the paper has an average elongation at break which is 1.03007 %, with the Young's Modulus of the paper is 41.67678 MPa. This indicates that the paper shows moderate stiffness. Meanwhile, biodegradability test results revealed that the average weight loss of the derived paper after 10 days is 36.43 %. This results highlights its ability to degrade into organic matter in a short period of time, which indicates well for long-term waste management strategies.

CONCLUSION

The study aimed to analyze the nutritional content and composition of banana peels at different ripeness stages. The paper derived from ripe banana peels showed potential for biodegradability and strength. Ripe peels were chosen for paper production due to their high moisture, crude fiber, and protein content. The paper exhibited moderate tensile strength and rapid biodegradation. The findings suggest that banana peels, especially at different ripeness stages, have potential for various applications, including dietary uses and eco-friendly packaging materials. To enhance the research, it is suggested to increase the sample size, explore different banana types, refine fiber extraction methods, and evaluate the environmental impact of using banana peels for various applications.

REFERENCES

Agustina, E. S. W., & Susanti, V. H. E. (2018a). Natural wrapping paper from banana (Musa paradisiaca Linn) peel waste with additive essential oils. *Journal of Physics: Conference Series*, *1022*(1), 012032.

Ahsan, M., Ashraf, H., Liaquat, A., Nayik, G. A., Ramniwas, S., Alfarraj, S., Ansari, M. J., & Gere, A. (2024). Exploring pectin from ripe and unripe Banana Peel: A novel functional fat replacers in muffins. *Food Chemistry: X*, 101539.

Alasalvar, H., Yildirim, Z., & Yildirim, M. (2023). Development and characterization of sustainable active pectin films: The role of choline chloride/glycerol-based natural deep eutectic solvent and lavender extracts. *Heliyon*, *9*(11).

Anjum, S., & Sundaram, S. (2022). Comparative study on nutrient composition and functional characteristics of tropical fruits with emphasis on banana fruit peel. *Int. J. Pharm. Pharm. Sci*, *14*, 25–35.

Arul Marcel Moshi, A., Ravindran, D., Sundara Bharathi, S. R., Suganthan, V., & Kennady Shaju Singh, G. (2019). Characterization of new natural cellulosic fibers–a comprehensive review. *IOP Conference Series: Materials Science and Engineering*, *574*(1), 012013.

Balda, S., Sharma, A., Capalash, N., & Sharma, P. (2021). Banana fibre: a natural and sustainable bioresource for eco-friendly applications. *Clean Technologies and Environmental Policy*, *23*, 1389–1401.

Chandrasekar, C. M., Krishnamachari, H., Farris, S., & Romano, D. (2023). Development and characterization of starch-based bioactive thermoplastic packaging films derived from banana peels. *Carbohydrate Polymer Technologies and Applications*, *5*, 100328.

Hassan, H. F., Hassan, U. F., Usher, O. A., Ibrahim, A. B., & Tabe, N. N. (2018). Exploring the potentials of banana (musa sapietum) peels in feed formulation. *International Journal of Advanced Research in Chemical Science*, *5*(5), 10–14.

Hikal, W. M., Said-Al Ahl, H. A. H., Bratovcic, A., Tkachenko, K. G., Sharifi-Rad, J., Kačániová, M., Elhourri, M., & Atanassova, M. (2022). Banana peels: A waste treasure for human being. *Evidence-Based Complementary and Alternative Medicine*, *2022*(1), 7616452.

Islam, M. R., Kamal, M. M., Kabir, M. R., Hasan, M. M., Haque, A. R., & Hasan, S. M. K. (2023). Phenolic compounds and antioxidants activity of banana peel extracts: Testing and optimization of enzyme-assisted conditions. *Measurement: Food*, *10*, 100085.

Issara, U., Chotiko, A., Phothisuwan, S., Kraithong, S., & Rungraeng, N. (2024). Banana peels: identification, quantification, and characterization. In *Banana Peels Valorization* (pp. 1–35). Elsevier.

Koni, T. N. I., Marambandima, Y. T., & Foenay, T. A. Y. (2023). Nutrient Content of Banana Peel (Musa paradisiaca) Fermented at Different Levels of Palmyra Sugar Liquid Addition. *3rd International Conference on Environmentally Sustainable Animal Industry 2022 (ICESAI 2022)*, 163–168.

Kumar, P. S., Shuprajhaa, T., Subramaniyan, P., Mohanasundaram, A., Shiva, K. N., Mayilvaganan, M., & Subbaraya, U. (2023). Ripening dependent changes in skin color, physicochemical attributes, in-vitro glycemic response and volatile profiling of banana varieties. *Food Bioscience*, *56*, 103274.

Ma, L., Liang, C., Cui, Y., Du, H., Liu, H., Zhu, L., Yu, Y., Lu, C., Benjakul, S., & Brennan, C. (2022). Prediction of banana maturity based on the sweetness and color values of different segments during ripening. *Current Research in Food Science*, *5*, 1808–1817.

Ruwali, A., Thakuri, M. S., Pandey, S., Mahat, J., & Shrestha, S. (2022). Effect of different ripening agents in storage life of banana (Musa paradisiaca) at Deukhuri, Dang, Nepal. *Journal of Agriculture and Food Research*, *10*, 100416.

Sojinu, O. S., Biliaminu, N. T., Mosaku, A. M., Makinde, K. O., Adeniji, T. H., & Adeboye, B. M. (2021a). The implications of ripening agents on chemical compositions of plantain (Musa paradisiaca). *Heliyon*, *7*(6).

Turker, S., Polat, A. A., & Bindak, R. (2022). Seasonal changes of carbohydrates in fruit peels, leaves and shoots of three pomegranate (Punica granatum L.) cultivars grown in upper Euphrates basin. *Scientia Horticulturae*, *304*, 111315.

Verma, P., Rani, R., Das, D., Rai, K. K., Gogoi, P., & Badwaik, L. S. (2024). Transformation of banana peel into biodegradable film added with starch and carboxymethyl cellulose and its characterization. *Sustainable Chemistry and Pharmacy*, *37*, 101356.

Vu, H. T., Scarlett, C. J., & Vuong, Q. V. (2018). Phenolic compounds within banana peel and their potential uses: A review. *Journal of Functional Foods*, *40*, 238–248.

Zaini, H. M., Roslan, J., Saallah, S., Munsu, E., Sulaiman, N. S., & Pindi, W. (2022). Banana peels as a bioactive ingredient and its potential application in the food industry. *Journal of Functional*

e ISBN 978-629-97630-3-1